Professur für Raumfahrtantriebe
Fakultät für Luftfahrt, Raumfahrt und Geodäsie
Technische Universität München

WALL HEAT TRANSFER MEASUREMENT AND PREDICTION IN METHANE/OXYGEN ROCKET ENGINES

NIKOLAOS PERAKIS

Vollständiger Abdruck der von der Fakultät für Luftfahrt, Raumfahrt und Geodäsie der Technischen Universität München zur Erlangung des akademischen Grades eines

Doktor-Ingenieurs (Dr.-Ing.)

genehmigten Dissertation.

Vorsitzender:
Prof. Dr.-Ing. Florian Holzapfel

Prüfende der Dissertation:
1. Prof. Dr.-Ing. Oskar J. Haidn
2. Prof. Dr.-Ing. Stefan Schlechtriem,
   Universität Stuttgart

Die Dissertation wurde am 15.12.2020 bei der Technischen Universität München eingereicht und durch die Fakultät für Luftfahrt, Raumfahrt und Geodäsie am 28.07.2021 angenommen.

NIKOLAOS PERAKIS

WALL HEAT TRANSFER MEASUREMENT AND PREDICTION IN METHANE/OXYGEN ROCKET ENGINES

Dedicated to my family.

ABSTRACT

In light of the rapid growth of the space launcher market and the increased efforts to privatize spaceflight as a commercial industry, the need for high-performing yet cost-effective rocket engines has emerged. Attempting to fulfill those requirements posed by the "NewSpace" movement, intensive investigations of the propellant combination of methane and oxygen are being carried out by research groups worldwide. The present work contributes to the advancement of experimental and numerical methods for the evaluation and prediction of combustion and heat transfer phenomena in methane/oxygen thrust chambers. Specifically with respect to the experimental task, a computationally-efficient inverse heat transfer method is developed and applied to the evaluation of test data for single-element and multi-element configurations. This leads to qualitative and quantitative insights into the injection, heat release and flame-wall interaction phenomena in the chamber. Parallel to that, the extension and application of a turbulent combustion numerical model is executed to complement the experimental methods. A tabulated-chemistry non-adiabatic flamelet model is adapted to allow for the prediction of exothermic recombination reaction effects close to the cooled chamber walls. The motivation for the inclusion of the recombination effects in chamber flow simulations is derived from three-dimensional reacting boundary layer Direct Numerical Simulations which quantify their influence on the wall heat loads. Finally, the derived model is successfully used for the simulation of sub-scale test cases in RANS and LES leading to good agreement with the experimental results obtained from the inverse method.

ZUSAMMENFASSUNG

Das rasante Wachstum des Trägerraketenmarkts, einhergehend mit der zunehmenden Privatisierung der Raumfahrt, lässt die Nachfrage an kosteneffizienten und leistungsstarken Raketentriebwerken stetig steigen. Eine vielverspechende Treibstoffkombination für die sogenannte NewSpace-Bewegung stellt Methan/Sauerstoff dar. Forschungsgruppen weltweit arbeiten intensiv daran die Eigenschaften dieses Treibstoffes besser zu verstehen. Die vorliegende Arbeit trägt zu der Weiterentwicklung von experimentellen und numerischen Methoden für die Auswertung und Vorhersage von CH_4/O_2 Verbrennungs- und Wärmetransportphänomenen bei. Im Rahmen der experimentellen Untersuchungen wird eine rechnereffiziente inverse Wärmetransportmethode entwickelt, welche anschließend bei der Auswertung von Testdaten in Single-Element und Multi-Element Konfigurationen Anwendung findet. Die Ergebnisse führen zu qualitativen und quantitativen Aussagen über die Einspritzung, Wärmefreisetzung und Flamme-Wandinteraktion in der Kammer. Ergänzend zu den experimentellen Methoden wird die Erweiterung und Anwendung eines numerischen Verbrennungsmodels erarbeitet. Dabei wird ein nicht-adiabates flamelet Model angepasst, um die exothermen Rekombinationsreaktionen in der Nähe der gekühlten Wand aufzulösen. Die Notwendigkeit für die Einbeziehung der Rekombinationseffekte resultiert aus dreidimensionalen Direkten Numerischen Simulationen einer reagierenden Grenzschicht. Aus den Ergebnissen der Grenzschichtsimulationen wird auch der Einfluss

der Rekombinationsreaktionen auf den auftretenden Wärmelasten quantifiziert. Schließlich wird das entwickelte Model für die Simulation von sub-scale Testfällen in RANS und in LES eingesetzt und führt zu einer guten Übereinstimmung mit den experimentellen Ergebnissen der inversen Methode.

I am not young enough to know everything.

— Oscar Wilde

ACKNOWLEDGMENTS

I would like to express the most sincere gratitude to my supervisor Prof. Dr.-Ing. Oskar Haidn for offering me the opportunity to work on this engaging project. Apart from the guidance he provided during the past three and a half years, Prof. Haidn has been a constant source of inspiration with his vast experience in propulsion as well as his ability to quickly identify the strengths and weaknesses of new ideas and assess their feasibility. Thank you for the long hours of insightful talks about the future of the space industry and for engaging in interesting thought experiments revolving around all possible topics with favorites including turbulence and chemical radicals. But most importantly, thank you for teaching me that when working on rockets, we are "in the fun business".

I would like to thank Prof. Dr.-Ing. Florian Holzapfel for chairing the thesis evaluation and Prof. Dr.-Ing. Stefan Schlechtriem for being the second examiner and for his valuable feedback.

My sincere gratefulness goes to Prof. Matthias Ihme for opening up a new chapter in my research path by accepting me as a visiting graduate student at his group. My experience at the Center of Turbulence Research at Stanford University was a very impactful part of my PhD and allowed me to gather invaluable experience in the topic of numerical combustion. Prof. Ihme's attention to detail and work ethic were definitely inspiring and his out-the-box thinking often delivered an extra spark to my creativity.

My appreciation extends to all colleagues from the CTR group but a special "thank you" goes to Dr. Quentin Douasbin and Danyal Mohaddes for the countless hours of thought-provoking discussions. Our talks in Building 500 accompanied by wild white-board brainstorming sessions on topics ranging from C++ debugging to drift terms and from porous burners to the Leidenfrost effect and other "creatures" will always be memorable to me.

Of course this work could also not have been possible without the support of my colleagues at the Chair of Space Propulsion of the TUM. Many thanks to Christof Roth for his help and the interesting conversations during the first stages of my thesis. Also big thanks to my then-supervisors and co-workers Dr.-Ing. Simona Silvestri, Dr.-Ing. Mariella Celano for believing in me during my first steps in the field of propulsion. Moreover, I am thankful to Christoph von Sethe for helping me re-explore my experimentalist-side, which had been well hidden under years of modeling, coding and simulating and to Ilaria De Dominicis and Mattia Straccia for keeping me sane during our lunch breaks. My gratitude extends to all other RFA colleagues: Alexander Fuchs, Andrej Sternin, Christian Bauer, Gregor Schlieben, Yongchuan Yu, Zhendong Yu, Hao Ma, Hongxin Wang, Julian Pauw, Lucrezia Veggi, Hong Ye, Fernanda Winter, Jianing Li.

I would also like to express my appreciation to Dr. Benedicte Cuenot (CERFACS) and Dr. Yu Daimon (JAXA) for some very insightful discussions during the past years.

The PhD project would not have been possible without the financial support of the German Science Foundation (DFG) in the framework of the Collaborative Research Center

TRR40. I am also grateful to the German Academic Exchange Service (DAAD) as well as the TUM Graduate Center for their support during my research and teaching visits at Stanford University and University of Tokyo.

I am lucky to be accompanied in this journey of the past three and a half years by a very loving and patient partner that made the frustrating moments of the PhD (and trust me there were a few) much more bearable. Thank you Jana for always being there and showing me love even on my grumpy days!

Finally, words cannot describe how grateful I am for my family, that has made all of this possible with their unconditional love and support over the last 26 years. Due to the lack of time during the PhD I did not visit home as much I would like to, but it was always motivating to know that I can count on you even when I am far away.

Μαμά, μπαμπά, Ματίνα και Ιάσων σας ευχαριστώ πολύ για όλα!

CONTENTS

LIST OF TABLES

ACRONYMS

ASM	Algebraic Stress Models
CARS	Coherent Anti-Stokes Raman Spectroscopy
CFD	Computational Fluid Dynamics
CFL	Courant–Friedrichs–Lewy
CMC	Conditional Moment Closure
CMR	Carcinogenic, Mutagenic and toxic to Reproduction
CNES	Centre National d'Etudes Spatiales (French Space Agency)
CNG	Compressed Natural Gas
DES	Detached Eddy Simulation
DFG	German Research Foundation (Deutsche Forschungsgemeinschaft)
DLR	Deutsches Zentrum für Luft- und Raumfahrt (German Aerospace Center)
DNS	Direct Numerical Simulation
ECHA	European Chemical Agency
EDC	Eddy Dissipation Concept
ESA	European Space Agency
FDM	Finite Difference Method
FEM	Finite Element Method
FLPP	Future Launcher Preparatory Program
FPL	Full Power Level
FPV	Flamelet Progress Variable
FRC	Finite-Rate Chemistry
FVM	Finite Volume Method
HPC	High Performance Computing
LEO	Low Earth Orbit
LOX	Liquid Oxygen
IG	Ideal Gas

ISP-1 In-Space Proulsion-1
ISRU In-Situ Resource Utilization
JAXA Japan Aerospace Exploration Agency
LES Large Eddy Simulation
LNG Liquified Natural Gas
LREs Liquid Rocket Engines
MMH Monomethylhydrazine
MPL Minimum Power Level
NASA National Aeronautics and Space Administration
NIST National Institute of Standards and Technology
NTO Nitrous Tetroxide
PDF Probability Density Function
PDI Phase-Doppler Interferometry
PLIF Planar Laser Induced Fluorescence
RANS Reynolds Averaged Navier-Stokes
REACH Registration, Evaluation, Authorisation and Restriction of Chemicals
RFA Chair of Space Propulsion (Professur für Raumfahrtantriebe)
RP-1 Rocket Propellant-1
RPL Rated Power Level
RSM Reynolds Stress Models
S-CO_2 Supercritical Carbon Dioxide
SGS subgrid scale
SSME Space Shuttle Main Engine
SST Shear-Stress Transport
SWCR Supercritical Water Cooled Reactors
TBLE Thin Boundary Layer Equations
TLAI Tomographic Laser Absorption Imaging
TUM Technical University of Munich
UDMH Unsymmetrical Dimethylhydrazine
ULA United Launch Alliance
WALE Wall-Adapting Local Eddy-viscosity

SYMBOLS

AR	aspect ratio [-]
C	progress variable [-]
$\mathcal{C}$	molar concentration [mol/m^3]
c^*	characteristic velocity [m/s]
c_e	effective exhaust velocity [m/s]
c_p	specific constant pressure heat capacity [J/(kg·K)]
c_v	specific constant volume heat capacity [J/(kg·K)]
D	diffusivity [m^2/s]
$\mathcal{D}$	Lenard-Jones collision diameter [m]
d	diameter [m]
Da	Damköhler number [-]
E	energy [J/kg]
$\mathcal{F}$	filter [-]
F	thrust [N]
G	Gibbs enthalpy [J/kg]
g_0	gravitational acceleration [m/s^2]
H	specific enthalpy [J/(kg·K)]
$\mathcal{H}$	normalized enthalpy difference [-]
h	heat transfer coefficient [W/(m^2·K)]
I_{sp}	specific impulse [s]
J	objective function [K^2]
j	species diffusive flux [kg/(m^2·s)]
K	equilibrium constant [-]
$\mathcal{K}$	reaction coefficient [kg/(mol·s)]
k_B	Boltzmann constant [m^2·kg/(s^2·K)]
L	length [m]
$\mathcal{M}$	species symbol [-]
M	molar mass [kg/mol]
m	molecular mass [kg]
$\dot{m}$	mass flow rate [kg/s]
Ma	Mach number [-]
Nu	Nusselt number [-]
$\mathbf{n}$	wall-normal vector [m]
O/F	oxidizer-to-fuel ratio [-]
P	probability density function [-]
$\mathbf{P}$	parameter heat flux values [W/m^2]
p	pressure [bar]
P_k	turbulence kinetic energy production [kg/(m·s^3)]
Pr	Prandtl number [-]
$\dot{Q}$	heat rate [W]
$\dot{\mathcal{Q}}$	heat release rate [W/m^3]
$\dot{q}$	heat flux [W/m^2]
R	ideal gas constant [J/(mol·K)]
$\mathcal{R}$	net reaction rate of progress [kg/(m^3·s)]
r	radial distance/radius [m]
Re	Reynolds number [-]
S	deformation tensor [1/s]
$\mathcal{S}$	specific entropy [J/(kg·K)]
$\mathbf{S}$	sensitivity matrix [K·m^2/W]
Sc	Schmidt number [-]
T	temperature [K]
t	time [s]
U	unmixedness [-]
u	velocity [m/s]
V	volume [m^3]
v	molar volume [m^3/mol]
w	width [m]
X	mole fraction [-]
x	axial coordinate [m]
Y	species mass fractions [-]
y	vertical coordinate [m]
Z	mixture fraction [-]
$\mathcal{Z}$	compressibility factor [-]
Z''^2	mixture fraction variance [-]
z	horizontal coordinate [m]

GREEK SYMBOLS

α	thermal diffusivity [m^2/s]
Γ	third-body factor [-]
γ	third-body efficiency [-]
Δ	filter width [m]
δ	distance/boundary layer thickness [m]
$\mathcal{E}$	emissivity [-]
ϵ	expansion ratio [-]

ε	turbulence kinetic energy dissipation [m^2/s]
η_r	recovery factor [-]
η_k	Kolmogorov scale [m]
ζ	normalized enthalpy [-]
Θ	cooling efficiency [-]
θ	angle [°]
κ	isentropic exponent [-]
Λ	pressure eigenvalue [$kg/(m^2 \cdot s)$]
λ	thermal conductivity [$W/(m \cdot K)$]
μ	dynamic viscosity [$Pa \cdot s$]
ν	kinematic viscosity [m^2/s]
ν'	stoichiometric coefficient [-]
ρ	density [kg/m^3]
Σ	Bartz coefficient [-]
σ	Stefan-Boltzmann constant [$W/(m^2 \cdot K^4)$]
τ	time-scale [s]
τ_{ij}	viscous tensor [Pa]
ϕ	generic variable [-]
χ	scalar dissipation rate [1/s]
ψ	apparent numerical order [1/s]
Ω	vorticity [1/s]
ω	specific rate of dissipation [1/s]
$\dot{\omega}$	molar reaction rate [$mol/(m^3 \cdot s)$]
Ω^*	collisional integral [m]

INDICES

a	activation
acc	accuracy
ad	adiabatic
atm	atmospheric
aw	adiabatic wall
c	critical
$calc$	calculated
cc	cooling channels
ch	chamber
$comp$	computed
CV	control volume
dev	deviation
e	exhaust
eff	effective
err	error
ext	exact
f	fluid
f	forward
fu	fuel
h	hydraulic
hg	hot gas
hgw	hot gas wall
IG	ideal gas
in	inlet
l	laminar
loc	location
mat	material
max	maximal
$meas$	measured
min	minimal
n	normalized
noz	nozzle
out	outlet
ox	oxidizer
$prec$	precision
r	reverse
rad	radiative
res	response
rot	rotational
sgs	Sub-Grid Scale
sp	species
st	stoichiometric
t	turbulent
tar	target
tc	throat curvature
th	throat
$thermo$	thermocouple
tot	total
$trans$	translational
$vibr$	vibrational
w	wall
∞	ambient

Part I

INTRODUCTION

The average introduction to almost any book is somewhat of a bore.

— Boris Karloff

1 INTRODUCTION

Rockets are cool. There's no getting around that.

— Elon Musk

Access into space has been traditionally enabled by high-performance liquid rocket engines (LREs) operating with well-established propellant combinations. Since the 1960s, most launcher stages have conventionally utilized liquid oxygen and liquid hydrogen due to the high specific impulse as well as liquid oxygen and kerosene due to the high energy density. For in-space propulsion systems requiring simplified system architectures, long operational duration and multiple-ignitions, hydrazine and its derivatives, especially the combination of monomethylhydrazine (MMH) with nitrous tetroxide (NTO) and unsymmetrical dimethylhydrazine (UDMH) with NTO, have been widely used due to their hypergolicity and long-term storability.

In the recent years however, the need for new propellant combinations has arisen. This need for new propellant technologies has emerged as a result of an increased interest towards environmental sustainability/compatibility, lower operational costs and commercialization of space.

With regards to the environmental impact, a significant contribution to the search for alternative fuels, is the Registration, Evaluation, Authorisation and Restriction of Chemicals (REACH) regulation[1] of the European Union, which aims at improving the protection of human health and the environment from the risks that can be posed by chemicals. Within the REACH regulation, hydrazine and its derivatives have been labeled as "substances of very high concern" and their future use is planned to be strictly reduced. The reasons for the induction of hydrazine to the list is its high toxicity, corrosivity as well as its classification as a carcinogenic, mutagenic and toxic to reproduction (CMR) substance. Those disadvantageous properties of hydrazine have always been a driver for strictly defined safety precautions during the production, transport and handling of the fuel and have been responsible for the associated high costs.

Within this framework, research efforts are being invested in the use of "green propellants" for in-space propulsion, which is the operational regime where hydrazine has been successfully used in the past. The class of "green propellants" describes propellants that are characterized by safer propellant handling (thereby mitigating the cost and risk associated with transport, storage, cleanup and human exposure), low toxicity, high fuel efficiency and minimal costs allowing for commercialization.

As far as space commercialization is concerned, several independent initiatives have emerged in the past years which act as a driving force towards the development of low-cost and low-turnaround-time propulsion systems, shaping the future satellite market. For example, projects like Starlink, OneWeb and Telesat [1] aiming at providing Internet

1 ECHA list of substances of very high concern for authorisation: https://echa.europa.eu/candidate-list-table (accessed on June 6th 2020)

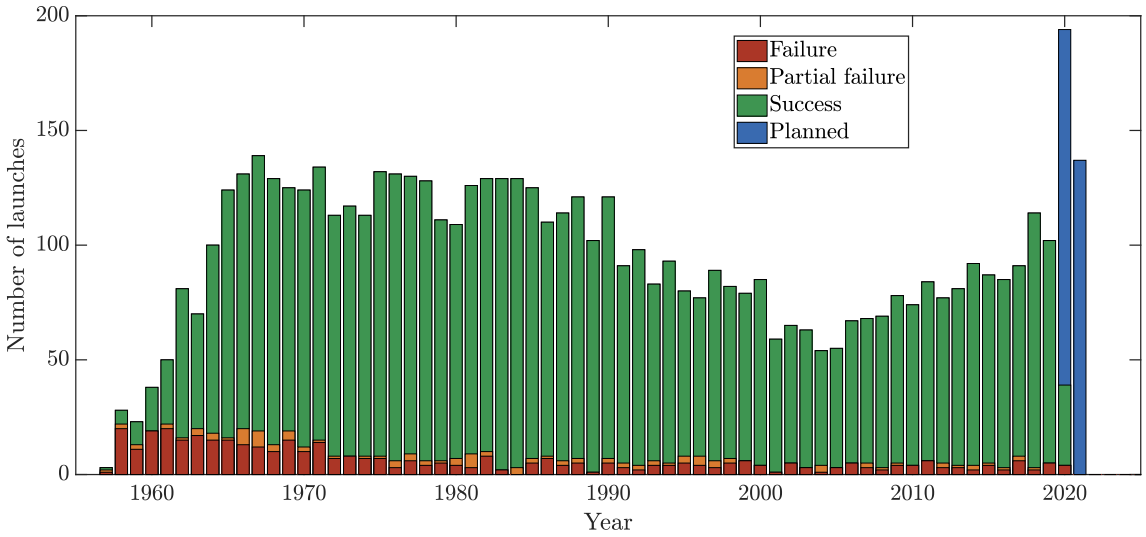

Figure 1.1: Number of launches per year for the period 1957-2021[2].

from space have re-gained popularity in the last years and consist of constellations with hundreds or thousands individual satellites in Low Earth Orbit (LEO). Furthermore, an increase in satellite systems aiming at understanding climate system and its changes, by quantifying processes of the atmosphere, land and oceans [2] using remote sensing as well as business and finance satellites [3] is observed. More ambitious projects involving asteroid mining for the extraction of water and rare metals such as platinum [4] as well as orbital fuel servicing and resupply missions [5, 6] have been proposed which would potential open up a whole new sector in the next generation space market.

This increase in commercial payloads as well as the the emergence of numerous private launch providers aiming to fill the small-satellite market [7] is expected to lead to a steady and rapid increase in the number of launches in the next years. Historically, the annual number of launches has been on the rise since 2005 as Figure 1.1 shows.

To ensure a frequent and sustainable access to space that satisfies the market needs and continues accommodating the ever-increasing number of scientific missions [8], low-cost, reusable launch vehicles are seen as an attractive option. SpaceX launch vehicle Falcon 9 has been the first orbital launcher to successfully achieve landing of the first stage booster and subsequent relaunch after refurbishment [9]. Other private companies and space agencies are looking into the development of reusable systems for a prospective cost reduction [10–12].

A propellant combination that appears to have the potential of satisfying the aforementioned challenges of in-space propulsion and launcher propulsion is LIQUID OXYGEN (LOX) and LIQUID METHANE. By being able to combine performance with reusability and sustainability, while also being considered a "green propellant", oxygen/methane ("methalox") has been the focus of multiple research studies in the past years. Apart from a pure research interest, methane as a fuel has gained a lot of attention from private companies envisioning Mars colonization such as SpaceX as it has undeniable benefits when applied for long-term manned interplanetary missions [13].

2 Data compiled from https://www.spacelaunchreport.com/logyear.html (Accessed on 8th of May 2020).

Property	CH_4	O_2	H_2	RP-1[3]
Freezing temperature [K]	90.7	54.4	14.0	226.0
Boiling temperature at 1 bar [K]	111.6	90.6	20.4	450.0
Critical temperature [K]	190.6	154.8	33.1	679.0
Critical pressure [bar]	46.0	50.4	12.9	23.4

Table 1.1: Thermodynamic properties of typical rocket propellants.

Given the traction that the idea of using methane as a space propulsion propellant has gained, it is important to understand its properties, benefits and drawbacks.

1.1 PROPERTIES OF THE LOX/METHANE PROPELLANT COMBINATION

Methane is a chemical substance with the chemical formula CH_4. It is the simplest of all alkanes and at ambient condition a colorless and odorless gas. Using oxygen as oxidizer the burning of methane at the stoichiometric mixture ratio $O/F \approx 4.0$ produces carbon dioxide and water:

$$CH_4 + 2\,O_2 \longrightarrow CO_2 + 2\,H_2O$$

Some important chemical and physical properties of methane and oxygen are summarized in Table 1.1. As a reference, the properties of the established fuels H_2 and kerosene (RP-1) are also included.

1.1.1 *Performance*

One of the major advantages of oxygen/methane in comparison to other propellant candidates is the high performance, expressed in terms of the specific impulse I_{sp}. The specific impulse is defined as the ratio of the spacecraft thrust F to the propellant flow rate $\dot{m}$, normalized by the gravitational acceleration at the surface of the earth g_0 and represents the normalized exhaust velocity c_e:

$$I_{sp} = \frac{F}{\dot{m}\,g_0} = \frac{c_e}{g_0} \tag{1.1}$$

For rocket relevant conditions (pressure $p = 100\,\text{bar}$ and expansion ratio $\epsilon = 45$ will be used as a representative set), the highest specific impulse is achieved for mixture ratios of about 3.5. The dependence of the specific impulse on the oxidizer-to-fuel ratio O/F for methalox is shown in Figure 1.2, where its performance is compared to other relevant propellant combinations.

3 The thermodynamic values for kerosene depend on the purity grade. The values for the RP-1 grade are reported in Table 1.1.

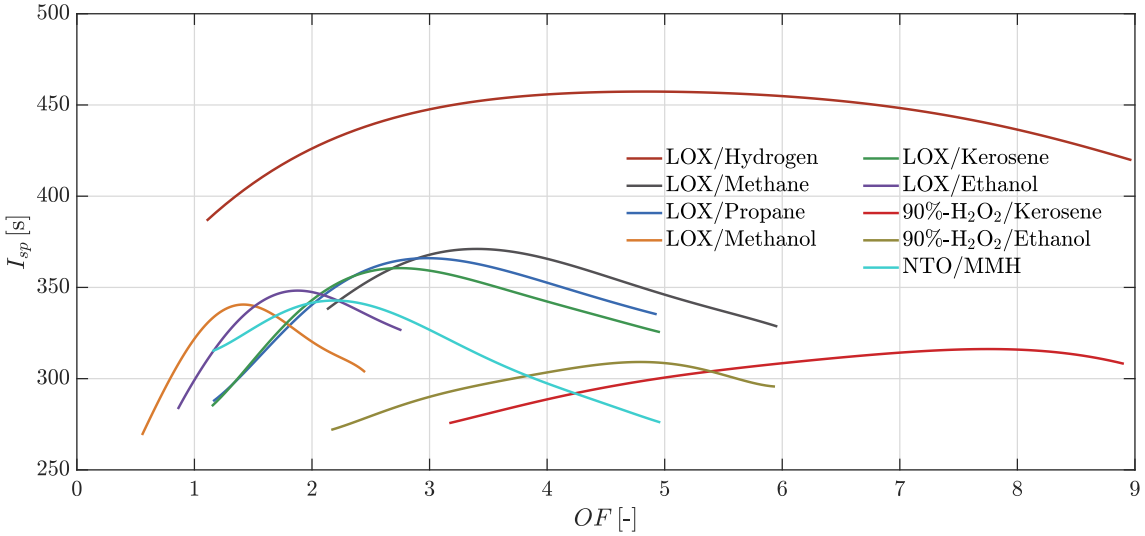

Figure 1.2: Ideal vacuum specific impulse for typical rocket propellant combinations. $p_c = 100\,\text{bar}$, $A_e/A_{th} = 45$. (Adapted from Haidn [14]).

Methane has the highest specific impulse among hydrocarbons[4], reaching values of up to 371 s for the examined operating point. This performance exceeds the specific impulse of the LOX/kerosene combination, which is the most widely used hydrocarbon propellant to date by up to 1.6%, which is significant in terms of payload capabilities. Before kerosene, the combination of LOX with alcohols (mainly ethanol and methanol) was widely researched upon in the early rocket engines, which however delivers lower performance by 6.6% and 9.1% respectively. Although ethanol has re-gained popularity in several recent propulsion projects [15, 16], it is inferior to methane from a performance point of view.

It is evident that compared to LOX/hydrogen, which can deliver up to 457 s of specific impulse, methane is not as powerful, but has other advantages as explained in the following sections. Compared to the widely established combination of NTO/MMH however, a superior I_{sp} by up to 8.0% is observed. This is a direct advantage of using methane to replace hypergolic hydrazine derivatives, as it combines the benefit of being a "green propellant" with a better performance.

Further hypergolic propellant combinations, using hydrogen peroxide (H_2O_2) as an oxidizer are also included in Figure 1.2 but the advantages they have due to the absence of external energy source for ignition are counteracted by the low specific impulse which is in the range of 310-320 s.

1.1.2 *Cooling properties*

A further important aspect when dealing with the choice of propellants for main-stage and upper-stage engines are the cooling properties. Since the fuel is the component that is typically used as a coolant, its thermodynamic properties can directly affect the

4 Note that only saturated hydrocarbons (alkanes and acohols) are plotted in Figure 1.2. Unsaturated hydrocarbons have a limited storage suitability due to resinification while aromatic hydrocarbons and cycloalcanes have a lower hydrogen content, which negatively influences the I_{sp} due to a higher molecular mass of the exhaust gases.

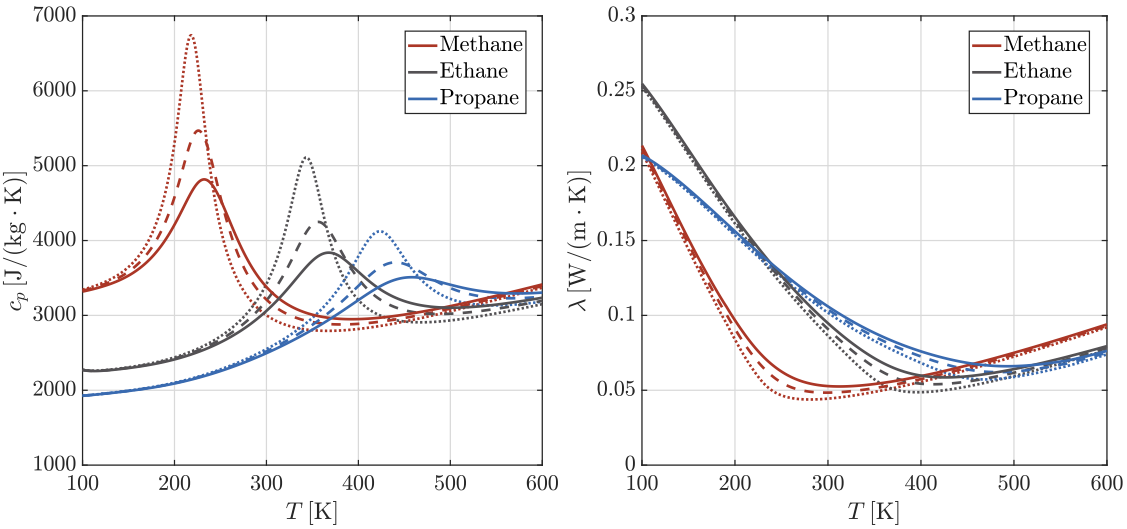

Figure 1.3: Specific heat capacity (left) and thermal conductivity (right) as a function of temperature for different hydrocarbons. The lines correspond to different pressure levels: $p = 100\,\text{bar}$ (·····), $p = 125\,\text{bar}$ (- - -), $p = 150\,\text{bar}$ (——). The NIST database was used for the thermodynamic data [17].

performance of the engine cycle, especially when it operates within an expander cycle, which uses the heat picked-up within the cooling channels to operate the turbine.

Compared to the other available hydrocarbons, the cooling properties of methane are superior, when nominal wall heat fluxes are considered[5] based on parametric analyses carried out by Urbano et al. [18]. The main advantage is the higher specific heat capacity compared to other alkanes as Figure 1.3 shows.

Apart from the thermodynamic properties that allow for a large heat pick-up within the cooling channels, methane with a high purity grade has the additional advantage of a very high coking limit. Soot deposition as a result of coking at high temperatures in the cooling channels significantly diminishes the cooling capabilities of the fuel and leads to a reduced engine lifetime. Tests carried out by Liang et al. [19] demonstrated that no coking was measured for methane within a large operating range ($50 - 300$ bar, heat fluxes up to $66\,\text{MW/m}^2$), while propane coking was reported in stainless steel tubes. At the same time, the onset for kerosene coking was found to be at wall temperatures as low as 650 K. This compares well to the results reported by Younglove et al. [20] and Gross [21], which show that soot deposition for kerosene occurs at around 560 K, for propane at 700 K, whereas for methane the threshold value is at around 970 K. Experimental results by Driscoll et al. [22] support those findings, as no significant carbon deposit was observed for pure methane. Although the formation of heavier hydrocarbons was found at higher temperatures, a much larger thermal stability was measured for methane compared to methane/propane mixtures. The increased thermal stability positively influences the maximal operating temperature range for the coolant and makes it suitable for use in an expander cycle [23]. It is important to note that the low carbon deposition occurs for pure methane and the influence of the fuel's impurity on the performance and cooling properties is further discussed in Section 1.1.6.

5 In the absence of high heat fluxes leading to heat transfer deterioration.

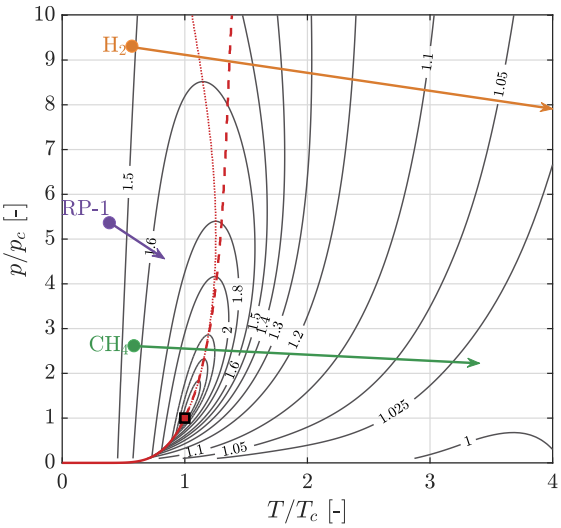

Figure 1.4: State change of different fuels within cooling channels. The iso-lines of the relative specific heat capacity ($c_p/c_{p,IG}$) for methane are plotted in the $p-T$ diagram. Saturation line: ——, Widom line: - - -, Maximum of $c_p/c_{p,IG}$: ·····. The NIST database was used for the thermodynamic data [17].

Despite the superior cooling properties compared to other hydrocarbons, methane can experience a phenomenon called "heat transfer deterioration" in the cooling channels when the ratio of wall heat flux to coolant mass flow rate becomes too high [24]. To understand the occurrence of heat transfer deterioration, the typical operating pressure and temperature range of rocket coolants has to be taken into account. An overview is given in Figure 1.4, where the evolution of temperature and pressure for three different coolants is plotted, with the round markers representing the inlet conditions and the arrow direction indicating the state change in the $p-T$ diagram. For all three fuels (H_2, RP-1 and CH_4), the same inlet pressure of 120 bar is chosen and an identical pressure loss of 10 bar is assumed[6]. In order to be able to compare the coolants despite their different thermodynamic properties, the comparison takes place in reduced thermodynamic units, where the pressure and temperature are normalized by their respective critical values p_c and T_c. The saturation line as well as the pseudo-boiling curve (Widom line [25]) are included along with the iso-lines of the ratio of the specific heat capacity c_p and the ideal gas (IG) specific heat capacity $c_{p,IG}$. A high $c_p/c_{p,IG}$ ratio indicates the presence of strong real-fluid effects.

Based on Figure 1.4, it is evident that although all three coolants enter the cooling channels in transcritical conditions, with supercritical pressure and subcritical temperature, they experience quite different behaviors. Hydrogen, having a critical pressure of 12.9 bar, is far away from its critical point in typical values for the cooling channel operating pressure. Hence upon crossing the pseudo-boiling line, no significant changes in its thermodynamic properties are observed. RP-1, due to the low temperature at which pyrolysis or thermal cracking and coking can take place [19], does not enter the gas-like regime when used as a coolant. Since it never crosses the Widom line, it remains in liquid-like conditions, which is the main reason why kerosene cannot be used as the fuel in expander cycle engines. Finally, by observing the transition of methane in Figure 1.4, it becomes clear that it enters the

6 The pressure loss also depends on the fuel properties, but the fuel-dependency is neglected for a first-order approximation of the coolant transition.

cooling channels at a relative pressure $p/p_c \approx 2.7$, which is very close to its critical point. As a consequence, the coolant flow behavior is strongly affected by the large property variations that occur in the near-critical region. In particular, variables such as specific heat at constant pressure, thermal conductivity and speed of sound exhibit a relevant peak value in the vicinity of the pseudo-critical temperature [26], as Figure 1.3 shows. Since the peak values decrease with increasing pressure, for sufficiently large pressure levels the influence of the near- critical region on the flow behavior is minimized, which is why hydrogen does not experience large property variations in the cooling channels.

This transition from subcritical to supercritical temperature for fluids with pressure slightly above the critical one, resembles a phase change and can lead to a heat transfer deterioration. Given a low mass flow rate and high wall heat flux, the density close to the heated wall sharply increases, leading to a local flow acceleration that modifies the flow field by reducing turbulence production [27, 28] and giving rise to regions of low shear stress as well as a thickening of the sub-viscous layer [29]. This impaired ability of the coolant to pick-up heat typically results in a sharp increase of the wall temperature, which has been experimentally measured for different operating conditions and configurations [30–33], with most of the studies focusing on supercritical water and carbon dioxide due to their application in Supercritical Water Cooled Reactors (SWCR) [34] and Supercritical Carbon Dioxide cycles (S-CO_2) [35] respectively.

For methane, this phenomenon has been measured experimentally as well [36] and several numerical studies have been carried out with efforts placed in deriving empirical correlations that can describe the heat flux coefficient in the near-critical operating conditions [18, 36–38]. Since the heat transfer deterioration is more prominent for methane compared to heavier hydrocarbons (due to their lower critical pressure), the cooling properties of methane can be worse than those of propane and ethane, for very high heat fluxes and low coolant flow rates [18]. Measures that can be taken to counter-act this effect would be ensuring a sufficiently high mass flow rate, increasing the coolant pressure or increasing the surface roughness that substantially prevents the onset of heat transfer deterioration in the expense of a higher pressure drop [26].

1.1.3 *System design*

From a system design point of view, methane offers significant advantages both with respect to in-space propulsion and rocket launchers.

Compared to hydrogen, the higher density of methane (by a factor of six for typical tank pressures) allows for smaller tanks [39, 40]. This results to a significant reduction in structural mass and compensates for the lower specific impulse. Launcher design studies which have been carried out comparing different propellants have shown a potential vehicle size reduction when using methane as fuel [41].

Additionally, the higher boiling temperature of methane (Table 1.1) allows for a reduction of the active tank cooling during storage, making long-term missions more favorable. At the same time, the boiling (and hence storage) temperature of methane and oxygen are quite similar, meaning that the thermal insulation between the fuel and oxidizer tanks can also be reduced compared to hydrogen. Finally, the density difference between methane and oxygen ($\rho = 425\,\mathrm{kg/m^3}$ and $\rho = 1142,\mathrm{kg/m^3}$ respectively at 1 bar) is much smaller compared to the equivalent difference for hydrogen ($\rho = 71\,\mathrm{kg/m^3}$ at 1 bar), allowing for

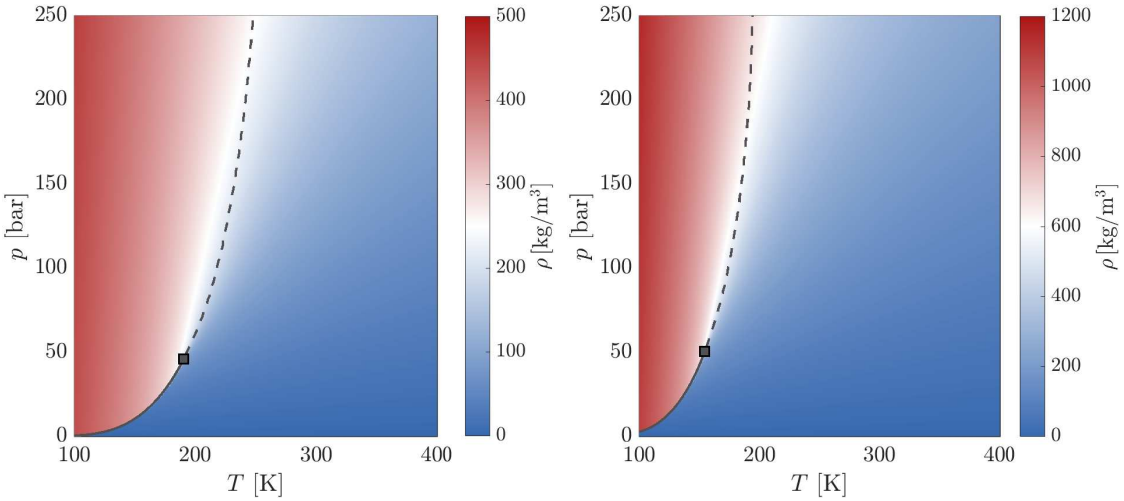

Figure 1.5: Density of methane (left) and oxygen (right). Saturation line: ——, Widom line: - - - . The NIST database was used for the thermodynamic data [17].

similar rotational speeds of the pump and the potential use of a single-shaft turbopump [42]. The individual densities of CH_4 and LOX are shown in Figure 1.5 as a function of pressure and temperature. Nevertheless, hydrocarbons with lower freezing temperature and higher density (like propane, which freezes at 85 K and has a density $\rho = 717\,\mathrm{kg/m^3}$ at 1 bar and 100 K) would reduce the requirements for insulation even further and allow for a denser storage, thereby shrinking the tank volume and mass, making them potentially even more advantageous from a launch vehicle design standpoint.

A significant number of studies has also dealt with the comparison between methane and kerosene as a fuel in rocket launch vehicles. Klepikov et al. [43] showed that launchers operating with LOX/methane could deliver the same payload as LOX/kerosene launchers, while Pempie et al. [44] and Burkhardt et al. [45, 46] demonstrated that both for expendable and reusable liquid booster stages, methane would be a viable alternative from a system design point of view, able to place the same payload to orbit as oxygen/kerosene. The main advantages reported in favor of methane were the lower operational and maintenance expenses. These are directly related to the topic of reusability, as explained in Section 1.1.4.

1.1.4 *Reusability*

The main source of additional costs, rendering the reusability of kerosene engines less attractive, is the intensive refurbishment potentially required due to the coking of the fuel in the cooling channels, as already explained in Section 1.1.2 [44].

Apart from kerosene however, the use of hydrogen in reusable liquid boosters also has certain disadvantages compared to methane. Although no thermal cracking and soot deposition occurs in the case of hydrogen, the higher thermal loads occurring at the chamber wall yield a lower fatigue life expectancy of the combustion chamber [47, 48]. Apart from the higher thermal loads, there is a larger thermal gradient within the chamber liner due to the increased temperature difference between coolant and hot gas mainly owing to the very low cooling channel inlet temperature of hydrogen. This has a significant

impact on the maximal amount of loading cycles of LOX/H_2 engines before mechanical failure [47].

1.1.5 *Sustainability*

A further factor that needs to be accounted for when comparing different propellant combinations is sustainability. In the current section the economic and environmental sustainability connected to the acquisition of each chosen fuel is examined. Environmental impact is expected to become a criterion for the choice of propellant when considering the scaling up of the number of launches to keep up with the needs of the market.

Kerosene is a substance created by fractional distillation of crude oil in a boiling range of 423 K to 623 K [49]. The projections of expected oil supply in the following decades is a complex and multifaceted topic, with several influencing variables and there is a high uncertainty regarding the future availability and price of oil and hence kerosene [50, 51]. In an attempt to increase the diversity of kerosene production sources and its sustainability, efforts are being carried out to produce renewable kerosene from thermochemical splitting of water and carbon dioxide [52] as well as bio-kerosene from Jatropha oil [53] and coconut oil [54]. The large-scale sustainability of those processes is however yet to be demonstrated.

On the other hand, hydrogen might be the most abundant element on earth but it is found rarely in its pure form and its production requires its extraction from a compound. The extraction of hydrogen is therefore connected to the use of external energy sources. Currently, close to 50% of the global demand for hydrogen is generated via steam reforming of natural gas, about 30% from oil/naphtha reforming from refinery/chemical industrial off-gases, 18% from coal gasification, 3.9% from water electrolysis and 0.1% from other sources [55]. Green hydrogen production technologies are not presently available with reasonable efficiency and cost. With regards to environmental sustainability, the only green hydrogen production method which can be considered as reference is the PV-electrolysis, which couples a photo-voltaic (PV) power generation system with a water electrolyzer but still has a low conversion efficiency [56]. Due to efforts however to increase the use of hydrogen as a fuel for power generation and transport (as opposed to its main function as a chemical substance in oil refineries and chemicals production processes [57]) an increase in the use of renewable energies for H_2 production is expected [58, 59] leading to a "greener" future prospect.

Currently however, the production of hydrogen is up to 10 times much more costly compared to methane [60]. Several industrial alternative processes for methane production are being utilized, with the majority of CH_4 being extracted from natural gas. Methane is the most important component of natural gas with a volume fraction of 80% up to 99%. The actual practice of processing natural gas to pipeline dry gas quality levels usually involves four main processes to remove the various impurities: oil and condensate removal, water removal, separation of natural gas liquids and sulfur and carbon dioxide removal. Apart from the extraction of natural gas however, the production of synthetic natural gas has also been demonstrated, promising a much more sustainable production source for methane [61–64]. Finally, using biomass and organic waste for the production of biomethane has been shown to be cost-efficient and allows for low-emission methane extraction [65]. Due to the diversity of low-cost processes that are already available for methane production

	CH_4	C_2H_6	C_3H_8	N_2
Mixture 1	92%	4.0%	2.2%	1.8%
Mixture 2	86%	9.5%	4.0%	0.5%
Mixture 3	93%	5.0%	1.5%	0.5%
Mixture 4	88%	5.0%	2.0%	5.0%

Table 1.2: Molar concentration of species for different LNG mixtures.

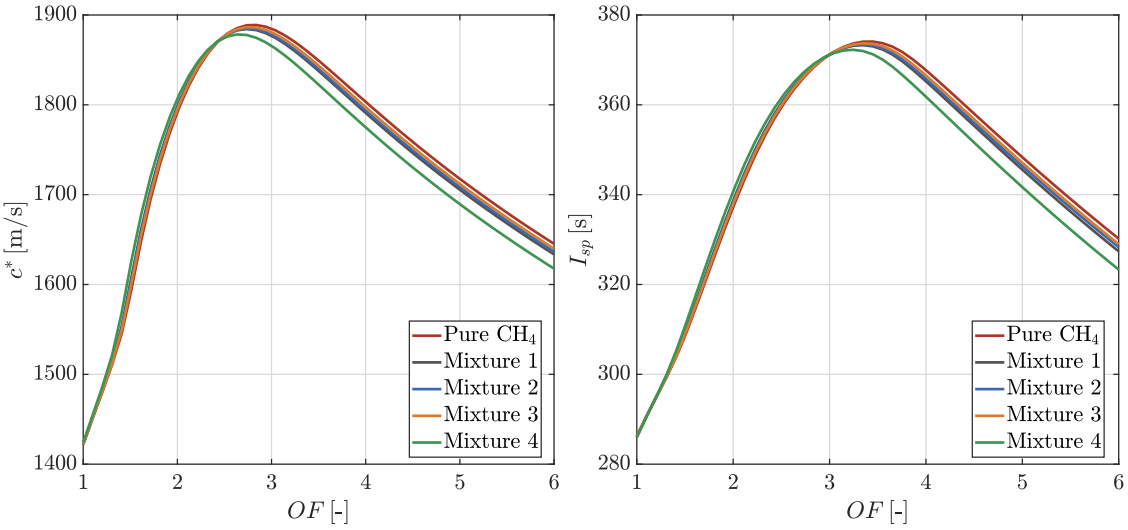

Figure 1.6: Characteristic velocity (left) and ideal vacuum specific impulse (right) for different LNG mixtures ($p_c = 100\,\text{bar}$, $A_e/A_{th} = 45$). Results obtained using CET93 [69].

together with the abundance of LNG makes methane a very promising fuel in terms of long-term sustainability.

1.1.6 *Effect of impurity on performance*

The MIL-PRF-32207 standard [66] describes the requirements for the purity grade of methane, distinguishing between grades A, B and C with 98.7%, 99.0% and 99.7% minimal volumetric concentration of CH_4 respectively. Nevertheless, several studies have been carried out proposing the use of compressed natural gas (CNG) or liquified natural gas (LNG) directly as a fuel, thereby avoiding the purification step [67].

To demonstrate the effect on the performance, four typical LNG mixtures are compared to pure methane in Figure 1.6. The mixtures are defined based on typical LNG concentrations and have been adapted from Urbano et al. [38] and Domashenko et al. [68] and the molar concentrations of their components are summarized in Table 1.2. The most dominant components apart from methane are heavier hydrocarbons (mainly ethane and propane) and nitrogen.

It is evident from Figure 1.6, that both the characteristic velocity c^* and the specific impulse are reduced when methane is not pure but the reduction is smaller than 1%. Even for higher impurity grades, the deterioration of specific impulse is minimal, as Figure 1.7

illustrates. The deviation of the maximal $I_{sp,max}$ for each mixture is compared to that of pure methane:

$$\Delta I_{sp,max} = \frac{I_{sp,max,mix} - I_{sp,max,\mathrm{CH_4}}}{I_{sp,max,\mathrm{CH_4}}} \cdot 100\% \tag{1.2}$$

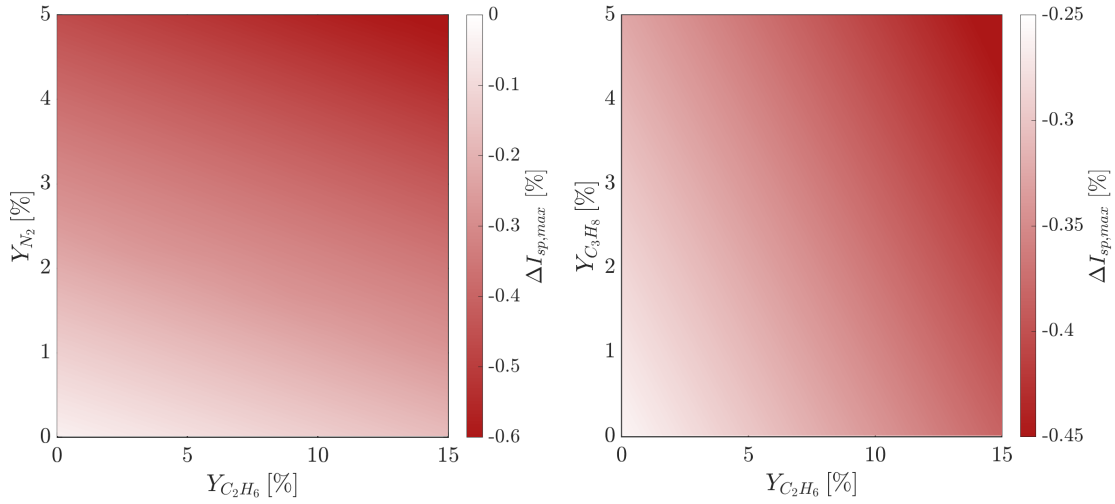

Figure 1.7: Deviation of LNG mixture specific impulse from the specific impulse of pure methane for $p_c = 100\,\mathrm{bar}$, $A_e/A_{th} = 45$. Constant propane mass fraction $Y_{\mathrm{C_3H_8}} = 3\%$ (left), constant nitrogen mass fraction $Y_{\mathrm{N_2}} = 3\%$ (right). Results obtained using CET93 [69].

Even for very large mass fractions of ethane (up to 15%) and nitrogen (up to 5%), the losses in specific impulse remain confined below 0.5-0.6%, indicating that using LNG instead of higher grade methane would not have a severe influence in performance.

Another aspect which is affected by the composition of the chosen LNG mixture is the behavior within the cooling channels. Specifically, a large sensitivity of the critical pressure and critical temperature on the mixture composition can be observed, which directly influences the thermodynamic properties of the coolant and the onset of heat transfer deterioration. The relative change of the critical pressure Δp_c and critical temperature ΔT_c defined in Equation 1.3 and Equation 1.4 is plotted in Figure 1.8.

$$\Delta p_c = \frac{p_{c,mix} - p_{c,\mathrm{CH_4}}}{p_{c,\mathrm{CH_4}}} \cdot 100\% \tag{1.3}$$

$$\Delta T_c = \frac{T_{c,mix} - T_{c,\mathrm{CH_4}}}{T_{c,\mathrm{CH_4}}} \cdot 100\% \tag{1.4}$$

An exact knowledge of the chemical composition of the fuel and hence the coolant is therefore necessary to account for the increase in critical properties of the mixture.

In addition to the critical properties, the coking and thermal cracking of LNG can be significantly different compared to pure methane. Experimental studies carried out by Driscoll et al. [22] and Higashino et al. [70] showed that thermal cracking and soot

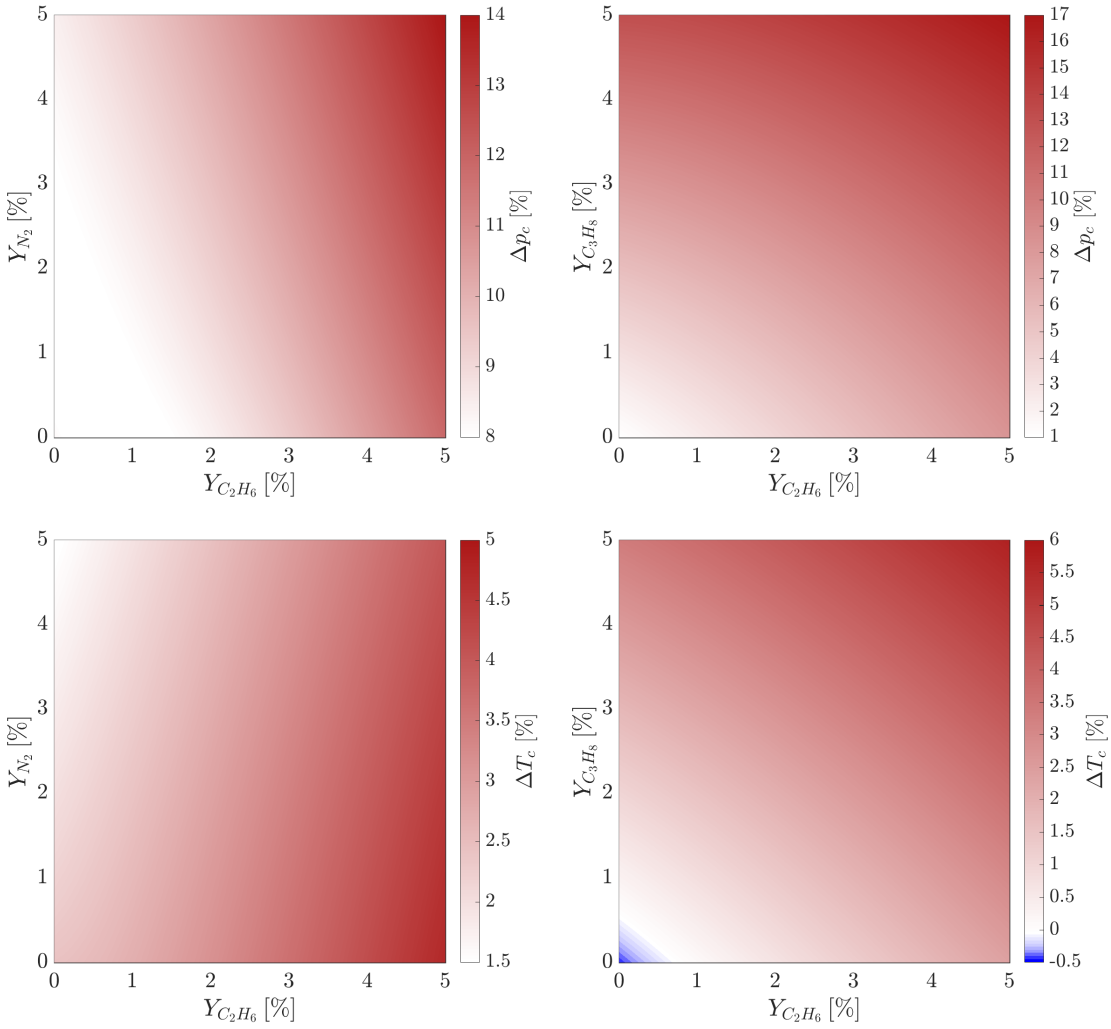

Figure 1.8: Deviation of LNG mixture critical pressure (top) and critical temperature (bottom) from the critical pressure of pure methane. Constant propane mass fraction $Y_{C_3H_8} = 3\%$ (left), constant nitrogen mass fraction $Y_{N_2} = 3\%$ (right). Results obtained from the NIST database [17].

deposition in the presence of heavier hydrocarbons occurs at much lower temperatures. For that reason, higher refurbishment costs are expected for LOX/LNG rockets and a high purity of methane is advantageous from a system point of view.

1.1.7 *In-Situ Resource Utilization*

A final property of methane, which makes it attractive for interplanetary missions is the possibility of In-Situ Resource Utilization (ISRU). One of the options for missions towards the outer planets is a potential re-fueling in the atmosphere of the gas giants (Jupiter, Saturn, Uranus and Neptune), where methane was the product of chemical processing of primordial solar nebula material [71]. Of special interest are the methane seas on the surface of Saturn's moon Titan [72], which would allow a significant reduction in propellant requirements upon a re-fueling.

For more near-future mission scenarios, the idea of generating methane on the surface of Mars and re-fueling the spacecraft has been extensively investigated from an engineering point of view [13]. The main idea relies in the utilization of the carbon dioxide from the Marsian atmosphere as well as water from the moisture of Marsian soil to feed into a Sabatier reactor [73]. Combined with a solid oxide electrolysis process [74, 75], oxygen both for life-support systems and as an oxidizer for the ascent propulsion system can be generated [76]. Preliminary studies have shown that using an electrolysis/Sabatier chemical synthesis system and small Stirling cycle refrigerators for cryogenic storage is likely to be practical, and the necessary development will probably represent a very small portion of the total cost of a Mars Sample Return mission [77]. Conversion rates of 96% have been reported from experimental full-scale demonstrators [77].

1.2 DEVELOPMENT EFFORTS OF METHANE/OXYGEN ROCKET ENGINES

Given the advantages associated with the use of methane for rocket propulsion applications, significant scientific efforts have been dedicated to developing and testing sub-scale and full-scale thrust chambers operating with LOX/CH_4 and GOX/CH_4. The most important projects are summarized in this section, with emphasis placed on full-scale engines.

In Europe, LOX/methane propulsion has been considered for the use in launchers by the European Space Agency (ESA) since the mid-2000's as a potential path to reducing the cost of access to space [78]. Launcher system studies were carried out, mostly limited to concepts and performance. Among the system studies, the Future Launcher Preparatory Program (FLPP) conducted feasibility studies regarding the use of methane for main stage engines with the introduction of new engines cycles [79]. At the same time, the FLPP aims to develop a staged combustion cycle engine able to deliver high thrust levels for use in the next generation European launchers [80, 81].

In 2015 the French Space Agency CNES (Centre National d'Etudes Spatiales) announced the development of the "Precursor Reusable Oxygen Methane Cost Effective Propulsion System" PROMETHEUS [82]. The project, which has currently been transferred into the FLPP aims at developing the new generation LOX/CH4 engines with the introduction of innovative manufacturing technologies based on additive manufacturing and a subsequent reduction of costs compared to current cryogenic engines by a factor of ten [83]. A cooperation has started between the DLR and the launcher directorate of CNES with the purpose of preparing the technologies and tools for the future LOX/CH_4 cryogenic engines like PROMETHEUS, in particular regarding ignition, combustion, chamber cooling, the system analysis of engine coupled with test bench and the turbopumps [84]. A digital rendering of the Prometheus engine is shown in Figure 1.9.

Parallel to the PROMETHEUS project, in 2015 the design and development of a LOX/LCH_4 demonstrator engine was carried out at the German Aerospace Center (DLR). This demonstrator is an expander-bleed cycle engine and was defined within the framework of the LUMEN (Liquid Upper stage demonstrator ENgine) project [85, 86]. Within this project, significant efforts have been carried out regarding the development of the turbopumps [87, 88], the design of the injector and the ignition system [89, 90]. Before the begin of the LUMEN project however, several studies had been completed by the DLR dealing with the investigation of methane's properties. Within the TEHORA program, analytical trade-off studies between methane and kerosene were carried out, while experimental

Figure 1.9: Digital rendering of Europe's proposed reusable rocket engine, Prometheus[7].

focus was placed on ignition and soot formation [80] whereas in the the frame of the In-Space Proulsion-1 (ISP-1) program, heat transfer processes and cooling methods were examined [91]. Before that, a demonstrator program was developed by ArianeGroup called Pathfinder Demonstrator Program, which targeted the expansion of the capabilities in operating reusable propulsion systems using hydrocarbons as propellants [92]. Apart from the development of a full scale gas-generator [93, 94] and a single-shaft turbopump [95], the project included the design and manufacturing of a 400kN class LOX/methane thrust chamber [96], which was also tested at the P3.2 high pressure test bench at DLR Lampoldshausen.

In Italy, efforts have been placed in using oxygen/methane propulsion technology for the upgrade of the VEGA launcher's upper stage since 2007. To demonstrate the technology, a 100kN class LOX/LNG expander cycle called LM10 MIRA has been developed and tested [97, 98]. The purpose of the project is the implementation of a low-cost LOX/methane upper stage solution to the VEGA Evolution (VEGA E) launcher, a decision which was approved by the ESA Council in 2016.

The development of the LM10 has been carried out by the Italian company AVIO in cooperation with the Russian KBKhA within the frame of the LYRA program [99]. For that reason, the outline of the LM10 demonstrator was based on an existing demonstrator by KBKhA, with a newly designed injector plate and fuel turbopump. In Russia, the extensive experience with hydrocarbons as rocket fuel, allowed for a transfer of knowledge into the development of oxygen/methane engines from existing kerosene engines. Specifically, a modified version of the RD0110 engine (which has successfully powered the third stage of the Soyuz rocket), was built operating with LNG and was named the RD0110M [100].

7 Image downloaded from https://www.esa.int/Enabling_Support/Space_Transportation/Prometheus_to_power_future_launchers. Retrieved on June 15th 2020.

Based on the success of the first RD0110M tests and given the heritage with the operation of LOX/hydrocarbon engines, hot firing tests of the modified RD0146Y expander cycle engine were performed with methane as fuel [101].

In Japan extensive research in field of designing and testing LOX/methane engines has been conducted since the beginning of the century. The LE-8 engine with a thrust level of 100kN started development in 2002 and completed more than 2000 seconds of firing tests [102, 103]. The design and experimental activities were carried out by the Japan Aerospace Exploration Agency (JAXA) and the company IHI and the initial design of impinging injectors and ablative cooling was updated to gas-liquid coaxial injectors and regenerative cooling to improve the performance [60, 104]. After the initial tests with the LE-8 engine, JAXA defined new targets regarding the expected performance (in terms of specific impulse) for their future LOX/LCH_4 engines. For thrust levels of 30kN and 100kN a full expander cycle was chosen, while for higher thrust levels between 100kN and 2000kN, a staged combustion cycle was chosen [102], based on the know-how heritage of the LE-5B and LE-7 engines respectively. After the initial sub-scale tests with a multi-element expander cycle engine [105], further component tests have been carried out, including characterization of the turbopumps [42] and the regeneratively cooled thrust chamber assembly [106].

In China, several studies on the requirements of LOX/LCH_4 engines have been carried out [107, 108] and they resulted in the definition of a gas-generator engine in 2006 [109]. For the characterization of the 600kN prototype gas-generator cycle engine's components, several sub-scale firing tests have been executed [110–112]. In 2011 the first full-scale tests of the prototype engine, along with methane cooling and gas-generator assembly were completed.

In the USA, the potential use of oxygen/methane as rocket propellants for an increased performance of liquid rocket boosters has been examined since the end of the 1970s [113]. In fact, detailed thermodynamic and hardware configuration sensitivity studies on the use of methane for expander cycles have been carried out [114] with conceptual investigations of modifying the successful RL-10 LOX/LH_2 engine to be operated with methane as fuel [115]. Apart from the conceptual modification studies of LOX/CH_4 upper stage engines, Aerojet also tested a 4kN LOX/methane engine, reaching combustion efficiencies of up to 97% [116]. In 2011 NASA's Johnson Space Center reported the first results from Project Morpheus, during the course of which a prototype planetary lander capable of vertical take-off and landing was successfully developed and tested [117, 118]. The project was part of the NASA Human Exploration Operations Mission Directorate's Advanced Exploration Systems programs. The lander vehicle was propelled by a LOX/LCH_4 engine and was designed to carry a 500 kg payload to the lunar surface at a relatively low cost [119]. One of the topics that was deeply researched during the operation of the pressure-fed LOX/methane Morpheus main engine was the occurrence of combustion instabilities. Specifically, first tangential and first radial modes were triggered during the ignition sequence. The problem was mitigated via a higher-chamber pressure start sequence which allowed the engine to successfully perform a 4:1 throttling [120].

The use of methane as a rocket fuel appears to be compliant with the vision of Blue Origin and SpaceX, two of the the private US companies developing the next generation of launch vehicles. The BE-4 engine, operating with a staged-combustion cycle, has been designed and tested by Blue Origin and is expected to power the main stage of both the

Figure 1.10: Full-scale hot-fire test of the BE-4 engine[8].

New Glenn heavy-lift orbital launch vehicle as well as the main stage of ULA's Vulcan launcher [121]. An image of a full-scale test of the BE-4 engine from April 2018 is shown in Figure 1.10. SpaceX has also announced the development of the Raptor engine, a full-flow staged combustion cycle operating with sub-cooled LOX/LCH_4. The engine has been designed with the goal of powering the interplanetary transport system [13], with the Raptor engine being utilized both in the main stage (31 engines planned) as well as the upper stage (6 engines planned) of the Starship launch vehicle.

1.3 THESIS MOTIVATION AND OUTLINE

Given the promising prospects of using methane as a fuel for in-space propulsion as well as for launcher propulsion systems, it is essential to develop the necessary know-how that allows a precise sub-component and engine assembly design as well as the prediction of performance. Because the experience of designing and operating LOX/methane engines is limited compared to the equivalent familiarity associated to more traditional propellants, technical challenges still prevail.

Some of the topics requiring special attention are the design of the injector system to ensure avoidance of combustion instabilities, the design of a reliable ignition system and the prediction of the injector/wall and flame/wall interactions to ensure accurate design of the cooling system and correct lifetime prognosis.

The ability to predict the performance and behavior of the thrust chamber given a geometry, operating point and start-up sequence is crucial in the design process of liquid rocket engines. This requires the availability of validated numerical tools that can be utilized for an efficient layout and optimization of the respective thrust chamber components and

8 Image used with permission from https://www.teslarati.com/spacex-competitor-blue-origin-25-reuse-future-rocket/. (Accessed on June 10th 2020)

the full-scale engine assembly. The use of numerical flow simulation tools in the early design phase is a promising approach as it allows the reduction of experimental tests and redesign efforts and consequently reduces development time and cost.

Due to the large amount of simultaneously occurring complex physical and chemical processes taking place within a rocket engine, including atomization, evaporation, mixing, chemical reactions, flame/wall interaction and supersonic expansion, the development of the computational tools is a challenging task which requires a comprehensive validation strategy [122]. To carry out the validation of such tools, a long-term process is required that comprises the mapping of numerous test cases ranging from lab-scale single-element tests up to full-scale engines operating in flight conditions.

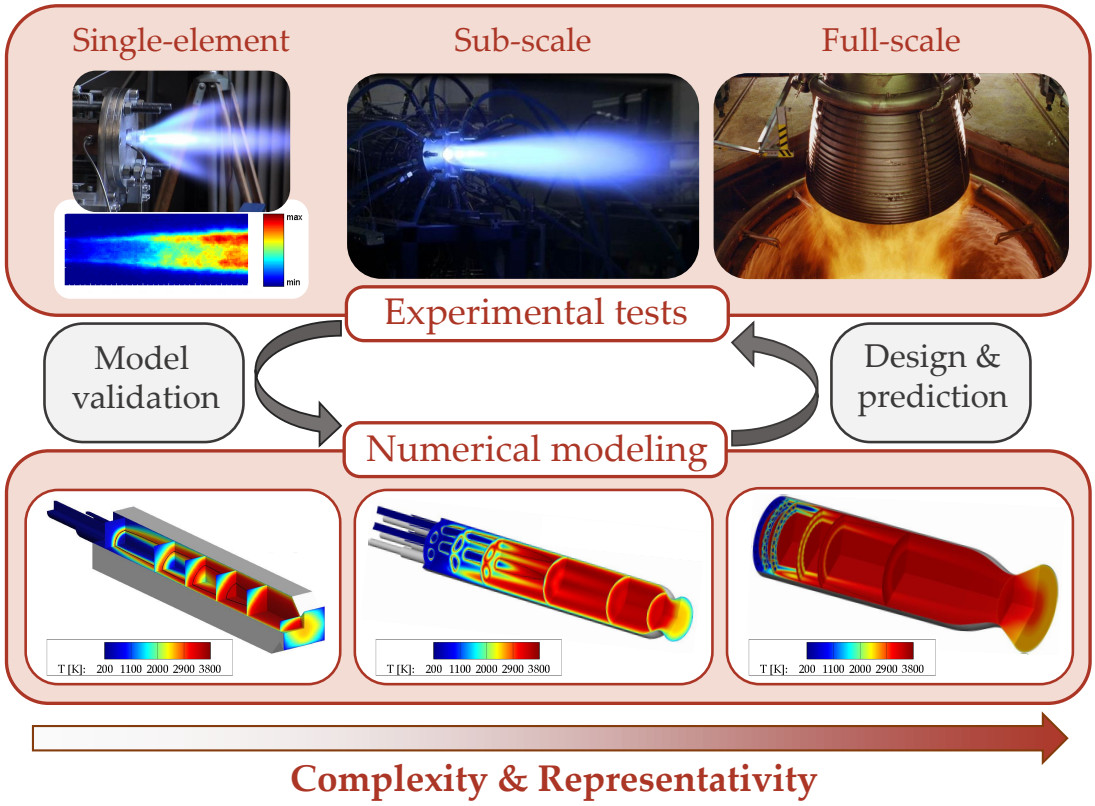

Figure 1.11: The role of experimental testing and numerical modeling in the design process of rocket engines. [9]

The process is schematically illustrated in Figure 1.11. The complexity of the examined systems increases from left to right, with the simplest configurations typically consisting of a single-element injector and a number of different instrumentation methods (optical access, pressure transducers, heat flux measurements) to allow for a detailed understanding of the fundamental processes occurring in the chamber. The next step typically involves the introduction of further injector elements. Such a multi-element configuration is more representative for the full-scale hardware, as additional flow and chemical effects like the

9 The images used in Figure 1.11 have been adapted from the following sources: Winter et al. [123] (single-element images), Perakis et al. [124] (sub-scale simulation image), Silvestri et al. [125] (sub-scale experimental image), Perakis et al. [126] (full-scale simulation image). The Vulcain 2 test image is provided by the DLR under a CC-BY 3.0 license (https://www.dlr.de/EN/Service/Imprint/imprint_node.html).

interaction of neighboring flames and the creation of secondary flow patterns is included. It is important to note that both the laboratory-scale single-element and sub-scale multi-element tests are to operate in conditions similar to the full-scale hardware, in order to allow for a validation in the relevant operating range. Using the test data from the simplified configurations, the numerical tools can be validated. Assuming that all relevant conditions are covered in the validation process, the inherent thermochemical complexity of the flow is mastered by the numerical tools and they can be applied to design and predict the performance of the real flight-hardware. Of course, it is important to note that during this scale-up to enlarged dimensions and additional configurational changes, the computational effort needed for the numerical simulations also scales-up. For that reason, a further requirement for a successful numerical tool is the representation of the physical and chemical phenomena while using minimal computational resources. Only this way it can deliver results in time frames short enough to allow actual design and optimization work, especially in the conceptual and design phases [122].

An important step which is usually overlooked in this verification and validation loop, is the validity of the acquired experimental data in the lab-scale and sub-scale experiments. Given that those data are often considered as the "ground truth" and lead to the modification of numerical models, reliable measurements, identification of potential error source and quantification of uncertainties needs to be guaranteed. This should also be possible within the practical limitations enforced by the finite space available for the installation of sensors on the test hardware. Reliable measurements and efficient evaluation algorithms of the raw data for the generation of validation test-cases are therefore equally important as the numerical tools.

Considering that the development of experimental test cases and the derivation and application of numerical models for the description of complex physical phenomena goes hand-in-hand, significant efforts have been placed at the Chair of Space Propulsion (RFA) of the Technical University of Munich (TUM) in order to progress those two aspects simultaneously. Those efforts have mainly been carried out within the Transregio TRR40 project entitled "Fundamental Technologies for the Development of Future Space-Transport-System Components under High Thermal and Mechanical Loads" [127]. One of the objectives of this DFG-funded project was increasing the experience around the propellant combination methane/oxygen for future space applications [128]. Within these goals, the RFA has designed and operated different sub-scale combustion chamber demonstrators ranging from single-element to multi-element configurations, at operating points relevant for real-flight hardware. In the design of the hardware and the chosen operating conditions, it was ensured that characteristic non-dimensional parameters like the chamber Mach number, Reynolds number as well as thermochemical parameters like the Prandtl, Schmidt and Damköhler numbers were kept constant across all chosen hardware and comparable to the ones of full-scale engines as defined by Penner [129].

The present thesis aims at providing new methods and models both to improve the available measurement techniques as well as to allow for more accurate numerical predictions, based on the experimental test cases derived within the TRR40. In both of those topics, the focus lies on the wall heat transfer in methane/oxygen engines, although the methods can be extended to other propellant combinations as well.

First, given the strong coupling between experimental results and numerical simulations presented in Figure 1.11, the challenges associated with the accurate measurement of wall

heat fluxes are described. As a solution fulfilling the requirements for low systematic uncertainty and high computational speed in the evaluation process of experimental data, a framework involving the use of an inverse heat transfer method is presented. The proposed method is developed as part of the RoqFITT code environment, and is applied to a variety of different hardware and operating conditions with varying number of injector elements and cooling types. Apart from the method validation and estimation of the systematic errors based on sample test cases, the use of the method in sub-scale GOX/GCH_4 test cases is found to deliver significant insights into the fluid-dynamic and thermochemical conditions within the combustion chamber. Of major interest are the transient heat loads due to the ignitor operation, as well as the axially and azimuthally evolving heat flux profiles. Accurate knowledge about those spatially and temporally varying loads is crucial for the calibration of hardware lifetime prediction tools and cooling system design.

Second, the development of numerical models and execution of turbulent combustion Computational Fluid Dynamics (CFD) simulations aiming to describe the conditions in the combustion chamber has a central place in the thesis. Due to the complex chemistry of methane/oxygen combustion including slow time-scales and a large number of reacting species, the development of models able to reproduce the energy release in the chamber is targeted in this work. Special focus is placed on the modeling of the near-wall reactions which are induced by the low-enthalpy environment of the cooled walls. Those recombination reactions are found to contribute up to 20% to the wall heat loads and hence their accurate prediction is of significance in the design process of engine cooling components. The effectiveness of the proposed numerical models is then assessed based on comparisons with the experimental measurements obtained with the inverse method.

The outline of the thesis follows this previously described thematic separation. For that reason it is composed of two parts. In the first part, the experimental methods are outlined. Chapter 2 presents an introduction to the heat transfer phenomena that are dominating in typical rocket engines. Various cooling methods and experimental wall heat transfer evaluation techniques including the inverse method are summarized. The results obtained with the proposed inverse methods appear in Chapter 3. The original peer-reviewed publications for the inverse method applied on different types of engines (capacitive and regeneratively cooled, single- and multi-injector) are shown. In the second part, focus is placed on numerical modeling. Starting off with the basic tools required for the description of turbulent combustion within rocket thrust chambers in Chapter 4, recombination reactions close to the wall are examined in Chapter 5. In this chapter, canonical configurations of increasing complexity are presented in order to shed light onto the physics behind the exothermic reactions occurring in the cooled boundary layer. Using the knowledge obtained by those findings, the development and validation of tabulated combustion models able to capture the effects of the recombination reactions is executed in Chapter 6. Finally, Chapter 7 summarizes the key findings of the thesis and stresses the importance of exchange between experimental and numerical studies for the improvement of our prediction capabilities.

Part II

EXPERIMENTAL WALL HEAT TRANSFER MEASUREMENT

It doesn't matter how beautiful your theory is,
it doesn't matter how smart you are.
If it doesn't agree with experiment, it's wrong.

— Richard P. Feynman

2 HEAT TRANSFER MEASUREMENT IN ROCKET ENGINES

The true method of knowledge is experiment.

— William Blake

Obtaining information about the conditions within a thrust chamber during an experimental test can be quite challenging and requires sophisticated instrumentation methods. One of the most accessible quantities characterizing the flow and combustion conditions is the wall pressure. This can be measured with pressure transducers and can be used to quantify the acceleration profile and progress of chemical reactions, as well as the overall combustion efficiency [130].

Due to the harsh environment within a rocket combustor with temperatures exceeding 3500 K however, direct measurements of the flame are not easy to implement. Typically, elaborate measurement techniques can be implemented in lab-scale rocket engines, provided that optical access to the chamber via a transparent window is granted. Among the most widely used non-intrusive optical techniques, OH^* chemiluminescence delivers an indication of the combustion zone and serves as a marker of the heat release rate [131] and has therefore been included in multiple studies of single-element [123, 132–135] and multi-element configurations [136, 137]. Similar qualitative measurements can be performed using CH^* radical chemiluminescence (for hydrocarbon fuels) [138, 139], blue radiation [137, 140] and OH-Planar Laser Induced Fluorescence (PLIF) [141–143]. Shadowgraph imaging is also a commonly employed method, typically used to identify the length of the liquid core and density variations due to shock-wave propagation in the chamber [133, 142, 144–146]. In the case of sub-critical injection conditions, information about the droplet size and velocity distribution can be obtained using Phase-Doppler Interferometry (PDI) [133, 147], while their temperature can be measured with a global rainbow refractometry method [148]. Finally, Coherent Anti-Stokes Raman Spectroscopy (CARS) and Tomographic Laser Absorption Imaging (TLAI) allow for more quantitative measurements of temperature [149, 150] and species concentrations [151], although they have their limitations for large pressures as they become susceptible to collisional line mixing and blending of the spectra [152]. Further disadvantages of using optical access is the limited accessible volume due to a restricted window size, the need for additional window cooling and hence potentially shorter experiment duration.

A further insight into into the flow and thermodynamic conditions within rocket combustion chambers can be obtained using wall heat flux measurements. The profile of the wall heat transfer along the chamber wall is strongly influenced by the propellant combination, operating point, injector geometry and chamber contour. Obtaining precise measurements of the heat flux and comparing between different configurations allows for an improved understanding of the injector/wall interaction, the progress of the chemical reactions and the injector/injector interaction. For a precise design of the experimental setup and the resulting design of flight hardware, it is hence important to understand the parameters that can potentially influence the wall heat transfer.

2.1 HEAT TRANSFER PHENOMENA IN ROCKET ENGINES

The operating principle of chemical rocket engines relies on the acceleration of gases to large exhaust velocities. The energy that becomes available for this acceleration is initially stored in form of chemical energy in the molecular bonds of the propellants. During combustion the chemical energy is released and transformed into thermal energy, increasing the temperature of the reaction products. The higher the energy content of the propellants, the higher the thermal energy will be, that is available to be converted to kinetic energy within the nozzle.

The interaction of the high-enthalpy gas with the chamber wall leads to a heat exchange and the deposition of energy into the liner material. The flow of heat from the gas to the wall is a result of the convective and radiative heat transfer.

2.1.1 *Convective heat transfer*

In rocket engines, forced convection is the main driver for heat transfer from the hot gases to the combustion chamber walls. The temperature gradient between hot gas and cooled wall causes a heat flux $\dot{q}$ which is described by Newton's law of cooling:

$$\dot{q} = h_{hg} \cdot (T_{aw} - T_w) \tag{2.1}$$

where h_{hg} stands for the heat transfer coefficient, T_{aw} the adiabatic wall temperature and T_w the actual wall temperature of the chamber.

T_{aw} is the temperature that the chamber wall would relax to in case the walls were adiabatic ($\dot{q} = 0$). Within the chamber, the total temperature of the gas is equal to T_{tot} and the static temperature equal to T. Given the Mach number of the fluid within the chamber Ma and the isentropic exponent of the gas κ, the relationship between T_{tot} and T is simply

$$T_{tot} = T \cdot \left(1 + \frac{\kappa - 1}{2} \cdot Ma^2\right) \tag{2.2}$$

In the boundary layer, where the velocity and hence the Mach number drop to zero, the temperature relaxes to T_{tot} if the assumption of ideal isentropic flow is made. In rocket engines however, the total temperature is not fully recovered at the wall. Due to radiative heat transfer within the boundary layer the resulting adiabatic wall temperature is always slightly below T_{tot} [153]. The difference between total temperature and adiabatic wall temperature is quantified by the recovery factor η_r:

$$T_{aw} = T \cdot \left(1 + \eta_r \cdot \frac{\kappa - 1}{2} \cdot Ma^2\right) \tag{2.3}$$

The recovery factor for turbulent flows is typically modeled as $\eta_r = \sqrt[3]{Pr}$, where Pr represents the Prandtl number of the flow. For practical purposes, since the Prandtl number is close to unity, the assumption $T_{aw} \approx T_{tot}$ can be made.

The heat transfer coefficient depends on the flow quantities like local fluid velocity, the thermodynamic and transport properties of the fluid such as specific heat capacity c_p, density ρ, viscosity μ, thermal conductivity λ.

In an effort to describe the average expected wall heat transfer coefficient and therefore heat flux as a function of the gas thermochemical state and flow properties, empirical correlations have been derived. Those correlations typically make use of the three dimensionless characteristic parameters that define heat transfer:

- Prandtl number $Pr = \frac{\mu \cdot c_p}{\lambda}$
- Reynolds number $Re = \frac{\rho \cdot u \cdot d_h}{\mu}$
- Nusselt number $Nu = \frac{h \cdot d_h}{\lambda}$

The Prandtl number Pr is defined as the ratio of momentum diffusivity to thermal diffusivity, the Reynolds number Re is the quotient of inertial forces to frictional forces, while the Nusselt number Nu is the ratio of convective heat transfer and diffusive heat transfer. The derived empirical correlations have the form

$$Nu = C \cdot Re^n \cdot Pr^m \cdot f_{correction} \tag{2.4}$$

where C, n and m are fitting parameters and $f_{correction}$ represents correction functions including the effects of curvature and boundary layer development. It is important to note that those correlations have been tailored based on experimental data for hydrogen, kerosene and MMH/NTO tests. Typically the composition corresponding to chemical equilibrium is taken to calculate the thermodynamic properties of the mixture. They are a crude approximation and are agnostic to the type of injector and hence to flow-dynamic phenomena like velocity and momentum ratios, injector/injector interaction, chemical reaction time-scales and other effects like the wall roughness that have shown to strongly affect the heat transfer. With those simplifications, the correlations are used as a first order approximation of the expected fluxes in the early design phase.

One of the most widely used correlations is the one derived by Bartz [154]. By using the definition of the characteristic velocity c^*:

$$c^* = \frac{p_{ch} \cdot A_{th}}{\dot{m}} \Rightarrow \rho \cdot v = \frac{\dot{m}}{0.25 \cdot \pi d_h^2} = \frac{p_{ch} \cdot d_{th}^2}{c^* \cdot d_h^2} \tag{2.5}$$

the Bartz formula can be written as:

$$h_{hg} = 0.026 \cdot \left(\frac{p_{ch} \cdot d_{th}^2}{c^* \cdot d_h^2} \right)^{0.8} \cdot \left(\frac{\mu c_p}{\lambda} \right)^{0.4} \cdot \left(\frac{d_{th}}{r_{tc}} \right)^{0.1} \cdot \Sigma \tag{2.6}$$

where d_{th} stands for the throat diameter and r_{tc} the curvature radius in the nozzle. In the original formulation, the factor Σ was equal to 1, but in an updated version, the factor was included in order to incorporate the effect of the temperature gradient in the boundary layer and the influence of the Mach number [155].

$$\Sigma = \left[\frac{1}{2}\cdot\frac{T_w}{T_{aw}}\left(1+\frac{\kappa-1}{2}Ma^2\right)+\frac{1}{2}\right]^{-0.68}\left[1+\frac{\kappa-1}{2}Ma^2\right]^{-0.12} \tag{2.7}$$

The proportionality of the heat transfer coefficient to the chamber pressure is hence evident.

$$h_{hg} \propto p_{ch}^{0.8} \tag{2.8}$$

Although the Bartz correlation is not the only empirical formula for heat transfer rate prediction, the close-to-linear dependency between heat transfer rate (and therefore heat flux) and chamber pressure is representative of all available formulas. In the works of Schacht et al. [156] and Sinyarev et al. [157], although the pre-factors, correction functions and reference temperature are different than in the work of Bartz, the pressure exponent is reported equal to 0.8 and 0.82 respectively.

Despite the simplifications used in the derivation of the Nusselt number correlations, they are able to capture some of the basic dependencies. Figure 2.1 shows a summary of the maximal measured heat flux in various high pressure LOX/LH_2 rocket engines. The experimentally determined pressure scaling seems to be in agreement with the first-order approximation presented in Equation 2.8.

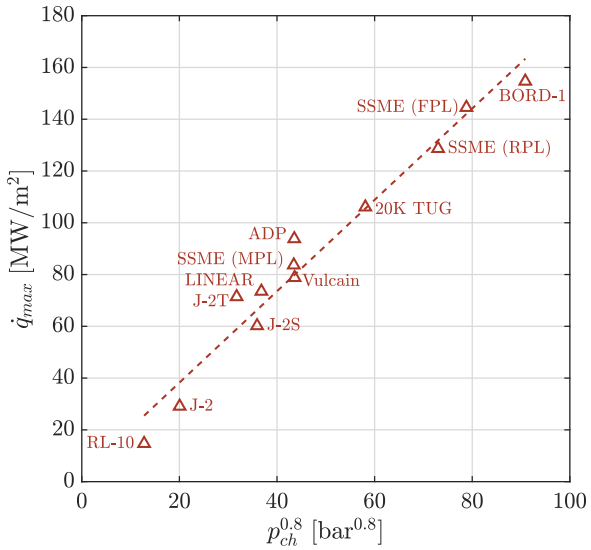

Figure 2.1: Throat peak heat flux trend for selected LOX/LH_2 engines. For the SSME: Minimum Power Level (MPL), Rated Power Level (RPL) and Full Power Level (FPL). (Adapted from Pempie [158]).

2.1.2 *Radiative heat transfer*

Within a rocket thrust chamber, radiative heat transfer takes place from the hot gas to the face-plate and to the chamber wall. The significance of the radiative heat transfer on the total heat transfer depends on the hot gas temperature, the composition of the products as well as geometry and material of the chamber wall.

The main reaction products that have been identified as strong radiation emitters are water and carbon dioxide. In the case of hydrocarbon engines, additional products like carbon monoxide are usually disregarded despite their large concentration, as their radiosity is at least one order of magnitude than the one of carbon dioxide [159, 160].

The analysis of radiative heat transfer is a very complicated part of heat transfer calculations as it requires the solution of radiative transfer equations that depend on spatial, directional and spectral variables [161]. Analytical and empirical formulas for the quantification of the heat deposition via radiative transfer have been proposed in order to quantify this contribution in the design process of engines. Barrére et al. [162] proposed a model for water and carbon dioxide given in Equation 2.9 and Equation 2.10.

$$\dot{q}_{rad,\mathrm{H_2O}} = 4.07 \cdot \left(p_{\mathrm{H_2O}}\right)^{0.8} \cdot \left(L_{eff}\right)^{0.6} \cdot \left(\left[\frac{T_{aw}}{100}\right]^3 - \left[\frac{T_w}{100}\right]^3 \right) \tag{2.9}$$

$$\dot{q}_{rad,\mathrm{CO_2}} = 4.07 \cdot \left(p_{\mathrm{CO_2}} \cdot L_{eff}\right)^{0.33} \cdot \left(\left[\frac{T_{aw}}{100}\right]^{3.5} - \left[\frac{T_w}{100}\right]^{3.5} \right) \tag{2.10}$$

where $p_{\mathrm{H_2O}}$ and $p_{\mathrm{CO_2}}$ are the partial pressures of the two radiating gases in the chamber and L_{eff} the effective radiation path. Models proposed by Schack [163, 164] have a similar dependency on the partial pressures, radiation path and temperature, with the temperature exponent ranging from 3 to 3.5.

More recent computational studies have been carried out in order to quantify the magnitude of the radiative contribution compared to the total wall heat transfer. Wang et al. [165] reported that the computed radiative heat flux is two orders of magnitude lower than the convective one in H_2/O_2 engines. Badinal et al. [166] found that the radiative heat flux could be important in the presence of shocks in the nozzle, as the Mach disk's high temperature increases the emissions, while the radiation could be neglected in shock-free flows. Goebel et al. [161] performed simulations of CH_4/O_2 and H_2/O_2 sub-scale and full-scale configurations and estimated the radiative fraction of the total heat flux to amount to 3%-5% for both propellant combinations using a non-homogeneous Weighted Sum of Gray Gases Model. Finally, in hydrocarbon engines operating in the fuel-rich regime, where soot is potentially formed, the soot particle radiation could be in the same order of magnitude as the radiation stemming from the gas-phase, but there is still large uncertainty in the estimation of the soot's molar concentration [167, 168]. The research findings support in general that the most dominant contribution to the wall heat flux is induced by the convective heat transfer.

2.2 COOLING METHODS

As Figure 2.1 shows, typical values of heat fluxes for the Vulcain main engine at 115 bar chamber pressure are up to 80 MW/m^2 and for the Space Shuttle Main Engine at 205 bar reach values close to 160 MW/m^2 [169]. Although higher pressures are favorable from a performance standpoint, their feasibility can be limited due to a continuous increase in expected heat flux levels. The reliable operation of rocket combustion chambers at such high thermal and mechanical loads is achieved by highly efficient cooling.

2.2.1 *Capacitive cooling*

Capacitive cooling (also called heat-sink cooling) is a passive cooling method, where the heat transferred to the chamber walls, diffuses into the structure and increases its temperature. In order for this method to be effective, a large thermal conductivity of the chamber material is required to diffuse the heat away from the hot gas wall, as well as a large heat capacity and density, to ensure a large heat-pickup without exceeding the operational temperature of the material. Copper alloys are typically used as they fulfill those requirements.

The temperature increase within the material is simply given by Fourier's law of heat conduction:

$$\frac{\partial T}{\partial t} = \frac{\lambda}{\rho c_p} \nabla^2 T \tag{2.11}$$

This leads to a transient temperature profile which does not reach steady state during the hot-run. The maximal testing duration is hence limited to ensure the thermal and mechanical integrity of the chamber liner. This fact, combined with the bulky dimensions of capacitive hardware (to ensure a sufficiently large heat-sink), renders the cooling method impractical for flight-hardware and it is therefore only used in laboratory-scale experimental combustors.

2.2.2 *Radiation cooling*

Cooling by radiative heat transfer is employed in small engines like the ones used for attitude and orbital control in satellite systems or in nozzle extensions of upper-stage engines. The operating principle relies in radiation of the hot-gas convective heat flux into the ambient. The heat flux radiated from the external wall of the thrust chamber is described by Equation 2.12.

$$\dot{q} = \sigma \cdot \mathcal{E} \cdot \left(T_w^4 - T_\infty^4 \right) \tag{2.12}$$

The performance increases with higher emissivity values $\mathcal{E}$ of the nozzle material and higher wall temperatures. In Equation 2.12, σ is the Stefan-Boltzmann constant and T_∞ is the ambient temperature. The materials chosen have to withstand large temperatures. Due to the practical limits in the acceptable material temperatures, the transmittable heat flux is limited.

2.2.3 *Ablative cooling*

Ablative material is designed to slowly burn away in a controlled manner, so that heat can be removed from the wall by the gases generated by ablation. Combustion gas-side wall material is hence sacrificed by melting, vaporization and chemical changes to dissipate heat. As a result, relatively cool gases flow over the wall surface, thus lowering the boundary-layer temperature and assisting the cooling process. In many applications, in-depth material pyrolysis (charring) and thermochemical surface ablation are the chosen methods of cooling. As the material is heated, one or more components of the original composite material pyrolyze and yield a pyrolysis gas and a porous residue. Due to the change in geometry and material properties, ablative cooling is not suitable for reusable engines as the cost of refurbishment is high.

2.2.4 *Film cooling*

Film cooling consists of injecting a fluid that is colder than the combustion gases close to the wall, in order to lower the temperature in the thermal boundary layer. The film coolant can be pure fuel or turbine exhaust gases from e.g. a gas generator and can hence be in a liquid, trans-critical or gaseous form. The film application occurs either via slots and holes or by changing the mixture ratio of the outer injectors towards fuel-rich conditions in a process called injector trimming.

The efficiency of film cooling Θ correlates wall temperatures with and without film cooling:

$$\Theta = \frac{T_{w,no\,film} - T_{w,film}}{T_{w,no\,film} - T_{film}} \tag{2.13}$$

This cooling method is usually applied in small satellite engines where the expected heat loads are small enough or as a secondary cooling system, complementing the regenerative cooling in larger engines. Losses are introduced to the system as the coolant mass flow may not at all or only to some extent take part in the combustion process leading to a decrease in combustion performance.

2.2.5 *Transpiration cooling*

Transpiration cooling is very similar to film cooling with the difference that the coolant is injected through a perforated or porous wall. This way, the heat exchange between hot gas stream and chamber wall is dampened by the existence of a thin coolant film, covering the wall's surface. Moreover, additional heat transfer takes place between the porous wall and the coolant flowing through it. Despite several experimental and numerical studies involved in the understanding of the flow-dynamic phenomena present in transpiration cooling, this method has not been yet employed in flight hardware.

2.2.6 *Regenerative cooling*

For high performance rocket engines with large operating pressures, such as the ones powering the main and upper stages of rocket launch system, regenerative cooling is deployed in order to maintain an acceptable wall temperature and avoid mechanical failure of the hardware. In regenerative cooling, one or two of the propellant components (most commonly the fuel) flow through cooling channels along the combustion chamber and nozzle wall, absorbing part of the heat resulting from combustion.

As the regenerative cooling operates very similar to a heat-exchanger, the coolant temperature is increased during its passing through the cooling channels. In the case of closed regenerative cooling, the heated propellants are injected into the main chamber, thereby keeping the energy loss to a minimum. The higher injection temperature is often favorable for combustion efficiency[1]. In expander cycles, the heat pick-up is also used to drive the turbopumps and hence an efficient extraction of thermal energy via the coolant is crucial for the system design. Typically, high specific heat capacity and thermal conductivity are desired for the coolant, combined with a low viscosity to minimize the pressure losses. Furthermore, possible thermal decomposition of the coolant and soot formation are factors that have to be considered. In experimental sub-scale engine tests, distilled water is also chosen as a coolant in order to simplify the setup.

The heat transfer from between the wall and the coolant is given by

$$\dot{q} = h_{cc} \cdot (T_w - T_{cc}) \tag{2.14}$$

where h_{cc} is the heat transfer coefficient of the coolant, T_{cc} is the temperature of the coolant in the channels and T_w the temperature of the channel walls.

Nusselt number correlations are typically employed for the estimation of h_{cc} and hence a first-order calculation of the absorbed heat fluxes based on Equation 2.14. The used correlations are derived from models for pipe flows but specific corrections tailored to flows for rocket cooling channels have been proposed.

One of the correlations that has been successfully applied for rocket cooling channels in the past is the one by Kraussold [170]. It reads:

$$Nu = 0.024 \cdot Re^{0.8} Pr^{0.37} \tag{2.15}$$

Additional corrections accounting for the effects of flow development and channel curvature have been proposed in the original work.

Similar correlations have been proposed by McAdams [171], and Gnielinski [172] for general pipe flows. More tailored formulas have been derived for hydrocarbon fuels by NASA [173–175], while Liang et al. [19] delivered a comprehensive literature review for correlations that are suitable for methane, propane and kerosene as coolants.

1 At the same time, higher injection temperatures could be unfavorable for the robustness of the system, when the combination of the injection pressure and temperature is close to the critical point. This is due to the large sensitivity of the fluid density on the thermodynamic state close to the critical conditions, which can lead to sharp changes in the injection velocity and which can subsequently influence the combustion stability.

The flow within the cooling channels is intrinsically three-dimensional due to the presence of secondary flows induced by the curvature of the thrust chamber contour and the asymmetric heating that leads to thermal stratification [176, 177]. Moreover, the aspect ratio is also significantly influencing the heat transfer from the chamber wall into the coolant, as it modifies both the flow pattern and the effective area of the coolant fins [178]. Additional effects like heat transfer deterioration in supercritical coolants [37, 179] and heat transfer enhancement via wall roughness [180, 181] also have to be considered.

As the 1D simplified formula in Equation 2.14 deals with homogeneous coolant temperature and neglects two- and three-dimensional effects, correction factors are usually employed in order to include corrections for wall roughness, curvature, stratification and the non-symmetrical heating of the cooling channel. For more accurate predictions however, 3D conjugate heat transfer simulations are usually performed, as they can include a larger amount of physical phenomena without the need for empirical corrections. Efforts are also being placed in replacing the use of Nusselt number correlations by artificial neural networks that take the multi-dimensional dependence of the heat transfer coefficient into account [182]. The development of such models however requires a large amount of data from high-fidelity simulations and experimental tests.

2.3 HEAT FLUX MEASUREMENT

The heat flowing from the gas products to the chamber wall is a quantity of vital importance for the design of the chamber and its sub-systems. For an optimal design of the cooling systems with minimum pressure losses the precise knowledge of heat transfer processes along the engine wall is required. In the case of the expander cycle, the wall heat flow dictates the available power to drive the turbopumps and hence the ability to predict the engine's performance is strongly coupled to the prediction ability of the heat fluxes. For reusable engines, life cycle estimation heavily depends on the accuracy of heat flux and wall temperature prediction, with an error of 40 K leading to 50% life reduction [183]. For the validation of the predictive numerical tools, which are used for engine lifetime estimations, a reliable experimental database is required, as explained in Figure 1.11. Also, apart from the implications it has on the cycle performance, cooling design and engine lifetime, the wall heat flux also serves as a footprint of the combustion processes which can be captured by installing sensors. This way it can convey information about the conditions within the chamber and the characteristics of sub-components such as the injector performance.

It is important to note the two-dimensional variability of the hot gas flow both in axial and circumferential direction. Typically, the axial development is influenced by the progress of the chemical reactions, while in circumferential direction the heat transfer varies due the variation of flow composition and temperature in the stratified flow especially near to the injector plate.

Those considerations result to the need for realistic, high-spatial resolution experimental heat transfer data at representative conditions, both at hot gas and at coolant side, for the determination of thermal loads of specific configurations as well as for the validation of numerical design tools. In the following sections, the most widely applied methods for heat transfer measurement in sub-scale thrust chambers will be presented along with some notable studies that employed each technique.

2.3.1 *Calorimetric method*

As a regenerative cooling system is employed for the majority of sub-scale demonstrators, information of the coolant heat pick-up can be readily obtained by measuring the inlet and outlet pressure and temperature of the cooling fluid. The increase in coolant enthalpy H corresponds to the average wall heat flux as Equation 2.16 shows.

$$\dot{q} = \frac{\dot{m}_{cc}}{A_w} \cdot (H(p,T)_{out} - H(p,T)_{in}) \tag{2.16}$$

As expected, a limited resolution is obtained with the calorimetric method, as it typically results in an azimuthally and axially averaged heat flux. An increase in the axial resolution can only occur by increasing the number of cooling segments, which typically leads to additional manufacturing costs and system complexity.

Nevertheless, axial heat flux profiles obtained via the calorimetric method can be used for identification of injector and film cooling performance as well as for a quantitative comparison with numerical simulations despite the restricted resolution. As early as in the 1960s, Welsh et al. [184] carried out experiments in a water-cooled rocket thrust chamber using NTO and hydrazine as propellants. The nozzle was equipped with 14 to 23 cooling segments allowing for a very high axial resolution. The results obtained for different injector and chamber configurations were then compared to the values predicted by the Bartz correlation [154], leading to a satisfying agreement for most examined load points. Studies in kerosene/oxygen combustion were performed by Kirchberger et al. [153, 185] and Schlieben et al. [186] using a single double-swirl injection element and four water-cooled chamber segments. Kerosene film and water film efficiencies were derived, which allowed for comparisons with numerical studies [187]. Further kerosene/oxygen studies with calorimetric heat flux measurement have been carried out by Masters et al. [188] and Ahn et al. [189].

Within the ISP-1 program, methane/oxygen combustion was investigated both experimentally and numerically in a sub-scale chamber with 15 coaxial injectors [190]. The 6 water-cooled chamber segments provided information about the wall heat flux, thereby quantifying the performance of the employed film cooling and the injector-wall interaction. Similar studies with the purpose of extracting wall heat flux data for the validation of numerical tools were performed by Silvestri et al. [125, 191, 192], where GCH_4/GOX combustion was investigated in a 7-element combustion chamber. The data provided by the five water-cooled segments was utilized to characterize the injector performance and to compare between different pressure levels and mixture ratios. The experimental test cases defined within this campaign, were used as a benchmark for several numerical studies by groups in industry and academia [193–195]. Finally, calorimetric heat flux results of a 19-element LOX/LH_2 using a 20-segment water cooling system have been reported by Preclik [196] and have been used to examine the validity of real-gas equations of state and wall heat transfer models by Masquelet et al. [197].

2.3.2 *Gradient method*

One of the simplest methods used in experimental rocket thrust chambers for the evaluation of the wall heat flux is the gradient method, which relies on the installation of two or more

temperature sensors at different radial positions r_1 and r_2 within the chamber wall. Using the assumption that the heat transfer within the material is in steady state, the analytical formula for the heat flux can be used, which is shown in Equation 2.17 for rectangular chambers and in Equation 2.18 for cylindrical chambers.

$$\dot{q} = \lambda \cdot \frac{T(r_2) - T(r_1)}{r_2 - r_1} \tag{2.17}$$

$$\dot{q} = \lambda \cdot \frac{T(r_2) - T(r_1)}{r_{ch} \cdot \ln(r_1/r_2)} \tag{2.18}$$

Due to the simplified instrumentation required for this method, a much smaller sensor spacing than in the calorimetric method can be obtained, while the resolution of heat flux is not restricted to only axial profiles but allows for azimuthal information extraction as well. However the use of equations Equation 2.17 and Equation 2.18 implies that the system is in temporal thermal equilibrium and that the influence from the presence of cooling channels is negligible. The validity of the second condition is analyzed in detail in Section 3.2.

Despite its shortcomings, the simplicity and minimal computational cost of the method makes it attractive for use in sub-scale engines. Suslov et al. [198] utilized 5 radially distributed thermocouples for the measurement of heat flux in a oxygen/hydrogen engine with regenerative cooling and LH_2 as well as water as coolants. Comparisons to the calorimetric method were also performed, demonstrating a fourfold increase in axial resolution [199]. Arnold et al. [200] employed a gradient method to evaluate typical film-cooling parameters such as film blowing rate, velocity ratio between film injection velocity and hot-gas velocity, circumferential slot positioning, and film injection slot in a LOX/GH_2 sub-scale engine at pressures up to 115 bar. In the same tests, a rotation of the hardware in azimuthal direction allowed for a two-dimensional thermal field measurement throughout the combustion chamber and to describe the circumferential behavior of wall temperature distribution and film cooling effectiveness [201].

2.3.3 *Transient method*

The transient method is the method of choice for test specimen with no active structural cooling but rather capacitive cooling, where the temperature field does not reach a steady-state. This implies a simple hardware design in the absence of regenerative cooling but also restricted test duration due to the thermal limits of the chamber material. In those types of laboratory-scale combustors, the instantaneous rate of change of temperature can be used as an indicator for the heat flux. The method requires the definition of the control volume which includes a thermocouple. Within this control volume with volume V_{CV}, it can be assumed that the temperature change at the sensor location is representative of the complete control volume. The wall heat flux is then given by:

$$\dot{q} = \frac{\rho V_{CV} c_p}{A_w} \cdot \frac{dT}{dt} + \dot{q}_{loss} \tag{2.19}$$

The factor $\dot{q}_{loss}$ stands for the heat flux that exits the control volume and does not contribute to the rise of its temperature.

Locke et al. [202] tested LOX/GCH4 single-element injectors over a range of pressure (20-80 bar) and mixture ratio (2.5, 3.0, 3.25) conditions and evaluated the heat flux using a multinode discretized transient method. This assumed axisymmetric heating and negligible longitudinal conduction and was used with the purpose of providing wall heat flux results that are valuable for both injector design and CFD code validation. Droppers et al. [203] carried out heat flux measurements in an oxygen/hydrogen model combustor using coaxial thermocouples which utilize a similar transient calculation method for the heat flux [204]. Celano et al. [205] utilized a zero-dimensional transient method in order to evaluate the axially evolving heat flux in a rectangular single-element chamber operating with GOX/GCH_4. For the estimation of the loss heat flux $\dot{q}_{loss}$, a shape factor for the control volume as well temperatures at different radial distances from the hot gas wall were employed. However, the obtained results showed too high heat flux levels compared to more elaborated methods. The transient method suffers from higher uncertainties and produces large systematic errors when the gradient of the temperature within the volume becomes too strong, since it is assumed that the complete control volume is subject to the same variation of temperature over time as in the measurement position.

2.3.4 *Inverse heat transfer method*

One of the most sophisticated methods of estimating wall heat loads in rocket thrust chambers is the use of inverse methods. These methods require the installation of thermocouples at different locations within the chamber material, similar to the gradient and transient techniques. The basic principle behind the use of most inverse methods is the iterative update of the unknown boundary conditions with the aim of minimizing the error between computed $\mathbf{T}_{comp}$ and measured $\mathbf{T}_{meas}$ temperature at the M sensor locations. This is mathematically formulated as the minimization of the residual function J [206]:

$$J = \frac{1}{M} \cdot \left[\mathbf{T}_{meas} - \mathbf{T}_{comp}\right]^T \left[\mathbf{T}_{meas} - \mathbf{T}_{comp}\right] \tag{2.20}$$

At each iteration step, the heat transfer problem is solved via Finite Difference Method (FDM), Finite Volume Method (FVM) or Finite Element Method (FEM), using the boundary values from the previous iteration. Based on the difference between the newly calculated temperature field and the experimentally measured temperature values, the boundary conditions are updated until convergence is reached. The method can be applied both for the solution of transient and steady-state problems and it can lead to the estimation of not only the hot gas wall heat flux but also the wall heat transfer coefficient in the cooling channels.

Outside of rocket combustors, inverse methods have been applied successfully in various engineering applications ranging from solar tower power plants [207], mold casting [208], internal combustion chambers [209], sounding rockets [210] and induction heating [211]. Although all methods have in common that an optimization of the unknown boundary conditions is carried out, the exact methods for finding the optimal solution are quite diverse. Studies can be found in literature including classical optimization based on adjoint methods [212], conjugate gradient methods [209], Newton-Raphson method [213],

Levenberg Marquardt algorithm [214, 215], genetic algorithms [216, 217], neural networks [208] as well as non-iterative boundary element methods [218, 219] and non-iterative finite element methods [220]

In rocket propulsion applications, inverse methods have the benefit of potentially requiring a lower degree of modeling and abstraction compared to other methods (and hence a lower number of potential sources of bias) while at the same time allowing for a temporal, axial and azimuthal resolution of the wall heat loads. Schacht et al. [156] calculated experimental heat flux distributions in oxygen/hydrogen rocket engines using an iterative method that minimized the error between the measured temperature and the one predicted by an analytical one-dimensional semi-infinite slab formula. In the work by Kuhl et al. [221] the solution of the transient heat conduction problem in a 2D domain was carried out with the optimization taking place via a conjugate direction method. This resulted to the simultaneous estimation of hot gas wall heat flux and coolant heat transfer coefficient for distinct axial locations. Suslov et al. [222] investigated the film cooling performance in a LOX/H_2 subscale combustion chamber using a similar method. A good agreement was obtained compared to the calorimetric heat flux evaluation, albeit having a 6 times finer axial resolution with the inverse results. Using a similar hardware as in the study by Suslov et al. [198], Haemisch et al. [36] employed an inverse heat transfer method to investigate heat transfer deterioration within cooling channels with cryogenic methane as coolant. Using the same hardware, Haemisch et al. [223] also examined the effects of thermal stratification in high aspect ratio cooling channels and derived Nusselt number correlations both for hydrogen and methane. Wang et al. [214] presented transient and axial profiles of wall heat flux in a capacitively cooled GO_2/GH_2 multi-element chamber. Celano et al. [205, 224] applied a conjugate gradient method in a three-dimensional domain to derive temporally and axially varying heat loads in single-element and multi-element GOX/GCH_4 rocket thrust chambers. Those were ultimately used as test cases for the validation of numerical tools [225–229]. Additional optical diagnostics data provided by Winter et al. [123] complemented the inverse heat flux data for operating pressures at 10 and 20 bar.

2.4 UNCERTAINTY QUANTIFICATION

In order to ensure a reliable set of experimental data that can be used for the prognosis of cycle performance, the optimal design of thrust chamber components and the validation of numerical tools, the uncertainty associated with the experimental procedures has to be quantified.

In the case of heat flux measurement, the relative uncertainty connected to the measurement $\dot{q}_{err}$ has been found to increase with larger heat flux levels. This is demonstrated in Figure 2.2, which has been adapted from the work by Oschwald et al. [230]. The values reported in the figure include various technological applications that required heat transfer measurement and are not restricted to rocket engines. As a reference, the heat fux levels of the Vulcain 2 and SSME engines are also shown. Given the nearly linear dependence of heat flux on pressure seen in Figure 2.1, it is expected that a large uncertainty is associated with measurements of representative rocket hardware. The reasons for the proportionality between heat flux level and relative uncertainty mainly has its roots on the increase in temperature gradients that occur within the chamber wall for larger heat loads.

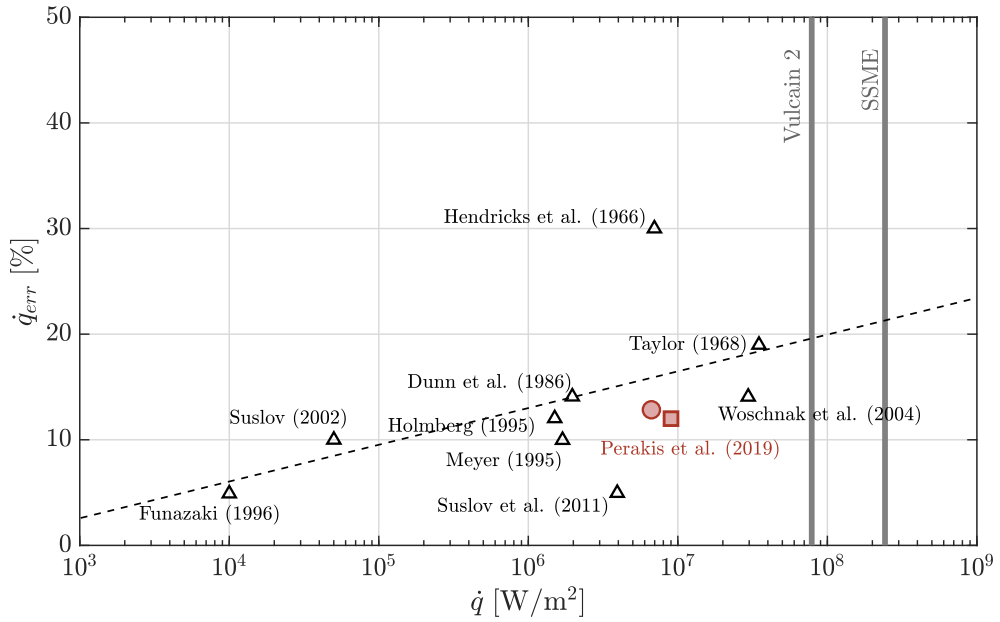

Figure 2.2: Measurement uncertainty in heat transfer experiments from various technological applications. (Adapted from Oschwald et al. [230]).[2]

However, the type of heat flux measurement also influences the source of error. When examining the most commonly used methods that have been presented in Section 2.3, different error sources can be identified. In the case of calorimetric evaluation, the main uncertainties stem from the mass flow metering and the temperature measurement in the coolant. In the case of fluids with strong thermophysical properties variations within the cooling channels such as cryogenic hydrogen, the influence of the temperature error is larger than for coolants with more linear properties such as water. The studies by Suslov et al. [222] and Woschnak et al. [231] included in Figure 2.2 mainly deal with those measurement uncertainties. In the work by Hendricks et al. [232] however, the high nickel content in test sections could have acted as a good catalyst for conversion of para- to ortho-hydrogen, leading to a coolant mixture with unknown properties and thereby increasing the systematic measurement error.

In the inverse and gradient methods, the main source of error is introduced by the accuracy and the correct placement of the thermocouples. Due to the large thermal gradients in the vicinity of the hot gas wall and the cooling channels, any temperature error is amplified leading to a very large uncertainty for the calculated heat flux. As the thermal contact between temperature sensor and chamber material as well as the exact positioning cannot always be determined with accuracy, systematic errors are expected and have to be quantified. Additional sources of error are the material properties of the chamber (mainly the thermal conductivity) and the response time of the thermocouples in the case of temporal heat flux profile estimation. Finally, when the heat transfer coefficient in the cooling channels is not directly measured but rather modeled, then an additional uncertainty arises depending on the choice of modeling approach.

2 The data points in Figure 2.2 are extracted from: Perakis et al. [213, 233], Funazaki [234], Dunn et al. [235], Holmberg et al. [236], Taylor [237], Meyer [238], Hendricks et al. [232], Suslov et al. [222, 239] and Woschnak et al. [231].

The sources of error explained in the previous paragraph are elaborated in detail in Section 3.1 and Section 3.3. The resulting uncertainty in the case of capacitively and regeneratively cooled engines has been included in Figure 2.2 with the red markers.

3

INVERSE HEAT TRANSFER PAPERS

It doesn't make a difference what temperature a room is,
it's always room temperature.

— Steven Wright

3.1 CAPACITIVELY COOLED ROCKET THRUST CHAMBERS

The development of an inverse method for the evaluation of experimental heat flux data in capacitive hardware is presented in this section. The passage corresponds to the paper entitled:

Inverse Heat Transfer Method Applied to Capacitively Cooled Rocket Thrust Chambers
Nikolaos Perakis, Oskar J. Haidn
International Journal of Heat and Mass Transfer (2019)
doi: https://doi.org/10.1016/j.ijheatmasstransfer.2018.11.048

As explained in Section 2.3.4, inverse methods for capacitive hardware have been successfully implemented in the past for rocket engine applications. In the present work, a 3*D sensitivity-matrix* based method has been developed and applied for the evaluation of *transient* temperature data.

The method has been developed within the code framework of RoqFITT: *Rocket q̇ Flux Inverse Thermal Tool*. The tool has the capability of performing wall heat flux and structural temperature evaluation given a sufficient number of thermocouple measurements. Due to the 3D nature of the computational domain used in the code, *both axially and azimuthally varying loads* can be resolved. This effect, combined with the transient capability of the tool, leads to a framework able to carry out the analysis of any experimental hardware with capacitive cooling, *independently of the number of injectors*.

Despite the use of a 3D domain, the *computational efficiency* of the chosen optimization method allows for short run-times. As each load point corresponding to test durations of approximately 3 seconds can be analyzed with a computational cost of 0.5 to 4 CPUhs, the tool can be applied in a batch mode to characterize the heat flux of multiple tests. The low computational cost arises from the use of a sensitivity matrix optimization, which converges within 10-15 iterations when combined with a Newton-Raphson method. A significant speed-up is provided by the calculation of this sensitivity matrix outside of the optimization loop by taking advantage of the linearity of the problem.

As described in the following paper, after a successful validation of the code, the method has been utilized to examine the experimental heat loads in three separate hardware: a round single-element chamber, a square single-element chamber and a rectangular multi-element chamber. For all three of the configurations, comparisons between the obtained heat

flux distributions has allowed for the understanding of the *injector performance and dynamics* and a description of the injector/wall interaction for different propellant combinations as well as for different pressures and mixture ratios.

In fact, apart from the examination of the steady-state results, the method has allowed for an analysis of the transient effects occurring during the engine start-up. Specifically, the *influence of the igniter* on the wall is a further effect that can be extracted from the results. Based on this analysis it was confirmed that the operation of the igniter leads to an additional heat deposition to the walls, which was quantified as a function of time.

Moreover, in the case of the multi-element chamber, where the use of a 3D domain is necessary, it was the first time that an inverse method was employed to obtain the heat flux profiles *in circumferential direction* as a result of the injector/injector interaction. As the experimental setup described by Celano et al. [224] allowed for temperature measurements both above and between injector elements, the heat load variation perpendicular to the flow direction was estimated.

However, this analysis also helped quantify the uncertainties associated with the heat flux measurement. Due to the large thermal gradients present in the first millimeters away from the hot gas wall, *inaccuracies in the placement of the thermocouples* lead to an amplified error in the heat flux evaluation. A large contributor to this effect is also the large thermal conductivity of the liner material, which leads to a large sensitivity of the temperature with respect to the wall heat flux. By accounting for the positioning error as well as additional sources of systematic uncertainties such as sensor accuracy, precision and response delay time and chamber material properties, the total expected error of the measurement was estimated. This amounts to approximately 10% for the chosen inverse method. In order to reduce the uncertainty related to the positioning of the thermocouples, the installment of multiple sensors for the same axial location at different wall distances is recommended. This way the statistical deviations in the exact installment position can be reduced.

International Journal of Heat and Mass Transfer 131 (2019) 150–166

Contents lists available at ScienceDirect

International Journal of Heat and Mass Transfer

journal homepage: www.elsevier.com/locate/ijhmt

Inverse heat transfer method applied to capacitively cooled rocket thrust chambers

Nikolaos Perakis *, Oskar J. Haidn

Technical University of Munich, Chair of Turbomachinery and Flight Propulsion, Boltzmannstr. 15, 85748 Garching, Germany

ARTICLE INFO

Article history:
Received 9 August 2018
Received in revised form 16 October 2018
Accepted 9 November 2018

Keywords:
Inverse method
Rocket engine
Methane combustion
Heat transfer

ABSTRACT

Measurements of the heat loads in experimental lab-scale rocket combustors are essential in order to obtain information about the mixing and energy release of the propellants, the injector/injector interaction as well as the injector/wall interaction. Usually the hardware used for single-element rocket thrust chambers is capacitively cooled in order to reduce the complexity of the system. The present work demonstrates an efficient method for estimating the time- and spatially resolved heat flux distribution at the hot gas wall of such engines using the information provided by temperature measurements in the material. The method is implemented in the code RoqFITT (Rocket q̇ Flux Inverse Thermal Tool) and is applied for the evaluation of test data of CH_4/O_2 and H_2/O_2 experiments. Three separate capacitive combustors are investigated, which are operated at the Chair of Turbomachinery and Flight Propulsion (LTF) of the Technical University of Munich (TUM): a single-element cylindrical, a single-element rectangular and a multi-element rectangular chamber. The use of the 3D inverse method for different load points gives significant information about the effect of the different propellant combinations, the choice of mixture ratio and pressure level, the spanwise heat flux distribution and hence injector/injector interaction as well as the transient effects during the igniter operation.

1. Introduction

The development process of new hardware and introduction of new technologies for rocket engines usually requires the design and testing of sub-scale engines. Specifically, before the design of full-scale engines, tests using single-element and multi-element sub-scale hardware are performed [1–4]. The knowledge about the performance of the injector elements, i.e. the mixing of the propellants, the injector/injector interaction and injector/wall interaction in the sub-scale experiments is used as an input for the improvement of the full-scale design without the need for costly full-scale testing.

Sub-scale configurations using single-element and multi-element rocket combustors are also used to provide validation data for numerical simulations. Over the past decades, significant effort has been placed in the numerical calculation of the combustion process in rocket engines. The necessity for a reliable prediction of the combustion characteristics and the heat loads within a combustion chamber and nozzle has promoted computational fluid dynamics (CFD) to become an integral part of the design process in the space propulsion industry. The validation of these numerical tools is usually done by comparing the calculated results for performance (Isp, c^*), pressure profiles along the axial position $p_c(x)$ as well as the heat flux values at the hot gas wall $\dot{q}(x)$ to the available experimental data. This implies that trustworthy measurements with sufficient axial resolution for those values have to be available by the experiments over a wide range of operational conditions. The need for this data is even more critical for the innovative propellant combination of methane (CH_4) and oxygen (O_2) due to the limited number of available tests [5–9].

Of the previously mentioned quantities, the one having the largest significance for the understanding of the physical and chemical phenomena is the heat flux. Due to the harsh environment within the chamber hot gas, the installation of sensors measuring temperature is almost impossible. Therefore, access to the burning gas is very limited and direct measurement is quite challenging and usually restricted to optical measurements of radicals emission or to spectroscopic methods like the Coherent anti-Stokes Raman (CARS) spectroscopy [10]. These methods however require the active film cooling of the optical window which can lead to a distortion of the flow field. Specifically, in single injector combustion chambers with strong film cooling the acceleration distribution due to hot gas expansion by combustion is not always

* Corresponding author.
E-mail address: nikolaos.perakis@tum.de (N. Perakis).

https://doi.org/10.1016/j.ijheatmasstransfer.2018.11.048
0017-9310/

representative due to the interaction with the film. Due to these difficulties, the heat flux distributions are usually utilized to deduce information about the conditions within the chamber.

Moreover the prediction of the engines lifetime, the design of an effective cooling system and the reliability of the chamber components after a specific number of tests is imminently connected to the heat loads applied onto the chamber wall thereby increasing the importance of this value even more.

The calculation of the heat flux in experiments where no active cooling system is present becomes challenging since the only information available consists of temperature readings at specific locations in the chamber material. The reconstruction of the heat flux profiles requires the solution of an inverse problem. The problem is considered to be an "inverse" one, since the causes (heat flux) that lead to a measured effect (temperature at specific locations) are sought.

The present work gives an overview of the capabilities of the inverse heat conduction method when applied to single- and multi-element chambers and the information about the flowfield and heat release that can be deduced from the resulting heat flux values. The hardware examined is operated at the Chair of Turbomachinery and Flight Propulsion (LTF) of the Technical University of Munich (TUM). Test data from experiments using gaseous methane (GCH_4) and gaseous oxygen (GO_2) as propellants as well as gaseous hydrogen (GH_2) and GO_2 are used for the validation of the method.

2. Inverse heat conduction method

Experimental lab-scale rocket combustors cooled by a water cycle or other cooling medium have the characteristic property of reaching a steady state temperature distribution after the first seconds of operation. This effect can be utilized when evaluating the heat flux profiles, since the latter ones can simply be obtained from the enthalpy difference of the outgoing and incoming coolant flow. When dealing with capacitively cooled engines however, the temperature field is not stationary during the test operation and hence a transient inverse heat conduction method is needed. Several efforts have been performed to calculate the transient heat flux profiles [11,12] in generic configurations as well as explicitely in rocket engines [13,14].

The main concept behind an inverse method for heat conduction problems lies in trying to estimate the boundary conditions (causes) which best fit the measured temperature values (effects) while keeping the physics of the problem intact. Similarly to the majority of inverse algorithms, the method shown in the present work is based on an iterative approach as outlined in Fig. 1. The goal of the optimization is to minimize the difference between the measured and calculated temperatures at the measurement locations.

The starting point of the code is to initialize the temperature in the computational domain and to choose an initial guess for the heat flux. With the initial conditions (temperature field) and the boundary conditions (guessed heat flux) the first step is solving the direct heat conduction problem. A restriction for the capacitively cooled chamber is that the starting point for the evaluation is always the beginning of the test. The reason is that the initial conditions in the entire domain have to be exactly known in order to initiate the calculation. The only time point where a known temperature field is present in the entire domain is at $t = 0$s, when the structural material is still at ambient temperature.

2.1. Direct solver

For the solution of the direct problem, a direct solver is required, which has to be computationally very efficient. This is a strict requirement due to the large number of direct problem evaluations until convergence of the heat flux is achieved. For the solution of the thermal conduction problem, RoqFITT uses a 3D finite difference (FD) code which was developed specifically for this purpose by the authors and has been validated in Celano et al. [15] and Perakis et al. [16]. The implementation of the direct solver is carried out in Matlab to avoid any extra interfaces between the optimization code and the direct solver. A central difference approximation of the second derivative in the heat conduction equation (Eq. (1)) is combined with an implicit Euler scheme for the time integration.

$$\frac{\partial T}{\partial t} = \frac{\lambda}{\rho c_p} \nabla^2 T \tag{1}$$

The FD solver is used to solve the heat conduction partial differential equation (PDE) in a simplified geometry. The geometry consists only of the copper combustion chamber (excluding the nozzle segment) and is in principle a block with a hole in the middle at the location where the hot gas combustion takes place. The exclusion of the nozzle is due to the fact that no temperature data are available in the nozzle block. As shown in Section 3 all of the combustors have a very short nozzle since the focus of the experiment is in understanding the combustion processes in the chamber and not to obtain high specific impulse and thrust performance. Eq. (1) is solved in Cartesian coordinates for the rectangular chambers and in cylindrical ones for the cylindrical hardware. The simplified

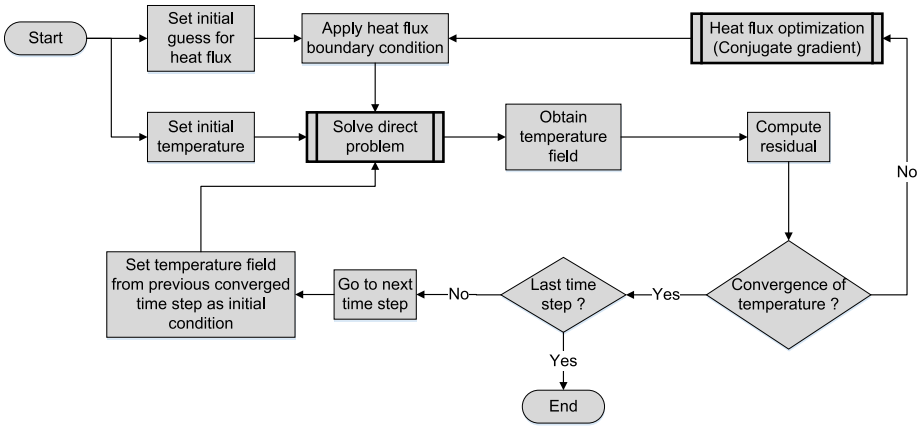

Fig. 1. Inverse heat conduction iterative algorithm.

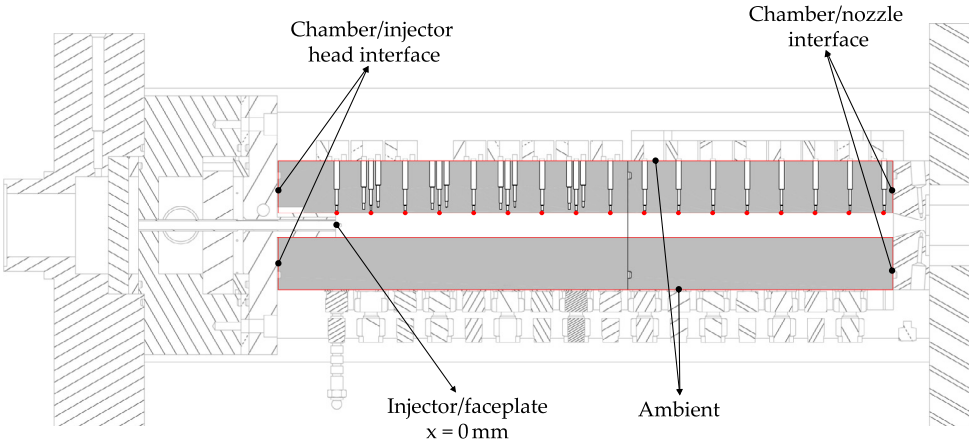

Fig. 2. Computational domain chosen for the inverse heat conduction method.

representation of the geometry constitutes the code very efficient from a computational standpoint and allows the iterative solution of the heat transfer problem in reasonable time.

The simplified computational domain is shown in Fig. 2 upon the example of a multi-element chamber. The grey area represents the computational domain and the red frame shows the boundaries. The thermocouple holes are also ignored in the computational model and the structure is modeled as a full-material block. The red points indicate the positions of the parameter points in the optimization problem, which are located at the axial positions of the thermocouples, projected onto the hot gas wall. Note that the computational domain in the presented method is three-dimensional and Fig. 2 shows only a 2D slice of the domain.

Apart from the boundary condition in contact with the hot gas, which is the sought variable, all the others must be defined a priori and are modeled with von Neumann and Robin boundary conditions. Specifically, an adiabatic boundary condition is used for the interface between the copper chamber and the injector head, whereas a natural convection boundary condition is applied to the outer wall with a convective heat transfer coefficient $h = 10\mathrm{W}/(\mathrm{m}^2 \cdot \mathrm{K})$and an ambient temperature corresponding to the one measured at each test.

For the boundary condition at the interface between combustion chamber and nozzle, an extensive sensitivity analysis has been performed. Specifically, an adiabatic boundary condition was compared to a time and spatially dependent heat flux, obtained by simulations performed with the in-house tool Thermtest [17]. The analysis resulted to the conclusion that the choice of this boundary condition has very small influence on the final heat flux profile. Specifically, between the solutions with the adiabatic and the Thermtest boundary condition, a maximal deviation of $\sim 5\%$ was observed in the heat flux value at the location of the last downstream thermocouple. All other positions upstream appeared to be unaffected by the choice of boundary condition, proving the low sensitivity of the final result on the treatment of this interface. For that reason and to ensure that the rebuilding of the thermal field is purely done on the basis of the measurements without relying on other inputs such as thermal simulations of the nozzle, an adiabatic boundary condition is imposed.

Upon solving the direct problem, the temperature field at the end of the first time step is known. The calculated value of the temperature at all the thermocouple positions can hence be extracted and compared with the measured ones. This residual temperature difference is given as an input to the optimization algorithm.

Fig. 3 shows a slice of the computational grid in the example of the rectangular single-element chamber. Only the upper-right

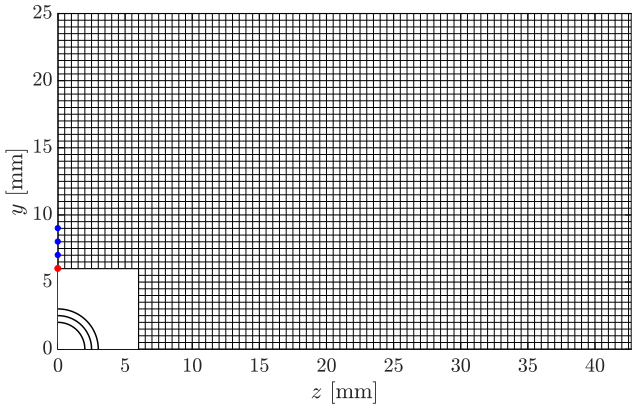

Fig. 3. Computational grid for the rectangular single-element chamber (every second node is shown).

quarter of the cross-section is shown due to the symmetry but the computational domain consists of the full chamber. A uniform spacing is used both in horizontal and vertical directions. Note than only every second node is shown in the figure for visualization purposes. In axial direction, a uniform spacing is used for the nodes, with a distance of 0.5 mm between neighboring nodes. The resolution was chosen after an extensive grid convergence study. In Fig. 3, the positions of the thermocouples at 1 mm, 2 mm and 3 mm from the hot gas wall are shown (blue points), as well as the projected parameter location (red point) as will be described in Section 2.2.

2.2. Optimization method

The purpose of the optimization is to minimize the difference between the calculated ($\mathbf{T}_c$) and measured ($\mathbf{T}_m$) temperatures at each time step. This residual J which is subject to minimization is defined as in Eq. (2):

$$J(\mathbf{P}) = [\mathbf{T}_m - \mathbf{T}_c(\mathbf{P})]^T [\mathbf{T}_m - \mathbf{T}_c(\mathbf{P})] \tag{2}$$

The vector $\mathbf{P}$ describes the heat flux values at the parameter points which are subject to optimization. The heat flux is a continuous variable being applied to all the points, however optimizing the heat flux value at every single point in contact with the hot gas would be computationally expensive and render the problem more ill-posed [18]. Having a larger number of optimization points increases the degrees of freedom of the problem without

increasing the information input (no additional thermocouple measurements). For that reason, for the method presented here, a parameter is placed only at locations which possess at least one temperature sensor, so the number of parameters N is always smaller or equal to the thermocouple number M. At each time step, the values of the N parameter points are changed to reduce the residual J.

For the determination of the amount by which each parameter value should be modified at every iteration, two separate methods have been applied and compared. Both of them are based on an iterative update by means of the Jacobi matrix $\mathbf{S}$, which serves as a sensitivity matrix describing the change of the temperature at a thermocouple position due to a small change at a specific heat flux parameter value. Its structure is presented in Eq. (3). It was shown in a sensitivity study that the linearity of the Fourier heat conduction equation allows for a calculation of the Jacobi matrix outside of the optimization loop. For that reason the computation of the matrix for both methods occurs as a pre-processing step before the calculation and it is saved for future calculations as well. As long as the number and locations of the thermocouples and parameters does not change, the matrix remains unaltered.

$$\mathbf{S} = \begin{bmatrix} \frac{\partial T_1}{\partial P_1} & \cdots & \frac{\partial T_M}{\partial P_1} \\ \vdots & \ddots & \vdots \\ \frac{\partial T_1}{\partial P_N} & \cdots & \frac{\partial T_M}{\partial P_N} \end{bmatrix} \tag{3}$$

The first method relies on a conjugate gradient method as described in Özisik [19]. After each iteration k, the values $\mathbf{P}^k$ are updated according to Eq. (4).

$$\mathbf{P}^{k+1} = \mathbf{P}^k - \beta^k \cdot \mathbf{d}^k \tag{4}$$

where β^k represents the search step size and $\mathbf{d}^k$ the direction of descent of the conjugate gradient method. Using the Fletcher-Reeves [20] expression for the conjugation coefficient and the gradient of the residual function from Eq. (5), the closure of the optimization algorithm is given by Eqs. (6)–(8) as described in Özisik [19].

$$\nabla J(\mathbf{P}^k) = -2[\mathbf{S}]^T \left[\mathbf{T}_m - \mathbf{T}_c(\mathbf{P}^k)\right] \tag{5}$$

$$\mathbf{d}^k = \nabla J(\mathbf{P}^k) + \gamma^k \mathbf{d}^{k-1} \tag{6}$$

$$\gamma^k = \frac{\sum_{j=1}^{N} \left[\nabla J(\mathbf{P}^k)\right]_j^2}{\sum_{j=1}^{N} \left[\nabla J(\mathbf{P}^{k-1})\right]_j^2} \tag{7}$$

$$\beta^k = -\frac{\left[\mathbf{S}\mathbf{d}^k\right]^T \left[\mathbf{T}_m - \mathbf{T}_c(\mathbf{P}^k)\right]}{\left[\mathbf{S}\mathbf{d}^k\right]^T \left[\mathbf{S}\mathbf{d}^k\right]} \tag{8}$$

The second method is based on a linearization of the problem and follows the Newton-Raphson formulation for the solution of non-linear systems [21]. The heat flux at each iteration step is obtained by solving the algebraic equation

$$\mathbf{S} \cdot \mathbf{P}^{k+1} = \left[\mathbf{T}_m - \mathbf{T}_c(\mathbf{P}^k)\right] + \mathbf{S} \cdot \mathbf{P}^k \tag{9}$$

In both cases, the process is repeated until convergence is achieved, i.e. until the residual drops beneath a predefined value ϵ. When this is the case, the calculation of the next time step takes place while the temperature is initialized with the converged temperature field of the previous time step. The stopping criterion ϵ was chosen to be proportional to the precision of the thermocouple measurements ΔT, to the time step Δt and the number of the thermocouples M using an empirical constant C. Due to the inherent uncertainty of the thermocouple measurements, the error ΔT was set to the accuracy of the used temperature measurement system.

$$\epsilon = C \cdot M(\Delta T)^2 \Delta t \tag{10}$$

It has been shown that both methods delivered identical results for the converged heat flux. However, the number of iterations required until convergence is lower by a factor 3 in the case of the Newton-Raphson method. For that reason this method is utilized for all results presented in Section 6.

2.3. Applying the heat flux on the boundary

As mentioned in the description of the optimization algorithm, the heat flux is updated only at specific locations and specifically only at the thermocouples' positions projected on the hot gas wall. Special care has to be taken to transform the heat flux from the few locations in the chamber to a continuous variable over the whole boundary domain. A cubic interpolation is used to transform the discrete values to a continuous profile in axial direction. However, the treatment along the perimeter is done differently for the single-element and multi-element configurations and will hence be described in Section 6.

3. Experimental setup

The inverse heat conduction method presented in this work was initially developed with the purpose of evaluating the experimental heat flux stemming from the hot runs of capacitively cooled rocket combustors operated at the Space Propulsion Division (RFA) of the Technical University of Munich (TUM). Within the framework of the German National Science Foundation (DFG) the DFG-TRR40 project entitled Fundamental Technologies for the Development of Future Space-Transport-System Components under High Thermal and Mechanical Loads has been funded, aiming at increasing the experience around the propellant combination methane/oxygen for future space applications [4].

In particular, the Space Propulsion Division of TUM has been working with these propellants for the last seven years employing different model combustors to provide detailed data about injector/injector and injector/wall interaction both for furthering identification and quantification of key phenomena and processes and for validation of engineering design tools [22,23]. For an optimum cooling system and specifically the cooling channel design it is essential to know in sufficient detail the axial and azimuthal heat load distributions for a particular injector geometry and their sensitivity towards variations of the operating condition.

In order to achieve these goals with a reasonable effort the following approach has been taken. In a first phase several single injector combustors (circular and square cross section and the later with an optional optical access to allow visualization of the near injector region) have been applied to investigate initial phenomena such as injector/wall interaction, combustion efficiency, film cooling and flow field from the injector with recess. In a second phase multi-injector combustors with rectangular and circular cross section have been operated to look additionally into injector/injector interaction and the effect of a smaller ratio of combustor surface to combustor volume.

For the evaluation of the heat flux profiles from the experiment, the RoqFITT code has been developed and applied to the different thrust chambers of the TUM. The object of the current investigation are the circular single-element, square single-element and rectangular multi-element rocket combustors, which are operated without an active cooling system and are hence subject to transient

temperature profiles within their structure. An overview of the hardware can be seen in Figs. 4–6 respectively.

All the model combustors are equipped with identical injectors, similar injector/wall distances and injector/injector distances and have the same contraction ratio ϵ_c. Due to the gaseous nature of the propellants such a design allows for similar injection velocities independently of combustion chamber pressure p_c, for similar chamber Mach numbers ($Ma \approx 0.25$) and thus convective transport characteristics and similar characteristic mixing lengths. For more information about the different combustors, see [24–27].

In all three of the examined combustors, type T thermocouples with 0.5 mm diameter are installed to measure the temperature within the oxygen-free copper material (Cu-HCP) of the structure. These measurements serve as the input for the inverse method, which aims at minimizing the error between the calculated and measured temperature signal for all time steps. The thermocouples are positioned at 1 mm, 2 mm and 3 mm distances from the hot gas walland their axial resolution is 17 mm. In the case of the circular and square single-element chambers, only one thermocouple is installed per plane, located directly above the injector element. The multi-element chamber can potentially accommodate up to seven thermocouples per axial plane, in order to measure the heat flux footprint created by the presence of five injector elements. As shown in the right sub-figure of Fig. 6, thermocouples are installed above each one of the five injectors and two additional ones are present left and right of the central injector element, right between two neighboring elements.

4. Error analysis

For a proper evaluation of the experimental data and a potential comparison with CFD simulations, knowledge of the different error sources as well as the magnitude of the individual errors is necessary. The error sources are usually due to statistical and systematical error of the measured data as well as due to the uncertainties used in the models.

In the case of the RoqFITT code the measurements are restricted to the thermocouple readings. As far as the model is concerned, RoqFITT uses the heat conduction equation with proper boundary conditions. The potential error sources are hence the material properties and the treatment of the boundary conditions at the interface with the nozzle as well as with the ambient environment.

Summarized, the uncertainties which have to be included in the error propagation are the following:

- Thermocouple accuracy
- Thermocouple precision
- Thermocouple positioning
- Thermocouple response delay
- Material properties
- Boundary conditions

The terms “accuracy” and “precision” are used in this context according to the definition by Taylor [28]: “accuracy” of a measurement is the deviation from the quantities “true value”, whereas “precision” refers to the reproducibility and repeatability of the measurement, i.e. the degree to which repeated measurements under unchanged conditions show the same results.

4.1. Thermocouple accuracy

For the accuracy of the thermocouples, the manufacturer’s instrument accuracy ΔT_{acc} can be used. Since the heat flux in the solution of the transient inverse problem is calculated based not on the absolute values of the temperature but in the form of a temperature increase within a time window, the total temperature error due to the instrument accuracy is doubled and hence has the magnitude $2 \cdot \Delta \mathbf{T}_{acc}$. Using the concept of linearization, the heat

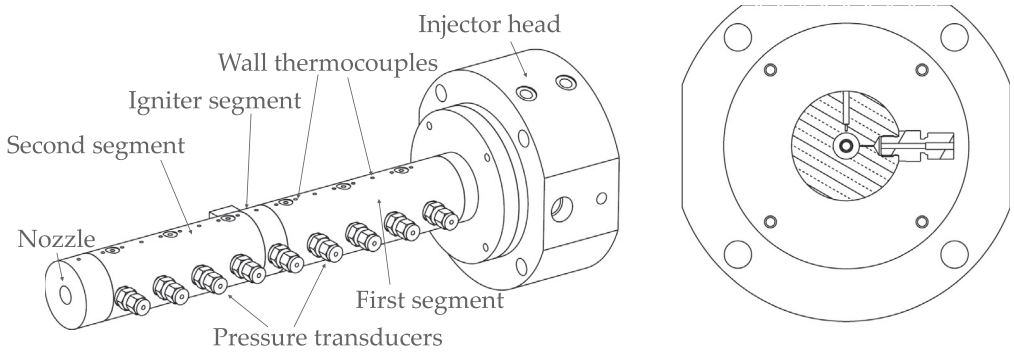

Fig. 4. Circular single-element combustion chamber hardware.

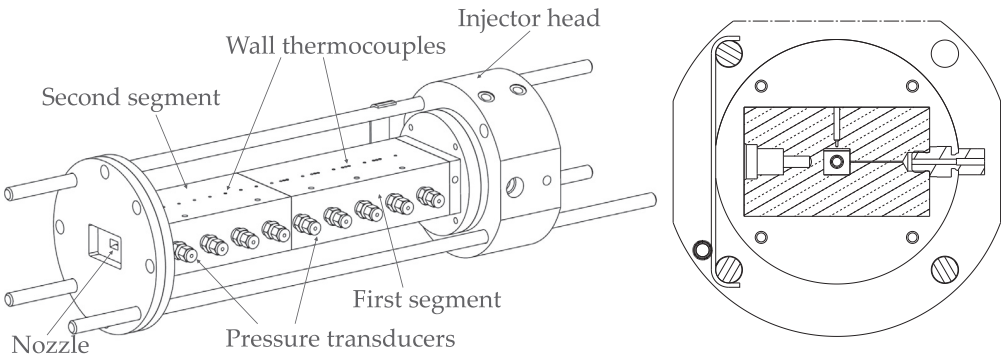

Fig. 5. Square single-element combustion chamber hardware.

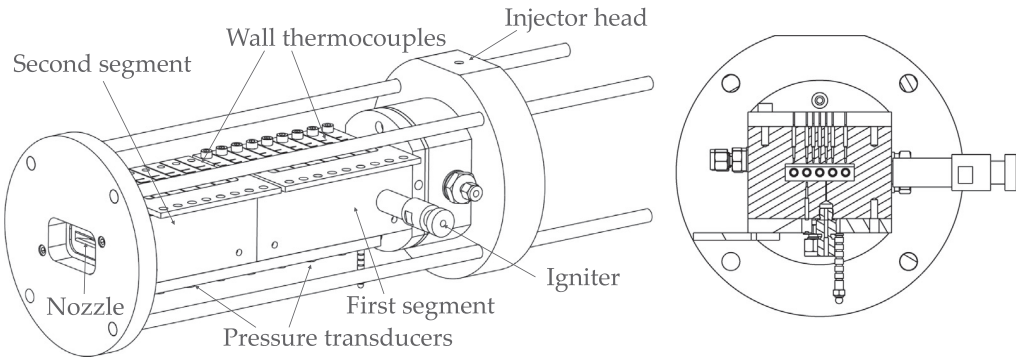

Fig. 6. Multi-element combustion chamber hardware.

flux error $\Delta\mathbf{P}_{acc}$ can be obtained by means of the Jacobi matrix, by solving the algebraic system in Eq. (11).

$$\Delta\mathbf{P}_{acc,i} = 2 \cdot \mathbf{S}^{-1} \cdot \Delta\mathbf{T}_{acc,i} \tag{11}$$

where the index i denotes the i-th time step.

4.2. Thermocouple precision

In case of the transient temperature measurements, the precision error is defined as the random fluctuation of the thermocouples readings. The raw thermocouple data is prone to high frequency noise and for that reason the transient profiles are smoothened before the start of the inverse method. The difference between the smoothed signal and the raw data is defined as the precision error and the corresponding heat flux error is defined as in Eq. (12)

$$\Delta\mathbf{P}_{prec,i} = \mathbf{S}^{-1} \cdot \Delta\mathbf{T}_{prec,i} \tag{12}$$

4.3. Thermocouple positioning

One of the largest sources of uncertainty when using thermocouples is the fact that their exact location is not always known. In order to take this into account, a post-processing step is introduced in RoqFITT, during which a systematic spatial deviation Δy is defined for all thermocouples. The initial position of the thermocouples y_0 is hence replaced by $y_0 + \Delta y$. Using the converged solution for the heat flux and the temperature field in the domain, the temperature at the new thermocouple positions can be found and it is used for the estimation of the temperature error:

$$\Delta\mathbf{T}_{loc,i} = \mathbf{T}_{c,i}(y_0) - \mathbf{T}_{c,i}(y_0 + \Delta y) \tag{13}$$

A maximal deviation equal to 0.5 mm is used for all hardware. The estimation of the resulting heat flux error is carried out with the Jacobi matrix similar to Eq. (12).

4.4. Thermocouple response delay

Apart from the position of the thermocouples, their thermal contact with the chamber material and their thermal inertia are not always ideal. Specifically, the combined effect of the contact thermal resistance (R_t) and the heat capacity (C_t) of the sensor give rise to a response delay time of each thermocouple $\tau = R_t \cdot C_t$. Any change in R_t and C_t will cause a body to respond differently to any changes in its thermal environment. Such a delay has to be taken into account when evaluating the heat flux for a capacitive hardware, since the measured temperature continues to increase after the combustion starts, resulting in unsteady temperature and heat flux at the wall. Because of the delayed response of the thermocouples, there is some discrepancy between the real time temperature and the experimental output.

In order to quantify the error resulting from the response delay time, the method presented by Wang et al. [29] is implemented, according to which, the real temperature at the thermocouple position T_{real} is related to the measured thermocouple output T_{meas} according to:

$$\frac{dT_{meas}}{dt} = \frac{T_{real} - T_{meas}}{\tau} \tag{14}$$

The effect of the response delay time on the measured thermocouple temperature is illustrated in Fig. 7. The thermocouple reading corresponds to $\tau = 0$ ms and represents the actual output without correction. The corrected temperature profiles for different values of the response delay are also shown in Fig. 7 and have larger values than the measured temperature for the entire duration of the experiment.

Typical response time values for 0.5 mm type T thermocouples are between 100 and 200 ms [15,29]. In the present study all thermocouple readings are corrected using Eq. (14) and a value of $\tau_0 = 100$ ms is assumed.

To estimate the heat flux uncertainty resulting from the thermocouple contact resistance and thermal inertia, Eq. (15) is used. The modified thermocouple measurement using the standard delay time τ_0 is compared to an increased standard delay time $\tau_0 + \Delta\tau$ and the heat flux error is obtained with the use of the sensitivity matrix. In the present framework a value of $\Delta\tau = 100$ ms is chosen.

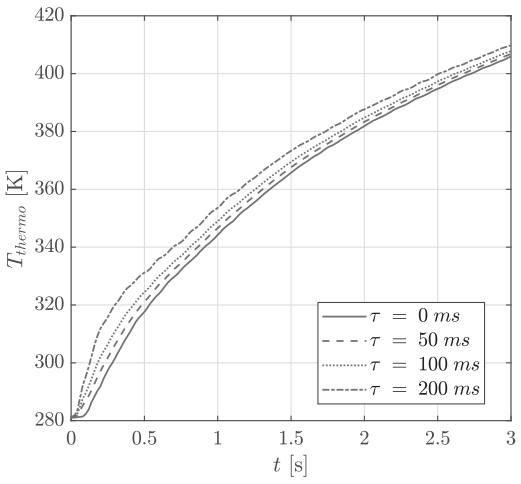

Fig. 7. Comparison of "real" and measured temperature at thermocouple position for different response delay times.

$$\Delta \mathbf{P}_{res,i} = \mathbf{S}^{-1} \cdot \Delta \mathbf{T}_{res,i} = \mathbf{S}^{-1} \cdot \left(\mathbf{T}_{m,i}(\tau_0) - \mathbf{T}_{m,i}(\tau_0 + \Delta\tau) \right) \quad (15)$$

4.5. Material properties

The material properties used in the solution of the direct problem are taken from the data sheet of the combustion chamber material. However there is some uncertainty connected to the choice of the thermal conductivity, density and heat capacity and for the quantification of its effect on the converged heat flux values is important.

The procedure for the calculation of the material-induced error goes as follows: Upon convergence of the inverse method, the converged heat flux values are used as input for the solution of a direct problem. In this direct problem however, the thermal diffusivity is replaced by a value which is modified compared to the nominal value α_0. The magnitude of the deviation $\Delta\alpha$ was estimated at 10%. The resulting heat flux error for each time step is simply given by Eq. (16).

$$\Delta \mathbf{P}_{mat,i} = \mathbf{S}^{-1} \cdot \Delta \mathbf{T}_{mat,i} = \mathbf{S}^{-1} \cdot \left(\mathbf{T}_{c,i}(\alpha_0) - \mathbf{T}_{c,i}(\alpha_0 + \Delta\alpha) \right) \quad (16)$$

4.6. Boundary conditions

In the computational domain of the rocket combustors shown in Fig. 2, the boundary conditions at the surfaces in contact with the nozzle and the outer surface have to be modeled. The natural convection was found to have a negligible effect on the final result of the hot gas heat flux and is hence not included in the error propagation analysis.

For the nozzle interface the adiabatic condition has been compared to a spatially and temporarily varying nozzle heat flux which is obtained by means of the in-house tool Thermtest [17]. Thermtest allows the simulation of steady as well as transient thermal behavior of cooled or uncooled structures over a wide scope of chamber materials and cooling fluids. While the heat conduction inside the chamber material is solved by a 3D finite difference method, the convective heat transfer from the hot gas side to the inner wall as well as for the coolant is modeled using empirical Nusselt correlations. The approximated thermal field at the interface between nozzle and combustion chamber stemming from the Thermtest simulation can be used to deduce the value of the conductive heat flux. This is applied directly as a von Neumann boundary condition in RoqFITT.

To quantify the uncertainty of this value, a comparison of the results with the nominal nozzle heat flux $\dot{q}_{noz,0}$ (=0, due to adiabatic conditions) was performed with the assumed deviation $\Delta\dot{q}_{noz}$ stemming from Thermtest. The resulting error in the heat flux parameters $\Delta \mathbf{P}_{noz,i}$ can be determined as in Eq. (17):

$$\Delta \mathbf{P}_{noz,i} = \mathbf{S}^{-1} \cdot \Delta \mathbf{T}_{noz,i} = \mathbf{S}^{-1} \cdot \left(\mathbf{T}_{c,i}(\dot{q}_{noz,0}) - \mathbf{T}_{c,i}(\dot{q}_{noz,0} + \Delta\dot{q}_{noz}) \right) \quad (17)$$

An extensive analysis showed that only the heat flux at the parameter point closest to the interface is influenced but the effect is kept below 10% even for large nozzle heat flux values.

Summing up all the error sources according to Eq. (18) results in a total uncertainty between 10% and 15% of the converged heat flux value at each parameter location.

$$\Delta \mathbf{P}_{tot,i} = \sqrt{\Delta \mathbf{P}^2_{acc,i} + \Delta \mathbf{P}^2_{prec,i} + \Delta \mathbf{P}^2_{loc,i} + \Delta \mathbf{P}^2_{res,i} + \Delta \mathbf{P}^2_{mat,i} + \Delta \mathbf{P}^2_{noz,i}} \quad (18)$$

The main contribution (around 80%) results from the thermocouple positioning and response delay time, whereas the boundary condition and precision errors are negligible.

4.7. Hot gas wall temperature error

Apart from the heat flux profile at the inner wall of the combustion chamber, a further result of the inverse heat conduction method is the wall temperature at the positions in contact with the hot gas. This is usually utilized as the thermal boundary condition in CFD simulations and is an important figure for the estimation of the engine's lifetime. Hence, knowing the uncertainty of the calculated values is also quite important.

This can be performed by means of the Jacobi matrix, estimated directly at the hot gas positions. With this information, the temperature errors at the hot gas can be evaluated by:

$$\Delta \mathbf{T}_{hot\,gas,i} = \mathbf{S}_{hot\,gas} \cdot \Delta \mathbf{P}_{tot,i} \quad (19)$$

Of course this implies the calculation of a second Jacobi matrix $S_{hot\,gas}$, which can be computationally expensive.

5. Validation

Before the application of the code to the evaluation of experimental data, a validation was carried out. Specifically, a validation of the direct solver and the inverse algorithm as well as a validation of the inverse method as a whole was performed.

5.1. Algorithm validation

For the validation of the direct solver, a comparison of the resulting temperature distribution given a specific heat flux as boundary input was done between RoqFITT and the commercial tool ANSYS [30]. The temperature results matched within an accuracy of 0.5 % leading to the conclusion that the direct solver is reliable.

For the validation of the inverse algorithm several tests were carried out. The purpose of the inverse algorithm is to determine the (unknown) applied heat flux based on temperature readings. Hence, to validate it, one has to provide measurements obtained with a precisely defined boundary condition. If the results from the inverse algorithm agree with the pre-defined conditions, then the algorithm can be considered as validated.

In the following, a time and spatially variable heat flux profile is applied to the hot gas wall of the square single element chamber. The profile is illustrated in Fig. 8 and is chosen with typical characteristics as the expected heat loads within the experimental combustor. Specifically, a transient increase of the heat flux level within the first second of operation is defined. Within this period, a small oscillation is imposed, resembling the effect of the igniter, which is located in the middle of the chamber. The effects of

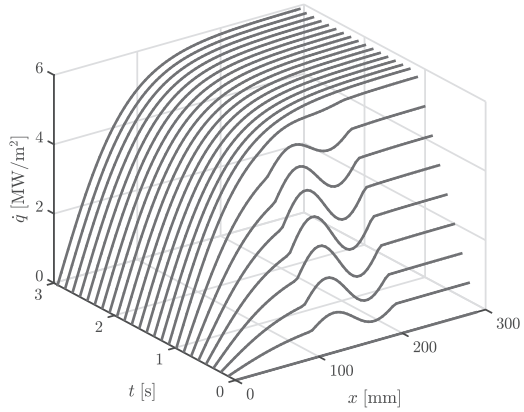

Fig. 8. Heat flux profile applied at the chamber wall for the validation.

ignition are usually measured within the first 0.5–1 s of the combustion tests. After the initial start-up, a steady state profile is obtained for the heat flux, which shows larger values for positions downstream of the injector and a subsequent constant plateau after approximately 200 mm from the faceplate. This resembles typical axial heat flux distributions where the heat flux increases for the first part of the combustion chamber since the mixing and energy release is not complete before reaching a nearly constant value upon completion of the combustion process. No variation of the heat flux is defined along the circumference of the square wall, i.e. a constant heat flux is applied for each axial position.

Using the profile from Fig. 8 a direct problem is run and the temperature values at the sensor locations are obtained. Using a random error of 0.5 K for the temperature data (to resemble the experimental noise), the "experimental" data are prepared. Those serve as input for the inverse heat conduction method. For the optimization, 18 parameters are used, located at the same axial locations as the thermocouples. The resulting heat flux profiles for some representative time steps are compared to the imposed ("direct") boundary condition (BC) in Fig. 9. Both the transient as well as the spatial variation is reproduced by the inverse method, with the maximal errors at the optimization positions remaining below 5%. During the steady state heat flux level, the errors were kept at below 1% and result mainly from the artificial thermocouple error imposed.

5.2. Method validation

The single-element chambers presented in Sections 6.1 and 6.2 can only be operated in capacitive mode and hence no available calorimetric measurements are available for comparison. Such comparison is however possible for the multi-element chamber and can be used for the validation of the inverse heat flux measurement. The multi-element chamber can be operated either in capacitive or in water-cooled mode. This is enabled by the modular form of the chamber segments which can be interchanged. In the water-cooled configuration, the segments are equipped with cooling channels which can be flown either counterflow or in co-flow with the hot gas. This makes a measurement of the heat flux based on the enthalpy difference of in- and outflowing water possible.

A test at O/F = 3.4 and pressure of 20 bar carried out once with the cooled hardware and once with the capacitive one is shown in Fig. 10. The test is taken from Perakis et al. [16]. Seven water-cooled separate segments are present, which provide the average heat flux for each one of them. In order to perform the comparison,

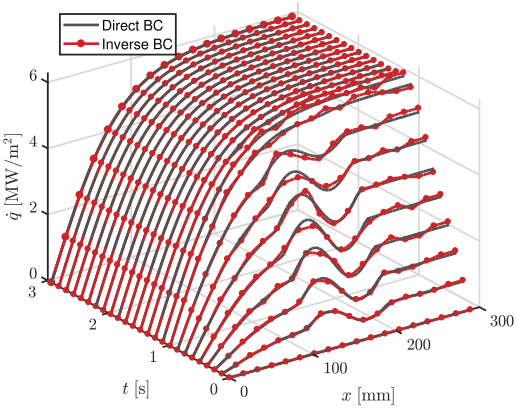

Fig. 9. Comparison of imposed direct boundary condition and resulting inverse boundary condition from RoqFITT.

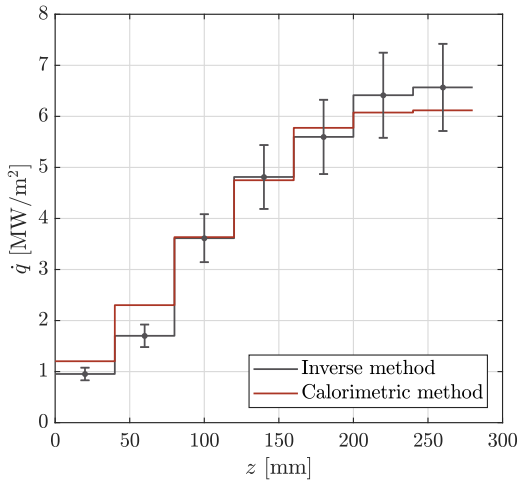

Fig. 10. Comparison between experimental heat flux obtained with the inverse and calorimetric method.

the results from the inverse method are also averaged along the same positions. It can be observed that the two curves demonstrate the same trend and have a difference of less than 3% in the segments located close to the middle of the chamber.

Planes closer to the injector plane and the nozzle show a higher deviation, which however remains within 7% with the exception of the second segment. The calorimetric method also contains some uncertainty which has not been quantified in the original experiment. Moreover, although efforts are made that the two hardware configurations (capacitive and water-cooled) are identical, it is still two different pieces of hardware and some discrepancies in the results could be attributed to this fact (slightly different material properties, installation of thermocouples etc.). The general trend however of the two methods is in good agreement, serving as a first validation of the inverse method.

6. Results

Selected results using the RoqFITT code for the evaluation of the heat flux profiles in the combustion tests of the hardware presented in Section 3 are outlined in this chapter. The main purpose is to demonstrate the capabilities of the code as far as the calculation of the heat loads is concerned. However, at the same time an investigation of the physical phenomena is given in order to explore whether the obtained heat flux values agree with the expected physical and chemical phenomena taking place within the chamber.

6.1. Circular single-element combustor

The single-element combustor shown in Fig. 4 can be operated either with CH_4/O_2 or H_2/O_2 in gaseous phase and at operating pressures up to 30 bar. The test operation is restricted to 3 s to avoid thermal and mechanical damage of the structure. For the estimation of the heat flux, thermocouples are installed at 17 positions, equally distributed along the axis of the chamber, with an axial separation of 17 mm from each other. The thermocouples used for the inverse method are located at 1 mm distance from the hot gas wall. Due to the axisymmetric nature of the problem, a uniform heat flux is applied along the perimeter for each axial position. The interpolation between the discrete parameter values occurs with a cubic scheme.

The only information available used by the inverse method for the reconstruction of the thermal field are the transient

thermocouple readings at distinct positions in the material. The transient readings at selected positions are presented in Fig. 11, where the solid lines represent the calculated values and the dashed lines the experimental ones. In the right sub-figure, the corresponding difference between the two is also shown. One observes that the inverse method is capable of reconstructing the temperature values at the thermocouple locations within an accuracy of approximately 2 K. Specifically, the largest discrepancy occurs during the initial sharp temperature rise due to the start of the experiment, while after 1 s of operation the difference between the two values is close to 1 K for most sensors. The data shown in Fig. 11 are from a CH_4/O_2 test at 20 bar and O/F = 3.0.

Due to the capacitive nature of the test hardware, the temperature profile is transient and does not reach a steady state within the 3 s of operation. A typical time-evolution of the pressure signal and a thermocouple measurement in the chamber is shown in the left sub-figure of Fig. 12. The valves are opened at 0 s and the combustion in the chamber takes place for approximately 3 s. During this duration, the pressure signal reaches a steady state shortly after the begin of the test and then oscillates around the nominal value. The temperature signal on the other hand steadily increases over time until the shut-off. The inverse method deals only with the time window of the test, i.e. only for the first 3 s of operation and hence the thermocouple readings within this time frame are taken as inputs.

Both the temperature and the heat flux however are transient values and in order to carry out an evaluation of the axial profiles of these values, an evaluation window must be chosen. In the present work this is done at 2/3 of the operational duration (i.e. at $t = 2$ s) and the window width is 0.5 s, when the pressure and heat flux profiles reach a steady state. The values within this window are averaged and can give insights about the axial distribution of heat loads. Although this method is described for the round single-element chamber in this section, it is the procedure followed for all three hardware. Some exemplary heat flux values at different axial positions are plotted over time in the right sub-figure of Fig. 12. It is evident that the initial start-up transient leads to an increasing heat flux for the first second of operation but after that an almost steady value is predicted in each position. Hence the choice of the evaluation window in the interval 2–2.5 s is justified, since within it the heat flux values are almost constant.

Using the inverse heat conduction method, important insights into the different heat loads stemming from the various propellant properties and pressure levels can be extracted. In Fig. 13, a comparison between the predicted heat flux results using H_2/O_2 and CH_4/O_2 at 10 and 20 bar nominal chamber pressure is shown. An

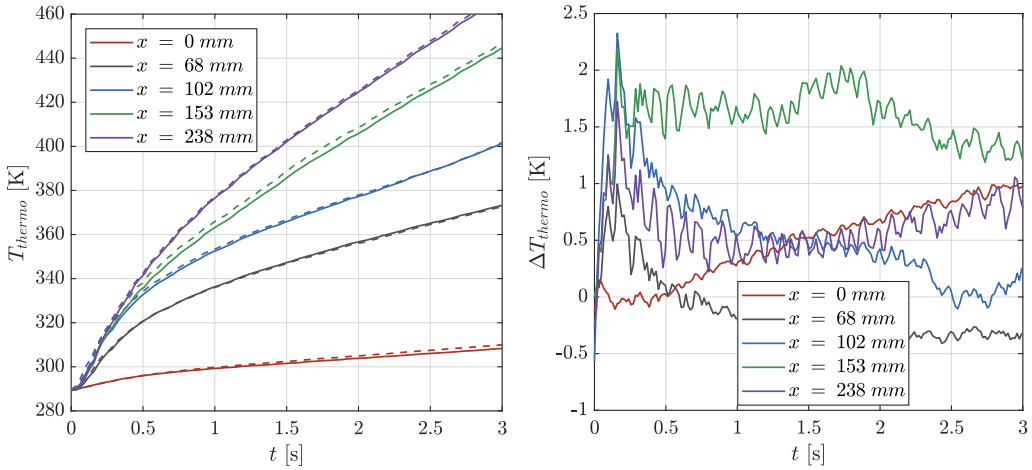

Fig. 11. Transient profiles of the calculated and measured temperature at selected thermocouple positions (left) and the corresponding difference between calculated and measured values (right) for the round chamber.

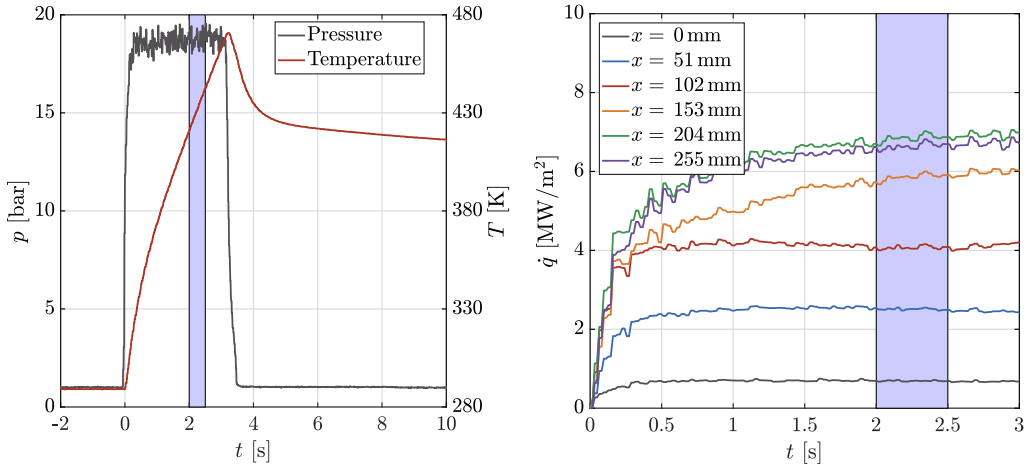

Fig. 12. Temperature, pressure and heat flux profiles along time. The evaluation window is indicated in blue color. (For interpretation of the references to colour in this figure legend, the reader is referred to the web version of this article.)

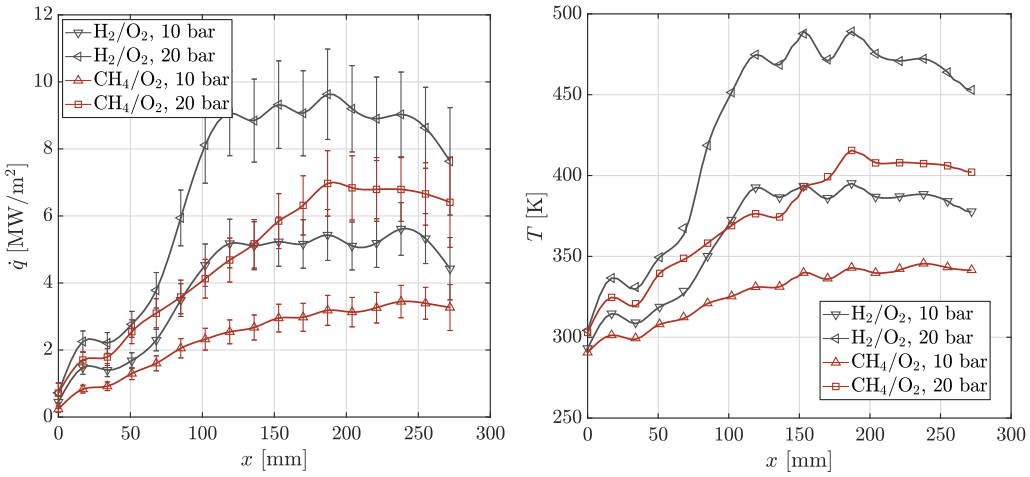

Fig. 13. Axial heat flux and temperature profile for H_2/O_2 and CH_4/O_2 load points using the circular rocket combustor at the evaluation time. The temperature profiles correspond to a 1 mm distance from the hot gas wall.

extensive comparison of the experimental data with results from CFD simulations is given in Roth et al. [31]. The nominal oxidizer to fuel ratio (O/F) in the hydrogen case is equal to 6.0 and for methane equal to 3.0.

In the right sub-figure of Fig. 13, the measured temperature values at 1 mm from the hot gas wall are plotted with symbols, whereas the solid lines represent the calculated temperature distribution from the inverse method. The shown profiles correspond to the averaged values within the evaluation window shown in Fig. 12, i.e. between 2 s and 2.5 s. An excellent agreement between the two values is observed, as expected since the goal of the method is to minimize the difference between the two. A higher temperature is shown in the case of H_2/O_2 compared to CH_4/O_2 both at 10 and 20 bar. This correlates to a higher heat flux predicted by the inverse method as shown in the left sub-figure. The uncertainty of the heat flux profile when taking into account all the error sources from Section 4, reaches approximately 13% for the majority of the axial positions. For axial positions between 100 mm and 200 mm a wavy pattern is observed in the thermocouple measurements. This translates to a heat flux oscillation at the same locations. The wavy pattern is visible for all time steps and does not experience an oscillatory behavior in time. This effect is attributed to a systematic error in the installation of the thermocouples either in terms of positioning or thermal contact with the chamber.

The results of the inverse method allow for a quantitative examination of the effects of higher pressure on the heat loads. In order to investigate the plausibility of the obtained results, an effort is made to explain the profiles based on the expected physical phenomena in the chamber.

According to Bartz [32], the heat transfer coefficient in a rocket engine correlates almost linearly according to $h \sim p_c^{0.8}$ with the combustion pressure p_c. Extensive data from Pempie [33] show that the same relationship holds true also for the maximal heat flux level in most LOX/LH_2 engines. In the data presented here, a clear increase of the heat flux with increasing pressure is seen, for both propellant combinations. To examine the applicability of this relationship to the examined combustion chamber, a fit of the data from the inverse method is carried out, according to $\dot{q} = C \cdot p_c^n$. Estimating the parameter n for methane and hydrogen results in values of 0.93 and 0.81 respectively. Hence it is found that for both the gaseous methane and the gaseous hydrogen tests, the qualitative trend of the Bartz correlation holds true and an almost linear heat flux level increase is expected with larger combustion chamber pressure.

Despite the similarity regarding the absolute level increase, the heat flux profiles for the two propellant combinations present several differences. Regarding the heat loads, hydrogen presents higher heat flux values for both operating points, which can be easily understood as it is a more energetic propellant with a higher combustion temperature. As far as the axial profile is concerned, in the case of hydrogen, a sharp increase is observed starting around 50 mm from the faceplate, followed by an almost constant heat flux plateau which sets in at 110 mm. Subsequently, a drop in the heat flux is observed, which takes place close to the end of the chamber, namely at $x = 250$ mm. In the case of methane on the other hand, the heat flux increase takes place much slower, and a constant level is reached after approximately 200 mm.

The sharper increase in the case of H_2 can be attributed both to hydrodynamic as well as chemical effects. Due to the large density difference between oxidizer and fuel, a large velocity ratio is imposed, which facilitates the mixing in the gaseous phase. Specifically, the velocity ratio for the CH_4/O_2 configuration is close to 1, whereas for H_2/O_2 it approaches a value of 8. Hence due to the efficient mixing in the shear layer of the coaxial element, the energy release takes place much closer to the injector plane, leading to a steep heat flux rise. At the same time, the fast chemical reaction rates occurring in hydrogen combustion result in the energy release being finished earlier than in the case of methane. This explains why a steady plateau is obtained around the middle of the combustor, which indicates the end of combustion. Since no further reactions take place, the hot gas starts losing energy through the walls and this fact in combination with the thermal boundary layer build-up leads to a slight drop in heat flux. Due to the lower chemical rates of the methane combustion and the slower mixing, the heat release takes place gradually over the entire chamber length and the end of combustion occurs further downstream.

6.2. Square single-element combustor

The single-element combustor with square cross-section has been operated with CH_4/O_2 at different load points ranging from 5 to 30 bar and oxidizer to fuel ratios between 2.2 and 3.4 [26], different injector recess lengths [24] and with optical access using OH^* emission imaging [34]. For the estimation of the heat flux, thermocouples at 18 axial positions are available, equally distributed along the axis of the chamber, with an axial separation of 17 mm from each other. For some axial positions, thermocouples at 1 mm, 2 mm and 3 mm from the hot gas wall are available,

whereas at other positions only thermocouples at 1 mm from the wall are available. In total 24 thermocouples are used for the inverse method of this hardware.

The ability of RoqFITT to correctly reconstruct the thermal field is evident in Fig. 14. A test case of CH_4/O_2 at 20 bar and O/F = 3.0 is taken as an example. The calculated transient profiles at the locations of selected thermocouples (solid lines) are plotted as a function of time, along with the corresponding measurements (dashed line) and their respective deviation. Again, a very good agreement is observed.

Apart from the transient thermocouple readings, the ability of the code to predict the spatial distribution of temperature in the chamber is also interesting. In Fig. 15 the iso-lines of temperature are shown at the $x = 255$ mm plane at the evaluation time. It can be observed that despite the rectangular shape of the inner wall, the contours are nearly circular close to the hot gas wall. Further outwards, the effect of the capacitive corner takes place: a fast cool-down is observed towards the right and left edges due to the presence of a large copper mass. In the vertical direction on the other hand, less material is available which leads to higher temperatures and a slower cool-down rate.

With the established ability of the code to correctly reconstruct the temperature at specific points, an effort can be made to explain the obtained heat flux profiles based on the expected physical phenomena. In this section the heat flux and temperature profiles for three CH_4/O_2 experiments at 20 bar nominal operating pressure are presented. A comparison between the profiles of the three O/F ratios is illustrated in Fig. 16 and can be used for the characterization of the injector element. The heat flux profile is namely largely dependent on the mixing and energy release processes, which in the vicinity of the faceplate are dictated by the injector design.

The temperature profiles correspond to the inverse method results at a distance of 1 mm from the hot gas wall and the markers represent the measured thermocouple values. All plotted curves are the averaged results within the evaluation window shown in Fig. 12. It can be seen in Fig. 16, that the absolute level of the heat flux and temperature at the end of the combustion chamber is increasing with increasing O/F. This effect is expected, as the stoichiometric composition in the case of methane/oxygen combustion lies at a value of O/F $\approx$ 4.0. Around this value the highest heat release and the largest gas temperature are anticipated, leading to a larger heat loss to the wall.

In the vicinity of the faceplate however, the heat release is not only dictated by the chemistry but is largely influenced by the injector design. In the first 50 mm from the wall, an opposite trend is observed: the lowest O/F operating points seem to have a larger heat flux. This is an effect of the difference in velocity ratios among the tests. For the lowest O/F = 2.6, the methane flowing through the outer annulus has a larger velocity than oxygen. This larger velocity leads to a higher expansion angle of the jet and therefore to a shorter distance between the flame and the wall. This directly increases the heat input into the structure.

In a sense, the flame for smaller O/F values is closer to the faceplate compared to larger O/F, where the flame appears to have shifted downstream. This downstream shift is also evident when examining the heat flux increase close to the end of combustion. For O/F = 2.6, the heat flux appears to reach a constant value after approximately 255 mm, whereas for O/F = 3.4 the heat flux increases until the end of the chamber. This indicates a continuous heat release over the entire chamber length and hence an incomplete combustion. This feature is attributed to the lower momentum flux ratio ($\rho_{CH_4} v_{CH_4}^2 / \rho_{O_2} v_{O_2}^2$) at higher O/F. The higher momentum of oxygen pushes the mixing region further downstream and leads to this observed shift of the flame to positions closer to the nozzle. This effect was both measured with the optical imaging methods as well as reproduced in the CFD simulations

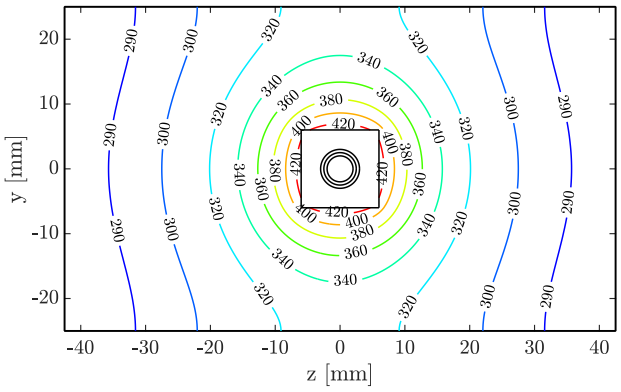

Fig. 15. Temperature field at the plane 255 mm downstream of the injector at evaluation time.

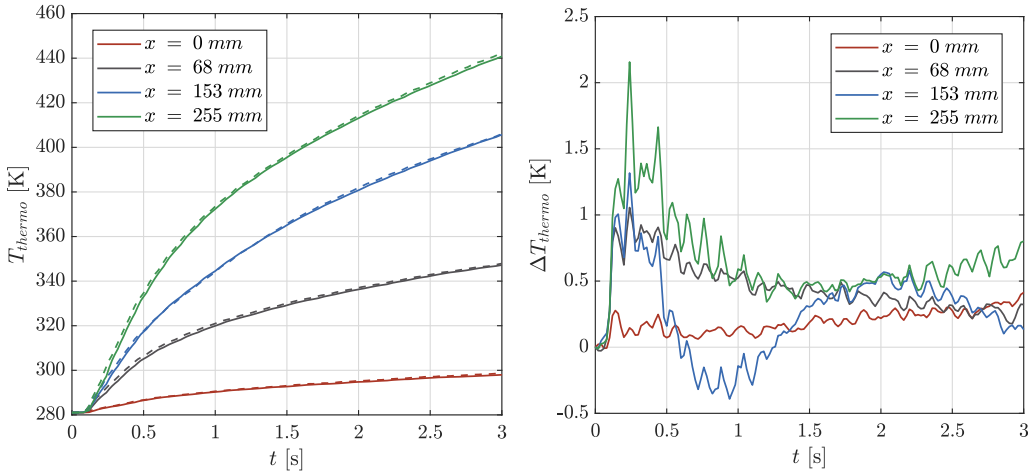

Fig. 14. Transient profiles of the calculated and measured temperature at selected thermocouple positions (left) and the corresponding difference between calculated and measured values (right) for the square chamber.

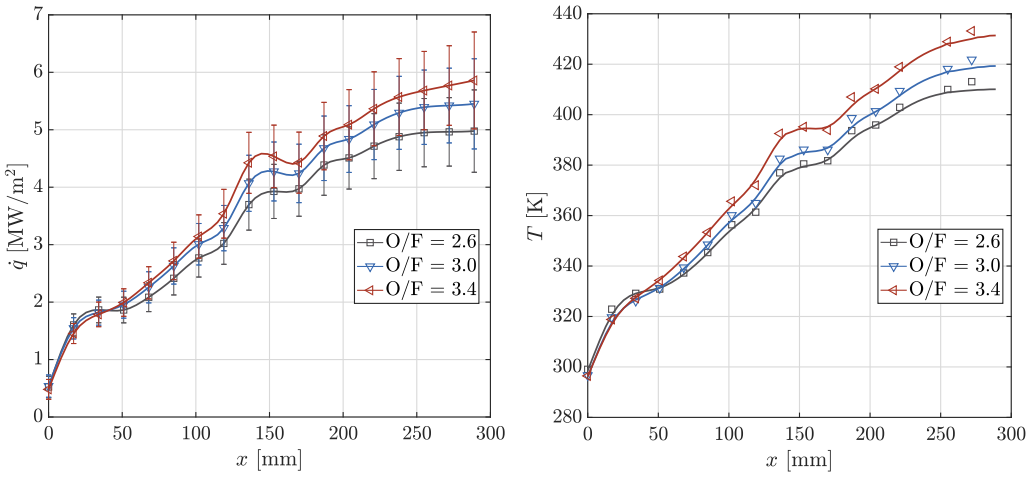

Fig. 16. Axial heat flux and temperature profile in the square single-element chamber for different operating points at the evaluation time.

presented in Winter et al. [34]. Hence using the inverse heat conduction method very significant information was able to be extracted from the available experimental data, essentially leading to a thorough understanding of the injector dynamics, mixing in gas phase and heat release.

In this evaluation, the optimization of the heat flux using RoqFITT occurs only at the specified parameter points, located at the positions of the thermocouples projected onto the hot gas wall. Along the perimeter of the rectangular cross section, a constant heat flux value is used. Physically, this assumption is not entirely motivating, since a lower heat flux is expected at the corners of the chamber due to the thermal boundary layer and the secondary flows, whereas the maximal heat flux should occur in the middle of each side. Due to the lack of further thermocouples in the present experimental configuration, no further information about the temperature outside of the middle plane is available, and hence no information about the heat flux distribution along the perimeter can be extracted.

An analysis has been carried out to examine the effect of the chosen heat flux profile along the perimeter. A large number of different profiles have been utilized, with all of them having a decreased corner heat flux value compared to the middle of the horizontal axis. It is namely expected that the heat flux approaches zero close to the corner. To demonstrate the effect of different profiles, the constant profile is compared to a variable profile, with the maximum placed in the middle of each side and the minimum of 0 at the corners. The shape of the profile is described by

$$\dot{q}(z) = \dot{q}_{max} \cdot \left(1 - \left(\frac{|2 \cdot z|}{w}\right)^n\right) \tag{20}$$

where w represents the width of the hot gas side and n a factor between 0 and 1 is.[1] Various values have been tested demonstrating similar results but for this study a value coming from the CFD simulation of the chamber in Winter et al. [34] is used with $n \approx 0.2$. For this comparison, the results of the test case with O/F = 3.0 are shown.

The results for the average heat flux along axial position are illustrated in Fig. 17. It can be seen that the two methods provide very similar distributions, with an offset which remains underneath 4% over the entire chamber length. Specifically, the variable profile predicts a slightly lower average heat flux compared to the constant one. This discrepancy can be better understood when examining the temperature and heat flux results of the inverse method along the spanwise direction (z axis) (see Fig. 18).

In the left sub-figure, it can be seen that both methods result in a maximal temperature in the middle of the horizontal side and minimal values at the sides. This is an effect created by the corners of the rectangular chamber, which act as a heat sink. Moreover, the temperature field with variable profile (dashed lines) shows a larger value at $z = 0$ mm. This is of course a result of the higher heat flux as shown in the right sub-figure. Although the temperature value directly at the wall is slightly higher with the variable profile, at 1 mm from the hot gas wall (i.e. at the location of the thermocouples) both methods deliver identical results by definition of the optimization problem. Due to the larger span-wise thermal gradient in the case of variable profile (steeper temperature drop towards the corners), the temperature decreases faster with increasing radial distance, leading to the same value with the constant profile at the measurement locations. Since the observed difference with both methods is so small however when evaluating the average heat flux values, both the variable and the constant profile are considered to be fully sufficient for this analysis.

6.3. Multi-element chamber

In contrast to the single-element combustors, in the multi-element one there is available information about the temperature values at more than one location in each axial position. As shown in Fig. 6, there is a maximal capacity of seven thermocouples per plane. Starting from left to right, the thermocouples are named 1C, 2C, 3L, 3C, 3R, 4C, 5C where "C" represents a position directly above an injector element, and "L", "R" the positions left and right of an element. Parameter points are placed at all the positions where thermocouple readings are available. It is important to note, that although seven measurements are possible at each plane, not all positions are equipped with thermocouples, and most planes possess only three measurements at 3L, 3C, 3R.

As mentioned in the description of the optimization algorithm, the heat flux is optimized only at specific locations and specifically only at the thermocouples' positions projected on the hot gas wall. Special care has to be taken to transform the heat flux from the few locations in the chamber to a continuous variable over the whole boundary domain. Along the z direction (horizontal side of the chamber), an interpolating procedure has to be implemented. A simple linear interpolation between two neighboring parameter values is in most cases prone to error. This is because locations named with the index "C" are directly above an injector element and are expected to have higher heat flux values (at least for loca-

[1] $z = 0$ mm corresponds to the middle of the horizontal side.

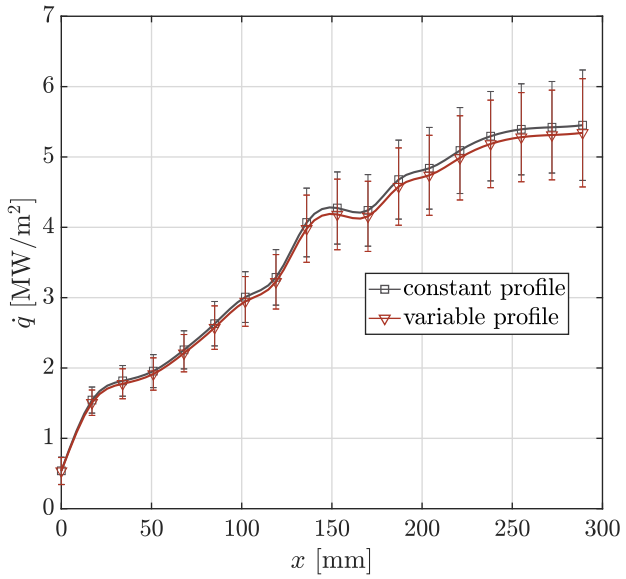

Fig. 17. Average heat flux profile for a constant and a variable distribution at the evaluation time.

tions close to the faceplate where the flame temperature's stratification is more dominant) compared to the locations between the two injectors (for example 3L). Hence a linear interpolation between 4C and 5C would be overestimating the flux between the injectors.

For that reason the heat flux at positions where the thermocouples are missing, are taken by averaging the remaining values at the same plane. This means that the missing values between the injectors 4 and 5 are taken by averaging the heat flux at 3R and 3L. In an analog fashion if the thermocouples at a position above an injector element are missing (e.g. 5C), then the average of the remaining central thermocouples are taken (e.g. 3C and 2C). This interpolation method assumes that the heat flux profiles above each one of the 5 injectors are similar for a specific plane. A cubic interpolation is used to convert the discrete parameter values to a continuous profile along the perimeter and the axial direction. Thermocouples are available at 16 equally spaced locations along the axial direction (separated by 17 mm from each other) and the total number of thermocouples used in the inverse method amounts to 66.

Only thermocouples at the upper wall are used and hence the heat flux profile at the bottom wall is defined identically to the upper wall, leading to a symmetric profile relative to the $y = 0$ plane. For the vertical walls of the hot gas side, a parabolic profile is defined. The corner value is known from the horizontal interpolation and the maximal value at the middle is defined as the average of the central values calculated for this plane (i.e. average of 1C, 2C, 3C, 4C, 5C). This can be used because the distance of the injector element from the vertical wall is the same as the one from the horizontal one, namely 3 mm.

Using those assumptions, the inverse method is used to evaluate a 20 bar, O/F = 3.4 CH_4/O_2 test case. The agreement of the calculated temperature values with the thermocouple readings is in accordance with the results presented in Figs. 11 and 14 for all sensor locations. Whereas the focus in Sections 6.1 and 6.2 was mainly on the axial profiles of the heat flux and temperature, in this section attention is specifically paid to the ability of RoqFITT to capture transient phenomena as well as information about the distributions along the perimeter.

Firstly, the pressure and heat loss profiles are compared in the left sub-figure of Fig. 19. The two variables are connected to each other since the combustion process has the effect of both raising the pressure within the chamber as well as increasing the energy release and hence the integral heat load to the wall. The values for the heat release calculated by the code refer only to the combustion chamber, excluding the nozzle since no heat flux values are available. The pressure measurement used here corresponds to the sensor located close to the faceplate, i.e. at $x = 0.5$ mm.

It is observed that the heat release starts increasing approximately at the same instant as the pressure at $t = 0$ s. After a sharp rise for the first 250 ms, the heat release increase seems to slow down at $t = 0.25$ s. The pressure profile also measures a small oscillation at the same time. The effect is attributed to the end of the igniter operation, which leads to a slight hold in the increase of the energy release. During the operation of the igniter, the presence of an additional transversal jet influences the injector flame, due to a local increase of mixing and therefore higher heat release, which is explained by the peak of the heat flux close to the faceplate. Immediately after the influence of the igniter is

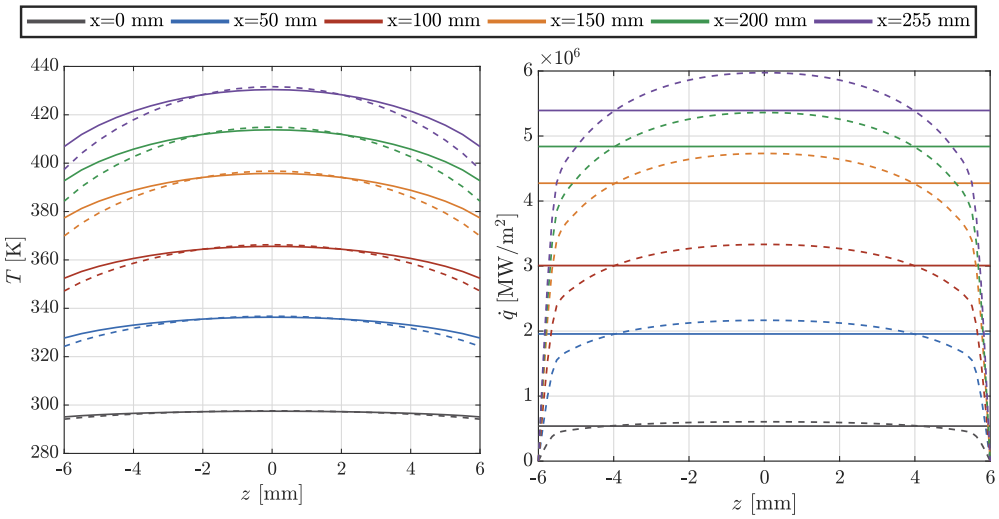

Fig. 18. Temperature and heat flux profile at the hot gas wall along the horizontal side (z axis) for a constant (solid line) and variable (dashed line) heat flux profile at evaluation time.

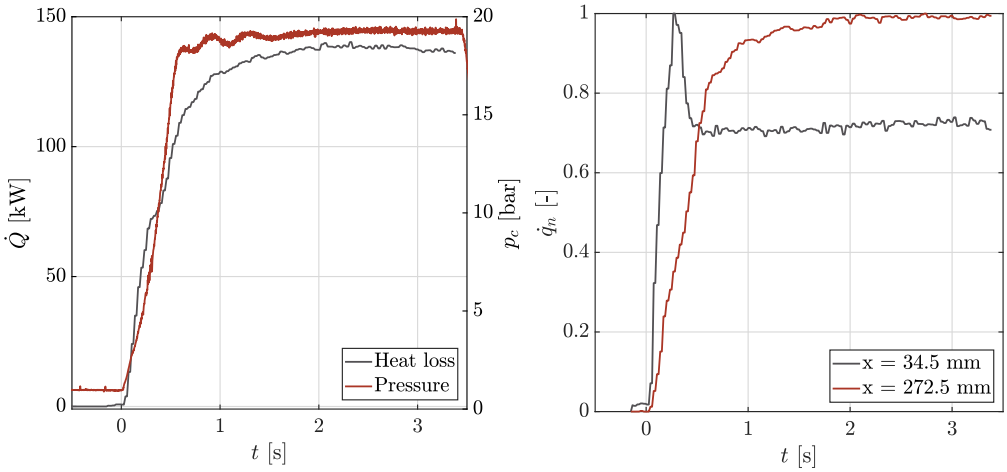

Fig. 19. Time-dependent profile of pressure and heat loss (left) and transient heat flux profiles at selected axial positions (right).

damped away, the energy release in the chamber continues to increase along with the pressure signal and reaches a constant plateau around the $t = 1.5$ s mark. Looking at the pressure signal, one notices that the pressure demonstrates a small oscillation from $t = 0.6$ s until $t = 1.5$ s. The cause of this transient phenomenon could be that the anchoring of the flame in all five injector elements does not happen simultaneously. The elements close to the igniter source are the ones being stabilized faster and the flame propagates to the others slightly later. When the flame is attached and stable, then a constant pressure level is expected. This is also the case at $t = 1.5$ s, which coincides with the time point at which the heat load gets to a plateau as well. Hence the inverse method is able to capture the qualitative transient development of the heat loss through the wall, which is verified by the pressure signal.

Apart from the time evolution of the integrated heat flux over the chamber area, examining the heat flux profile over time at specific locations in the chamber also gives information about the combustion characteristics. In the right sub-figure of Fig. 19, the temporal profile of the heat flux at the 3C location for two different axial planes ($x = 34.5$ mm and $x = 272.5$ mm) is plotted. The heat flux values have been normalized with their respective maximal value in order to emphasize the qualitative effect of the time evolution without taking into account the effect of the difference in absolute value. The values at $x = 34.5$ mm demonstrate a peak after around 0.25 s before reaching a constant level. As explained earlier, this is the effect of the igniter which is located at the same axial position. The results further downstream right before the nozzle segment ($x = 272.5$ mm) seem to be uninfluenced from the igniter effect, since there is no peak present along time. This behavior is expected since start-up effects should be located close to the ignition source and should have disappeared before reaching the end of the combustion chamber.

Therefore it is evident that the inverse method can distinguish between the transient and spatially varying heat loads and the resulting profiles appear to be in agreement with the expected behavior due to the hardware configuration and test sequence.

The main difference between an inverse method used for the heat flux evaluation in a multi-element chamber compared to a single element one is the azimuthal variation of the heat flux profile. In the case of a rectangular combustor as in this case, the variation occurs along the z axis. In order to examine the capability of the method to predict the heat flux variation along the horizontal hot gas wall, the temperature profiles at 1 mm distance from the wall for some selected axial positions and the corresponding heat flux values are examined in Fig. 20.

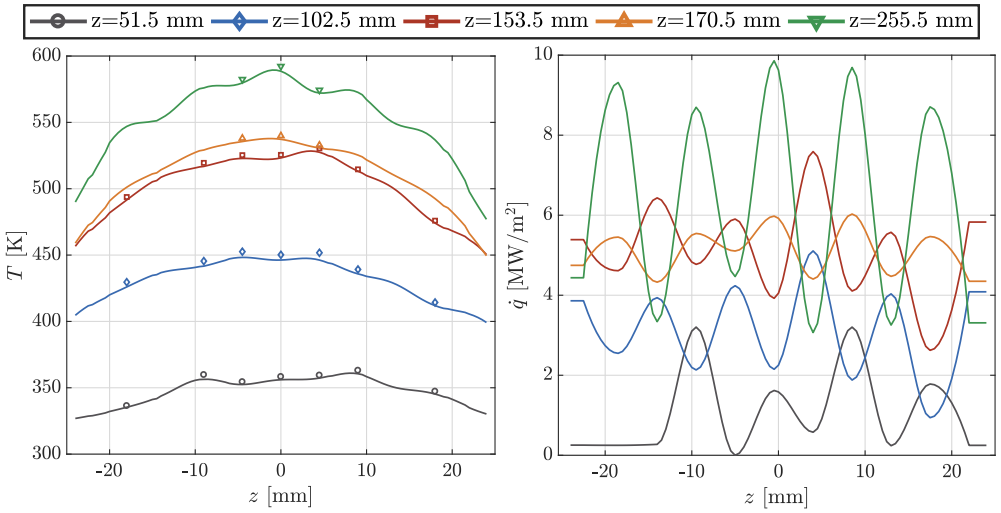

Fig. 20. Temperature at 1 mm from the hot gas wall (left) and heat flux profile at the hot gas wall along the horizontal side (z axis) at evaluation time.

In Fig. 20, the measured values are indicated with symbols and the solid line represents the calculated values stemming from the inverse method. The results are shown at the defined evaluation time window (t = 2-2.5 s). The planes at x = 51.5 mm, x = 102.5 mm and x = 153.5 mm are equipped with all seven thermocouples, whereas at x = 170.5 mm and x = 255.5 mm only the 3L, 3C and 3R positions are filled. Starting with the plane closest to the faceplate (x = 51.5 mm) one notices that the temperature values directly above the injector elements (2C, 3C and 4C) are higher than the measurements between the injectors (3L, 3R). This is also captured in the heat flux profile for the same plane, which demonstrates peaks at the positions 1C, 2C, 3C, 4C and 5C and lower values at the locations in between. This effect of temperature stratification and specifically of higher heat release directly above the elements is expected close to the faceplate where the individual streams have not been mixed and the flow-field can be imagined as five separate cylindrical flames.

The same pattern of maximal heat flux values at the "C" locations is observed at the planes x = 170.5 mm and x = 255.5 mm as shown in Fig. 20. However, planes x = 102.5 mm and x = 153.5 mm show the exact opposite effect, with the heat flux values between the injectors being higher than directly above the elements. This results can be deduced by simply looking at the 3L, 3C and 3R temperature measurements for these planes. The effect of the shift in the maximal heat flux azimuthal position has been observed in other sub-scale engines as well. CFD simulations preformed on various engines such as the TUM 7-element sub-scale combustor [23] showed that downstream of a specific location at the chamber, the heat flux values above the injector elements were lower than the ones between two elements of the outer row. This effect was attributed to the presence of strong secondary vortices pushing hot gas out of the injector plane. It is assumed that a similar process takes place in the case of the TUM rectangular combustor.

For positions further downstream than this "shifted" peak, it is expected that the heat flux should be smoother along the z direction, with fewer variations between the maximal and minimal values due to an increase in mixing, leading to a smaller stratification degree. This is indeed observed at the x = 170.5 mm where the differences between the heat flux values remain underneath 1 MW/m^2. This is also depicted in the temperature profile which almost has the form of a parabola, with very small variations. In general, observing the trend for all four planes up to the x = 170.5 mm location, one sees that the stratification decreases indicating a better mixing of the hot gas.

However the plane at x = 255.5 mm demonstrates a further increase in stratification, larger variations of the thermocouple readings and hence obtained heat flux values. Since this would correspond to a decrease in the mixing degree of the burnt gas compared to positions further upstream, the results have to be treated with caution. A possible explanation for this behavior could be a problem with the installation of the thermocouples. If the thermal contact between sensor and chamber material is not adequate then a bigger response time and hence slower measurement can be expected. This could be the case for the 3L and 3R sensors in this plane. Also the sensitivity of the thermocouples' distances from the hot gas wall is also an issue. If the position deviates from the nominal 1 mm, then due to a high sensitivity of the calculated heat flux on the measurement, a bigger heat flux error has to be accounted for. Nevertheless, some flow-dynamic effects could also influence the heat release in this part due to the presence of the truncated nozzle. Due to the sharp edge and the presence of more chamber material at this location, a more detailed CFD analysis is required to fully understand the dynamics of heat release close to the end of combustion. Therefore CFD simulations are also planned to examine whether this effect could be physically possible or if it is a byproduct of the hardware installation.

The high sensitivity of the thermocouple position on the obtained heat flux profile can be grasped by examining Fig. 21. Here the temperature field at the last axial plane before the nozzle is plotted at the evaluation time. The isolines close to the hot gas wall (within the first 2–3 mm) show a "wavy" pattern indicating the variation of the heat flux along the axial position. For distances farther away however, the temperature variation seems to vanish and the isolines show a nearly elliptical form. This implies that positioning the thermocouples in a smallest possible distance from

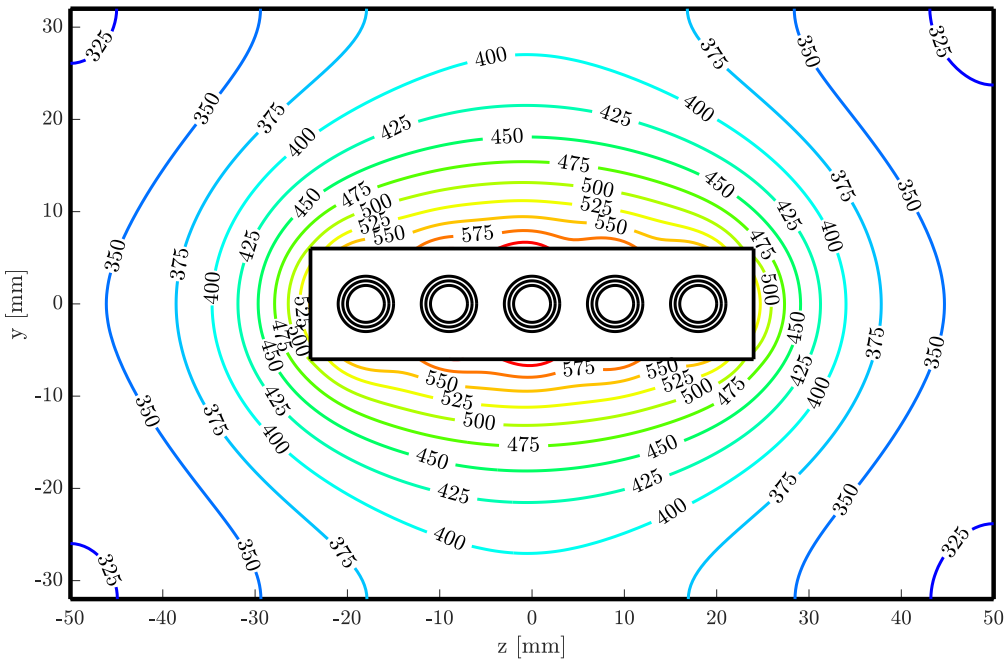

Fig. 21. Temperature field at the plane 272.5 mm downstream of the injector at evaluation time.

the chamber wall is needed for accurate heat flux evaluation. This also implies that a small deviation of the thermocouple from the nominal position or a faulty thermal contact would produce a large heat flux uncertainty because of the high sensitivity.

7. Conclusion

The evaluation of heat flux profiles in single-element and sub-scale engines is crucial for the understanding of the underlying physical and chemical processes defining the injector performance, the injector/injector and injector/wall interaction, mixing and energy release in the chamber. The inverse heat conduction method implemented in RoqFITT is intended for the analysis of transient temperature and heat flux distributions in capacitively cooled rocket thrust chambers and was developed at the Chair of Turbomachinery and Flight Propulsion of the Technical University of Munich.

The inverse method relies on an iterative optimization method with the objective of minimizing the temperature difference between the measured and the calculated values. The optimization variable is the heat flux at discrete locations at the hot gas wall of the chamber. The iterative process requires an efficient direct thermal solver, which has been developed using a finite difference approach on a simplified computational domain. The update of the heat flux parameters at each iteration is carried out using the Jacobi matrix either via the conjugate gradient or the Newton-Raphson method, with the latter one showing a higher computational efficiency. Extensive validation studies of the direct solver and the inverse algorithm have been carried out for operating conditions in a range relevant for sub-scale engine tests.

The inverse heat conduction method has been applied on three capacitively cooled combustors operated at the TUM. Using the algorithm for the evaluation procedure of the tests, important information was extracted from the obtained heat flux profiles regarding the performance of the injector. The qualitative difference in the mixing and energy release process of H_2/O_2 and CH_4/O_2 was captured based on the heat flux profile gradient, allowing for information about the performance characteristics of each propellant combination. The effects of pressure and mixture ratio variations onto the mixing and combustion were also deduced based on the heat flux footprint at the hot gas wall. Moreover, transient effects due to the igniter's operation were identified and validated based on the measured pressure signal. Finally, the heat flux profile along the spanwise direction in a multi-element chamber could also be calculated, showing that the resulting distribution is highly sensitive to measurement noise and systematic errors due to the high thermal conductivity of the structure material.

It has been shown that the inverse heat conduction method can be successfully applied to numerous rocket engine applications for the estimation of the heat loads with reasonable computational resources. Both steady state as well as transient effects can be captured by the use of the method, rendering it a necessary tool for the evaluation of sub-scale experiments.

Conflict of interest

Declarations of interest: none.

Acknowledgements

The authors would like to thank Mr. Cosimo Ciraci and Mr. Alessandro Villani for their assistance in the validation of the code as well as Ms. Simona Silvestri, Ms. Maria Palma Celano and Ms. Fernanda Winter for providing the experimental data. Financial support has been provided by the German Research Foundation (Deutsche Forschungsgemeinschaft DFG) in the framework of the Sonderforschungsbereich Transregio 40.

References

[1] H. Asakawa, H. Nanri, K. Aoki, I. Kubota, H. Mori, Y. Ishikawa, K. Kimoto, S. Ishihara, S. Ishizaki, The status of the research and development of LNG rocket engines in Japan, in: Chemical Rocket Propulsion, Springer, 2017, pp. 463–487.
[2] T. Kato, D. Terakado, H. Nanri, T. Morito, I. Masuda, H. Asakawa, H. Sakaguchi, Y. Ishikawa, T. Inoue, S. Ishihara, et al., Subscale firing test for regenerative cooling LOx/methane rocket engine, in: 7th European Conference for Aeronautics and Space Sciences (EUCASS), 2017. https://doi.org/10.13009/EUCASS2017-381.
[3] O. Knab, M. Frey, J. Görgen, K. Quering, D. Wiedmann, C. Mäding, Progress in combustion and heat transfer modelling in rocket thrust chamber applied engineering, in: 45th AIAA/ASME/SAE/ASEE Joint Propulsion Conference & Exhibit, 2009, p. 5477.
[4] O.J. Haidn, N. Adams, R. Radespiel, W. Schröder, C. Stemmer, T. Sattelmayer, B. Weigand, Fundamental Technologies for the development of future space transport system components under high thermal and mechanical loads, in: 54th AIAA/SAE/ASEE Joint Propulsion Conference, 2018, p. 4466.
[5] F. Cuoco, B. Yang, M. Oschwald, Experimental investigation of LOX/H2 and LOX/CH4 sprays and flames, in: 24th International Symposium on Space Technology and Science, 2004.
[6] J. Lux, D. Suslov, M. Bechle, M. Oschwald, O.J. Haidn, Investigation of sub-and supercritical LOX/methane injection using optical diagnostics, in: 42nd AIAA/ASME/SAE/ASEE Joint Propulsion Conference & Exhibit.
[7] M. Shim, K. Noh, W. Yoon, Flame structure of methane/oxygen shear coaxial jet with velocity ratio using high-speed imaging and OH*, CH* chemiluminescence, Acta Astronaut. 147 (2018) 127–132.
[8] F. Grisch, E. Bertseva, M. Habiballah, E. Jourdanneau, F. Chaussard, R. Saint-Loup, T. Gabard, H. Berger, CARS spectroscopy of CH_4 for implication of temperature measurements in supercritical LOX/CH_4 combustion, Aerosp. Sci. Technol. 11 (1) (2007) 48–54.
[9] D. Suslov, B. Betti, T. Aichner, S. Soller, F. Nasuti, O. Haidn, Experimental investigation and CFD-simulation of the film cooling in an O_2/CH_4 subscale combustion chamber, in: Space Propulsion Conference, 2012.
[10] F. Grisch, P. Bouchardy, W. Clauss, CARS thermometry in high pressure rocket combustors, Aerosp. Sci. Technol. 7 (4) (2003) 317–330.
[11] C.-H. Huang, S.-P. Wang, A three-dimensional inverse heat conduction problem in estimating surface heat flux by conjugate gradient method, Int. J. Heat Mass Transf. 42 (18) (1999) 3387–3403.
[12] C.-H. Huang, Y.-L. Tsai, A transient 3-D inverse problem in imaging the time-dependent local heat transfer coefficients for plate fin, Appl. Therm. Eng. 25 (14–15) (2005) 2478–2495.
[13] E.B. Coy, Measurement of transient heat flux and surface temperature using embedded temperature sensors, J. Thermophys. Heat Transf. 24 (1) (2010) 77–84.
[14] A. Vaidyanathan, J. Gustavsson, C. Segal, One-and three-dimensional wall heat flux calculations in a O_2/H_2 system, J. Propul. Power 26 (1) (2010) 186–189.
[15] M.P. Celano, S. Silvestri, J. Pauw, N. Perakis, F. Schily, D. Suslov, O.J. Haidn, Heat flux evaluation methods for a single element heat-sink chamber, in: 6th European Conference for Aeronautics and Space Sciences (EUCASS), 2015.
[16] N. Perakis, M.P. Celano, O.J. Haidn, Heat flux and temperature evaluation in a rectangular multi-element GOX/GCH4 combustion chamber using an inverse heat conduction method, in: 7th European Conference for Aeronautics and Space Sciences (EUCASS), 2017.
[17] C.U. Kirchberger, Investigation on heat transfer in small hydrocarbon rocket combustion chambers (Ph.D. thesis), Technische Universität München, 2014.
[18] E. Artioukhine, Heat transfer and inverse analysis, in Educational Notes RDP, NATO Unclassified, https://doi.org/10.14339/RTO-EN-AVT-117.
[19] M.N. Özisik, Inverse Heat Transfer: Fundamentals and Applications, CRC Press, 2000.
[20] R. Fletcher, C.M. Reeves, Function minimization by conjugate gradients, Comput. J. 7 (2) (1964) 149–154.
[21] R. Fletcher, Practical Methods of Optimization, John Wiley & Sons, 2013.
[22] C.M. Roth, O.J. Haidn, A. Chemnitz, T. Sattelmayer, G. Frank, H. Müller, J. Zips, R. Keller, P.M. Gerlinger, D. Maestro, et al., Numerical investigation of flow and combustion in a single element GCH4/GOx rocket combustor, in: 52nd AIAA/SAE/ASEE Joint Propulsion Conference, 2016, p. 4995.
[23] N. Perakis, D. Rahn, D. Eiringhaus, Y. Daimon, S. Zhang, S. Karl, T. Horchler, O.J. Haidn, Qualitative and quantitative comparison of RANS simulation results for a 7 element GOX/GCH4 rocket combustor, in: 54th AIAA/SAE/ASEE Joint Propulsion Conference, 2018.
[24] S. Silvestri, F. Winter, M. Garulli, M.P. Celano, G. Schlieben, O.J. Haidn, O. Knab, Investigation on recess variation of a shear coaxial injector in a GOX-GCH4 rectangular combustion chamber with optical access, in: 7th European Conference for Aeronautics and Space Sciences (EUCASS), 2017.
[25] S. Silvestri, C. Kirchberger, G. Schlieben, M.P. Celano, O.J. Haidn, Experimental and numerical investigation of a multi-injector GOX-GCH4 combustion chamber, Trans. Jpn. Soc. Aeronaut. Space Sci. Aerosp. Technol. Jpn. 16 (5) (2018) 374–381.
[26] M.P. Celano, S. Silvestri, C. Bauer, N. Perakis, G. Schlieben, O.J. Haidn, Comparison of single and multi-injector GOX/CH_4 combustion chambers, in: 52nd AIAA/SAE/ASEE Joint Propulsion Conference, 2016, p. 4990.

[27] S. Silvestri, M.P. Celano, G. Schlieben, O.J. Haidn, Characterization of a multi-injector GOX/CH_4 combustion chamber, in: 52nd AIAA/SAE/ASEE Joint Propulsion Conference, 2016, p. 4992.
[28] J. Taylor, Introduction to error analysis, the study of uncertainties in physical measurements, University Science Books, New York, 1997.
[29] X. Wang, Y. Gao, G. Cai, H. Huo, Wall heat transfer measurements in high-pressure combustion devices, J. Aerosp. Eng. 26 (4) (2011) 698–707.
[30] Fluent, 18.0 ANSYS Fluent Theory Guide 18.0, Ansys Inc.
[31] C. Roth, S. Silvestri, N. Perakis, O.J. Haidn, Experimental and numerical investigation of flow and combustion in a single element rocket combustor using GH2/GOX and GCH4/GOX as propellants, in: International Symposium on Space Technology and Science, 2017.
[32] D.R. Bartz, A simple equation for rapid estimation of rocket nozzle convective heat transfer coefficients, J. Jet Propulsion 27 (1) (1957) 49–53.
[33] P. Pempie, Moteur fusees a ergols liquides, Tech. rep., CNES/DLA/AET/A 331/00, 2000.
[34] F.F. Winter, N. Perakis, O.J. Haidn, Emission imaging and CFD simulation of a coaxial single-element GOX/GCH4 rocket combustor, in: 54th AIAA/SAE/ASEE Joint Propulsion Conference, 2018, p. 4764.

3.2 REGENERATIVELY COOLED ROCKET THRUST CHAMBERS

The investigation of different approaches for the estimation of wall heat loads in regenerative rocket thrust chambers using inverse methods is presented in this section. The passage corresponds to the paper entitled:

Wall Heat Flux Evaluation in Regeneratively Cooled Rocket Thrust Chambers
Nikolaos Perakis, Lukas Preis, Oskar J. Haidn
Journal of Thermophysics and Heat Transfer (2020)
doi: https://doi.org/10.2514/1.T6056

The main objective of the present study was the extension of the RoqFITT code to enable the evaluation of experimental configurations *with cooling channels*, as opposed to the already established method for capacitive hardware shown in Section 3.1.

In order to be able to compare different evaluation methods with respect to their ability to capture the experimental heat loads, precise knowledge of the heat loads and temperature fields is required. As this data is not available in real experimental applications, data for this analysis were *generated by means of a forward model*. In this forward model, the raw temperature sensor readings were generated by a running a *full-fledged CFD simulation of the turbulent combustion* within the chamber, coupled with a conjugate heat transfer simulation in the walls and convection in the cooling channels. The temperature data at embedded locations of the thermocouple sensors were then used to represent experimental measurements in order to validate and compare the different methods. The test case chosen for the analysis corresponds to an upper-stage expander engine in the 100 kN thrust regime which is described in the work of Eiringhaus et al. [240].

The thermocouple readings were first used to estimate the *systematic errors introduced by the gradient method*. By varying the distance of the sensors from the hot gas wall, it was demonstrated that the temperature field in the structure of the chamber is *significantly distorted by the presence of the cooling channels*, to a degree that errors in heat flux of up to 85% were measured. According to the results, thermocouples placement further away than the first 0.5 mm from the hot gas wall could lead to unacceptable measurement uncertainties. This strongly restricts the applicability of the method. Although the absolute errors in heat flux and wall temperature are derived only from this specific configuration, they are representative and it is therefore important to note that the shortcoming of this method is expected for other geometries and operating points.

As far as the use of the inverse method is concerned, a classification of *three different approaches* is presented, based on the number of available sensors per axial location. The difference amongst the three methods is based on the treatment of the additional boundary condition, namely the cooling channel walls. A larger number of installed sensors allows for the estimation of the heat transfer coefficients simultaneously to the estimation of the hot gas wall heat flux. In summary, the following three categories are analyzed:

- Method requiring at least *one* thermocouple per axial position: Nusselt-number correlation for the cooling channel boundary.
- Method requiring at least *two* thermocouples per axial position: Inverse estimation of an average heat transfer coefficient for the entire cooling channel circumference.

- Method requiring at least *three* thermocouples per axial position: Inverse estimation of separate heat transfer coefficients at the top and bottom walls of the cooling channels.

Using the second and third method has the advantage that a *simultaneous inverse calculation of both hot gas heat flux and cooling heat transfer coefficient* can be derived. This is similar to the methods used by Kuhl et al. [221] and Haemisch et al. [36]. The benefit of the approach shown in the current section is the use of a *pre-processed sensitivity matrix* which allows for a *computationally efficient* inverse optimization, despite the 3D nature of the domain. With this method, the need for additional modeling is obsolete and a distinction between the heat transfer characteristics at the upper and lower walls can be performed, which allows for a better understanding of the coolant flow conditions. In the absence of a Nusselt correlation, the bias of the method is reduced.

Despite those undeniable benefits, the installation of thermocouples in multiple radial locations for each axial position is a complicated process, due to the small thickness of the fins between individual cooling channels and the lack of sufficient space for a large number of sensors. For that reason, specific emphasis is placed on the method using one thermocouple per axial location. To enable an estimation of the heat flux, the use of a Nusselt number correlation is proposed, which models the coolant's interaction with the wall. This approach can deliver heat flux data in regeneratively cooled chambers with a *much higher resolution than calorimetric data, while employing the least amount of sensors possible*. However, it has to be ensured that the used empirical correlations are validated for the operating conditions of interest. Failure to choose a tailored Nusselt number correlation introduces a bias in the obtained inverse results. This is shown in the paper together with a *parametric study on the sensor location*, in order to quantify the different sources of systematic error. The errors introduced due to a faulty positioning of the thermocouples are not investigated in this work, but are given in detail in Section 3.3.

JOURNAL OF THERMOPHYSICS AND HEAT TRANSFER

Wall Heat Flux Evaluation in Regeneratively Cooled Rocket Thrust Chambers

Nikolaos Perakis,* Lukas Preis,† and Oskar J. Haidn‡
Technical University of Munich, 85748 Garching, Germany

https://doi.org/10.2514/1.T6056

In the present Paper, different wall heat flux evaluation methods for rocket engines are analyzed and compared. The test case for the comparison is a supercritical load point of an H_2/O_2 upper-stage engine. The evaluation of the heat flux using existing gradient methods shows unacceptable deviations, whereas significant improvements are found with an inverse heat transfer method. Using a Nusselt number correlation for the modeling of the cooling channel heat transfer coefficient, good agreement with the experimental profiles is achieved, while the number of installed thermocouples is held at a minimum. However, the choice of the Nusselt number correlation directly influences the obtained results and strongly depends on the fuel and geometry of the system. Using a simultaneous optimization of the heat flux and heat transfer coefficient, on the other hand, seems to eliminate the need for additional modeling and leads to great agreement with the experiment. A new optimization method proposed in this Paper based on a preprocessed Jacobi matrix significantly speeds up the estimation of the free parameters. With the obtained results, the placement of the thermocouples before the design of the hardware can be optimized, leading to reduction of manufacturing costs.

Nomenclature

A	=	area, m^2
AR	=	aspect ratio
c^*	=	characteristic velocity, m/s
c_p	=	specific heat capacity, $J/(kg \cdot K)$
D	=	diameter, m
d	=	absolute thermocouple distance, m
H	=	specific enthalpy, J/kg
$\boldsymbol{H}$	=	heat transfer coefficient parameters, $W/(m^2 \cdot K)$
h	=	heat transfer coefficient, $W/(m^2 \cdot K)$
I_{sp}	=	specific impulse, s
J	=	residual/objective function, K^2
M	=	number of thermocouples
$\dot{m}$	=	mass flow rate, s
N	=	number of optimization parameters
Nu	=	Nusselt number
$\boldsymbol{n}$	=	wall normal, m
O/F	=	oxidizer to fuel ratio
p	=	pressure, bar
Pr	=	Prandtl number
$\boldsymbol{Q}$	=	wall heat flux parameters, W/m^2
$\dot{q}$	=	wall heat flux, W/m^2
Re	=	Reynolds number
r	=	radial distance, m
$\boldsymbol{S}$	=	sensitivity matrix, $(K \cdot m^2)/W$
T	=	temperature, K
t	=	wall thickness, m
x	=	axial distance, m
y	=	wall distance, m
z	=	spanwise distance, m
δ	=	relative thermocouple distance, m
λ	=	thermal conductivity, $W/(m \cdot K)$

Subscripts

bottom	=	bottom wall
c	=	calculated
cc	=	cooling channel
ch	=	combustion chamber
dev	=	standard deviation
err	=	error
f	=	fluid (coolant)
h	=	hydraulic
hgw	=	hot gas wall
in	=	inlet
m	=	measured
n	=	normalized
out	=	outlet
$side$	=	side wall
t	=	turbulent
top	=	top wall
w	=	wall

I. Introduction

THE high velocity flows within liquid propellant rocket engines combined with the hot gas temperatures of around 3500 K give rise to extreme heat loads at the wall of a typical rocket thrust chamber. When designing a rocket engine, a high chamber pressure is typically beneficial, as it helps achieve a high specific impulse and increases the compactness of the chamber [1]. A higher combustion chamber pressure, however, has a direct impact on the wall heat loads, because the heat transfer coefficient is proportional to the chamber pressure ($\dot{q} \sim p^{0.8}$) [2].

To ensure the reliable operation of rocket thrust chambers at those high operating thermal loads, efficient cooling methods need to be implemented such as film cooling, regenerative cooling, or a combination of the two. The proper design of the cooling system requires sufficient understanding of the heat transfer methods within the chamber and the wall structure not only to minimize the plastic deformation and ensure the desired component life but also because in some engine cycles the performance relies on the heat transfer characteristics between the hot gas and the wall. A typical example is the expander cycle, where the turbopumps are driven by the enthalpy that the cooling fluid picks up while flowing through the channels along the chamber wall.

To design a rocket engine, numerical methods are often implemented in order to simulate the flow structures within the thrust

Received 7 April 2020; revision received 20 May 2020; accepted for publication 9 July 2020; published online 30 September 2020.

*Graduate Student, Chair of Space Propulsion, Boltzmannstrasse 15; nikolaos.perakis@ltf.mw.tum.de.

†Graduate Student, Chair of Space Propulsion, Boltzmannstrasse 15.

‡Professor, Chair of Space Propulsion, Boltzmannstrasse 15.

chamber. These computational fluid dynamics (CFD) simulations are important in the first stages of an engine design because they can replace expensive trial-and-error firing tests. Nevertheless, for those models and simulations to be considered reliable, sufficient validation is mandatory. This is usually done by comparing their predicted heat flux, pressure, and performance (c^*, I_{sp}) against predefined experimental test cases [3,4]. For this validation, it is hence essential that the provided heat flux measurements are reliable and that sources of potential systematic errors are known.

It is therefore evident that the ability to accurately determine the heat loads of a rocket engine are very important for the design of future hardware, for the evaluation of hot-gas experiments and the validation of CFD models. Heat flux measurements can, however, be quite challenging. Although pressure, mass flow rate, thrust, and combustion efficiency are not challenging to measure during a hot run test, information on the temperature and heat loads at the chamber walls can be difficult to obtain due to the harsh environment. To improve the heat flux prediction accuracy in rocket combustors, significant efforts have been put into designing experimental research combustors, allowing for precise heat transfer measurements [5–9].

The purpose of the present Paper is to present the benefits of using inverse heat transfer methods for estimating the locally varying heat loads in regeneratively cooled rocket engines. Using a baseline reference case of a full-scale upper-stage engine described in Sec. III, a comparison between the different heat flux evaluation methods is presented. The main focus and innovation of this Paper lie in identifying the influence of the thermocouple placement on the achieved accuracy of each method shown in Sec. IV. Based on the available number of installed thermocouple sensors, the most accurate evaluation method is assessed. We are able to show that even a single thermocouple for each axial position is sufficient for an accurate heat flux retrieval. For a computationally efficient evaluation of the three-dimensional problem with arbitrary number of sensors, an optimization algorithm is presented in Secs. IV.B and IV.C. Although the idea of simultaneous optimization of wall heat flux and coolant heat transfer coefficient shown in these sections is not new, the proposed algorithm for the inversion significantly reduces the computational resources needed compared to methods used in the past.

II. Heat Flux Measurement Methods

In most rocket engines, the heat flux distribution has a three-dimensional nature with variations along the azimuthal direction (especially close to the face plate due to thermal and species stratification) and along the axial direction due to the progress in chemical reaction and the acceleration in the nozzle. Therefore, heat transfer measurements, apart from performing accurate estimations of the maximal heat loads, are required to resolve the spatial distribution of the thermal fields in order to deliver information about the mixing and reactions in the chamber.

Measurement specimens such as thermal barrier coatings have been developed in order to carry out a direct heat flux measurement; however, they are usually prone to large measurement uncertainty [10]. Heat flux sensors such as the Gardon sensor [11], the anisotropic heat flux sensors, and high-temperature heat flux sensors [12] were also developed for heat measurements but for other engineering applications. Although they can provide acceptable local resolution, their disadvantages include a difficult integration, disturbance of the temperature field due to the hot-island effect, a limited maximal operating temperature, and low maximal heat flux. Because of their lacking reliability when dealing with high thermal loads, they are rarely implemented in rocket engines. Instead, the most common methods for measuring heat fluxes are the calorimetric method, the transient method, the gradient method, and the inverse method. Most transient methods are applied in capacitively cooled chambers and are hence not relevant in the case of actively cooled thrusters. More information can be found in the work by Celano et al. [13].

A. Calorimetric Method

The presence of an active regenerative cooling system in most rocket engines experiencing high thermal loads allows for the application of the calorimetric method to determine the wall heat loads. Specifically, if the structure being cooled by a cooling fluid is in thermal equilibrium (no transient phenomena) and the natural convection of the outer walls is neglected, then the heat flow rate into the structure is equal to the heat flow rate from the material into the cooling fluid. The total heat rate coming from the hot-gas wall can therefore be determined by measuring the enthalpy increase of the coolant between the inlet and outlet of the channel. The average heat flux in the segment can then be calculated according to Eq. (1):

$$\dot{q} = \frac{\dot{m}_f}{A_w} \cdot [H_f(p,T)_{\text{out}} - H_f(p,T)_{\text{in}}] \tag{1}$$

The wall area A_w refers to the total area exposed to the hot gas within the segment. The method is very common, because it requires only the measurement of the coolant mass flow rate $\dot{m}_f$ and the pressure and temperature of the fluid at the inlet and outlet positions. Because the accuracy of those three individual measurements is within 1%, the errors in the average heat flux estimation using the calorimetric principle are limited. Note, that in order for the method to be effective the axial heat transfer between separate segments has to be negligible; otherwise, an additional source of error is introduced as seen in the work by Perakis et al. [14]. This can be achieved if the coolant of the first segment is used as well for the subsequent segments to minimize coolant temperature differences at the interface.

Therefore, global heat flux characteristics can be estimated with confidence using the calorimetric method. However, the resolution of this method is limited by the number of cooling segments present in the configuration. Most of the times, the method is connected to limited spatial resolution due to the additional complexity in the case of a large cooling segment number. When a more detailed resolution is required, other methods would have to be implemented, allowing for a more dense heat flux measurement distribution. A further disadvantage of the calorimetric method is the difficulty in determining the wall temperature from the heat flux measurement. Because only an average heat flux is estimated, the local profile of wall temperature is very challenging to calculate.

B. Gradient Method

The gradient method is a simplified procedure which allows for the estimation of local heat flux and wall temperature not only for actively cooled but also capacitively cooled chambers and relies on the measurement of temperature at several radial distances from the hot-gas wall (usually 2 to 5). By estimating the temperature gradient in the direction normal to the structure wall, the heat flux can be approximated. In the case of cylindrical chambers, the heat flux is given by

$$\dot{q}(r) = \frac{\lambda(T_2 - T_1)}{\ln(r_1/r_2) \cdot r_{\text{ch}}} \tag{2}$$

Calculating the heat flux requires at least two thermocouple measurements in different radial positions r_i. The benefit of the method is its very low computational complexity. Although the method is very accurate when dealing with capacitive cooling, the approximation that the heat flux follows the form given in Eq. (2) can become invalid when cooling channels are employed. The distortion of the temperature field by the cooling system leads to a more complex, nonanalytic expression for the wall heat flux, and the use of Eq. (2) can cause large systematic deviations.

C. Inverse Heat Transfer Method

A more reliable method for the evaluation of the wall heat transfer is based on the inverse solution of the thermal heat transfer problem. Inverse methods for heat transfer are typically iterative methods, which employ an optimization procedure to estimate the value of an

unknown boundary conditions that best matches the experimentally measured temperatures [15].

Inverse methods have been applied successfully in various engineering applications ranging from solar tower power plants [16], mold casting [17], internal combustion chambers [18], rocket combustion thrust chambers [4,19,20], sounding rockets [21], and induction heating [22]. Although all methods have in common that an optimization of the unknown boundary conditions is carried out, the exact methods for finding the optimal solution are quite diverse. Studies can be found in the literature including classical optimization based on adjoint methods [23], conjugate gradient methods [18], the Newton–Raphson method [4], the Levenberg–Marquardt algorithm [24,25], genetic algorithms [26,27], neural networks [17] as well as noniterative boundary element methods [28,29], and noniterative finite element methods [30]. In all of them, however, the objective is the minimization of the residual J,

$$J(\boldsymbol{Q}) = \frac{1}{M} \cdot [\boldsymbol{T}_m - \boldsymbol{T}_c(\boldsymbol{Q})]^T [\boldsymbol{T}_m - \boldsymbol{T}_c(\boldsymbol{Q})] \tag{3}$$

which describes the differences between the measured $\boldsymbol{T}_m$ and calculated $\boldsymbol{T}_c$ temperature vectors for a given choice of heat flux parameters $\boldsymbol{Q}$.

When dealing with experimental inverse methods, the available information consists of temperature measurements in M distinct positions within the material. For the problem to be well posed, the number of optimization variables N on the unknown boundary (the heat flux $\dot{q}$ in most applications) has to be smaller than or equal to the number of available measurement positions M [15]. Choosing the positioning of the thermocouples is hence very important when designing the experiment. In general, choosing thermocouple positions as close to the location of the optimization parameter as possible is beneficial in order to ensure the highest sensitivity and avoid parameter interference [31,32].

In the case of rocket thrust chambers used for main and upper stages of launch vehicles, a regenerative cooling system is typical [1]. On the one hand, the cooling system simplifies the inverse simulation as it eliminates the need for a transient solution, when the chamber operates in study state (excluding the startup and shutdown phases) as opposed to capacitively cooled chambers [20]. On the other hand, a further unknown boundary conditions is introduced to the system, namely, the heat transfer coefficient between the structure and the cooling channels h_{cc}.

The prediction of this additional unknown boundary simultaneously to the hot gas wall heat load can be performed with two different methods: modeling and optimizing.

1. Modeling Cooling Channel Heat Transfer Coefficient

In the first method, the interaction between the coolant and the structure is carried out either using a CFD simulation or with a simpler correlation (e.g., a Nusselt number correlation for h_{cc}). In the case of CFD, the sophistication and accuracy is expected to be higher than for simpler one-dimensional expressions. The higher accuracy is expected due to the threedimensional nature of the cooling channel simulation, which allows for the prediction of local variations of the heat transfer coefficient, both in axial and circumferential direction, while also capturing physical effects like thermal stratification [33] and heat flux deterioration [34,35]. Nevertheless, the computational time can be significantly higher, due to the iterative nature of the optimization algorithms, requiring multiple solutions of the CFD algorithm.

In the case of Nusselt number correlations, on the other hand, the computational resources needed are minimal. However, because of the simplified nature of the correlations which typically provide only a one-dimensional profile of h_{cc} along the channel axis, a higher uncertainty is expected, especially for supercritical conditions. Efforts are being carried out, however, to improve the correlations and increase their complexity by incorporating corrections for heat flux deterioration phenomena [36], supercritical conditions [37], and curvature effects [38]. Using new advances in neural networks can also assist in improving the existing correlations for hydrocarbon rocket engines [39].

Regardless of the chosen modeling option, a further benefit of this method is the reduction of the free optimization parameters. Because the calculation of the heat transfer coefficient is carried out with CFD or a correlation, the only remaining unknown parameter is the wall heat flux $\dot{q}$. For that reason, the use of only one thermocouple per position is sufficient to ensure well-posed-ness. This method uses the minimal amount of installed sensors and has been successfully applied in water-cooled rocket thrust chambers [4].

2. Optimizing Cooling Channels Heat Transfer Coefficient

The second option classifies the cooling channel heat transfer coefficient as an additional unknown, similar to the wall heat flux. The benefit of this method is that no additional modeling is required for the solution of the thermal problem. Because both the hot-gas wall boundary and the cooling channel wall boundary are modeled as black boxes, the domain only consists of the chamber material, and the only modeling parameters are the material properties like thermal conductivity, heat capacity, and density. The accumulated effect of thermal stratification, heat transfer deterioration, curvature, and wall roughness is captured without the need of additional models.

Nevertheless, because of the increased number in free optimization parameters, the demand for more thermocouple measurements is also higher, resulting in $M \geq 2 \cdot N$. Because of the larger number of free parameters, the simultaneous optimization of $\dot{q}$ and h_{cc} can become computationally intensive. In Sec. IV.C, a computationally efficient method based on the sensitivity matrix is introduced.

III. Test Case Description

To demonstrate the performance of each heat transfer evaluation method, a representative test case has been defined. Heat flux measurement methods are used both in subscale experimental chambers as well as in full-scale hardware being tested for qualification and acceptance. To ensure that the results of the current analysis are representative for flight hardware applications, a full-scale expander engine is used, operated with Liquid oxygen/liquid hydrogen.

The chosen hardware corresponds to the virtual thrust chamber demonstrator (TCD) presented in the work of Eiringhaus et al. [40]. The full-scale demonstrator TCD1 has been defined and designed with the purpose of testing the available numerical and analytical methods of combustion and heat transfer modeling [41].

The TCD1 concept is an upper-stage engine operating with an expander cycle and producing a nominal thrust of 100 kN, similar to the RL-10C engine [42]. The combination of LOX and LH_2 for the oxidizer and fuel are chosen as propellants. A nominal combustion chamber pressure of 55 bar and an a/F equal to 5.6 are chosen as a reference operating point. The nozzle extension has been designed according to the truncated ideal contour (TIC) principle. For the cooling of the combustion chamber as well as the nozzle extension (up to an expansion ratio of 22), liquid hydrogen flows through a cooling channel in a coflow configuration. In total, 138 cooling channels are present, equally distributed along the perimeter. The chamber and the liner are manufactured using oxygen-free copper due to its high conductivity, whereas the outer structural jacket consists of nickel. Despite the TCD1 being a virtual engine, not intended to be built and tested, its design underwent all engineering steps found at the development process of a real engine, and it therefore constitutes a realistic example for the implementation of the inverse heat transfer method.

For an estimation of each heat transfer evaluation method's accuracy, the knowledge of the real wall heat flux, coolant heat transfer rate, and wall temperature has to be known for the entirety of the domain. In experimental configurations, this can never be achieved, and hence a virtual experimental test case is set up. The process for the generation of the experimental data is illustrated in Fig. 1.

To obtain a realistic wall heat flux profile for the chosen load point, a CFD simulation of the flow and turbulent combustion within the chamber is carried out. The models used are briefly described in Sec. III.A. Using the obtained experimental wall heat load, a simulation of the chamber structure with the cooling channels is carried out as outlined in III.B. This delivers a representative temperature

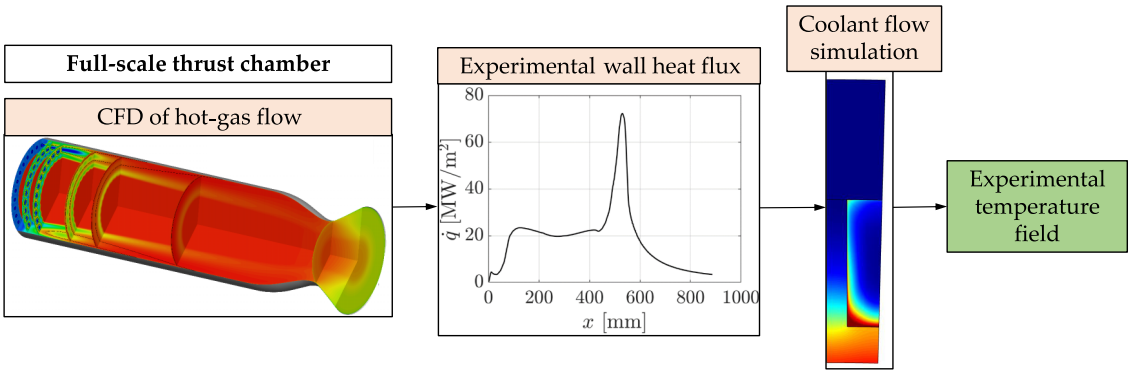

Fig. 1 Schematic illustration of the method used to generate the experimental test data.

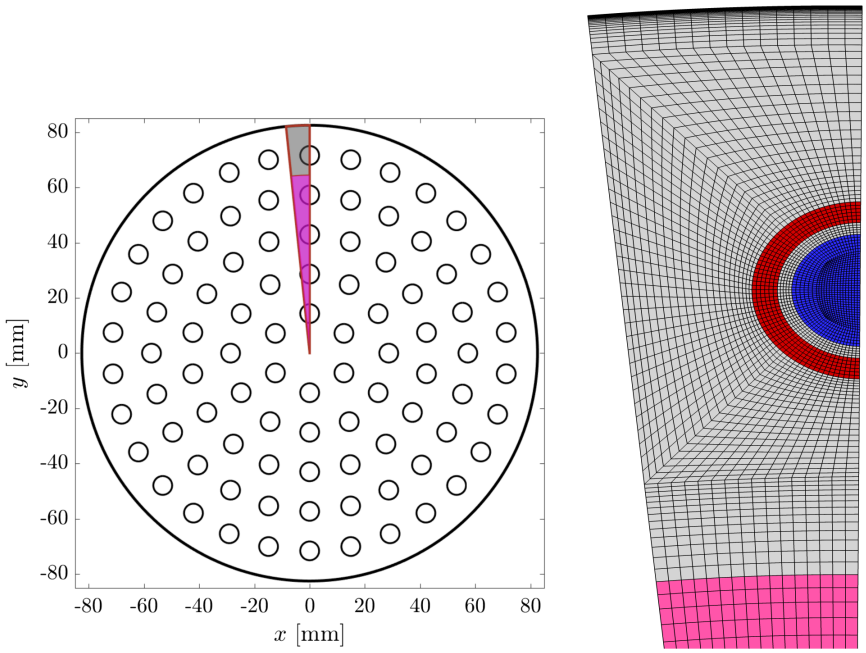

Fig. 2 Computational domain and mesh on the face plate. Note that every second grid point is shown.

field within the entire structure, which is used to generate the virtual thermocouple measurements.

A. Simulation of Hot-Gas Flow

A three-dimensional Reynolds-averaged Navier–Stokes (RANS) simulation of the supercritical combustion case within the TCD engine is carried out. The commercial code ANSYS Fluent has been used for the simulations [43]. To reduce the computational effort for the simulation of the hot-gas flow in the domain, only a thin sector of the engine is computed. In fact, the smallest possible symmetry is used, consisting of only half an injector in the outer row. The face plate as well as the chosen sector are illustrated in Fig. 4. To ensure that the symmetry of the injector configuration is attained, only the outermost injector is resolved, whereas the remaining mass flow rate is injected in premixed and preburnt conditions. The injection area of the preburnt mixture is indicated with the magenta color in Fig. 2. The red and blue colors represent the fuel and oxidizer inlet, respectively. This method of reducing the number of resolved injectors has been used in the past for simulations of full-scale engines [44,45] as it significantly reduces the computational cost while still preserving the three-dimensional nature of the flowfield and the injector/wall interaction. The resulting mesh consists of $2.3 \cdot 10^6$ cells, and its wall resolution is chosen so as to fulfill the $y^+ < 1$ condition. At the wall boundary, an axially varying temperature profile is applied, obtained from the work of Eiringhaus et al. [40].

Because of the fast chemical processes occurring in hydrogen/oxygen engines, a chemical equilibrium model has been employed for the turbulent combustion simulation. To account for the cryogenic injection temperatures of the liquid oxygen ($T_{ox} = 95$ K), a Peng–Robinson cubic equation of state is used [46], with the volume correction by Abudour et al. [47]. For the turbulence closure, the standard $k-\varepsilon$ model proposed by Launder and Spalding [48] is implemented, extended by the two-layer approach by Wolfshtein [49] to account for the proper treatment of the wall. A presumed

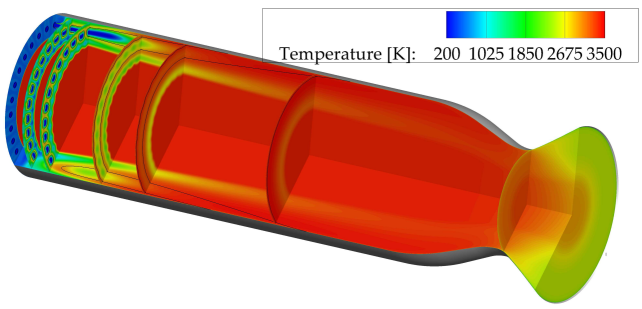

Fig. 3 Temperature field in the thrust chamber domain. The solid lines represent the stoichiometric composition.

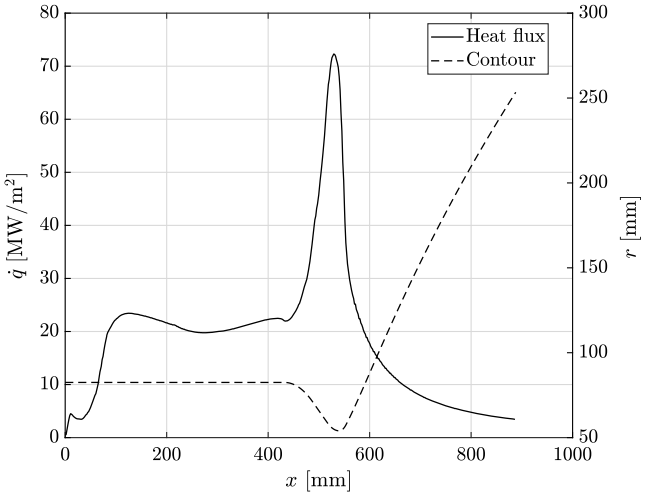

Fig. 4 Heat flux profile and chamber contour along the axial direction.

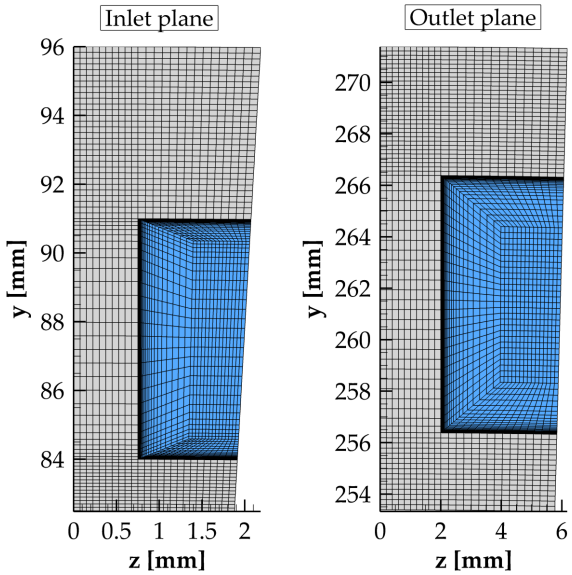

Fig. 6 Mesh at the inlet and outlet planes of the cooling channel.

β Probability Density Function is used for the turbulence/chemistry interaction, whereas constant turbulent Prandtl and Schmidt numbers equal to 0.9 and 0.6, respectively, are defined for the turbulent heat and mass fluxes. Finally, the molecular kinetic properties are defined using the model by Chung et al. [50], and for the thermodynamic data, NASA polynomials are used.

The resulting temperature distribution in the thrust chamber (excluding the nozzle extension) is shown in Fig. 3, in which the domain has been mirrored in the circumferential direction. The fact that the outer injector row is resolved gives rise to a temperature stratification close to the chamber wall. A liquid oxygen core can be identified, surrounded by a thin flame. The core flow, however, is injected in a preburnt state and hence remains uniform for the entire length of the domain. Because of mixing within the chamber, the gas composition and temperature become more homogeneous further downstream of the face plate. The resulting (circumferentially averaged) heat flux profile along with the chamber contour is plotted in Fig. 4. As expected, a rise in heat flux occurs within the first 100 mm from the injection plane, as the mixing and energy release within the outer injector is intensified. Farther downstream, the heat flux obtains a nearly constant value before increasing again in the converging part of the nozzle.

It is important to note here that the obtained heat flux values and combustion simulation results are not evaluated with regard to their validity and accuracy. Instead, they serve as realistic reference values, used for the generation of the experimental temperatures in Sec. B.

B. Numerical Setup of the Coolant Side

To calculate the material temperatures for the virtual reference experiment, a simulation of the hydrogen cooling channels and the chamber domain is carried out. To take advantage of the geometry's symmetry, only half of the 138 channels is included in the computational domain, leading to a simulation of only 1.3 deg. The domain with labels indicating the individual parts is illustrated in Fig. 5. A symmetry boundary condition is used for the other half of the cooling channel, which leads to $1.4 \cdot 10^6$ cells in the domain. A closeup of the mesh in the inlet and outlet planes is given in Fig. 6, in which the blue region indicates the fluid domain.

The hydrogen flow in the channel is modeled by solving the RANS equations. The $k-\omega$ shear-stress transport model by Menter [51] is chosen, and the wall is resolved to values of the dimensionless wall distance $y+$ of around 1. In all calculations, the closure of the turbulence flux terms is done with a constant turbulent Prandtl number $Pr_t = 0.9$. For the temperature-dependent properties of supercritical hydrogen, data from the National Institute of Standards and Technology library [52] have been used, accounting for pressure and temperature-dependent density, specific heat, viscosity, and thermal conductivity.

At the LH_2 inlet, the mass flow rate and the inlet temperature are given, whereas at the outlet, the expected pressure of 175 bar is set. The hot gas wall is given a von Neumann boundary condition with the applied heat flux from Fig. 1. Finally, the external jacket wall is defined as adiabatic. For the copper and nickel, temperature-dependent values for the density, heat capacity, and thermal conductivity are used. Only the energy equation is solved in the chamber material, and hence no significant modeling is required for the structure.

The temperature field within the chamber wall and hydrogen coolant is plotted in Fig. 7 for four locations within the chamber ($x = 100, 200, 300, 400$ mm) and the nozzle throat ($x = 541$ mm). As expected, due to the asymmetrical heating, the material and fluid

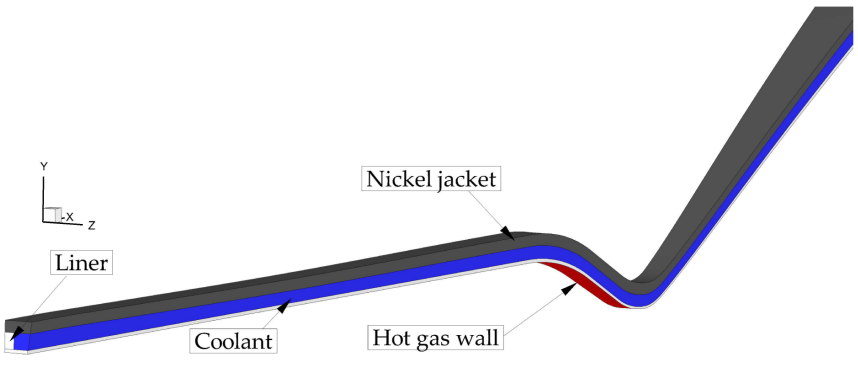

Fig. 5 Setup of the cooling channel simulation domain.

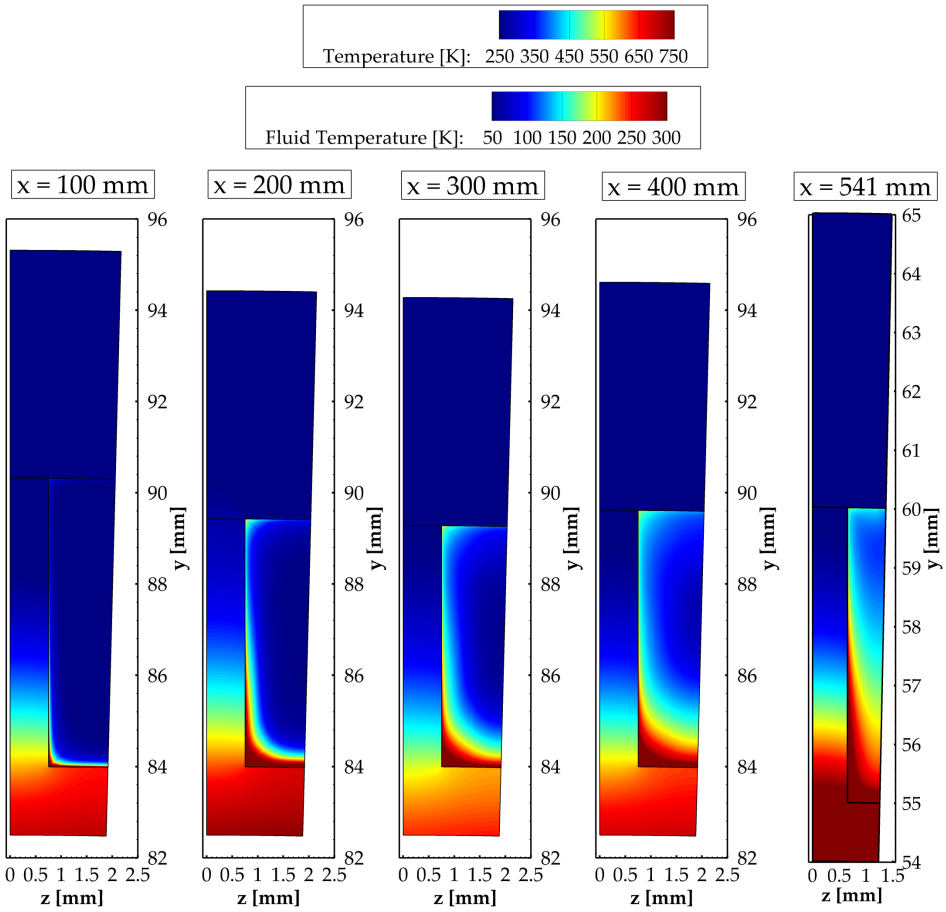

Fig. 7 Temperature field in the cooling channel for different axial positions.

temperatures close to the hot-gas wall are higher than the remaining locations. Moreover, because of the high thermal conductivity of the copper liner, a significant part of the heat is transferred radially outward, heating up the fluid in contact with the fins. This effects leads to an amplification of the thermal boundary layer dimensions along the bottom and vertical walls. This asymmetric heat attenuation leads to large deviations of the local temperature from the bulk flow temperature, i.e., to thermal stratification.

To describe the stratification more quantitatively, the standard deviation of the fluid temperature for each axial position $T_{f,\mathrm{dev}}$ is defined as the mass flow averaged discrepancy from the mean fluid temperature $T_{f,\mathrm{mean}}$:

$$T_{f,\mathrm{mean}} = \frac{\oint\!\!\oint_S T_f \, d\dot{m}}{\dot{m}} \tag{4}$$

$$T_{f,\mathrm{dev}} = \sqrt{\frac{\oint\!\!\oint_S (T_f - T_{f,\mathrm{mean}})^2 \, d\dot{m}}{\dot{m}}} \tag{5}$$

The axial profiles of both the mean temperature and the deviation are plotted in Fig. 8. For the bulk fluid temperature, a constant increase along the axial direction is observed. The temperature deviation, on the other hand, demonstrates a more complex profile. Specifically, it appears to be steadily increasing within the cylindrical part of the chamber and up to the throat (first 540 mm from the face plate). When entering the divergent part of the nozzle, a sudden drop in the standard deviation of the temperature occurs, indicating a more homogeneous fluid. The physical processes behind this phenomenon are not the subject to the present analysis but have been investigated in the past and are attributed to the secondary flows which change direction depending on the curvature of the channels [53]. The correlation between the performance of the inverse method and the temperature stratification will be discussed in Sec. IV.B.

Finally, the stratification of the temperature field gives rise in locally varying heat transfer coefficients along the channel circumference. In this context, the local heat transfer coefficient h is defined using the local wall temperature T_w and local channel heat flux $\dot{q}_w$:

$$h_{\mathrm{cc}} = \frac{\dot{q}_w}{T_w - T_{f,\mathrm{mean}}} \tag{6}$$

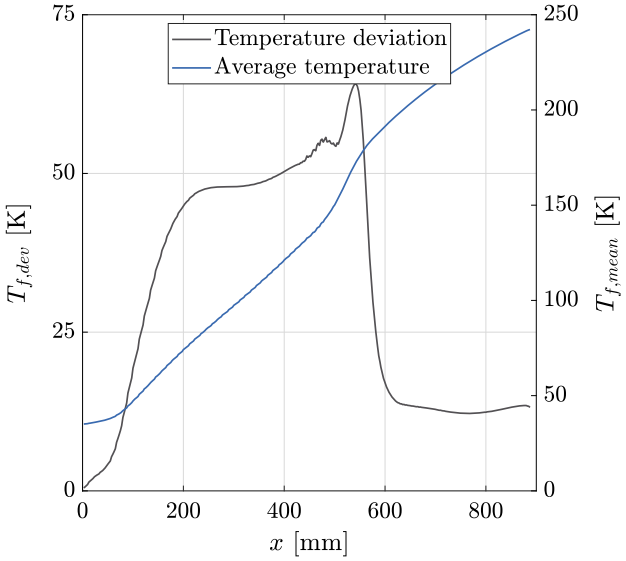

Fig. 8 Average coolant temperature and temperature stratification in the cooling channels.

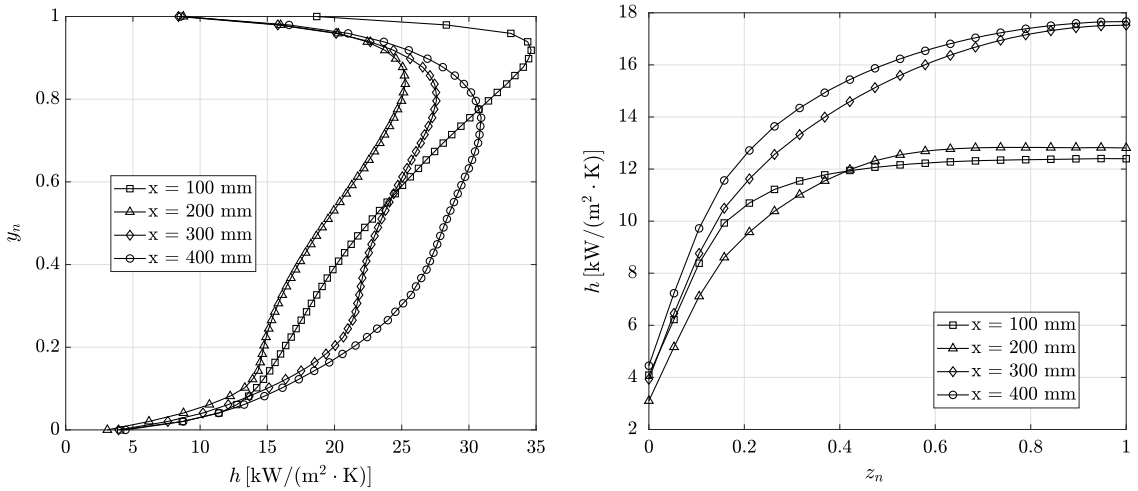

Fig. 9 Heat transfer coefficient for different axial positions along the vertical wall (left) and the horizontal bottom wall (right).

The variation along the normalized channel height y_n and the normalized channel width z_n is shown in Fig. 9. Note that $z_n = 1$ corresponds to the middle of the channel, $y_n = 0$ corresponds to the bottom wall, and $y_n = 1$ corresponds to the bottom wall. Given the observed variations of heat transfer coefficient along the channel circumference, the performance of the inverse heat transfer methods which approximate h_{cc} with a constant value for each axial position will be discussed in Sec. IV.D.

IV. Comparison of Heat Flux Evaluation Methods

Having established the test case used to generate the thermocouple measurements, we proceed with the analysis of the individual methods that were introduced in Sec. II. It is important to note that in this section only steady-state results are presented. The extension of the presented inverse methods to time-varying heat loads could also be carried out similar to the work by Perakis and Haidn [20].

Although the presented methods can be applied similarly to both the combustion chamber and the nozzle, the results within the chamber will be given more detailed focus. The reason is that the main mixing and combustion processes occur in the cylindrical part of the chamber. This is therefore the area which is typically intensively instrumented in order to obtain enough information to characterize the injector performance and injector/wall interaction. Also, installing multiple thermocouples close to the throat can become mechanically challenging due to the small distance between the cooling channels.

Moreover, throughout this section, the position of the thermocouples will be referenced as described in Fig. 10. The first thermocouple is at distance d_1 from the wall, whereas the position of the second thermocouple is given by the relative distance δ with respect to the first sensor. The third thermocouple is located at a distance d_3 from the hot-gas wall. To generalize the results, all distances are given relative to the wall thickness t.

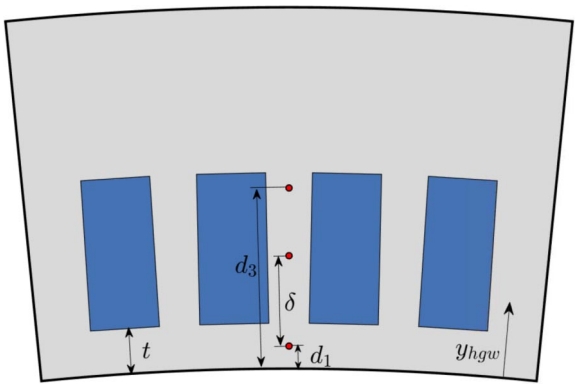

Fig. 10 Overview of the thermocouple positions.

To provide a sufficient axial resolution, 30 thermocouple positions are chosen, with a relative distance of approximately 40 mm from each other. Note that for all analyses the error due to the positioning of the thermocouples, the accuracy of the sensors, and the axial spacing are neglected, as they affect all different methods similarly. Their effect has been discussed in previous studies [4]. For that reason, although the experimental measurements in this Paper are replaced by conjugate heat transfer CFD results, no random error is added to the thermocouple readings. The effect of random measurement noise $\Delta \boldsymbol{T}_{\text{noise}}$ on the obtained inverse heat flux results has been analyzed in previous studies and scales as $\Delta \boldsymbol{Q} = \boldsymbol{S}^{-1} \cdot \Delta \boldsymbol{T}_{\text{noise}}$ [20] and has the same effect on all inverse methods presented in this section. In this context, $\boldsymbol{S}$ is the sensitivity matrix introduced in Eq. (13).

A metric used for comparison of each method's performance is the average heat flux and hot-gas wall temperature error. Those are defined as the average systematic error for all K axial positions as elaborated in Eqs. (7) and (8):

$$\dot{q}_{\text{err}}(d_1, \delta) = \frac{1}{K} \sum_{k=1}^{K} \frac{|\dot{q}_{\text{exact}} - \dot{q}_{\text{calc}}(d_1, \delta)|}{\dot{q}_{\text{exact}}} \tag{7}$$

$$T_{\text{err}}(d_1, \delta) = \frac{1}{K} \sum_{k=1}^{K} \frac{|T_{\text{exact}} - T_{\text{calc}}(d_1, \delta)|}{T_{\text{exact}}} \tag{8}$$

A. Gradient Method

The gradient method is the computationally least expensive one and is shown here as a reference, as it has been applied in various studies in the past. In the presence of cooling channels, the validity of Eq. (2) deteriorates, and an error is expected both for the calculated heat flux and the wall temperature.

The dependence of the magnitude of the resulting errors as a function of the thermocouple positions is plotted in Fig. 11. Note that the upper right corner corresponds to combinations that are not in the liner domain and are hence unfeasible.

Starting with the heat flux error, a rather complex behavior is observed, with high gradients in the resulting error, inferring a large sensitivity on the location of the sensors. For small values of d_1 and δ, the deviation is smaller than 10% (white isoline), but only in a very limited region. Increasing the radial distance of either sensor leads to a rapid increase in the error of the measured heat flux, with the highest deviation reaching up to 85%. A further increase of the sensor position d_1 seems to counterintuitively improve the situation, leading to the existence of a narrow band where $\dot{q}_{\text{err}} \leq 10\%$. This region is, however, the location where the error in heat flux changes sign, going from an overestimation of the heat loads to an underestimation and cannot be predicted a priori. Because no predictions about this region can be made, there cannot be a systematic positioning of the sensors within this region.

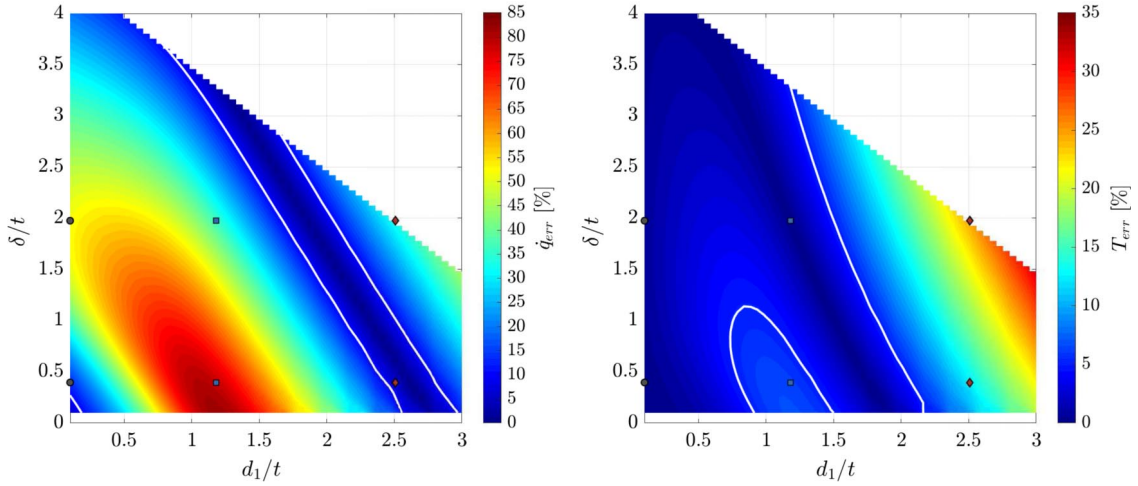

Fig. 11 Heat flux (left) and hot gas wall temperature (right) error for the gradient method. The white isoline corresponds to 10 and 5% error, respectively.

Moreover, looking at the temperature error in the right subfigure, it becomes clear that, even if the heat flux accidentally matches the exact values in this region, the temperature error is not negligible, as it lies outside the region with $T_{\text{err}} \leq 5\%$. It has to be mentioned that the dependence of T_{err} on the thermocouple positions seems to be less sensitive than for the heat flux. Although a larger error is to be expected for larger d_1 values, the gradients remain small, and a large region can be found where the $T_{\text{err}} \leq 5\%$ constraint is met.

It is evident, however, that in order to minimize both the heat flux and hot-gas wall temperature simultaneously the options for the sensor placement are hugely restricted to positions in the imminent vicinity of the wall. Because this is often not feasible from a manufacturing point of view (long thin thermocouple holes combined with a small wall thickness), errors larger than 10% in heat flux are usually the norm.

To better understand the error source of the method, the axial heat flux profiles and structural temperatures for six representative sensor combinations are shown in Fig. 12. The combinations correspond to the marker locations in Fig. 11. Focusing on the temperature profiles in the right subfigure, it is obvious that the simplified logarithmic profile of the gradient method cannot capture the dynamics of the cooling channels which lead to a significant distortion of the exact temperature profile.

B. Inverse Method with Nusselt Number Correlation

As explained in Sec. II, one of the options for modeling the heat transfer coefficient in the cooling channels is the use of a simplified one-dimensional Nusselt number correlations. For the present analysis, the correlation proposed by Kraussold [54] has been used due to its previous applications in rocket engine simulations [4,55]. The heat transfer coefficient is then modeled as a function of the Reynolds Re and Prandtl Pr numbers, as well as the channel hydraulic diameter D_h and coolant thermal conductivity λ_f according to Eq. (9):

$$Nu = \frac{h_{\text{cc}} \cdot D_h}{\lambda_f} = 0.024 \cdot Re^{0.8} \cdot Pr^{0.37} \tag{9}$$

It is then applied to the channel boundary as a von Neumann boundary condition along the normal direction $\boldsymbol{n}$:

$$h_{\text{cc}}(T_f - T_w) = \lambda \frac{\partial T}{\partial \boldsymbol{n}}\bigg|_S \tag{10}$$

For the average (bulk) coolant temperature $T_f(x)$, the heat pickup based on the calculated wall heat flux $\dot{q}$ is used,

$$T_f(x) = T_{f,\text{in}} + \int_0^x \frac{2\pi r_{\text{ch}}}{N_{\text{cc}}} \frac{\dot{q}}{\dot{m} c_p} \text{dx} \tag{11}$$

where N_{cc} stands for the number of the cooling channels.

The solution of the direct problem is carried out using the commercial code ANSYS Fluent [43]. An extensive mesh convergence study has been performed for the grid of the chamber's structure, and

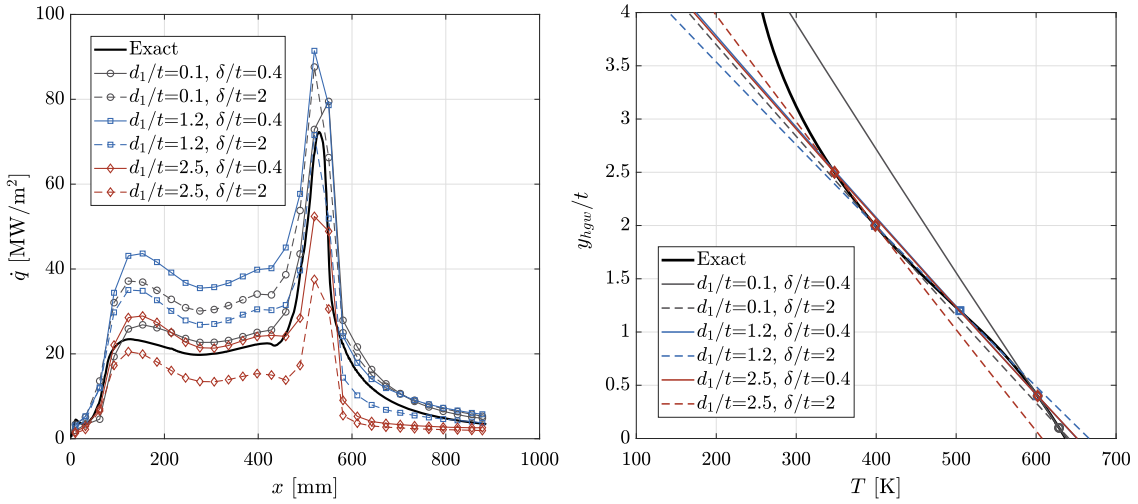

Fig. 12 Axial heat flux profiles for the gradient method (left) and liner temperature profiles for $x = 300$ mm (right).

it was found that the temperature error resulting from the solution of the energy equation in the numerical domain is two orders of magnitude smaller than the sesnors' statistical measurement uncertainty. For that reason, the effect of the computational grid on the retrieved heat flux is not analyzed further.

The calculation of the unknowns, namely, the heat flux at the boundary, is based on a linearization of the problem and follows the Newton–Raphson formulation for the solution of nonlinear systems [56]. The heat flux at each iteration step k is obtained by solving the algebraic equation

$$\boldsymbol{S}\cdot\boldsymbol{Q}^{k+1} = [\boldsymbol{T}_m - \boldsymbol{T}_c(\boldsymbol{Q}^k)] + \boldsymbol{S}\cdot\boldsymbol{Q}^k \tag{12}$$

Solving the system of equations defined in Eq. (12) is carried out using the inversion of the pseudoinverse Moore–Penrose matrix [57], because in the generalized case the problem can be overdetermined (meaning $M \geq N$). It is important to note that the inversion of Eq. (12) is applied on all optimization points simultaneously. Applying the inversion on a reduced set of optimization points (e.g., separately for each axial plane) would lead to a slower convergence due to the neglect of cross-correlation effects.

As shown in previous studies, the Jacobi matrix $\boldsymbol{S}$, which serves as a sensitivity matrix describing the change of the temperature at a thermocouple position due to a small change at a specific heat flux parameter value, can be computed outside of the optimization loop in a preprocessing step [4,20]. This dramatically improves the convergence speed of the algorithm. Its structure is presented in Eq. (13):

$$\boldsymbol{S} = \frac{\partial \boldsymbol{T}}{\partial \boldsymbol{Q}} = \begin{bmatrix} \frac{\partial T_1}{\partial Q_1} & \cdots & \frac{\partial T_M}{\partial Q_1} \\ \vdots & \ddots & \vdots \\ \frac{\partial T_1}{\partial Q_N} & \cdots & \frac{\partial T_M}{\partial Q_N} \end{bmatrix} \tag{13}$$

One of the major benefits of using this method is the need for only one thermocouple for each axial location, as there is only one free parameter to calculate. For that reason, in the analysis shown here, the radial position d_1 is varied, and the resulting heat flux profiles are shown in Fig. 13.

A large discrepancy between the exact and the inverse heat flux profiles can be observed for the largest part of the combustion chamber and up until the throat. The inverse method appears to overestimate the heat flux in the cylindrical part, even for low values of d_1. In general, an increase in the radial distance of the sensor from the wall leads to a lower sensitivity of the method and hence an even further degradation of the agreement with the exact heat flux. This can be supported by the right subfigure of Fig. 13, in which the average temperature and heat flux errors are shown with the black lines and a clear monotonic behavior can be found. Specifically, the average heat flux deviation in the thrust chamber exceeds 40%, whereas the wall temperature prediction is within 5% only for sensor locations very close to the wall ($d_1/t \leq 0.5$).

The smallest chosen value for d_1/t lies at 0.33 (0.5 mm absolute distance in the cylindrical part) and corresponds to an average heat flux error of 40%. It can be observed, however, that the heat flux profile close to the injection plane (first 100 mm) and within the divergent part of the nozzle ($x \leq 600$ mm) matches the exact values with great accuracy, independent of the d_1 value. The reason for the better performance in those locations is the lower stratification of the coolant temperature, as seen when comparing with Fig. 8. Larger stratification caused by large aspect ratios introduces a greater uncertainty in the simplified Nusselt equation, rendering its applicability critical.

The corresponding temperature profiles along the radial direction within the copper liner can be found in Fig. 14. It is evident that the inverse temperature profile is matching the exact one only at the measurement location but shows very large discrepancies for all remaining positions. Increasing the number of thermocouples does not provide any improvement to the solution as the right subfigure of Fig. 14 indicates. Because the form of the temperature profile is strongly influenced by the chosen Nusselt number correlation, the introduction of additional sensors is not sufficient to alter the obtained temperature profile. Instead, for each combination of d_1 and δ, one of the measurements is overestimated, and one of them is underestimated, leading to the local minimum of the optimization algorithm.

Hence, it can be inferred that in the absence of correction functions the use of simplified Nusselt number correlations is not suitable for compressible, supercritical channels flows with high aspect ratio. For that reason, the performance of a correlation, explicitly tailored for supercritical hydrogen cooling channels with high aspect ratios, is assessed. The correlation proposed by Haemisch et al. [58] was derived by examining cooling channels with aspect ratios between 1.7 and 30 and pressure levels up to 160 bar. For hydrogen, the correlation reads

$$Nu = \frac{h_{cc}\cdot D_h}{\lambda_f} = C\cdot Re^{0.8}\cdot Pr^{0.4} \tag{14}$$

where the factor C includes the dependence on the aspect ratio AR:

$$C = 0.005545\cdot e^{-0.2015\cdot \mathrm{AR}} + 0.005207 \tag{15}$$

Applying this correlation to the framework of the inverse method delivers a significant improvement of the heat flux results, which

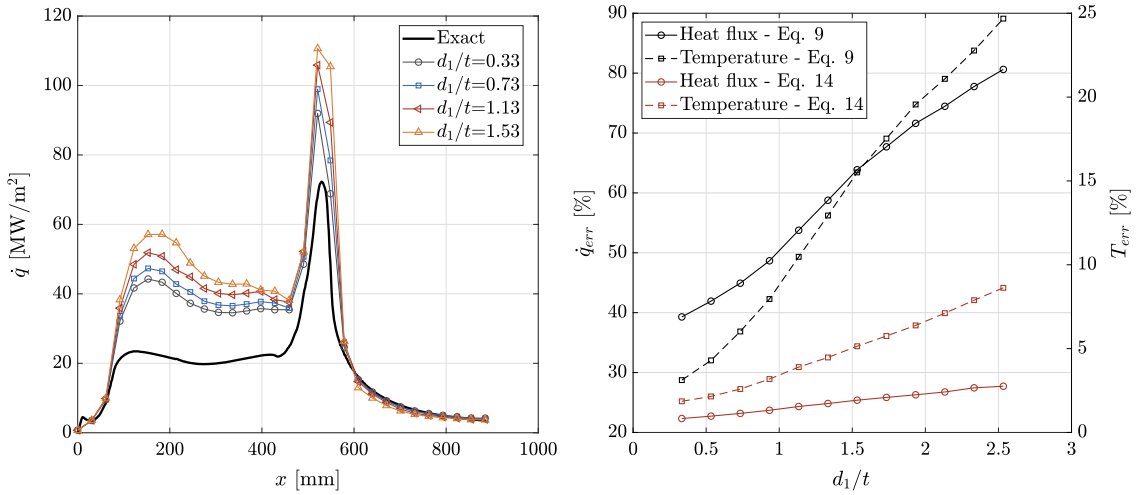

Fig. 13 Axial heat flux profiles (left) and average measurement error (right) for the inverse method using the Kraussold correlation [54] and a single thermocouple.

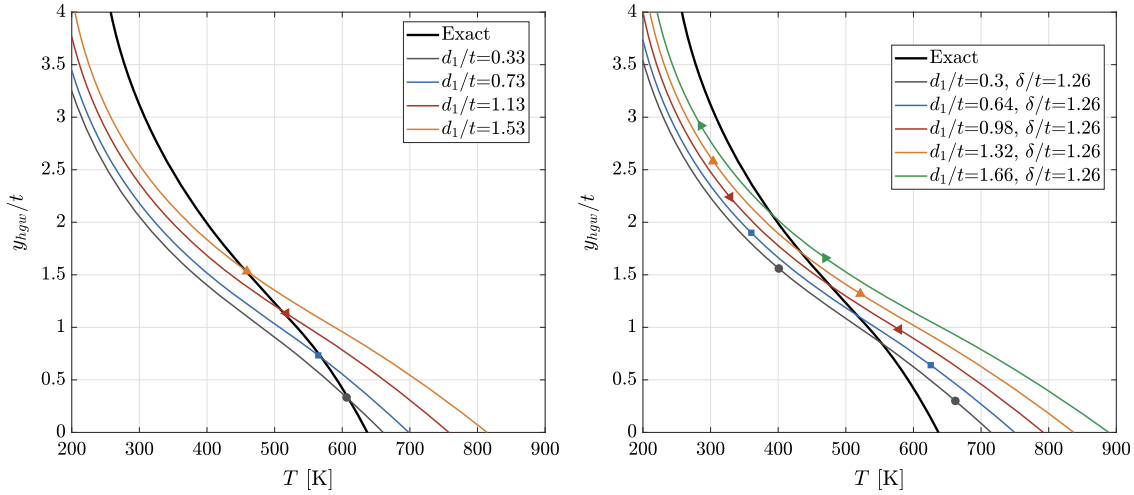

Fig. 14 Liner temperature profiles for $x = 300$ mm using one sensor (left) and two sensors (right) with the Kraussold [54] correlation.

are plotted in Fig. 15. The deviation of the inverse profile remains within 10–15% in the cylindrical part of the chamber and only shows larger discrepancies in the vicinity of the throat. This is expected as the correlation was derived for straight cooling channels and has not been adapted for curvature effects. Still, the average heat flux and wall temperature errors shown in the right subfigure of Fig. 13 in red are in an acceptable range, given the simplicity of the method. Similar to the use of the Kraussold correlation, an increase in d_1 leads to a less accurate prediction, but the sensitivity of the exact thermocouple placement is lower, as the flatter curves indicate.

C. Inverse Method with Simultaneous $\dot{q} - h$ Estimation

It is obvious that using a Nusselt number correlation for the estimation of the heat flux needs to be accompanied by a small uncertainty of the chosen equation and certainty that it captures all the fuel-specific and geometry-specific physical effects. To alleviate the need for fulfillment of those requirements, the heat transfer coefficient can be treated as an unknown optimization parameter of the inverse method and be estimated simultaneously to the heat flux. This way, the cooling channel is treated like a black box, and the need for modeling is kept at a minimum.

This method has been employed in the past to evaluate experimental data [59]. However, because of the large number of unknowns, the inverse algorithm can easily become computationally slow, and an efficient optimization method is required for three-dimensional problems. Taking advantage of the linearity of the problem, the Jacobi-based inversing algorithm from Eq. (12) can be extended to account for the heat transfer coefficient parameter set $\boldsymbol{H}$.

Using the Newton–Raphson method, the update of the unknown parameters is carried out using Eq. (16),

$$\left[c_1 \cdot \frac{\partial \boldsymbol{T}}{\partial \boldsymbol{Q}}, c_2 \cdot \frac{\partial \boldsymbol{T}}{\partial \boldsymbol{H}}\right] \cdot \begin{bmatrix} \boldsymbol{Q}^{k+1} \\ \boldsymbol{H}^{k+1} \end{bmatrix} = [\boldsymbol{T}_m - \boldsymbol{T}_c(\boldsymbol{Q}^k, \boldsymbol{H}^k)] + \left[c_1 \cdot \frac{\partial \boldsymbol{T}}{\partial \boldsymbol{Q}}, c_2 \cdot \frac{\partial \boldsymbol{T}}{\partial \boldsymbol{H}}\right] \cdot \begin{bmatrix} \boldsymbol{Q}^k \\ \boldsymbol{H}^k \end{bmatrix} \tag{16}$$

where the c_1 and c_2 prefactors ensure that the Jacobians of $\boldsymbol{Q}$ and $\boldsymbol{H}$ have similar orders of magnitude to avoid close-to-singular matrices. For the method to be computationally efficient, the calculation of the sensitivity matrix $\partial \boldsymbol{T}/\partial \boldsymbol{H}$ has to be carried out in a preprocessing step, outside the main optimization loop. This is done by means of a forward finite difference method,

$$\frac{\partial \boldsymbol{T}}{\partial H_i} = \frac{\boldsymbol{T}_c(\boldsymbol{Q}^0, \boldsymbol{H}^0 + \epsilon \cdot \boldsymbol{H}_i^0) - \boldsymbol{T}_c(\boldsymbol{Q}^0, \boldsymbol{H}^0)}{\epsilon \cdot \boldsymbol{H}_i^0} \tag{17}$$

with ϵ being a number small enough for the first-order approximation of the finite difference to be valid. $\boldsymbol{H}_i^0$ is a vector, and its elements $H_{i,j}^0$ are defined as

$$H_{i,j}^0 = \begin{cases} 0 & i \neq j \\ H_i^0 & i = j \end{cases} \tag{18}$$

The choice of the initial guess for the heat flux $\boldsymbol{Q}^0$ and $\boldsymbol{H}^0$ has to be close to the expected results in order to ensure that the linearity of the problem is preserved. For the current analysis, the empirical profiles from Bartz [2] and Haemisch et al. [58] are used for $\boldsymbol{Q}^0$ and $\boldsymbol{H}^0$, respectively. With this newly proposed optimization method, the convergence of the three-dimensional problem with 30 optimization positions (60 free parameters in total) has been found to converge to residuals as low as $J = 0.1$ K^2 within 10–20 iterations, amounting to 2–4 processor hours (CPUh) in total on a workstation with Intel Core i7-6700 3.4 GHz using four cores.

Using this method, two separate studies are carried out, in which the location of the thermocouples are varied. In the first study, two thermocouples are used with varying d_1 and δ, whereas in the second one, a third sensor at a constant position $d_3/t = 4$ is added.

In the first case, using two thermocouples leads to the error distribution shown in Fig. 16. A large region where the heat flux and wall temperature deviations do not exceed 10 and 5%, respectively, can be

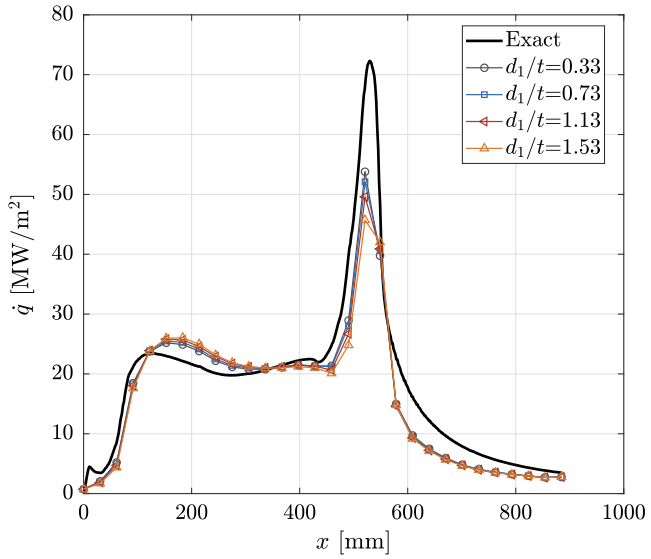

Fig. 15 Axial heat flux profiles for the inverse method using the Haemisch et al. correlation [58] and a single thermocouple.

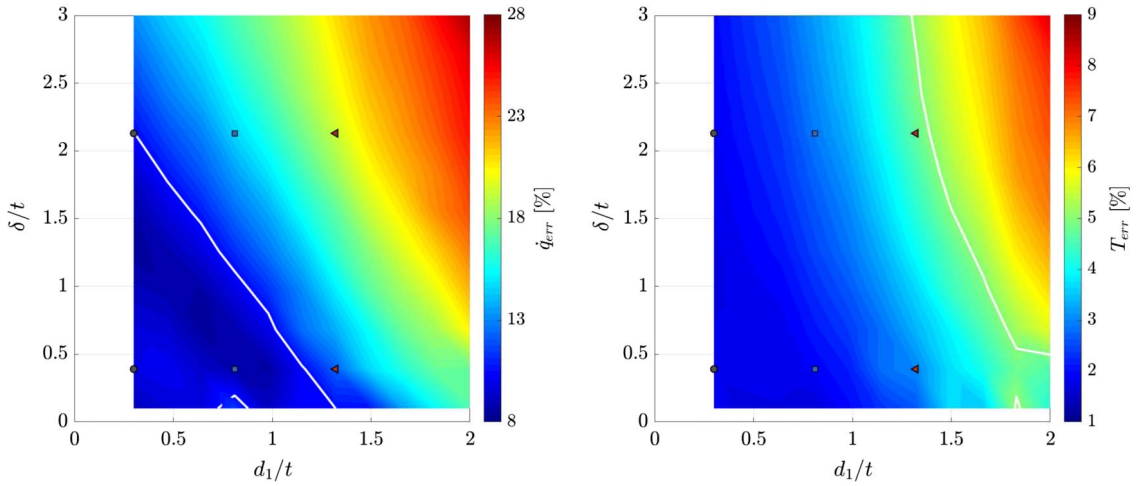

Fig. 16 Heat flux (left) and hot gas wall temperature (right) error for the $\dot{q} - h$ method using two thermocouples. The white isoline corresponds to 10 and 5% error, respectively.

identified. This implies that the positioning of the thermocouples is not as strict as in the case of the Nusselt number correlations. The expected trend seen already in Sec. IV.B is reproduced, with higher values for d_1 leading to an increase in the measurement error.

The axial evolution of the heat flux profiles for selected $d_1 - \delta$ combinations is shown in the diagram of Fig. 17. It can be observed that the exact heat flux profile is reproduced accurately for the entirety of the chamber length. At the same time, the prediction of the average cooling channel heat transfer coefficient can now be compared to the exact profile from the virtual experiment as displayed in the right subfigure of Fig. 17. It has to be noted that the h profiles are not expected to match the exact values perfectly, as the real profiles exhibit a strong variability as shown in Fig. 9 and the assumption of homogeneous h_{cc} coefficient is an oversimplification.

Nevertheless, the obtained curves are demonstrating a qualitative agreement with the exact values. They capture both the initial large values due to the buildup of the boundary layer, the increase in the throat, and the subsequent drop in the divergent nozzle part. Contrary to the heat flux estimation, however, where thermocouples closer to the wall delivered a superior accuracy, in the case of the cooling channels, larger values of d_1 and δ give rise to a better agreement. This is understandable because higher radial positions capture a larger domain of influence of the coolant flow.

To balance out the tradeoff between wall heat flux and cooling channel coefficient accuracy, a further thermocouple is introduced to the system, at the position $d_3/t = 4$. An improvement is observed in the prediction of the heat transfer coefficient in Fig. 18, while the heat flux prediction is not influenced significantly. The improved predictive accuracy of the method is also reflected in the temperature profiles shown in Fig. 19. Including an additional measurement point at $d_3/t = 4$ provides a better matching of the temperature profile, especially for larger radial distances, without significantly changing the hot-gas wall temperature.

D. Inverse Method with Simultaneous $\dot{q} - h_{\text{top}} - h_{\text{bottom}}$ Estimation

A very satisfying agreement with regard to heat flux and wall temperature is achieved using the simultaneous $\dot{q} - h$ optimization while employing two and three sensors. However, because a single value is obtained for the average heat transfer coefficient, little information can be inferred regarding the degree of stratification and the nature of the secondary flows in the channel. If the goal of the experiment and thermocouple measurements is to evaluate the conditions within the cooling channels apart from only the hot-gas heat flux and wall temperature, then the parameterization of the cooling channel using more than one unknowns is recommended.

To demonstrate this effect, the cooling channels are discretized in three separate boundaries: the top, side, and bottom walls. To simplify the problem and based on the expected results from Fig. 9, only the coefficient on the top and bottom boundaries is calculated, and a linear profile is used on the side wall. The linear profile is defined as

$$h_{\text{side}}(y_n) = h_{\text{bottom}} + (h_{\text{top}} - h_{\text{bottom}}) \cdot y_n \tag{19}$$

This discretization method has been applied in the past but with a reduced number of free parameters due to the linear profile assumed for the wall heat load [19].

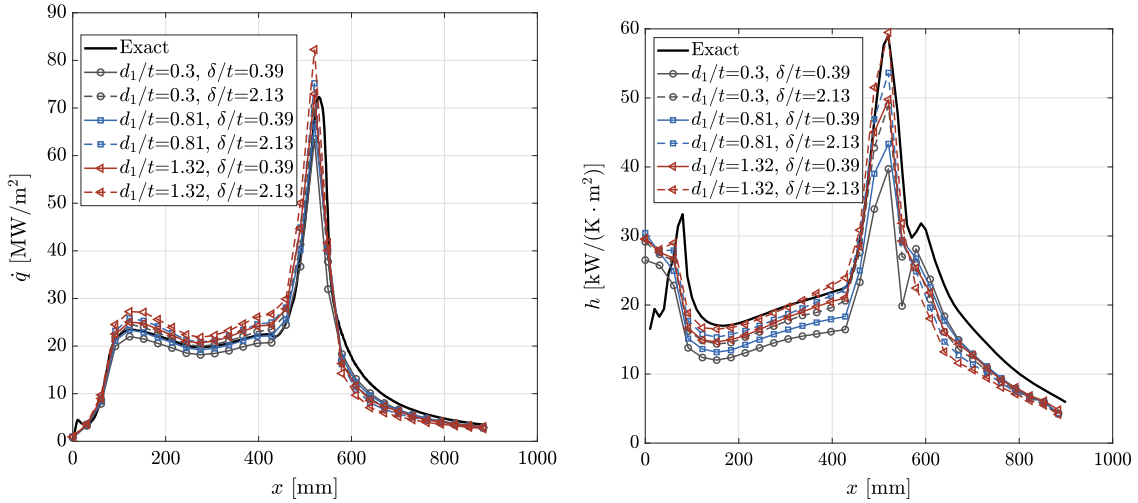

Fig. 17 Axial heat flux profiles (left) and cooling channel heat transfer coefficient profiles (right) for the $\dot{q} - h$ optimization with two sensors.

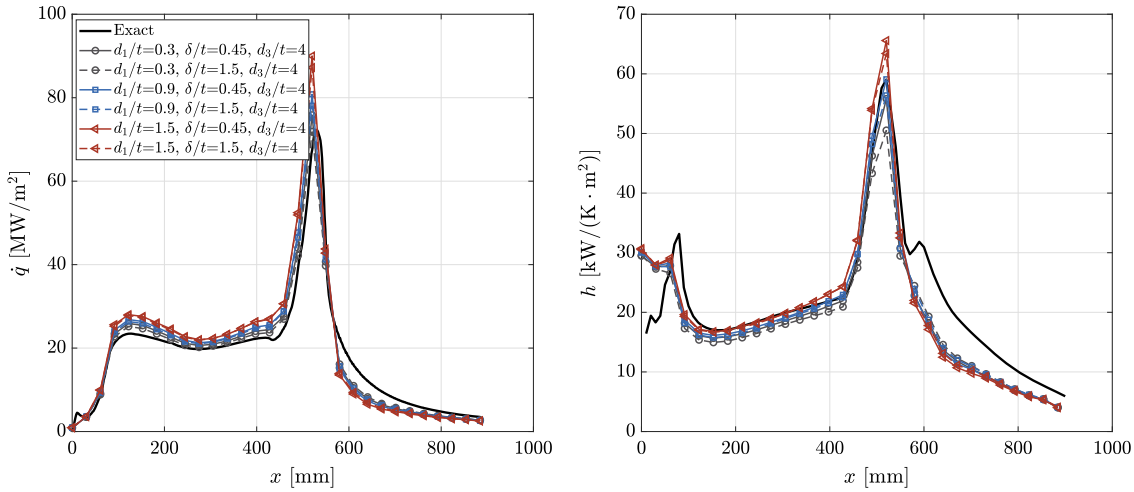

Fig. 18 Axial heat flux profiles (left) and cooling channel heat transfer coefficient profiles (right) for the $\dot{q} - h$ optimization with three sensors. The left and right subfigures share the same legend.

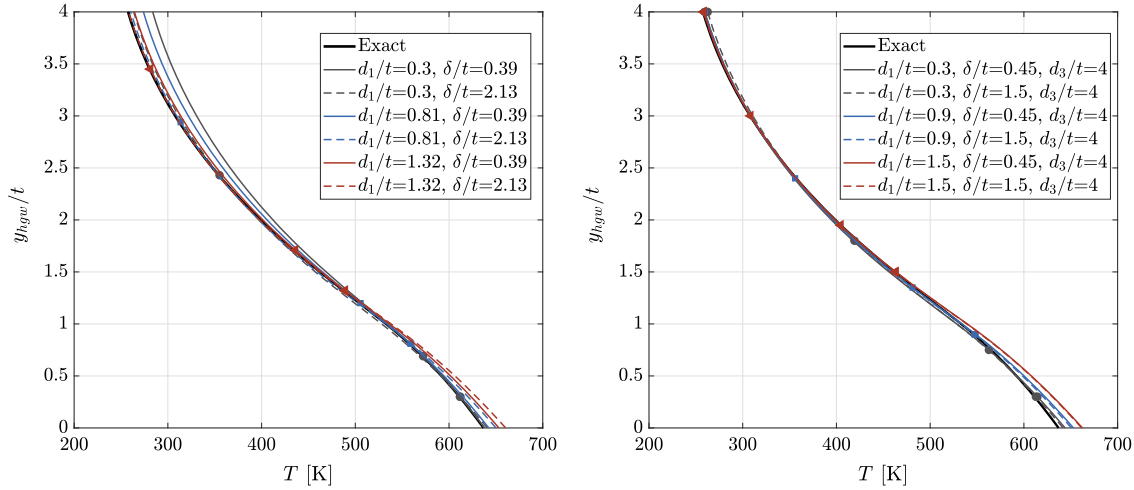

Fig. 19 Liner temperature profiles for the $\dot{q} - h$ optimization using two sensors (left) and three sensors (right) at $x = 300$ mm.

In the present Paper, the optimization method introduced in Eq. (16) is extended to three variables for $\boldsymbol{Q}$, $\boldsymbol{H}_{\text{top}}$, and $\boldsymbol{H}_{\text{bottom}}$. However, because of the introduction of the new variable and the assumed profile of the side wall, the assumption of constant Jacobian is no longer as robust as with two variables. For that reason, first a $\dot{q} - h$ optimization is carried out as a precursor run. Given the converged values for $\boldsymbol{Q}$ and $\boldsymbol{H}$, a new Jacobian is calculated, which can be used for the $\dot{q} - h_{\text{top}} - h_{\text{bottom}}$ run, thereby accelerating the optimization algorithm. Per run, a total of 40–70 iterations was needed, amounting to 8–15 CPUh in total on a workstation with Intel Core i7-6700 at 3.4 GHz using four cores.

The results for the bottom and top walls are shown in Fig. 20. Both profiles appear to be captured by the inverse method throughout the entirety of the domain, with the exception of the throat, where larger

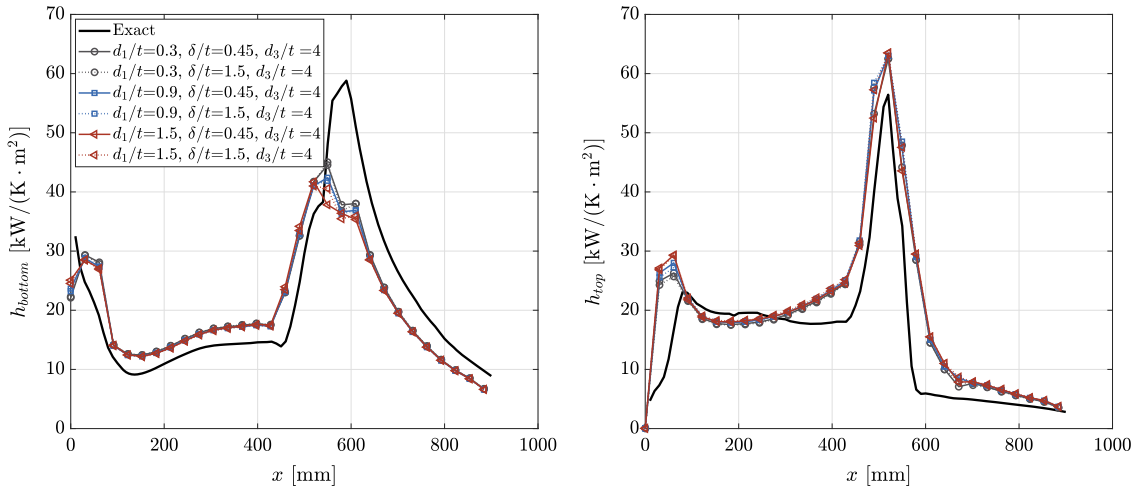

Fig. 20 Cooling channel heat transfer coefficient for the bottom and top walls. The left and right subfigures share the same legend.

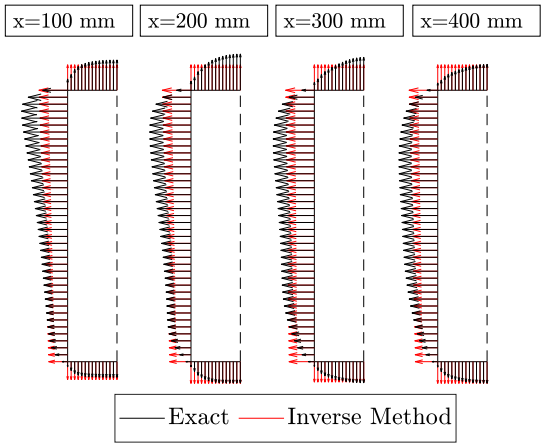

Fig. 21 Heat transfer coefficient along the channel circumference for different axial positions.

deviations are observed. Moreover, the exact positions of the thermocouples do not influence the obtained results significantly, which is encouraging regarding the placement of the sensors. The relative magnitude of the two wall coefficients is also reproduced accurately: in the cylindrical part, the upper wall has a higher average heat transfer coefficient, whereas in the divergent part of the nozzle, the reverse situation holds.

This is also illustrated schematically in Fig. 21, in which the heat transfer coefficient along the entire circumference is plotted in form of a vector field. Again, it is evident that the exact profile is much more complex than the linear trend assumed for the side wall. Increasing the complexity of the presumed profile would be possible but would necessitate additional thermocouples.

V. Conclusions

In the present Paper, the different options for the evaluation of experimental heat flux profiles in subscale and full-scale engines have been assessed for their performance. Obtaining accurate results for the heat flux using the smallest amount of thermocouples is crucial for the design of the testing hardware, as it can simplify cost- and time-intensive manufacturing steps needed for the placement of the sensors.

For the performed analysis, a full-scale upper-stage expander engine operated with LOX/LH_2 has been chosen. To generate the reference experimental heat flux and temperature fields, a CFD coupled simulation of the hot gas flow, structure, and cooling channels has been carried out. The obtained profiles from CFD represent the exact experimental values, and the different inverse methods have been assessed in their ability to match those values.

The results of the gradient method have been included because of the simplicity of the method. Because of the simplification of neglecting the effect of cooling channels, the possible thermocouple locations which allow for an accurate wall temperature and heat flux calculation are very restricted. Hence, the method is considered to be obsolete when dealing with regenerative cooling.

A major improvement can be achieved with the use of inverse methods and the modeling of the cooling channel heat transfer with an algebraic Nusselt number model. The benefit of this method is the large computational speed and the need for only one temperature sensor per axial location, which leads to the smallest possible installation of thermocouples. However, the studies carried out in this Paper display the need for well-validated Nusselt number correlations, which capture the physical phenomena of the fuel-specific properties, the thruster geometry, and the thermodynamic conditions. With increased CFD and experimental studies dealing with the improvement of those correlations and the use of data-based approaches, the method's robustness and range of application are expected to significantly increase.

Finally, to avoid the need for modeling of the cooling channels, the simultaneous optimization of both the wall heat flux and cooling coefficient has been presented. A Jacobi-based approach has been introduced, which significantly accelerates the convergence of the algorithm. This method requires at least two sensors per axial position but delivers heat flux data and cooling channel heat transfer coefficients with an accuracy of 5–12%. Because of the high accuracy of the method, the installation of the thermocouples does not have to be too close at the hot-gas wall, which can reduce the manufacturing costs and increase the liner wall thickness at the measurement locations. With this method, predicting the heat transfer in each one of the three channel walls (top, bottom, and side) has also been demonstrated, at the expense of installing three sensors per axial position.

For all methods presented in this Paper, the systematic error resulting from the placement of the temperature sensors has been analyzed allowing for a better quantification of the expected heat flux experimental uncertainties in future tests. This, combined with the computational efficiency of the proposed Jacobi-based optimization, allows for an increase in reliability and reduction of numerical cost for the evaluation of three-dimensional full-scale rocket test data.

Acknowledgments

Financial support has been provided by the German Research Foundation in the framework of the Sonderforschungsbereich Transregio 40. The authors gratefully acknowledge the Gauss Centre for Supercomputing e.V. (https://www.gauss-centre.eu) for funding this project by providing computing time on the GCS Supercomputer SuperMUC at Leibniz Supercomputing Centre (https://www.lrz.de/). The authors also thank Christof Roth and Maximilian Mörtl for their contribution to the preliminary computational fluid dynamics studies.

References

[1] Sutton, G. P., *History of Liquid Propellant Rocket Engines*, AIAA, Reston, VA, 2006, Chap. 3. https://doi.org/10.2514/4.868870

[2] Bartz, D. R., "A Simple Equation for Rapid Estimation of Rocket Nozzle Convective Heat Transfer Coefficients," *Jet Propulsion*, Vol. 27, No. 1, 1957, pp. 49–51. https://doi.org/10.2514/8.12572

[3] Chemnitz, A., Sattelmayer, T., Roth, C., Haidn, O., Daimon, Y., Keller, R., Gerlinger, P., Zips, J., and Pfitzner, M., "Numerical Investigation of Reacting Flow in a Methane Rocket Combustor: Turbulence Modeling," *Journal of Propulsion and Power*, Vol. 34, No. 4, 2018, pp. 864–877. https://doi.org/10.2514/1.B36565

[4] Perakis, N., Strauß, J., and Haidn, O. J., "Heat Flux Evaluation in a Multi-Element CH4/O2 Rocket Combustor Using an Inverse Heat Transfer Method," *International Journal of Heat and Mass Transfer*, Vol. 142, Oct. 2019, Paper 118425. https://doi.org/10.1016/j.ijheatmasstransfer.2019.07.075

[5] Suslov, D., Betti, B., Aichner, T., Soller, S., Nasuti, F., and Haidn, O., "Experimental Investigation and CFD-Simulation of the Film Cooling in an O2/CH4 Subscale Combustion Chamber," *Space Propulsion Conference*, Association Aéronautique et Astronautique de France, Paris, France, 2012.

[6] Celano, M. P., Silvestri, S., Bauer, C., Perakis, N., Schlieben, G., and Haidn, O. J., "Comparison of Single and Multi-Injector GOC/CH4 Combustion Chambers," *52nd AIAA/SAE/ASEE Joint Propulsion Conference*, AIAA Paper 2016-4990, 2016. https://doi.org/10.2514/6.2016-4990

[7] Arnold, R., Suslov, D., and Haidn, O., "Circumferential Film Cooling Effectiveness in a LOX/H2 Subscale Combustion Chamber," *Journal of Propulsion and Power*, Vol. 25, No. 3, 2009, pp. 760–770. https://doi.org/10.2514/1.40305

[8] Deridder, M. A., and Anderson, W. E., "Heat Flux and Pressure Profiles in an Oxygen/Hydrogen Multielement Rocket Combustor," *Journal of Propulsion and Power*, Vol. 26, No. 4, 2010, pp. 696–705. https://doi.org/10.2514/1.48060

[9] Daimon, Y., Negishi, H., Koshi, M., and Suslov, D., "Numerical and Experimental Investigation of the Methane Film Cooling in Subscale Combustion Chamber," *Progress in Propulsion Physics*, Vol. 8, 2016, pp. 129–144. https://doi.org/10.1051/eucass/2016081290

[10] Oschwald, M., Suslov, D., Haemisch, J., Haidn, O., Celano, M., Kirchberger, C., Rackemann, N., Preuß, A., and Wiedmann, D., *Measurement of Heat Transfer in Liquid Rocket Combustors*, AIAA, Reston, VA, 2020, Chap. 7, pp. 281–331. https://doi.org/10.2514/5.9781624105814.0281.0332

[11] Ash, R., and Wright, R., Jr., "Design Considerations for Gardon Heat Flux Sensors," *6th Thermophysics Conference*, AIAA Paper 1971-470, 1971. https://doi.org/10.2514/6.1971-470
[12] Mityakov, A. V., Sapozhnikov, S. Z., Mityakov, V. Y., Snarskii, A. A., Zhenirovsky, M. I., and Pyrhönen, J. J., "Gradient Heat Flux Sensors for High Temperature Environments," *Sensors and Actuators A: Physical*, Vol. 176, April 2012, pp. 1–9. https://doi.org/10.1016/j.sna.2011.12.020
[13] Celano, M., Silvestri, S., Pauw, J., Perakis, N., Schily, F., Suslov, D., and Haidn, O., "Heat Flux Evaluation Methods for a Single Element Heat-Sink Chamber," *6th European Conference of Aeronautics and Space Science*, EUCAS, Saix, France, 2015.
[14] Perakis, N., Rahn, D., Haidn, O. J., and Eiringhaus, D., "Heat Transfer and Combustion Simulation of Seven-Element O2/CH4 Rocket Combustor," *Journal of Propulsion and Power*, Vol. 35, No. 6, 2019, pp. 1080–1097. https://doi.org/10.2514/1.B37402
[15] Ozisik, M. N., *Inverse Heat Transfer: Fundamentals and Applications*, CRC Press, Boca Raton, FL, 2000, Chap. 2.
[16] Fernández-Torrijos, M., Sobrino, C., Almendros-Ibáñez, J., Marugán-Cruz, C., and Santana, D., "Inverse Heat Problem of Determining Unknown Surface Heat Flux in a Molten Salt Loop," *International Journal of Heat and Mass Transfer*, Vol. 139, Aug. 2019, pp. 503–516. https://doi.org/10.1016/j.ijheatmasstransfer.2019.05.002
[17] Zhang, L., Li, L., Ju, H., and Zhu, B., "Inverse Identification of Interfacial Heat Transfer Coefficient Between the Casting and Metal Mold Using Neural Network," *Energy Conversion and Management*, Vol. 51, No. 10, 2010, pp. 1898–1904. https://doi.org/10.1016/j.enconman.2010.02.020
[18] Huang, C.-H., and Lee, C.-T., "An Inverse Problem to Estimate Simultaneously Six Internal Heat Fluxes for a Square Combustion Chamber," *International Journal of Thermal Sciences*, Vol. 88, Feb. 2015, pp. 59–76. https://doi.org/10.1016/j.ijthermalsci.2014.08.021
[19] Haemisch, J., Suslov, D., and Oschwald, M., "Experimental Analysis of Heat Transfer Deterioration and Pseudoboiling Phenomena in a Methane Cooled Combustion Chamber at Real Conditions," *2018 Joint Propulsion Conference*, AIAA Paper 2018-4943, 2018. https://doi.org/10.2514/6.2018-4943
[20] Perakis, N., and Haidn, O. J., "Inverse Heat Transfer Method Applied to Capacitively Cooled Rocket Thrust Chambers," *International Journal of Heat and Mass Transfer*, Vol. 131, March 2019, pp. 150–166. https://doi.org/10.1016/j.ijheatmasstransfer.2018.11.048
[21] Dabrowski, A., and Dabrowski, L., "Inverse Heat Transfer Problem Solution of Sounding Rocket Using Moving Window Optimization," *PLOS One*, Vol. 14, No. 6, 2019, Paper e0218600. https://doi.org/10.1371/journal.pone.0218600
[22] Luo, J., and Shih, A. J., "Inverse Heat Transfer Solution of the Heat Flux due to Induction Heating," *Journal of Manufacturing Science and Engineering*, Vol. 127, No. 3, 2005, pp. 555–563. https://doi.org/10.1115/1.1949617
[23] Huang, C.-H., and Tsai, Y.-L., "A Transient 3-D Inverse Problem in Imaging the Time-Dependent Local Heat Transfer Coefficients for Plate Fin," *Applied Thermal Engineering*, Vol. 25, Nos. 14–15, 2005, pp. 2478–2495. https://doi.org/10.1016/j.applthermaleng.2004.12.003
[24] Wang, T., Sun, B., Xiang, J., and Liu, D., "Wall Heat Flux Measurements in a GO2/GH2 Heat-Sink Combustion Chamber," *Journal of Thermal Science and Technology*, Vol. 13, No. 1, 2018, Paper JTST0016. https://doi.org/10.1299/jtst.2018jtst0016
[25] Singh, S. K., Yadav, M. K., Sonawane, R., Khandekar, S., and Muralidhar, K., "Estimation of Time-Dependent Wall Heat Flux from Single Thermocouple Data," *International Journal of Thermal Sciences*, Vol. 115, May 2017, pp. 1–15. https://doi.org/10.1016/j.ijthermalsci.2017.01.010
[26] Raudenský, M., Woodbury, K. A., Kral, J., and Brezina, T., "Genetic Algorithm in Solution of Inverse Heat Conduction Problems," *Numerical Heat Transfer, Part B Fundamentals*, Vol. 28, No. 3, 1995, pp. 293–306. https://doi.org/10.1080/10407799508928835
[27] Szénási, S., and Felde, I., "Configuring Genetic Algorithm to Solve the Inverse Heat Conduction Problem," *2017 IEEE 15th International Symposium on Applied Machine Intelligence and Informatics (SAMI)*, Inst. of Electrical and Electronics Engineers, Piscataway, NJ, 2017, pp. 387–392. https://doi.org/10.1109/SAMI.2017.7880340
[28] Yu, B., Yao, W., Gao, Q., Zhou, H., and Xu, C., "A Novel Non-Iterative Inverse Method for Estimating Boundary Condition of the Furnace Inner Wall," *International Communications in Heat and Mass Transfer*, Vol. 87, Oct. 2017, pp. 91–97. https://doi.org/10.1016/j.icheatmasstransfer.2017.06.017
[29] Yu, B., Xu, C., Yao, W., and Meng, Z., "Estimation of Boundary Condition on the Furnace Inner Wall Based on Precise Integration BEM Without Iteration," *International Journal of Heat and Mass Transfer*, Vol. 122, July 2018, pp. 823–845. https://doi.org/10.1016/j.ijheatmasstransfer.2018.02.039
[30] Nie, C., and Yu, B., "Inversing Heat Flux Boundary Conditions Based on Precise Integration FEM Without Iteration and Estimation of Thermal Stress in FGMs," *International Journal of Thermal Sciences*, Vol. 140, June 2019, pp. 201–224. https://doi.org/10.1016/j.ijthermalsci.2019.03.003
[31] Fadale, T. D., Nenarokomov, A. V., and Emery, A. F., "Two Approaches to Optimal Sensor Locations," *Journal of Heat Transfer*, Vol. 117, No. 2, 1995, pp. 373–379. https://doi.org/10.1115/1.2822532
[32] Wan, S., Xu, P., Wang, K., and Li, S., "Estimation of Distributed Thermal Boundary Based on Fuzzy Clustering of Temperature Observable Points," *International Journal of Heat and Mass Transfer*, Vol. 147, Feb. 2020, Paper 118920. https://doi.org/10.1016/j.ijheatmasstransfer.2019.118920
[33] Pizzarelli, M., Nasuti, F., Paciorri, R., and Onofri, M., "Numerical Analysis of Three-Dimensional Flow of Supercritical Fluid in Cooling Channels," *AIAA Journal*, Vol. 47, No. 11, 2009, pp. 2534–2543. https://doi.org/10.2514/1.38542
[34] Dang, G., Zhong, F., Zhang, Y., and Zhang, X., "Numerical Study of Heat Transfer Deterioration of Turbulent Supercritical Kerosene Flow in Heated Circular Tube," *International Journal of Heat and Mass Transfer*, Vol. 85, June 2015, pp. 1003–1011. https://doi.org/10.1016/j.ijheatmasstransfer.2015.02.052
[35] Pizzarelli, M., Urbano, A., and Nasuti, F., "Numerical Analysis of Deterioration in Heat Transfer to Near-Critical Rocket Propellants," *Numerical Heat Transfer, Part A: Applications*, Vol. 57, No. 5, 2010, pp. 297–314. https://doi.org/10.1080/10407780903583016
[36] Pizzarelli, M., "A CFD-Derived Correlation for Methane Heat Transfer Deterioration," *Numerical Heat Transfer, Part A: Applications*, Vol. 69, No. 3, 2016, pp. 242–264. https://doi.org/10.1080/10407782.2015.1080575
[37] Pioro, I. L., Khartabil, H. F., and Duffey, R. B., "Heat Transfer to Supercritical Fluids Flowing in Channels–Empirical Correlations (Survey)," *Nuclear Engineering and Design*, Vol. 230, Nos. 1–3, 2004, pp. 69–91. https://doi.org/10.1016/j.nucengdes.2003.10.010
[38] Naraghi, M., and Dassonville, R., "Improved Correlations for Curvature Effects in Cooling Channels of Rocket Engines," *48th AIAA/ASME/SAE/ASEE Joint Propulsion Conference & Exhibit*, AIAA Paper 2012-3992, 2012. https://doi.org/10.2514/6.2012-3992
[39] Waxenegger-Wilfing, G., Dresia, K., Deeken, J. C., and Oschwald, M., "Heat Transfer Prediction for Methane in Regenerative Cooling Channels with Neural Networks," *Journal of Thermophysics and Heat Transfer*, Vol. 34, No. 2, 2020, pp. 347–357. https://doi.org/10.2514/1.T5865
[40] Eiringhaus, D., Riedmann, H., Knab, O., and Haidn, O. J., "Full-Scale Virtual Thrust Chamber Demonstrators as Numerical Testbeds Within SFB-TRR 40," *Joint Propulsion Conference*, AIAA Paper 2018-4469, 2018. https://doi.org/10.2514/6.2018-4469
[41] Haidn, O. J., Adams, N., Radespiel, R., Schröder, W., Stemmer, C., Sattelmayer, T., and Weigand, B., "Fundamental Technologies for the Development of Future Space Transport System Components Under High Thermal and Mechanical Loads," *Joint Propulsion Conference*, AIAA Paper 2018-4466, 2018. https://doi.org/10.2514/6.2018-4466
[42] Santiago, J., "Evolution of the RL10 Liquid Rocket Engine for a New Upperstage Application," *32nd Joint Propulsion Conference and Exhibit*, AIAA Paper 1996-3013, 1996. https://doi.org/10.2514/6.1996-3013
[43] Fluent, A., *Ansys Fluent Theory Guide*, ANSYS, Inc., Canonsburg, PA, 2011.
[44] Traxinger, C., Zips, J., and Pfitzner, M., "Large-Eddy Simulation of a Multi-Element LOx/CH4 Thrust Chamber Demonstrator of a Liquid Rocket Engine," *8th European Conference of Aeronautics and Space Science*, EUCAS, Saix, France, 2019. https://doi.org/10.13009/EUCASS2019-731
[45] Negishi, H., Daimon, Y., and Kawashima, H., "Flowfield and Heat Transfer Characteristics in the LE-X Expander Bleed Cycle Combustion Chamber," *50th AIAA/ASME/SAE/ASEE Joint Propulsion Conference*, AIAA Paper 2014-4010, 2014. https://doi.org/10.2514/6.2014-4010
[46] Peng, D.-Y., and Robinson, D. B., "A New Two-Constant Equation of State," *Industrial and Engineering Chemistry Fundamentals*, Vol. 15, No. 1, 1976, pp. 59–64. https://doi.org/10.1021/i160057a011

[47] Abudour, A. M., Mohammad, S. A., Robinson, R. L., Jr., and Gasem, K. A., "Volume-Translated Peng-Robinson Equation of State for Liquid Densities of Diverse Binary Mixtures," *Fluid Phase Equilibria*, Vol. 349, July 2013, pp. 37–55.
https://doi.org/10.1016/j.fluid.2013.04.002

[48] Launder, B. E., and Spalding, D. B., *Mathematical Models of Turbulence*, Academic Press, London, 1972, pp. 101–108.

[49] Wolfshtein, M., "The Velocity and Temperature Distribution in One-Dimensional Flow with Turbulence Augmentation and Pressure Gradient," *International Journal of Heat and Mass Transfer*, Vol. 12, No. 3, 1969, pp. 301–318.
https://doi.org/10.1016/0017-9310(69)90012-X

[50] Chung, T. H., Ajlan, M., Lee, L. L., and Starling, K. E., "Generalized Multiparameter Correlation for Nonpolar and Polar Fluid Transport Properties," *Industrial and Engineering Chemistry Research*, Vol. 27, No. 4, 1988, pp. 671–679.
https://doi.org/10.1021/ie00076a024

[51] Menter, F. R., "Two-Equation Eddy-Viscosity Turbulence Models for Engineering Applications," *AIAA Journal*, Vol. 32, No. 8, 1994, pp. 1598–1605.
https://doi.org/10.2514/3.12149

[52] Lemmon, E., McLinden, M., Friend, D., Linstrom, P., and Mallard, W., *NIST Chemistry WebBook*, NIST Standard Reference Database Number 69, National Inst. of Standards and Technology, Gaithersburg, MD, 2011.

[53] DiValentin, J., and Naraghi, M., "Effects Cooling Channel Curvature on Coolant Secondary Flow and Heat Transfer," *46th AIAA/ASME/SAE/ASEE Joint Propulsion Conference & Exhibit*, AIAA Paper 2010-6973, 2010.
https://doi.org/10.2514/6.2010-6973

[54] Kraussold, H., "Die Wärmeübertragung an Flüssigkeiten in Rohren bei Turbulenter Strömung," *Forschung auf dem Gebiet des Ingenieurwesens A*, Vol. 4, No. 1, 1933, pp. 39–44.
https://doi.org/10.1007/BF02716945

[55] Kirchberger, C., Wagner, R., Kau, H.-P., Soller, S., Martin, P., Bouchez, M., and Bonzom, C., "Prediction and Analysis of Heat Transfer in Small Rocket Chambers," *46th AIAA Aerospace Sciences Meeting and Exhibit*, AIAA Paper 2008-1260, 2008.
https://doi.org/10.2514/6.2008-1260

[56] Fletcher, R., *Practical Methods of Optimization*, Wiley, Hoboken, NJ, 2013, pp. 44–79.

[57] Strang, G., *Linear Algebra and Its Applications*, Hartcourt Brace Jovanovich College, San Diego, CA, 1988, pp. 211–214.

[58] Haemisch, J., Suslov, D., and Oschwald, M., "Experimental Analysis of Heat Transfer Processes in Cooling Channels of a Subscale Combustion Chamber at Real Thermal Conditions for Cryogenic Hydrogen and Methane," *6th Space Propulsion Conference*, Association Aéronautique et Astronautique de France, Paris, France, 2018.

[59] Kuhl, D., Haidn, O., and Holzer, A., "Computational Solution of the Inverse Heat Conduction Problem of Rocket Combustion Chambers," *35th Joint Propulsion Conference and Exhibit*, AIAA Paper 1999-2913, 1999.
https://doi.org/10.2514/6.1999-2913

3.3 REGENERATIVELY COOLED MULTI-ELEMENT ROCKET THRUST CHAMBERS

The application of an inverse method for the evaluation of experimental heat flux data in multi-element regenerative thrust chambers is presented in this section. The passage corresponds to the paper entitled:

Heat Flux Evaluation in a Multi-Element CH_4/O_2 rocket Combustor Using an Inverse Heat Transfer Method
Nikolaos Perakis, Julian Strauß, Oskar J. Haidn
International Journal of Heat and Mass Transfer (2019)
doi: https://doi.org/10.1016/j.ijheatmasstransfer.2019.07.075

The motivation behind this work is to apply the methods that have been validated in Section 3.2 for the evaluation of *real experimental data*. For that reason, a multi-element GOX/GCH_4 chamber using a water-cooling cycle is investigated. The configuration of the chamber and the experimental test envelope are described in detail in Silvestri et al. [192].

An additional feature which has been investigated for the first time in this study is the evaluation of the *circumferential variation in heat flux* simultaneously to its axial resolution. As large deviations from the average heat flux value can be experienced locally due to the interaction of neighboring injector elements, the evaluation of the circumferentially resolved loads is crucial for precise lifetime predictions of the chamber hardware. Some of the previous studies aiming at measuring the azimuthal heat flux and temperature variation, have employed a repetition of tests with a rotation of the cylindrical chamber segment relative to the injector head [201, 222]. Wang et al. [241] performed an analysis of the two-dimensional heat loads in a GH_2/GO_2 capacitive chamber using an inverse method, thereby eliminating the need for test repetition and hardware rotation. Recently, Liu et al. [242] identified a horseshoe-like heat flux pattern in an experimental GH_2/GO_2 water-cooled demonstrator and quantified the effect that the azimuthal load variation has on the thermal stresses and cooling channel deformation. Suslov et al. [243] carried out the evaluation of the thermal loads in a LOX/H_2 sub-scale chamber with an inverse method, showing the dependence of the heat load variation on the chamber pressure.

In the work presented in this section, an instantaneous inverse evaluation of the azimuthal heat load profile without rotation of the hardware is carried out, using thermocouple measurements placed in different azimuthal locations. For the optimization, the sensitivity matrix method is utilized, with a *Nusselt number correlation* for the description of the cooling channels. This is enforced by the fact that only one thermocouple is placed per axial location which does not allow the use of a simultaneous measurement of both wall loads and cooling performance. Despite the simplicity of the cooling channel boundary condition, a reasonable agreement with the calorimetric data is found for the average heat flux. At the same time, the inverse method provides *an 8-fold increase in resolution* of the axial wall heat loads.

In azimuthal direction, thermocouples placed directly above and between neighboring injector elements were used as input. The resulting inverse profiles led to a better understanding of the physical processes occurring during the expansion of the individual flames and their interaction. Specifically, a *shift in the azimuthal position of the local heat flux maximum*

was obtained using the inverse method which has been attributed to a secondary flow pattern and which is numerically investigated in Section 6.1.

Finally, a quantification of the expected systematic error sources has been realized, leading to a heat flux uncertainty of approximately 10-12%. The major contributions of the uncertainty arise from the utilized Nusselt number correlation and the placement accuracy of the thermocouples. Although the inverse method is able to deliver results by using a single thermocouple per axial/azimuthal position, the uncertainty introduced by the faulty sensor installation can be significantly reduced by adding a larger number of sensors at different radial positions and is an option that should be preferred when designing the chamber instrumentation. As far as the minimization of the bias stemming from the Nusselt number model is concerned, the use of correlations specifically tailored for a specific operational configuration are recommended.

International Journal of Heat and Mass Transfer 142 (2019) 118425

Contents lists available at ScienceDirect

International Journal of Heat and Mass Transfer

journal homepage: www.elsevier.com/locate/ijhmt

Heat flux evaluation in a multi-element CH_4/O_2 rocket combustor using an inverse heat transfer method

Nikolaos Perakis *, Julian Strauß, Oskar J. Haidn

Technical University of Munich, Chair of Turbomachinery and Flight Propulsion, Boltzmannstr. 15, 85748 Garching, Germany

ARTICLE INFO

Article history:
Received 11 December 2018
Received in revised form 6 May 2019
Accepted 15 July 2019

Keywords:
Inverse method
Rocket engine
Methane combustion
Heat transfer

ABSTRACT

Heat load measurements in experimental lab-scale rocket combustors are essential in order to obtain information about the mixing and energy release of the propellants, the injector/injector interaction as well as the injector/wall interaction. The present work demonstrates an efficient inverse method for estimating the spatially resolved heat flux distribution at the hot gas wall of multi-element, actively cooled engines using the information provided by temperature measurements in the material. This inverse method implements Nusselt-correlations for the estimation of the wall heat transfer coefficient in the cooling channels and a Jacobi-matrix based optimization algorithm for the calculation of the hot gas side heat flux. The method is applied for the evaluation of CH_4/O_2 test data. A water-cooled 7-injector rocket combustor is investigated, which is operated at the Chair of Turbomachinery and Flight Propulsion (LTF) of the Technical University of Munich (TUM). The use of the inverse method gives significant information about the axial and azimuthal distribution of the heat flux. The azimuthal distribution sheds light into the interaction between the individual flames. Specifically, the angular position of maximal heat flux appears to shift from directly above the injector elements towards the positions between two neighboring elements, implying the presence of a strong vortex system pushing hot gas directly onto the wall. The obtained results agree qualitatively with RANS simulations of the hot gas flow.

1. Introduction

In an effort to decrease launch costs and to produce reliable and efficient propulsion devices for space applications, significant research efforts have been placed in advancing the maturity level of the propellant combination methane/oxygen. Within the past decades many space-faring nations have investigated and developed technologies for liquid propellant rocket engines operating with methane/oxygen. NASA has successfully developed and tested a prototype planetary lander propelled by a LOX/LCH_4 20kN class engine within the Morpheus project [1,2], whereas in Europe a low cost LOX/LCH_4 engine prototype named Prometheus is scheduled [3] with the purpose of powering the next generation of launchers after Ariane 6. The collaboration of industry and space agencies in Europe is manifested in the development of the LM-10 MIRA engine for the upper stage of the VEGA-E launcher [4] and the ACE-42R reusable engine for a space plane concept. The interest of private companies in the LOX/LCH_4 propellant is also evident from the development of the BE-4 and Raptor engines, which will power the Vulcan and ITS launch vehicles respectively [5]. Finally, South Korea is also looking into advancing the status of methane/oxygen engines [6], whereas in Japan the LE-8 engine, as well as a 30 kN- and a 100 kN-class engine have been successfully tested [7,8].

The reasons for the increased research interest in methane/oxygen are mainly the fact that it combines great performance with reusability and sustainability. Apart from the high specific impulse (highest among hydrocarbons) and the large density which leads to small tank volumes [9], the large boiling temperature compared to hydrogen allows for less demanding cooling and thermal insulation of the tanks to minimize vaporization and heat-exchange with the oxygen tank. Reusability is achieved by the low coking-rate of methane under the thermal conditions typical for cooling channels [10] and the lower thermal strain induced to the engine structure due to the temperature difference of coolant and hot gas compared to hydrogen engines [11]. Sustainability is ensured by the existence of various methods for obtaining bio-methane and the methods for renewable natural gas production [12,13]. Finally, the costs can be further reduced by substituting the costly helium with nitrogen for the pressurization of the tanks.

* Corresponding author.
E-mail address: nikolaos.perakis@tum.de (N. Perakis).

https://doi.org/10.1016/j.ijheatmasstransfer.2019.07.075
0017-9310/

Nomenclature

c^*	characteristic velocity [m/s]
c_p	specific heat capacity [J/(kg · K)]
d	diameter [m]
h	heat transfer coefficient [W/(m^2 · K)]
J	residual function [K^2]
k	iteration index [–]
$\dot{m}$	mass flow rate [kg/s]
M	number of thermocouples [–]
N	number of parameter points [–]
$\mathbf{n}$	outwards pointing normal direction [m]
Nu	Nusselt number [–]
p	chamber pressure [bar]
Pr	Prandtl number [–]
r	radius [m]
$\dot{q}$	heat flux [W/m^2]
Re	Reynolds number [–]
$\mathbf{S}$	Jacobi matrix [K · m^2/W]
T	temperature [K]
x	axial coordinate [m]
ε	residual convergence limit [K^2]
ϵ	error [%]
θ	circumferential coordinate [°]
λ	thermal conductivity [W/(m · K)]
μ	dynamic viscosity [Pa · s]

Subscripts

0	reference
acc	accuracy
c	calculated
cc	cooling channel
corr	correlation
fu	fuel
inj	injector
loc	location
m	measured
mat	material
ox	oxidizer
prec	precision
tot	total
w	wall

In order to better understand the characteristics of this promising propellant combination, the design and testing of sub-scale engines is required. Specifically, before the design of full-scale engines, tests using single-element and multi-element sub-scale hardware are performed [7,8,14,15]. The knowledge about the performance of the injector elements, i.e. the mixing of the propellants, the injector/injector interaction and injector/wall interaction in the sub-scale experiments is used as an input for the improvement of the full-scale design without the need for costly full-scale testing.

The test data obtained from the sub-scale configurations are also used to provide validation data for numerical simulations. The necessity for a reliable prediction of the combustion characteristics and the heat loads within a combustion chamber and nozzle has promoted computational fluid dynamics (CFD) to become an integral part of the design process in the space propulsion industry. Apart from the prediction of performance merits such as the specific impulse and the characteristic velocity c^*, the calculated pressure profiles along the axial position $p(x)$ as well as the heat flux values at the hot gas wall $\dot{q}(x)$ are compared to the available experimental data. The need for this data over a wide range of operational conditions is even more critical for the innovative propellant combination of methane/oxygen due to the limited number of available tests [16–20].

Of the previously mentioned quantities, the one having the largest significance for the understanding of the physical and chemical phenomena is the heat flux. Due to the harsh environment within the chamber hot gas, the installation of sensors measuring gas temperature is almost impossible. Given the limited access to the burning gas, the heat flux distributions are usually utilized to deduce information about the conditions within the chamber. Moreover the prediction of the engine's lifetime, the design of an effective cooling system and the reliability of the chamber components after a specific number of tests is imminently connected to the heat loads applied onto the chamber wall thereby increasing the importance of this quantity even more.

The calculation of the average heat flux in experiments with active cooling system is easily carried out by means of the calorimetric method. However, the axial resolution of this method is restricted since it is defined by the number of cooling segments present in the hardware. Moreover, obtaining information about the azimuthal distribution becomes challenging and is usually not an option since the inlet and outlet temperature is measured in mixing manifolds [20]. Using temperature readings within the chamber material however, a reconstruction of the axially and azimuthally resolved heat flux profiles is possible. This method requires the solution of an inverse problem. The problem is considered to be an "inverse" one, since the causes (heat flux) that lead to a measured effect (temperature at specific locations) are sought.

Of particular interest are heat flux data for multi-element sub-scale engines due to the additional complexity introduced in the presence of flame-flame interaction. The interaction of the individual injectors leads to a local variation of the wall heat flux along the azimuthal direction, a phenomenon which is representative for full-scale hardware as well [21]. Extensive studies of wall heat flux evaluation in multi-element configurations with the purpose of resolving the azimuthal distributions are however limited. Conjugated heat transfer simulations of combustion and heat transfer in sub-scale and full-scale engines by Negishi et al. [22,23], Song et al. [24] as well as Daimon et al. [25] have demonstrated that the local heat flux values can significantly be increased by the secondary flow structures induced by the interaction of the individual flames. Similar results have been reported in experimental studies by Suslov et al. [26].

The present work introduces an inverse method for the evaluation of the heat loads in actively cooled rocket engines. The method can be applied to the evaluation of axially and circumferentially varying heat loads in multi-element sub-scale and full-scale rocket thrust chambers without a large computational cost. The main attributes of the method are the use of a Newton-Raphson optimization method and the approximation of the wall heat transfer in the cooling channels with a Nusselt-correlation. The method is applied for the evaluation of the heat loads in a GOX/GCH$_4$ multi-element chamber. Information about the flow-field, heat release and injector/injector interaction can be deduced from the resulting heat flux values and compared to existing CFD results.

In Section 2 a description of the chosen hardware is presented, whereas in Section 3 the properties of the inverse method are outlined in detail. The error analysis in Section 4 aims to quantify the uncertainties of the heat flux and temperature evaluation. The results of the inverse method as well as the comparison with the calorimetric method and previous CFD results is given in Section 5.

2. Experimental setup

The inverse heat conduction method presented in this work was initially developed with the purpose of evaluating the experimental heat flux stemming from the hot runs of capacitively and actively cooled rocket combustors operated at the Space Propulsion Division (RFA) of the Technical University of Munich (TUM). Within the framework of the German National Science Foundation (DFG) the DFG-TRR40 project entitled "Fundamental Technologies for the Development of Future Space-Transport-System Components under High Thermal and Mechanical Loads" has been funded, aiming at increasing the experience around the propellant combination methane/oxygen for future space applications [15].

In particular, the Space Propulsion Division of TUM has been working with these propellants for the past years employing different model combustors to provide detailed data about injector/injector and injector/wall interaction both for furthering identification and quantification of key phenomena and processes and for validation of engineering design tools [27,28]. For an optimum cooling system and specifically the cooling channel design, it is essential to know in sufficient detail the axial and azimuthal heat load distributions for a particular injector geometry and their sensitivity towards variations of the operating condition.

The examined multi-injector combustion chamber was designed for GOX and GCH_4 allowing high chamber pressures (up to 100 bar) and film cooling behavior examination. One of the key aspects of the project is to improve the knowledge on heat transfer processes and cooling methods in the combustion chamber, which is mandatory for the engine design. The attention is focused, in particular, on injector-injector and injector-wall interaction. In order to have a first characterization of the injectors' behavior, the multi-element combustion chamber is tested at low combustion chamber pressures and for a wide range of mixture ratios [29].

The seven-element rocket combustion chamber has an inner diameter of 30 mm and a contraction ratio of 2.5 in order to achieve Mach numbers similar to the ones in most rocket engine applications. The combustion chamber, depicted in Fig. 1, consists of four cylindrical water cooled chamber segments, as well as a nozzle segment (individually cooled), adding up to a total length of 382 mm. For the current study, shear coaxial injector elements are integrated. The test configuration includes the GOX post being mounted flush with respect to the injection face. The geometry of the injector is described in Table 1 and shown in Fig. 2.

In the present work, operating points with mean combustion chamber pressure of 20 and 30 bar and mixture ratios between 2.6 and 3.4 are chosen. The experimental data made available for the numerical evaluation include the mass flow rates of water at the inlet, the water pressure, the wall temperature at distinct locations and the integral heat flux values. For the determination of the heat flux values in the four chamber segments (A-D) and the nozzle (N), a calorimetric method is applied. The average heat flux of each chamber segment is determined by the enthalpy difference of the coolant between inlet and outlet. This is obtained by precise temperature measurements in the water manifolds between the test segments. Two separate cooling cycles are implemented: one for the first four segments in the combustion chamber and an additional cooling cycle for the nozzle segment, both in co-flow configuration with the hot gas. As described in Section 3, the present study focuses on chamber segment A, in which the cooling channels have a rectangular cross section. The geometry of the cooling channels and the operating conditions for the coolant in the first chamber segment are summarized in Table 2.

The wall temperature values available as inputs for the inverse method are obtained at radial distances of 0.7–1.5 mm from the hot gas wall. Each of the 8 axial positions equipped with thermocouples, alternates between 0.7 and 1.5 mm, with the first location at 2.5 mm downstream of the injector having a hot gas wall distance of 1.5 mm. Type T thermocouples with 0.5 mm diameter are installed to measure the temperature within the structure.

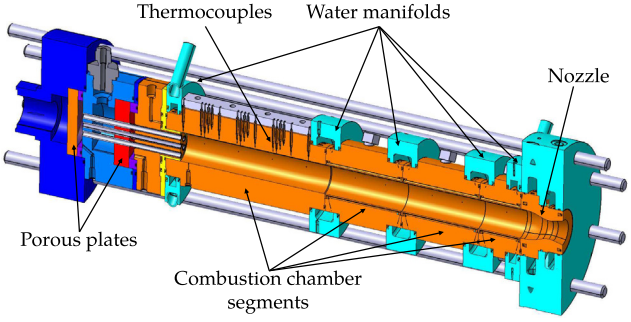

Fig. 1. Sketch of the combustion chamber.

Table 1
Summary of injector dimensions.

Dimension	Value
Oxygen port diameter d_{ox}	4.0 mm
Methane annulus inner diameter $d_{fu,in}$	5.0 mm
Methane annulus outer diameter $d_{fu,out}$	6.0 mm
Distance between injector centers $d_{inj,inj}$	9.0 mm
Distance between injector center and wall $d_{inj,wall}$	6.0 mm

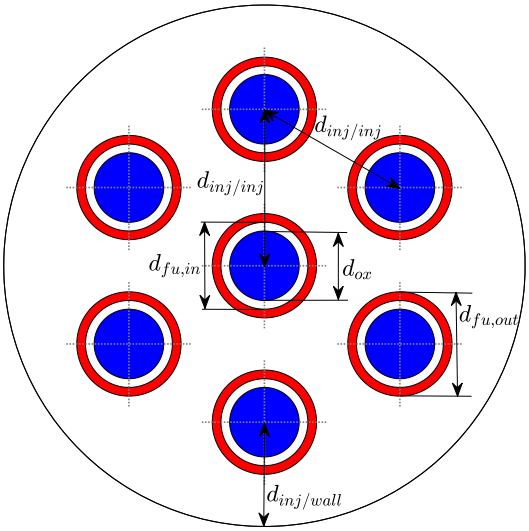

Fig. 2. Sketch of the injector faceplate.

Table 2
Summary of cooling channels geometry and operating point.

Dimension	Value
Cooling channel height	3.5 mm
Cooling channel width	1.5 mm
Aspect ratio	2.33
Distance of cooling channel to hot gas wall	1.5 mm
Mass flow rate (per channel)	13.89 g/s
Inlet pressure	40 bar
Inlet temperature segment A	285.0 K
Outlet temperature segment A	304.5 K
Reynolds number	5550

The locations of the thermocouples relative to the cooling channels are shown in the right sub-figure of Fig. 6. The inner part of the chamber (until the radius corresponding to the end of the cooling channels) consists of a CuCrZr alloy, whereas the outer part has been manufactured using copper electroplating.

3. Inverse heat transfer method

Experimental lab-scale rocket combustors cooled by a water cycle or other cooling medium have the characteristic property of reaching a steady state temperature distribution after the first seconds of operation. This effect is utilized when evaluating the heat flux profiles, since the latter ones can simply be obtained from the enthalpy difference of the outgoing and incoming coolant flow. The calorimetric method however only provides average values and its resolution is given by the number of cooling segments. For a more detailed distribution, the temperature field has to be reconstructed using an inverse method.

Inverse heat transfer methods have been successfully applied for the heat flux estimation in capacitively cooled engines where the temperature field is not stationary during the test operation and hence a transient inverse heat conduction method is needed [30–32].

The main concept behind an inverse method for heat conduction problems lies in trying to estimate the boundary conditions (causes) which best fit the measured temperature values (effects) while keeping the physics of the problem intact. In contrast to the capacitive method, no transient calculation is required, since the temperature is in steady-state. Nevertheless, the complexity of the problem increases because a second boundary condition is present in the system, namely the heat transfer between the coolant and the structure. This can be represented by the heat transfer coefficient and the bulk coolant temperature, which are unknown.

Three methods are the most promising for quantifying this additional unknown boundary condition. First, a simultaneous optimization of the heat flux and the heat transfer coefficient at each wall position is possible. This implies that the set of parameters, which are the outputs of the optimization problem, is increased by a factor two (one value for the hot gas wall heat flux and one for the coolant heat transfer coefficient). At the same time, at least two thermocouple measurements are required at the same axial and azimuthal position (for example at different radial positions) to ensure that the number of available information values (thermocouples) is larger than or equal the number of optimization parameters. This method is quite accurate since no modeling of the heat transfer coefficient is required and has been successfully applied for the evaluation of methane/oxygen sub-scale tests [26,33]. The second method would be to utilize a CFD simulation for the coolant side. This significantly increases the computational resources required for the inverse calculation since the flow simulation has to be carried out in each iteration of the optimization loop. Despite the larger computational effort, there is still uncertainty connected to the resulting heat transfer coefficient from the CFD simulation due to the limits of the available turbulence models. Finally, the modeling of the heat transfer can be performed using one-dimensional Nusselt correlations. Despite their empirical nature and lower sophistication level compared to CFD, their fast implementation and minimal computational resources render them attractive for test data evaluation.

In the present work, due to the limited number of thermocouples installed on the examined hardware and the need for short evaluation times, the method utilizing Nusselt correlations is implemented. Similarly to the majority of inverse algorithms, the method is based on an iterative approach as outlined in Fig. 3. The goal of the optimization is to minimize the difference between the measured and calculated temperatures at the measurement locations. The inverse method is implemented in the RoqFITT code which has already been validated for the evaluation of sub-scale rocket engines in Perakis et al. [30].

The starting point of the code is to initialize the temperature in the computational domain and to choose an initial guess for the heat flux. With the initial conditions (temperature field) and the boundary conditions (guessed heat flux) the material properties of the coolant are calculated and the heat transfer coefficient is obtained via the Nusselt correlation. After that, the first step is solving the direct heat transfer problem.

3.1. Direct solver

For the solution of the direct problem, a direct solver is required, which has to be computationally very efficient. This is a strict requirement due to the large number of direct problem evaluations until convergence of the heat flux is achieved. For the solution of the thermal conduction problem, the commercial tool ANSYS Fluent [34] is used and a file-based interface to the code RoqFITT is programmed. The heat conduction equation (Eq. (1)) is solved using a finite volume method in an unstructured grid consisting of 7.5 million cells.

$$\nabla^2 T = 0 \tag{1}$$

The direct solver is used to solve the heat conduction partial differential equation (PDE) in a simplified geometry. The geometry consists only of the combustion chamber and does not include the fluid domain. The effect of the coolant on the temperature field of the structure is included by specifying the modeled boundary conditions.

Only the first segment of the combustion chamber is included in the computational domain. Since the number of the installed thermocouples in the other segments is too low for a sufficient resolution of the heat flux profiles using the inverse method, only the

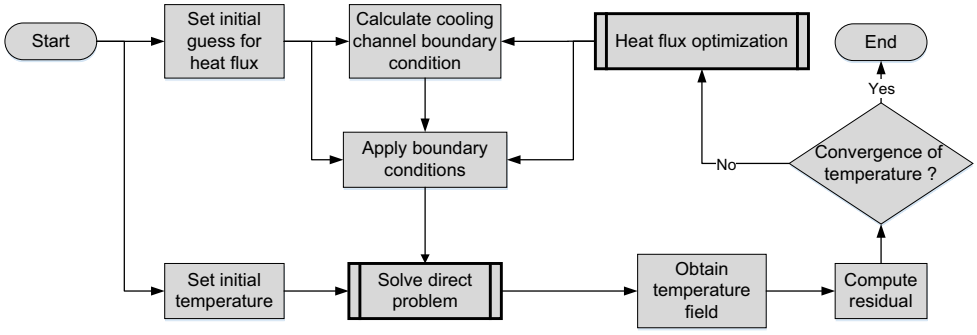

Fig. 3. Inverse heat transfer iterative algorithm.

first part is modeled. The interfaces between the first and second segment as well as between the injector head and the first segment are defined as adiabatic. For the boundary condition at the interface between the first and final combustion chamber segments, an extensive sensitivity analysis has been performed. Specifically, the adiabatic boundary condition was compared to a spatially dependent heat flux, obtained by coupled simulations of the chamber as shown in Rahn et al. [35]. The analysis resulted to the conclusion that the choice of this boundary condition has very small influence on the final heat flux profile. Specifically, between the solutions with the adiabatic and the variable boundary condition, a deviation of ~1% was observed in the heat flux value at the location of the last downstream thermocouple. All other positions upstream appeared to be unaffected by the choice of boundary condition, proving the low sensitivity of the final result on the treatment of this interface. For that reason and to ensure that the rebuilding of the thermal field is purely done on the basis of the measurements without relying on other inputs such as coupled CFD simulations, an adiabatic boundary condition is imposed.

Finally, a natural convection boundary condition is applied to the outer wall with a convective heat transfer coefficient $h = 10\,\mathrm{W}/(\mathrm{m}^2 \cdot \mathrm{K})$ and an ambient temperature corresponding to the one measured at each test. An overview of the computational domain and the corresponding boundaries is given in Fig. 4. The shape of the cooling channels is also easy to identify: they begin going almost radially inward towards the hot gas wall and then continue axially parallel to the main flow before bending again radially outwards towards the outlet.

The orientation of the chosen segment with regards to the injector elements is given in Fig. 5. The light gray area shows the entire chamber domain, whereas the area highlighted in dark grey is the modeled domain. The red lines represent the boundaries of the domain. The $\theta = 0^\circ$ and $\theta = 60^\circ$ positions correspond to azimuthal locations directly above an injector element, whereas $\theta = 30^\circ$ and $\theta = 90^\circ$ are symmetry planes between two adjacent elements. Note that the outer radius in Fig. 5 has been reduced from 80 mm down to 40 mm for visualization purposes.

The optimized (hot gas wall) and the modeled (cooling channel) boundary conditions are applied respectively as

$$\dot{q} = \lambda \frac{\partial T}{\partial \mathbf{n}}\bigg|_S \tag{2}$$

$$h_{cc}(T_{cc} - T_w) = \lambda \frac{\partial T}{\partial \mathbf{n}}\bigg|_S \tag{3}$$

In this context $\mathbf{n}$ is the outward pointing normal vector. Upon solving the direct problem, the temperature field is known and hence the calculated value of the temperature at all the thermocouple positions can be extracted and compared with the measured ones. This residual temperature difference is given as an input to the optimization algorithm.

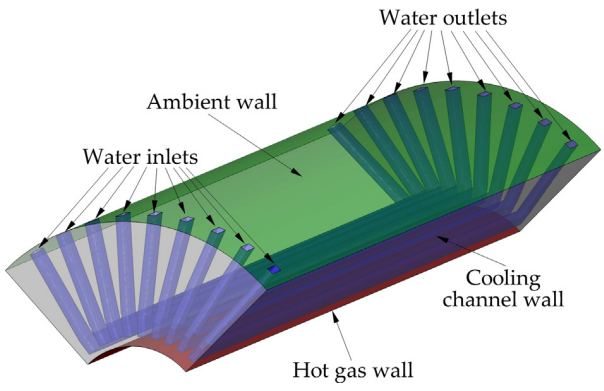

Fig. 4. Schematic view of the first chamber segment.

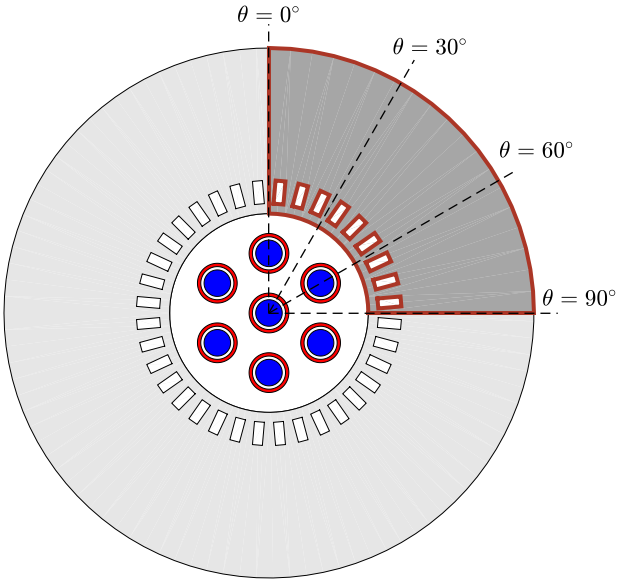

Fig. 5. Cut through the combustion chamber.

3.2. Optimization method

The purpose of the optimization is to minimize the difference between the calculated ($\mathbf{T}_c$) and measured ($\mathbf{T}_m$) temperatures. This residual J which is subject to minimization is defined as in Eq. (4):

$$J(\mathbf{P}) = [\mathbf{T}_m - \mathbf{T}_c(\mathbf{P})]^T [\mathbf{T}_m - \mathbf{T}_c(\mathbf{P})] \tag{4}$$

The vector $\mathbf{P}$ describes the heat flux values at the parameter points which are subject to optimization. The heat flux is a continuous variable being applied to all the points, however optimizing the heat flux value at every single point in contact with the hot gas would be computationally expensive and render the problem more ill-posed [36]. Having a larger number of optimization points increases the degrees of freedom of the problem without increasing the information input (no additional thermocouple measurements). For that reason, for the method presented here, a parameter is placed only at locations which possess at least one temperature sensor, so the number of parameters N is always smaller or equal to the thermocouple number M. At each time step, the values of the N parameter points are changed to reduce the residual J.

RoqFITT utilizes an iterative update by means of the Jacobi matrix $\mathbf{S}$, which serves as a sensitivity matrix describing the change of the temperature at a thermocouple position due to a small change at a specific heat flux parameter value. Its structure is presented in Eq. (5). It was shown in a sensitivity study that the linearity of the Fourier heat conduction equation allows for a calculation of the Jacobi matrix outside of the optimization loop. For that reason the computation of the matrix occurs as a preprocessing step before the calculation and it is saved for future calculations as well. As long as the number and locations of the thermocouples and parameters do not change, the matrix remains unaltered.

$$\mathbf{S} = \begin{bmatrix} \frac{\partial T_1}{\partial P_1} & \cdots & \frac{\partial T_M}{\partial P_1} \\ \vdots & \ddots & \vdots \\ \frac{\partial T_1}{\partial P_N} & \cdots & \frac{\partial T_M}{\partial P_N} \end{bmatrix} \tag{5}$$

The implemented optimization method is based on a linearization of the problem and follows the Newton-Raphson formulation for the solution of non-linear systems [37]. The heat flux at each iteration step k is obtained by solving the algebraic equation

$$\mathbf{S} \cdot \mathbf{P}^{k+1} = \left[\mathbf{T}_m - \mathbf{T}_c(\mathbf{P}^k)\right] + \mathbf{S} \cdot \mathbf{P}^k \tag{6}$$

The process is repeated until convergence is achieved, i.e. until the residual drops beneath a predefined value ε. When this is the case, the calculation is finished and the post-processing and visualization of the results starts. For the present study the convergence condition is that each individual sensor measurement drops beneath the inherent uncertainty of the thermocouple measurements ΔT. Hence ε is set to the accuracy of the used temperature measurement system.

The fact that a Jacobian is obtained outside of the optimization loop increases the computational efficiency of the algorithm dramatically. Convergence occurs in less than 15 iterations with a total computational cost of approximately 4 CPUh on four Intel Core i7-6700 at 3.40 GHz. The calculation of the Jacobian (which has to be performed only once for a given geometry and thermocouple configuration) required less than 10 CPUh on the same workstation.

3.3. Applying the heat flux on the boundary

At each axial position with available temperature measurements, four thermocouples are installed, each one at 0°, 30°, 60° or 90°. In total 8 axial positions are equipped with thermocouples leading to 32 sensors used in each calculation. The possible locations of the thermocouples are shown in the right sub-figure of Fig. 6, where the orange markers represent the 1.5 mm and the red ones the 0.5 mm distance from the hot gas wall.

As mentioned in the description of the optimization algorithm, the heat flux is updated only at specific locations and specifically only at the thermocouples positions projected on the hot gas wall, as indicated in Fig. 6. Special care has to be taken to transform the heat flux from the few locations in the chamber to a continuous variable over the whole boundary domain. A cubic interpolation is used to transform the discrete values to a continuous profile in axial and azimuthal direction. At the symmetry planes (0° and 90°) a symmetry condition is applied for the interpolation of the heat flux in azimuthal direction, meaning $\partial \dot{q}/\partial \theta = 0$. For the axial positions between the last thermocouple and the end of the chamber segment, a linear extrapolation is applied.

3.4. Modeling the cooling channels

For the unknown heat transfer coefficient in the cooling channels, Nusselt correlations for generic pipe flows are implemented. Using the work of Kirchberger et al. [38,39] where correlations where used for the description of the cooling channel heat transfer, the most prominent correlations are examined. Although both the models by Gnielinski [40] and Kraussold [41] showed similar profiles, only the Kraussold model will be discussed. The Kraussold correlation which reads

$$Nu_{cc} = \frac{h_{cc} \cdot d_h}{\lambda} = 0.024 \cdot Re^{0.8} \cdot Pr^{0.37} \tag{7}$$

is a function of the geometry (hydraulic diameter d_h) and material properties as it depends on the heat capacity c_p, thermal conductivity λ, dynamic viscosity μ as well as on the mass flow rate $\dot{m}_{cc}$ (which is needed for the Reynolds number). The temperature dependent properties are obtained using the NIST database [42]. The correction factors for the start-up of the flow [39] was also investigated.

At this point it is important to note that due to the complex geometry of the cooling channels (transition from radially inwards flow to axial flow, rectangular shape), the use of any Nusselt-based correlations will only approximate the real heat transfer coefficient. Studies are planned in order to obtain a more detailed correlation for the coolant heat transfer by running parametric CFD simulations of the geometry and obtaining a correlation using machine learning as in the works of Chang et al. [43] and Scalabrin et al. [44]. For the present analysis a classical correlation by Kraussold, shown to produce reasonable results for rocket engine cooling channels [39] will be shown but the inverse method presented here is not restricted to the use of this particular approximation.

In order to use Eq. (3) for the estimation of the boundary condition and to calculate the aforementioned fluid properties, the average bulk coolant temperature is required. The heating of the coolant (in this case water) is carried out by assuming that the system is in steady state and hence the whole heat is effectively flowing into the coolant. Therefore the coolant temperature at axial position x is given by

$$T_{cc}(x) = T_{cc,in} + \int_0^x \frac{2\pi r_c}{N_{cc}} \frac{\dot{q}}{\dot{m}_{cc} c_p} \mathrm{dx} \tag{8}$$

with heat flux $\dot{q}$ as the average heat flux at the considered differential wall surface.

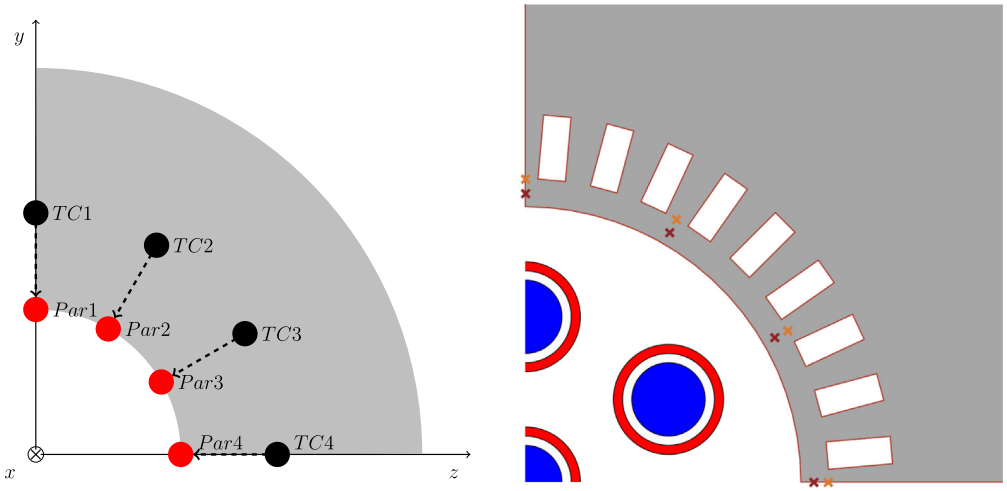

Fig. 6. Definition of parameter points (left) and the locations of installed thermocouples (right).

The computational domain possesses nine cooling channels. Fig. 7 illustrates the contour of the cooling channels projected onto the hot gas surface. The division of the surface above the axial cooling channel parts into nine equally sized strips is visualized, too. The integral heat flow over one of these strips is the energy that heats up the coolant in the corresponding cooling channel. To obtain the coolant bulk temperature distribution in x-direction, the cooling channels are discretized (cf. cooling channel at 5° azimuthal position in Fig. 7). Then the bulk temperature increment is calculated for each cell of the length dx_{cc} by evaluating Eq. (8). For that the integral heat flow within the blue rectangle in Fig. 7 is calculated.

4. Error analysis

For a proper evaluation of the experimental data and a potential comparison with CFD simulations, knowledge of the different error sources as well as the magnitude of the individual errors is necessary. The error sources are usually due to statistical and systematical error of the measured data as well as due to the uncertainties used in the models.

In the case of the RoqFITT code the measurements are restricted to the thermocouple readings. As far as the model is concerned, RoqFITT uses the heat conduction equation with modeled boundary conditions, which introduces additional uncertainty to the system. The potential error sources also comprise the material properties and the treatment of the boundary conditions at the interface with the second segment. Due to the steady-state nature of the problem, thermocouple response delay is not included in the analysis.

Summarized, the uncertainties which have to be included in the error propagation are the following:

- Thermocouple accuracy.
- Thermocouple precision.
- Thermocouple positioning.
- Material properties.
- Boundary conditions.

The individual error sources are documented in detail in Perakis et al. [30] and in this chapter only the specific issues applicable to the multi-element chamber will be discussed.

4.1. Thermocouple accuracy

For the accuracy of the thermocouples, the manufacturer's instrument accuracy ΔT_{acc} is used, which is set to 1.0 K for type T thermocouples. Using the concept of linearization, the heat flux error $\Delta \mathbf{P}_{acc}$ can be obtained by means of the Jacobi matrix, by solving the algebraic system in Eq. (9).

$$\Delta \mathbf{P}_{acc} = \mathbf{S}^{-1} \cdot \Delta \mathbf{T}_{acc} \tag{9}$$

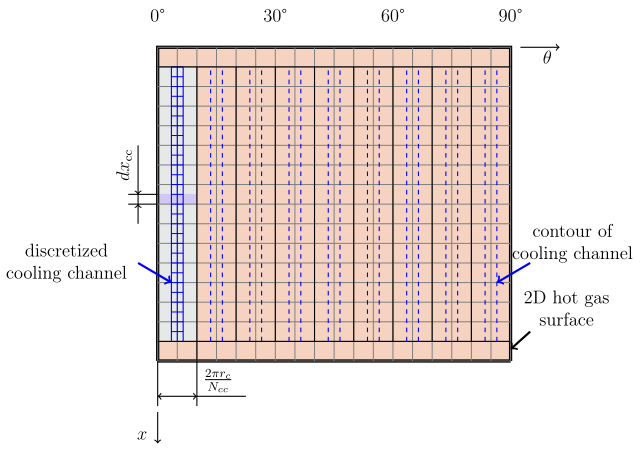

Fig. 7. Discretization of the cooling channels for the water heat-up calculation.

4.2. Thermocouple precision

In case of the steady-state temperature measurements, the precision error is defined as the random fluctuation of the thermocouples readings within a specific time window. The raw thermocouple data is prone to high frequency noise and for that reason the standard deviation of the transient profiles within a time window of 1 s is used. The corresponding heat flux error is given similar to Eq. (9).

4.3. Thermocouple positioning

A further source of uncertainty when using thermocouples is the fact that their exact location is not always known. Due to manufacturing tolerances of the drilling hole in which the sensor is installed, the exact contact point between the copper material of the chamber and the thermocouple tip cannot be predicted with 100% accuracy. In order to take this into account, a post-processing step is introduced in RoqFITT, during which a systematic radial deviation Δr is defined for all thermocouples. The initial radial position of the thermocouples r_0 is hence replaced by $r_0 + \Delta r$. Using the converged solution for the heat flux and the temperature field in the domain, the temperature at the new thermocouple positions can be found and it is used for the estimation of the temperature error:

$$\Delta \mathbf{T}_{loc} = \mathbf{T}_c(r_0) - \mathbf{T}_c(r_0 + \Delta r) \tag{10}$$

A maximal deviation equal to 0.1 mm is used for this hardware. Extensive measurements of the depth of the drilling hole were carried out before the installation of the sensors, and this is the reason for the relatively small devation used in this study. The estimation of the resulting heat flux error is carried out with the Jacobi matrix similar to Eq. (9). This calculation of the positioning error was also carried out by repeating the inverse calculation with modified positions for the thermocouples and the result was compared to the approximation in Eq. (10). Both methods deliver almost identical results for the small location errors assumed here.

4.4. Material properties

For the solution of the steady state heat equation only the thermal conductivity of the material is required and this value is bound to some uncertainty. A deviation from the nominal value λ_0 with the magnitude $\Delta\lambda$ = 10% is assumed.

Due to the steady-state nature of the problem, the inverse calculation is not computationally expensive and hence the repetition of the solution with the modified material properties is not prohibitive. For that reason, the inverse solution is repeated and the resulting heat flux error is simply given by Eq. (11).

$$\Delta \mathbf{P}_{mat} = \mathbf{P}(\lambda_0) - \mathbf{P}(\lambda_0 + \Delta\lambda) \tag{11}$$

4.5. Boundary conditions

In the computational domain of the rocket combustors, the boundary conditions at the surfaces in contact with the second segment and the outer surface have to be modeled. The natural convection was found to have a negligible effect on the final result of the hot gas heat flux and is hence not included in the error prop-

agation analysis. For the second segment interface the adiabatic condition has been compared to a spatially heat flux obtained by Rahn et al. [35]. Upon comparison of the values obtained with adiabatic and variable boundaries, no significant difference was observed and therefore the adiabatic condition is maintained. This is physically justified by the fact that both segments are run in coflow with the hot gas and hence the axial heat transfer is minimal.

On the other hand, the effect of the coolant heat transfer coefficient and coolant temperature on the uncertainty of the final heat flux is not negligible. In order to quantify this error, using a linear approach as in Eq. (11) is not straightforward, since the bulk coolant temperature is also dependent on the converged heat flux. For that reason the inverse calculation is repeated after convergence with the modified $h_{cc} = 1.15 \cdot h_{cc,Kraussold}$. Here an uncertainty of 15% is assumed for the heat transfer coefficient. Determining this value is difficult since it strongly depends on the geometry and requires detailed CFD simulations for each load point. The quantification of the error introduced when using a Nusselt correlation for the description of wall heat transfer in rocket cooling channels has been examined by Haemisch et al. [33] for methane and hydrogen but there are limited works dealing with water as coolant. The uncertainty of 15% is chosen only to provide a reference for the propagated wall heat flux error. Studies which are beyond the scope of the present work have been planned in order to quantify the actual deviation of the chosen correlation and to provide an improved correlation by the use of parametric studies and deep learning algorithms [43].

The resulting heat flux uncertainty is given by

$$\Delta \mathbf{P}_{corr} = \mathbf{P}(h_{cc}) - \mathbf{P}(h_{cc,Kraussold}) \tag{12}$$

For the water temperature at inlet, a similar method is implemented, with a temperature deviation $\Delta T_w = 1$ K.

$$\Delta \mathbf{P}_{Tw} = \mathbf{P}(T_w + \Delta T_w) - \mathbf{P}(T_w) \tag{13}$$

Summing up all the error sources according to Eq. (14) results in a total uncertainty $\Delta \mathbf{P}_{tot}$ between 10% and 30% of the converged heat flux value at each parameter location.

$$\Delta \mathbf{P}_{tot} = \sqrt{\Delta \mathbf{P}_{acc}^2 + \Delta \mathbf{P}_{prec}^2 + \Delta \mathbf{P}_{loc}^2 + \Delta \mathbf{P}_{mat}^2 + \Delta \mathbf{P}_{corr}^2 + \Delta \mathbf{P}_{Tw}^2} \tag{14}$$

The relative magnitude of the uncertainty compared to the calculated value for each of the axial positions is given in the left subfigure of Fig. 8. The relative total error is largest for the first axial position. This is expected due to the small temperature increase and heat flux value at this location, which makes the temperature measurement errors (both in material and in the water) more significant. For all remaining axial positions, relative values between 10% and 15% are obtained.

The main contribution (around 90%) results from the used cooling channel correlation, whereas the accuracy, precision and water temperature errors are negligible with the exception of the first axial position. A detailed analysis of each contribution is shown in the right sub-figure of Fig. 8. It is observed that the magnitude of the error induced by the material properties alternates between two consecutive axial positions. This is due to the different radial distances of the thermocouples in each plane. Planes with thermocouples closer to the hot gas wall are less tolerant to the variation of the heat flux conductivity, since the thermal gradients are higher at their position. In the same note, they are also more affected by the positioning error, whereas they appear to be more resistant to the correlation, because of the larger distance from the cooling channels.

5. Results

In this chapter we present the heat flux results obtained with the inverse method implemented in RoqFITT for different operating conditions.

In the context of the national research program Transregio SFB-TRR 40 on "Technological Foundation for the design of thermally and mechanically high loaded components of Future Space Transportation System", a test case using the multi-element chamber was defined during the Summer Program 2017 with the purpose of motivating groups to simulate the flow conditions in the combustion chamber and accurately predict the pressure and heat flux profiles at the wall. The available experimental data included pressure measurements and average calorimetric heat flux values for each segment due to the absence of a reliable inverse method. The test case comprises an operational point at 20 bar and O/F = 2.6, with the fuel and oxidizer being injected at ambient temperature in gaseous form.

A large number of groups carried out independent calculations of the turbulent combustion in the rocket engine and the results were compared to each other and to the available measurements [28,35,45,25]. Deviations between the solutions of the individual groups regarding the azimuthal distribution of the wall heat flux increased the motivation for an inverse method with high spatial resolution.

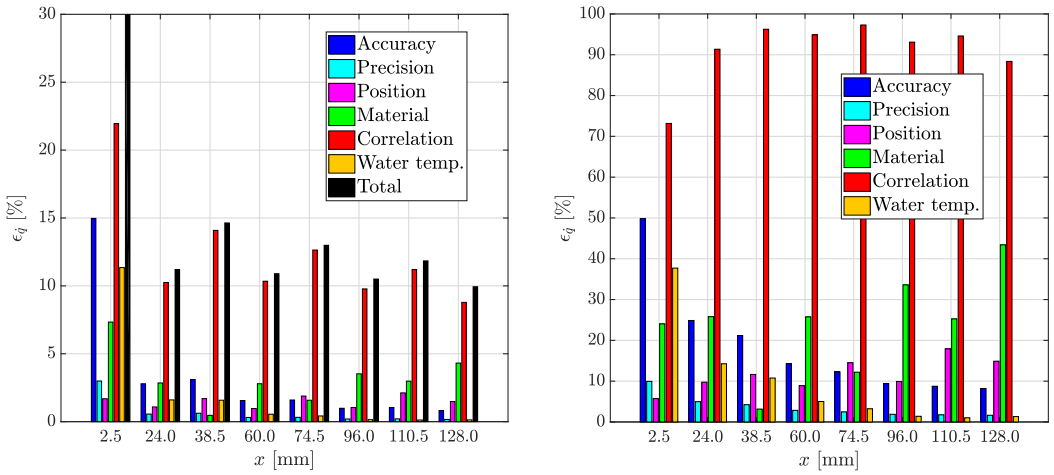

Fig. 8. Relative error (left) and individual error contributions (right) at different axial positions.

5.1. Temperature profiles

The only information available used by the inverse method for the reconstruction of the thermal field are the temperature sensor measurements. Those are shown in Fig. 9, where the circles represent the measurements at 1.5 mm from the hot gas wall and the diamonds the ones at 0.7 mm. In the same graph the reconstructed temperature field stemming from the inverse method is also shown. 0° and 60° correspond to the two neighboring injector elements.

As far as the measurements are concerned, a general increase of the temperature with increasing axial position is observed. Since the mixing and energy release is still ongoing in the first segment, an increasing heat load and hence temperature reading is expected as the flow moves downstream of the injector. Moreover, a slight asymmetry in the readings is observed. It would be expected that positions 0° and 60° have almost identical results, as should 30° and 90°. Since this deviation appears to be systematic, i.e. the values at 0° appear to be larger than the ones at 60° for all axial positions, a faulty thermocouple installation is excluded since that would be an error of statistical nature. Instead a slight asymmetry of the co-axial injectors (either due to the manufacturing or the assembly) is assumed to be the cause.

The reconstructed field shown in Fig. 9 matches the measured values within the defined tolerance of the inverse method. The profiles at 0.7 mm (solid lines) have higher values since they are closer to the hot gas wall, whereas the 1.5 mm show a much more prominent cooling channel footprint, as they are closer to the cooling channels. Specifically, the wavy pattern results from the geometry of the cooling channels, with the temperature minimums corresponding to positions between two channels, and the maximums to positions directly under the channels.

5.2. Azimuthal heat flux profiles

The corresponding heat flux profiles are illustrated in Fig. 10. For each axial position, the heat flux resulting from the inverse method is plotted with the markers representing the values at the parameter points and the solid lines representing the azimuthal heat flux profile applied at the wall. The uncertainty intervals calculated as described in Section 4 are shown as shadows and amount to ±10–30% of the average values.

It is easy to notice by looking at Fig. 10 that an injector footprint is visible in the heat flux data. Specifically, for the first 60 mm of the chamber a local maximum directly above the injector is observed with a local minimum at the positions between two elements (30° and 90°). Despite the asymmetry produced by the temperature readings, all four available axial positions show a similar trend.

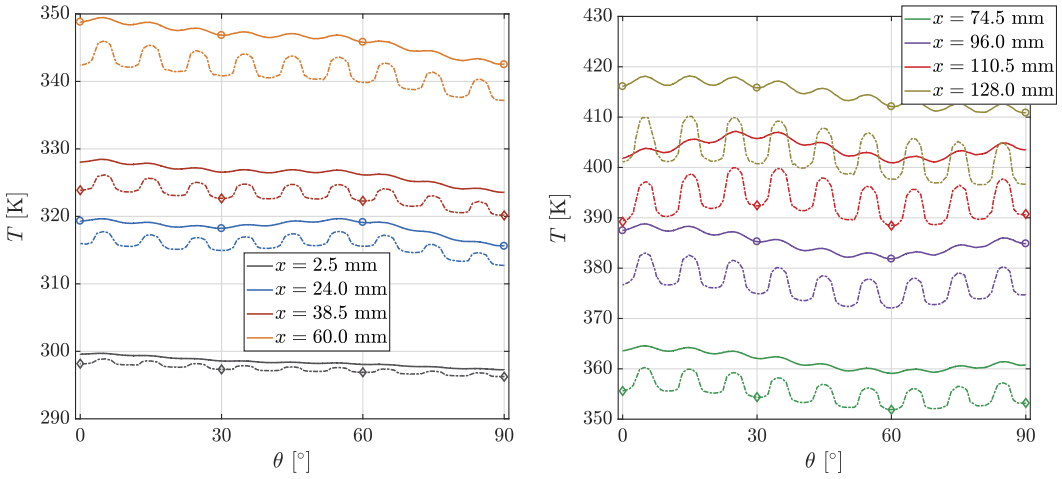

Fig. 9. Measured and calculated temperature at 0.7 and 1.5 mm from the hot gas wall. Solid lines correspond to 0.7 mm and the dashed ones to 1.5 mm.

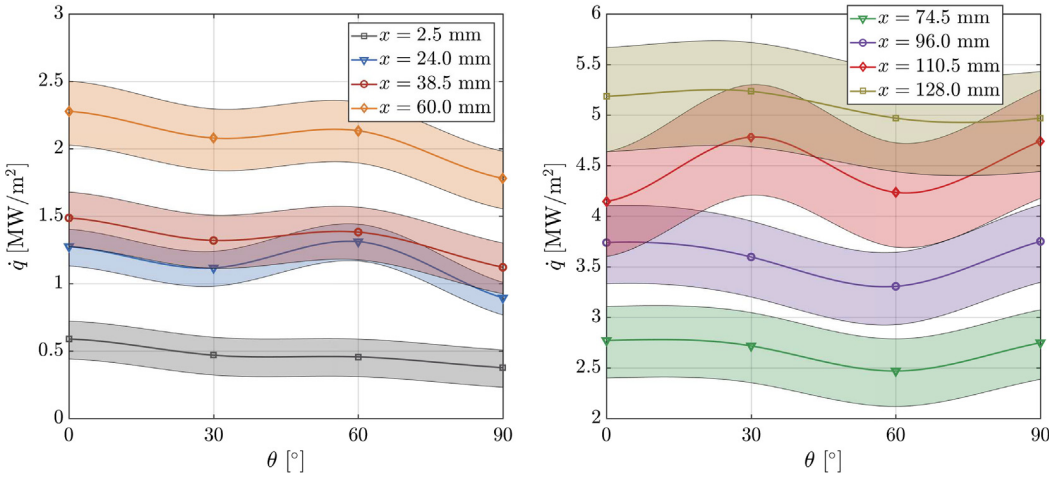

Fig. 10. Heat flux profiles along the azimuthal direction for different axial positions. The corresponding uncertainty intervals are also shown.

Moving towards positions downstream, a shift is observed in the measured heat flux profiles. Starting at around 74.5 mm the heat flux at the 60° position appears to drop below the values at 30° and 90°, indicating a change in the injector/injector and injector/wall interaction. Due to the asymmetry in the measured temperatures, the 0° heat flux undergoes this shift at a later downstream position and the profile becomes symmetric again at the 110.5 mm position. After this axial location, the injector footprint is inverted compared to the initial positions close to the face-plate.

For axial positions close to the face-plate, the flames from the individual injector elements are almost cylindrical and interact minimally with each other. Therefore, the heat transfer coefficient directly above the injector is maximal due to the distance between element and wall being smallest. As the heat release in the coaxial shear layer of each element increases and leads to a radial expansion of the jet outwards, the interaction between the jets is amplified. In an effort to expand radially against each other, the flames build a stagnation flow between two neighboring elements. Due to the central element jet also expanding radially outwards, the stagnation flow is forced towards the wall and increases the local heat transfer at the locations between the injectors. Further downstream (for positions which are unfortunately in the other 3 segments of the TUM chamber and hence not shown in the inverse method results) the mixing is further increased and a homogeneous flow is achieved, leading to a smoother heat flux distribution where the injector footprint is no longer visible. This pattern is also observed in CFD simulations in Section 5.4.

It is important to note that the injector footprint observed in Fig. 10 is not directly visible in the thermocouple readings shown in Fig. 9. Although some of the effects can be identified (different behavior in the first and second part of the segment), due to the asymmetry of the measurements, the injector footprint is obscured. Only after the evaluation of the test data with the inverse method is the footprint visible in terms of heat load profiles. This is an additional motivation for the use of the inverse method for the evaluation of the test results, as the raw thermocouple data cannot convey all the physical information, since they are the result of multiple physical effects which have to be separated.

The circumferential variations in heat flux appear to be in agreement with the physical arguments resulting from the consideration of the flame/flame interaction within the chamber. Nevertheless, it has to be noted that the observed variations are of the same order as the error bands in Fig. 10. When trying to assess the reliability of the obtained profiles it is essential to include the nature of the uncertainties in the discussion. Specifically, as demonstrated in Section 4, the correlation for the cooling water heat transfer coefficient contributed by approximately 90% to the total uncertainty. This error source is however systematic and acts more as a bias to the obtained results. Since all cooling channels have identical geometry and mass flow rates, it is expected that their flow-field is very similar for the same axial position. For that reason they should also exhibit similar heat transfer coefficients, which is confirmed in the left sub-figure of Fig. 13. There, the relative deviations in each axial plane do not exceed 1%. From this argument follows that even if the modeled heat transfer coefficient has a large deviation from the experimental one, the error should act as a bias for all azimuthal positions, thereby leading to a shift of the entire heat flux profile, while preserving the circumferential variations.

The effect of the injector footprint that the inverse method tries to capture requires a resolution of at least 30°, namely equal to half the angular distance between the injectors. The chosen hardware is equipped with sensors satisfying this minimal angular resolution, meaning that any heat flux information with a shorter angular wavelength will not be captured by the method. An increase in the number of installed sensors or a rotation of the hardware after every test repetition as in the work of Suslov et al. [26] would be required for a more detailed profile.

Finally, the effect of the domain size was also investigated in order to quantify the influence of the temperature asymmetry which was reported in Section 5.1. For this study the 90° domain presented in the results so far was compared to simulations using a smaller, 60° domain. For the smaller domain, two separate studies were performed: one using the measurements at 0°, 30° and 60° and with the 30°, 60° and 90° values. The results in Fig. 11 illustrate that all three measurement sets lead to similar results. Both the magnitude and the form of the profile are in good agreement for the different domain choices. The only measurable difference occurs at the 30° location. At this point the asymmetry of the measurements is more prominent and the assumption of $\partial\dot{q}/\partial\theta$ at the symmetry plane is violated. This results in a maximal error of 5% compared to the full 90° domain. Hence, this study shows that a smaller domain could also be used, consisting of only 60°. The benefits of reducing the domain size however are not so dominant, as the computational speed of the method is already very low as reported in Section 3.

5.3. Comparison with calorimetric method

The axial evolution of the heat flux values for the four azimuthal positions which are equipped with thermocouples is shown in the left sub-figure of Fig. 12. The uncertainty intervals are omitted for visualisation purposes. One observes that although the 0° and 60° profiles start higher than the 30° and 90° ones, at approximately 70 mm from the face-plate, the 90° heat flux surpasses the 60° value, and after 100 mm the same occurs between 0° and 30°. The heat flux keeps increasing for all axial positions, indicating that the combustion is not complete yet, which is expected as the length of the first segment does not exceed 150 mm.

Looking at the azimuthally averaged profile and globally average heat flux value in the right sub-figure of Fig. 12, a comparison with the calorimetrically determined value can be made. Using the difference of incoming and outcoming water enthalpy flow, the calorimetric heat flux lies at 3.40 MW/m^2 with a relative error of approximately 10%. The error comes from the uncertainty of the water mass flow measurement (around 1% of the nominal value) and a 1 K accuracy of each water thermocouple. The average value obtained via the inverse method on the other hand is equal to

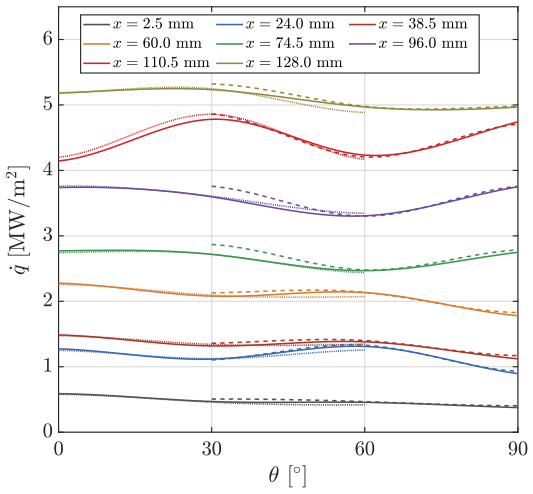

Fig. 11. Azimuthal heat flux results for different sets of measurement. The solid lines represent the 0–30–60–90° configuration, the dotted one the 0–30–60° and the dashed one the 30–60–90°.

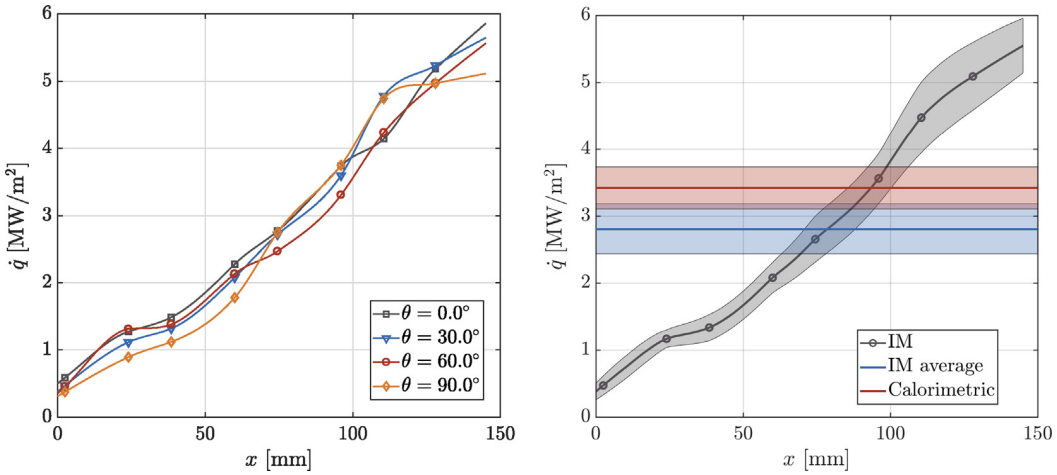

Fig. 12. Heat flux profiles along the axial direction for different angular positions (left) and average heat flux along axial position (right).

2.85 MW/m^2 with a 11.5% uncertainty. Note that this uncertainty strongly depends on the assumed error induced by the Kraussold correlation, which was arbitrarily set to 15%. The uncertainty intervals of the two heat flux evaluation methods intersect, which serves as a validation for the heat flux level predicted by the inverse method.

The deviation between the two methods is attributed to the error introduced by the generic Nusselt correlation for the specific geometry, which could underestimate the heat transfer coefficient within the cooling channels. Due to the shape of the channels, a recirculation zone is namely expected at the interface between the radial part and the flow-parallel part of the channel, which could theoretical increase the local turbulence and heat pickup. The heat flux obtained by the inverse method is directly proportional to the heat flux exiting the domain through the cooling channels. Hence too small a value for h_{cc} would directly cause a lower wall heat flux compared to the experiment. Further studies are planned in order to evaluate the validity of the chosen correlation using comparison with CFD simulations of the cooling channels and to derive a new correlation fitted for the present flow configuration.

The lower heat flux compared to the calorimetric method, also affects the calculated water temperatures. In Fig. 13 the temperature profile for four of the nine cooling channels is shown along with the average calculated and average measured water outlet temperature. The injector footprint has an impact on the water heat-up, as the cooling channels close to the injector elements (5° and 55°) start with a higher temperature than the corresponding ones between the elements (25° and 85°). As soon as the shift in the location of the heat flux maximum occurs, the gradient of the water temperature at 25° and 85° also rises faster, and the values catch up close to the outlet.

The average water outlet temperature of all nine channels originating from the inverse method is 302.5 K, which lies approximately 2.3 K lower then the measured value. The difference can be attributed to the lower heat flux predicted than the inverse method, as the water heat-up is directly proportional to the integral heat load. The difference of 2.3 K corresponds to a relative error of around 11.5%, which is comparable to the deviation of the calorimetric and inverse heat flux evaluations.

5.4. Comparison with CFD

The previously described test case has been the subject of numerical investigation by various groups, which have utilized CFD models to describe the physical phenomena taking place within the combustor with special focus in the injector/injector and injector/wall interaction. A summary of the RANS simulations

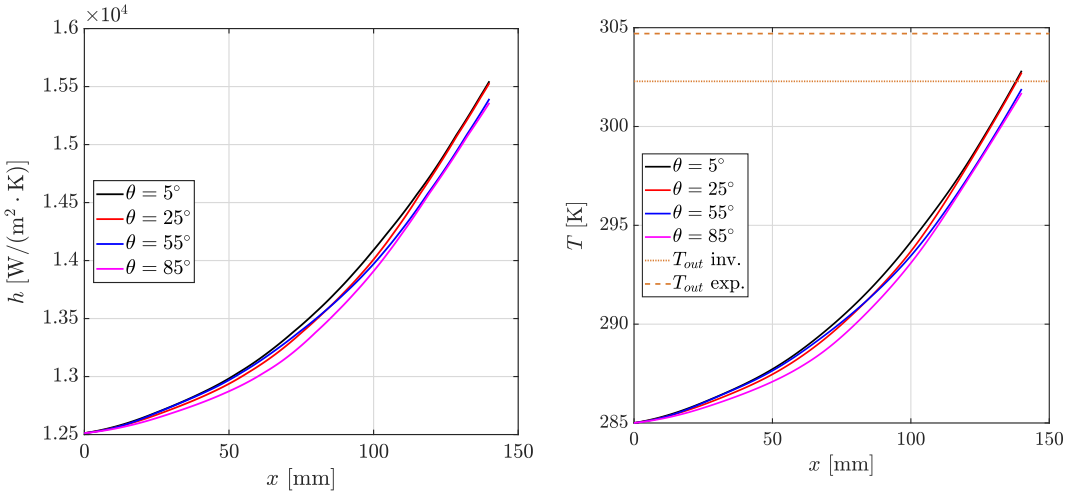

Fig. 13. Heat transfer coefficient (left) and water temperature (right) in the cooling channels.

results can be found in Perakis et al. [28]. Due to the availability of CFD results, it is interesting to compare the results acquired with the inverse method with the ones using RANS models for the simulation of the turbulent combustion. This comparison does not serve as a validation of the inverse method but rather as an effort to examine whether the profiles obtained by RoQFITT can be explained by effects observed in the CFD results and which cannot be measured directly in the experiment as they are linked to flow and energy release properties.

The results presented in this section are generated from a simulation of the hot gas in the thrust chamber using the frozen flamelet model [46] with the skeletal chemical mechanism by Slaviskaya et al. [47] for the chemistry modeling. For the turbulence modeling the standard k-ϵ model proposed by Launder and Spalding [48] is implemented. A 3D domain consisting of 30° (corresponding to the minimal symmetry of the chamber) is utilized and the Reynolds-Averaged Navier-Stokes equations are solved with the ideal gas equation for state. For the wall boundary condition, two methods were compared to each other: one using the experimental thermocouple measurements as Dirichlet boundary conditions and a second one where a conjugate heat transfer was applied by fully-coupling the hot gas, structure and cooling channels. Both methods showed almost identical results for the heat flux in the first segment and hence no distinction is required in the present comparison. More details about the setup can be found in Perakis et al. [45].

First a comparison between the average axial heat flux profile of the two methods is given in Fig. 14. The error-bars are shown only for the axial profile and omitted for the average values (both calorimetric and inverse) to make the figure easier to read. The first observation is that the axial profile of the CFD heat flux is quite similar to the inverse one. Starting from the positions close to the injector, the heat flux appears to rise before dropping shortly at around 10 mm from the face-plate. This indicates the location of a recirculation zone, which creates a stagnation point and hence an increase in the local heat transfer. The inverse profile shows a similar trend, but not so prominent, as a slight plateau is achieved at 25 mm. Due to the axial resolution of the heat flux, it is difficult to resolve the small recirculation zone which is predicted by the CFD, but the small drop in the heat flux increase indicates that this effect is still captured by the temperature measurements.

Downstream of this position both method predict a steady increase of the heat flux value and after 110 mm they both show a slower increment, as the profile starts flattening out. This is caused by the build-up of the thermal boundary layer at the wall and the fact that the heat release in the chamber is reduced for positions further downstream.

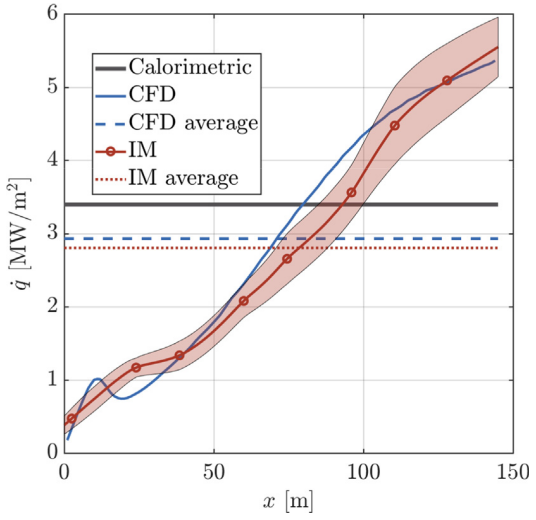

Fig. 14. Axial and average heat flux profile for the CFD simulation and the inverse method. The calorimetric method is also shown for reference.

When examining the average values, the CFD simulation delivers 2.93 MW/m^2, which is comparable to the inverse method result and lies around 14.5% lower than the calorimetric value for this segment.

The azimuthal profiles are also topics of large interest and therefore selected axial planes are shown in Fig. 15. The CFD results are copied along the azimuthal direction as they are symmetric (RANS simulation). Regarding the absolute value of the heat flux, both the simulation as well as the inverse evaluation of the test data show similar levels, which can also be deduced by looking at Fig. 14. Some discrepancies are however noticed in the qualitative form of the profiles. It is evident that the low resolution caused by the positioning of the thermocouples does not allow for a detailed profile as in the case of the CFD. Specifically, the presence of a complicated pattern for positions between two injector elements (0° and 60°) is visible. Since this large-scale structure is finer than the resolution allowed by the thermocouple installation, this cannot be detected with our method.

Despite the inverse method profiles being coarser, they are still able to capture some of the effects found in the CFD. Starting with the first positions close to the face-plate (left sub-figure), both CFD and inverse method show a higher heat flux above the injectors (0°, 60°) than between them (30°, 90°). An additional local maximum at the ±10° positions left and right of each injector is also a result of the CFD simulation, which is a consequence of a secondary flow pattern as explained in detail in [45,28]. For the positions further downstream (right sub-figure), both methods show a shift in the maximum location. After 110 mm, the CFD heat flux values appear to shift, leading to global minima directly above the injector locations (0° and 60°). The main culprit for this change of the pattern is the increasing interaction of neighboring jets, which leads to hot gas being pushed towards the wall between the elements. It is hence quite assuring that the pattern observed in the inverse results and which was described in detail in Section 5.2, is not an artifact of the thermocouple measurements but rather a physical phenomenon supported by the CFD result.

For a more detailed comparison it is suggested that additional instrumentation shall be installed and a repetition of the tests shall be carried out.

5.5. Load points comparison

Apart from the 20 bar, O/F = 2.6 test case presented so far, the chamber has also been operated at mixture ratios 3.0 and 3.4 and all three load points have also been repeated for a 30 bar nominal chamber pressure. Due to the gaseous injection of the propellants, the mixture ratio influences the velocity ratio and momentum flux ratio of methane and oxygen and hence the dynamics in the vicinity of the injection system.

These effects are visible in the axial profiles of Fig. 16, where the heat flux of the 20 and 30 bar cases is plotted. Along with the axial profiles, the average values are shown (solid line) as well as the calorimetric measurement (dashed line). The error bars are not included for visualization purposes.

It is observed that all three load points have quite similar average heat flux values in this segment. In fact, the discrepancy between the inverse and the calorimetric method appears to be almost identical for all O/Fs and both pressure levels. It is important to note that the maximal heat flux for the inverse evaluation of the 20 bar case is around 6 MW/m^2, whereas for the 30 bar case it is 8 MW/m^2. The expected rise in the heat load with increasing pressure is also reflected in the calorimetric measurements.

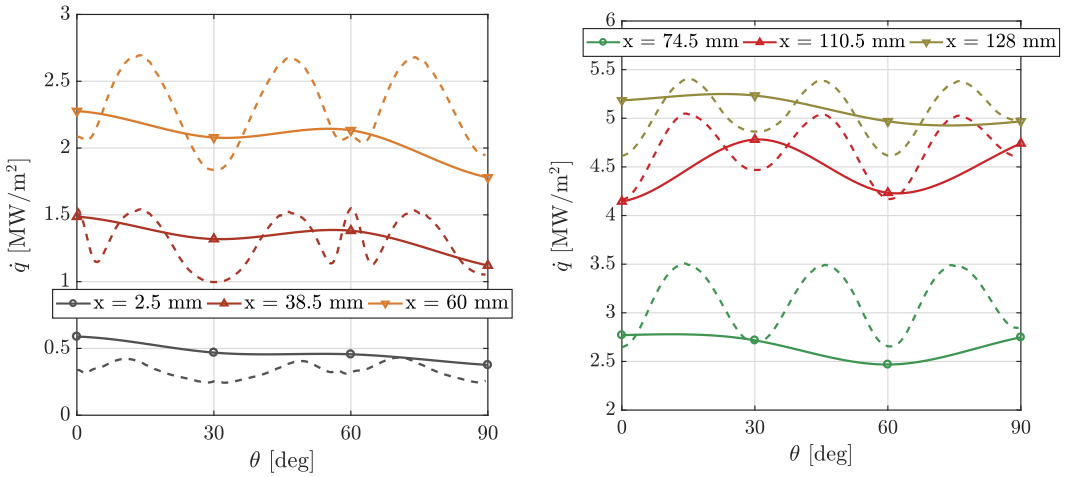

Fig. 15. Heat flux profiles along the azimuthal direction for different axial positions for the inverse method (solid line) and the CFD simulation (dashed line).

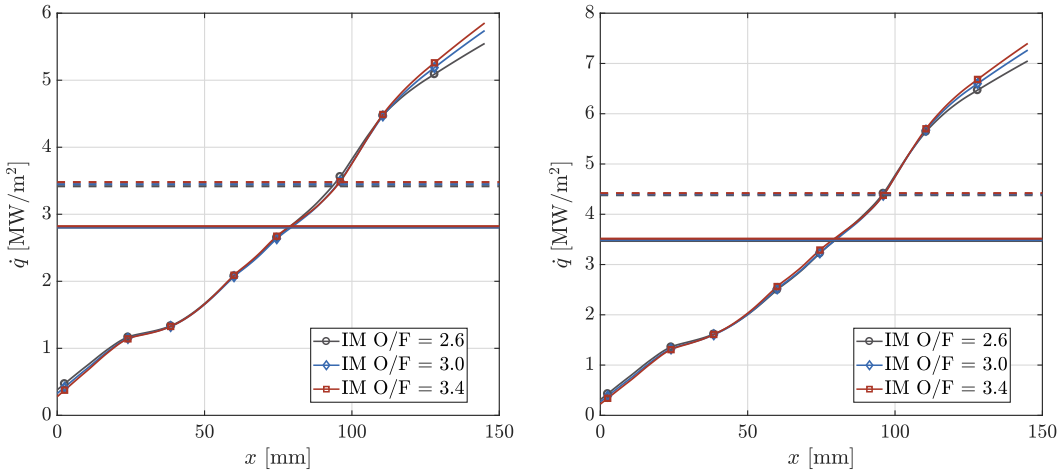

Fig. 16. Heat flux profiles along the axial direction for different O/F values for the 20 bar (left) and 30 bar (right) cases.

A more detailed look into the exact profiles is given in the plots of the azimuthal distributions in Figs. 17 and 18. Starting with the positions close to the injector, the lower O/F (O/F = 2.6, solid line) produces the highest heat flux. Moving downstream, for the first 60 mm the higher O/F test cases (O/F = 3.4, dashed line) appear to lead to a larger thermal stratification compared to the O/F = 2.6, i.e. to a more visible injector footprint. The values at 0° and 60° appear to increase with increasing O/F, whereas the positions between the elements (30°, 90°) show the opposite pattern. The explanation is given by the difference in momentum flux ratio and velocity ratio. If the mixing is shifted downstream in the high O/F cases due to the large inertia of oxygen pulling the methane annulus with it, it is expected that the jets retain their almost cylindrical form and do not mix laterally with the neighboring flames. For lower O/F on the other hand, due to the higher methane velocity, a larger expansion is predicted and therefore a better mixing close to the face-plate inducing a more homogeneous flow and a reduced stratification.

This effect prevails up until the first 74.5 mm. At this point the chemistry becomes more dominant and a break-even point is observed where the hydrodynamic and chemical effects cancel out and the heat flux values appear almost independent of the O/F. For the final downstream location however (128 mm), the mixing has progressed and the chemical effects have definitely overtaken the initial footprint, leading to the higher O/F cases having a larger overall heat flux due to the higher gas temperature).

This phenomenon has been explored in previous studies with rocket combustor demonstrators operated using the same injector elements as the 7-element chamber of this work [49,30]. Due to the higher momentum of the central oxygen jet with higher O/F, the mixing and energy release zone is shifted downstream, and for positions closer to the injector, a lower heat load is achieved. For positions further downstream however, the chemistry dominates and since the combustion temperature of the higher O/F is larger (closer to stoichiometry), the heat flux is also expected to be higher. This explains why the lower O/Fs start with a higher heat flux for $x = 0$ mm and end up with a lower value at the end of the segment.

All the observed effects are within the uncertainty limits which result from the error analysis presented in Section 4. However, the physical motivation behind the interpretation of those phenomena has been shown in previous studies and validated with CFD simulations of similar configurations [49]. Moreover, using the same argumentation as in Section 5.2, the main contribution of the uncertainty is the heat transfer correlation error and it should lead to a homogeneous bias in the heat flux results, hence not affecting the relative profiles and the resulting physical interpretation.

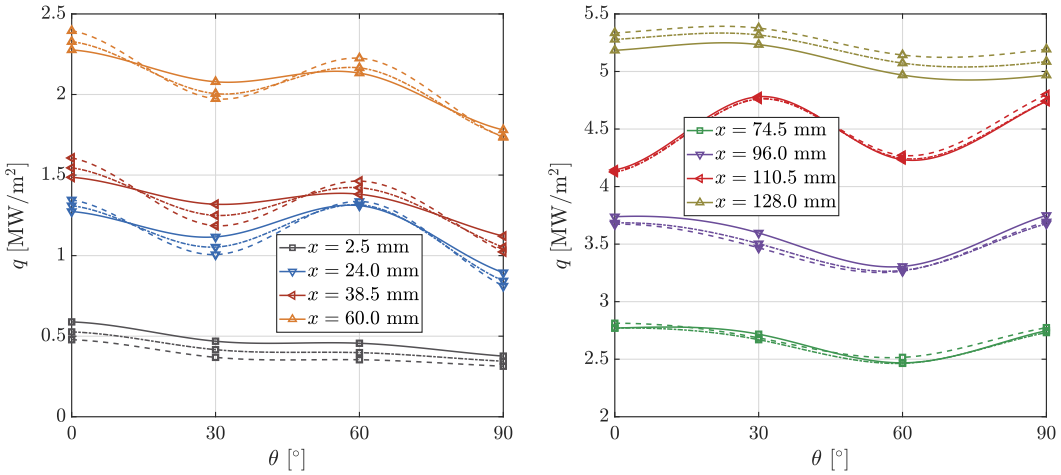

Fig. 17. Heat flux profiles along the axial direction for different axial positions at 20 bar. Solid line: O/F = 2.6, dash-dot line: O/F = 3.0 and dashed line: O/F = 3.4.

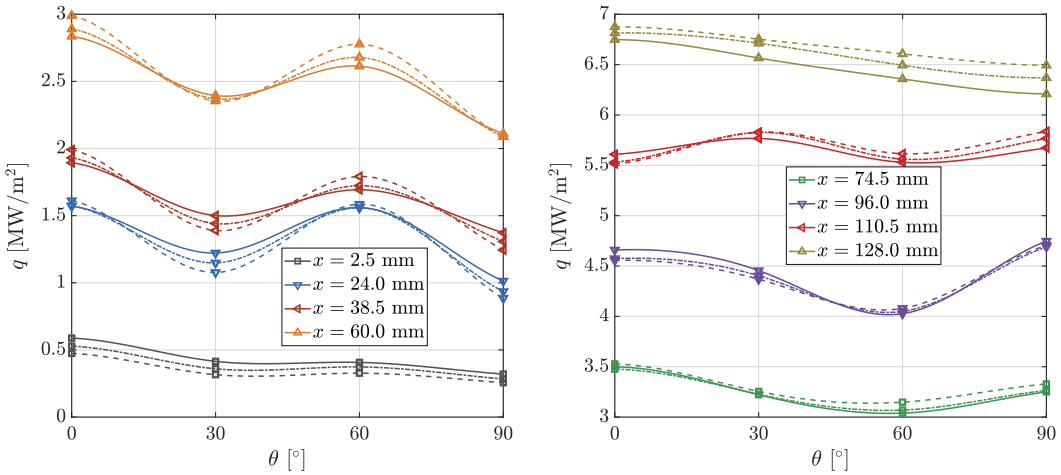

Fig. 18. Heat flux profiles along the azimuthal direction for different axial positions at 30 bar. Solid line: O/F = 2.6, dash-dot line: O/F = 3.0 and dashed line: O/F = 3.4.

6. Conclusion

The evaluation of heat flux profiles in sub-scale engines is crucial for the understanding of the underlying physical and chemical processes defining the injector performance, the injector/injector and injector/wall interaction, mixing and energy release in the chamber. The inverse heat transfer method implemented in RoqFITT is intended for the analysis of temperature and heat flux distributions in actively cooled rocket thrust chambers.

Similar to previous methods used for the estimation of heat fluxes in capacitive hardware, the inverse method presented in this work relies on an iterative optimization method with the objective of minimizing the temperature difference between the measured and the calculated values. The update of the heat flux parameters at each iteration is carried out using a pre-calculated Jacobi matrix via the Newton-Raphson method. This results to a very efficient optimization algorithm requiring minimal computational resources. The use of thermocouple measurements at different circumferential and axial positions allows for the resolution of axially and azimuthally varying heat loads.

The method can complement calorimetric methods for the evaluation of experimental tests, as it can resolve axially varying loads with much higher spatial accuracy. Compared to gradient methods which require at least two thermocouples per location, the inverse method has demonstrated that one thermocouple per location is sufficient. Compared to the calorimetric method, an axial evolution of the heat flux with much higher resolution is achieved. The two methods agree within 15% with the main reason for this deviation being attributed to the chosen correlation for the heat transfer in the cooling channels. Studies are planned in order to improve the Nusselt correlations by adjusting them to the specific flow conditions examined. Moreover, compared to inverse methods using CFD for the modeling of the coolant flow, a dramatic speed-up is introduced, whereas compared to inverse methods based on simultaneous optimization of wall heat flux and coolant heat transfer coefficient, the number of required installed thermocouples is reduced by a factor of at least 2.

The attractiveness of the new method is its ability to also resolve the azimuthal variation of the heat flux. Using the coarsest possible thermocouple installation in circumferential direction, it was shown that injector footprints can be obtained. This gives information about the interaction of the injector elements without the need for the repetition of the experiments with rotation of the hardware as was proposed by previous methods. Of course, to increase the resolution of the heat transfer in azimuthal direction and to provide a more quantitative comparison with the CFD simulations, a higher number of sensors would be needed. The uncertainty introduced by the Nusselt correlation is expected to

introduce a bias error in the heat flux levels, influencing their absolute level but not their relative variation, hence still allowing the deduction of physical arguments from the obtained azimuthal trends.

When applied for the evaluation of a GCH_4/GOX multi-injector rocket combustor operated at 20 and 30 bar, insights into the physical phenomena in the chamber were obtained. An interesting effect in the circumferential heat flux profile is an observed shift in the location of the local maxima, occurring at around 70 mm distance from the injection plane. This also appeared to be in agreement with CFD simulations of the same load point and can be explained by the secondary flow structures created by the flame/flame interaction. Finally, a comparison between different load points demonstrated that the effect of the velocity and momentum flux ratio on the wall heat loads can be captured by the inverse method. The results confirm that the hydrodynamic effects close to the face-plate dominate leading to higher heat flux for low O/F load points, whereas further downstream the higher O/F produces a larger thermal exchange due to the higher temperature.

It has been shown that the inverse heat transfer method can be applied to rocket engine applications with active cooling for the estimation of the heat loads with minimal computational resources leading to a higher spatial resolution than calorimetric methods. Although only steady state effects were examined in this work, the method could be implemented in a time loop, leading to the capturing of transient effects which may apply during start-up transients and potential combustion instabilities. Finally, the method will be applied for the evaluation of further experimental load points and serve as a validation for new CFD models describing the hot gas flow.

Declaration of Competing Interest

None.

Acknowledgements

The authors would like to thank Ms. Simona Silvestri for providing the experimental data and Mr. Daniel Rahn for providing the heat flux data at the interface with the second chamber segment. Financial support has been provided by the German Research Foundation (Deutsche Forschungsgemeinschaft DFG) in the framework of the Sonderforschungsbereich Transregio 40.

References

[1] J.B. Olansen, Project morpheus: Lander technology development, in: AIAA SPACE 2014 Conference and Exposition, 2014, p. 4314.
[2] J.C. Melcher, R.L. Morehead, Combustion stability characteristics of the project Morpheus liquid oxygen/liquid methane main engine, in: 50th AIAA/ASME/SAE/ASEE Joint Propulsion Conference, 2014, p. 3681.
[3] A. Iannetti, N. Girard, N. Ravier, E. Edeline, D. Tchou-Kien, PROMETHEUS, a low cost LOX/CH4 engine prototype, in: 53rd AIAA/SAE/ASEE Joint Propulsion Conference, 2017, p. 4750.
[4] M. Rudnykh, S. Carapellese, D. Liuzzi, L. Arione, G. Caggiano, P. Bellomi, E. D'Aversa, R. Pellegrini, S. Lobov, A. Gurtovoy, et al., Development of LM10-MIRA LOX/LNG expander cycle demonstrator engine, Acta Astronaut. 126 (2016) 364–374.
[5] E. Musk, Making humans a multi-planetary species, New Space 5 (2) (2017) 46–61.
[6] J.S. Kim, H. Jung, J.H. Kim, State of the art in the development of methane/oxygen liquid-bipropellant rocket engine, J. Korean Soc. Propul. Eng. 17 (6) (2013) 120–130.
[7] T. Kato, D. Terakado, H. Nanri, T. Morito, I. Masuda, H. Asakawa, H. Sakaguchi, Y. Ishikawa, T. Inoue, S. Ishihara, et al., Subscale firing test for regenerative cooling LOX/methane rocket engine, in: 7th European Conference for Aeronautics and Space Sciences (EUCASS), 2017.
[8] H. Asakawa, H. Nanri, K. Aoki, I. Kubota, H. Mori, Y. Ishikawa, K. Kimoto, S. Ishihara, S. Ishizaki, The status of the research and development of LNG rocket engines in japan, in: Chemical Rocket Propulsion, Springer, 2017, pp. 463–487.
[9] O.J. Haidn, Advanced rocket engines, Adv. Propul. Technol. High-Speed Aircraft 1 (2008) 1–6.
[10] K. Liang, B. Yang, Z. Zhang, Investigation of heat transfer and coking characteristics of hydrocarbon fuels, J. Propul. Power 14 (5) (1998) 789–796.
[11] D. Preclik, G. Hagemann, O. Knab, L. Brummer, C. Mading, D. Wiedmann, P. Vuillermoz, LOX/hydrocarbon propellant trade considerations for future reusable liquid booster engines, in: 41st AIAA/ASME/SAE/ASEE Joint Propulsion Conference & Exhibit, 2005, p. 3567.
[12] J.P. Stempien, M. Ni, Q. Sun, S.H. Chan, Production of sustainable methane from renewable energy and captured carbon dioxide with the use of solid oxide electrolyzer: a thermodynamic assessment, Energy 82 (2015) 714–721.
[13] T. Amon, B. Amon, V. Kryvoruchko, A. Machmüller, K. Hopfner-Sixt, V. Bodiroza, R. Hrbek, J. Friedel, E. Pötsch, H. Wagentristl, et al., Methane production through anaerobic digestion of various energy crops grown in sustainable crop rotations, Bioresource Technol. 98 (17) (2007) 3204–3212.
[14] O. Knab, M. Frey, J. Görgen, K. Quering, D. Wiedmann, C. Mäding, Progress in combustion and heat transfer modelling in rocket thrust chamber applied engineering, in: 45th AIAA/ASME/SAE/ASEE Joint Propulsion Conference & Exhibit, 2009, p. 5477.
[15] O.J. Haidn, N. Adams, R. Radespiel, W. Schröder, C. Stemmer, T. Sattelmayer, B. Weigand, Fundamental technologies for the development of future space transport system components under high thermal and mechanical loads, in: 54th AIAA/SAE/ASEE Joint Propulsion Conference, 2018, p. 4466.
[16] F. Cuoco, B. Yang, M. Oschwald, Experimental investigation of LOX/H2 and LOX/CH4 sprays and flames, in: 24th International Symposium on Space Technology and Science, 2004.
[17] J. Lux, D. Suslov, M. Bechle, M. Oschwald, O.J. Haidn, Investigation of sub-and supercritical LOX/methane injection using optical diagnostics, in: 42nd AIAA/ASME/SAE/ASEE Joint Propulsion Conference & Exhibit.
[18] M. Shim, K. Noh, W. Yoon, Flame structure of methane/oxygen shear coaxial jet with velocity ratio using high-speed imaging and OH∗, CH∗ chemiluminescence, Acta Astronaut. 147 (2018) 127–132.
[19] F. Grisch, E. Bertseva, M. Habiballah, E. Jourdanneau, F. Chaussard, R. Saint-Loup, T. Gabard, H. Berger, CARS spectroscopy of CH4 for implication of temperature measurements in supercritical LOX/CH4 combustion, Aerospace Sci. Technol. 11 (1) (2007) 48–54.
[20] D. Suslov, B. Betti, T. Aichner, S. Soller, F. Nasuti, O. Haidn, Experimental investigation and CFD-simulation of the film cooling in an O2/CH4 subscale combustion chamber, in: Space Propulsion Conference, 2012.
[21] D. Eiringhaus, H. Riedmann, O. Knab, O.J. Haidn, Full-scale virtual thrust chamber demonstrators as numerical testbeds within sfb-trr 40, in: 54th AIAA/SAE/ASEE Joint Propulsion Conference, AIAA 2018-4469, 2018, p. 4469. doi:https://doi.org/10.2514/6.2018-4469.
[22] H. Negishi, Y. Daimon, H. Kawashima, Flowfield and heat transfer characteristics in the le-x expander bleed cycle combustion chamber, in: 50th AIAA/ASME/SAE/ASEE Joint Propulsion Conference, AIAA 2014-4010, 2014, p. 4010. doi:https://doi.org/10.2514/6.2014-4010.
[23] H. Negishi, Y. Daimon, H. Kawashima, N. Yamanishi, Conjugated combustion and heat transfer modeling for full-scale regeneratively cooled thrust chambers, in: 49th AIAA/ASME/SAE/ASEE Joint Propulsion Conference, 2013, p. 3997.
[24] J. Song, B. Sun, Coupled numerical simulation of combustion and regenerative cooling in lox/methane rocket engines, Appl. Therm. Eng. 106 (2016) 762–773, https://doi.org/10.1016/j.applthermaleng.2016.05.130.
[25] Y. Daimon, H. Negishi, S. Silvestri, O. Haidn, Conjugated combustion and heat transfer simulation for a 7 element GOX/GCH4 rocket combustor, in: 2018 Joint Propulsion Conference, AIAA Paper 2018-4553, 2018, p. 4553. doi:https://doi.org/10.2514/6.2018-4553.
[26] D. Suslov, R. Arnold, O. Haidn, Investigation of film cooling efficiency in a high pressure subscale lox/h2 combustion chamber, in: 47th AIAA/ASME/SAE/ASEE Joint Propulsion Conference & Exhibit, AIAA 2011-5778, 2011, p. 5778. doi:https://doi.org/10.2514/6.2011-5778.
[27] C.M. Roth, O.J. Haidn, A. Chemnitz, T. Sattelmayer, G. Frank, H. Müller, J. Zips, R. Keller, P.M. Gerlinger, D. Maestro, et al., Numerical investigation of flow and combustion in a single element GCH4/GOx rocket combustor, in: 52nd AIAA/SAE/ASEE Joint Propulsion Conference, 2016, p. 4995.
[28] N. Perakis, D. Rahn, D. Eiringhaus, Y. Daimon, S. Zhang, S. Karl, T. Horchler, O.J. Haidn, Qualitative and quantitative comparison of RANS simulation results for a 7 element GOX/GCH4 rocket combustor, in: 54th AIAA/SAE/ASEE Joint Propulsion Conference, 2018.
[29] S. Silvestri, M.P. Celano, G. Schlieben, O.J. Haidn, Characterization of a multi-injector GOX/CH4 combustion chamber, in: 52nd AIAA/SAE/ASEE Joint Propulsion Conference, 2016, p. 4992.
[30] N. Perakis, O.J. Haidn, Inverse heat transfer method applied to capacitively cooled rocket thrust chambers, Int. J. Heat Mass Transfer 131 (2019) 150–166.
[31] E.B. Coy, Measurement of transient heat flux and surface temperature using embedded temperature sensors, J. Thermophys. Heat Transfer 24 (1) (2010) 77–84.
[32] A. Vaidyanathan, J. Gustavsson, C. Segal, One-and three-dimensional wall heat flux calculations in a O2/H2 system, J. Propul. Power 26 (1) (2010) 186–189.
[33] J. Haemisch, D. Suslov, M. Oschwald, Experimental analysis of heat transfer in cooling channels of a subscale combustion chamber at real thermal conditions for cryogenic hydrogen and methane, in: Space Propulsion Conference, 2018.
[34] Fluent, 18.0 ANSYS Fluent Theory Guide 18.0, Ansys Inc.
[35] D. Rahn, D. Eiringhaus, H. Riedmann, R. Behr, O. Haidn, Characterization of an adiabatic flamelet combustion model for gaseous CH4/O2 combustion in rocket thrust chambers, in: Space Propulsion Conference 2018, 2018.
[36] E. Artioukhine, Heat Transfer and Inverse Analysis, RTO-EN-AVT-117.

[37] R. Fletcher, Practical Methods of Optimization, John Wiley & Sons, 2013.
[38] C. Kirchberger, R. Wagner, H.-P. Kau, S. Soller, P. Martin, M. Bouchez, C. Bonzom, Prediction and analysis of heat transfer in small rocket chambers, in: 46th AIAA Aerospace Sciences meeting and Exhibit, AIAA-2008-1260, Reno (NV), USA, 2008, pp. 07–11, https://doi.org/10.2514/6.2008-1260.
[39] C.U. Kirchberger, Investigation on heat transfer in small hydrocarbon rocket combustion chambers, Ph.D. thesis, Technische Universität München, 2014.
[40] V. Gnielinski, New equations for heat and mass transfer in turbulent pipe and channel flow, Int. Chem. Eng. 16 (2) (1976) 359–368.
[41] H. Kraussold, Die Wärmeübertragung an Flüssigkeiten in Rohren bei turbulenter Strömung, For. Gebiet Ingenieurwes. A 4 (1) (1933) 39–44.
[42] E. Lemmon, M. McLinden, D. Friend, P. Linstrom, W. Mallard, NIST Chemistry WebBook, Nist Standard Reference Database Number 69, National Institute of Standards and Technology, Gaithersburg.
[43] W. Chang, X. Chu, A.F.B.S. Fareed, S. Pandey, J. Luo, B. Weigand, E. Laurien, Heat transfer prediction of supercritical water with artificial neural networks, Appl. Therm. Eng. 131 (2018) 815–824, https://doi.org/10.1016/j.applthermaleng.2017.12.063.
[44] G. Scalabrin, L. Piazza, Analysis of forced convection heat transfer to supercritical carbon dioxide inside tubes using neural networks, Int. J. Heat Mass Transfer 46 (7) (2003) 1139–1154, https://doi.org/10.1016/s0017-9310(02)00382-4.
[45] N. Perakis, D. Rahn, D. Eiringhaus, O.J. Haidn, Heat transfer and combustion simulation of a 7-element GOX/GCH4 rocket combustor, in: 2018 Joint Propulsion Conference, AIAA Paper 2018-4554, 2018, p. 4554. doi: https://doi.org/10.2514/6.2018-4554.
[46] N. Peters, Laminar diffusion flamelet models in non-premixed turbulent combustion, Prog. Energy Combust. Sci. 10 (3) (1984) 319–339, https://doi.org/10.1016/0360-1285(84)9011-X.
[47] N. Slavinskaya, M. Abbasi, J.-H. Starcke, A. Mirzayeva, O.J. Haidn, Skeletal mechanism of the methane oxidation for space propulsion applications, in: 52nd AIAA/SAE/ASEE Joint Propulsion Conference, American Institute of Aeronautics and Astronautics, AIAA Paper 2016-4781, 2016, p. 4781. doi: https://doi.org/10.2514/6.2016-4781.
[48] B.E. Launder, D.B. Spalding, Mathematical Models of Turbulence, Academic Press, 1972.
[49] F.F. Winter, N. Perakis, O.J. Haidn, Emission imaging and CFD simulation of a coaxial single-element GOX/GCH4 rocket combustor, in: 54th AIAA/SAE/ASEE Joint Propulsion Conference, 2018, p. 4764.

Part III

COMBUSTION AND HEAT TRANSFER MODELING

All models are wrong, but some are useful.

— George E.P. Box

4 NUMERICAL TURBULENT COMBUSTION

Engineering is done with numbers.
Analysis without numbers is only an opinion.

— Akin's first law of spacecraft design

The aim of this chapter is to introduce the basic methods used to numerically describe turbulent reacting flows. Emphasis is placed on the approaches used to generate the results shown in Chapter 6.

4.1 NAVIER-STOKES EQUATIONS

The Navier-Stokes equations for multi-species mixtures are given in Equation 4.1 through Equation 4.4.

$$\frac{\partial \rho}{\partial t} + \frac{\partial}{\partial x_i}\left(\rho u_i\right) = 0 \tag{4.1}$$

$$\frac{\partial \rho u_j}{\partial t} + \frac{\partial \rho u_i u_j}{\partial x_i} + \frac{\partial p \delta_{ij}}{\partial x_i} = -\frac{\partial \tau_{ij}}{\partial x_i} \quad \text{for } j = [1,3] \tag{4.2}$$

$$\frac{\partial \rho Y_k}{\partial t} + \frac{\partial \rho u_i Y_k}{\partial x_i} = -\frac{\partial j_{i,k}}{\partial x_i} + M_k \dot{\omega}_k \quad \text{for } k = [1, N_{sp}] \tag{4.3}$$

$$\frac{\partial \rho E}{\partial t} + \frac{\partial \rho u_i E}{\partial x_i} + \frac{\partial u_j p \delta_{ij}}{\partial x_i} = -\frac{\partial q_i}{\partial x_i} + \frac{\partial u_j \tau_{ij}}{\partial x_i} + \dot{\omega}_T \tag{4.4}$$

where u_j is the j-th component of the velocity vector, p the static pressure, E the total energy, ρ the density and Y_k the species mass fraction of species k. τ_{ij} represents the viscous tensor, $j_{i,k}$ the i-th component of the k-th species diffusive flux, q_i the i-th component of the energy flux, while $\dot{\omega}_k$ and $\dot{\omega}_T$ are the species and energy chemical source terms respectively.

The viscous stress tensor is given by Equation 4.5, under the assumption of having a Newtonian fluid that fulfills the Stokes hypothesis.

$$\tau_{ij} = 2\mu\left(S_{ij} - \frac{1}{3}\delta_{ij} S_{kk}\right) \tag{4.5}$$

μ is the dynamic viscosity of the fluid and S_{ij} is the deformation tensor:

$$S_{ij} = \frac{1}{2}\left(\frac{\partial u_j}{\partial x_i} + \frac{\partial u_i}{\partial x_j}\right) \tag{4.6}$$

The diffusive flux of species k into the mixture $j_{i,k}$ is given by a mixture-averaged approach following the approximation by Hirschfelder and Curtiss [244]:

$$j_{i,k} = \rho Y_k V_{k,i} = -\rho \left(D_k \frac{M_k}{M} \frac{\partial X_k}{\partial x_i} - Y_k \sum_{l=1}^{N_{sp}} D_l \frac{M_l}{M} \frac{\partial X_l}{\partial x_i} \right) \tag{4.7}$$

where X_k is the molar fraction of species k and M the mixture molar mass given by the weighted sum of the individual species molar masses M_k by $M = \sum_{k=1}^{N_{sp}} X_k M_k$. The mixture-averaged diffusion coefficient is given as a function of the binary diffusion coefficients of species j into species k, D_{jk}:

$$D_k = \frac{1 - Y_k}{\sum_{j \neq k} X_j / D_{jk}} \tag{4.8}$$

The energy flux is composed by the conduction component and the species diffusion enthalpy flux:

$$q_i = -\lambda \frac{\partial T}{\partial x_i} + \sum_{k=1}^{N} j_{i,k} H_k \tag{4.9}$$

The closure of the equations requires a relationship between the pressure, density and temperature, which is delivered by the ideal gas equation:

$$p = \rho \frac{R}{M} T \tag{4.10}$$

with R being the ideal gas constant.

It has to be noted here that the ideal gas equation, although valid in the high-temperature regions within the main reacting zone, is not a valid equation of state for typical rocket engine propellant injections, where the oxidizer and/or the fuel are experiencing real-gas effects. This is essentially the case with most systems where liquid oxygen is injected in transcritical thermodynamic conditions. Proper treatment of the real-gas phenomena has to be employed in those cases for the simulation of the supercritical mixing and combustion [245–247].

To achieve that, cubic equations of state are commonly employed, with the following format:

$$p = \frac{RT}{v - b} - \frac{a}{v^2 + 2bv - b^2} \tag{4.11}$$

where $v = M/\rho$ is the molar volume and a, b are coefficients that account for inter-molecular attractive forces and the reduction of free volume, respectively. They are calculated using van-der-Waals type mixing rules and depend on the critical properties p_c and T_c.

For the present thesis however, real-gas effects are not considered, as only test-cases with gaseous propellant injection are examined as Chapter 6 shows. To justify the use of the ideal gas equation of state, the compressibility factor $\mathcal{Z}$ for both methane and oxygen

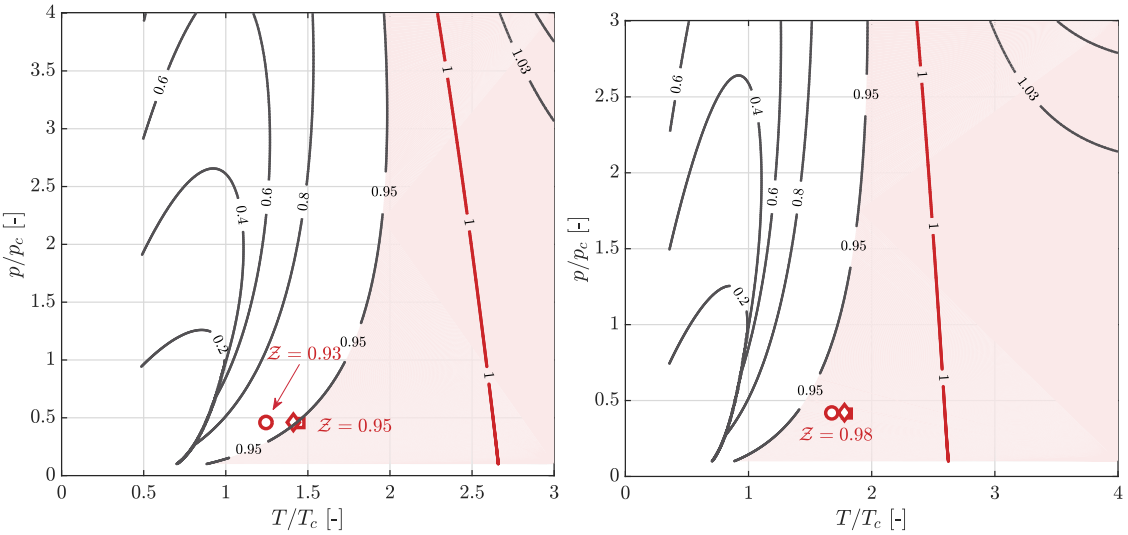

Figure 4.1: Isolines of the compressibility factor for methane (left) and oxygen (right) as a function of the reduced pressure and temperature. The symbols indicate the injection conditions for the simulations shown in Chapter 6. Circle: Section 6.1, square: Section 6.2, diamond: Section 6.3. The shaded region indicates the states with deviation of ±5% from the ideal gas behavior.

is shown in Figure 4.1. $\mathcal{Z}$ quantifies the deviation from the ideal gas assumption and is defined as:

$$\mathcal{Z} = \frac{pv}{RT} \tag{4.12}$$

Given that the maximal deviation from the ideal gas remains within 7% for the chosen load points (signified with the markers in Figure 4.1), the choice of the equation of state is justified.

4.2 THERMODYNAMIC AND TRANSPORT PROPERTIES

For the description of the specific heat capacity, enthalpy and entropy of the individual species, the NASA polynomials are employed. They consist of 7 parameters for each species and lead to a following format for the thermodynamic variables as a function of temperature:

$$c_{p,k}(T) = \frac{R}{M}\left(a_1 + a_2 T + a_3 T^2 + a_4 T^3 + a_5 T^4\right) \tag{4.13}$$

$$H_k(T) = \frac{R}{M}\left(a_1 T + a_2 \frac{T^2}{2} + a_3 \frac{T^3}{3} + a_4 \frac{T^4}{4} + a_5 \frac{T^5}{5} + a_6\right) \tag{4.14}$$

$$\mathcal{S}_k(T) = \frac{R}{M}\left(a_1 \ln(T) + a_2 T + a_3 \frac{T^2}{2} + a_4 \frac{T^3}{3} + a_5 \frac{T^4}{4} + a_7\right) \tag{4.15}$$

The specific heat capacity c_p, enthalpy H and entropy $\mathcal{S}$ of the gas mixture are then given as a weighted average of the component values:

$$c_p = \sum_{k=1}^{N_{sp}} Y_k c_{p,k} \tag{4.16}$$

$$H = \sum_{k=1}^{N_{sp}} Y_k H_k \tag{4.17}$$

$$\mathcal{S} = \sum_{k=1}^{N_{sp}} Y_k \mathcal{S}_k \tag{4.18}$$

In case of real-gas effects, departure functions would have to be utilized, accounting for the deviation of the thermodynamic properties from the ideal gas values [248].

As far as the transport properties are concerned, a kinetic theory model is employed as proposed by Hirschfelder et al. [244]. The dynamic viscosity of each species is then described by

$$\mu_k = \frac{5}{16} \frac{\sqrt{\pi m_k k_B T}}{\pi \mathcal{D}_k^2 \Omega^{(2,2)^*}} \tag{4.19}$$

where k_B is the Boltzmann constant, m_k is the molecular mass, $\mathcal{D}_k$ is the Lenard-Jones collision diameter and $\Omega^{(2,2)^*}$ the collisional integral depending on the temperature and the reduced dipole moment of the molecule.

Based on the same approach, the binary diffusivity is obtained as shown in Equation 4.20.

$$D_{jk} = \frac{3}{16} \frac{\sqrt{2\pi k_B^3 T^3 / M_{jk}}}{p \pi \mathcal{D}_{jk}^2 \Omega^{(1,1)^*}} \tag{4.20}$$

where the reduced molecular mass m_{jk} and reduced collisional parameter $\mathcal{D}_{jk}$ for the pair are calculated by:

$$m_{jk} = \frac{m_j m_k}{m_j + m_k} \tag{4.21}$$

$$\mathcal{D}_{jk} = \frac{1}{2}(\mathcal{D}_k + \mathcal{D}_j) \tag{4.22}$$

Finally, the thermal conductivity of each gas constituent is given by consideration of its degrees of freedom:

$$\lambda_k = \mu_k \left(f_{trans} c_{v,trans} + f_{rot} c_{v,rot} + f_{vibr} c_{v,vibr} \right) \tag{4.23}$$

The individual contributions for the translational, rotational and vibrational components f can be found in Warnatz et al. [249], while the specific heat capacity contributions c_v depend on the type of molecule (single-atom, linear or non-linear).

The mixture-average values for the viscosity and thermal conductivity are finally obtained by means of Equation 4.24 and Equation 4.26, as explained in the work by Wilke [250] and Mathur et al. [251] respectively.

$$\mu = \sum_{k=1}^{N_{sp}} \frac{X_k \mu_k}{\sum_{j=1}^{N_{sp}} X_j \Phi_{kj}} \tag{4.24}$$

$$\Phi_{kj} = \frac{1}{\sqrt{8}} \left(1 + \frac{M_k}{M_j}\right)^{-\frac{1}{2}} \left(1 + \left(\frac{\mu_k}{\mu_j}\right)^{\frac{1}{2}} \left(\frac{M_j}{M_k}\right)^{\frac{1}{4}}\right)^2 \tag{4.25}$$

$$\lambda = \frac{1}{2} \left(\sum_{k=1}^{N_{sp}} X_k \lambda_k + \frac{1}{\sum_{k=1}^{N_{sp}} X_k / \lambda_k} \right) \tag{4.26}$$

4.3 CHEMICAL KINETICS

The reactions taking place between the species in the gas mixture are described by means of chemical kinetics. Considering a set of N_{reac} reactions and N_{sp} species, the general form of a reaction equation between different species $\mathcal{M}_k$ is given by Equation 4.27

$$\sum_{k=1}^{N_{sp}} \nu'_{kj} \mathcal{M}_k \Longleftrightarrow \sum_{k=1}^{N_{sp}} \nu''_{kj} \mathcal{M}_k \quad \text{for } j = [1, N_{reac}] \tag{4.27}$$

where ν'_{kj} and ν''_{kj} represent the molar stoichiometric coefficients of the reactants and products respectively.

The molar reaction rate of species k is defined as the sum of the reaction rates for each individual reaction $\dot{\omega}_{k,j}$:

$$\dot{\omega}_k = \sum_{j=1}^{N_{reac}} \dot{\omega}_{k,j} = \sum_{j=1}^{N_{reac}} \left(\nu''_{kj} - \nu'_{kj}\right) \mathcal{R}_j \tag{4.28}$$

The net rate of progress for reaction j is given as a function of the forward and reverse reaction rates $\mathcal{K}_{fj}$ and $\mathcal{K}_{rj}$:

$$\mathcal{R}_j = \Gamma_j \cdot \left(\mathcal{K}_{fj} \prod_{k=1}^{N_{sp}} \mathcal{C}_k^{\nu'_{kj}} - \mathcal{K}_{rj} \prod_{k=1}^{N_{sp}} \mathcal{C}_k^{\nu''_{kj}} \right) \tag{4.29}$$

with the molar concentration defined as $\mathcal{C}_k = \frac{\rho X_k}{M}$.

The forward reaction coefficient is described with the Arrhenius law:

$$\mathcal{K}_{fj} = A_j T^{\beta} \exp\left(\frac{-E_{aj}}{RT}\right) \tag{4.30}$$

If not explicitly specified by a separate set of Arrhenius coefficients, the reaction coefficient for the reverse reaction $\mathcal{K}_{rj}$ is described by making use of the equilibrium constant K_j:

$$\mathcal{K}_{rj} = \frac{\mathcal{K}_{fj}}{K_j} \tag{4.31}$$

$$K_j = \exp\left(\frac{\Delta\mathcal{S}_j}{R} - \frac{\Delta H_j}{RT}\right)\left(\frac{p_{\text{atm}}}{RT}\right)^{\sum_{k=1}^{N_{sp}}\left(\nu''_{kj}-\nu'_{kj}\right)} \tag{4.32}$$

where p_{atm} denotes atmospheric pressure. The term in the exponential represents the change in Gibbs free enthalpy and its components (the enthalpy and entropy changes for the reaction ΔH_j and $\Delta\mathcal{S}_j$) are given by their respective net change between products and reactants:

$$\frac{\Delta\mathcal{S}_j}{R} = \sum_{k=1}^{N_{sp}}\left(\nu''_{kj} - \nu'_{kj}\right)\frac{\mathcal{S}_k}{R} \tag{4.33}$$

$$\frac{\Delta H_j}{RT} = \sum_{k=1}^{N_{sp}}\left(\nu''_{kj} - \nu'_{kj}\right)\frac{H_k}{RT} \tag{4.34}$$

The factor Γ_j in Equation 4.29 describes the net effect of third bodies on the reaction rate. Using the third body efficiency γ_{kj} of each species, the total efficiency is given by:

$$\Gamma_j = \sum_{k=1}^{N_{sp}} \gamma_{kj}\mathcal{C}_k \tag{4.35}$$

Finally, the net heat release rate of each reaction $\dot{\mathcal{Q}}_j$ is given by the product of the net rate of progress and the reaction enthalpy

$$\dot{\mathcal{Q}}_j = \mathcal{R}_j \cdot \Delta H_j \tag{4.36}$$

leading to a total heat release of $\dot{\mathcal{Q}} = \sum_{j=1}^{N_{reac}} \dot{\mathcal{Q}}_j$.

4.4 NUMERICAL SIMULATION APPROACHES

Despite the impressive advances in the field of High Performance Computing (HPC), the computational resources required for a full resolution of all turbulent scales in complex engineering geometries is still out of reach. This is particularly true for high speed flows,

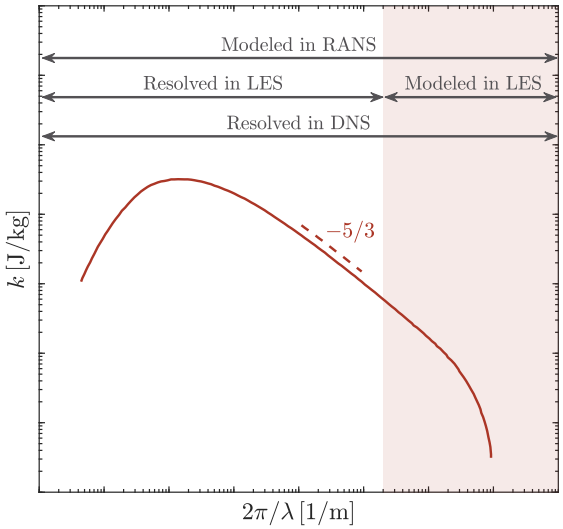

Figure 4.2: Turbulence kinetic energy spectrum plotted as a function of the wave number. The range of spatial wave numbers explicitly resolved and modeled in different CFD approaches is indicated.

as the smallest scales that need to be resolved (Kolmogorov scale η_k) decrease for higher Reynolds numbers Re [252]:

$$\eta_k \propto Re^{-3/4} \tag{4.37}$$

This implies that for a sufficient resolution of all turbulent length scales, the required number of discretization points scales with $Re^{9/4}$ for a 3D flow. Combined with the large number of species and reactions needed to be resolved in combustion applications which increase the stiffness of the numerical problem, the development of models is employed, aiming to reduce the computational cost. This modeling effort results in different numerical simulation strategies.

Depending on the modeling effort required, different CFD methodologies are available for the solution of the compressible Navier-Stokes equations. The range of spatial wave numbers explicitly resolved and modeled in each of the approaches (DNS, LES and RANS) is shown in Figure 4.2.

4.4.1 *Direct Numerical Simulation - DNS*

In Direct Numerical Simulation (DNS) the entire spectrum of turbulent length scales is resolved, by explicitly solving the full instantaneous Navier-Stokes equations. As there is a minimal amount of modeling required, the method can be characterized as a brute-force method. Due to the absence of model and the aforementioned scaling of the grid size with the Reynolds number ($\propto Re^{9/4}$), DNS of complex engineering configurations such as gas turbines and rocket thrust chambers is not yet feasible. For that reason, the application of DNS is restricted to more affordable, academic setups with simplified configurations and moderate Reynolds numbers. Nevertheless, the simulation of those configurations is crucial for the understanding of physical phenomena in turbulent combustion and is therefore employed to derive improved models that can be implemented in LES and RANS.

4.4.2 *Large Eddy Simulation - LES*

As the name of the approach suggests, in Large Eddy Simulation (LES), the larger turbulent scales are resolved and explicitly calculated, whereas the smaller scales are modeled. The basis of this scale separation is that larger scales are significantly influenced by the geometry of the problem and hence have to be solved for in each individual case, whereas the smaller ones have a self-similar nature, allowing for modeling. Similar to DNS, LES allows for investigation of unsteady phenomena, as the evolution of the large turbulent scales is resolved both spatially and temporally.

To perform the scale separation, a filter operator is introduced in LES, and is applied onto the governing equations. For any quantity ϕ, the filtered quantity $\overline{\phi}$ can be defined as

$$\overline{\phi}\left(\mathbf{x}\right) = \int \phi(\mathbf{r}) \mathcal{F}_{\Delta}(\mathbf{x}-\mathbf{r}) \mathrm{d}\mathbf{r} \tag{4.38}$$

where $\mathcal{F}_{\Delta}$ stands for the spatial filter kernel, operating at a filter width Δ. For flows with variable density like the ones present in rocket engines, a Favre-filtering is carried out to account for the density variations.

$$\widetilde{\phi}\left(\mathbf{x}\right) = \frac{\overline{\rho\phi}}{\overline{\rho}} = \frac{\int \rho\phi(\mathbf{r}) \mathcal{F}_{\Delta}(\mathbf{x}-\mathbf{r}) \mathrm{d}\mathbf{r}}{\overline{\rho}} \tag{4.39}$$

$\widetilde{\phi}$ corresponds to the value that is resolved in the numerical simulation, whereas the unresolved, subgrid scale (SGS) contributions are defined by:

$$\phi^{'}\left(\mathbf{x}, t\right) = \phi(\mathbf{x}, t) - \overline{\phi}\left(\mathbf{x}\right) \tag{4.40}$$

Filtering the instantaneous balance equations leads to the following equations for continuity, momentum, species and energy:

$$\frac{\partial \overline{\rho}}{\partial t} + \frac{\partial \overline{\rho}\widetilde{u}_i}{\partial x_i} = 0 \tag{4.41}$$

$$\frac{\partial \overline{\rho}\widetilde{u}_j}{\partial t} + \frac{\partial \overline{\rho}\widetilde{u}_i\widetilde{u}_j}{\partial x_i} + \frac{\partial \overline{p\delta_{ij}}}{\partial x_i} = \frac{\partial}{\partial x_i}\left[\overline{\tau}_{ij} - \overline{\rho}\left(\widetilde{u_i u_j} - \widetilde{u}_i\widetilde{u}_j\right)\right] \tag{4.42}$$

$$\frac{\partial \overline{\rho}\widetilde{Y}_k}{\partial t} + \frac{\partial \overline{\rho}\widetilde{u}_i\widetilde{Y}_k}{\partial x_i} = -\frac{\partial}{\partial x_i}\left[\overline{j}_{i,k} - \overline{\rho}\left(\widetilde{u_i Y_k} - \widetilde{u}_i\widetilde{Y}_k\right)\right] + \overline{\dot{\omega}}_k \tag{4.43}$$

$$\frac{\partial \overline{\rho}\widetilde{E}}{\partial t} + \frac{\partial \overline{\rho}\widetilde{u}_i\widetilde{E}}{\partial x_i} + \frac{\overline{\partial u_i p\delta_{ij}}}{\partial x_i} = -\frac{\partial}{\partial x_i}\left[\overline{q_i} - \overline{\rho}\left(\widetilde{u_i E} - \widetilde{u}_i\widetilde{E}\right)\right] + \overline{\tau_{ij}\frac{\partial u_i}{\partial x_j}} + \overline{\dot{\omega}}_T \tag{4.44}$$

For the filtered viscous terms, following approximations are used:

STRESS TENSOR The laminar stress tensor $\overline{\tau}_{ij}$ is given by

$$\overline{\tau_{ij}} = \overline{2\mu\left(S_{ij} - \frac{1}{3}\delta_{ij}S_{kk}\right)} \tag{4.45}$$

and approximated by

$$\overline{\tau}_{ij} \simeq 2\bar{\mu}\left(\widetilde{S}_{ij} - \frac{1}{3}\delta_{ij}\widetilde{S}_{kk}\right) \tag{4.46}$$

The filtered deformation tensor is defined as $\widetilde{S}_{ij} = \frac{1}{2}\left(\frac{\partial \widetilde{u}_j}{\partial x_i} + \frac{\partial \widetilde{u}_i}{\partial x_j}\right)$ and the filtered viscosity is calculated as a function of the filtered temperature ($\bar{\mu} \simeq \mu(\widetilde{T})$), using the formulas in Section 4.2.

Apart from the resolved laminar stress tensor, a subgrid flux is also introduced in Equation 4.42. Specifically the term $\overline{\tau}_{ij}^{sgs} = -\bar{\rho}\left(\widetilde{u_i u_j} - \widetilde{u}_i\widetilde{u}_j\right)$ is the unresolved Reynolds tensor. Following the Boussinesq hypothesis [253], the Reynolds tensor is modeled similar to the laminar, resolved term $\overline{\tau_{ij}}$ by introducing the turbulent viscosity μ_t:

$$\overline{\tau}_{ij}^{sgs} = 2\mu_t\left(\widetilde{S}_{ij} - \frac{1}{3}\delta_{ij}\widetilde{S}_{kk}\right) \tag{4.47}$$

For the description of the turbulent viscosity, several models have been proposed in LES, that will be explored in Section 4.4.2.1.

SPECIES FLUX The diffusive species flux vector $\bar{j}_{i,k}$ is approximated as

$$\bar{j}_{i,k} \simeq -\overline{\rho}\left(\overline{D}_k\frac{M_k}{\overline{M}}\frac{\partial \widetilde{X}_k}{\partial x_i} - \widetilde{Y}_k\sum_{k=1}^{N_{sp}}\overline{D}_k\frac{\partial \widetilde{X}_k}{\partial x_i}\right) \tag{4.48}$$

and the filtered binary diffusion coefficient is again defined as a function of the filtered temperature, using Equation 4.20.

The unresolved species flux $\bar{j}_{i,k}^{sgs} = -\overline{\rho}\left(\widetilde{u_i Y_k} - \widetilde{u}_i\widetilde{Y}_k\right)$ is modeled using a diffusive contribution, following an analogy to the momentum flux closure. In this case, the turbulent diffusivity D_t is introduced resulting to the following approximation for $\bar{j}_{i,k}^{sgs}$:

$$\bar{j}_{i,k}^{sgs} = -\overline{\rho}\left(D_t\frac{M_k}{\overline{M}}\frac{\partial \widetilde{X}_k}{\partial x_i} - \widetilde{Y}_k\sum_{k=1}^{N_{sp}}\overline{D}\frac{\partial \widetilde{X}_k}{\partial x_i}\right) \tag{4.49}$$

Similar to the definition of the laminar diffusivity, the turbulent one is given as a function of the turbulent viscosity and the turbulent Schmidt number Sc_t.

$$D_t = \frac{\mu_t}{\rho Sc_t} \tag{4.50}$$

ENERGY FLUX Finally, the laminar heat flux is approximated by

$$\overline{q_i} \simeq -\bar{\lambda}\frac{\partial \widetilde{T}}{\partial x_i} + \sum_{k=1}^{N_{sp}} \bar{j}_{i,k}\widetilde{H}_k \tag{4.51}$$

and the laminar thermal conductivity is calculated using Equation 4.23 with $\overline{\lambda} \simeq \lambda(\widetilde{T})$.

The unresolved part of the energy flux $\overline{q}_i^{sgs} = -\overline{\rho}\left(\widetilde{u_i E} - \widetilde{u}_i\widetilde{E}\right)$ is modeled by means of the turbulent thermal conductivity λ_t:

$$\overline{q}_i^{sgs} = -\lambda_t\frac{\partial \widetilde{T}}{\partial x_i} + \sum_{k=1}^{N_{sp}} \bar{j}_{i,k}\widetilde{H}_k \tag{4.52}$$

In an analog fashion as for the turbulent diffusivity, where the turbulent Schmidt number was introduced, the turbulent conductivity is defined by employing the turbulent Prandtl number Pr_t:

$$\lambda_t = \frac{\mu_t \bar{c}_p}{Pr_t} \tag{4.53}$$

4.4.2.1 *Turbulent viscosity models*

The most widely used approach for the description of the interaction between the resolved and unresolved scales when modeling the subgrid scale stress tensor, is the use of a turbulent viscosity model. Typically, it is assumed that the subgrid scales have a universal behavior, with a dissipative nature according to the cascade theory proposed by Kolmogorov [252]. The modeled dissipative nature of the subgrid eddies implies that no backscatter, i.e. transfer of energy from the unresolved scales to the integral scales is included. This is however not necessarily the case in complex turbulent flows, as Lesli et al. [254] showed that energy transfer from small residual scales to the larger ones is possible.

Some of the most common subgrid scale models are being presented in this section, while more detailed discussions on the subrgid modeling can be found in the works of Ferzinger [255], Lesieur [256] and Piomelli [257].

SMAGORINSKY MODEL The Smagorinsky SGS model was first proposed in the work of Smagorisky [258] and is one of the most popular models due to its simple formulation. It is based on a mixing length analogy, according to which the subgrid scale turbulent kinetic viscosity $\nu_t = \mu_t/\overline{\rho}$ is expressed as:

$$\nu_t = C_S^2\Delta^{4/3}l_t^{2/3}\left(2\widetilde{S}_{ij}\widetilde{S}_{ij}\right)^{1/2} \tag{4.54}$$

where l_t is the turbulence integral length scale and C_S a model constant. Equation 4.54 is simplified by assuming that the integral scale is of the order of the grid size Δ, leading to:

$$\nu_t = (C_S\Delta)^2\left(2\widetilde{S}_{ij}\widetilde{S}_{ij}\right)^{1/2} \tag{4.55}$$

In the case of homogeneous isotropic turbulence, the model constant is estimated as $C_S = 0.17$ [259] but it depends on the flow configuration. The Smagorinsky model is also known as being too dissipative [260], especially near walls, making it less suitable for wall-bounded flows.

GERMANO DYNAMIC MODEL The objective of the Germano dynamic model [260] is to estimate small scale dissipation from the knowledge of the resolved eddies. It leads to an extension of the Smagorisky model, by evaluating the constant C_S locally, insteady of using a pre-defined value. In this model, a test filter with size $\widehat{\Delta} > \Delta$ is used. The unknown unresolved Reynolds stresses at the filter level and at the test filter level are connected via the Germano identity [261], which provides five independent equations for the unknown model constant C_S so that C_S may be determined using optimization procedures.

WALE MODEL The Wall-Adapting Local Eddy-viscosity (WALE) model was proposed by Ducros et al. [262] in order to obtain correct scaling laws in the vicinity of the wall. The turbulent viscosity reads

$$\mu_t = \overline{\rho} \left(C_w \Delta\right)^2 \frac{\left(s_{ij} s_{ij}\right)^{3/2}}{\left(\widetilde{S}_{ij} \widetilde{S}_{ij}\right)^{5/2} + \left(s_{ij} s_{ij}\right)^{5/4}} \tag{4.56}$$

with the factor s_{ij} being defined as

$$s_{ij} = \frac{1}{2}\left(\left(\frac{\partial \widetilde{u}_i}{\partial x_j}\right)^2 + \left(\frac{\partial \widetilde{u}_j}{\partial x_i}\right)^2\right) - \frac{1}{3}\left(\frac{\partial \widetilde{u}_k}{\partial x_k}\right)^2 \delta_{ij} \tag{4.57}$$

and with C_W being a model constant equal to 0.5.

σ- MODEL Nicoud et al. [263] proposed an eddy-viscosity based, subgrid-scale model for Large Eddy Simulations derived from the analysis of the singular values of the resolved velocity gradient tensor. Using those singular values σ_1, σ_2 and σ_3 and the model constant C_σ, the turbulent viscosity is defined as:

$$\nu_t = \left(C_\sigma \Delta\right)^2 \frac{\sigma_3 \left(\sigma_1 - \sigma_2\right)\left(\sigma_2 - \sigma_3\right)}{\sigma_1^2} \tag{4.58}$$

The model is able to correctly capture the behavior of the dissipation in near-wall regions, as the order of ν_t scales with the wall distance y_w as $\nu_t = \mathcal{O}(y_w^3)$

VREMAN MODEL Vreman [264] introduced an eddy-viscosity model and applied it in LES of turbulent shear flows with quite satisfactory results. The model is constructed in such a way that its dissipation is relatively small in transitional and near-wall regions, allowing for the description of wall-bounded flows, while at the same time it does not involve explicit filtering and averaging, rendering it well suited for engineering applications.

The turbulent viscosity is defined as:

$$\nu_t = c\sqrt{\frac{B_\beta}{\alpha_{ij}\alpha_{ij}}} \tag{4.59}$$

with

$$\alpha_{ij} = \frac{\partial \widetilde{u}_j}{\partial x_i} \tag{4.60}$$

$$\beta_{ij} = \Delta_m^2 \alpha_{mi} \alpha_{mj} \tag{4.61}$$

$$B_\beta = \beta_{11}\beta_{22} - \beta_{12}^2 + \beta_{11}\beta_{33} - \beta_{13}^2 + \beta_{22}\beta_{33} - \beta_{23}^2 \tag{4.62}$$

The model constant c is related to the Smagorisky constant by $c \approx 2.5 C_S^2$.

4.4.3 *Reynolds Averaged Navier Stokes - RANS*

The Reynolds Averaged Navier-Stokes (RANS) equations result from performing a time-averaging of the instantaneous Navier-Stokes equations. They are based on the decomposition of the flow quantities into a mean and a fluctuating part:

$$\phi = \widetilde{\phi} + \phi'' \tag{4.63}$$

The $\widetilde{\phi}$ notation corresponds to a density-weighted averaging (Favre averaging [265]) defined as

$$\widetilde{\phi} = \frac{\overline{\rho\phi}}{\overline{\rho}} \tag{4.64}$$

and simplifies several unclosed correlation compared to the Reynolds averaging in the case of variable density flows.

In contrast to the subgrid component in the LES-filtering, for which $\widetilde{\phi''} \neq 0$, in the case of RANS averaging, the time-average of the fluctuations is indeed zero by definition ($\widetilde{\phi''} = 0$).

As Figure 4.2 indicates, the entire turbulence spectrum, which is represented by the unclosed terms that appear in the RANS equations is modeled in RANS. As only the average quantities are calculated and there is no need for resolution of small turbulent scales, RANS simulations are attractive for use in industry due to their low computational cost compared to LES. However, as the larger scales of the turbulent motion usually strongly depend on the geometric configuration being simulated, RANS closure models often lack universality.

Using the averaging formalism in Equation 4.64, the averaged balance equations become:

$$\frac{\partial \overline{\rho}}{\partial t} + \frac{\partial \overline{\rho}\widetilde{u}_i}{\partial x_i} = 0 \tag{4.65}$$

$$\frac{\partial \overline{\rho}\widetilde{u}_j}{\partial t} + \frac{\partial \overline{\rho}\widetilde{u}_i\widetilde{u}_j}{\partial x_i} + \frac{\partial \overline{p\delta_{ij}}}{\partial x_i} = \frac{\partial}{\partial x_i}\left(\overline{\tau}_{ij} - \overline{\rho}\widetilde{u_i''u_j''}\right) \tag{4.66}$$

$$\frac{\partial \overline{\rho}\widetilde{Y}_k}{\partial t} + \frac{\partial \overline{\rho}\widetilde{u}_i\widetilde{Y}_k}{\partial x_i} = -\frac{\partial}{\partial x_i}\left(\overline{j}_{i,k} - \overline{\rho}\widetilde{u_i''Y_k''}\right) + \overline{\dot{\omega}}_k \tag{4.67}$$

$$\frac{\partial \overline{\rho}\widetilde{E}}{\partial t} + \frac{\partial \overline{\rho}\widetilde{u}_i\widetilde{E}}{\partial x_i} + \frac{\overline{\partial u_i p \delta_{ij}}}{\partial x_i} = -\frac{\partial}{\partial x_i}\left(\overline{q_i} - \overline{\rho}\widetilde{u_i''E''}\right) + \overline{\tau_{ij}\frac{\partial u_i}{\partial x_j}} + \overline{\dot{\omega}}_T \tag{4.68}$$

The laminar fluxes for momentum $\overline{\tau}_{ij}$, species $\overline{j}_{i,k}$ and heat $\overline{q_i}$ are treated in the same way as in the LES formulation, using the gradient assumption shown in Equation 4.46, Equation 4.48 and Equation 4.51 respectively.

The unclosed Reynolds stress appearing in Equation 4.66 $\overline{\rho}\widetilde{u_i''u_j''}$, is modeled following the turbulence viscosity assumption proposed by Boussinesq and hence reads:

$$\overline{\rho}\widetilde{u_i''u_j''} = 2\mu_t\left(\widetilde{S}_{ij} - \frac{1}{3}\delta_{ij}\widetilde{S}_{kk}\right) \tag{4.69}$$

Finally, for the closure of the turbulent fluxes $\overline{\rho}\widetilde{u_i''Y_k''}$ and $\overline{\rho}\widetilde{u_i''E''}$, the turbulent Schmidt and Prandtl numbers are utilized, in an analog manner as for the LES subgrid terms.

4.4.4 *Turbulent viscosity models*

Turbulent viscosity models are typically used for the closure of the Reynolds stress term.

PRANDTL MIXING LENGTH MODEL The simplest approach consists of a zero-equation model, where the turbulent viscosity is estimated based on an algebraic equation proposed by Prandtl [266]:

$$\mu_t = \overline{\rho} l_m^2 \left|\widetilde{S}\right| \tag{4.70}$$

Various empirical relations have been proposed to model the mixing length l_m but depend strongly on the flow geometry. For that reason, the simple algebraic model is rarely used for engineering flow configurations.

SPALART-ALLMARAS MODEL The Spalart–Allmaras model is a one-equation model that solves a modelled transport equation for the kinematic eddy turbulent viscosity [267]. The Spalart–Allmaras model was designed specifically for aerospace applications involving wall-bounded flows.

A transport equation for a viscosity-like variable $\widetilde{\nu} = \nu / f_{v1}$ is solved, which is referred to as the Spalart–Allmaras variable. The definition of the transport equation and the normalization function f_{v1} can be found in Spalart et al. [267].

k-ε MODEL Two-equation turbulence models allow the determination of both a turbulent length and time-scale by solving two separate transport equations. The standard k-ε belongs to this class of models and has become the workhorse of practical engineering

flow calculations in the time since it was proposed by Launder et al. [268]. In this model, a transport equation for the turbulence kinetic energy k and one for its dissipation rate ε are solved.

$$\frac{\partial}{\partial t}(\overline{\rho}k) + \frac{\partial}{\partial x_i}(\overline{\rho}\widetilde{u}_i k) = \frac{\partial}{\partial x_i}\left[\left(\mu + \frac{\mu_t}{\sigma_k}\right)\frac{\partial k}{\partial x_i}\right] + P_k - \overline{\rho}\varepsilon \tag{4.71}$$

$$\frac{\partial}{\partial t}(\overline{\rho}\varepsilon) + \frac{\partial}{\partial x_i}(\overline{\rho}\widetilde{u}_i \varepsilon) = \frac{\partial}{\partial x_i}\left[\left(\mu + \frac{\mu_t}{\sigma_\varepsilon}\right)\frac{\partial \varepsilon}{\partial x_i}\right] + C_{\varepsilon 1}\frac{\varepsilon}{k}P_k - C_{\varepsilon 2}\overline{\rho}\frac{\varepsilon^2}{k} \tag{4.72}$$

where the turbulence kinetic energy production source P_k is given by

$$P_k = -\overline{\rho}\widetilde{u_i'' u_j''}\frac{\partial \widetilde{u}_i}{\partial x_j} \tag{4.73}$$

.

By solving the two equations, the turbulent viscosity is given by

$$\mu_t = \overline{\rho}C_\mu \frac{k^2}{\varepsilon} \tag{4.74}$$

σ_k, σ_ε, $C_{\varepsilon 1}$, $C_{\varepsilon 2}$ and C_μ are model constants.

Equation 4.71 and Equation 4.72 implicitly assume high Reynolds number, homogeneous and isotropic turbulence and have to be adapted for low Reynolds number flows. As the strengths and weaknesses of the standard k-ε model have become known, modifications have been introduced to improve its performance, with two of these variants being the RNG k-ε [269] and the realizable k-ε model [270].

k-ω SST model k-ω models solve transport equations for the turbulence kinetic energy k and the specific dissipation rate ω , which can also be thought of as the ratio of ε to k. Compared to the standard k-ω model proposed by Wilcox [271], the k-ω Shear-Stress Transport (SST) model introduces a gradual change from the standard k-ω model in the inner region of the boundary layer to a high-Reynolds number version of the k-ε model in the outer part of the boundary layer. It also includes a modified turbulent viscosity formulation to account for the transport effects of the principal turbulent shear stress. For that reason it is considered to be better suited for flows including both free-jet turbulence and jet-wall interaction.

The transport equations are defined as:

$$\frac{\partial}{\partial t}(\overline{\rho}k) + \frac{\partial}{\partial x_i}(\overline{\rho}\widetilde{u}_i k) = \frac{\partial}{\partial x_i}\left[\left(\mu + \frac{\mu_t}{\sigma_k}\right)\frac{\partial k}{\partial x_i}\right] + P_k - \rho\beta^* f_{\beta^*} k\omega \tag{4.75}$$

$$\frac{\partial}{\partial t}(\overline{\rho}\omega) + \frac{\partial}{\partial x_i}(\overline{\rho}\widetilde{u}_i \omega) = \frac{\partial}{\partial x_i}\left[\left(\mu + \frac{\mu_t}{\sigma_\omega}\right)\frac{\partial k}{\partial x_i}\right] + \alpha\frac{\omega}{k}P_k - \rho\beta f_\beta \omega^2 \tag{4.76}$$

The blending functions β, β^*, f_{β^*}, α, as well as the constant σ_ω are defined in the work of Menter [272].

HIGHER LEVEL TURBULENCE CLOSURES Two-equation models such as k-ε and k-ω assume isotropic turbulence, but practical flows very often exhibit strong anisotropic features. Such phenomena can be incorporated through more sophisticated modeling. For example, in Algebraic Stress Models (ASM) and Reynolds Stress Models (RSM), the Boussinesq formulation is abandoned and instead algebraic equations and balance equations respectively are derived for the Reynolds stresses $\overline{\rho}\widetilde{u_i'' u_j''}$. As the use of higher level turbulence closures is not part of this thesis, the models are not explained in further detail. An overview can be found in the work of Hallback et al. [273].

4.5 COMBUSTION MODELING

Both in LES and RANS models, there is a need to find closure for the reaction rate $\overline{\dot{\omega}}_k$. In LES this term represents the resolved reaction rate, whereas in RANS it stands for the mean reaction rate.

Different models are developed based on the nature of the combustion problem, with separate approaches followed for premixed and non-premixed flame configurations. As the combustion regime in rocket engines predominantly consists of non-premixed flames, those models will be mainly described in the following sections.

For the mean reaction rate in RANS, rate closures are generally developed from physical analysis, comparing chemical and turbulent time-scales. The strong non-linearity of the Arrhenius law with temperature makes averaging a difficult issue, because the average of a strongly non-linear function cannot be estimated using the evaluation of the function with the mean of the arguments:

$$\overline{\dot{\omega}(T, Y_k)} \neq \dot{\omega}(\widetilde{T}, \widetilde{Y}_k) \tag{4.77}$$

Based on the work of Veynante et al. [274], most of the models are derived from geometrical analysis (like the flamelet model), turbulent mixing assumptions (like the Eddy-Dissipation Concept) or one-point statistics (probability-density function methods).

For LES, the simplest model is to assume perfect mixing at the subgrid scale level, neglecting subgrid scale fluctuations. The model for the filtered reaction rate then implicitly assumes that the turbulent subgrid time-scale is shorter than all chemical time-scales. As this assumption often deviates from the reality in combustion applications, scale similarity assumptions, similar to those used for the description of Reynolds stresses can be employed for the unresolved reaction rate [275, 276].

One of the most common approaches in modeling non-premixed turbulent combustion and the one that is predominantly used in this thesis, consists of decomposing the entire flame structure into laminar flames called flamelets, which are the building blocks of turbulent flames.

When a flamelet-type method is used, then the solution of the diffusion flame can be reduced to two steps, that will substitute Equation 4.43 and Equation 4.67. In such a flame, the two problems to solve are:

- A mixing problem that will provide a solution for the mixture fraction field $\widetilde{Z}$ and some of its higher moments ($\widetilde{Z''^2}$).

- A flame structure problem where temperature T and species mass fractions, Y_k are expressed as a function of the mixture fraction.

The solution of the mixing problem takes place by solving the transport equation for the mixture fraction $\widetilde{Z}$:

$$\frac{\partial \bar{\rho}\widetilde{Z}}{\partial t} + \frac{\partial}{\partial x_i}\left(\bar{\rho}\widetilde{u_i}\widetilde{Z}\right) = \frac{\partial}{\partial x_i}\left(\overline{\rho\mathcal{D}\frac{\partial Z}{\partial x_i}} - \bar{\rho}\widetilde{u_i''Z''}\right) \tag{4.78}$$

The complexity added by turbulence, compared to laminar diffusion flames, comes from the averaging procedures. To determine average values, the mean value of Z is not sufficient. Instead higher moments need to be included, in the form of a Probability Density Function (PDF). When the PDF $P(Z)$ is known, the averaged quantities can be obtained via integration of the conditional averages and the PDF:

$$\bar{\rho}\widetilde{Y_k} = \int_0^1 (\overline{\rho Y_k \mid Z^*}) P\left(Z^*\right) \mathrm{d}Z^* \tag{4.79}$$

$$\bar{\rho}\widetilde{T} = \int_0^1 (\overline{\rho T \mid Z^*}) P\left(Z^*\right) \mathrm{d}Z^* \tag{4.80}$$

$$\bar{\rho}\overline{\dot{\omega}_k} = \int_0^1 (\overline{\rho\dot{\omega}_k \mid Z^*}) P\left(Z^*\right) \mathrm{d}Z^* \tag{4.81}$$

where $(\overline{\phi \mid Z^*})$ denotes the conditional average of quantity ϕ for a given value of the mixture fraction $Z = Z^*$.

In primitive variable approaches, assumptions are being made for the flame structure in order to deliver the conditional means $(\overline{\rho T \mid Z^*})$ and $(\overline{\rho Y_k \mid Z^*})$ from pre-computed libraries like in flamelet models [1]. This way, species mass fractions equations are no longer required and mean reaction rates do not need to be modeled. Instead, the CFD code only solves for the flow variables and mixture fraction variables to estimate, directly or indirectly, the probability density function $P(Z)$.

In reaction rate approaches on the other hand, balance equations for species mass fractions are solved and the mean reaction rates are modeled. Typical models used for this closure are the Eddy Dissipation Concept (EDC) [277], flame surface density flamelet models [278] and transported PDF models [279].

The primitive variable method is computationally more efficient than the reaction rate approach because species mass fractions balance equations are no longer required; but it is valid only under restrictive assumptions. In this section only primitive variable methods will be described.

1 Apart from tabulated methods, balance equations can be used for the estimation of the conditional means as in the case of Conditional Moment Closure (CMC) models [280].

4.5.1 *Chemical equilibrium model*

One of the simplest models includes the assumption of infinitely fast chemistry and the use of chemical equilibrium conditions. Under chemical equilibrium conditions, the flame structure only depends on the local mixture fraction, pressure and enthalpy. The conditional averages then reduce to:

$$\left(\overline{\rho Y_k \mid Z^*}\right) = \rho\left(Z^*\right) Y_k\left(Z^*\right) \quad ; \quad \left(\overline{\rho T \mid Z^*}\right) = \rho\left(Z^*\right) T\left(Z^*\right) \tag{4.82}$$

and hence the determination of $\widetilde{Y}_k$ and $\widetilde{T}$ reduces to the determination of the probability density function $P(Z)$ of the mixture fraction.

For engineering computations, a widely used, but approximate, solution is to presume the shape of the PDF using simple analytical functions. The β-function is the most popular presumed PDF function and depends only on two parameters, the mean mixture fraction $\widetilde{Z}$ and its variance $\widetilde{Z''^2}$:

$$P(Z) = \frac{\Gamma(a+b)}{\Gamma(a)\Gamma(b)} Z^{a-1}(1-Z)^{b-1} \tag{4.83}$$

with

$$a = \widetilde{Z}\left[\frac{\widetilde{Z}(1-\widetilde{Z})}{\overline{Z''^2}} - 1\right] \quad ; \quad b = \frac{a}{\widetilde{Z}} - a \tag{4.84}$$

The mixture fraction variance is typically modeled as:

$$\frac{\partial \bar{\rho}\widetilde{Z''^2}}{\partial t} + \frac{\partial \bar{\rho}\widetilde{u}_j\widetilde{Z''^2}}{\partial x_j} = \frac{\partial}{\partial x_j}\left(\left(\frac{\bar{\mu}}{Sc} + \frac{\mu_t}{Sc_t}\right)\frac{\partial \widetilde{Z''^2}}{\partial x_j}\right) - 2\bar{\rho}\widetilde{\chi} + 2\left(\frac{\bar{\mu}}{Sc} + \frac{\mu_t}{Sc_t}\right)\left(\frac{\partial \widetilde{Z}}{\partial x_j}\right)^2 \tag{4.85}$$

where $\widetilde{\chi}$ represents the scalar dissipation rate, defined as:

$$\bar{\rho}\tilde{\chi} = 2\rho\mathcal{D}\overline{\frac{\partial Z}{\partial x_i}\frac{\partial Z}{\partial x_i}} \tag{4.86}$$

The equilibrium model can be useful when simulating systems where the chemical time-scales are much faster than the turbulent ones, which is often the case when hydrogen/oxygen combustion is involved. For slower chemical reaction rates however, as in the case of hydrocarbon combustion, equilibrium conditions significantly overestimate the heat release and are no longer suitable.

4.5.2 *Steady flamelet model*

In order to include finite rate effects in tabulated methods, flamelet models are instead used. The basic idea of flamelet modeling is to assume that a small instantaneous flame element embedded in a turbulent flow has the structure of a laminar flame. This concept is

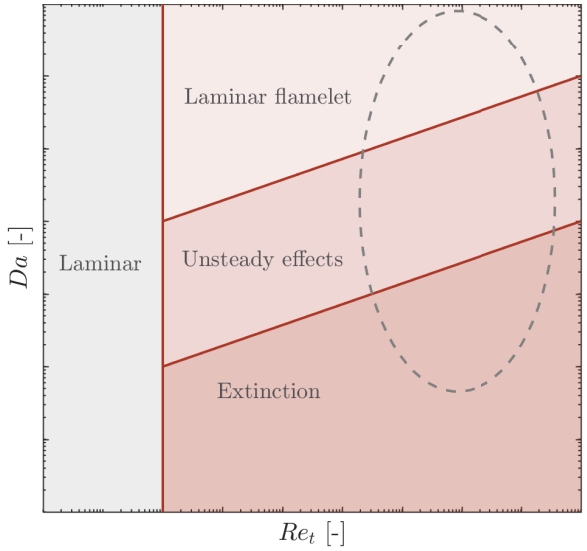

Figure 4.3: Non-premixed combustion diagram (adapted from Cuenot et al. [282]). The dashed line represents typical conditions found within rocket thrust chambers.

schematically illustrated in Figure 4.4. This assumption requires all reaction zones to be thin compared to turbulent flow scales, i.e. large Damköhler numbers.

It is important to note that in contrast to premixed flames, which have intrinsic properties and can typically be described by combustion regime diagrams (Borghi [281]), non-premixed structures lack those characteristic scales. The structure of diffusion flames is governed by the scalar dissipation rate and establishing a universal combustion diagram is not straightforward. Efforts to identify regimes based on the local Damköhler number Da and the turbulent Reynolds number Re_t have been carried out by Cuenot et al. [282]. A schematic representation of this classification is shown in Figure 4.3. In the turbulent regime range (higher Re_t values), the flame structure is not affected by turbulence and hence the assumption of laminar flamelet can be applied. This occurs up to a characteristic Damköhler number, underneath which unsteady effects come into play. For even lower Damköhler numbers, the chemical time-scales are much larger than the flow time-scales and hence quenching of the flame is reached. All three of the states can be found in typical thrust chambers. Within the reacting zone, where temperatures upwards of 3500 K are reached, the assumption of laminar flamelet is typically valid in the absence of transient effects. For re-ignition and local flame extinction however, the assumption does no longer hold.

In the steady flamelet model, the flame structure is first described as a function of the mixture fraction and the scalar dissipation rate at the flame location χ_{st}. The scalar dissipation χ_{st} is equivalent to the flame stretch and including this parameter allows to account for stretch effects and quenching. [283].

The flame structure is then given by a set of functions $T(Z, \chi_{st})$, $Y_k(Z, \chi_{st})$ which are calculated in a pre-processing step by solving multiple instances of laminar counterflow diffusion flames.

To solve the laminar counterflow diffusion flames two separate methodologies can be used:

- The solution of the counterflow diffusion equations in physical coordinates

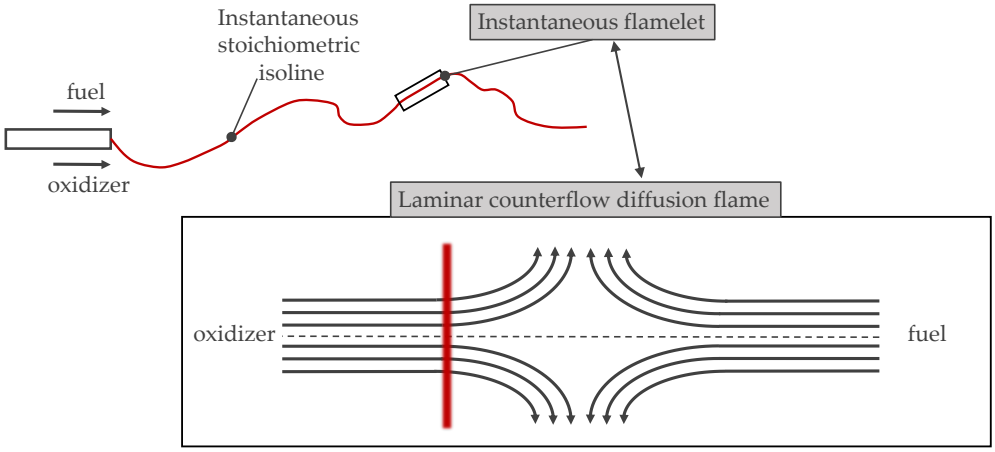

Figure 4.4: Flamelet concept for turbulent non-premixed flames. Adapted from Poinsot et al. [261].

- The solution of the flamelet equations in mixture-fraction space.

In the first case, an axisymmetric stagnation flow is solved, with conservation equations for continuity, radial momentum, energy and species being included in the set of equations. The set of equations is described in Section 5.3 in detail.

The second alternative is based on a coordinate transformation proposed by Peters, where the mixture fraction coordinate is used to describe the flame structure normal to the surface of the stoichiometric mixture. The flamelet equations under assumption of unity Lewis number consist of an equation for each species and one for the temperature or enthalpy, for which several formulations have been proposed [283–285]. The one employed in the work by Peters [286] is shown here:

$$\frac{\partial Y_k}{\partial t} = \frac{1}{2}\chi\frac{\partial^2 Y_k}{\partial Z^2} + M_k\frac{\dot{\omega}_k}{\rho} \tag{4.87}$$

$$\frac{\partial T}{\partial t} = \frac{\chi}{2}\frac{\partial^2 T}{\partial Z^2} - \frac{1}{\rho c_p}\sum_{k=1}^{N_{sp}} M_k\dot{\omega}_k H_k \tag{4.88}$$

A typical profile for the scalar dissipation rate χ as a function of the mixture fraction is given by the parametric distribution in Equation 4.89, following the work of Peters [283], whereas further parametrizations have been put forward by Pitsch et al. [284] and Kim et al. [285].

$$\chi(Z) = \chi_{st}\exp\left[2\left[\text{erfc}^{-1}\left(2Z_{st}\right)\right]^2 - 2\left[\text{erfc}^{-1}(2Z)\right]^2\right] \tag{4.89}$$

Upon solution of the laminar flamelets, the profiles are stored in flamelet libraries. The mean turbulent temperature and species mass fractions are then evaluated by using the presumed PDF:

$$\bar{\rho}\widetilde{Y}_k = \int_0^\infty\int_0^1 \rho Y_k\left(Z,\chi_{st}\right)P\left(Z,\chi_{st}\right)\mathrm{d}Z\mathrm{d}\chi_{st} \tag{4.90}$$

$$\bar{\rho}\widetilde{T} = \int_0^\infty \int_0^1 \rho T\left(Z, \chi_{st}\right) P\left(Z, \chi_{st}\right) \mathrm{d}Z\mathrm{d}\chi_{st} \tag{4.91}$$

Statistical independence of the mixture fraction Z and its scalar dissipation rate χ_{st} is often assumed leading to $P(Z, \chi_{st}) = P(Z) \cdot P(\chi_{st})$. For the mixture fraction PDF, β functions are typically used, whereas the scalar dissipation PDF is modeled either via a Dirac function [287] or via log-normal distribution [288].

After the PDF integration, the resulting turbulent tables are parametrized based on the mean mixture fraction $\widetilde{Z}$, its variance $\widetilde{Z''^2}$ and the scalar dissipation rate at stoichiometry $\widetilde{\chi_{st}}$. During the CFD simulation, the fields for $\widetilde{Z}$ and $\widetilde{Z''^2}$ are obtained via solution of the corresponding transport equations (Equation 4.78 and Equation 4.85), whereas χ_{st} is evaluated using an algebraic expression

$$\chi_{st} = 2(\mu + \mu_t)\left(\frac{\partial \widetilde{Z''^2}}{\partial x_j}\right)^2 \tag{4.92}$$

In RANS simulations, it is often replaced by:

$$\widetilde{\chi_{st}} = 2\frac{\varepsilon}{k}\widetilde{Z''^2} \tag{4.93}$$

Compared to models assuming infinitely fast chemistry, in the steady flamelet model, finite rate chemistry effects are measured through scalar dissipation rates at the stoichiometric conditions. The scalar dissipation rate is hence quantifying the deviation from chemical equilibrium conditions and is correlated to available resolved quantities (usually mixture fraction distribution and turbulent time scales) as shown in Equation 4.93.

4.5.3 *Flamelet progress variable model*

The Flamelet Progress Variable (FPV) model was proposed by Pierce et al. [289] as an alternative modeling method for non-premixed turbulent combustion. Similar to the steady flamelet model, the FPV model is also based on an indirect mapping approach, whereby all of the detailed chemical processes are mapped to a reduced system of tracking scalars. In this case, the scalars considered are the mixture fraction variable, which tracks the mixing of fuel and oxidizer, and the progress variable, which tracks the global extent of reaction of the local mixture. The motivation behind this model is that the mixture fraction alone does not contain any intrinsic information about chemical reactions and hence a non-conserved quantity like the progress variable is required, in order to be independent from mixture fraction.

The progress variable C is commonly defined from a combination of reactive scalars such as chemical species or temperature and represents the completeness of the combustion. Although its definition is not unique, the choice of a suitable progress variable is typically guided by ensuring that the definition of C results in a transport equation that can be conveniently solved in a combustion simulation. Moreover it is essential that all parameters which define the manifold are independent of one another and that the set of parameters

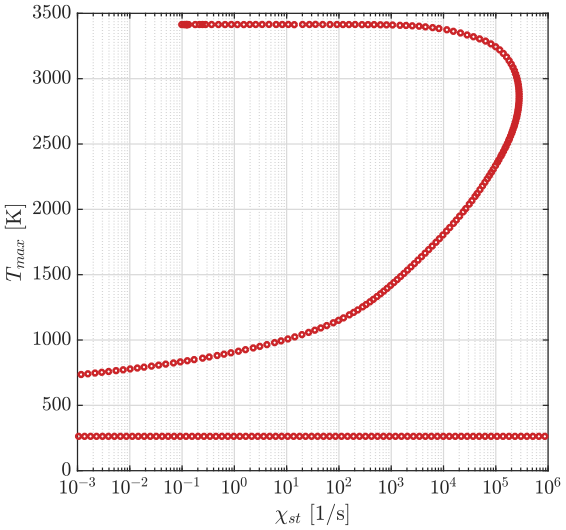

Figure 4.5: S-curve for methane/oxygen diffusion flame at $p = 20\,\text{bar}$. The inlet temperature for oxidizer and fuel are set to 270 K. Each point corresponds to a laminar counterflow diffusion flame.

from which the manifold is formed uniquely characterize each point in the thermochemical state-space [290]. Although several definitions based on sum of major species have been proposed [289, 291, 292] and studies dealing with the optimal definition of C have been carried out [292], for combustion applications of methane/oxygen, the definition by Ihme et al. [292] is usually employed:

$$C = Y_{H_2O} + Y_{H_2} + Y_{CO_2} + Y_{CO} \tag{4.94}$$

In order to produce the laminar flamelet tables $Y_k = Y_k(Z, C)$ and $T = T(Z, C)$, several instances of the counterflow diffusion flame are solved, in a similar manner as for the steady flamelet approach. The complete range of flame states, from completely extinguished (mixing without reaction) to completely reacted (equilibrium chemistry) including the unstable branch, is represented in the library. An example for the S-curve resulting from this calculation in a CH_4/O_2 combustion case is shown in Figure 4.5. This is one of the major differences to the steady flamelet model, where only the stable branch in included in the tables as explained in Figure 4.3. Each of the laminar flamelets is then mapped to a value of the progress variable C.

Note, that apart from the species mass fractions and temperature, the progress variable reaction rate is also tabulated as a function of Z and C:

$$\dot{\omega}_C = \dot{\omega}_C(Z, C) \tag{4.95}$$

This results from the fact that C is a non-conserved variable (as it represents the sum of species mass fractions) and its transport equation is given by Equation 4.97. As a reference

the transport equation for the resolved mixture fraction in the LES framework is given by Equation 4.96.

$$\frac{\partial}{\partial t}(\overline{\rho}\widetilde{Z}) + \frac{\partial}{\partial x_i}\left(\overline{\rho}\widetilde{u_i}\widetilde{Z}\right) = \frac{\partial}{\partial x_i}\left[\left(\rho D + \frac{\mu_t}{Sc_t}\right)\frac{\partial \widetilde{Z}}{\partial x_i}\right] \tag{4.96}$$

$$\frac{\partial}{\partial t}(\overline{\rho}\widetilde{C}) + \frac{\partial}{\partial x_i}\left(\overline{\rho}\widetilde{u_i}\widetilde{C}\right) = \frac{\partial}{\partial x_i}\left[\left(\rho D + \frac{\mu_t}{Sc_t}\right)\frac{\partial \widetilde{C}}{\partial x_i}\right] + \widetilde{\dot{\omega}_C} \tag{4.97}$$

Once the flamelet library is computed and assumed subgrid PDF integrals are evaluated[2]similar to the steady flamelet case, lookup tables can be generated to provide the filtered chemical functions of the quantities readily available from LES, namely $\widetilde{Z}$, $\widetilde{Z''^2}$ and $\widetilde{C}$.

With the FPV model, one of the more conspicuous limitations of the steady-flamelet model, which is its inability to properly account for ignition and extinction phenomena is bridged. This way unsteady, lifted flame dynamics can be simulated.

4.6 MODELING OF NON-ADIABATIC EFFECTS

The classical flamelet model is based on the generation of libraries resulting from adiabatic counterflow diffusion flames. The effect of heat losses on the reaction rates and on the chemical composition of the gas is hence not accounted for. As most engineering applications including rocket thrust chambers consist of wall-bounded flows with heat losses, this effect has to be included as an additional dimension in the flamelet tables.

Previous studies have included a radiation source term in the flamelet equations [293, 294], which is however not suitable to describe thermal losses due to convective heat transfer. In the works of Proch et al. [295] and Kishimoto et al. [296] on the other hand, the chemical reaction rates were reduced by a constant factor in the counterflow diffusion flame equations. The use of this additional dimension for the flamelet tables in [296] led to satisfactory agreement of the wall heat fluxes with experimental data for a $GH_2/GO2$ rocket combustor. Although effective, applying a uniform scaling factor to the reaction term is restrictive with regards to the heat loss profiles that can be prescribed. For that reason, more representative profiles resulting from conductive heat loss considerations have been applied by Cecere et al. [297] and Fiorina et al. [291].

Further methods include the inclusion of a source term in the temperature equation, the direct prescription of an enthalpy profile and the introduction of a permeable isothermal wall. Those methods are inspected in more detail as they are used in Chapter 6.

4.6.1 *Energy source term*

The energy source method involves the introduction of a heat loss source term $\dot{\mathcal{Q}}$ in the heat equation of the counterflow diffusion flame. This can be done either in physical or in

2 The joint subgrid PDF for C and Z assumes statistical independence, with $P(Z,C) = P(C \mid Z) \cdot P(Z)$ and with the $P(C \mid Z)$ PDF being modeled as a delta Dirac function.

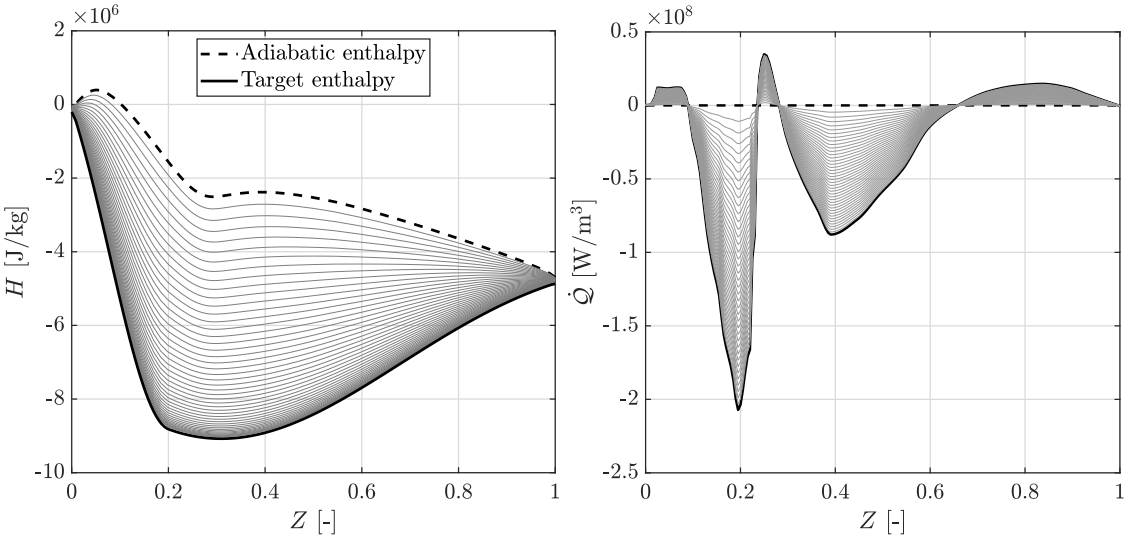

Figure 4.6: Enthalpy profile (left) and heat loss source term (right) in mixture fraction space. The light curves represent intermediate iterations.

mixture fraction space. In the case of physical coordinates, the modified energy equation (Equation 5.4) reads:

$$\rho c_p u \frac{\partial T}{\partial x} = \frac{\partial}{\partial x}\left(\lambda \frac{\partial T}{\partial x}\right) - \sum_k j_k c_{p,k} \frac{\partial T}{\partial x} - \sum_k H_k M_k \dot{\omega}_k + \dot{\mathcal{Q}}(x) \tag{4.98}$$

The source term $\dot{\mathcal{Q}}(x)$ is defined as a function of the axial coordinate and it is modified iteratively until the desired enthalpy profile is achieved. An example for the target enthalpy together with the starting enthalpy profile corresponding to the adiabatic conditions[3] are shown in the left sub-figure of Figure 4.6. Intermediate solutions as well as the resulting heat source are plotted in the same figure.

The method was utilized in the works of Perakis et al. [298] and Rahn et al. [299]. In the first work, the optimization of the source term to achieve the desired enthalpy profile was performed with the Levenberg-Marquardt method. The update for iteration i, using the Jacobian (sensitivity) matrix $\mathbf{S}$ is shown in Equation 4.99[4] .

$$\dot{\mathcal{Q}}^{i+1}(x) = \dot{\mathcal{Q}}^{i}(x) + \left[\left(\mathbf{S}^i\right)^T \mathbf{S}^i + \xi^i I\right]^{-1} \left(\mathbf{S}^i\right)^T \cdot \left(H^i(x) - H_{tar}(x)\right) \tag{4.99}$$

4.6.2 *Enthalpy prescription*

Similar to the source term method, in the enthalpy prescription approach, a target enthalpy profile is defined. The idea is based on replacing the energy flamelet equation (Equation 4.88) by imposing an enthalpy profile as an equality constraint in the mixture space

3 Note that in this example, the adiabatic enthalpy profile in mixture fraction space is not simply a straight line, as preferential diffusion effects are included. A linear profile is obtained only when the assumption of unity Lewis number is made.

4 The damping factor ξ accounts for the fact that this optimization problem is ill-conditioned, i.e. $\left|\left(\mathbf{S}^i\right)^T \mathbf{S}^i\right| \approx 0$.

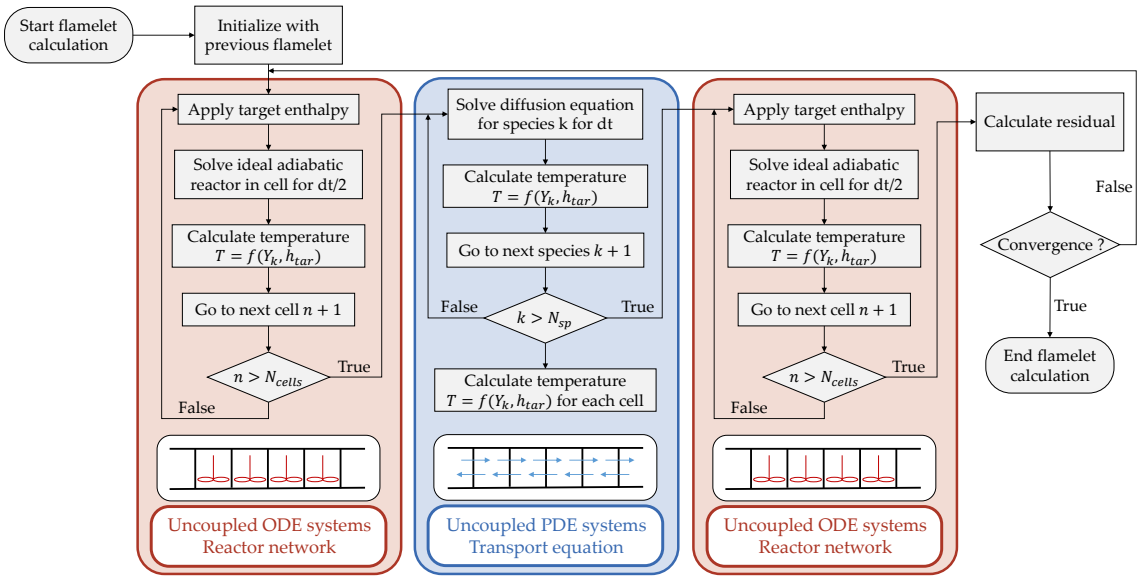

Figure 4.7: Flow chart of the splitting algorithm for the solution of the flamelet equations.

frame. By omitting the energy/temperature equation, the flamelet calculation is reduced to a boundary vale problem consisting of the mass fraction equations (Equation 4.87) and an optimality constraint: $H(Z) = H_{tar}(Z)$.

This approach was used by Kim et al. [300] and was also adapted in the work of Perakis et al. [298]. For the solution of the resulting boundary value problem, an operator splitting technique proposed by Strang [301] and Yanenko [302] can be applied, leading to a computationally efficient solution. By employing the operator splitting, the non-linear algebraic equations resulting from the discretization of Equation 4.87 are broken into two smaller systems:

- A chemical kinetics equation at each cell in the Z-space, decoupled from other cells (initial value problem)
- A diffusion equation for each chemical species, decoupled from the mass fractions of the other species (parabolic problem)

The solution of the two problems is alternated repeatedly making it possible to match the accuracy of the fully coupled problem, and the process is schematically illustrated in the flow chart of Figure 4.7.

Both the source term method and the enthalpy prescription method deliver the same results for species and temperature, when the same target enthalpy level is defined and when the same assumptions about the transport properties (e.g. unity Lewis number) are made [298]. The choice of the enthalpy profiles for the tabulation of the non-adiabatic effects is important for these two methods, as it can influence the resulting reaction rates and consequently mass fractions [303].

4.6.3 *Permeable wall method*

Modeling of wall-heat loss effects and flame/wall interaction in the context of the laminar flamelet formulation using an additional thermal boundary condition was proposed in

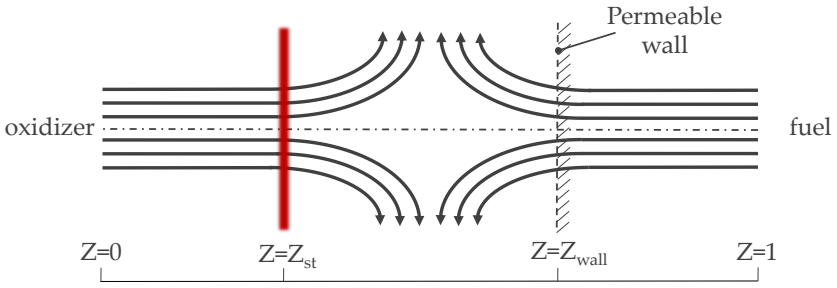

Figure 4.8: Schematic of a counterflow diffusion flame configuration with permeable wall.

the work of Wu et al. [304]. In this model, the direction of heat flux is assumed to be primarily aligned with the gradient of mixture fraction, i.e. normal to the flame surface. As a result, the effect of heat-loss can be introduced by assuming the presence of a permeable wall boundary condition, the location of which is denoted by Z_{wall} in the mixture fraction coordinate system.

By adding this permeable isothermal and chemically inert wall into the counterflow diffusion flame, the gas temperature is kept low from the fuel inlet up to the Z_{wall} location. This configuration results in a heat flux normal to the flame surface toward the permeable wall. Based on this modeling concept, Wu et al. [304] and later Ma et al. [305] formulated the flamelet equations for the domain $0 < Z < Z_{wall}$, which correspond to the classical flamelet equations (Equation 4.87 and Equation 4.88). For $Z_{wall} < Z < 1$, the source terms are set to zero, and hence an inert mixing process is solved. The coupling of the two domains is completed by enforcing the boundary conditions $T = T_{wall}$, $Y_k(Z^+_{wall}) = Y_k(Z^-_{wall})$ and $\frac{\partial Y_k}{\partial Z}(Z^+_{wall}) = \frac{\partial Y_k}{\partial Z}(Z^-_{wall})$. By varying the permeable wall position in mixture fraction space Z_{wall} and its temperature T_{wall}, the flame can be exposed to increasing heat loss until thermal quenching occurs.

The introduction of the Z_{wall} as an additional dimension in the flamelet manifold allows for the quantification of the heat loss effects. The value of the look-up variable Z_{wall} during the CFD is calculated by using the cell values for energy and temperature as described in Ma et al. [305]. The method has been successfully applied both using the FPV approach [304, 305] as well as the steady flamelet model [303, 306].

Recently, comparisons between the enthalpy-prescription method and the permeable wall method for the introduction of heat-loss effects in the flamelet tables were reported in the work of Breda et al. [303]. When the enthalpy profiles from the permeable-wall simulations are used in the enthalpy-prescription model, identical results for both the temperature and the species profiles were obtained. This agreement is shown in Figure 4.9.

4.7 WALL TREATMENT

The two main approaches for the wall treatment when dealing with wall-bounded flows is either resolving the wall down to the viscous sub-layer or using wall models. The main motivation behind the use of wall models is that the computational time connected to resolving the wall in LES poses a significant obstacle in industrial applications.

Chapman [307] estimated that the resolution required to resolve the outer layer of a growing boundary layer is proportional to $Re^{0.4}$, whereas for the viscous sub-layer (which

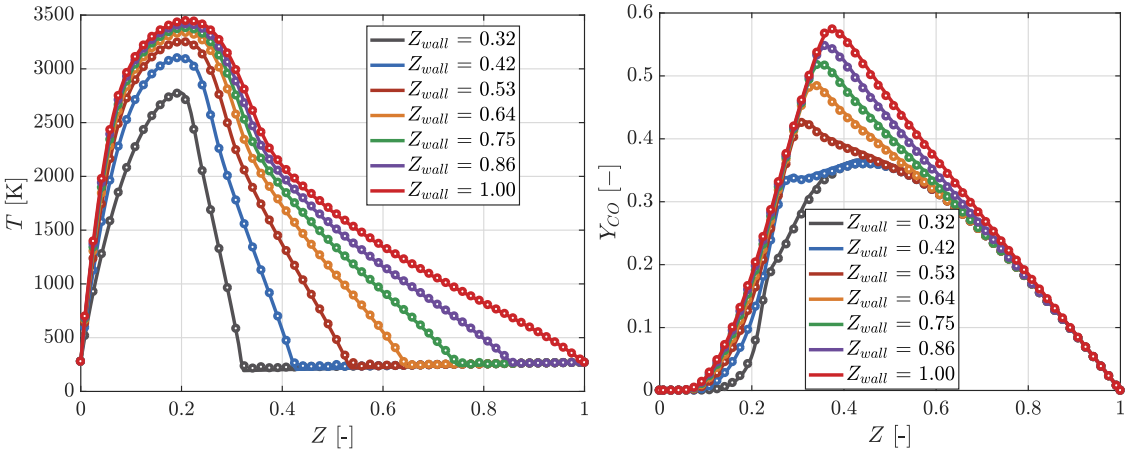

Figure 4.9: Comparison of temperature (left) and CO mass fraction (right) profiles for two different non-adiabatic models. The lines represent the results of the permeable wall method and the circles the results of the enthalpy-prescription [303].

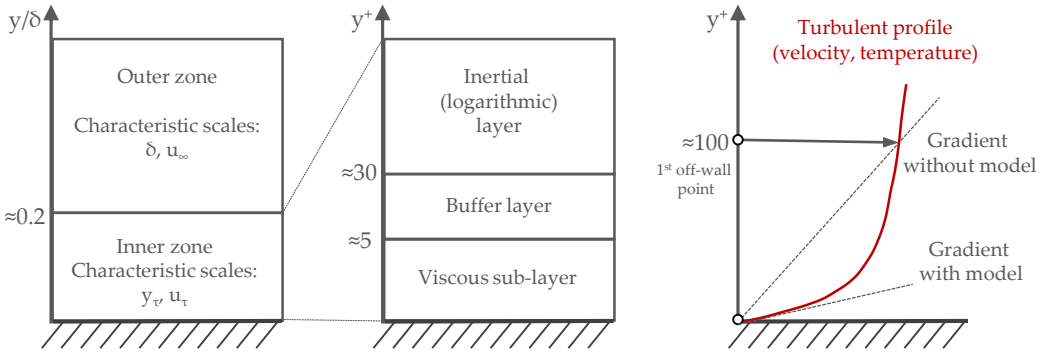

Figure 4.10: Schematic of the turbulent boundary layer in different zones (left) and wall gradient estimation (right). Adapted from Potier [309].

only accounts for approximately 1-5% of the boundary-layer thickness) the number of points needed increases at least like $\mathrm{Re}^{1.8}$. The reason is that in the near-wall region, the Re-dependence of the resolution is much steeper, as the near-wall eddies that need to be resolved scale with wall units. As the Reynolds number is increased, the physical dimensions of these eddies decrease much more rapidly than the boundary-layer thickness, resulting in more stringent grid requirements. An overview of the different regions within a turbulent boundary layer are schematically shown in Figure 4.10.

Apart from the number of cells, the time-step also has to be taken into account. This is generally determined by a Courant–Friedrichs–Lewy (CFL) condition $dt \propto \Delta x/u$, which means that the number of time steps required to perform a simulation is proportional to the number of grid points in one direction, with $N_t \propto Re^{0.2}$ for the outer layer and $N_t \propto Re^{0.6}$ for the inner layer[5]. The total cost of a calculation, therefore, scales like $Re^{0.6}$ for the outer layer and like $Re^{2.4}$ if the inner layer is to be resolved [308].

In the inner layer, the molecular and turbulent diffusion phenomena compete. It can be divided into three sub-layers:

5 This is based on the scaling of the boundary layer thickness as $\delta \propto Re^{-0.2}$ [308]

- The viscous sub-layer, where molecular diffusion dominates and the flow is practically laminar
- The inertial or logarithmic sub-layer, where turbulent diffusion dominates
- The buffer sub-layer, which is the intermediate zone between the other two sub-layers and where turbulent and molecular diffusion phenomena are of the same order.

To describe the characteristic scales in this zone, the friction velocity $u_\tau = \sqrt{\tau_w/\rho_w}$, friction distance $y_\tau = \nu_w/u_\tau$ and friction temperature $T_w = \dot{q}_w/(\rho_w c_{p,w} u_\tau)$ are used and lead to the definition of the normalized units $u^+ = u/u_\tau$, $y^+ = y/y_\tau$ and $T^+ = (T - T_w)/T_\tau$.

There have been many proposed methods for modeling of the inner layer in LES, which are summarized in the the reviews by Piomelli and Balaras [310] and Spalart [311]. These wall-modeled approaches generally fall into one of two categories: methods that model the wall shear stress and wall heat flux directly, and methods that switch to a RANS description in the inner layer. The second category includes hybrid LES/RANS and Detached Eddy Simulation (DES) and will not be further investigated in this work.

For the direct estimation of the the wall stress τ_w and wall heat flux, wall laws are typically employed in order to correctly estimate the velocity and temperature gradients without resolving the inner layer (as shown in the left sub-figure of Figure 4.10). The standard wall law [312] predicts a linear profile for both velocity and temperature in the viscous sub-layer:

$$u^+ = y^+ \tag{4.100}$$

$$T^+ = Pry^+ \tag{4.101}$$

and a logarithmic profile in the inertial sub-layer:

$$u^+ = \frac{1}{0.41} \ln\left(y^+\right) + 0.55 \tag{4.102}$$

$$T^+ = \frac{Pr_t}{0.41} \ln\left(y^+\right) + \left(3.85 Pr^{1/3} - 1.3\right)^2 + 2.12 \ln(Pr) \tag{4.103}$$

It has been demonstrated in the work of Cabrit [313] that the assumptions made to derive standard wall laws do not hold for compressible boundary layers where the ratio of gas temperature to wall temperature is high. In that case temperature and density gradients have to be accounted for in the boundary layer, resulting to a "coupled" wall law. This requires the simultaneous solution of the coupled velocity and temperature laws in order to retrieve the wall stress and heat flux.

A further wall-modeling approach involves the solution of the unsteady Thin Boundary Layer Equations (TBLE) as a two-layer model on an embedded grid. The TBLE are a set of simplified partial differential equations derived from the Navier-Stokes equations under the assumption that in the very thin wall region, the wall-tangential length scales are much

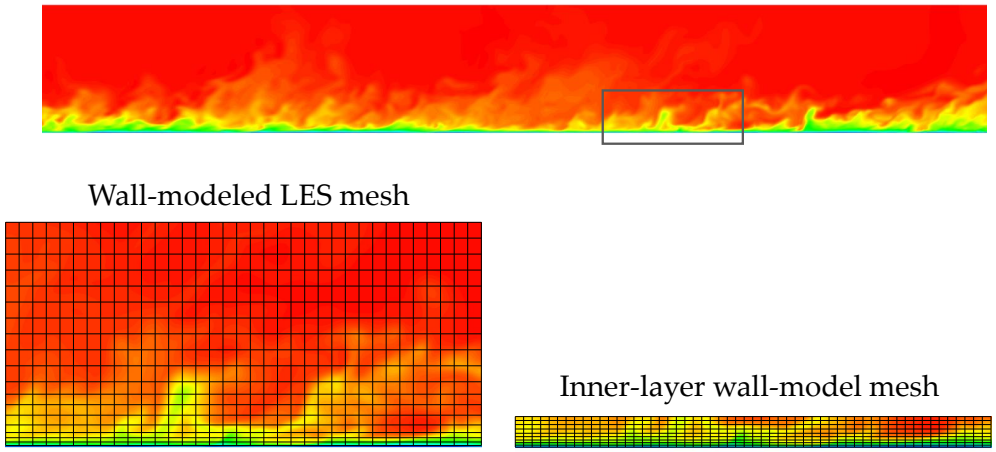

Figure 4.11: Sample of meshes for wall-modeled LES. LES grid based on outer length scales only (left) and auxiliary wall-model grid in the inner layer (refined in the wall-normal direction) for estimation of the wall shear stress and heat flux. Adapted from Kawai et al. [316].

larger than the wall-normal ones, and wall-normal direction derivatives are much bigger than derivatives of wall-tangential directions [314]. This method allows the inclusion of more dynamics in the near-wall region, compared to regular wall laws [315].

The LES mesh is designed to resolve only the outer-layer scales but not the viscous motions in the inner layer. Therefore, the necessary grid resolution scales with the boundary layer thickness δ, and the grid spacing in viscous units is irrelevant. The wall shear stress τ_w and wall heat flux $\dot{q}_w$ are computed by solving the TBLE equations on an auxiliary grid in the inner layer to be provided to the concurrent LES as approximate flux wall boundary conditions. This grid is embedded in the LES mesh and refined in the wall-normal direction, as illustrated in Figure 4.11.

The wall-model equations are forced at their top boundary by the instantaneous solution in the LES at the corresponding point. Although the inner-layer wall-model mesh is embedded in the LES mesh, the only information transferred between the models is at the top of the wall-modeled layer (instantaneous LES solution imposed on wall-model) and at the wall (instantaneous wall shear stress and heat flux from the wall-model imposed on the LES). For that reason the term "approximate boundary condition" model is also used to describe the approach. The development of the model for compressible flows with heat transfer has been carried out by Kawai et al. [316] and Devesa [317]. For reacting flows, Muto et al. [318] included the effects of chemical reactions and variable properties into the boundary layer equations and applied the model to the simulation of hydrogen/oxygen rocket combustors. The reactions were assumed to be in chemical equilibrium in the inner layer, which is however not a suitable approach when dealing with methane/oxygen chemistry, as the results in Chapter 5 show.

5 ANALYSIS OF RECOMBINATION REACTIONS

The world of chemical reactions is like a stage,
on which scene after scene is ceaselessly played.
The actors on it are the elements.

— Clemens Winkler

The heat losses occurring in the vicinity of cooled walls in rocket thrust chambers, lead to a non-adiabatic environment. The reduced enthalpy (compared to the adiabatic conditions) initiates additional chemical reactions in the turbulent boundary layer, which are typically exothermic in nature, thereby enhancing the energy release close to the wall. As this extra contribution to the heat release can have a non-negligible impact on the experienced heat loads, it has to be accounted for in numerical models dealing with the prediction of flow and combustion conditions within rocket engines.

In the present chapter, an effort to understand the nature of the aforementioned recombination reactions is carried out. Specifically, the conditions at which the reactions are initiated and the time-scales at which they progress is evaluated. Moreover, the impact that they have on the wall heat loads is isolated and quantified.

This investigation is performed by examining representative canonical test-cases with increasing degree of complexity as Figure 5.1 indicates.

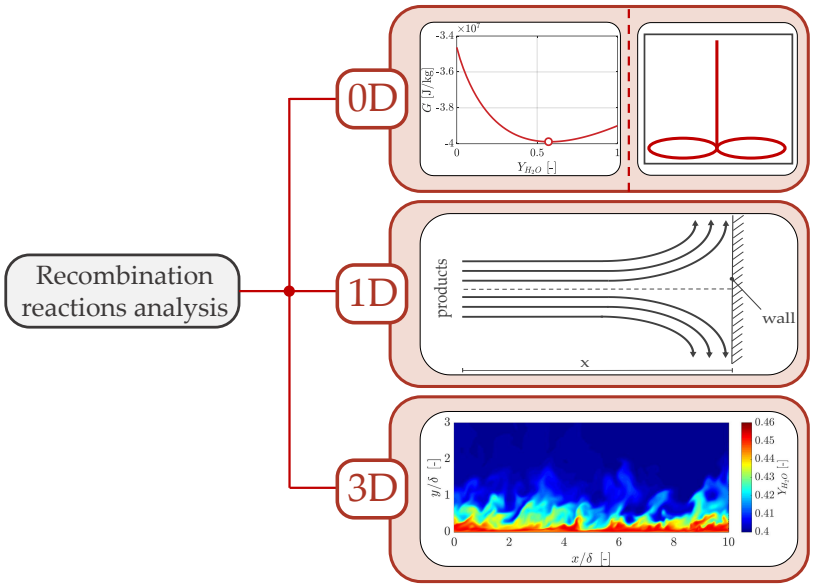

Figure 5.1: Schematic layout of the canonical test-cases included in the analysis of the recombination reactions.

First, two zero-dimensional problems are presented: a chemical equilibrium computation and an isothermal, isobaric, perfectly stirred reactor. In the equilibrium computations,

the minimization of the systems Gibb's enthalpy G is carried out. In the ideal reactor simulation, a perfect mixing is assumed and the gas mixture is observed while evolving in time. As the time approaches infinity, the reactor thermochemical state, asymptotically reaches the chemical equilibrium solution. The open-source tool Cantera [319] is employed for the computation.

The dimensionality of the problem is then increased by one, as an axisymmetric stagnation flow is investigated. Hot products corresponding to the equilibrium solution are released in a flow impinging against an isothermal, inert wall. The recombination reactions and resulting wall loads are then analyzed.

Finally, a high-fidelity three-dimensional DNS of a reacting boundary layer is carried out. The evaluation of the results gives significant insights into the locations at which the bulk of the chemical energy is released, the main reaction pathways leading to the recombinations, and the interaction with the turbulent structures.

For all four computations, operating points which are typical for rocket engines applications are chosen. The examined pressure values range from 20 bar up to 100 bar, which covers a significant portion of sub-scale and flight hardware. However, the main focus is placed in the lower band of the pressure spectrum, which is mainly found in sub-scale combustors, as well as pressure-fed engines used on upper stages and satellite systems. As the typical mixture load points in methane/oxygen applications are fuel-rich, conditions corresponding to $O/F < 4$ are mainly presented.

5.1 CHEMICAL EQUILIBRIUM

In the first step, the chemical equilibrium thermochemical state is computed for the methane/oxygen mixture in the entire range of mixture fraction values. The results for the temperature and species composition from the adiabatic chemical equilibrium calculation are shown in Figure 5.2 and Figure 5.3[1]. The maximal temperature occurs close to the stoichiometric mixture fraction ($Z_{st} = 0.2$), while the temperature approaches the pure oxidizer and pure fuel values on either side of its maximum. Close to $Z \approx 0.4$, a reduction in the slope of the temperature profile can be observed. By comparing it to the mass fractions of CH_4 and H_2O, a correlation between the temperature and species profiles can be found, as the change in the slope coincides with the mixture fraction at which the methane mass fraction drops to 0 with a subsequent increase in the production of water. Apart from water, the hydroxyl radical OH, carbon dioxide CO_2 and the H and O radicals have local maxima in the vicinity of stoichiometry. Carbon monoxide, also appears in large mass fractions, approaching 70% in the fuel-rich region.

The pressure dependency of the chemical equilibrium species is also included in Figure 5.2 and Figure 5.3, as three distinct levels ranging from 20 bar to 100 bar are shown. A higher combustion pressure expedites an increase in exothermic recombination reactions leading to larger temperature values in chemical equilibrium. This can be confirmed when observing that the O, H, OH, H_2 concentrations decrease with increasing pressure, whereas H_2O and CO_2 experience larger values. The effect of the shift in chemical composition on the temperature mostly prevails close to stoichiometry ($Z \approx 0.1 - 0.3$) and in the fuel-rich region ($Z \approx 0.42 - 0.8$). As elaborated on in the following sections however, the time-scales at which the reactions responsible for the shift in equilibrium evolve, are very slow.

1 For each mixture fraction value, the initial temperature of the oxygen/methane mixture is set at 270 K.

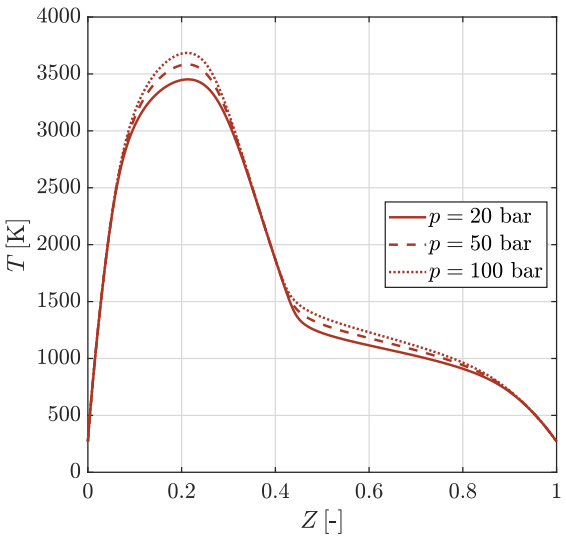

Figure 5.2: Temperature as a function of mixture fraction for the methane/oxygen chemical equilibrium calculation.

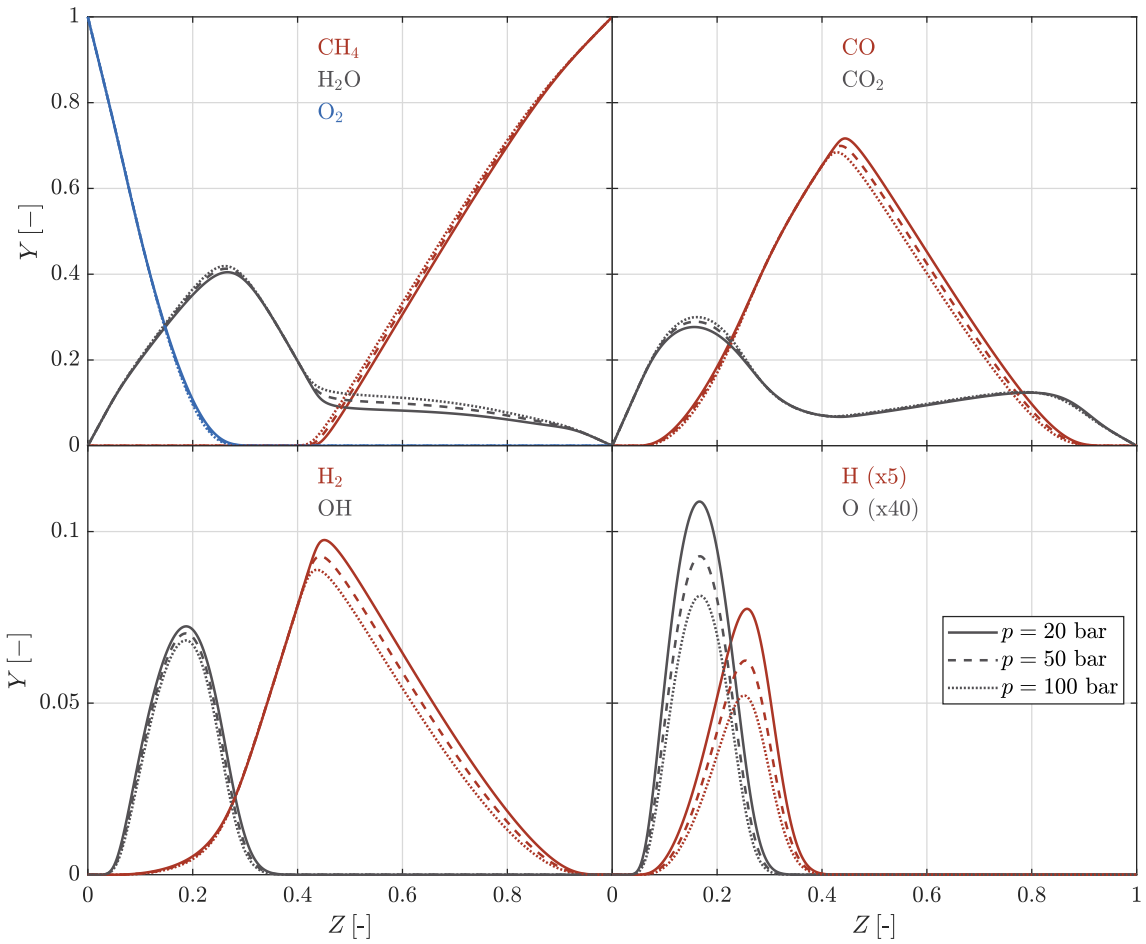

Figure 5.3: Species mass fractions as a function of mixture fraction for the methane/oxygen chemical equilibrium calculation.

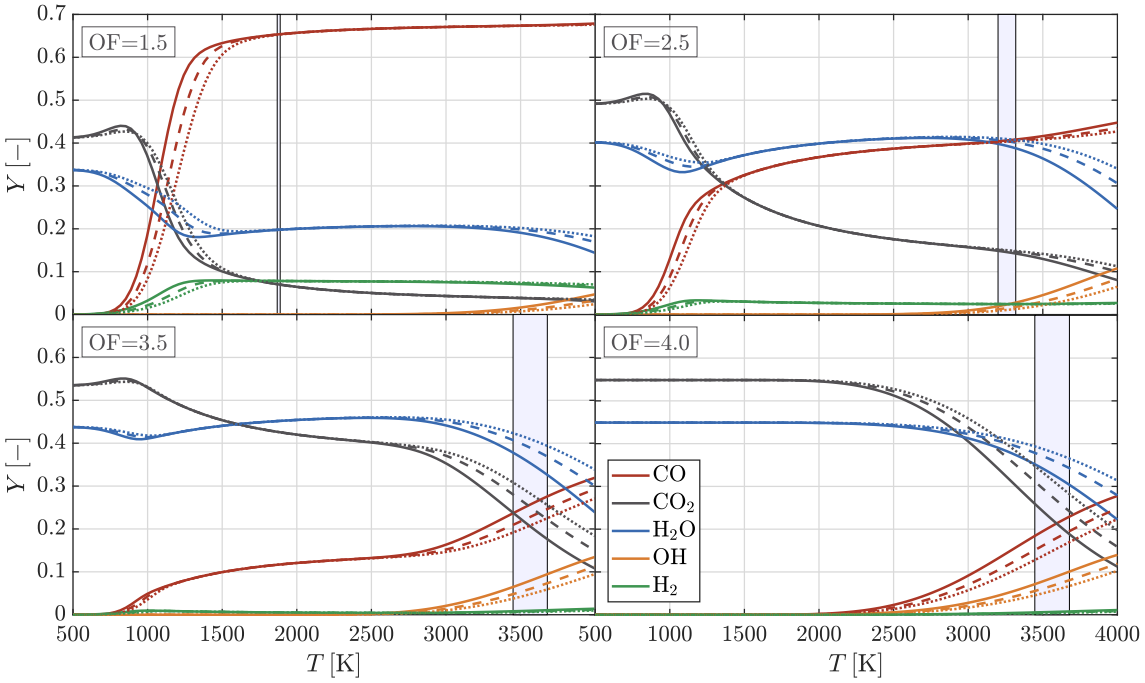

Figure 5.4: Species mass fractions as a function of temperature for the chemical equilibrium calculations. The different types of lines correspond to different pressure levels: $p = 20$ bar (——), $p = 50$ bar (- - -) and $p = 100$ bar (·····).

The results shown in Figure 5.2 and Figure 5.3 correspond to adiabatic chemical equilibrium calculations given a constant enthalpy level. In order to understand the effect of low-enthalpy environment and heat-loss on the gas composition, chemical equilibirum results at different temperature levels are shown in Figure 5.4. In this figure, results for four different O/F values are presented[2]. The areas shaded in blue correspond to the adiabatic conditions and can be hence compared to the results from Figure 5.3[3]. Temperature values on the left of the shaded region correspond to sub-adiabatic enthalpies and values to the right to super-adiabatic conditions.

A common occurrence in all four O/F points, is the fact that a reduction in temperature gives rise to two major recombination processes: the recombination of CO to CO_2 and the recombination of OH to H_2O. This leads to a drop in the CO and OH mass fractions and a resulting increase in CO_2 and H_2O. As the temperature approaches values which are typical for rocket engine walls (between 500 K and 1000 K), a complete depletion of CO is predicted, which occurs for different temperature values in each O/F. The OH depletion happens even sooner, as OH mass fractions drop below 0.1% already at 2000 K. For temperatures below the value of full recombination of carbon monoxide and hydroxyl radical, the mass fractions of water and carbon dioxide reach an approximately constant plateau and no further changes in composition are observed. Similar to the observations made for the adiabatic conditions, the effect of the pressure on the species mass fractions is that it favors the recombinations and hence the production of water and carbon dioxide.

2 Each O/F point corresponds to a mixture fraction value. For the chosen points: $O/F = 1.5$ corresponds to $Z = 0.4$, $O/F = 2.5$ to $Z = 0.286$, $O/F = 0.35$ to $Z = 0.222$ and $O/F = 4.0$ to $Z = 0.2$.

3 Note that it is a temperature range and not a single value, as multiple pressure levels are plotted in each sub-figure and the equilibrium temperature is pressure-dependent.

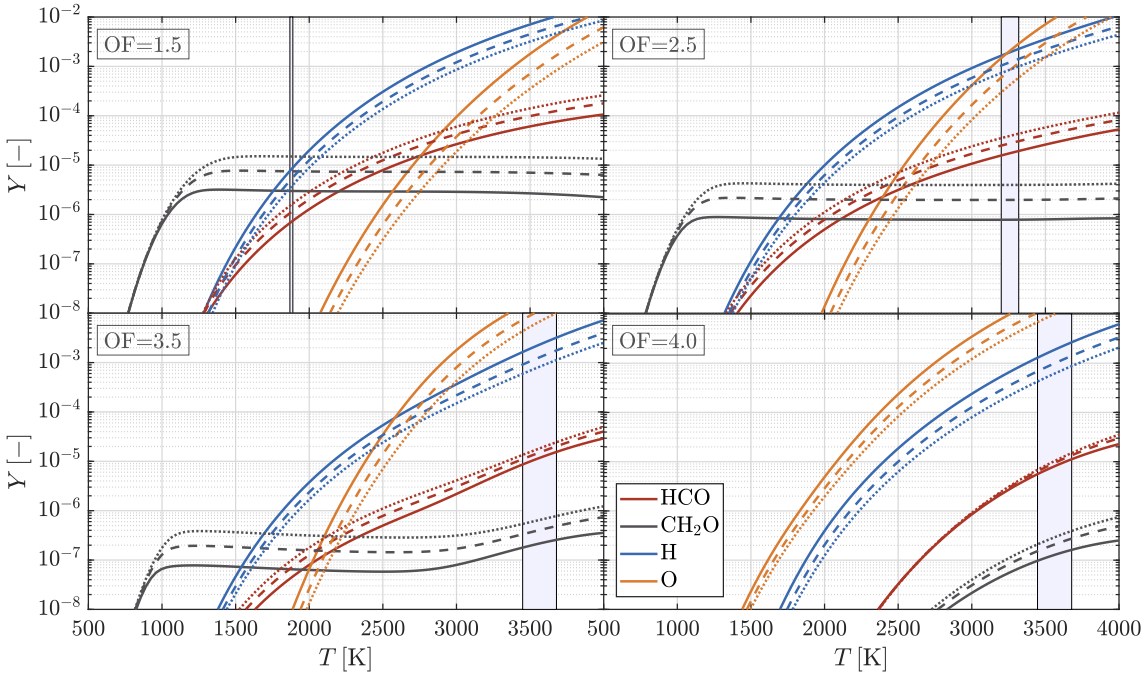

Figure 5.5: Minor species mass fractions as a function of temperature for the chemical equilibrium calculations. The different types of lines correspond to different pressure levels: $p = 20$ bar (——), $p = 50$ bar (- - -) and $p = 100$ bar (·····).

Similar to the mass fractions of major species that are illustrated in Figure 5.4, the minor mass fractions in Figure 5.5 also confirm the increase in the degree of recombination at lower temperatures. All chemical radicals shown in this figure appear to sharply recombine when reaching sub-adiabatic conditions.

The response of the system to a reduction in temperature is a direct result of Le Chatelier's principle [320] according to which:

"When any system at equilibrium for a long period of time is subjected to a change in concentration, temperature, volume, or pressure, the system changes to a new equilibrium, and this change partly counteracts the applied change."

A reduction of the gas temperature will lead to a new system equilibirum that will try to counteract this change. As shown in Section 5.2, the recombination reactions are exothermic and potentially lead to an increase in temperature. Therefore, the reduction of temperature shifts the composition towards more stable species like H_2O and CO_2 in an effort to counteract the applied change.

The same principle can be applied for an increase in pressure. If a system at equilibrium is compressed, then the reaction will tend to adjust so as to minimize the increase in pressure. This it can do by reducing the number of particles in the gas phase, which implies a reduction of the "degree of dissociation" [320] and correspondingly an increase in the "degree of recombination".

5.2 ISOTHERMAL REACTOR

Using the chemical equilibrium composition and temperature is important in order to understand the direction at which the chemical reactions will develop. However, it is also crucial to quantify the time-scales at which the chemical equilibrium is reached.

The least computationally expensive way of analyzing the time-evolution of the chemical system is performing a zero-dimensional simulation of a perfectly stirred reactor. In order to isolate the composition evolution from variations in temperature and pressure, an isothermal constant-pressure reactor is employed, similar to the work of Betti et al. [321]. In this analysis, a mixture of combustion gases, with composition corresponding to the chemical equilibrium at a given pressure, temperature and mixture ratio, is suddenly introduced to a lower temperature environment, and then is left to evolve in time. During the temporal evolution, the composition is changed according to the chemical kinetics and after a sufficient amount of time, the new chemical equilibrium is reached. This zero-dimensional test aims to reproduce the evolution of the mixture in conditions similar to those occurring in the thermal boundary layer, which develops between the hot core flow and the cold wall in a basically constant-pressure environment.

The evolution of the species mass fractions and temperature in the isothermal reactor is described by Equation 5.1.

$$\frac{\partial Y_k}{\partial t} = \frac{M_k \dot{\omega}_k}{\rho} \quad \text{and} \quad \frac{\partial T}{\partial t} = 0 \tag{5.1}$$

For the study (as well as all the following studies in Chapter 5), the GRI-MECH 3.0 chemical mechanism consisting of 53 species and 325 reversible reactions has been utilized [322]. A comparison between the results obtained with this mechanism and the results delivered by a more detailed one is shown in Appendix A.

Figure 5.6 shows the evolution of the species mass fractions over time for an isothermal constant-pressure reactor at $T_w = 1000\,\mathrm{K}$ and $p = 20\,\mathrm{bar}$. For all 4 different O/F values shown, the species mass fractions appear to change in a step-wise manner, due to the different reaction pathways being activated as a function of time. As expected, the final concentrations of CO and OH are lower than the starting values, indicating once again the effect of recombination reactions.

Although the recombination occurs for all O/F load points, a significant variation in the elapsed time before the arrival at chemical equilibrium can be observed. Specifically, O/F values closer to stoichiometry seem to enforce shorter time durations. While equilibrium is reached after approximately 1 second in the $O/F = 4.0$ case, the gas with mixture ratio equal to 1.5 requires a approximately 10^9 seconds before relaxing to its new equilibrium. This implies that the chemical time-scales in fuel-rich conditions are significantly slower than practical flow time-scales in rocket engines and hence the assumption of chemical equilibrium close to the cooled walls is not representative.

The heat release rate associated to the chemical reactions taking place within the 0D-reactor is plotted in Figure 5.7. Data points corresponding to a positive net energy release (exothermic) are drawn in red, whereas data points representing a net energy consumption (endothermic) are plotted in blue. As expected, the magnitude of the heat release is approaching zero, as the time advances. The reason is that close to the chemical equilibrium,

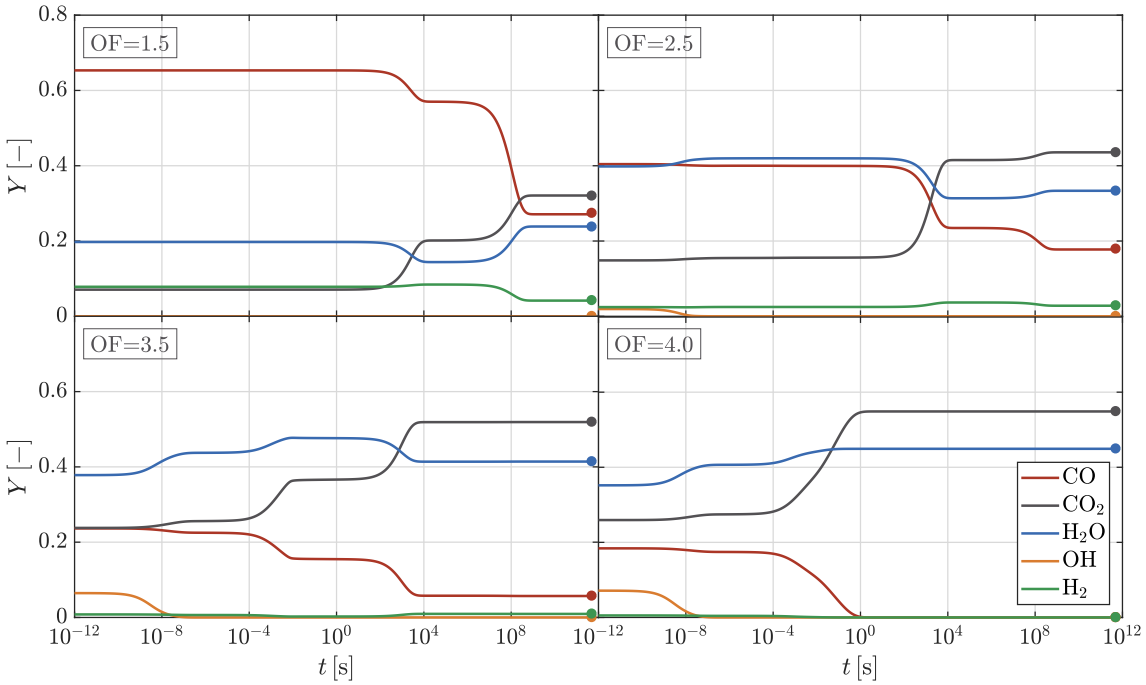

Figure 5.6: Temporal evolution of major species mass fractions in the isothermal, constant-pressure reactor with $T_w = 1000\,\mathrm{K}$ and $p = 20\,\mathrm{bar}$ for different O/F values.

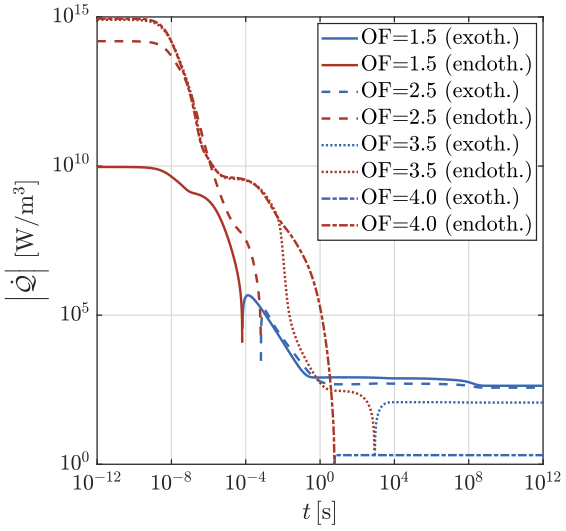

Figure 5.7: Temporal evolution of heat release rate in the isothermal, constant-pressure reactor with $T_w = 1000\,\mathrm{K}$ and $p = 20\,\mathrm{bar}$ for different O/F values.

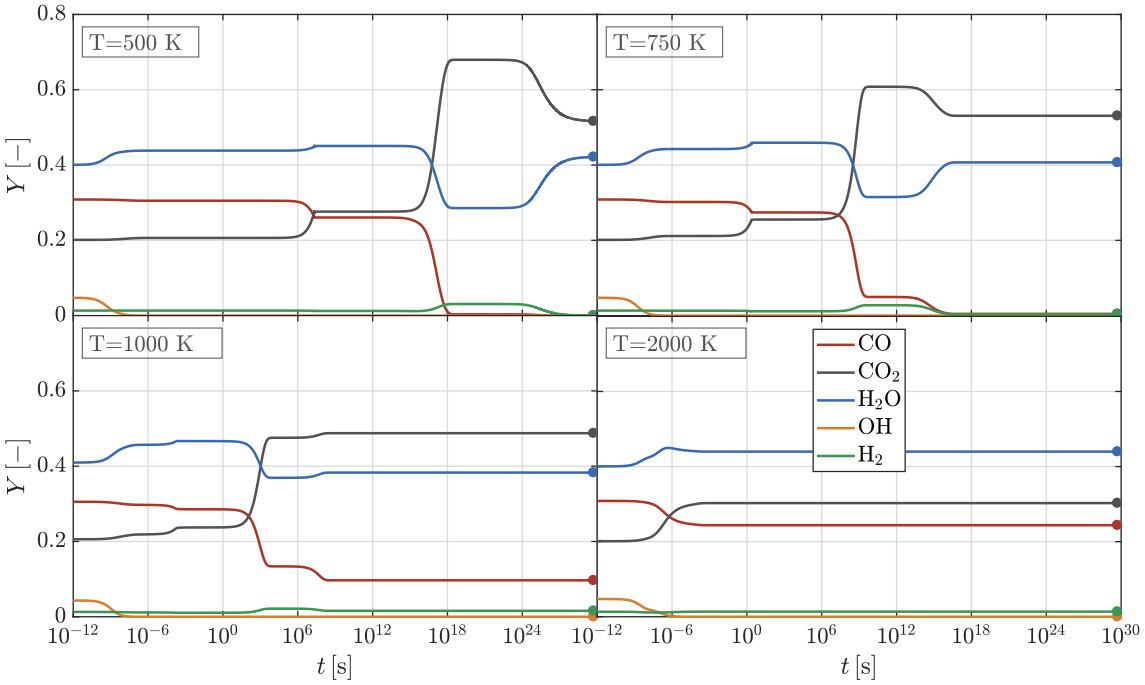

Figure 5.8: Temporal evolution of major species mass fractions in the isothermal, constant-pressure reactor for $O/F = 3.0$, $p = 20\,\text{bar}$ and different wall temperature values.

the forward and backward reaction rates are neutralized, leading to a zero net heat release rate.

Moreover, it is can be seen that the gas responds to the initial abrupt reduction change in temperature with a net release of energy, i.e. exothermic reactions. The magnitude of the initial heat release is higher for mixture ratios close to stoichiometry. This effect can also be explained when considering that fuel-rich conditions are connected to slow reaction rates and hence a smaller volumetric heat release rate.

Apart from the variation of O/F, a variation of wall temperature has also been carried out and is illustrated in Figure 5.8. The plots correspond to a mixture fraction $O/F = 3.0$ and a reactor pressure of 20 bar.

A strong dependence of the required time for reaching the new chemical equilibrium is observed as a function of temperature. Higher reactor temperatures significantly reduce the equilibrium time scales, with a temperature of 2000 K corresponding to approximately 10^{-3} s, while a temperature of 500 K requires as much as 10^{30} s before the completion of the reactions.

The reason for the vast inconsistency in duration is dual. First, for higher temperatures, the new target chemical equilibrium is closer to the initial conditions and hence requires shorter times to be reached. Second, higher temperatures give rise to higher reaction rates due to the Arrhenius temperature dependence, which promotes shorter time-scales.

In order to examine the chemical reactions producing the shift in chemical equilibrium, the heat release rate of each individual reaction is plotted against time in Figure 5.9 and Figure 5.10. Only the regions where the net heat release is exothermic are plotted for each reaction. In the legend, the direction at which the net reaction rate is taking place has been

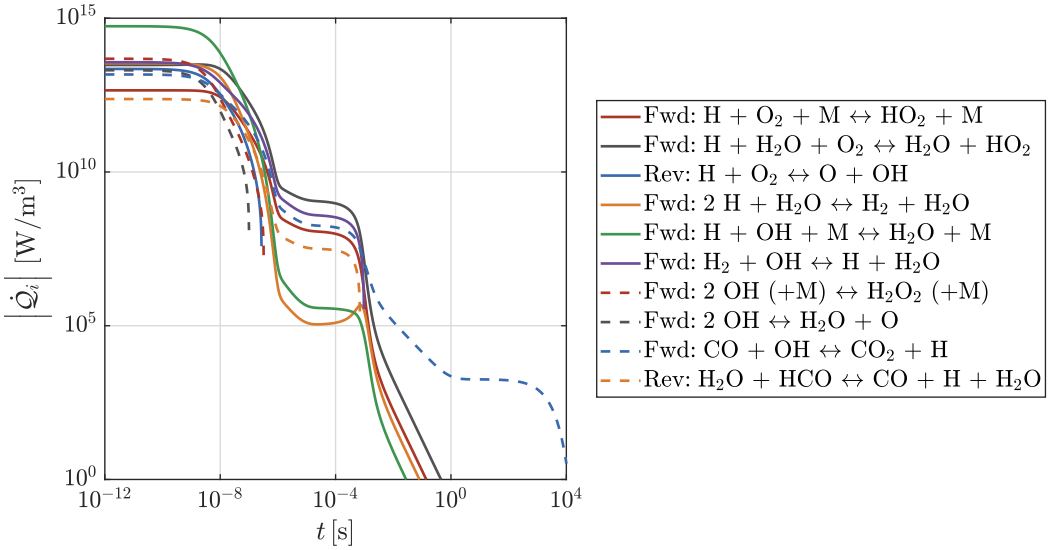

Figure 5.9: Temporal evolution of each reaction's heat release rate in the isothermal, constant-pressure reactor for $O/F = 3.0$, $p = 20\,\text{bar}$ and $T_w = 1000\,\text{K}$. Only the regions where the net heat release is exothermic are plotted for each reaction.

indicated with "Fwd." corresponding to the forward reaction direction and "Rev." to the reverse one[4].

Starting with the results for the $O/F = 3.0$ case, it is evident that the majority of the energy being released for the first 10^{-8} s is a result of hydrogen reactions, containing no carbon. The most dominant reaction is the direct recombination of H and OH radicals to form H_2O:

$$H + OH + M \longrightarrow H_2O + M$$

In the time period from 10^{-7} s to 10^{-3} s, the recombination of the hydrogen radical and oxygen to form hydroperoxyl (with water as collisional partner) is most intense:

$$H + O_2 + H_2O \longrightarrow H_2O + HO_2$$

Within the ten most dominant reactions (from a heat release perspective), only the recombination of CO to CO_2 contains carbon chemistry:

$$CO + OH \longrightarrow CO_2 + H$$

Although the reaction has a high heat release throughout the entire duration, it becomes the most dominant reaction after 10^{-3} s, when the reaction rates of the hydrogen chemical reactions sharply decline. For the remaining 10^4 s, the CO recombination becomes the main source of exothermic heat release.

In the case of lower O/F values, the heat release profiles differ from the ones at $O/F = 3.0$, as Figure 5.10 indicates. Apart from the absolute level of the release rate which is approximately 5 orders of magnitude lower, different individual reactions are

4 This has been done so as to keep the chemical reaction equation identical to its original formulation from Smith et al. [322].

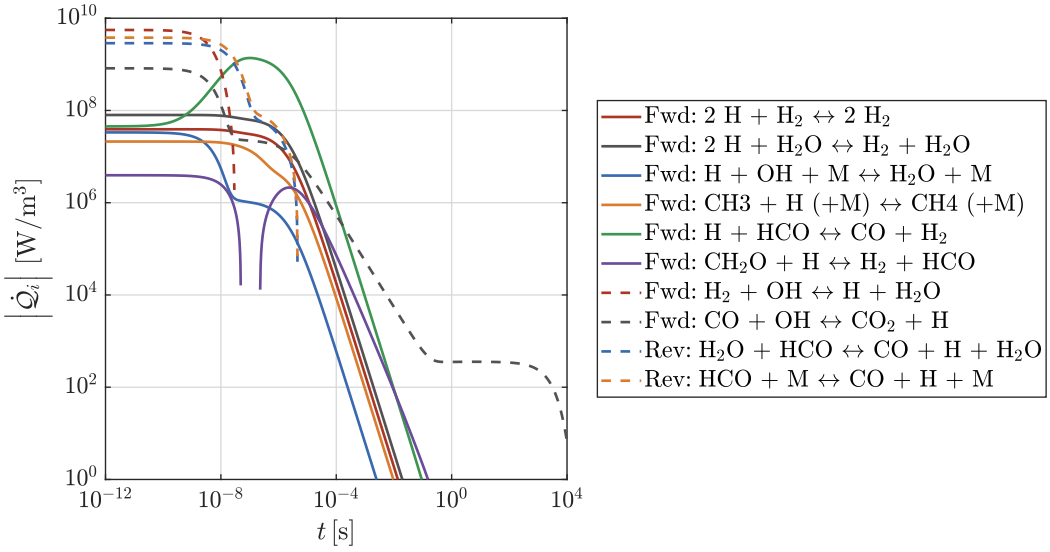

Figure 5.10: Temporal evolution of each reaction's heat release rate in the isothermal, constant-pressure reactor for $O/F = 1.5$, $p = 20\,\text{bar}$ and $T_w = 1000\,\text{K}$. Only the regions where the net heat release is exothermic are plotted for each reaction.

activated. Specifically, a much larger contribution takes place from the recombination of carbon containing molecules, with the recombination of the methyl radical (CH_3) and formaldehyde (CH_2O) playing a non-negligible role. The recombination of CO still remains dominant but now appears with a secondary pathway, forming formyl radical:

$$\text{CO + OH + M} \longrightarrow \text{HCO + M}$$

In order to obtain a more comprehensive overview of the pathways that are relevant for each mixture fraction at different instantaneous time stamps, Figure 5.11 and Figure 5.12 are provided and show the reaction path diagram for the oxygen atom [5].

Starting with the lower mixture fraction ($O/F = 1.5$), the reaction path diagram in Figure 5.11 demonstrates that for the first 10^{-8} s (sub-figures a and b), the main fluxes occur in the conversion of OH and CO to H_2O and HCO, with a minor contribution towards the production of CO_2. After $2 \cdot 10^{-3}$ s (sub-figure c), the formation of CO_2 becomes more dominant, while at the same time, CH_2O is also created. The conversion of CO to CO_2 prevails even after 1 second (sub-figure d), while the OH required for the recombination of CO is provided by the dissociation of H_2O.

For the operating point closer to stoichiometry ($O/F = 3.0$) in Figure 5.12, a larger amount of radicals is present (due to the higher initial temperature of the mixture), that leads to a more complex reaction path diagram. Within the first $7 \cdot 10^{-9}$ s, the formation of CO_2, H_2O a well as HO_2 and H_2O_2 is observed. The creation of those products takes place with a large number of intermediate species including O_2, OH and O. Starting at $3 \cdot 10^{-6}$ s (sub-figure c), a lower number of final products is observed, as HO_2 and H_2O_2 now play

5 To interpret the results, the labeling convention has to be explained. Next to each arrow, the normalized net atomic flux is indicated, while its normalization factor is shown at the bottom of the figure, labeled as "Scale". The forward and reverse fluxes are also indicated (as long as they exceed 5% of the net flux). Finally, the reactions that comprise the forward and backward conversion rates are shown by indication of the reacting partners and the relative flux in parenthesis.

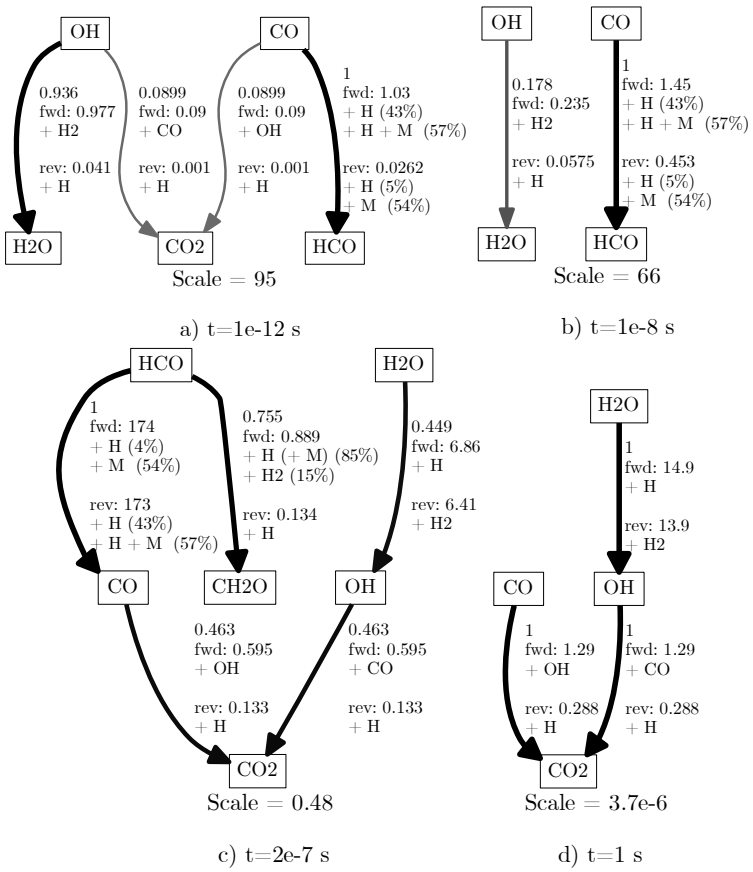

Figure 5.11: Reaction path diagram of oxygen atom for different snapshots in the isothermal, constant-pressure reactor for $O/F = 1.5$, $p = 20\,\text{bar}$ and $T_w = 1000\,\text{K}$.

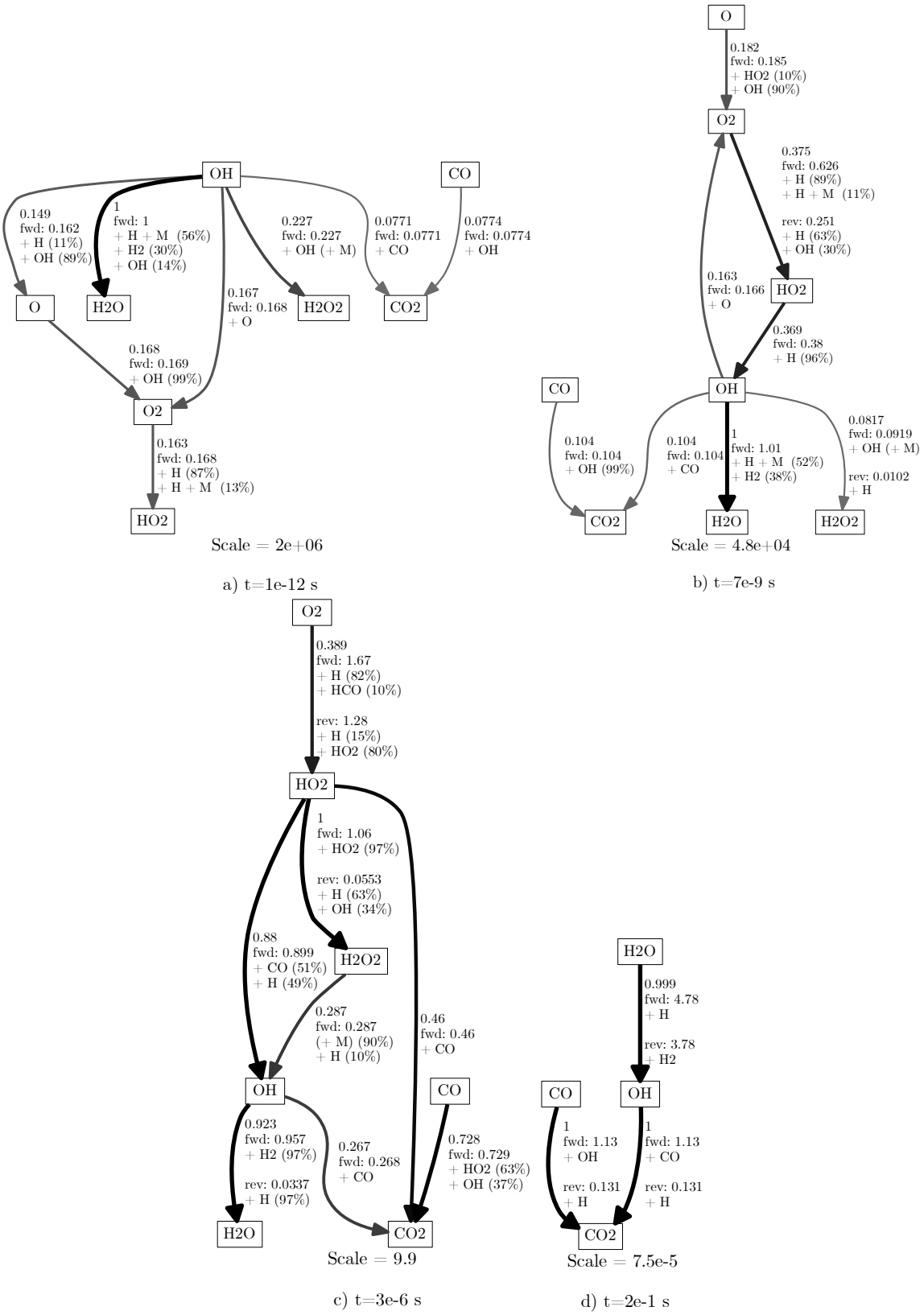

Figure 5.12: Reaction path diagram for different snapshots in the isothermal, constant-pressure reactor for $O/F = 3.0$, $p = 20\,\text{bar}$ and $T_w = 1000\,\text{K}$.

the role of intermediate species and only water and carbon dioxide are created as a net result. Finally, most of the radicals are depleted by the first $2 \cdot 10^{-1}$ s, which significantly simplifies the reaction pathways and leads to the production of CO_2 from CO and OH, similar to the sub-figure d) of Figure 5.11.

5.3 STAGNATION FLOW

Despite its simplicity, the examination of the zero-dimensional isothermal reactor gives significant insights into the individual recombination reactions taking place in the vicinity of cooled chamber walls.

In order to examine the influence of the recombination reactions on the expected wall heat flux using a reduced-order modeling approach, one-dimensional reacting stagnation flow simulations have been carried out. The concept of a stagnation flow is schematically illustrated in Figure 5.13. Combustion products enter the domain through the inlet at $x = 0$, with an initial velocity perpendicular to the isothermal wall.

The flow has been modeled using a one-dimensional axisymmetric domain, using the open-source chemistry tool Cantera [319]. Cantera models flames that are stabilized in an axisymmetric stagnation flow, and computes the solution along the stagnation streamline ($r = 0$), using a similarity solution to reduce the three-dimensional governing equations to a single dimension. The governing equations for a steady axisymmetric stagnation flow follow those derived in Kee et al. [323]. The conservation equations for continuity (Equation 5.2), radial momentum (Equation 5.3), energy (Equation 5.4) and species (Equation 5.5) are solved:

$$\frac{\partial \rho u}{\partial x} + 2\rho V = 0 \tag{5.2}$$

$$\rho u \frac{\partial V}{\partial x} + \rho V^2 = -\Lambda + \frac{\partial}{\partial x}\left(\mu \frac{\partial V}{\partial x}\right) \tag{5.3}$$

$$\rho c_p u \frac{\partial T}{\partial x} = \frac{\partial}{\partial x}\left(\lambda \frac{\partial T}{\partial x}\right) - \sum_k j_k c_{p,k} \frac{\partial T}{\partial x} - \sum_k H_k M_k \dot{\omega}_k \tag{5.4}$$

$$\rho u \frac{\partial Y_k}{\partial x} = -\frac{\partial j_k}{\partial x} + M_k \dot{\omega}_k \tag{5.5}$$

where u is the axial velocity, v is the radial velocity, $V = v/r$ is the scaled radial velocity and Λ is the pressure eigenvalue (independent of the axial coordinate x with $d\Lambda/dx = 0$). The tangential velocity has been assumed to be zero, and the fluid has been assumed to behave as an ideal gas. The species diffusive mass fluxes j_k is computed according to a mixture-averaged formulation:

$$\begin{aligned} j_k^* &= \rho \frac{M_k}{\bar{M}} D'_{km} \frac{\partial X_k}{\partial x} \\ j_k &= j_k^* - Y_k \sum_i j_i^* \end{aligned} \tag{5.6}$$

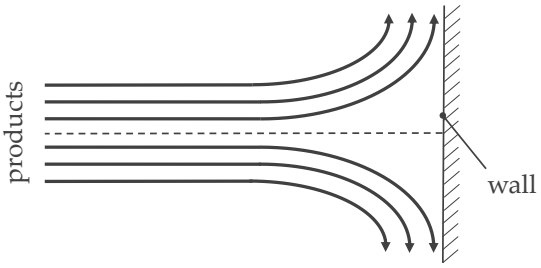

Figure 5.13: Schematic illustration of stagnation flow perpendicular to a non-reacting wall.

At the inlet, values are supplied for the temperature, and the species mass fractions corresponding to the adiabatic equilibrium conditions at the chosen mixture ratio. The inlet axial velocity is set to the laminar flame speed, while the scaled radial velocity is set to zero. At the wall boundary, both velocity components are set to zero, as well as the diffusive fluxes for all species, while the gas temperature is set to the wall temperature.

The 1D simulations have been carried out at an operating pressure of 20 bar and the wall temperature as well as mixture fraction have been varied. For each combination of O/F and T_{wall}, two simulations have been carried out: one reacting case and one frozen case. For both runs, the same equations are solved, with the only difference being that in the frozen case, the reaction rates $\dot{\omega}_k$ are set to zero. This way, the effect of the recombination effects can be isolated and its impact on the temperature profile and wall heat flux can be estimated.

The results for the species profiles as a function of the normalized coordinate x/d (with d being the length of the domain), are shown in Figure 5.14 for $O/F = 3.0$. The zoomed-in regions correspond to the locations in the direct vicinity of the non-catalytic wall. Apart from the reacting and frozen results, the species corresponding to the chemical equilibrium conditions are also plotted in dotted lines. Note that this is not a separate simulation but rather a post-processing evaluation of the reacting results, where the chemical equilibrium composition is calculated for each cell, given the local pressure, mixture ratio and temperature.

As expected based on the stirred reactor results, in lower-enthalpy environments closer to the wall, recombination reactions alter the gas composition. By comparing to the local chemical equilibrium conditions, it is evident that the reactions are not fast enough to reach their target equilibrium close to the wall. The reason is that the chemical time-scales become slower in the vicinity of the wall, due to the drop in temperature. Therefore, significant deviations from the equilibrium concentration are observed, especially for CO, CO_2 and H_2O. Similar to the findings of Section 5.2, OH is depleted fast enough and is therefore very close to its equilibrium for the entirety of the domain.

Given the important deviations from both the frozen composition and the equilibrium solution, it is evident that the recombination reactions in methane/oxygen follow time-scales which do not agree with neither extremes of infinitely slow and infinitely fast chemistry. The need for modeling is also apparent when comparing those results with a representative case of recombinations in H_2/O_2 mixtures. In Figure 5.15, the combustion products of a hydrogen/oxygen flame are used at the inlets of the stagnation flow simulation. Specifically, a mixture ratio $O/F = 6.0$ is chosen, as this corresponds to the same equivalence ratio as for the $O/F = 3.0$ case in methane/oxygen combustion (equivalence ratio $\phi \approx 1.33$).

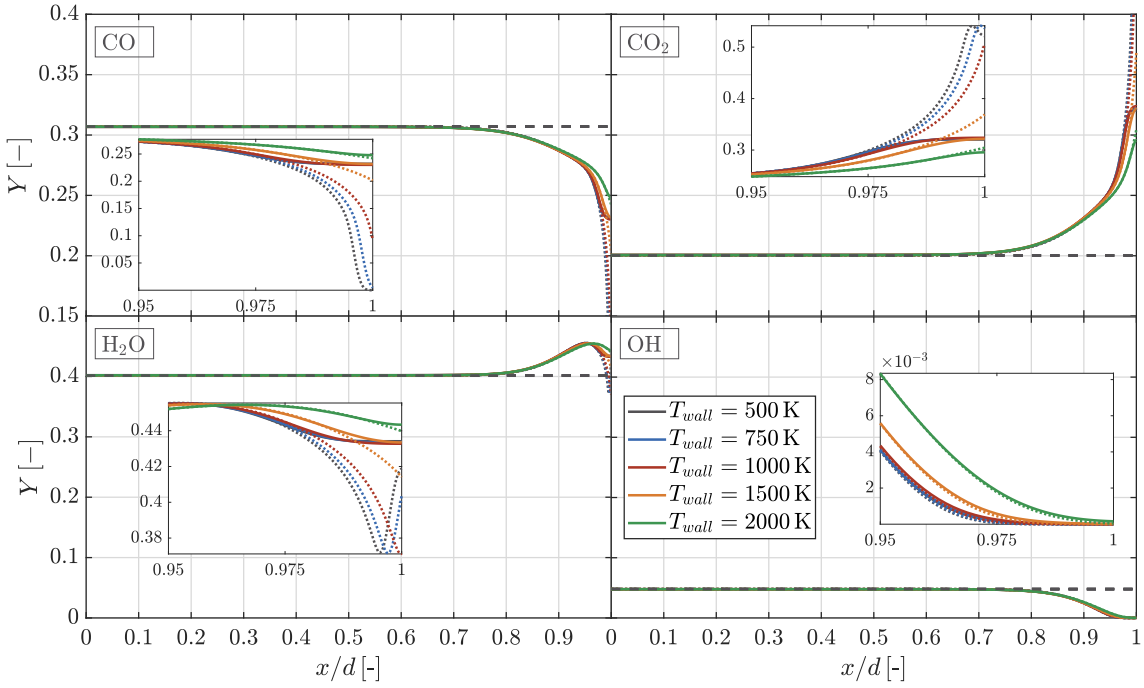

Figure 5.14: Species profiles in the stagnation flow simulation as a function of the normalized axial coordinate for $p = 20\,\text{bar}$ and $O/F = 3.0$. The reacting case is plotted with solid lines (——), the frozen case with dashed lines (- - -) and the chemical equilibrium composition with dotted lines (·····).

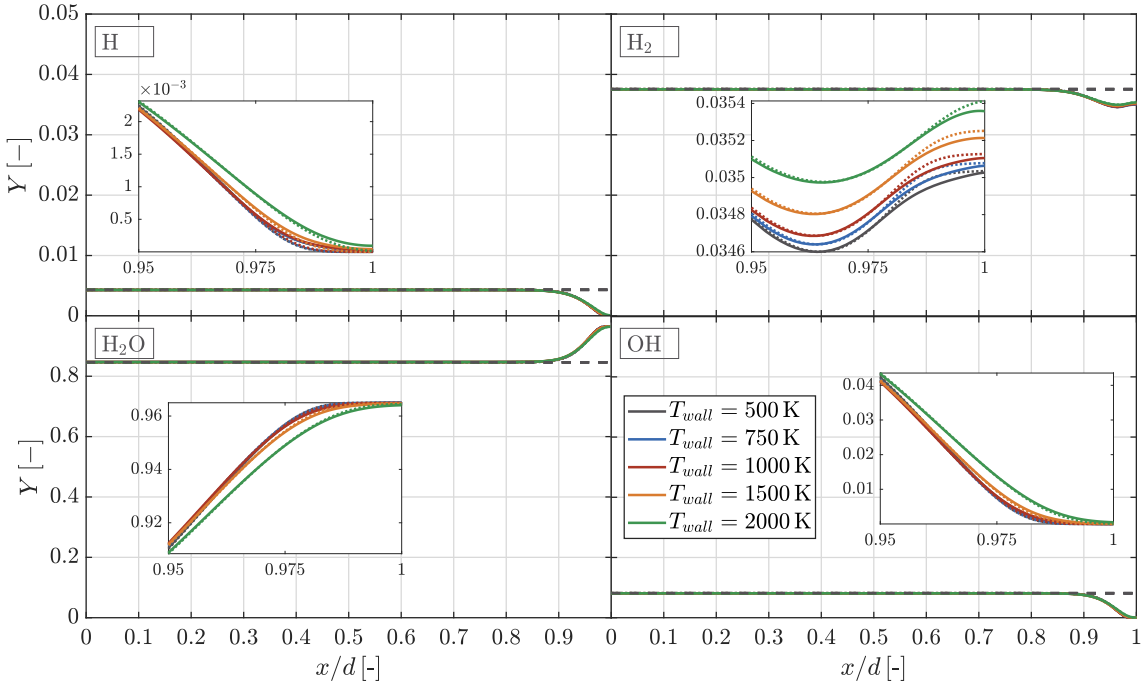

Figure 5.15: Species profiles in the stagnation flow simulation as a function of the normalized axial coordinate for $p = 20\,\text{bar}$ and $O/F = 6.0$ for the H_2/O_2 mixture. The reacting case is plotted with solid lines (——), the frozen case with dashed lines (- - -) and the chemical equilibrium composition with dotted lines (·····).

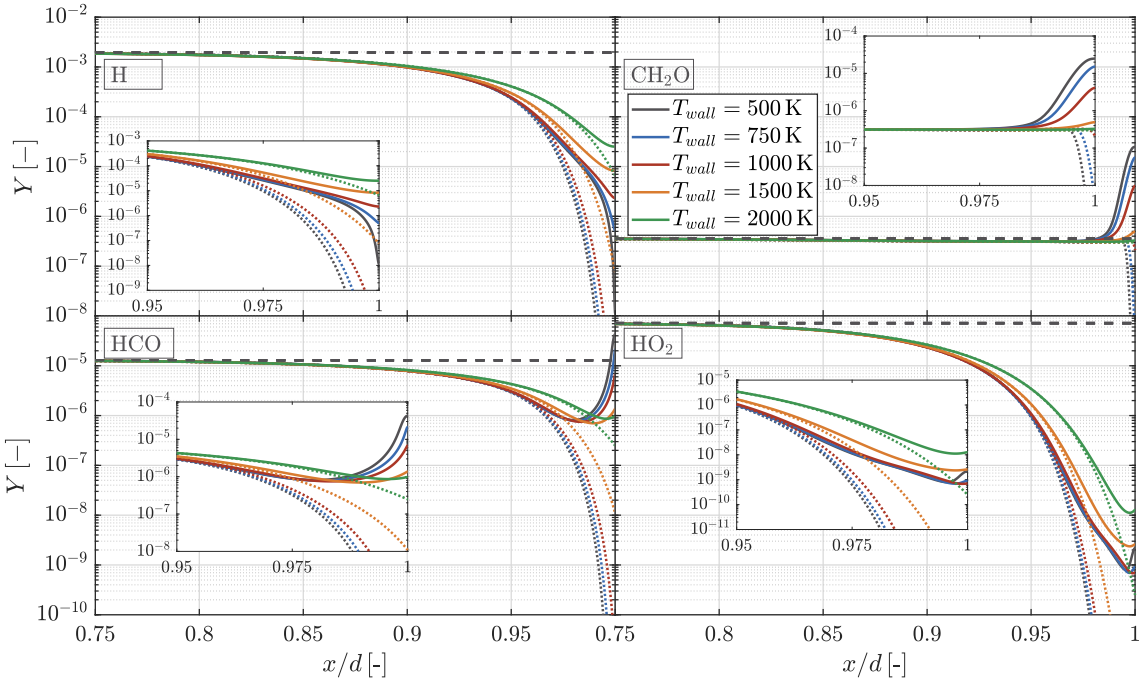

Figure 5.16: Minor species profiles in the stagnation flow simulation as a function of the normalized axial coordinate for $p = 20\,\text{bar}$ and $O/F = 3.0$ for the CH_4/O_2. The reacting case is plotted with solid lines (——) and the frozen case with dashed lines (- - -).

It is noticeable from Figure 5.15, that all dominant products of the hydrogen/oxygen flame are following their equilibrium composition without significant deviations. This effect seems to be independent of the wall temperature, as the discrepancy from chemical equilibrium is negligible even for the lowest T_{wall} values. This puts in perspective the different orders of magnitude for the chemical time-scales of methane reactions compared to hydrogen. It also serves as a further justification for the use of the chemical equilibrium model when simulating hydrogen/oxygen rocket engines.

Apart from the major species concentrations shown in Figure 5.14 and Figure 5.15, the minor species mass fractions in Figure 5.16 and Figure 5.17 also show an interesting behavior. Although the reactions involving those radicals are not responsible for the bulk energy release in the turbulent boundary layer (as seen in Figure 5.10), their concentration is important for the initiation of the main exothermic reactions. As expected based on the results obtained from the 0D calculations in Figure 5.5, the mass fractions in the post-processed chemical equilibrium conditions of the stagnation flow are decreasing in the vicinity of the wall, both for the methane/oxygen and the hydrogen/oxygen case. When resolving the reactions with finite-rate however, it becomes apparent that some of the species exhibit a quantitatively different behavior in the imminent vicinity of the wall. Specifically, for HCO, while a drop in concentration is found starting at $x/d \approx 0.75$ that coincides with the direction of chemical equilibrium, when moving closer to the wall (at $x/d \approx 0.98$), a subsequent rapid increase in concentration is observed. This second mode is dissimilar to the behavior exhibited by major recombining species like CO, which do not experience any positive net production near the wall. Comparably, the CH_2O mass fraction demonstrates an increase for $x/d > 0.98$, which does not conform to the predicted equilibrium state. The rise in HCO and CH_2O mass fractions appears to be

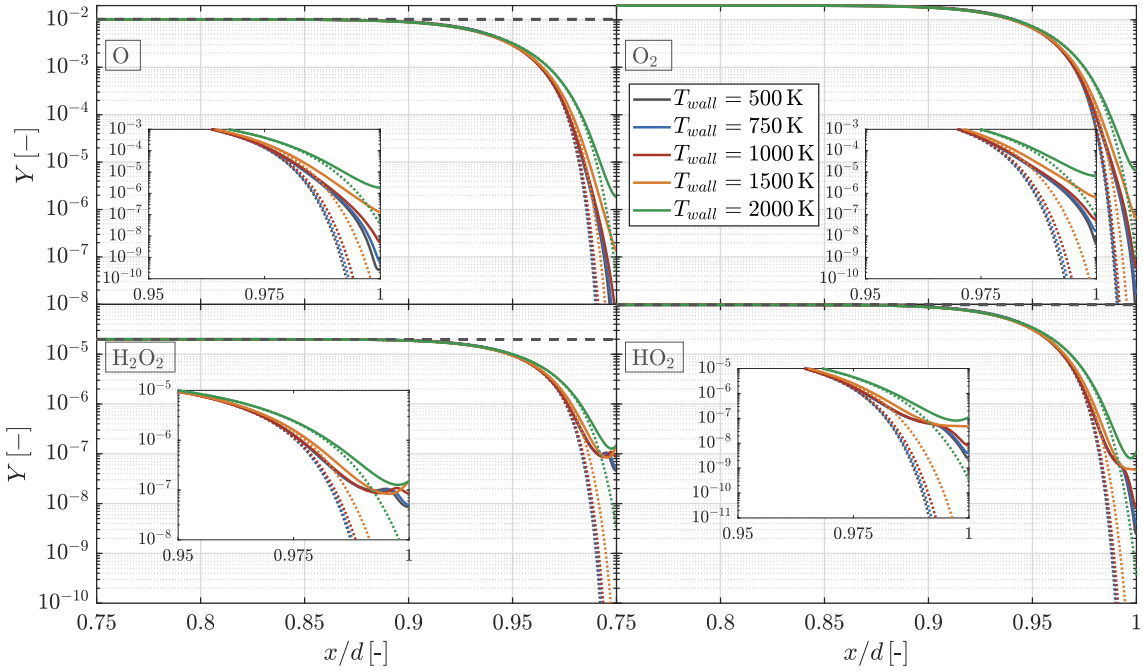

Figure 5.17: Minor species profiles in the stagnation flow simulation as a function of the normalized axial coordinate for $p = 20\,\text{bar}$ and $O/F = 6.0$ for the H_2/O_2. The reacting case is plotted with solid lines (——) and the frozen case with dashed lines (- - -).

temperature-dependent with lower wall temperatures favoring the production of both species.

To obtain a deeper understanding of the activated chemical pathways in the wall region, a reaction flux diagram for different wall temperatures is illustrated in Figure 5.18. For higher temperatures, the conversion of OH and CO into CO_2 is established as the dominant path, while no significant formaldehyde formation is reported. By reducing the temperature though, the absorption of an H radical by HCO to form CH_2O gains importance, with the atomic fluxes of the reaction being larger than for the conversion of CO to CO_2. A further temperature drop to 500 K shows that the HCO and CH_2O formations become the most significant pathways, while the formation of carbon dioxide ceases, as the "freezing" of the chemical conversion in Figure 5.14 has implied. The main reason for the sharp increase of the formyl (HCO) and formaldehyde (CH_2O) mass fractions is that they are the products in recombination reactions with zero or negative activation energy. Therefore, lower temperatures facilitate their production, as the molar concentration $\mathcal{C}$ increases with decreasing temperature (and hence increasing density).

In order to quantify the isolated effect of the recombination reactions in the CH_4/O_2 case, Figure 5.19 provides the temperature profiles of the reacting and frozen cases for various mixture ratio and wall temperature combinations. The exothermic heat release of the recombination reactions leads to a substantial increase in temperature compared to the non-reacting case. It can also be inferred from the figure, that the deviations between the two cases become larger for mixture ratios closer to stoichiometry. This can be confirmed by examining the low O/F case ($O/F = 1.5$), where minimal differences between the frozen and reacting cases are seen. This is caused by the slower reaction time-scales in the fuel-rich

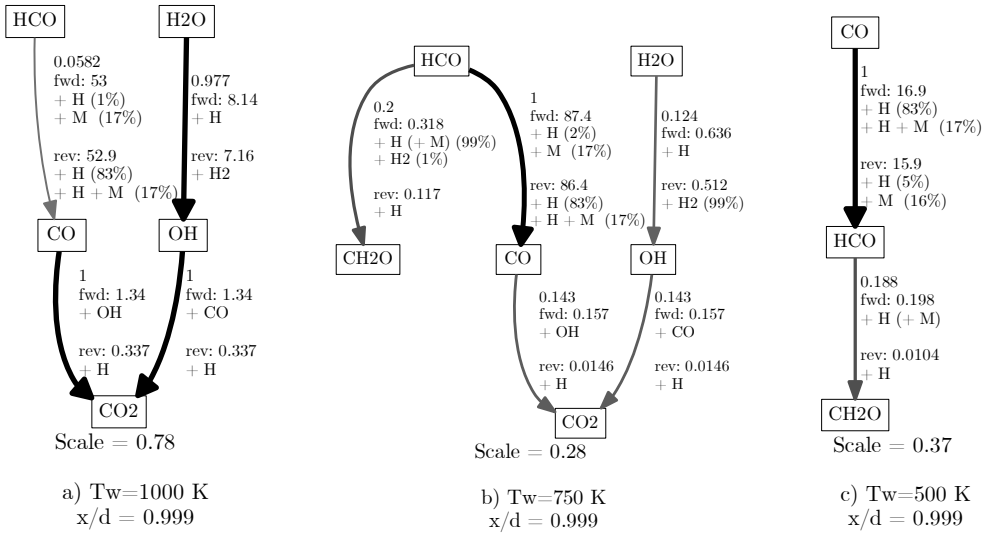

Figure 5.18: Reaction path diagram of oxygen atom for different wall temperatures in the stagnation flow of CH_4/O_2, for $O/F = 3.0$, $p = 20\,\text{bar}$.

region, which can cause the chemistry to "freeze" in the presence of faster flow time-scales. For higher O/F values, however discrepancies of up to 600 K are predicted.

The larger temperature level is also manifested in a larger temperature gradient at the wall and hence an amplification of the wall heat transfer. This effect is depicted in Figure 5.20, where the wall heat flux defined as $\dot{q} = \lambda_w \cdot (\partial T/\partial x)_w$ is plotted. Each point in the two-dimensional contour plots of Figure 5.20 corresponds to a combination of O/F and wall temperature and hence represents the results of a single 1D simulation. Results are shown only for T_{wall} values which do not exceed the adiabatic equilibrium temperature of the gas T_{ad}.

Starting with the reacting results in the top left sub-figure, it can be inferred that the maximal heat flux occurs close to the stoichiometric mixture ratio and for a wall temperature of approximately 1000 K. On the other hand, the results from the frozen case behave differently, having a smaller absolute heat flux level and a maximal heat flux for $O/F = 3.5$ and $T_{wall} \approx 500\,\text{K}$. In the frozen case, due to the absence of exothermic reactions, the heat flux is driven by the temperature difference between the inlet temperature (adiabatic equilibrium temperature) and the wall temperature. For a given O/F, the lower wall temperatures are expected to give rise to a larger thermal gradient and therefore to a larger heat flux. The only reason why the heat flux shows a maximum at $T_{wall} \approx 500\,\text{K}$ instead of continuously increasing with decreasing wall temperature, is that the thermal conductivity of the gas is proportional to its temperature. Hence a further decrease in wall temperature results in a drop of the product of thermal conductivity λ_w and temperature gradient $(\partial T/\partial x)_w$. In the reacting case however, apart from the thermal conductivity and the initial temperature difference between inlet and wall, the heat release due to recombination reactions is a further driver. As higher temperatures enhance the reaction rates and energy release of the major recombination reactions, the maximal heat flux occurs at a higher T_{wall} value than for the frozen composition. Also, since the heat release is also larger in the vicinity of the stoichiometry, the maximal heat flux is found for $O/F \approx 4.1$.

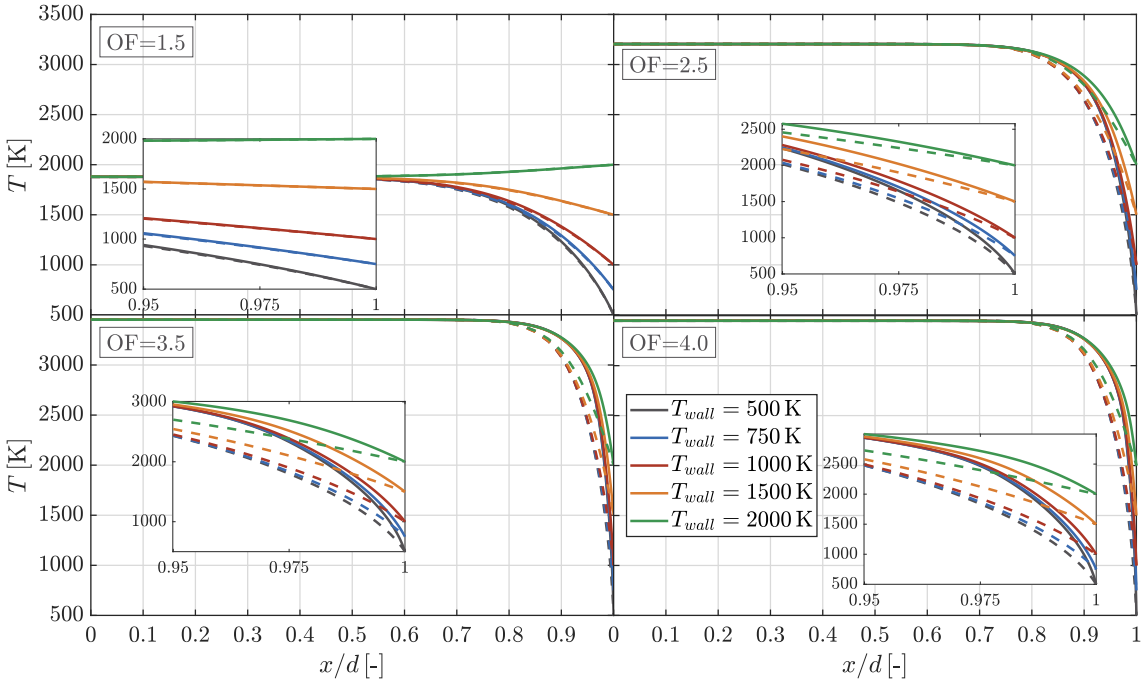

Figure 5.19: Temperature profiles in the stagnation flow simulation as a function of the normalized axial coordinate for $p = 20$ bar. The reacting case is plotted with solid lines (——) and the frozen case with dashed lines (- - -).

The difference between the two solutions is defined as $\Delta\dot{q} = \dot{q}_{reacting} - \dot{q}_{frozen}$, while the relative difference is given by:

$$\Delta\dot{q}_{rel} = \frac{\dot{q}_{reacting} - \dot{q}_{frozen}}{\dot{q}_{reacting}} \cdot 100\% \tag{5.7}$$

The effect of the recombination reactions is therefore quantified and is found to make up for up to 80% of the total heat transfer rate. By examining the relative difference in the bottom right sub-figure of Figure 5.20, it is obvious that the effect of the reactions is most dominant for larger wall temperatures, where the temperature difference is low and hence the frozen heat flux approaches zero.

A further metric that can isolate the effect of the reactions is the normalized heat flux $\dot{q}_n$, which has been used in numerical studies of head-on flame quenching configurations [324]. This is defined as

$$\dot{q}_n = \frac{\dot{q}}{\rho c_p u_l \Delta T} \tag{5.8}$$

with u_l being the laminar flame speed and ΔT being the difference between burnt and unburnt gases. The normalized wall heat flux isolates the effect of the recombination reactions from the initial temperature difference between the hot products and the wall. Its dependence on the wall temperature and mixture ratio is portrayed in the left sub-figure of

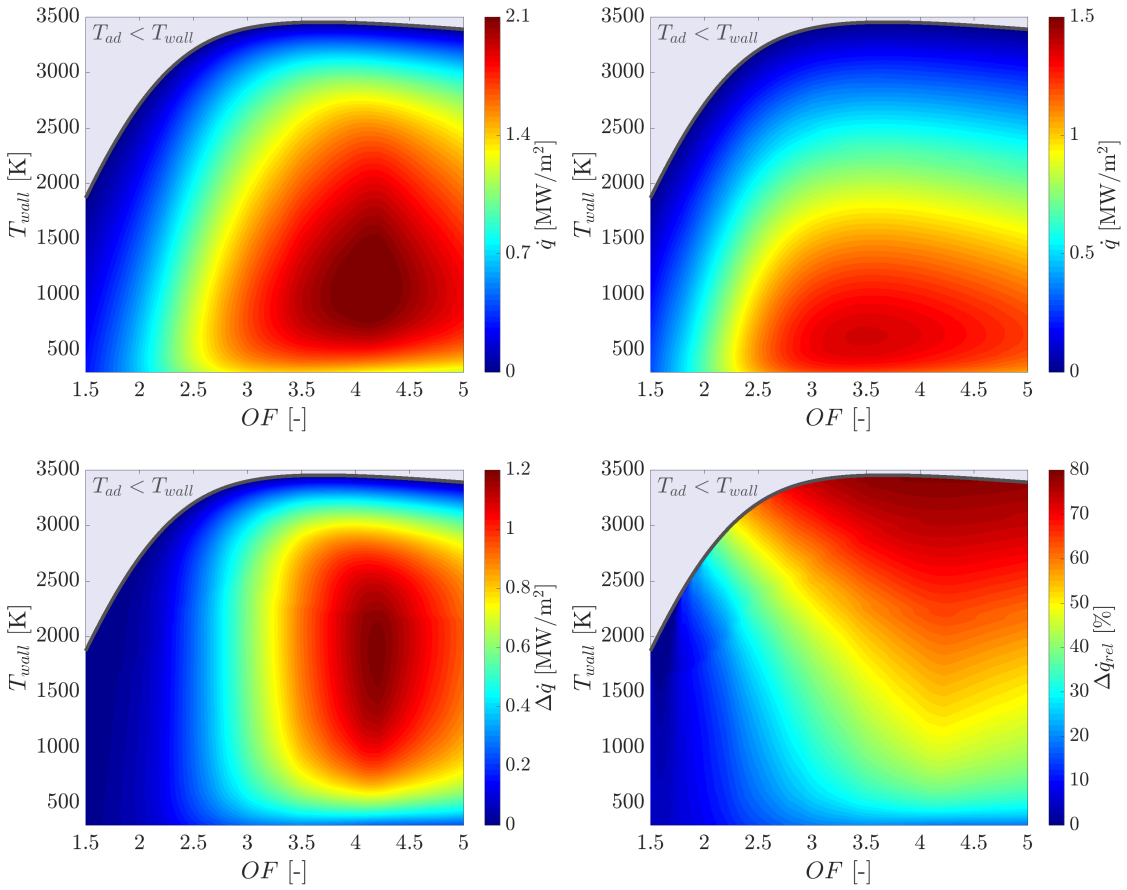

Figure 5.20: Wall heat flux from the stagnation flow simulations at 20 bar. The top row shows the heat flux results for the reacting (left) and frozen (right) cases, while the bottom row shows the absolute (left) and relative (right) heat flux differences.

Figure 5.21. Higher temperature values lead to an increase in the normalized heat flux, as the laminar species production rates are amplified. A link between the normalized heat flux and the cumulative heat release $\dot{Q}_{sum}$ is obtained by comparing the left and right sub-figures of Figure 5.21. $\dot{Q}_{sum}$ is calculated as the integral of the total heat release rate within the domain:

$$\dot{Q}_{sum} = A \cdot \int_0^d \dot{Q} dx \tag{5.9}$$

A reference area of $A = 1\,\mathrm{m}^2$ is used for this 1D flow. It can be seen, that in the combinations of O/F and T_{wall} where a significant amount of heat is being released as a result of the recombination reactions, the normalized heat flux also experience a high value. However, it is also discernible that the effect is mostly dominant for temperatures upwards of 2000 K, which are not representative for typical combustion chamber liner walls.

In the following section, high-fidelity DNS are carried out, and the wall temperatures in the range of 500 to 1000 K are examined, as they are common for sub-scale and full-scale combustion chambers and they fall within the region where the 1D simulations predict

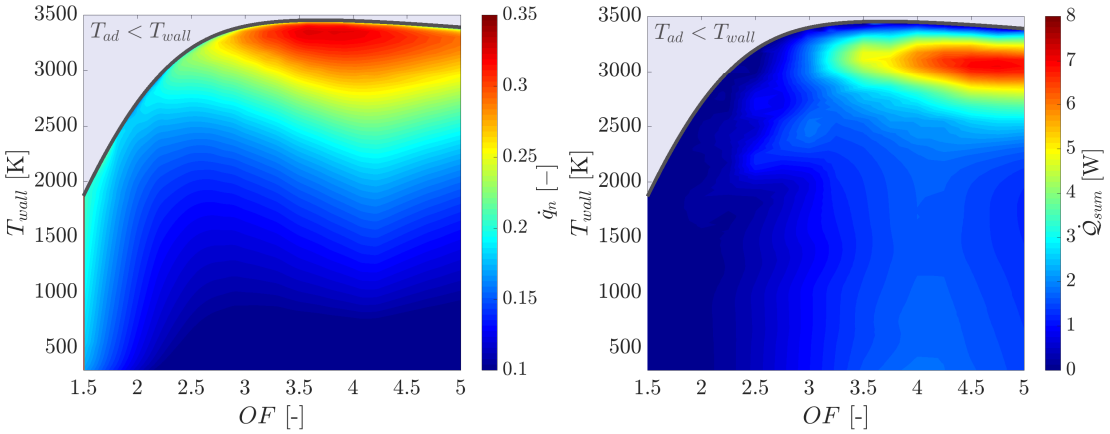

Figure 5.21: Normalized wall heat flux from the stagnation flow simulations at 20 bar (left) and integral heat release (right) for the $p = 20$ bar CH_4/O_2 case.

the largest absolute heat flux difference between frozen and reacting flows (bottom left sub-figure in Figure 5.20.

5.4 DIRECT NUMERICAL SIMULATION

A study of a reacting boundary layer flow with heat transfer at conditions typical for sub-scale methane/oxygen rocket thrust chambers has been performed using a set of Direct Numerical Simulations. The passage corresponds to the paper entitled:
Heat transfer augmentation by recombination reactions in turbulent reacting boundary layers at elevated pressures
Nikolaos Perakis, Oskar J. Haidn, Matthias Ihme
International Journal of Heat and Mass Transfer (2021)
doi: https://doi.org/10.1016/j.ijheatmasstransfer.2021.121628
Simulations using both frozen and reacting conditions are carried out in order to quantify the effect of the recombination reactions within the boundary layer. It is found that the chemical reactions can be responsible for an *increase of up to* 20% *on the wall heat loads*.

The recombination of H and H_2O to form OH and H_2 and a subsequent reaction of the produced OH with CO to form CO_2 are identified as the chemical reactions responsible for the majority of the energy release in the boundary layer. The mass fractions are found to deviate from the theoretical chemical equilibrium values, inferring strong non-equilibrium effects which result from the large chemical time-scales of hydrocarbon combustion. In this paper an estimate for the chemical-time scale using a detailed chemical mechanism is carried out for the first time in high-fidelity DNS. The results of the time-scale analysis clearly show regions where the gas is close to chemical equilibrium within the free stream and areas in the wall vicinity with chemically frozen behavior. In between the two extremes, regions described by finite chemical rates are present.

This effect leads to a limited extent for the reacting zone, which is mainly dominant from $y^+ \approx 10$ to $y^+ \approx 200$. For positions closer to the wall, *freezing of the chemical reactions* takes place, as the Kolmogorov and integral turbulent scales become the rate defining factors. In this region within the logarithimic sub-layer is also where the bulk of the chemical energy

is being released. The additional energy results in a significant temperature rise and a corresponding amplification of the wall heat transfer rate.

Although the reactions responsible for the bulk heat release (predominantly the recombination of CO to CO_2) cease to have a significant impact within the viscous sub-layer due to the freezing of the reactions, a *secondary recombination zone producing HCO and* CH_2O is formed for $y^+ < 10$ (in alignment with the stagnation flow results from Section 5.3). This low-temperature chemical pathway is a result of the recombination reactions with zero activation energy, that produce formyl and formaldehyde. Due to the constraint volume in which these reactions operate, there energy release constitutes only 5% of the total heat release within the boundary layer.

International Journal of Heat and Mass Transfer 178 (2021) 121628

Contents lists available at ScienceDirect

International Journal of Heat and Mass Transfer

journal homepage: www.elsevier.com/locate/hmt

Heat transfer augmentation by recombination reactions in turbulent reacting boundary layers at elevated pressures

Nikolaos Perakis [a,b,a,*], Oskar J. Haidn [a], Matthias Ihme [b]

[a] Chair of Space Propulsion, Technical University of Munich, Boltzmannstr. 15, Garching 85748, Germany
[b] Department of Mechanical Engineering, Stanford University, Stanford, CA 94305, USA

ARTICLE INFO

Article history:
Received 19 February 2021
Revised 12 June 2021
Accepted 19 June 2021

Keywords:
Reacting boundary layer
Recombination reactions
Chemical time-scales
Heat transfer

ABSTRACT

A study of a reacting boundary layer flow with heat transfer at conditions typical for configurations at elevated pressures has been performed using a set of direct numerical simulations. Effects of wall temperatures are investigated, representative for cooled walls of gas turbines and sub-scale rocket engines operating with hydrocarbon as fuels. The results show that exothermic chemical reactions induced by the low-enthalpy in the boundary layer take place predominantly in the logarithimic sub-layer. The majority of the heat release is attributed to the exothermic recombination of OH and CO to produce CO_2 and H_2O. The recombination reactions result in an increase of the wall heat loads by up to 20% compared to the inert flow. The gas composition experiences strong deviations from the chemical equilibrium conditions. In fact, a quenching of the major species is observed within the viscous sub-layer and the transition region. Analysis of chemical time-scales shows that the location of quenched composition coincides with the region where the Damköhler number decreases below unity. Within the viscous sub-layer, a secondary reaction zone is detected, involving the production of formyl and formaldehyde radicals that provide an additional source of energy release. The analysis of the reaction paths showed that reactions with zero activation energy are responsible for this change in gas composition, which also account for the initial branching of hydrocarbon fuels decomposition according to previous auto-ignition studies. The effect of the secondary recombination reactions is more prominent for the lower wall temperature case. Finally, the role of turbulent fluctuations on the species net chemical production rates is evaluated, showing a strong correlation between species and temperature fluctuations. This leads to a pronounced deviation of the mean reaction rates $\overline{\dot{\omega}(Y_k, T)}$ from the reaction rates obtained under the assumption of laminar finite rate.

1. Introduction

Accurate predictions of the flame-wall interaction are crucial in the design of combustion systems. In most industrial applications that operate in confined geometries including rocket thrust chambers, gas-turbine combustors and automotive engines, flame-wall interaction strongly affects fuel consumption and pollutant formation [1,2], while temporal and spatial fluctuations induced by it can influence the thermal loads and engine lifetime. Classical turbulent combustion models [3] do not account for the wall effects. Hence a better understanding of the flame-wall interaction is required for the development of predictive combustion models.

A major physical phenomenon that introduces substantial uncertainties on the prediction of heat transfer is the effect of exothermic recombination reactions within the reacting boundary layer. In particular for rocket applications, modeling these reactions is especially critical in hydrocarbon combustion, where the chemical time-scales are lower than in the case of hydrogen/oxygen chemistry. Efforts to model the influence of non-adiabatic effects on the gas composition, the associated heat release and expected wall heat loads have been carried out using flamelet methods [4–8]. Studies aiming at quantifying the importance of the recombination reactions on heat loads augmentation have been carried out by considering methane/oxygen mixtures in rocket combustion chambers [9–12]. At the same time, wall model extensions have been proposed in an effort to capture the near-wall chemical kinetics, but so far are limited to hydrogen/oxygen studies, which can be safely assumed to be in chemical equilibrium even in the cold boundary layer [13].

Despite ongoing modeling efforts, the physical mechanisms controlling turbulent flame-wall interaction, recombination reactions and the related wall heat fluxes have not been completely

* Corresponding author.
E-mail address: nikolaos.perakis@tum.de (N. Perakis).

https://doi.org/10.1016/j.ijheatmasstransfer.2021.121628
0017-9310/

Nomenclature

$\mathcal{C}$	species molar concentration $\left[\mathrm{mol/m^3}\right]$
c_p	specific heat capacity $[\mathrm{J/(kg \cdot K)}]$
D	species diffusion coefficient $\left[\mathrm{m^2/s}\right]$
Da	Damköhler number $[-]$
E	specific total energy [J/kg]
h	specific enthalpy [J/kg]
$\mathcal{H}$	normalized enthalpy $[-]$
$\boldsymbol{I}$	identity matrix $[-]$
$\boldsymbol{j}$	species diffusion flux $\left[\mathrm{kg/(m^2 \cdot s)}\right]$
$\boldsymbol{J}$	chemical Jacobi matrix [1/s]
k	turbulence kinetic energy $\left[\mathrm{m^2/s^2}\right]$
$\mathcal{K}$	reaction coefficient $[\mathrm{kg/(mol \cdot s)}]$
M	molecular weight [kg/mol]
p	pressure [bar]
Pr	Prandtl number $[-]$
$\dot{\mathcal{Q}}$	heat release $\left[\mathrm{W/m^3}\right]$
$\dot{q}$	heat flux $\left[\mathrm{W/m^2}\right]$
Re	Reynolds number $[-]$
R	universal gas constant $[\mathrm{J/(kg \cdot K)}]$
$\mathcal{R}_j$	reaction rate of progress $\left[kg/(\mathrm{m^3 \cdot s})\right]$
Sc	Schmidt number $[-]$
T	temperature [K]
t	time [s]
u	wall-parallel velocity [m/s]
v	wall-normal velocity [m/s]
$\boldsymbol{u}$	velocity vector [m/s]
x, y, z	spatial coordinates [m]
X	species molar fractions $[-]$
Y	species mass fractions $[-]$
Γ	third-body factor $[-]$
δ	boundary layer thickness [m]
ε	turbulence dissipation rate $\left[\mathrm{m^2/s^3}\right]$
η	length scale [m]
θ	temperature difference [K]
κ	von Karman constant $[-]$
λ	thermal conductivity $[\mathrm{W/(m \cdot K)}]$
μ	viscosity $[\mathrm{Pa \cdot s}]$
ν	stoichiometric coefficient $[-]$
ρ	density $\left[\mathrm{kg/m^3}\right]$
τ	time-scale [s]
$\boldsymbol{\tau}$	stress tensor $\left[\mathrm{N/m^2}\right]$
$\dot{\omega}$	molar reaction rate $\left[\mathrm{mol/(m^3 \cdot s)}\right]$
ad	adiabatic
c	chemical
$cumul$	cumulative
f	forward
j	reaction index
k	species index
K	Kolmogorov
r	reverse
t	turbulent
T	thermal
S	species
VD	van Driest
w	quantity at the wall
z	spanwise direction
τ	friction
∞	free stream conditions

understood. Because of the difficulties in obtaining accurate near-wall experimental measurements, Direct Numerical Simulation (DNS) represents an alternative for studying the processes taking place in the near-wal region.

As far as high-fidelity simulations of flame-wall interaction are concerned, head-on quenching configurations have often been chosen, where premixed laminar hydrocarbon flames are propagated perpendicular to the wall. One-dimensional simulations of head-on quenching are reported in the works of Westbrook et al. [14], Hocks et al. [15], Popp et al. [16,17]. These studies concur that low-activation energy recombination reactions of chemical radicals enhance the wall heat loads and require consideration for the flame-wall interaction processes. Based on these results it is also evident that detailed chemical kinetic mechanisms are required for capturing these effects. The importance of radical recombination reactions at the wall is also emphasized in simulations of H_2/O_2 flames, as in the work of Dabireau et al. [18].

Due to the large computational costs of multi-dimensional DNS of turbulent flame-wall interaction, only few investigations have been reported. Two-dimensional DNS of head-on quenching within a reactive boundary layer was performed by Poinsot et al. [19] while Bruneaux et al. [20] studied a three-dimensional configuration of a premixed flame propagating in constant density turbulent channel flow. Alshaalan et al. [21] investigated sidewall quenching of a three-dimensional V-shaped premixed flame with a single-step chemistry approximation. More recently Gruber et al. [22] simulated the same configuration with H_2/air with a detailed chemical mechanism.

As far as reacting turbulent boundary layer simulations are concerned, an even smaller number of studies can be found in literature, especially for configurations that are relevant to rocket thrust chambers. Martin et al. [23,24] performed DNS of hypersonic boundary layers with a single-step reaction scheme examining the feedback mechanisms between chemistry and turbulence, showing an increase in temperature fluctuations, induced by exothermic chemical reactions. Cabrit et al. [25] performed DNS and wall-resolved LES of multi-component mixtures in rectangular isothermal channels. Configurations with large temperature gradients and small Mach numbers were simulated, resembling rocket-like applications. However, the gas mixture that was introduced consisted to a large degree of inert nitrogen and a simplified chemical model was utilized, rendering the simulations less applicable to the thermochemical states experiences in modern methane/oxygen rocket engine hardware.

In the case of combustion devices at elevated pressures such as gas turbines and rocket combustion chambers, it is recognized that the effect of the reacting boundary layer can have a leading order effect on the performance and wall heat transfer. However, there is still insufficient understanding of the processes controlling the evolution of chemical reactions within the boundary layer, which leads to the absence of suitable models able to describe them. The present work addresses this knowledge gap in the context of recombinations in low-enthalpy environments using DNS of a reacting turbulent boundary layer. A canonical configuration is chosen for the study, with the selected operating conditions being representative for rocket combustion chamber applications. A reacting methane/oxygen gas mixture is chosen due to the relevance of methane as a fuel in the design of future space transportation vehicles.

2. Computational setup

In order to investigate the occurrence of recombination reactions in reacting boundary layers, direct numerical simulations of spatially evolving turbulent boundary layer over an isothermal flat plate are performed. The computational setup consists of a three-

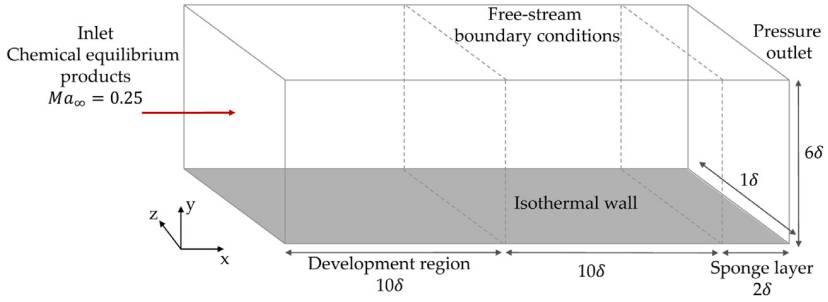

Fig. 1. Computational setup for the DNS.

dimensional, spanwise periodic domain, which is schematically illustrated in Fig. 1.

For the thermodynamic state at the inlet, the chemical equilibrium composition and temperature for a methane/oxygen mixture with mass mixture ratio equal to 3.0 is chosen, whereas the Mach number is 0.25 and the pressure is 20 bar. This represents the typical composition and velocity conditions found downstream of the main reaction zone in sub-scale rocket engines [26]. A boundary layer thickness of $\delta = 1$ mm is chosen, leading to a Reynolds number $Re_\delta = \rho_\infty u_\infty \delta/\mu_\infty = 4678$. The inlet velocity u_∞ is 327 m/s, while ρ_∞ and μ_∞ are calculated from the chemical equilibrium thermochemical state and are equal to 1.41 kg/m^3 and 9.87×10^{-5} Pa s respectively.

As described in Xu et al. [27], the specification of appropriate methods to generate inflow boundary conditions for LES and DNS of compressible boundary layers is important for the development of the turbulence in the domain. In spatially evolving boundary layers, the most convenient procedure involves the definition of a laminar profile with disturbances far upstream, allowing for a transition to turbulence. This approach is typically used to investigate transition [28–30] and is not generally applicable to turbulence simulations as it is very costly especially when coupled to the resolution of chemical reactions. It was hence not considered. Instead, more cost-efficient methods include the recycling of time series of instantaneous velocity planes from an auxiliary simulation similar to the work of Li et al. [31], the specification of the inflow by superposition of random fluctuations on mean flows as done by Lee et al. [32] and the parallel-flow boundary layer method used by Lund et al. [33,34]. In practice, the inflow boundary typically has to be displaced upstream of the region of interest in order to allow for relaxation of the errors made in approximating the inflow conditions. The inclusion of such a "development section" adds to the overall cost of the simulation and therefore one would like to minimize its extent while at the same time, trying to minimize the cost associated with generating the inflow data themselves.

In the present work, the velocity inflow profile is prescribed by a synthetic turbulent flow, of which the mean flow obeys the law of the wall [35] with boundary-layer thickness of $\delta = 1$ mm. The turbulent perturbations with turbulence intensity of 0.2 in the freestream are generated using the method of Klein et al. [36]. This method is able to generate pseudoturbulent inflow conditions based on digital filtering of random data and is able to reproduce prescribed second order statistics as well as auto-correlation functions. It hence provides advantages over the classical approach of using random fluctuations, by reducing the long development section which is induced due to the lack of proper phase information and non-linear energy transfer in random methods.

Based on these considerations and on typical development lengths reported for inflow turbulence [37,38], a development region of 10 boundary layer thicknesses is considered. Also, a sponge layer is applied before the outlet to suppress any numerical wave propagation. In the following analysis, $x = 0$ represents the start of the domain after the development region and not the inflow boundary.

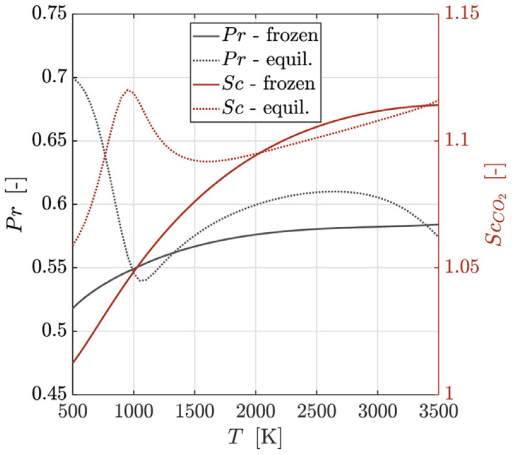

Fig. 2. Prandtl and Schmidt numbers as a function of temperature for the mixture at 20 bar and O/F = 3.0.

The mesh in wall-normal distance is discretized using 236 grid points following a geometric growth rate with a first-cell height corresponding to $y^+ \approx 0.3$ and adequate points to resolve the viscous sublayer following the recommendations in Moser et al. [39]. The mesh in the streamwise and spanwise directions consists of 1400 and 80 equidistant points, respectively. This corresponds to grid resolutions of $\Delta x^+ \approx 11$ and $\Delta z^+ \approx 12$ in the area of interest (after the development region).

For locations further away from the wall, the flow is dominated by energy-transferring motions and there, the grid resolution is better evaluated in terms of the Kolmogorov length scale $\eta_K = ((\mu/\rho)^3\rho/\epsilon)^{1/4}$, where ϵ is the dissipation rate. Due to the presence of heat and mass transfer, apart from the Kolmogorov scale, the thermal Batchelor scale $\eta_T = \eta_K/\sqrt{Pr}$ [40] and scalar Batchelor scale $\eta_S = \eta_K/\sqrt{Sc}$ [41] have to be resolved as well. As the Prandtl Pr and Schmidt Sc numbers of the examined mixture are close to unity for the entire temperature range, η_K, η_T and η_S are all on the same order of magnitude. The variations of the non-dimensional numbers for the mixture are shown in Fig. 2 for the two extreme cases of frozen chemistry and equilibrium conditions. The Schmidt number of CO_2 is chosen as it has the lowest diffusivity among the dominant reaction species. The values are within the resolution requirements of $\Delta x < 12\eta_T$, $\Delta y < 2\eta_T$ and $\Delta z < 6\eta_T$, as also reported in other DNS studies [42–44].

The spanwise extent of the domain was chosen to ensure that it exceeds the minimal size of $l_z^+ = 100$, reported in Jimenez et al. [45]. For a periodic boundary condition to be reasonably accurate the two-point correlations are required to be close to zero at a distance of half the domain size. In Fig. 3, we show the two-point cor-

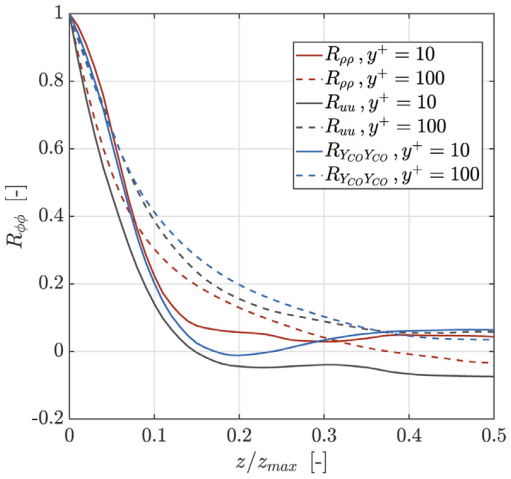

Fig. 3. Two-point correlation for downstream position $x/\delta = 5$.

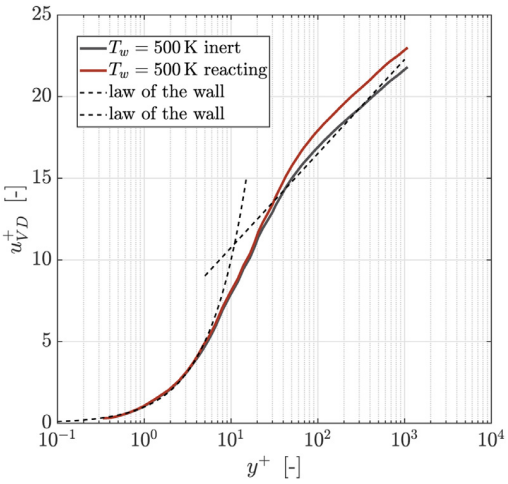

Fig. 4. Normalized velocity profile of the inert and reacting DNS using the van Driest transformation.

relations for density ($R_{\rho\rho}$), streamwise velocity (R_{uu}) and CO mass fractions ($R_{Y_{CO}Y_{CO}}$) at wall-normal positions $y^+ = 10$ and $y^+ = 1000$ and streamwise location $x/\delta = 5$.

For the simulations presented in the following sections, the governing equations for continuity, momentum, energy and transported scalars in the compressible flow are solved as follows [46,47]

$$\partial_t \rho + \nabla \cdot (\rho \boldsymbol{u}) = 0 \tag{1}$$

$$\partial_t (\rho \boldsymbol{u}) + \nabla \cdot (\rho \boldsymbol{u}\boldsymbol{u} + p\boldsymbol{I}) = \nabla \cdot \boldsymbol{\tau} \tag{2}$$

$$\partial_t (\rho E) + \nabla \cdot [\boldsymbol{u}(\rho E + p)] = \nabla \cdot (\boldsymbol{\tau} \cdot \boldsymbol{u}) - \nabla \cdot \dot{\mathbf{q}} \tag{3}$$

$$\partial_t (\rho Y_k) + \nabla \cdot (\boldsymbol{u}\rho Y_k) = -\nabla \cdot \boldsymbol{j}_k + \dot{\omega}_k M_k \tag{4}$$

where ρ is the density, $\boldsymbol{u}$ is the velocity vector, p is the pressure, $\boldsymbol{\tau}$ is the viscous stress tensor, $\dot{\boldsymbol{q}}$ is the heat flux vector and E is the specific total energy defined as the sum of the specific internal energy e and the kinetic energy $|\boldsymbol{u}|^2/2$. The ideal gas equation of state is used as closure for the system of equations.

The viscous stress tensor, heat flux and species diffusion terms are given by:

$$\boldsymbol{\tau} = \mu\left[\nabla \boldsymbol{u} + (\nabla \boldsymbol{u})^T\right] - \frac{2}{3}\mu(\nabla \cdot \boldsymbol{u})\boldsymbol{I}, \tag{5}$$

$$\boldsymbol{q} = -\lambda \nabla T, \tag{6}$$

$$\boldsymbol{j}_k = -\rho\left(D_k \frac{M_k}{M}\nabla X_k - Y_k \sum_{l=1}^{N} D_l \frac{M_l}{M}\nabla X_l\right). \tag{7}$$

To account for the chemical reactions and the production term $\dot{\omega}_k$ the present DNS study considers the detailed GRI 3.0 chemical mechanism [48]. In the case of the inert simulations, the chemical source term is set to zero.

The system of equations is discretized based on a finite-volume approach and a high-order non-dissipative scheme is used for the convective flux discretization [46], which is fourth-order accurate on uniform meshes. A strong stability-preserving third-order Runge-Kutta scheme is used for time advancement [49]. A Strang-splitting scheme [47,50] is employed to separate the convection operator from the remaining operators of the system. A sensor-based hybrid central-ENO scheme is used to capture flows with large density gradients and to minimize the numerical dissipation while stabilizing the simulation. For regions where the density ratio between the reconstructed face value and the neighboring cells exceeds 25%, a second-order ENO reconstruction is used on the left- and right-biased face values, followed by an HLLC Riemann flux evaluation. The flow is well resolved and the ENO scheme is active on less than 0.01% of all cell faces.

3. Results

The results of the DNS are presented in this section for four different computational setups. Reacting and inert simulations are carried out for two different values of the wall temperature (500 K and 1000 K) resulting in a total of four cases. In this section will mainly focus on the results of the case with 500 K wall temperature and we only consider the 1000 K case to show qualitative differences.

3.1. Velocity scaling

For constant-property wall-bounded turbulent flows, the near-wall time-averaged velocity follows the law of the wall [35] with the wall-normalized velocity given by $u^+ = y^+$ in the viscous sublayer ($y^+ < 5$) and by the logarithimic relationship $u^+ = \frac{1}{\kappa}\log(y^+) + B$ in the logarithimic layer ($30 \leq y^+ \leq 0.1\delta$).

For variable-property flows, both the fluid density and the dynamic viscosity are functions of temperature and pressure, leading to additional complexities. One commonly used velocity transformation that allows the scaled velocity to collapse with the incompressible law of the wall is the van Driest transformation [51]:

$$u^+_{\mathrm{VD}} = \int_0^{u^+} \left(\frac{\bar{\rho}}{\bar{\rho}_w}\right)^{1/2} du^+. \tag{8}$$

A comparison of the velocity profiles from the DNS is shown in Fig. 4, where the data support the validity of the van Driest transformation for compressible reacting flows. This can be attributed to the density fluctuations in compressible low-Mach number flows, arising from mean fluid-property variations. This confirms the Morkovin hypothesis [52], which has been used in the past to investigate the compressible turbulent boundary layer in the same line as for the incompressible one by accounting for the effects of mean density variations [53]. In the range of Mach numbers explored in the present study, our DNS results support

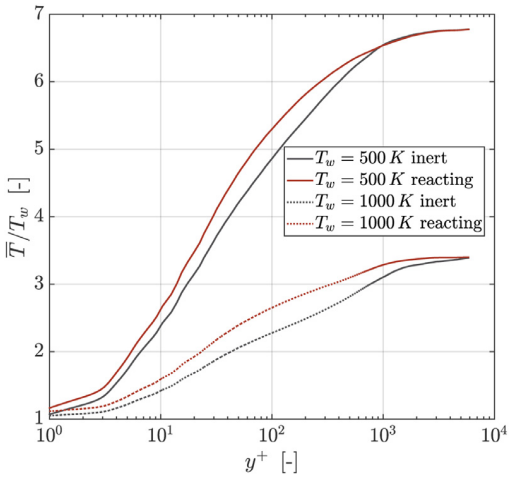

Fig. 5. Temperature profile within the turbulent boundary layer.

previous experimental and numerical studies that showed the validity of the van Driest transformation in scaling the velocity profile with wall heat transfer and even chemical reactions [25,54–57]. In the presence of higher Mach-number flows and real-fluid effects [58], it is expected that additional effects require consideration, related to the compressible nature of the fluid.

3.2. Temperature and species mass fractions

The mean temperature profiles (normalized by the wall temperature) are shown as a function of wall-normal distance in Fig. 5. The effect of chemical reactions in the boundary layer is evident for both wall temperatures. Specifically, the temperature profiles for the reacting cases show higher values in the range $10 \leq y^+ \leq 1000$. The increased temperature is a result of the exothermic reactions that are induced in the low-enthalpy boundary-layer region.

Fig. 6 (a) shows the profile of the mean transformed temperature T^+, which is defined as the temperature difference $\theta = \overline{T} - T_w$ normalized by the friction temperature $T_\tau = \overline{q_w}/\left(\overline{\rho_w}\,\overline{c_{p,w}}\,u_\tau\right)$.

$$T^+ = \frac{\overline{T} - T_w}{T_\tau}. \tag{9}$$

The discrepancies observed between the reacting and inert cases indicate that the wall heat flux is sensitive to chemistry. Specifically, the values for the inert case are higher than the reacting case, indicating the presence of an appreciable heat transfer augmentation due to the chemical reactions.

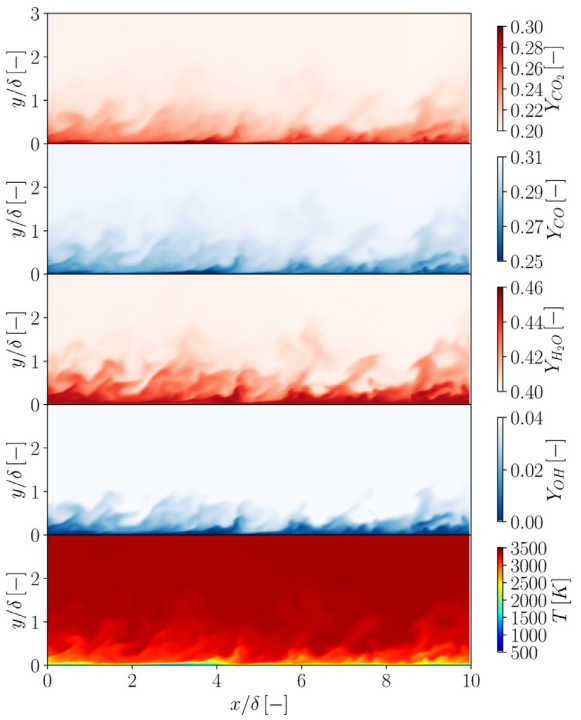

Fig. 7. Instantaneous species mass fractions and temperature field for the reacting case with wall temperature equal to 500 K.

Using the van Driest transformed temperature profile [44]

$$T^+_{\mathrm{VD}} = \int_0^{T^+} \left(\frac{\bar{\rho}}{\bar{\rho}_w}\right)^{1/2} dT^+ \tag{10}$$

as shown in Fig. 6(b), does not lead to a collapse of the inert and reacting profiles. Compared to the findings in Fig. 4, where the velocity profiles for the reacting and inert cases showed similar properties, it is clear that the chemical reactions have an important effect on the fluxes at the wall, even if they do not influence the mean velocity profiles. This finding aligns with the results reported by Carbit et al. [25] and justifies the need of taking care of fluid heterogeneity in wall models.

To illustrate the effect of the chemical reactions, the instantaneous fields of major species and temperature are shown in Fig. 7. The formation of a distinctive species boundary layer in the vicinity of the cooled wall is evident. Specifically, the recombination of CO to CO_2 and that of OH to H_2O is prominent throughout the

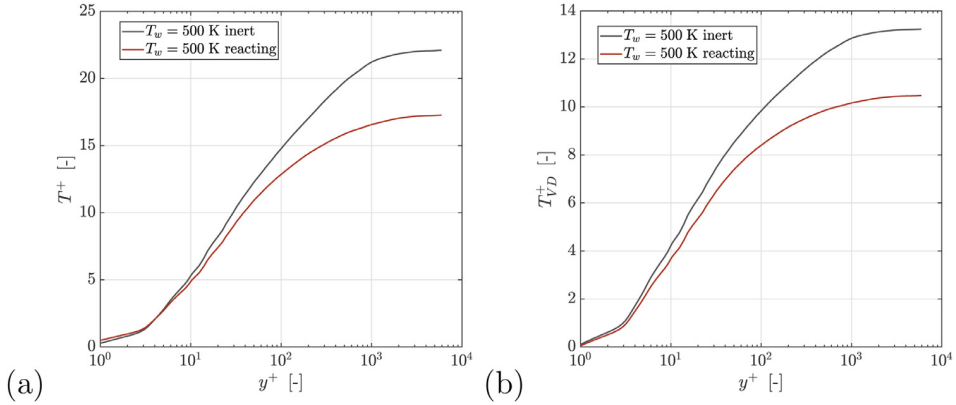

Fig. 6. Profiles of the (a) transformed temperature T^+ and (b) van Driest scaled temperature T^+_{VD} within the turbulent boundary layer.

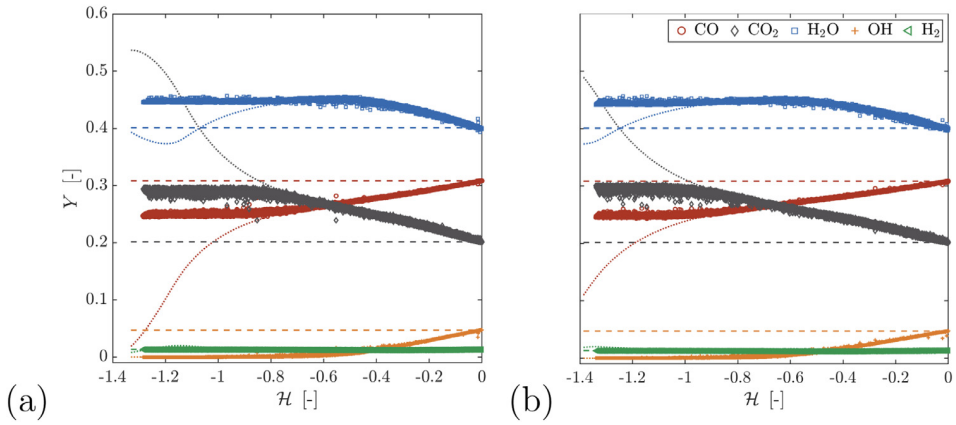

Fig. 8. Instantaneous enthalpy conditioned mass fractions for wall temperature equal to (a) 500 K and (b) 1000 K. Dotted lines correspond to equilibrium mass fractions and dashed lines correspond to frozen mass fractions.

entire domain. Although only major species are shown here, the recombination reactions influence all radicals that also react and form stable species. The locations with increased CO_2 mass fraction and hence reduced CO mass fraction are directly correlated to regions with lower temperature.

In order to obtain a better understanding of where those reactions occur and to quantify the correlation between species mass fractions and enthalpy, we examine Fig. 8, which illustrates the distribution of the major species as a function of the normalized enthalpy loss. $\mathcal{H}$, which is defined as:

$$\mathcal{H} = \frac{h - h_{ad}}{h_w - h_{ad}}, \tag{11}$$

and lower values of $\mathcal{H}$ correspond to conditions closer to the wall. h_{ad} represents the adiabatic enthalpy of the mixture, i.e. the enthalpy of the hot products at the inlet and h_w the enthalpy that the gas would have when cooled down to the wall temperature without changing its composition.

The scatter plots in Fig. 8 show a clear correlation between the normalized enthalpy loss and the species concentration. Compared to the adiabatic values ($\mathcal{H} = 0$), a decrease in enthalpy appears to promote the recombination of OH to H_2O and of CO to CO_2. A noteworthy remark is the small dispersion of the instantaneous data in the enthalpy space, as a very small variation is observed with the point cloud being concentrated around a well established average for each species. We compare the change in concentration with the theoretical chemical equilibrium for each enthalpy level, which is illustrated by the dotted lines in Fig. 8. For enthalpy losses $\mathcal{H} \geq -0.8$ the results follow the chemical equilibrium concentration, indicating that the reaction rates are faster than the competing physical phenomena. In lower enthalpy environment, however, the deviation increases, which implies that the rate of change of the gas composition is now dictated by larger time-scales. Finally, the shift towards the recombined products is not continuously increasing with lower enthalpy but rather reaches a plateau, indicating a freezing of the reactions directly at the wall.

It is noteworthy that the minimum value of $\mathcal{H}$ in the domain is smaller than -1, which corresponds to a quenched (non-reacting) mixture that is cooled to the wall temperature. This arises from the fact that the major combustion products H_2O and CO_2 have a lower formation enthalpy and a lower specific heat capacity than OH and CO. As the gas approaches the wall, the heat loss favors the formation of stable products and results in a lower enthalpy compared to its frozen equivalent.

The spatial distribution of the species composition is illustrated in Fig. 9, where the average mass fraction of the major species is plotted as a function of the wall-normal distance for the reacting cases with $T_w = 500\,\mathrm{K}$ and $T_w = 1000\,\mathrm{K}$. Distinct regions can be identified when examining the species mass fraction profiles. Starting from locations away from the wall ($y^+ \geq 3000$), it appears that no significant change occurs in the composition of the gas, leading to non-varying mass fractions. However at $y^+ \approx 3000$, a species boundary layer starts to develop. The conversion of CO to CO_2 is observed, along with the recombination of OH to H_2O. The mass fraction of H_2 on the other hand is unaltered. For both wall temperatures, the normalized wall-distance at which the chemical reactions take effect are comparable. In accordance with the enthalpy conditioned diagram in Fig. 8 which provides information about a "freezing" of the reactions in enthalpy space, a similar termination of the chemical recombinations is evident in physical space as well. For wall-normal distances with $y^+ < 10$, all major species have reached a constant value, which infers a suppression of the reaction rates because of the low temperature.

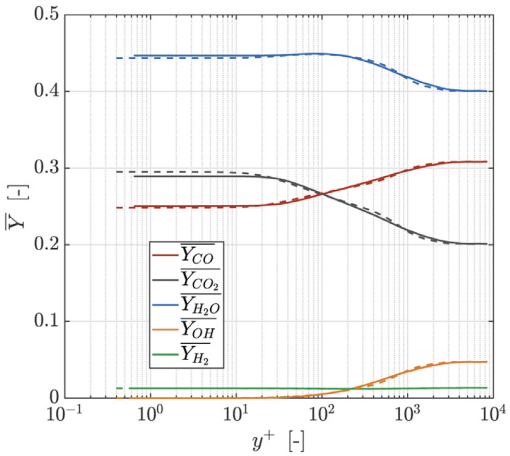

Fig. 9. Mass fractions of the major species as a function of the wall-normal distance for the reacting cases with $T_w = 500\,\mathrm{K}$ (solid line) and $T_w = 1000\,\mathrm{K}$ (dashed line).

Apart from the major species, shown in Fig. 9, the mass fraction profiles of the radical species are depicted in Fig. 10. Similar to the behavior of major species, the radical species concentrations are nearly constant further away from the wall, where the gas is in a state of chemical equilibrium ($y^+ > 2000$). At locations closer to the isothermal wall, the exothermic recombination reactions result in a reduction in the mass fractions of all radicals. This remains for most of the species until a quenching of the reactions is reached at $y^+ < 10$. For the formyl radical (HCO) and formaldehyde (CH_2O), however, a distinct increase in mass fraction is observed starting

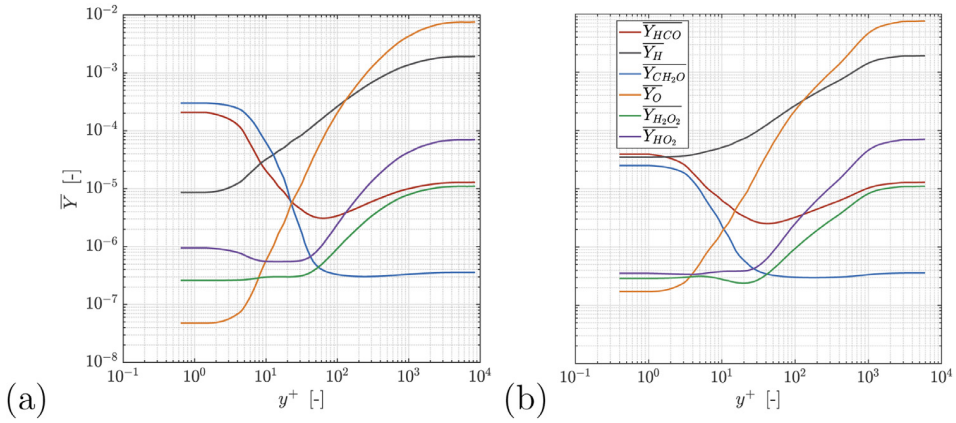

Fig. 10. Minor and radical species mass fractions for the reacting cases as a function of the wall-normal distance for (a) $T_w = 500\,\mathrm{K}$ and (b) $T_w = 1000\,\mathrm{K}$.

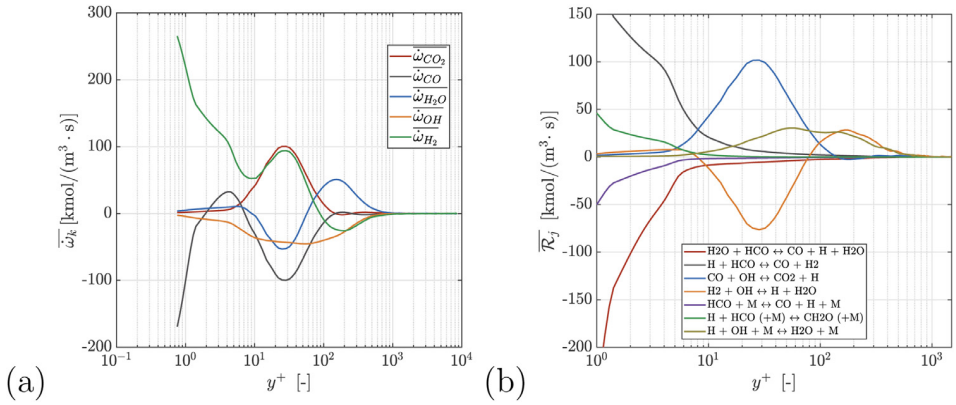

Fig. 11. Profiles of (a) mean net chemical production rates of the major species and (b) mean net rates of progress for the most dominant reactions for the reacting case with $T_w = 500\,\mathrm{K}$.

at $y^+ \approx 100$. A second reaction zone is hence present, in which the formation of HCO and CH_2O is favored.

The results of the species profiles both in conditional and physical space are qualitatively similar for the tow wall temperatures. For that reason, only the case with $T_w = 500\,\mathrm{K}$ is examined in the remaining sections.

3.3. Reaction path analysis

In order to understand the origin of the recombination reactions, the mean net species molar reaction rates $\dot{\omega}_k$ are plotted in Fig. 11(a). In agreement with the species plots in Fig. 9, the reaction rates for $y^+ > 1000$ are exactly zero, whereas the main reaction zone extends from $y^+ \approx 10$ until $y^+ \approx 1000$. Starting at locations further from the wall, it is evident that the hydrogen chemistry is activated first, with the reaction rates of H_2O, H_2 and OH increasing in magnitude already at $y^+ \approx 1000$. The carbon chemistry on the other hand (represented here by the reaction rates of CO and CO_2) is more localized, with non-negligible values for the reaction rates beginning at $y^+ \approx 100$. As far as the net production and destruction of the species is concerned, in the area where the bulk of the reactions takes place (between $y^+ \approx 1000$ and $y^+ \approx 10$), there are regions with positive net production of water and regions with net consumption of water, with the transition occurring at $y^+ \approx 500$. For OH, on the other hand, only net consumption rates are shown. Moreover, as expected based on the scatter results (Fig. 8), CO_2 is predominantly being created in regions where CO has a net consumption rate.

Although the mass fraction of CO appears to be unaffected in regions closer to the wall due to the freezing of the reactions that was established in Fig. 9, a sharp increase in the consumption rate of CO is observed for distances $y^+ < 10$, with a simultaneous increase in the H_2 net creation rate. This effect, which is most prominent for the case with lower wall temperature, occurs at wall-distances that coincide with the regions of increased HCO and CH_2O abundance (from Fig. 10). This secondary reaction zone is hence activated at low temperatures and is confined within the viscous sub-layer.

In order to investigate the nature of this secondary recombination layer, the reactions with the highest mean net rates of progress $\overline{\mathcal{R}_j}$ are explored in Fig. 11(b). The instantaneous rate of progress of reaction j is defined as:

$$\mathcal{R}_j = \Gamma_j \cdot \left(\mathcal{K}_{fj} \prod_{k=1}^{N_{sp}} \mathcal{C}_k^{\nu'_{kj}} - \mathcal{K}_{rj} \prod_{k=1}^{N_{sp}} \mathcal{C}_k^{\nu''_{kj}} \right) \tag{12}$$

where Γ_j is the third-body coefficient, $\mathcal{K}_{fj}$ and $\mathcal{K}_{rj}$ are the forward and reverse reaction coefficients, $\mathcal{C}_k$ is the molar concentration of species k, while ν'_{kj} and ν''_{kj} are the forward and reverse stoichiometric coefficients.

Within the viscous sub-layer, it is apparent that reactions involving HCO are dominant. Specifically, the recombination of CO and H to form HCO using H_2O as collision partner as well as the recombination of HCO and H to CO and H_2 demonstrate the largest rates of progress. The net effect is a net production rate for HCO and a subsequent increase in its mass fraction as shown in Fig. 10. At the same time, the recombination of some of the excess HCO

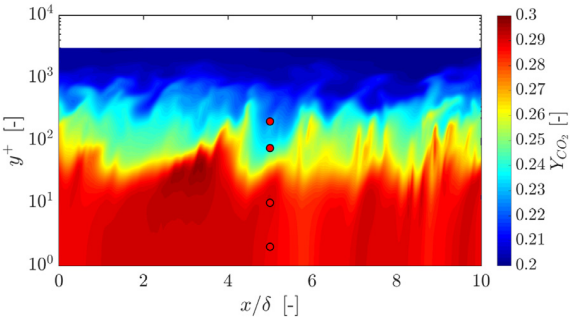

Fig. 12. Instantaneous CO_2 species mass fraction for the reacting case with wall temperature equal to 500 K. The wall-normal distances used in Fig. 13 are indicated with the red markers. (For interpretation of the references to color in this figure legend, the reader is referred to the web version of this article.)

with H to form formaldehyde is also activated in this low temperature region.

The reason for the sharp increase in the mass fractions of HCO and CH_2O is the absence of activation energy for the aforementioned reactions. The formation of formaldehyde is driven by a negative activation energy, which promotes the formation of the molecules in low enthalpy environments. As the temperature drops in the vicinity of the wall, the other reaction rates with positive activation energy start decaying, leading to a freezing of the reactions. For the case of HCO and CH_2O production reactions however, the rates of progress keep increasing as the density and hence radical concentration increase. This agrees with the results reported by Westbrook et al. [14], who investigated the importance of radical recombination reactions with low activation energy and found that radical recombination reactions become the dominant means of consumption of radical species when the temperatures drop below 700–800 K and the rates of radical-fuel reactions fall to very low values.

The paths leading to the production of formyl and formaldehyde in the reacting DNS are illustrated in the reaction flux diagram of Figs. 13. Reaction path diagrams at different wall-normal distances for a representative instantaneous snapshot are included. The forward and backward rates of the most dominant reactions are also used as labels in the diagrams. Going from left to right in Fig. 13, the normalized distances $y^+ = 2$, $y^+ = 10$, $y^+ = 75$ and $y^+ = 200$ are shown. Those distinct locations are also indicated with red markers in Fig. 12. In the regions further from the wall ($y^+ = 200$), the production of H_2O remains most prominent, as the temperature is still high and the reaction rates of the hydrogen chemistry dominate. Approaching the wall, in the lower temperature environment ($y^+ = 75$ and $y^+ = 10$), the recombination of OH and CO to form CO_2 is established as the main reaction path. Directly within the viscous sub-layer nevertheless ($y^+ = 2$), the reaction rates of the CO-to-CO_2 recombination die out and CO feeds the production of HCO via the CO + H and CO + H + M paths. Further absorption of a H-atom leads to the production of formaldehyde.

Given the presence of two distinct reaction zones (one where OH and CO recombine to form carbon dioxide and water and the other where CO recombines to formyl and formaldehyde), the individual contributions of these two modes to the total heat release rate are quantified in Fig. 14. The mean local heat release rate $\overline{\dot{Q}}$ as well as the integrated cumulative heat release $\overline{\dot{Q}}_{cumul}$ are shown for the two reacting cases. The cumulative heat release is defined as the percentage of the total energy release starting from the wall and moving towards the free stream:

$$\overline{\dot{Q}}_{cumul} = \cdot \frac{\int_0^y \overline{\dot{Q}}(y)dy}{\int_0^\infty \overline{\dot{Q}}(y)dy} \tag{13}$$

As expected from the results of the species production rates in Fig. 11, the total heat release rate has a local maximum close to $y^+ \approx 60$ and a further maximum with a larger value directly at the wall ($y^+ = 1$). For the case with $T_w = 500$ K, the maximum corresponding to the HCO recombination is more prominent. However, looking at the distribution of $\overline{\dot{Q}}_{cumul}$ in Fig. 14, it becomes evident that the HCO production reactions do not have a significant contribution to the total heat release. Within the viscous sub-layer ($y^+ < 10$), approximately 6% of the total energy is set free. The bulk majority of the chemical energy is released between $y^+ \approx 10$ and $y^+ \approx 1000$, with a subsequent ceasing of the energy production in the regions with high temperature. The low-temperature recombination reactions with zero activation energy have hence a minimal impact on the total energy release, as they are only activated in a region with restricted volume in the direct vicinity of the wall.

By comparing the total heat release rate with the net rate of progress for the most dominant reaction in Fig. 11(b), it can be inferred that the two reactions responsible for the majority of the energy being released in the boundary layer are the production of OH following the path H + H_2O → H_2 + OH and the subsequent recombination of OH and CO following the path CO + OH → CO_2 + H. The latter reaction path has also been identified as the most dominant reaction in the boundary layer of rocket thrust chambers in prior work [9].

3.4. Chemical time-scales

The exothermic CO recombination reaction that is activated in the low-temperature environment can be explained by Le Chatelier's principle, as the initially equilibrated gas is subjected to a change in enthalpy and reacts by undergoing exothermic reactions that aim at counteracting the applied change. However, with decreasing temperature near the wall, the reaction rates also approach zero which gives rise to two competing effects: the low temperature, which is the initiator for the reactions is also the limiting factor that does not allow the composition to reach its new equilibrium. This results in a significant increase in the chemical time-scales and is expressed by an apparent "quenching" of the chemical reactions.

To understand the competing effects that dominate the change in chemical composition, we choose to describe the chemical time-scale along the wall normal direction using the Computational Singular Perturbation (CSP) technique by Lam et al. [59] which is used in the Chemical Explosive Mode Analysis (CEMA) as introduced by Lu et al. [60]. The time-scale is then defined as:

$$\tau_c = \frac{\|\dot{\boldsymbol{\omega}}\|}{\|\boldsymbol{J} \cdot \dot{\boldsymbol{\omega}}\|}, \tag{14}$$

where the species Jacobi matrix is given by the sensitivity of the net species reaction rates to a change in the species mass fractions.

The mean chemical time-scale τ_c for the reacting cases is shown in Fig. 15 along with the local Damköhler number. Two different definitions for the Dahmköhler number are included, one based on the Kolmogorov time-scale τ_K and one based on the integral turbulent time-scale τ_t. The respective time-scales and Damköhler numbers are given as:

$$\tau_K = \sqrt{\frac{\mu}{\rho\epsilon}}, \quad Da_K = \tau_K/\tau_c \tag{15}$$

$$\tau_t = \frac{k}{\epsilon}, \quad Da_t = \tau_t/\tau_c \tag{16}$$

Fig. 15 shows that, the chemical time-scale is small in regions away from the wall, indicating that the gas mixture is close to its equilibrium concentration. Moving towards the wall however, as the temperature decreases, a slowing-down of the reactions takes

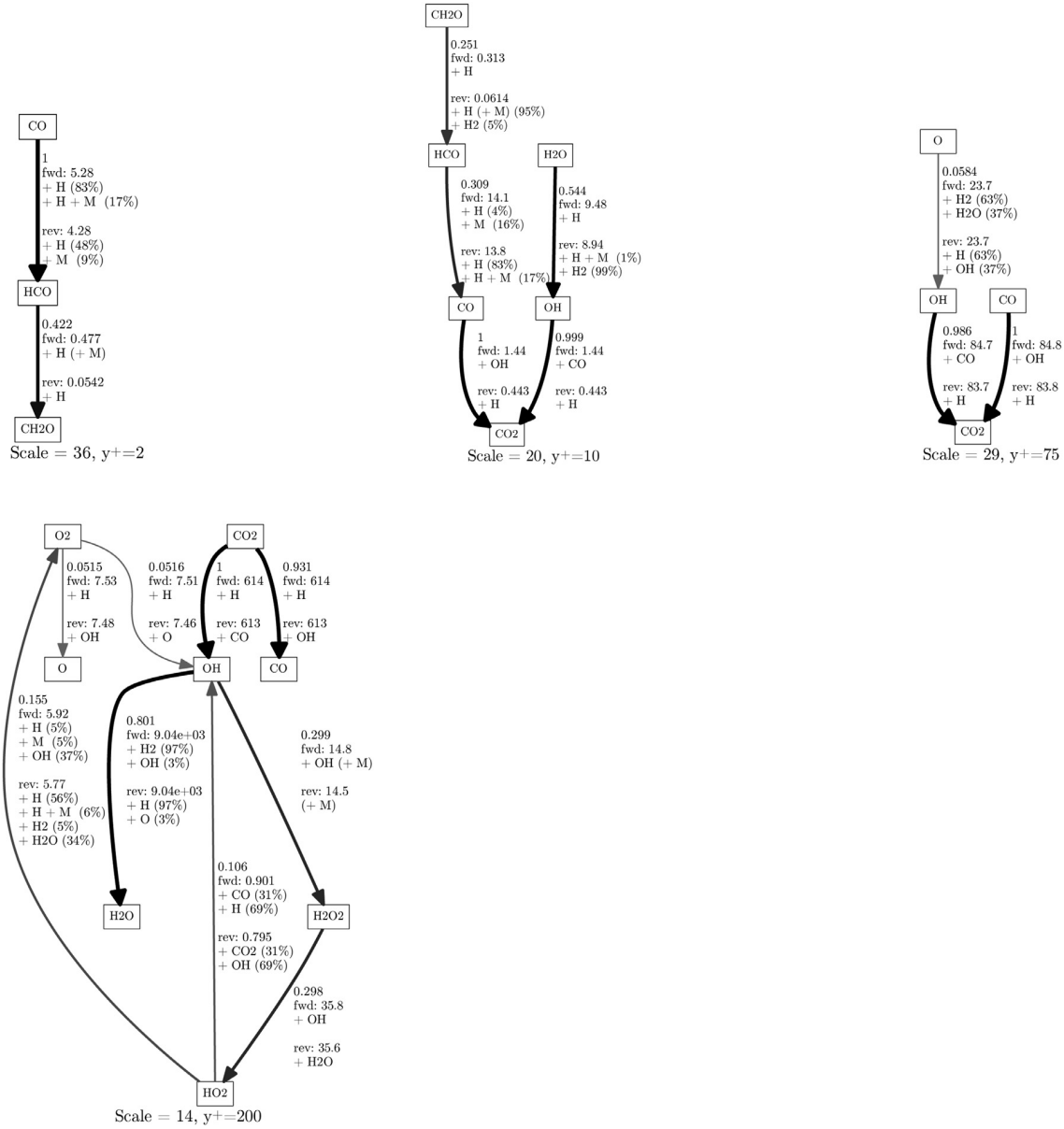

Fig. 13. Reaction flux path diagram for the oxygen atom at different wall-distances in the reacting case with $T_w = 500\,\mathrm{K}$.

place. This trend persists up until $y^+ \approx 30$, where the chemical time-scale has a local maximum and then subsequently reduces further. This secondary reduction in the time-scale represents the zone where the formyl and formaldehyde production become dominant. At the same time, both the turbulent time-scale and the Kolmogorov time-scale are monotonically reduced for locations closer to the wall.

This leads to comparable results for Da_K and Da_t. Both of them have large values between 4×10^4 and 9×10^5 outside the boundary layer and reach values between 0.1 and 5 within the viscous sub-layer. In the region where the reaction rates of the main exothermic recombination reactions of CO and OH start diminishing ($y^+ < 10$), the Damköhler number reaches values close to unity. This implies that after this point the turbulent and Kolmogorov time-scales dictate the evolution of the species which confirms the assumption that the freezing of the chemical reactions is due to the large chemical time-scales in the low-temperature environment.

3.5. Wall heat transfer amplification

Understanding the conditions that lead to the enhancement of the exothermic recombination reactions in the cooled boundary layer is of major importance for the prediction of wall heat loads in rocket thrust chambers and other propulsion systems. Using the comparison between the inert and reacting cases, the effect of the additional energy release in the wall vicinity can be isolated and quantified. The results for the mean wall heat loads for the different DNS cases examined here are summarized in Table 1.

These results show that, lower wall temperatures lead to a higher heat flux, as this is proportional to the temperature difference between the wall and the free stream temperature (which is equal to the adiabatic equilibrium temperature). The same is true when comparing the two reacting cases to each other, with the lower wall temperature leading to a higher wall heat transfer rate. For a given wall temperature, an increase of approximately 20% is obtained from the effect of the chemical recombinations.

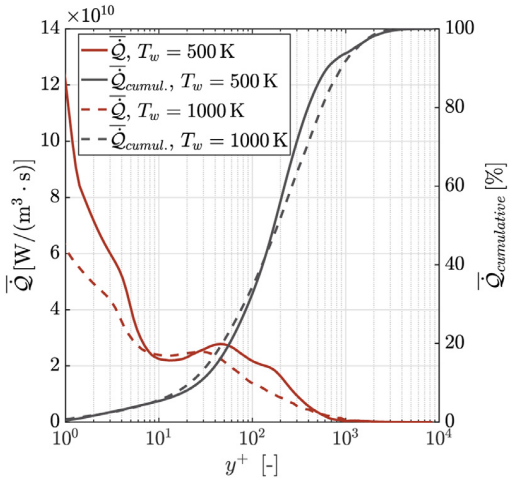

Fig. 14. Mean heat release rate and cumulative energy release for the reacting cases with $T_w = 500$ K and $T_w = 1000$ K.

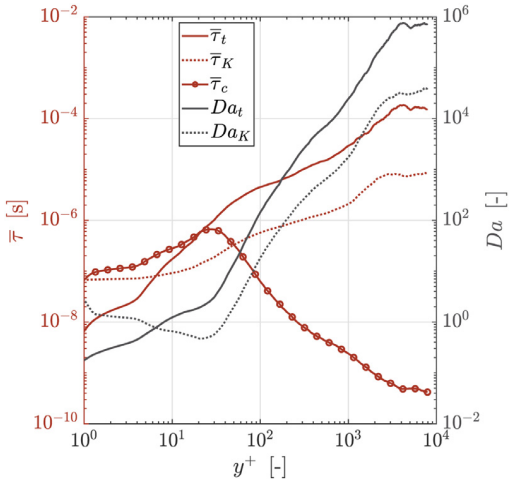

Fig. 15. Chemical time-scale and Damköhler number for the reacting case with $T_w = 1000$ K.

Table 1
Mean wall heat flux for the different cases.

Case	Mean heat flux
Reacting, $T_w = 500$ K	11.93 MW/m^2
Reacting, $T_w = 1000$ K	9.87 MW/m^2
Inert, $T_w = 500$ K	10.01 MW/m^2
Inert, $T_w = 1000$ K	8.27 MW/m^2

This degree of under-prediction of the heat loads when using models that do not account for recombination reactions is comparable with the values reported by Betti et al. [10] for low-pressure methane/oxygen rocket engines. It was also reported in the same work that the difference between inert and reacting treatment for the boundary layer reduces with increasing operating pressures.

Apart from the averaged values for the heat loads reported in Table 1, the local variation of the heat flux is plotted in Fig. 16 for representative instantaneous snapshots. Localized "hot islands" with heat flux values two times larger than the mean average are visible. This is also illustrated in Fig. 17, where the Probability Density Function (PDF) of the instantaneous local heat flux values is plotted for each of the four simulations. A consequence of the overall higher heat flux level, the reacting cases have a wider distribution compared to the respective inert ones. The presence of strong

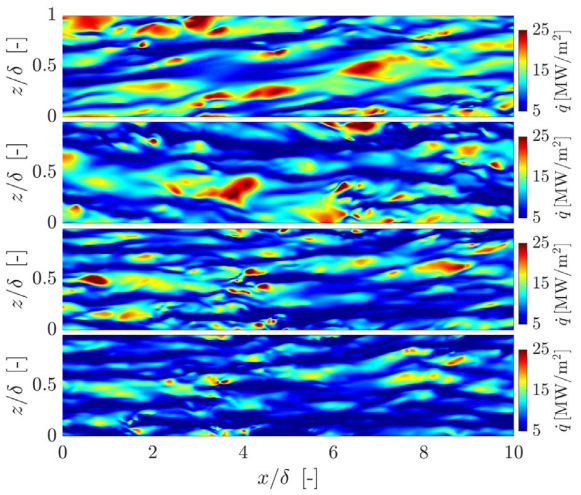

Fig. 16. Instantaneous wall heat flux. From top to bottom: reacting case with $T_w = 500$ K, reacting case with $T_w = 1000$ K, inert case with $T_w = 500$ K, inert case with $T_w = 1000$ K.

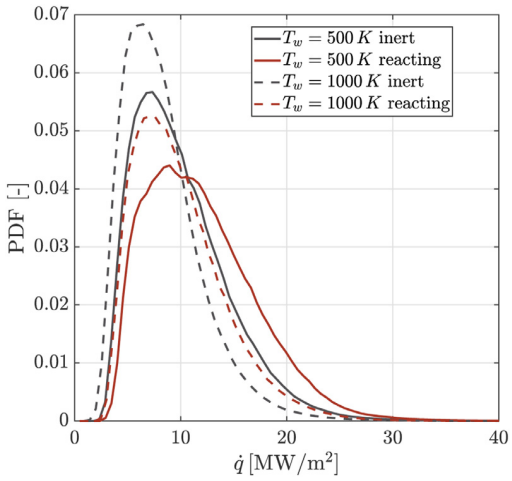

Fig. 17. PDFs for the wall heat flux distribution.

fluctuations in the experienced wall heat loads can lead to significant deviations from the mean values which in turn could lead to strong temperature gradients and higher thermal stresses on the walls. However, the time-scales of the turbulent fluctuations which are responsible for the spatial variation, shown in Fig. 16 and 17, are much shorter than typical conduction time-scales in the material and hence do not pose an issue for the design of cooling systems.

3.6. Turbulent fluctuations

In an effort to examine the sensitivity of reaction rates to compositional variations, Figs. 18 and 19 show PDFs of Y_k, T and $\dot{\omega}_k$ at three distinct distances from the wall. The case with $T_w = 500$ K is shown here and the results obtained with the higher wall temperature are qualitatively similar. In contrast to the enthalpy-conditioned distribution from Fig. 8, which clearly showed a minimal variation of the species mass fractions around its average, the PDFs at different spatial locations show a much larger variability. Wider distributions for both the temperature as well as major species mass fractions are observed within the logarithmic region of the boundary layer ($y^+ = 75$). Approaching the wall and entering the viscous sub-layer where turbulent effects are less promi-

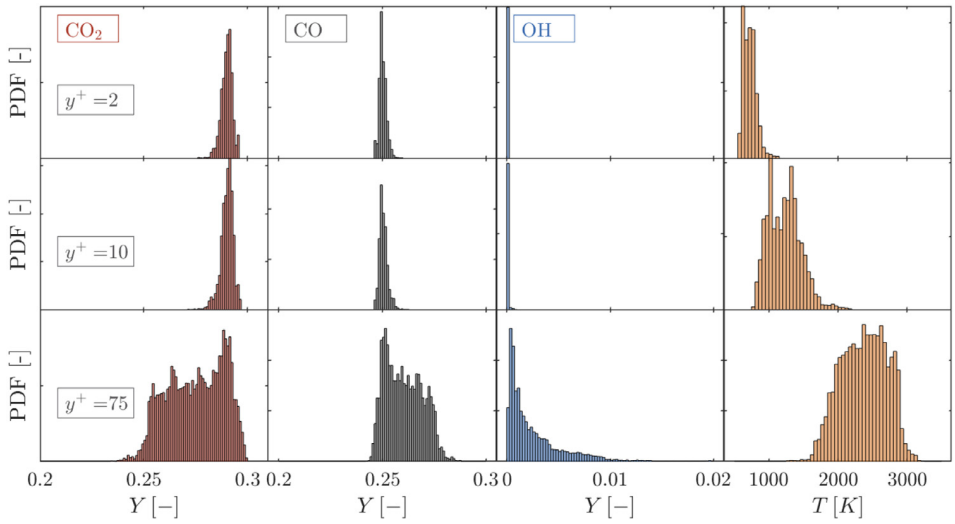

Fig. 18. PDFs of species mass fractions and temperature at different wall distances for the reacting case with $T_w = 500$ K.

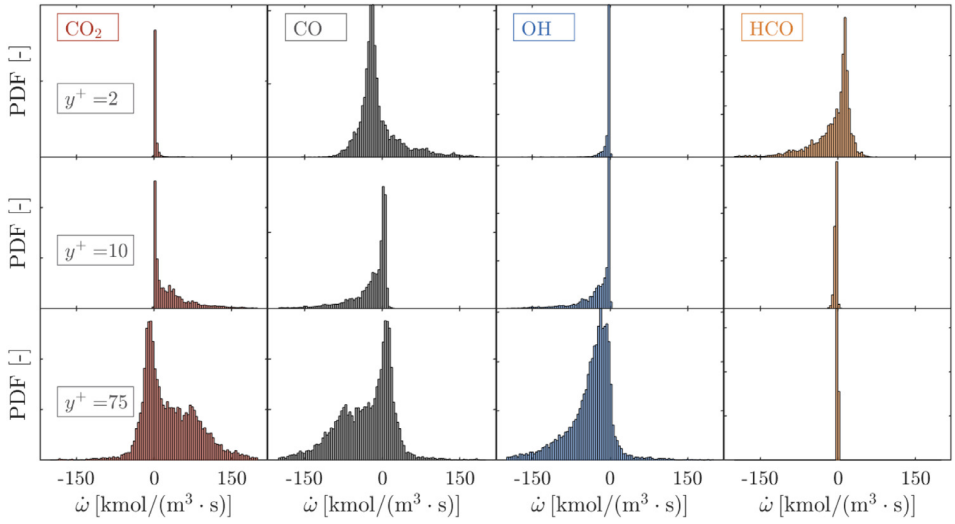

Fig. 19. Probability density function of species molar reaction rates at different wall distances for the reacting case with $T_w = 500$ K.

nent, the width of the distributions quickly shrinks. For OH in fact, the PDF of the mass fraction converges to a Dirac function around zero, as most of the OH is consumed before the begin of the viscous sub-layer.

The net molar production rates at $y^+ = 75$ demonstrate a clear correlation between the consumption of CO and the production of CO_2 and exhibit a large variation which extends in the range from - 150 to 150 kmol/(m^3s), while the average value lies at $\pm$ 35 kmol/(m^3s for CO_2 and CO, respectively. Closer to the wall, the correlation between the CO and CO_2 reaction rates ceases to be dominant, as carbon dioxide no longer undergoes any further chemical reactions in alignment with the results in Fig. 11. Instead, as the reaction path including HCO is activated, a correlation between the reaction rates of formyl and carbon monoxide is visible. It is also noteworthy that the reaction rate of HCO was close to zero for locations within the log-layer, whereas it exhibits a large variability in the vicinity of the wall owing to non-negligible variations in temperature and CO mass fraction.

To further examine the non-linearity of mass fractions and reaction rates, a scatter plot of instantaneous and averaged net species production rates are given in Fig. 20. The grey points represent instantaneous results, mapped onto the conditional $Y_k - T$ space, while the dashed line corresponds to the projection of the averaged quantities, i.e. to the manifold $\overline{Y}_k - \overline{T}$.

It is evident that the estimation of the reactions rates using the averaged fields for mass fractions and temperature $\dot{\omega}_k(\overline{Y}_i, \overline{T})$ leads to significant overestimation compared to the time-averaged production rates $\overline{\dot{\omega}_k(Y_i, T)}$ (which correspond to the results from Fig. 11) both for CO and CO_2. The two results for the production rates deliver similar values in the hot regions (where the gas is near its chemical equilibrium) as well as in the direct vicinity of the wall, where a quenching of the reactions occur. For the intermediate positions however, differences larger than one order of magnitude are observed. This is an indication for strong turbulence-chemistry interaction, which leads to the confirmation that the closure of the chemical source term is inadequately described by a first-order approximation of the reaction rate:

$$\overline{\dot{\omega}_k(Y_i, T)} \neq \dot{\omega}_k(\overline{Y}_i, \overline{T}) \tag{17}$$

The deviation between the two quantities can be attributed to the correlation between mass fraction fluctuations and temperature fluctuations. This is shown in Fig. 21, which clearly illustrates that a positive correlation holds in the reacting zone for CO, while a negative correlation can be found for CO_2. No significant differ-

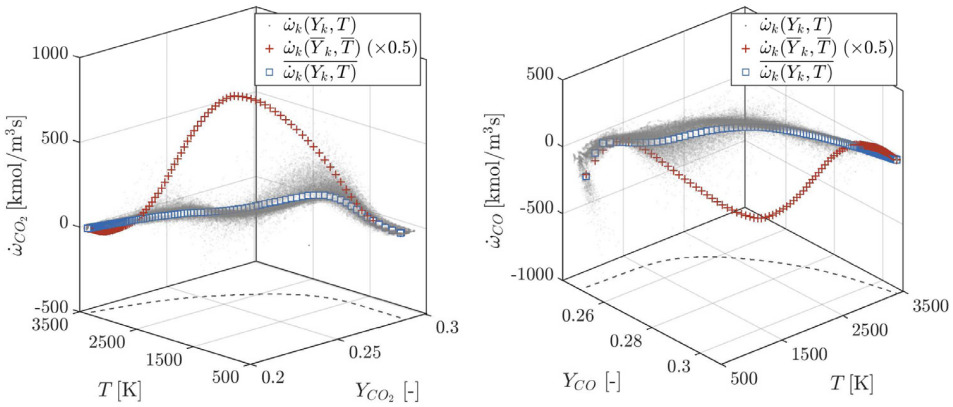

Fig. 20. Scatter plot of the instantaneous and averaged chemical source terms for (a) CO_2 and (b) CO in conditional space for $T_w = 500$ K. The dashed lines correspond to the manifold correlating mean temperature and mean mass fractions.

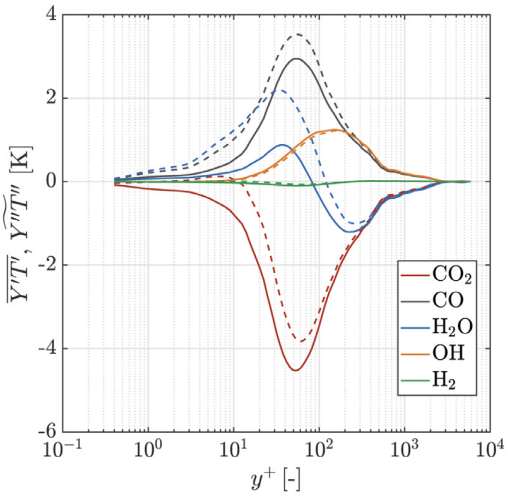

Fig. 21. Correlation of turbulent fluctuations for species mass fractions and temperature for the reacting case with $T_w = 500$ K. The solid line represents the Reynolds averaged quantity $\overline{Y'T'}$, while the dashed line represents the Favre averaged $\widetilde{Y''T''}$.

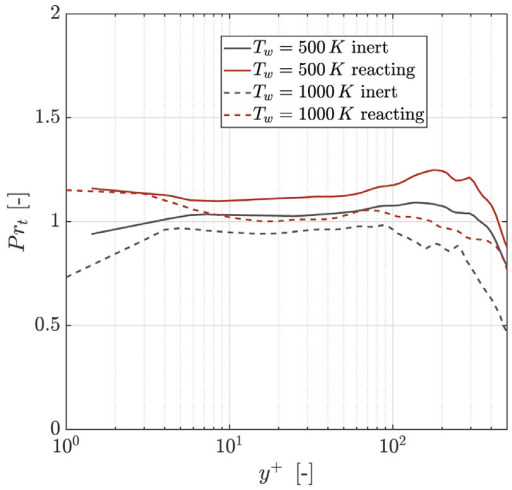

Fig. 22. Turbulent Prandtl number for the four DNS cases as a function of the wall-normal distance.

ence can be found between the compressible and incompressible definitions ($\widetilde{Y''T''}$ and $\overline{Y'T'}$), as they both give qualitatively identical results.

Finally, we investigate whether the turbulent fluctuations and the feedback produced by the chemical reactions give rise to an enhancement of the turbulent heat transfer. To quantify this, the turbulent Prandtl number is calculated for all four DNS cases. The turbulent Prandtl number is defined as the ratio of the turbulent thermal diffusivity α_T and the turbulent viscosity α_M. The strong Reynolds analogy assumes that the turbulent heat transfer and the turbulent momentum transfer are similar, resulting in a turbulent Prandtl number equal to unity. Based on experimental and numerical studies, it has been found that the Reynolds analogy is valid for most boundary layer flows, although departures from $Pr_t = 1.0$ have been reported [61].

Common practice in most turbulence models for RANS, is to approximate Pr_t by a constant value, which in some cases, can lead to incorrect heat transfer predictions. This is typically the case in supercritical flows, where strong gradients in the molecular Prandtl number give rise to spatial variations for Pr_t [62]. For gases at high-temperature conditions, with nearly constant molecular Prandtl number (as in the present operating point) and high turbulent Peclet number, the Prandtl number is nearly constant within the log region with values around 0.85 and 1, while in the "wake" region of external turbulent boundary layers it was found to decrease in the neighborhood of 0.5-0.7 [61]. Previous studies of reacting turbulent boundary layers performed by Cabrit et al. [25] found that the turbulent Prandtl number varies from around 0.5 in the middle of their turbulent channel up to values close to 1.2 in the wall vicinity. No qualitative differences were obtained in the Pr_t profiles between inert and reacting cases.

Similar findings are reported in Fig. 22 by analyzing the results of the present DNS. The compressible definition was employed for the calculation:

$$Pr_t = \frac{\widetilde{u''v''}}{\widetilde{v''h''}} \frac{\partial \widetilde{h}/\partial y}{\partial \widetilde{u}/\partial y} \tag{18}$$

For all cases, the turbulent Prandtl number appears to be nearly constant throughout the logarithmic and viscous sub-layer regions. Differences between the individual cases are small, with the reacting cases having the tendency of producing higher turbulent Prandtl numbers. Values between 0.9 and 1.2 are found within the region where the bulk energy release takes place ($y^+ \approx 10$ to $y^+ \approx 100$). Further from the wall, a drop of the turbulent Prandtl number to values as low as 0.5 is observed.

4. Conclusions

In the present study, DNS of a reacting boundary layer have been carried out. Mixtures representative of the conditions within

rocket engines and high-pressure propulsion systems have been chosen, corresponding to an equilibrated mixture of methane and oxygen at 20 bar. In order to isolate effects of chemical reactions resulting from the low-enthalpy environment in the vicinity of the isothermal wall, inert and reacting simulations were carried out for the same operating conditions. A detailed chemical mechanism was employed to account for the role of chemical radical recombinations in the vicinity of the wall.

Evaluation of the temperature profile showed that deviations between the inert and reacting cases were prominent, resulting from the energy release within the boundary layer. The energy released from the recombination of CO and OH to form H_2O and CO_2 was identified as the main effect for the temperature increase. This effect was found to be qualitatively similar for both wall conditions.

The analysis of reaction rates showed strong non-equilibrium effects. Although a clear correlation between the degree of recombination of CO and the local enthalpy value was found, the species mass fractions profiles deviated from the theoretical equilibrium values. Moreover, for regions up until the begin of the viscous sub-layer ($y^+ \approx 10$), a quenching of the major species mass fractions was observed. Further examination of the chemical reaction rates confirmed that the occurrence of this layer with chemically quenched composition arises from the low temperature and resulting long chemical time-scales. In fact, the chemical time-scales at the locations where the recombination rates start diminishing reach values that are larger than the turbulent and Komlmogorov time-scales and hence chemistry is no longer the rate-defining process.

Closer to the wall, despite the termination of the CO recombination, the recombination of CO to HCO and the subsequent formation of CH_2O is activated. This reaction path was detected using reaction flux diagrams and showed that the production of formyl and formaldehyde is favored by low wall temperatures. Due to the restricted extent of the region in which the temperatures are low enough to activate the aforementioned reactions, the total energy released from this reaction path amounted to approximately 5% of the total heat release in the boundary layer.

As far as the wall heat transfer is concerned, the exothermic reactions contributed to an additional 20% in heat flux compared to the equivalent inert cases. No qualitative difference was observed between the results with low (500 K) and high (1000 K) wall temperature. The non-negligible augmentation of the heat transfer puts additional emphasis on the importance of the recombination reactions in modeling efforts of flame-wall interaction, like in the case of non-adiabatic flamelet manifolds.

A strong coupling between turbulence and chemistry was also inferred from the results. Strong variations in mass fractions and temperature within the reacting zone resulted in a large variance of the resulting reaction rates and broad PDFs for the source terms. The assumption of first-order representation of the reaction rate was hence assessed as inadequate to describe the turbulence-chemistry interaction processes in the reaction zone. Despite the strong correlation of species and temperature fluctuations and the additional energy released via the chemical reactions, no significant enhancement of the turbulent heat transfer was observed. Evaluation of the turbulent number for both the reacting and inert cases delivered values for Pr_t close to unity with fairly constant profiles along the entirety of the logarithmic and viscous sub-layers.

The strong presence of non-equilibrium effects, dictated by the competition between turbulent and chemical time-scales as well as the intensity of the TCI throughout the turbulent boundary layer, highlight the difficulty of modeling the near-wall region in the presence of chemically reacting flows and strong temperature gradients. Examination of further operating points and fuels is of interest in order to understand the processes occurring within the reacting boundary layer of rocket engines and gas turbines for a broad spectrum of applications. Based on the representative load point chosen for this analysis however, the importance of the recombination effects on the wall heat flux augmentation is illustrated. For that reason, future models developed for the treatment of near-wall effects in reacting simulations should account for the quenching of the reactions within the buffer and viscous sub-layers.

Declaration of Competing Interest

None.

CRediT authorship contribution statement

Nikolaos Perakis: Conceptualization, Methodology, Software, Writing - original draft, Visualization. **Oskar J. Haidn:** Resources, Supervision. **Matthias Ihme:** Conceptualization, Resources, Supervision, Writing - review & editing.

Acknowledgements

Resources supporting the DNS study were provided by the NASA High-End Computing Program through the NASA Advanced Supercomputing Division at Ames Research Center (Award No. NNX15AV04A) and by the GCS Supercomputer SuperMUC at Leibniz Supercomputing Centre. Financial support has been provided by the German Research Foundation (Deutsche Forschungsgemeinschaft DFG) in the framework of the Sonderforschungsbereich Transregio 40.

References

[1] A. Dreizler, B. Böhm, Advanced laser diagnostics for an improved understanding of premixed flame-wall interactions, Proc. Combust. Inst. 35 (1) (2015) 37–64, doi:10.1016/j.proci.2014.08.014.
[2] M. Mann, C. Jainski, M. Euler, B. Böhm, A. Dreizler, Transient flame–wall interactions: experimental analysis using spectroscopic temperature and co concentration measurements, Combust. Flame 161 (9) (2014) 2371–2386, doi:10.1016/j.combustflame.2014.02.008.
[3] N. Peters, Laminar diffusion flamelet models in non-premixed turbulent combustion, Prog. Energy Combust. Sci. 10 (3) (1984) 319–339.
[4] P.C. Ma, H. Wu, M. Ihme, J.-P. Hickey, Nonadiabatic flamelet formulation for predicting wall heat transfer in rocket engines, AIAA J. 56 (6) (2018) 2336–2349, doi:10.2514/1.J056539.
[5] P. Breda, M. Pfitzner, N. Perakis, O. Haidn, Generation of non-adiabatic flamelet manifolds: comparison of two approaches applied on a single-element GCH4/GO2 combustion chamber, in: 8th European Conference for Aeronautics and Space Sciences (EUCASS), 2019.
[6] N. Perakis, C. Roth, O.J. Haidn, Development of a non-adiabatic flamelet model for reacting flows with heat loss, in: Space Propulsion Conference 2018, 2018.
[7] D. Cecere, E. Giacomazzi, F.R. Picchia, N. Arcidiacono, F. Donato, R. Verzicco, A non-adiabatic flamelet progress variable approach for LES of turbulent premixed flames, Flow Turbul. Combust. 86 (3) (2011) 667–688, doi:10.1007/s10494-010-9319-7.
[8] B. Fiorina, R. Baron, O. Gicquel, D. Thevenin, S. Carpentier, N. Darabiha, et al., Modelling non-adiabatic partially premixed flames using flame-prolongation of ILDM, Combust. Theor. Model. 7 (3) (2003) 449–470, doi:10.1088/1364-7830/7/3/301.
[9] N. Perakis, O. Haidn, M. Ihme, Investigation of CO recombination in the boundary layer of CH4/O2 rocket engines, Proc. Combust. Inst. 80 (7) (2020), doi:10.1016/j.proci.2020.07.080.
[10] B. Betti, D. Bianchi, F. Nasuti, E. Martelli, Chemical reaction effects on heat loads of CH4/O2 and H2/O2 rockets, AIAA J. 54 (1) (2016) 1693–1703, doi:10.2514/1.J054606.
[11] D. Rahn, H. Riedmann, O. Haidn, Conjugate heat transfer simulation of a subscale rocket thrust chamber using a timescale based frozen non-adiabatic flamelet combustion model, AIAA Propulsion and Energy 2019 Forum, AIAA Paper 2019–3864, 2019, doi:10.2514/6.2019-3864.
[12] N. Perakis, O.J. Haidn, Wall heat transfer prediction in CH4/O2 and H2/O2 rocket thrust chambers using a non-adiabatic flamelet model, Acta Astronaut. 174 (2020) 254–269.
[13] D. Muto, Y. Daimon, T. Shimizu, H. Negishi, An equilibrium wall model for reacting turbulent flows with heat transfer, Int. J. Heat Mass Transf. 141 (2019) 1187–1195, doi:10.1016/j.ijheatmasstransfer.2019.05.101.

[14] C.K. Westbrook, A.A. Adamczyk, G.A. Lavoie, A numerical study of laminar flame wall quenching, Combust. Flame 40 (1981) 81–99, doi:10.1016/0010-2180(81)90112-7.
[15] W. Hocks, N. Peters, G. Adomeit, Flame quenching in front of a cold wall under two-step kinetics, Combust. Flame 41 (1981) 157–170, doi:10.1016/0010-2180(81)90049-3.
[16] P. Popp, M. Smooke, M. Baum, Heterogeneous/homogeneous reaction and transport coupling during flame-wall interaction, Symp. (Int.) Combust. 26 (2) (1996) 2693–2700, doi:10.1016/S0082-0784(96)80105-6.
[17] P. Popp, M. Baum, Analysis of wall heat fluxes, reaction mechanisms, and unburnt hydrocarbons during the head-on quenching of a laminar methane flame, Combust. Flame 108 (3) (1997) 327–348, doi:10.1016/S0010-2180(96)00144-7.
[18] F. Dabireau, B. Cuenot, O. Vermorel, T. Poinsot, Interaction of flames of H2 and O2 with inert walls, Combust. Flame 135 (1–2) (2003) 123–133, doi:10.1016/S0010-2180(03)00154-8.
[19] T. Poinsot, D.C. Haworth, G. Bruneaux, Direct simulation and modeling of flame-wall interaction for premixed turbulent combustion, Combust. Flame 95 (1–2) (1993) 118–132, doi:10.1016/0010-2180(93)90056-9.
[20] G. Bruneaux, K. Akselvoll, T. Poinsot, J. Ferziger, Flame-wall interaction simulation in a turbulent channel flow, Combust. Flame 107 (1–2) (1996) 27–44, doi:10.1016/0010-2180(95)00263-4.
[21] T.M. Alshaalan, C.J. Rutland, Turbulence, scalar transport, and reaction rates in flame-wall interaction, Symp. Combust. 27 (1) (1998) 793–799, doi:10.1016/S0082-0784(98)80474-8.
[22] A. Gruber, R. Sankaran, E.R. Hawkes, J.H. Chen, Turbulent flame-wall interaction: a direct numerical simulation study, J. Fluid Mech. 658 (2010) 5, doi:10.1017/S0022112010001278.
[23] M.P. Martin, G.V. Candler, DNS of a Mach 4 boundary layer with chemical reactions, 38th Aerospace Sciences Meeting and Exhibit 2000, AIAA Paper 2000-399, 2000.
[24] M.P. Martin, G.V. Candler, Temperature fluctuation scaling in reacting boundary layers, in: 15th AIAA Computational Fluid Dynamics Conference, AIAA Paper 2001–2717, 2001, doi:10.2514/6.2001-2717.
[25] O. Cabrit, F. Nicoud, Direct simulations for wall modeling of multicomponent reacting compressible turbulent flows, Phys. Fluids 21 (5) (2009) 055108, doi:10.1063/1.3123528.
[26] N. Perakis, D. Rahn, O.J. Haidn, D. Eiringhaus, Heat transfer and combustion simulation of seven-element O2/CH4 rocket combustor, J. Propul. Power 35 (6) (2019) 1080–1097, doi:10.2514/1.B37402.
[27] S. Xu, M.P. Martin, Assessment of inflow boundary conditions for compressible turbulent boundary layers, Phys. Fluids 16 (7) (2004) 2623–2639.
[28] M. Rai, P. Moin, Direct numerical simulation of transition and turbulence in a spatially evolving boundary layer, in: 10th Computational Fluid Dynamics Conference, 1993, pp. 890–914.
[29] K. Bhaganagar, D. Rempfer, J. Lumley, Direct numerical simulation of spatial transition to turbulence using fourth-order vertical velocity second-order vertical vorticity formulation, J. Comput. Phys. 180 (1) (2002) 200–228.
[30] F. Ducros, P. Comte, M. Lesieur, Large-eddy simulation of transition to turbulence in a boundary layer developing spatially over a flat plate, J. Fluid Mech. 326 (1996) 1–36.
[31] N. Li, E. Balaras, U. Piomelli, Inflow conditions for large-eddy simulations of mixing layers, Phys. Fluids 12 (4) (2000) 935–938.
[32] S. Lee, S.K. Lele, P. Moin, Simulation of spatially evolving turbulence and the applicability of Taylors hypothesis in compressible flow, Phys. Fluids A 4 (7) (1992) 1521–1530, doi:10.1063/1.858425.
[33] T.S. Lund, Large-eddy simulation of a boundary layer with concave streamwise curvature (1994).
[34] T.S. Lund, P. Moin, Large-eddy simulation of a concave wall boundary layer, 17, 1996, pp. 290–295.
[35] S.B. Pope, Turbulent Flows, Cambridge University Press, 2001.
[36] M. Klein, A. Sadiki, J. Janicka, A digital filter based generation of inflow data for spatially developing direct numerical or large eddy simulations, J. Comput. Phys. 186 (2) (2003) 652–665, doi:10.1016/S0021-9991(03)00090-1.
[37] T.S. Lund, X. Wu, K.D. Squires, Generation of turbulent inflow data for spatially-developing boundary layer simulations, J. Comput. Phys. 140 (2) (1998) 233–258.
[38] H. Le, P. Moin, Direct numerical simulation of turbulent flow over a backward–facing step, J. Fluid Mech. 330 (1993) 349–374.
[39] R.D. Moser, J. Kim, N.N. Mansour, Direct numerical simulation of turbulent channel flow up to Reτ = 590, Phys. Fluids 11 (4) (1999) 943–945.
[40] G.K. Batchelor, Small-scale variation of convected quantities like temperature in turbulent fluid part 1. General discussion and the case of small conductivity, J. Fluid Mech. 5 (1) (1959) 113–133.
[41] F. Schwertfirm, M. Manhart, DNS Of passive scalar transport in turbulent channel flow at high schmidt numbers, Int. J. Heat Fluid Flow 28 (6) (2007) 1204–1214.
[42] F. Zonta, C. Marchioli, A. Soldati, Modulation of turbulence in forced convection by temperature-dependent viscosity, J. Fluid Mech. 697 (2012) 150, doi:10.1017/jfm.2012.67.
[43] J. Lee, S.Y. Jung, H.J. Sung, T.A. Zaki, Effect of wall heating on turbulent boundary layers with temperature-dependent viscosity, J. Fluid Mech. 726 (2013) 196–225, doi:10.1017/jfm.2013.211.
[44] A. Patel, B.J. Boersma, R. Pecnik, Scalar statistics in variable property turbulent channel flows, Phys. Rev. Fluids 2 (8) (2017) 084604.
[45] J. Jiménez, P. Moin, The minimal flow unit in near-wall turbulence, J. Fluid Mech. 225 (1991) 213–240, doi:10.1017/S0022112091002033.
[46] P.C. Ma, Y. Lv, M. Ihme, An entropy-stable hybrid scheme for simulations of transcritical real-fluid flows, J. Comput. Phys. 340 (2017) 330–357, doi:10.1016/j.jcp.2017.03.022.
[47] H. Wu, P.C. Ma, M. Ihme, Efficient time-stepping techniques for simulating turbulent reactive flows with stiff chemistry, Comput. Phys. Commun. 243 (2019) 81–96, doi:10.1016/j.cpc.2019.04.016.
[48] G.P. Smith, D.M. Golden, M. Frenklach, et al., GRI-Mech 3.0, http://combustion.berkeley.edu/gri-mech/(2000).
[49] S. Gottlieb, C.-W. Shu, E. Tadmor, Strong stability-preserving high-order time discretization methods, SIAM Rev. 43 (1) (2001) 89–112, doi:10.1137/S003614450036757X.
[50] G. Strang, On the construction and comparison of difference schemes, SIAM J. Numer. Anal. 5 (3) (1968) 506–517, doi:10.1137/0705041.
[51] E.R. Van Driest, Turbulent boundary layer in compressible fluids, J. Aeronaut. Sci. 18 (3) (1951) 145–160.
[52] M.V. Morkovin, Effects of compressibility on turbulent flows, Mécanique Turbul. 367 (1962) 380.
[53] R. So, T. Gatski, T. Sommer, Morkovin hypothesis and the modeling of wall-bounded compressible turbulent flows, AIAA J. 36 (9) (1998) 1583–1592, doi:10.2514/2.584.
[54] P.G. Huang, P. Bradshaw, T.J. Coakley, Skin friction and velocity profile family for compressible turbulent boundary layers, AIAA J. 31 (9) (1993) 1600–1604, doi:10.2514/3.11820.
[55] R. So, H. Zhang, T. Gatski, C. Speziale, Logarithmic laws from compressible turbulent boundary layers, AIAA J. 32 (11) (1994) 2162–2168, doi:10.2514/3.12273.
[56] Y. Morinishi, S. Tamano, K. Nakabayashi, Direct numerical simulation of compressible turbulent channel flow between adiabatic and isothermal walls, J Fluid Mech 502 (2004) 273, doi:10.1017/S0022112003007705.
[57] W.-P. Wang, R.H. Pletcher, On the large eddy simulation of a turbulent channel flow with significant heat transfer, Physics of Fluids 8 (12) (1996) 3354–3366, doi:10.1063/1.869110.
[58] P.C. Ma, X.I. Yang, M. Ihme, Structure of wall-bounded flows at transcritical conditions, Phys. Rev. Fluids 3 (3) (2018) 034609.
[59] S. Lam, D. Goussis, Understanding complex chemical kinetics with computational singular perturbation, in: Symposium (International) on Combustion, 22, Elsevier, 1989, pp. 931–941.
[60] T. Lu, C.S. Yoo, J. Chen, C.K. Law, Three-dimensional direct numerical simulation of a turbulent lifted hydrogen jet flame in heated coflow: a chemical explosive mode analysis, J. Fluid Mech. 652 (2010) 45.
[61] W.M. Kays, Turbulent Prandtl number. Where are we? J. Heat Transf. 116 (2) (1994) 284–295.
[62] J.Y. Yoo, The turbulent flows of supercritical fluids with heat transfer, Annu. Rev. Fluid Mech. 45 (2013) 495–525, doi:10.1146/annurev-fluid-120710-101234.

6 NUMERICAL MODELING PAPERS

However beautiful the strategy, you should occasionally look at the results.

— Winston Churchill

6.1 FROZEN FLAMELET

The application of frozen flamelet model for the simulation of a multi-element methane/oxygen rocket thrust chamber is presented in this section. Despite the sufficiently accurate heat load description (within the experimental uncertainties), the shortcomings of the frozen flamelet are evident when comparing the pressure results from the simulation to the experimental measurements. The passage corresponds to the paper entitled:

Heat Transfer and Combustion Simulation of Seven-Element O_2/CH_4 Rocket Combustor
Nikolaos Perakis, Daniel Rahn, Oskar J. Haidn, Daniel Eiringhaus
Journal of Propulsion and Power (2019)
doi: https://doi.org/10.2514/1.B37402

As described in Section 4.5.2, the use of flamelet models is quite common for the simulation of engineering combustion configurations including hydrocarbons as fuel. Using already available RANS models for the turbulence modeling and combustion modeling, the obtained RANS results are compared to experimental values for pressure and heat flux. The choice of the turbulence model (standard k-ε) is justified after a comparison with the SST k-ω model, which delivers a *substantially reduced mixing efficiency* of fuel and oxidizer in the chamber.

In order to account for the experimental setup conditions consisting of water-cooled calorimetric segments, a *conjugate heat transfer simulation is carried out* by modeling the heat transfer within the liner wall and resolving the flow in the cooling channels. Both a *one-way coupling and a two-way coupling* were performed, demonstrating that *the one-way coupling is sufficient for the correct prediction of the wall heat flux loads*. Although the wall heat flux is not as sensitive, for a more accurate of the wall temperatures, a two-way coupled simulation procedure is recommended.

Apart from the calorimetric heat flux values which were found to agree with the experimental values with sufficient accuracy, the *azimuthal distribution of the wall heat flux* was also investigated. This showed an interesting pattern, with a local maximum corresponding to locations *between the injector elements* for positions downstream of the face-plate. This behavior is found to be also in agreement with the experimental results obtained with an inverse heat transfer method as presented in Section 3.3. The azimuthal heat flux profile was further investigated by comparing the present results with other groups [193]. The

enhanced heat transfer coefficient for positions between neighboring injector elements was attributed to a *secondary vortex system* which feeds hot gas from the flame zone into an impinging trajectory with respect to the chamber wall. The vortex system was found to weaken for positions closer to the end of the cylindrical combustion chamber, leading to a homogeneous distribution in the nozzle. Previous numerical studies have also investigated the origins of the circumferential heat flux variation. Song et al. [325] found the unburnt methane between injectors being the culprit for the varying heat flux distribution, whereas Negishi et al. [326] and Perakis [327] attributed the observed local heat flux minima to the accumulation of unburnt oxygen in LOX/GH_2 and LOX/GCH_4 sub-scale chambers respectively.

Despite the satisfactory agreement with the experimental wall heat fluxes, the shortcomings of the frozen steady flamelet model are visible when examining the pressure profiles. Although the general form of the axial pressure distribution resembles the experimental one, an *offset of approximately* 0.5 *bar* (equivalent to 2.6%) in the absolute level is found in the entire chamber domain. This implies an insufficient energy release that leads to a lower combustion efficiency. This issue *is attributed to the absence of proper treatment for the recombination reactions in the vicinity of the wall*, which release additional energy due to their exothermic nature. The gas composition in the frozen flamelet model is independent of the local enthalpy and for that reason, this additional contribution is ignored, leading to the lower pressure level. This enhances the motivation for the development of non-adiabatic flamelet models, able to describe the effect of the aforementioned reactions.

JOURNAL OF PROPULSION AND POWER
Vol. 35, No. 6, November–December 2019

Heat Transfer and Combustion Simulation of Seven-Element O_2/CH_4 Rocket Combustor

Nikolaos Perakis,* Daniel Rahn,† and Oskar J. Haidn‡
Technical University of Munich, 85748 Garching, Germany
and
Daniel Eiringhaus§
ArianeGroup, GmbH, 82024 Taufkirchen, Germany

DOI: 10.2514/1.B37402

In the present Paper, the simulation of the flow inside an experimental GOX/GCH_4 rocket thrust chamber is undertaken. The combustor's injector consists of seven individual coaxial injector elements, while the chamber and nozzle segments are water cooled. The results presented in this Paper are obtained with three-dimensional Reynolds-averaged Navier–Stokes simulations using an adiabatic flamelet formulation for the chemistry modeling. The main focus is placed on examining the effect of the different turbulence models on the flame structure and on the resulting pressure and wall heat flux. The obtained numerical values are compared to experimental measurements, delivering good agreement in the heat flux profile at the combustion chamber wall and a slight underestimation of the pressure profile of approximately 2.5%. Greater discrepancies are observed in the heat flux of the nozzle segment but are largely attributed to the experimental setup. A conjugate heat transfer simulation of the structure and cooling channel flow confirms this assumption, and results for both one-way and two-way couplings are shown. It is demonstrated that a one-way coupling between hot gas and structure is sufficient due to the low sensitivity of the wall heat flux on the wall temperature. The azimuthal variation of the heat flux is also examined, and interestingly the heat flux showcases a local minimum at the position directly above the injector element. It is shown that an increased concentration of colder fuel-rich gas directly above the injector due to a strong vortex system leads to the local minimum in heat flux values and is strongly influenced by the injector/injector interaction near the face plate.

Nomenclature

c_p	=	specific heat capacity, J/(kg · K)
H	=	specific total enthalpy, J/kg
h	=	specific enthalpy, J/kg
k	=	turbulence kinetic energy, m^2/s^2
M	=	molar mass, kg/mol
$\dot{m}$	=	mass flow rate, kg/s
P	=	probability density function
Pr_t	=	turbulent Prandtl number
p	=	pressure, bar
$\dot{q}$	=	heat flux, W/m^2
R	=	universal gas constant, J/(mol · K)
r	=	grid refinement ratio
Sc_t	=	turbulent Schmidt number
T	=	temperature, K
t	=	time, s
U	=	unmixedness
u	=	velocity, m/s
x, y, z	=	spatial coordinates, m
Y	=	species mass fraction
y^+	=	dimensionless wall distance
Z	=	mixture fraction
Z''^2	=	mixture fraction variance
ϵ	=	turbulent dissipation, m^2/s^3
ε	=	numerical error
θ	=	angle, deg
λ	=	heat conductivity, W/(m · K)
μ	=	viscosity, Pa · s
ρ	=	density, kg/m^3
τ	=	stress tensor, N/m^2
ϕ	=	generic variable
χ	=	scalar dissipation rate, 1/s
ψ	=	apparent numerical order
ω	=	specific rate of dissipation, 1/s
Ω	=	vorticity, 1/s
$\dot{\omega}$	=	chemical reaction rate, 1/s

Subscripts

c	=	chamber
ext	=	exact
flow	=	flow
fu	=	fuel
k	=	species index
max	=	maximal value
N	=	nozzle
ox	=	oxidizer
sp	=	species
st	=	stoichiometric value
t	=	turbulent value

Presented as Paper 2018-4554 at the 2018 Joint Propulsion Conference, AIAA Propulsion and Energy Forum, Cincinnati, OH, 9–11 July 2018; received 2 October 2018; revision received 24 June 2019; accepted for publication 13 July 2019; published online 22 August 2019.

*Graduate Student, Chair of Turbomachinery and Flight Propulsion, Boltzmannstrasse 15; nikolaos.perakis@ltf.mw.tum.de.
†Graduate Student, Chair of Turbomachinery and Flight Propulsion.
‡Prof. Dr.-Ing., Chair of Turbomachinery and Flight Propulsion.
§Graduate Student, Robert-Koch-Strasse 1.

I. Introduction

A VERY important step in the process of designing and optimizing new components or subsystems for rocket propulsion devices is the numerical simulation of the flow and combustion in them. Implementing computational fluid dynamics (CFD) tools in the design process significantly reduces the development time and cost and allows for greater flexibility. The main requirements that a successful CFD tool must fulfill in order to be suitable for rocket engine applications is providing an accurate description of the heat loads on the chamber wall, the combustion pressure, the combustion efficiency, and the performance parameters such as the specific impulse [1]. Other design problems that can be

tackled with the use of CFD are prediction and simulation of combustion-acoustic instabilities [2].

The reliability of a numerical tool lies in accurately describing the physical and chemical processes taking place within the thrust chamber. This is done by a set of models (and the corresponding numerical methods to solve them), which must be validated for the wide range of operating conditions that can occur in different types of rocket engines (e.g., attitude control thrusters and launcher propulsion). To make CFD attractive in the design process, the choice of the used models should be such that the computational time does not become prohibitive, while still capturing the physics of the underlying phenomena with sufficient accuracy.

A significant step during the development of numerical tools for combustion and turbulence modeling in rocket engines is the validation of the models. Several studies have been carried out in an effort to describe the chemical and physical processes taking place in single-element rocket combustion chambers over the years. Oefelein and Yang [3] examined the flow and combustion in LOX/H_2 rocket engine configurations, whereas Zhukov [4] performed an analysis of a GOX/GH_2 single-element combustor. Cutrone et al. [5], on the other hand, performed Reynolds-averaged Navier–Stokes (RANS) simulations on single-element chambers operated with LOX/CH_4 using a real-gas flamelet/progress variable model, whereas Zips et al. [6] used a real-gas steady flamelet model for large-eddy simulation of a LOX/CH_4 combustor.

Compared to single-element chamber simulations, the available studies for multi-injector rocket thrust chambers are limited. Furthermore, most of the available multi-injector studies are devoted to LOX/hydrogen thrust chambers. Urbano et al. [2] examined the triggering of combustion instabilities in LOX/H_2 rocket engines, whereas Negishi et al. [7,8] carried out simulations of the combustion and wall heat transfer in multi-element oxygen/hydrogen rocket thrust chambers. In the case of hydrocarbon engines, a simplified approach for the prediction of wall heat transfer of methane combustion was proposed by Betti et al. [9] using a pseudoinjector RANS approach, which, however, tends to overestimate the heat flux in the near injection region and does not provide any information about the azimuthal heat load distribution. A similar approach using a uniform pseudoinjection with a nonadiabatic flamelet model was implemented by Kim et al. [10], who carried out simulations of multi-element rocket engines with hydrocarbons as fuel, without, however, performing an analysis of the wall heat transfer. Song and Sun [11], on the other hand, focused on the coupled wall heat transfer in multi-element methane rocket engines but did not provide a comparison of the simulations with experimental data.

Within the framework of facilitating the development of CFD for rocket engines, several different configurations of rocket combustors and propellant combinations have been tested as shown by Silvestri et al. [12], building an experimental database that can be used in the validation process of CFD models. In a similar manner as with the single-element GOX/GCH_4 rocket combustor described by Chemnitz et al. [13], a test case from the available experimental database is defined. The experimental rocket combustor is operated with gaseous oxygen (GOX) and gaseous methane (GCH_4) and has a multi-element injector. A detailed description of the test campaign can be found in the work by Silvestri et al. [14]. Section II gives a short summary of the relevant experimental data used in the simulations.

In the present Paper, the numerical results from the simulation of the seven-element chamber are presented. Having identified the absence of available numerical studies dealing with the combustion and wall heat transfer simulation of multi-element methane rocket combustors, the goal of this study is to examine the ability of existing turbulent combustion models to accurately predict performance and wall heat loads. A three-dimensional (3D) RANS approach is used, and the combustion modeling is based on the adiabatic flamelet approach. Compared to single-element combustors, multi-injector engines introduce additional physical phenomena needed to be described such as the interaction between individual jets and the wall flame impingement between neighboring elements. The objective of the study is not to introduce a new model but rather to evaluate the capability of existing ones to predict the mixing and interaction of the flames in multi-element methane/oxygen configurations.

To assess the strengths and weaknesses of the model, comparison with experimental data is necessary. Since the available measurements for the present test case only include calorimetric heat flux values for the coolant, a conjugate heat transfer simulation of structure and coolant is also applied. This step is, however, only considered in order to allow for a direct comparison with the measurements and to analyze the effect of the wall temperature on the wall heat transfer.

The present Paper is organized as follows. The experimental test case chosen for this analysis is described in Sec. II. Section III deals with the numerical setup and models applied in the hot gas simulation, whereas the results of the turbulent combustion are presented in Sec. IV. For the comparison with the experimental data, a one-way coupling as well as a fully conjugated heat transfer coupling with the structure and cooling channels is carried out, since the experimental calorimetric measurements do not coincide with the wall heat transfer as explained in Sec. V. The effect of the flame/flame interaction on the heat transfer characteristics is analyzed in Sec. VI. Finally, Sec. VII gives an overall conclusion and summary of the results and points out the potential areas of improvement.

II. Description of Test Case

The examined multi-injector combustion chamber was designed for GOX and GCH_4, allowing high chamber pressures (up to 100 bar) and film cooling behavior examination. One of the key aspects of the project is to improve the knowledge of heat transfer processes and cooling methods in the combustion chamber, which is mandatory for the engine design. The attention is focused, in particular, on injector/injector and injector/wall interaction. To have a first characterization of the injectors' behavior, the multi-element combustion chamber is tested at low combustion chamber pressures and for a wide range of mixture ratios [12].

The seven-element rocket combustion chamber has an inner diameter of 30 mm and a contraction ratio of 2.5 in order to achieve Mach numbers similar to the ones in most rocket engine applications. The combustion chamber, depicted in Fig. 1, consists of four cylindrical water-cooled chamber segments as well as a nozzle segment (individually cooled), adding up to a total length of 382 mm. For the current study, shear coaxial injector elements are integrated. The test configuration includes the GOX post being mounted flush with respect to the injection face. Table 1 gives an overview of the chamber and injector dimensions. Figure 2 shows the injector configuration as well as the locations of the cooling channels. The centers of the six outer injectors are located at a radial distance equal to 9 mm from the center of the central injector, which corresponds to 1.5 times the outer methane diameter D_{fu}, whereas their distance from the wall is equal to $D_{fu} = 6$ mm.

For the present test case, an operating point with mean combustion chamber pressure of 18.3 bar and mixture ratio of 2.65 is chosen. The experimental data made available for the numerical simulations include the mass flow rates of oxygen and methane, the wall temperature, the pressure profile, and integral heat flux values. A summary of the test data is given in Table 2. For the determination of

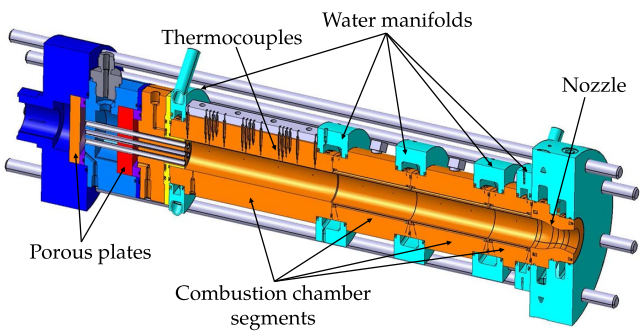

Fig. 1 Sketch of the combustion chamber.

Table 1 Summary of chamber dimensions

Dimension	Value, mm
Chamber diameter	30.0
Axial location end of segment A	145.0
Axial location end of segment B	222.0
Axial location end of segment C	299.0
Axial location end of segment D	340.0
Nozzle length	42.0
Total chamber length	382.0
Oxygen port diameter	4.0
Methane annulus inner diameter	5.0
Methane annulus outer diameter	6.0

Table 2 Summary of experimental data

Measured quantity	Value
Mean chamber pressure p_c, bar	18.3
Oxidizer to fuel ratio O/F	2.65
Oxidizer mass flow rate $\dot{m}_{ox}$, kg/s	0.211
Fuel mass flow rate $\dot{m}_{fu}$, kg/s	0.080
Average heat flux $\dot{q}_A$, MW/m^2	3.40
Average heat flux $\dot{q}_B$, MW/m^2	6.47
Average heat flux $\dot{q}_C$, MW/m^2	6.72
Average heat flux $\dot{q}_D$, MW/m^2	5.37
Average heat flux $\dot{q}_N$, MW/m^2	13.18

the heat flux values in the four chamber segments (A–D) and the nozzle (N), a calorimetric method is applied. The average heat flux of each chamber segment is determined by the enthalpy difference of the coolant between the inlet and outlet. This is obtained by precise temperature measurements in the water manifolds between the test segments. Two separate cooling cycles are implemented: one for the first four segments in the combustion chamber and an additional cooling cycle for the nozzle segment. The cross sections of the cooling channels in segments A–D are shown in Fig. 2 and further elaborated in Sec. IV. The temperature values available are obtained at radial distances of 0.7–1.0 mm from the hot gas wall and are used as boundary conditions for the calculation, as will be elaborated on in Sec. III.

III. Computational Setup of Hot Gas Simulation

The numerical simulation of the turbulent combustion within the seven-element chamber is carried out using the pressure-based code ANSYS Fluent, in which the 3D RANS equations are solved with the SIMPLE algorithm.

A. Computational Domain

The computational domain considered in the RANS calculation of the turbulent combustion consists of a 30 deg segment of the thrust chamber, which includes only a half-injector in the outer row and corresponds to 1/12th of the whole chamber. To create a developed velocity profile at the injection plane, the injector tubes are also modeled as can be seen in Fig. 3. The final mesh consists of approximately 2.9 million cells and is chosen after a mesh convergence study. To resolve the boundary layer appropriately and to facilitate a correct heat load prediction, the mesh in the vicinity of walls is refined to satisfy the condition $y^+ \approx 1$. A close-up view of the mesh at the injector and face plate is shown in Fig. 4. The black cells represent the posttip between oxygen and fuel, and the red and blue cells represent the CH_4 and O_2 inlets respectively. As can be seen in the right subfigure of Fig. 4, the x axis represents the axial direction, a notation that will be used throughout the entirety of the Paper. The origin of the x axis is located at the axial location of the face plate, i.e., at the location where the injector elements end and the chamber begins.

The grid is chosen after an extensive grid convergence study. To assess the influence of grid resolution, the maximal pressure and maximal heat flux on the thrust chamber wall are chosen as characteristic quantities, and the simulation is carried out using the standard $k-\epsilon$ model for the turbulence closure. Four meshes are evaluated, with the coarsest one consisting of approximately 1.8 million cells and the finest one consisting of 6.2 million cells.

To evaluate the convergence of the solution, the theory of the Richardson extrapolation [15] is employed. The numerical error is calculated by comparing the solutions on each grid to a value gained from Richardson extrapolation according to

$$\phi_{\text{ext}} = \frac{r^{\psi} \cdot \phi_1 - \phi_2}{r^{\psi} - 1} \tag{1}$$

where the lower indices represent the finer mesh solutions, r is the grid refinement ratio, and ψ is the achieved numerical order.

The results are summarized in Table 3, whereas Fig. 5 shows the numerical error as a function of the grid points. Although only the results for the maximal pressure and heat flux values are shown, the analysis has been carried out for a larger set of representative points along the chamber wall, all of which demonstrate a similar behavior. All simulations are carried out with a second-order upwind scheme for all transport equations. The achieved order ψ of convergence is also estimated for each of the three variables, using the method shown in Eq. (2):

$$\psi = \frac{\log((\phi_3 - \phi_2)/(\phi_2 - \phi_1))}{\log r} \tag{2}$$

For all monitored variables, apparent orders between 1.75 and 1.90 are obtained.

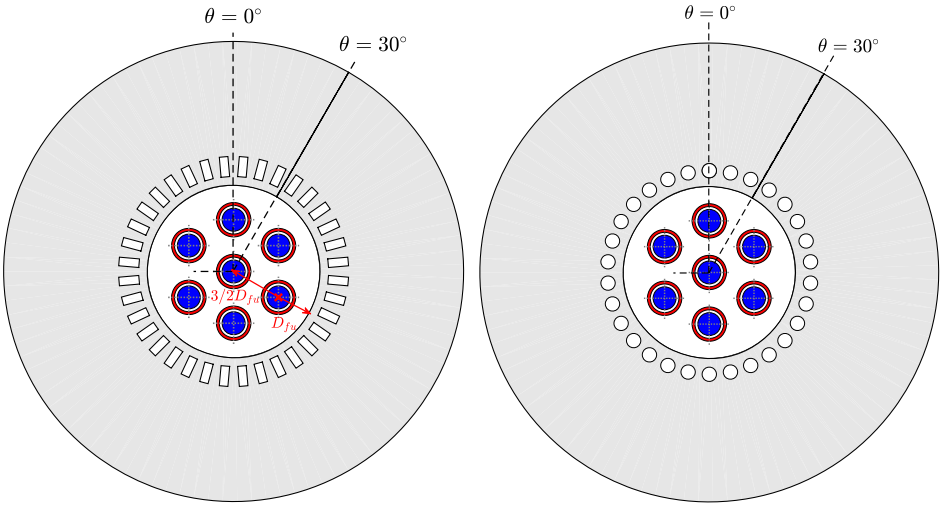

Fig. 2 View of the injector configuration and cross-section of the chamber in segment A (left) and in segments B, C, and D (right).

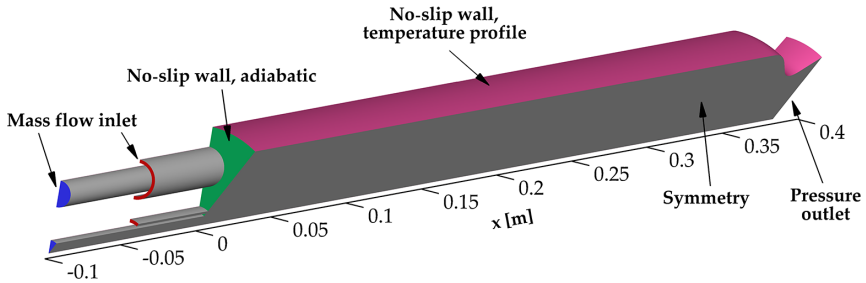

Fig. 3 Computational domain and applied boundary conditions.

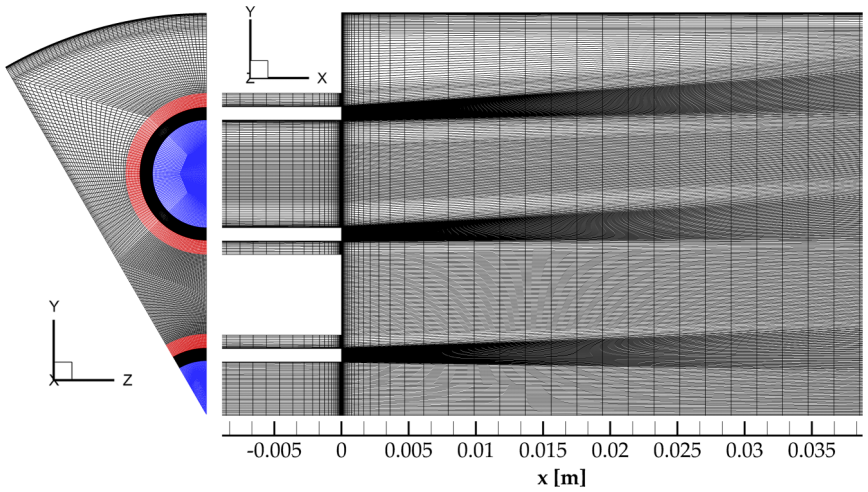

Fig. 4 Mesh at injector elements, face plate, and symmetry plane.

The relative numerical errors for the chosen grid ("Middle 1") remain underneath 2%, and for that reason, all simulations presented in this Paper are performed with it.

B. Boundary Conditions

A schematic representation of the applied boundary conditions can be seen in Fig. 3. The oxygen and methane inlets of the coaxial injector are defined as mass flow inlets by prescribing the appropriate values from the experiments. For the outlet, a pressure boundary condition is applied. The planes corresponding to 0 and 30 deg are defined as symmetry boundary conditions. This is chosen to reduce the computational time of the simulation and to take advantage of the RANS formulation, which gives only the mean flow values. A further justification of this choice for the boundary condition is given in Sec. VI. At the chamber wall, a prescribed temperature profile is defined. This profile is obtained by the experimental values. Since the temperature measurements directly at the hot gas wall are not available, the ones measured by the thermocouples located at radial distances of 0.7 and 1.0 mm from the hot gas wall are chosen instead. Since no temperature data are known at the nozzle, the last temperature value from the combustion chamber is defined at the nozzle wall. The resulting temperature profile at the wall is shown in Fig. 6. The validity of this boundary condition is assessed in Sec. V. All remaining walls are defined as adiabatic thermal boundaries and are given a no-slip condition.

Table 3 Results of the grid convergence study

Quantity	Coarse	Middle 1	Middle 2	Fine	Exact
Cells	$1.80 \cdot 10^6$	$2.91 \cdot 10^6$	$4.35 \cdot 10^6$	$6.1 \cdot 10^6$	— —
$p_{\max}$, bar	18.31	18.44	18.50	18.53	18.55
$\epsilon_{p_{\max}}$, %	1.27	0.57	0.25	0.09	— —
$\dot{q}_{\max}$, MW/m^2	17.42	16.95	16.78	16.70	16.69
$\epsilon_{\dot{q}_{\max}}$, %	4.37	1.55	0.53	0.11	— —

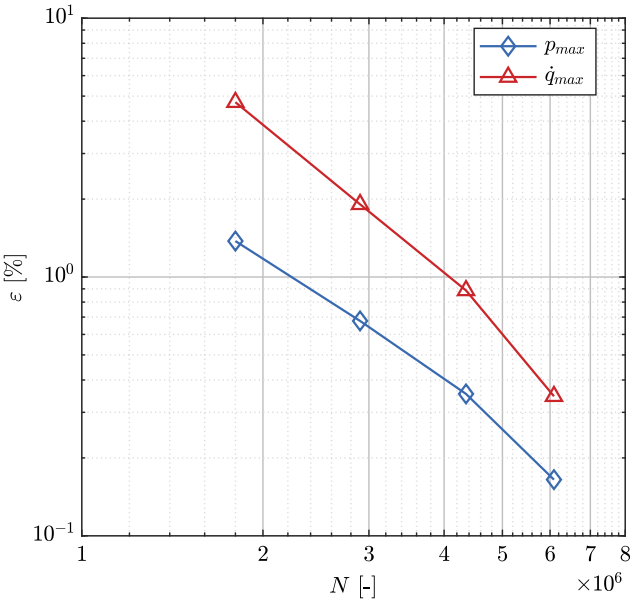

Fig. 5 Numerical error as a function of node number.

C. Numerical Models

The flowfield in the combustion chamber is described by the conservation equations for mass, momentum, and energy in three-dimensional space,

$$\frac{\partial \rho}{\partial t} + \frac{\partial (\rho \tilde{u}_i)}{\partial x_i} = 0 \tag{3}$$

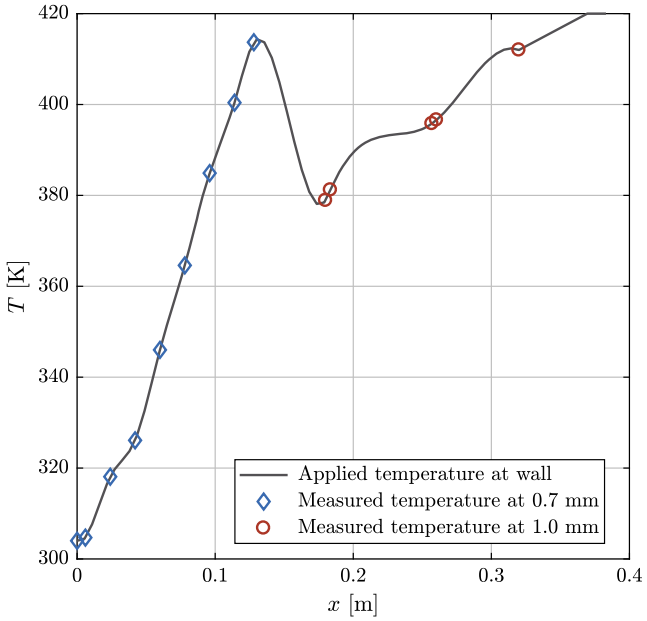

Fig. 6 Temperature at thrust chamber wall.

$$\frac{\partial(\bar{\rho}\tilde{u}_i)}{\partial t} + \frac{\partial(\bar{\rho}\tilde{u}_i\tilde{u}_j)}{\partial x_j} = -\frac{\partial \bar{p}}{\partial x_i} + \frac{\partial}{\partial x_i}(\bar{\tau}_{ij} - \bar{\rho}\,\widetilde{u_i''u_j''}) \tag{4}$$

$$\frac{\partial(\bar{\rho}\tilde{H})}{\partial t} + \frac{\partial(\bar{\rho}\tilde{H}\tilde{u}_i)}{\partial x_i} = \frac{\partial}{\partial x_i}\left(\frac{\bar{\lambda}}{\bar{c}_p}\frac{\partial \tilde{H}}{\partial x_i} - \bar{\rho}\,\widetilde{u_i''H''}\right) \tag{5}$$

where ρ and p are the Reynolds-averaged density and pressure, respectively, and $\tilde{u}_i$ are the Favre-averaged velocity components in the spatial directions x_i. The viscous stress tensor τ_{ij} is given as

$$\bar{\tau}_{ij} = \mu\left(\frac{\partial \tilde{u}_i}{\partial x_j} + \frac{\partial \tilde{u}_j}{\partial x_i} - \frac{2}{3}\delta_{ij}\frac{\partial \tilde{u}_k}{\partial x_k}\right) \tag{6}$$

with μ being the dynamic viscosity. The total specific enthalpy is $\tilde{H}$ and is defined as the sum of the static specific enthalpy $\tilde{h}$ and the specific kinetic energy $1/2\tilde{u}_i\tilde{u}_i$, while c_p and λ are the specific heat capacity and the thermal conductivity of the fluid. NASA polynomials are implemented for the enthalpy and heat capacity of the individual species. The mixture values are obtained using a mass fraction averaging:

$$\tilde{h} = \sum_{k=1}^{N_{sp}} \tilde{Y}_k \cdot \tilde{h}_k \tag{7}$$

$$\bar{c}_p = \sum_{k=1}^{N_{sp}} \tilde{Y}_k \cdot \bar{c}_{p,k} \tag{8}$$

A pressure-based scheme is used for the solution of the discretized equations. Density and pressure are coupled through the ideal gas equation of state,

$$\rho = \frac{pM}{R\tilde{T}} \tag{9}$$

where R is the universal gas constant and $\tilde{T}$ and M are the fluid mixture temperature and molecular weight, respectively.

1. *Turbulence Modeling*

The turbulent closure of the unclosed terms introduced by the Reynolds averaging of the Navier–Stokes equations is achieved by employing the Boussinesq hypothesis, relating the Reynolds stresses to the mean velocity gradients. Hence, the momentum stresses in Eq. (4) are modeled as

$$\bar{\rho}\,\widetilde{u_i''u_j''} = -\mu_t\left(\frac{\partial \tilde{u}_i}{\partial x_j} + \frac{\partial \tilde{u}_j}{\partial x_i} - \frac{2}{3}\delta_{ij}\frac{\partial \tilde{u}_k}{\partial x_k}\right) + \frac{2}{3}\bar{\rho}\,\tilde{k} \tag{10}$$

In this formulation, μ_t is the turbulent viscosity, and k is the turbulent kinetic energy.

Similarly, the closure of the turbulent heat flux in Eq. (5) is achieved using the turbulent Prandtl number Pr_t:

$$\bar{\rho}\,\widetilde{u_i''H''} = -\frac{\lambda_t}{\bar{c}_p}\frac{\partial \tilde{H}}{\partial x_i} = -\frac{\mu_t}{Pr_t}\frac{\partial \tilde{H}}{\partial x_i} \tag{11}$$

Rather than being a fixed species property, the value of the turbulent Prandtl number depends on the studied case. The evaluation of this quantity from an experimental point of view is found in the work by Kays [16], whereas Riedmann et al. [17] have analyzed the relevance of this number in the context of rocket combustor simulations. A constant value equal to 0.9 was chosen for the present study.

To evaluate the fluxes as defined previously, the turbulent viscosity needs to be modeled. In this Paper, two-equation models are considered, within which the turbulent viscosity is calculated from a turbulent length and time scale.

Specifically, in the standard k-ϵ model proposed by Launder and Spalding [18], one transport equation is solved for the turbulence kinetic energy $\tilde{k} = 1/2 \cdot \widetilde{u_i''u_i''}$, and one is solved for its dissipation $\tilde{\epsilon}$. To account for the proper treatment of the wall when using the $k-\epsilon$ model, the two-layer approach by Wolfshtein [19] is implemented.

In the $k-\omega$ shear-stress transport (SST) model by Menter et al. [20], on the other hand, two additional transport equations for the turbulent kinetic energy $\tilde{k}$ and the specific dissipation rate $\tilde{\omega}$ are solved instead.

The turbulent viscosity for the two models is then found by the relation

$$\mu_t \sim \bar{\rho}\frac{\tilde{k}^2}{\tilde{\epsilon}} \quad \text{and} \quad \mu_t \sim \bar{\rho}\frac{\tilde{k}}{\tilde{\omega}} \tag{12}$$

All modeling constants and blending functions are set to the proposed standard values by Launder and Spalding [18], Menter [20], and Wilcox [21].

2. *Chemistry Modeling*

As already mentioned, the chemistry modeling takes place by using the flamelet approach. This model significantly reduces the computational resources required for combustion simulations by reducing the number of transport equations. This is done by replacing the transport equations for the chemical species by only two equations: one for the mean mixture fraction $\tilde{Z}$ and one for its variance $\tilde{Z}''^2$, which is included in order to account for the interaction between the chemistry and the turbulence,

$$\frac{\partial(\bar{\rho}\tilde{Z})}{\partial t} + \frac{\partial(\bar{\rho}\tilde{u}_i\tilde{Z})}{\partial x_i} = \frac{\partial}{\partial x_i}\left(\frac{\mu + \mu_t}{Sc_t}\frac{\partial \tilde{Z}}{\partial x_i}\right) \tag{13}$$

$$\frac{\partial(\bar{\rho}\,\widetilde{Z''^2})}{\partial t} + \frac{\partial(\bar{\rho}\tilde{u}_i\widetilde{Z''^2})}{\partial x_i} = \frac{\partial}{\partial x_i}\left(\frac{\mu + \mu_t}{Sc_t}\frac{\partial \widetilde{Z''^2}}{\partial x_i}\right) + C_g\mu_t\frac{\partial \tilde{Z}}{\partial x_i}\frac{\partial \tilde{Z}}{\partial x_i} - C_d\bar{\rho}\frac{\tilde{\epsilon}}{\tilde{k}}\widetilde{Z''^2} \tag{14}$$

Here, Sc_t is the turbulent Schmidt number, which is set to a constant value of $Sc_t = 0.6$ throughout the domain, and C_g and C_d are constants with values of 2.86 and 2.0, respectively [22].

A third variable, which is calculated by the model (but with an algebraic equation instead of a transport one), is the scalar dissipation rate $\tilde{\chi}$. This represents the dissipative term in the equation for the mixture fraction variance and is a measure for the deviation of the flow from equilibrium. A value of $\tilde{\chi}$ equal to zero would imply a perfect mixing and a low strain rate in the flow and would correspond to chemical equilibrium. For much higher values of this quantity, the extinction limit of the flame is reached [23],

$$\tilde{\chi} = \frac{C_\chi \tilde{\epsilon} \widetilde{Z''^2}}{\tilde{k}} \tag{15}$$

where C_χ is a constant with a value of 2.0.

The properties of the mixture such as the mixture fractions of the individual species as well as the temperature are pretabulated as a function of the laminar variables Z and χ_{st}. This is done by solving the flamelet equations in a preprocessing step. They consist of a transport equation for the temperature T and for the species mass fractions Y_i as shown in Eqs. (16) and (17) [24]:

$$\rho \frac{\partial T}{\partial t} = \frac{1}{2}\rho\chi \frac{\partial^2 T}{\partial Z^2} - \frac{1}{c_p}\sum_k^{N_{sp}} h_k \dot{\omega}_k + \frac{1}{2c_p}\rho\chi\left[\frac{\partial c_p}{\partial Z} + \sum_k^{N_{sp}} c_{p,k}\frac{\partial Y_k}{\partial Z}\right]\frac{\partial T}{\partial Z} \tag{16}$$

$$\rho \frac{\partial Y_k}{\partial t} = \frac{1}{2}\rho\chi \frac{\partial^2 Y_k}{\partial Z^2} + \dot{\omega}_k \tag{17}$$

In this context, $\dot{\omega}_k$ represents the species reaction rate, and h_k is the specific enthalpy of each species. The scalar dissipation rate is modeled using the one-parametric distribution [23]:

$$\chi(Z) = \chi_{st} \cdot \exp[2(erfc^{-1}(2Z_{st}))^2 - 2(erfc^{-1}(2Z))^2] \tag{18}$$

The flamelet equations are solved for different values of the scalar dissipation, and pressure leading to a laminar table $T, Y_k, \phi = f(Z, \chi_{st}, p)$, with ϕ representing the rest of the thermochemical variables such as density, specific heat capacity, and transport properties. To account for the turbulence/chemistry interaction, a further step is undertaken during preprocessing. A statistical treatment of turbulence is included by performing an integration using a presumed probability density function (PPDF). The resulting mean species mass fractions and mean temperature are hence tabulated as a function of the flow variables $\tilde{Z}, \tilde{Z}''^2, \tilde{\chi}_{st}, \bar{p}$. The PPDF chosen in this work is a decoupled probability density function (PDF), i.e., $P(Z, \chi_{st}, p) = P(Z) \cdot P(\chi_{st}) \cdot P(p)$, with a beta PDF for the mixture fraction and a Dirac function for the scalar dissipation and pressure.

During the CFD computation, the transport equations for the mean mixture fraction and its variance are solved, while the scalar dissipation is computed algebraically for each cell. The pressure is available from the pressure-based solver (using the SIMPLE algorithm). With this information, the species mass fractions are interpolated from the precomputed flamelet table. With the specific enthalpy of the cell, the temperature can be obtained. In the present Paper, an adiabatic (or else frozen) flamelet approach is used. This means that the mass fractions are not tabulated as a function of the enthalpy. This simplification suppresses further reactions, which could take place in the presence of a lower enthalpy, for example, recombinations close to the wall. Although this effect is considered to be significant and is probably not negligible, in the present Paper, the model has been simplified, and the enthalpy is only used to correct the resulting temperature (and hence density as well). One the other hand, the pressure dependence in the table accounts for the change in density during expansion in the rocket engine nozzle.

Various methods have been introduced in an effort to account for the additional reactions in the presence of the low-enthalpy environment, which is introduced in the vicinity of cooled walls. Methods using additional source terms in the flamelet equations [25–27], conductive heat losses [28,29], radiative losses [30,31], reductions of the chemical source term [32,33], permeable thermal walls [34], and enthalpy prescription methods [27] have been developed. Despite the simplification introduced, the adiabatic flamelet model is still widely used in the design process of rocket thrust chambers. For that reason, the present Paper aims at assessing its performance in dealing with multi-injector rocket combustor configurations.

The reaction mechanism used for the solution of the flamelets is the one by Slavinskaya et al. [35] and consists of 21 species and 97 reactions, whereas the thermodynamic properties were calculated using NASA polynomials. For the molecular transport (viscosity and thermal conductivity), the Chapman–Enskog kinetic theory [36,37] is used for the individual species, combined with the Wilke mixture rule [38], leading to species- and temperature-dependent properties. Different turbulence models are compared as seen in Sec. IV, but the standard $k-\epsilon$ model [18] shows the most promising results, using a two-layer model for the wall treatment [19].

IV. Results of Hot Gas Simulation

In this section, the results of the CFD calculations will be presented and compared with the experimental values. In the first approach, the standard $k-\epsilon$ [18], combined with the two-layer model [19] at the wall, is implemented and compared to the $k-\omega$ SST [20]. For both approaches, the closure of the turbulent flux terms is done with a turbulent Schmidt number $Sc_t = 0.6$ and a turbulent Prandtl number $Pr_t = 0.9$.

In Fig. 7, the temperature field inside the thrust chamber is plotted. Although a 30 deg domain is simulated, a larger domain (150 deg) is shown in the plots for a more intuitive visual representation. In the same plot, the line corresponding to stoichiometric composition ($Z_{st} = 0.2$) in the case of CH_4/O_2 combustion is indicated. This is included to give insight into the shape of the flame and consequently its length.

A. Effect of Turbulence Model on Mixing and Combustion

By examining the two distributions, it is evident that the $k-\epsilon$ models tends to better capture the mixing within the combustion chamber. Using the SST model, the temperature stratification remains prominent even in axial positions close to the nozzle. The temperature demonstrates namely a wavy pattern especially close to the wall, which is an indication for inefficient mixing of the individual flames. In the $k-\epsilon$, however, this temperature stratification is restricted to the first two-thirds of the engine, and a more homogeneous field is present farther downstream. The effect of the less efficient mixing is also evident by the length of the individual flames. In the $k-\epsilon$ solution, the outer and inner flames are almost equally long and extend up until the middle of the chamber. The SST, on the other hand, produces a sufficiently longer flame length, more dominantly in the outer flame implying a smaller flame/flame and flame/wall interaction.

The effect is attributed to a lower production in the turbulent viscosity of the SST model. Figure 8 demonstrates that the turbulent viscosity resulting from the $k-\epsilon$ calculation has a higher value throughout the whole combustion chamber, leading to a higher dissipation and hence a more uniform temperature field. The effect is mainly prominent in the area of the individual flame jets and in the core flow. The $k-\epsilon$ calculation is performed with the use of a limiter for the turbulent kinetic energy according to Menter [20]. Calculations without the limiter resulted in the presence of a large area with very high turbulent viscosity at the nozzle. This effect was restrained close to the axis of the nozzle and was dampened out closer to the wall. Although the production limiter led to the disappearance of this hot spot, making the μ_t field more intuitive, no measurable changes in the macroscopic values such as pressure or heat flux in the nozzle were observed.

A more quantitative examination of the inefficient mixing in the chamber is given by evaluating the unmixedness and the average O_2 mass fraction in the thrust chamber. The unmixedness is a dimensionless number that describes the degree of mixing in the chamber. For an ideal mixture, it reaches the value 0, whereas for

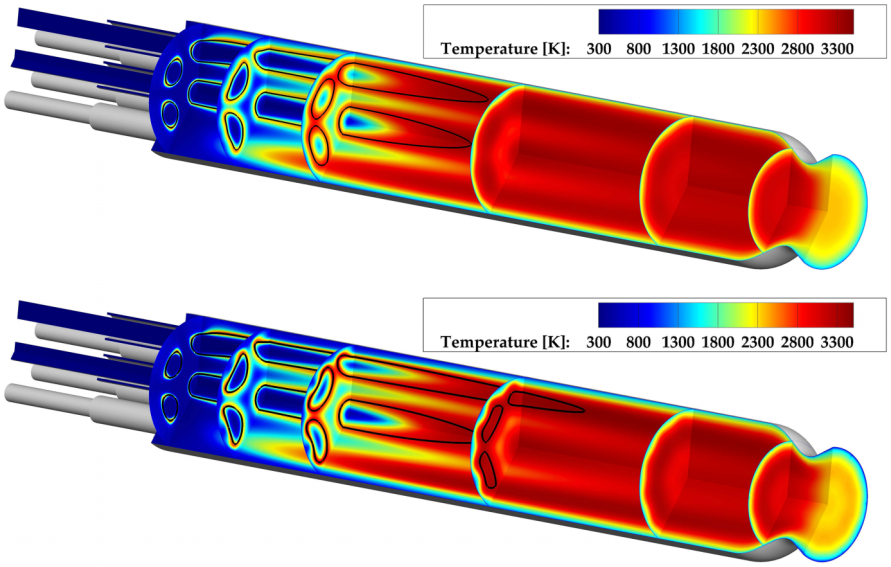

Fig. 7 Temperature field in the thrust chamber using the standard $k-\epsilon$ model (top) and the $k-\omega$ SST model (bottom). The black line corresponds to the stoichiometric mixture fraction. Axial scaling 50%.

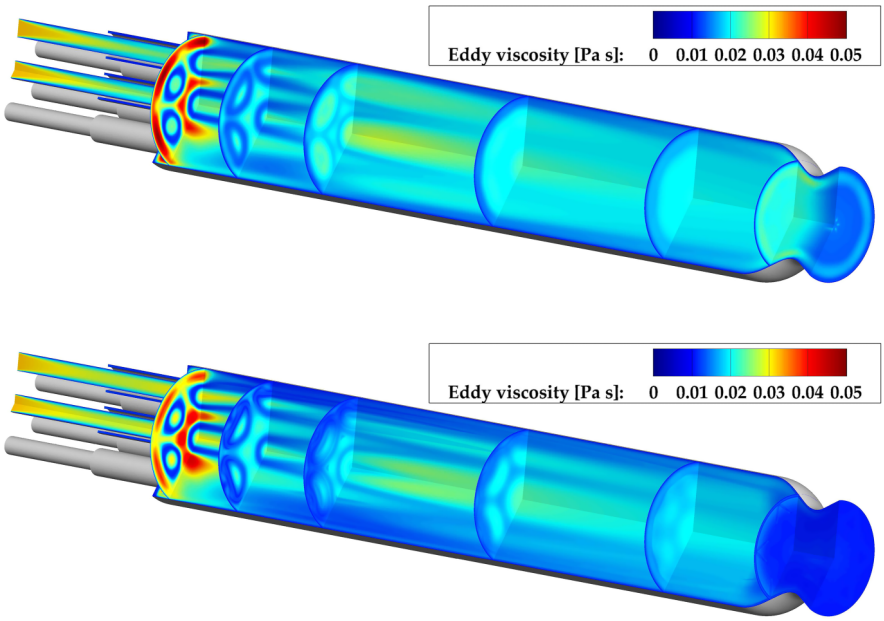

Fig. 8 Turbulent viscosity field in the thrust chamber using the standard $k-\epsilon$ model (top) and the $k-\omega$ SST model (bottom). Axial scaling 50%.

totally unmixed compounds, it is equal to 1. Its formula is given by Eq. (19):

$$U = \frac{\langle Z'^2 \rangle}{\langle Z \rangle (1 - \langle Z \rangle)} \tag{19}$$

$\langle Z \rangle$ stands for the average mixture fraction along all the nodes of a cross-sectional plane, and $\langle Z'^2 \rangle$ stands for the variance of the mixture fraction values on these points. The unmixedness should approach zero toward the exit plane of the nozzle, due to increasingly better mixing of the gas. In Fig. 9, the $k-\epsilon$ shows an unmixedness value approximately five times smaller at the exhaust plane and a generally lower value along the whole domain of the chamber, which confirms the fact that the mixing is calculated more effectively.

The fields of the heat release rate in Fig. 10 confirm these findings. We would like to point out that in the steady flamelet model the heat release rate is not a variable required by the solver, since the temperature is directly interpolated from the table for a given enthalpy, pressure, mixture fraction, variance, and scalar dissipation. However, similar to the thermochemical variables from the solution of the flamelet equations such as species mass fractions and temperature, it can be tabulated in the preprocessing state. The fields at the two symmetry planes as well as the $x = 0.2$ m plane are shown. As expected, the main heat release takes place within the shear layer, where the scalar dissipation rate is the highest. The energy release continues along the stoichiometric lines farther downstream and drops below 1% of the maximal value before the end of the chamber. In the case of SST, it can be observed that the heat release zones are much thinner and less diffuse than for the simulation with the $k-\epsilon$ model. This results in the energy being released for positions farther downstream, indicating that the mixing is not as efficient and that the combustion requires a longer length to be complete. This result is also in accordance with the heat flux values from Fig. 11.

A further quantity that acts as a measure for the degree of mixing and the completion of combustion is the concentration of oxygen in the combustion chamber. To achieve the maximum yield from the reaction of the propellants and hence the highest possible energy release, the amount of unburnt oxygen leaving the chamber should be

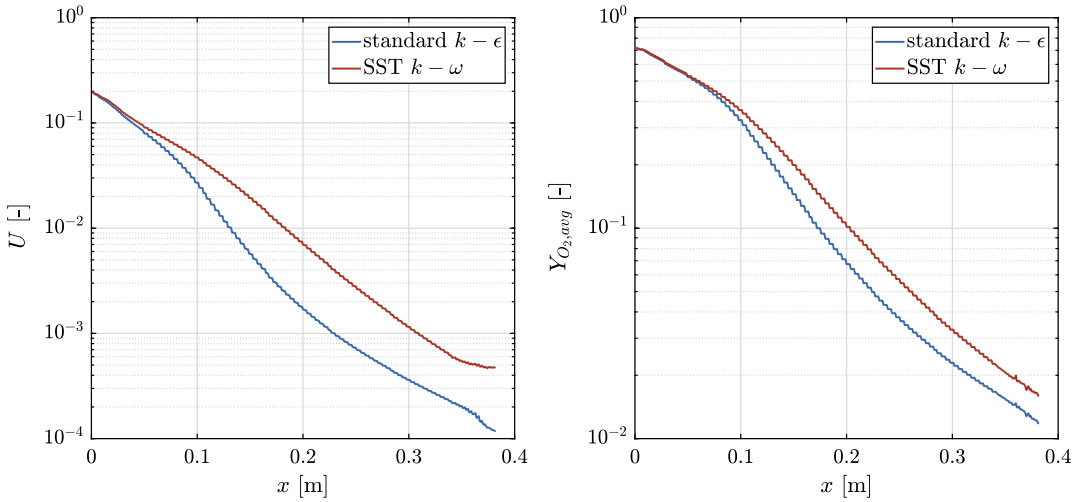

Fig. 9 Unmixedness (left) and average O_2 mass fraction (right) along the axial position.

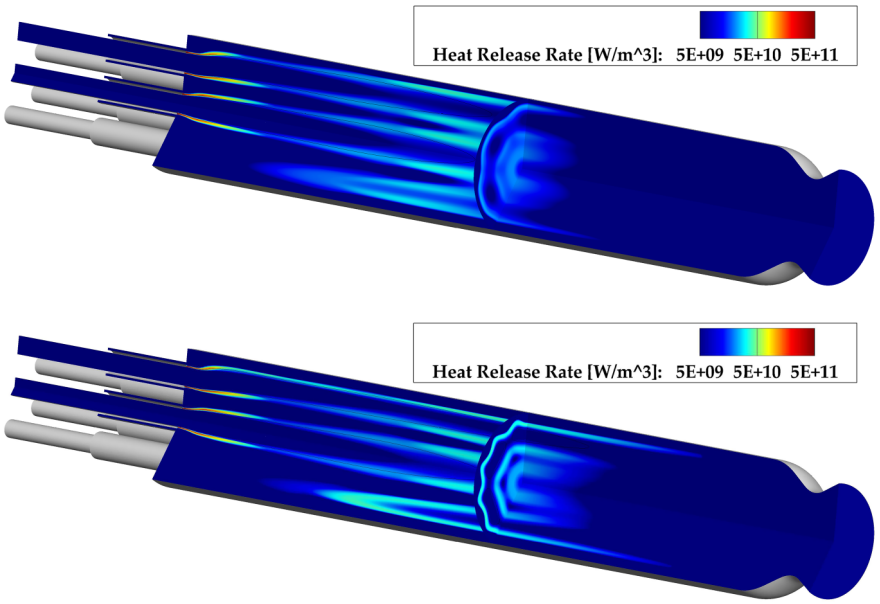

Fig. 10 Heat release field in the thrust chamber using the standard $k-\epsilon$ model (top) and the $k-\omega$ SST model (bottom). Axial scaling 50%.

held at a minimum. Chemical equilibrium calculations using the minimization of Gibb's free enthalpy showed that a mass fraction of approximately 0.2–0.4% O_2 is expected at equilibrium (depending on the pressure at the outlet plane). The O_2 mass fraction profiles along x are shown in Fig. 9. Both turbulence models seem to overpredict the oxygen at the outlet, thereby underpredicting the mixing and the energy release in the chamber. The $k-\epsilon$ and SST models show that approximately 1.40 and 1.75% O_2 remain unburnt, respectively. Therefore, although the $k-\epsilon$ produces better results than the SST, it still fails to capture the mixing and energy release correctly when combined with the flamelet model.

Finally, the fields of some major species are plotted in Fig. 12. Since the balance between CO and CO_2 is very important in methane/oxygen combustion and also affects the wall heat transfer characteristics, those species are chosen. It is observed that CO_2 is mainly generated in the areas around stoichiometry, as it is one of the two stoichiometric combustion products along with H_2O. CO, on the other hand, is mainly produced in regions with an absence of sufficient oxygen to generate CO_2. Since the common coaxial injector includes the fuel being injected in the outer annulus, the region close to the wall is fuel rich and facilitates the production of CO. As the mixing progresses, sufficient oxygen-rich gas reaches the wall and allows for the CO to react further and get converted to CO_2.

This effect is quantitatively shown in Fig. 13, in which the CO and CO_2 concentrations at the wall are presented as a function of the axial direction. For the simulation with SST, due to the poorer mixing, the production of CO at the wall is delayed. As a result, the point of maximal CO concentration is closer to the end of the chamber. This is also affecting the production of CO_2 at the wall; as the mixing is delayed, the gas at the wall starts getting leaner (closer to the global mixture fraction) at positions farther downstream, and then the transition of CO to CO_2 takes place. Furthermore, the SST model seems to predict a peak with higher concentrations of both CO and CO_2 at around $x = 0.02$ m from the face plate. This corresponds to the position of the stagnation point resulting from the recirculation zone (a shown in Sec. VI). This effect is less prominent in the simulation using the $k-\epsilon$. This higher concentration of reactants implies a stronger vortex formation and higher heat transfer at the stagnation point in the SST. This is verified in Fig. 11, in which the heat flux at the stagnation point is higher in the SST case.

Using an adiabatic flamelet model implies that no additional changes in the composition due to enthalpy defects are taken into account. Specifically, if a physically more intuitive nonadiabatic formulation were to be applied, the balance of CO and CO_2 at the wall would be different. As previous studies of methane/oxygen combustors have demonstrated, the low-enthalpy environment

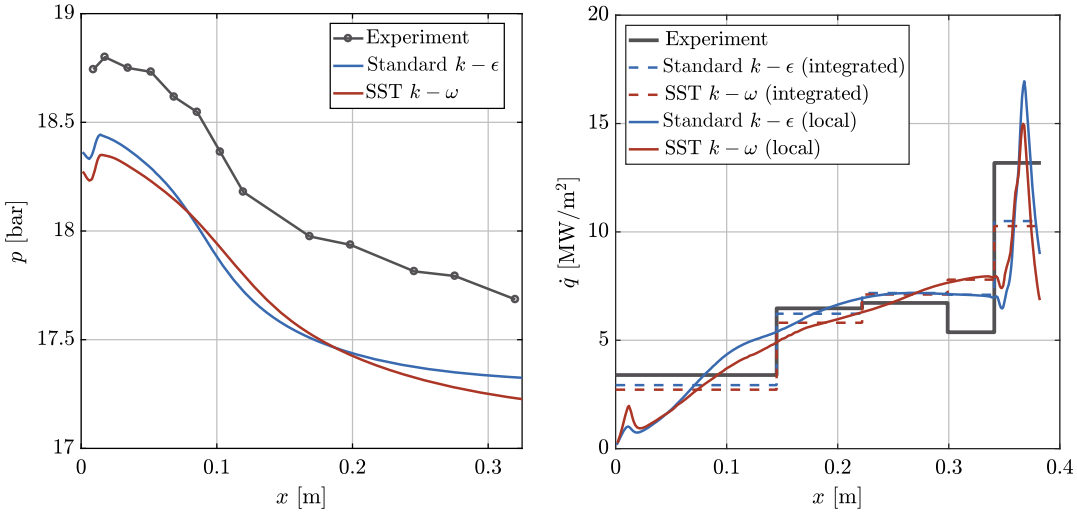

Fig. 11 Average pressure (left) and average wall heat flux (right) along the axial position.

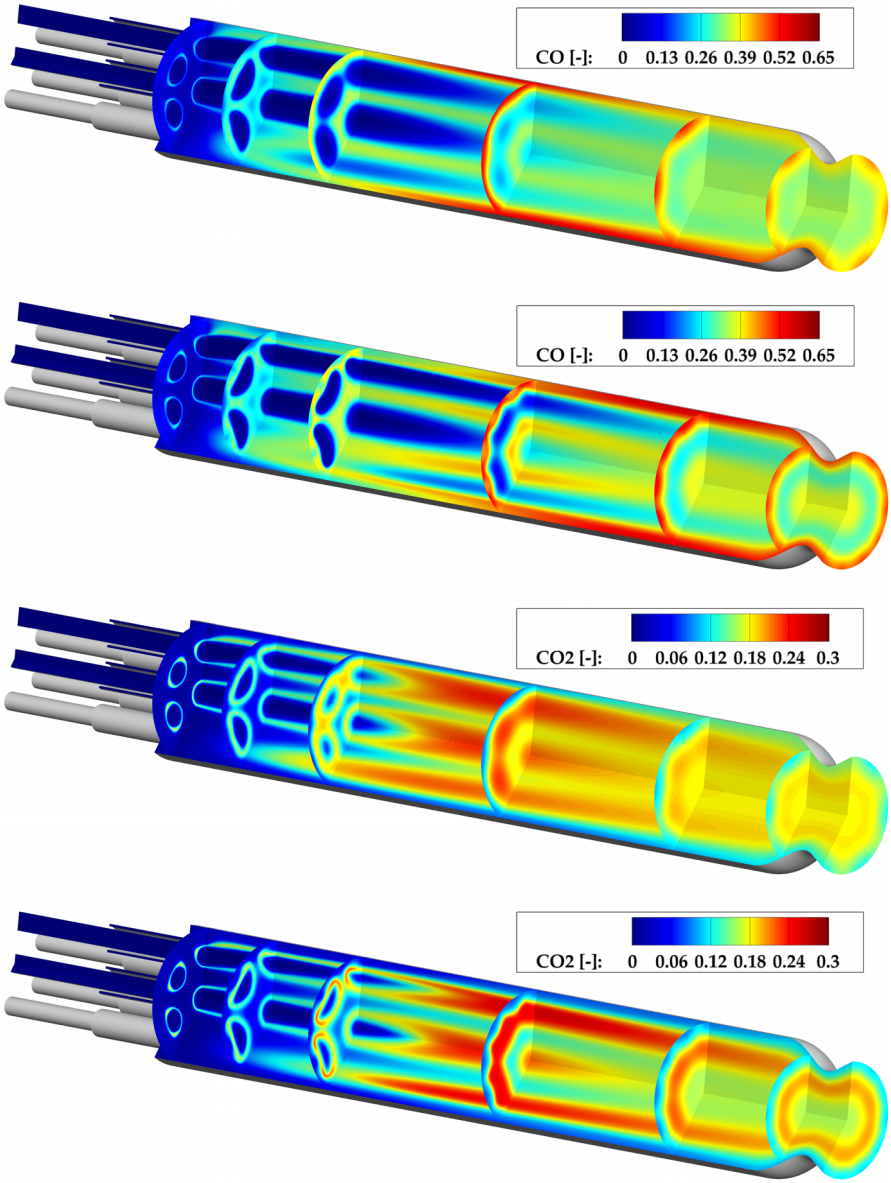

Fig. 12 CO and CO_2 fields in the thrust chamber using the standard $k-\epsilon$ model (top) and the $k-\omega$ SST model (bottom). Axial scaling 50%.

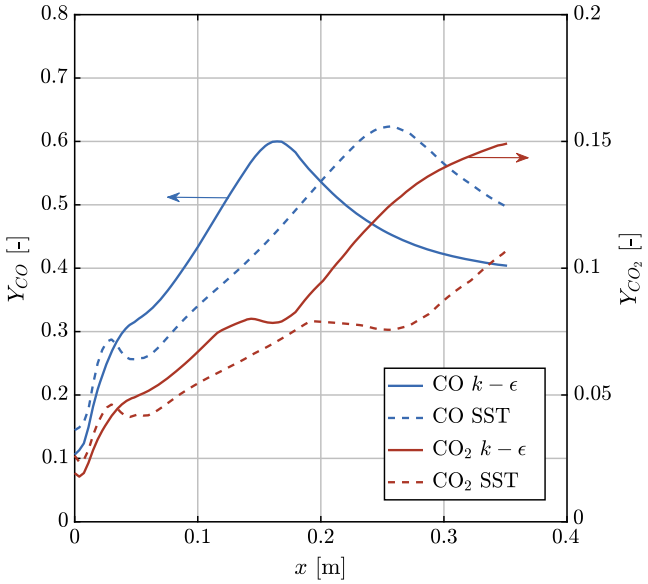

Fig. 13 CO and CO_2 concentrations at the chamber wall.

facilitates the recombination of CO to CO_2 [39]. This results in a faster depletion of CO compared to the frozen flamelet model in the vicinity of the wall and an increase in the heat transfer coefficient due to the exothermic nature of the recombination reaction.

B. Comparison with Experimental Results

The experimental pressure profile is displayed in Fig. 11. The profile shows a slight increase in the first axial positions, which corresponds to the presence of a stagnation point stemming from the injector recirculation zone, whereas after this point, a drop in the pressure values is observed. Both the increase at the stagnation point and the pressure drop are captured by the simulations. Comparing the absolute level gives as an additional indicator for the incompleteness of the combustion. Specifically, both turbulence models underestimate the pressure in the chamber by approximately 0.4 bar. The shape of the pressure profile seems to be very similar with the experimental one, implying similar acceleration profiles for the hot gas in the simulation and the experiment, but the absolute level is lower by around 2.5%. In the presence of recombination reactions due to the $k-\omega$ SST, the pressure profile seems to be slightly steeper close to the exit of the combustion chamber and the start of the nozzle, meaning that the energy release and the acceleration of the gas are still ongoing.

This is also the case with the heat flux, which keeps increasing even in the last chamber segment for the $k-\omega$ SST case, as can be seen in the right subfigure of Fig. 11, in which the local average heat flux (solid line) as well as the integrated heat flux for each segment (dashed line) are illustrated. Both the pressure and the heat flux profiles from the experiment demonstrate better agreement with the $k-\epsilon$ results. This fact combined with the unmixedness and O_2 profiles shown in Fig. 9 imply the ability of the $k-\epsilon$ to capture the mixing process more effectively.

Both models deliver a good match with the experimental data in the first three segments of the chamber. Similar slopes and average values are exhibited by both models. One difference is the heat flux directly at the stagnation point of the recirculation zone, which seems to be higher in the case for the SST $k-\omega$ model. This result agrees with the species profiles of Fig. 13. Apart from the stagnation point, the $k-\epsilon$ results show an increase of the heat flux over the first two segments and a flatter profile for the last two, indicating that the heat release has ended. In segment D, however, a drop in the heat flux was measured in the experiments, whereas the simulation predicted either a flat profile ($k-\epsilon$) or an increase of the heat loss to the wall ($k-\omega$ SST). This and the very high heat flux measured in the nozzle (compared to the CFD) are the main discrepancies between simulation and experiment. In fact, the nozzle heat flux has an error of approximately 25%. Further CFD tests were carried out by decreasing the wall temperature boundary condition since the actual value of the temperature is unknown. Even values of 300 K at the wall and simulations using a chemical equilibrium model were still unable to capture such a high increase in the nozzle heat flux. Changing the turbulence closure numbers for heat and mass transfer (Pr_t and Sc_t) did not introduce any improvement in this aspect.

A further investigation of the results and discussion with the publishers of the experimental results attributed the discrepancies in segments D and N to the experimental setup. Specifically, the nozzle had a separate cooling cycle, and for this test case, a very large water mass flow rate was chosen, in order to avoid any mechanical damage of the copper. The overly large coolant flow led to lower temperatures in the material and therefore to an axial heat flow from segment D into the nozzle segment. Energy that was originally applied to the wall of the fourth segment diffused axially toward the lower temperature domain of the nozzle segment. The consequence was that the water in the nozzle picked up a higher energy, whereas the water in the last segment was not heated as much as expected, thereby producing a significant drop in the heat flux of the third segment and a high increase in the nozzle.

V. Conjugate Heat Transfer

The effect of the cooling in the nozzle was also shown by Silvestri et al. [14] using an in-house engineering thermal code called Thermtest [40]. Thermtest allows the simulation of steady as well as transient thermal behavior of cooled or uncooled structures over a wide scope of chamber materials and cooling fluids. This demonstrated that the heat flux applied directly at the wall deviates from the one measured in the water manifolds, even in steady-state conditions. This effect is prominent only in the last two segments (D and N).

The basic assumption of the calorimetric measurement is that the integrated wall heat flux is identical to the water heat pickup. Hence, measuring the enthalpy difference of the incoming and outgoing water reproduces the average wall heat flux. In the present configuration, however, the assumption appears to be violated following the findings by Silvestri et al. [14]. Therefore, no wall heat flux data are available for segments D and N, and no comparison with the CFD results can be carried out.

To compare the CFD results with the available calorimetric data, an additional step has to be performed, in order to transform the obtained wall heat flux into a water enthalpy increase. To achieve that, a conjugate heat transfer (CHT) simulation of the copper structure and the cooling channels is carried out. Specifically, a 60 deg domain of the structure and coolant is modeled, and the commercial code ANSYS CFX is used for the numerical simulation of the coolant flow and heat conduction in the solid copper part of the thrust chamber. The first segment of the combustion chamber and the nozzle segment have rectangular cooling channels, whereas segments B, C, and D have circular channels, as shown by Silvestri et al. [12] and illustrated in Fig. 2. The 60 deg domain results in the incorporation of six rectangular cooling channels and five circular cooling channels, and corresponds to the smallest symmetrical domain. For the simulation, a block-structured grid with 27.8 million cells is used with the goal of fully resolving the boundary layer ($y^+ < 1$) at the cooling channel walls on the fluid domain side. The mesh of the cooling channels at the interface between segment D and segment N is shown in Fig. 14. Note that the mesh of the solid part is not shown in the figure but is included in the computational domain.

The boundary conditions for the cooling water with constant properties are defined according to the experiments, using a mass flow inlet condition together with a static pressure outlet condition. Because of numerical instabilities, the inflow of the combustion chamber cooling cycle is, however, approached by a total pressure boundary condition, which is dynamically adapted to keep the experimental target mass flow rate constant. Turbulence modeling is done by using Menter's $k-\omega$ SST model [20], neglecting any surface roughness effects. The heat conductivity of copper is modeled as a function of temperature. Between the combustion

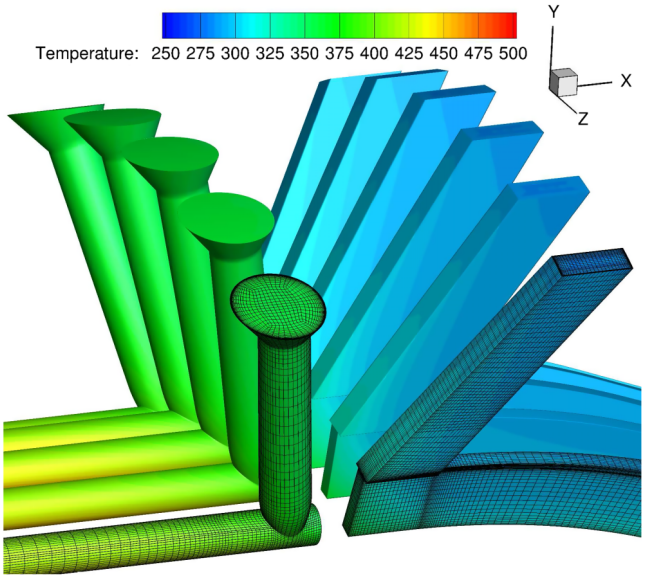

Fig. 14 Mesh of the cooling channels at the interface between segments D and N.

chamber segments, perfect heat transfer is assumed, while an adiabatic wall is set on the outer surfaces. For the simulation of the coolant flow, the equations for continuity, momentum, and energy are solved along with the transport equations for the turbulence kinetic energy and the specific dissipation rate, as shown in Sec. III. The setup is shown in detail in the work by Rahn et al. [41].

The study is carried out in two steps. In the first step, a one-way coupling is performed. The heat flux results obtained with a the one-dimensional wall temperature profile (Fig. 6) described in the previous section are fed to the model of the structure and coolant as von Neumann boundary conditions, and the resulting flow and heat transfer problem is solved. A single iteration of this coupling is carried out. In the second step, a fully coupled conjugate heat transfer simulation between the hot gas, structure, and coolant is performed. This implies a periodic exchange of the boundary conditions at the thrust chamber wall. Specifically, the heat flux obtained by the CFD of the hot gas is applied as a boundary condition at the structure wall and upon the solution of the structure and water simulation, the resulting wall temperature is applied as a boundary condition of the hot gas CFD. This process is iterated until convergence of the wall temperature and heat flux. Carrying out the fully coupled CHT is done to assess the validity of the one-way coupled results.

In the following subsections, the results using the heat flux from the hot gas simulation with the $k-\epsilon$ model as a boundary condition for the structure and cooling will be shown. The coupling with the SST hot gas simulation was also carried out but will be not used for the phenomenological description of the nozzle heat flux, as the previous sections demonstrated that the $k-\epsilon$ results are more reliable. The better agreement of the $k-\epsilon$ coupling with the experimental heat flux data will be demonstrated, however, once more in Fig. 15.

A. One-Way Coupling

The numerical results for the coolant and structural side resulting from the one-way conjugate heat transfer simulation are shown in Fig. 16 by using the temperature distribution. For the first cooling cycle covering the cylindrical combustion chamber part, a continuous increase in the fluid temperature through the channels together with a respective increase of the structural temperature is observed. This trend is locally interrupted by regions of colder temperatures near the hot gas wall in the vicinity of the cooling channels feeding lines.

The 3D effects of the wall temperature profile are shown in Fig. 17. As a result of the conjugate heat transfer simulation, an additional circumferential variation appears with higher temperatures occurring at a position of 0 deg above the injection element of the outer row. This highlights the importance of a 3D computation allowing one to resolve local peaks in the numerical simulation in order to evaluate the structural integrity. In contrast, the assumed boundary condition for the noncoupled hot gas simulation (black line) shows much lower temperatures with relative local deviations of the respective curves greater than 70 K in the combustion chamber. A similar relationship is observed when comparing the temperature values in the copper structure, which are evaluated at the exact positions of the thermocouple sensors used in the experimental setup. While very good agreement between the calculated and measured values is achieved in the chamber segment A, the simulation shows higher structural temperatures for the segments farther downstream. Similar behavior was reported in previous works carried out by Daimon et al. [42].

Possible sources causing this difference could also be found on the experimental side in the form of measurement errors, thermocouple positioning errors, or a deviation of the actual geometry from the CAD used as modeling input. Errors that could be introduced on the numerical side could be geometric simplifications in the form of omitting drilling tips together with adapting the diameter transition from the feeding channels to the main channel. Furthermore, not including any surface roughness effects could have an impact.

Both Figs. 16 and 17 also reveal a relatively low temperature of the throat and nozzle segment. This occurs due to the high experimental

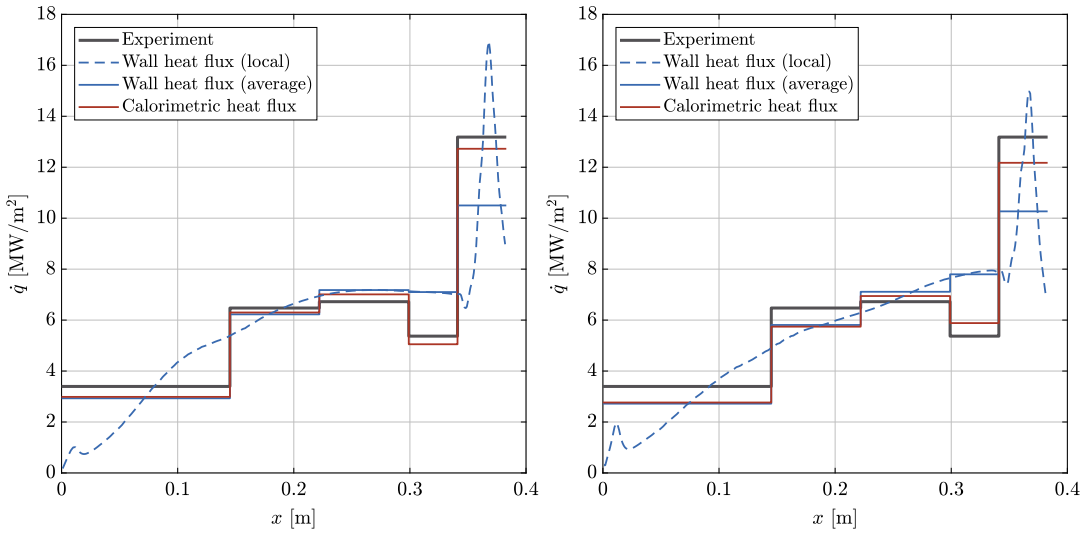

Fig. 15 Local and average wall heat flux compared to the experimental values and the calorimetric heat flux from the one-way coupling. Results with heat flux from hot gas simulation with $k-\epsilon$ (left) and SST (right).

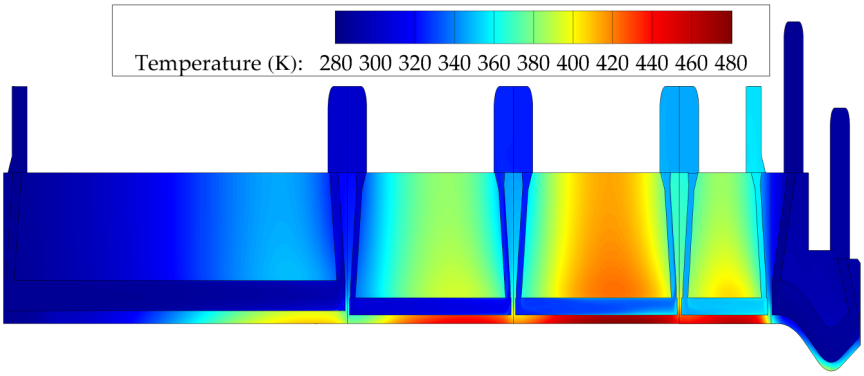

Fig. 16 Coolant side temperature field (axial scaling 25%) at the 0 deg plane (segments B, C, and D) and the 6 deg plane (segments A and N) to visualize all cooling channels above the outer injection element.

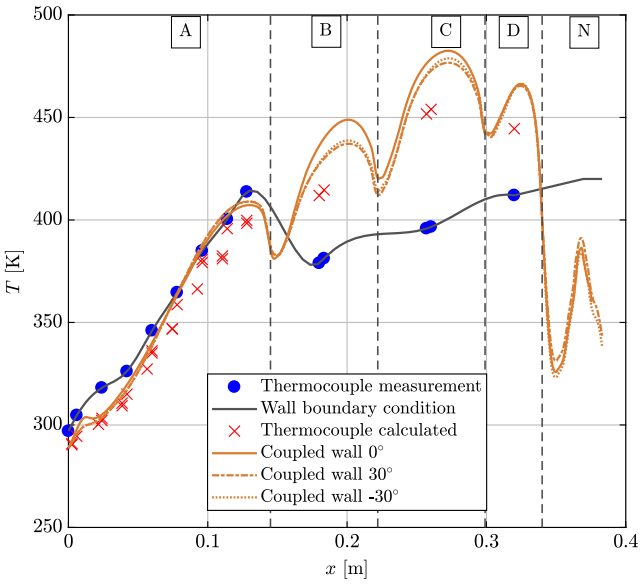

Fig. 17 Measured and calculated temperature values in the copper structure (points) and wall temperature boundary condition data (lines).

water mass flow rate in the nozzle cooling cycle, amounting to 5.5 times higher than the one in the cylindrical part. Moreover, the fact that both cycles are run in coflow operation results in hot water at the outlet of segment D being close to the fresh water flowing into the cooling channel of segment N. The resulting thermal gradient between segments D and N triggers axial heat conduction through the unisolated copper interface. Therefore, the nozzle cooling cycle extracts additional heat from the end of the chamber cooling cycle. Hence, the combustion chamber wall along the throat and nozzle segment has a much lower temperature compared to most of the cylindrical part, which has an additional impact on the wall heat flux prediction for the nozzle cooling cycle.

These effects have a large influence on the calorimetric wall heat flux prediction, as the data in Fig. 15 show. The calorimetric heat flux resulting from the one-way coupling of the hot gas and cooling channel simulations was evaluated as in the experiment, namely, according to Eq. (20).

$$\dot{q} = \dot{m}_w \frac{h_{\text{out}} - h_{\text{in}}}{A_w} \tag{20}$$

using the volume-averaged enthalpy difference between each manifold, the cooling cycle mass flow $\dot{m}_w$, and the combustion chamber wall surface area A_w. Both the results for $k-\epsilon$ (left) as well as SST (right) are shown. When comparing this calorimetric heat pickup (red line) to the experimental data (black line), better agreement between simulation and measurement is achieved. Compared to the heat flux directly at the wall (blue line), the calorimetric heat pickup shows a large deviation in the last two segments (D and N). As explained before, the effects discussed with regard to the throat and nozzle segment lower the heat pickup in segment D, while leading to a respective increase for segment N. In the remaining segments, however (A, B, and C), the differences between the wall heat flux and the calorimetric one are minimal.

This analysis shows that the experimental assumption of the wall heat flux and the calorimetric heat flux (resulting from the water enthalpy difference) being identical is not valid when large thermal gradients are present. With the one-sided coupling, the assumption of the axial heat flux altering the experimental data was confirmed, and a direct comparison between the nozzle results from CFD and from the experiment was carried out.

The relative deviation of the numerical calorimetric values from the experimental one shown in Table 4 defined as

$$\Delta\dot{q}_i = \frac{\dot{q}_{\text{exp}} - \dot{q}_i}{\dot{q}_{\text{exp}}} \tag{21}$$

provides a direct comparison between the performance of the standard $k-\epsilon$ and SST $k-\omega$. As expected, based on the results of Sec. IV, the less effective mixing of the SST model, which pushes the zone of heat release farther downstream, leads to a larger discrepancy in the heat flux values. Still, the error even with the SST model remains below 12% for most of the segments, with the exception of segment A. The larger deviation in segment A, which holds true also for the $k-\epsilon$ results, can be attributed to the fact that the heat flux in this region is highly dependent on the resolution of the recirculation zone. Since both the $k-\epsilon$ and the SST $k-\omega$ are eddy viscosity models and the recirculation zone is a region of anisotropic turbulence, they are not able to capture the turbulent heat flux accurately. However, for the remaining positions, the $k-\epsilon$ results manage to approximate the experimental values to an accuracy better than 6%. Therefore, the one-way coupling shows that the CFD heat flux results using the flamelet and $k-\epsilon$ models are able to match the experimental measurement with good agreement.

B. Two-Way Coupling

The two-way coupling is carried out by periodically exchanging the boundary conditions between the hot gas simulation and the structure/cooling channel simulation until the change between two subsequent iterations is smaller than a predefined threshold. Specifically, the simulation terminates when the maximal heat flux change between two iterations falls beneath 0.2%. For the hot gas

Table 4 Comparison of experimental and numerical calorimetric heat flux values

Model	$\Delta\dot{q}_A$, %	$\Delta\dot{q}_B$, %	$\Delta\dot{q}_C$, %	$\Delta\dot{q}_D$, %	$\Delta\dot{q}_N$, %
Standard $k-\epsilon$	12.07	2.71	−4.27	5.93	3.48
SST $k-\omega$	18.56	11.30	−3.30	−9.54	7.66

simulations, the Haswell nodes of the SuperMUC at the Leibniz Supercomputing Centre were used. The first iteration required approximately 25,000 CPU hours, whereas the subsequent iterations required approximately 1000 CPU hours each on 140 cores. The coolant simulation was performed using 15 CPUs (Intel Xeon CPU E5-2667 v3, 3.20 GHz) with 1000 CPU hours per iteration.

It was observed that the system achieved convergence after a small number of iterations (five iterations). This is an indicator for the fact that the initial solution provided (heat flux from the uncoupled hot gas simulation) is very close to the converged solution.

This is confirmed in Fig. 18. In the left subfigure, the uncoupled heat flux profile (shown already in Sec. IV) is compared to the converged solution of the coupled heat flux. In the right subfigure the relative difference between the two solutions is illustrated. The temperature difference in the same figure corresponds to the deviation of the converged wall temperature from the assumed initial wall boundary condition. It is observed in the right subfigure that the temperature applied as a boundary condition for the hot gas simulation in the converged CHT is up to 70 K higher than the initially applied thermal boundary condition in the chamber and up to 100 K lower in the nozzle. Despite this significant deviation, the two heat flux profiles are very similar, and their local discrepancies do not exceed 4% in any axial position. This implies that the wall temperature does not have a significant influence on the final heat flux profile as long as an adequately accurate first estimate is used, as was the case with the thermocouple measurements at 0.7 and 1.1 mm from the hot gas wall.

The reason for this low sensitivity is the fact that the wall heat transfer is driven by the difference in total enthalpy between the hot gas flow and the wall. For the present case with adiabatic temperatures of approximately 3500 K, the driving force is proportional to $T_{\mathrm{ad}} - T_w = 3500\ \mathrm{K} - 400\ \mathrm{K}$. The heat flux increase at the points of maximal deviation (assuming a temperature difference of 100 K) is hence expected to be in first order proportional to $(500-400)/(3500-400) \approx 3.2\%$, which is of the same order of magnitude as the observed values. Since the effect on the wall heat flux is minimal and since the correct wall temperature is almost never available a priori, the choice of an approximate temperature profile as a boundary condition of the hot gas CFD (e.g., like the one from Fig. 6) is justified.

The effect of the two-way coupling on the quantities of interest, namely, calorimetric heat flux and wall temperature, is given in Fig. 19. In the left subfigure, the calorimetric heat flux from the one-way coupling demonstrates only a minor deviation from the fully coupled simulation, which remains below 2%. For the nozzle segment, a slightly larger deviation is observed, which is expected, as this is the position with the highest wall temperature deviation as reported in Fig. 18.

Similarly, the temperature directly at the wall shows deviations that are constrained below 10 K. Therefore, one can safely deduce that the one-way coupling in this case is a sufficient approximation of a fully coupled simulation for the purpose of comparing with the experimental results, especially when considering the significantly lower computational cost.

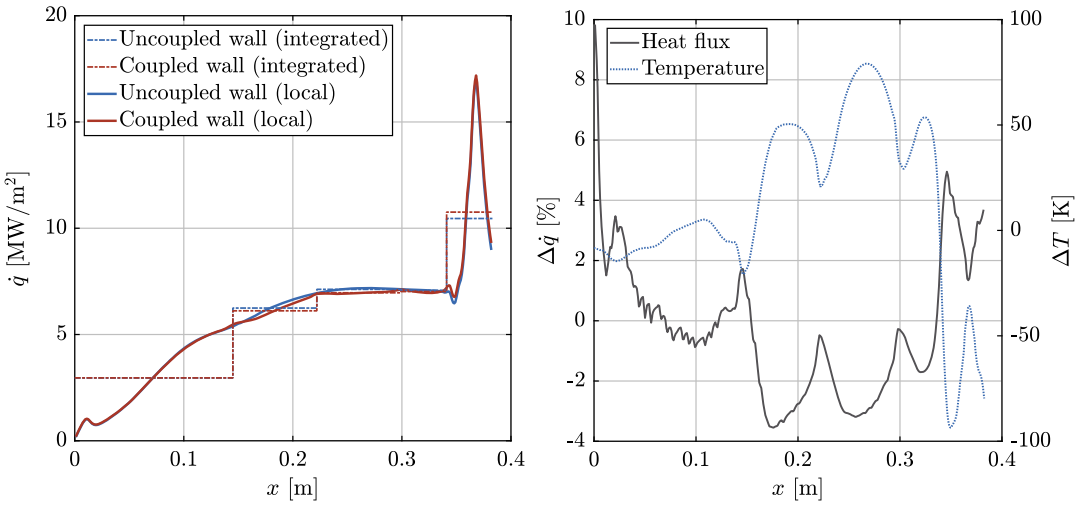

Fig. 18 Initial and converged wall heat flux (left). Wall temperature difference with corresponding relative heat flux change (right).

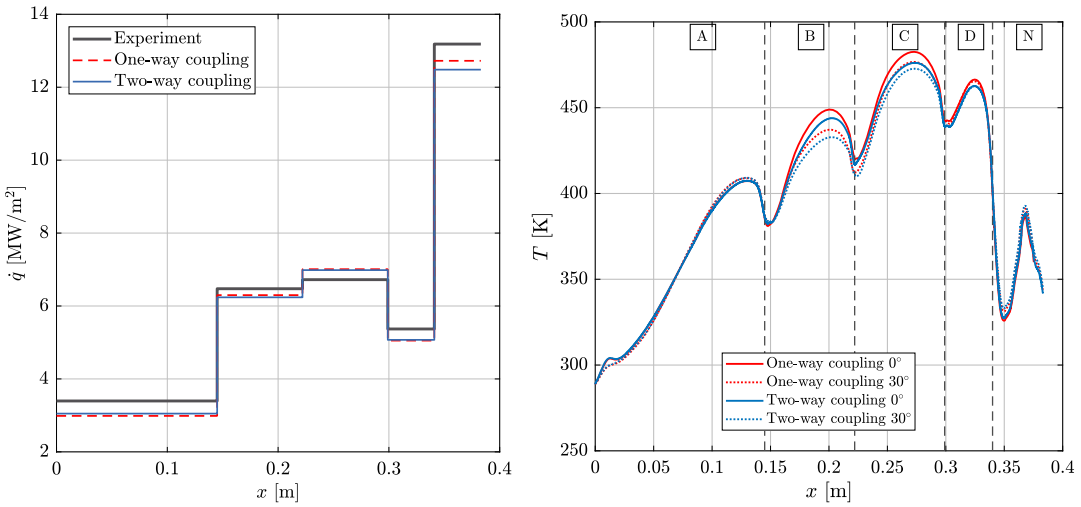

Fig. 19 Calorimetric heat flux (left) and wall temperature (right) from the one-way and two-way coupling.

VI. Azimuthal Heat Flux Profile

A very interesting observation occurs when investigating the variation of the heat flux along the chamber angle. The azimuthal profile of the heat flux at the wall is shown in Fig. 20. Here, 0 deg corresponds to the position directly above the injector, and −30, 30 deg corresponds to the symmetry planes, while 0 mm refers to the face plate, and 300 mm is a plane approximately 40 mm before the end of the combustion chamber and the beginning of the nozzle. As expected, the SST model produces a much larger variation of the heat flux value along the perimeter, since it has a higher temperature stratification even at positions close to the nozzle. The $k-\epsilon$ solution, on the other hand, demonstrates a flat heat flux profile for positions after 200 mm, in agreement with the temperature field (Fig. 7), which becomes homogeneous.

An unexpected effect is that for both models the heat flux has a local minimum at the position directly above the injector (0 deg) and its maximum at approximately 15 deg. This effect starts after about 50 mm downstream of the injector and continues for the rest of the chamber. To better understand the origin of this phenomenon, the temperature at the center of the first cell from the wall is plotted as seen in Fig. 21. At the wall position, the mixture fraction variance and the scalar dissipation tend to zero, and hence the temperature becomes a function of the mixture fraction solely (and the enthalpy, which, however, does not alter the chemical composition in the adiabatic flamelet formulation). For that reason, the mixture fraction is also plotted in Fig. 21. This is done only for the $k-\epsilon$ model, since it is the one producing the more physical results.

As expected, the temperature has a maximum directly at the positions where the heat flux is also maximal and a minimum at 0 deg. This is a result of the mixture fraction profiles at the wall; after the stoichiometric mixture fraction $Z_{st} = 0.2$, the temperature decreases with increasing mixture fraction, and hence the local maximum of the heat flux corresponds to a lower value of Z, i.e., a leaner composition, and vice versa. This is validated in the right subfigure of Fig. 21 and in Figs. 22 and 23. For positions closer to the injector, a recirculation zone is created, which leads to a maximum in temperature and heat flux right above the injector. Farther downstream, pockets of fuel-rich mixture are created directly at 0 deg, which leads to a decrease in temperature and heat flux. The shift in mixture fraction values above the injector is also visible in Fig. 22. Up until $x = 50$ mm, the mixture fraction at 0 deg is smaller than between the injectors, and downstream of that point, a shift occurs leading to colder, high- Z gas pockets being concentrated at 0 deg.

The streamlines in Figs. 24 and 25 verify that. In Fig. 24, the length of the recirculation zone is visible, amounting to approximately 10 mm, whereas in Fig. 25, the cause of the higher mixture fraction at 0 deg is illustrated. It can be observed that after the location of the recirculation zone a twist in the flow takes place. Specifically, due to the interaction of the injector jet with the symmetry boundary condition (i.e., with the neighboring injector), areas with a high mixture fraction are pushed toward the middle. This leads to an accumulation of the fuel-rich zones above the injector, leading to a lower temperature.

The presence of a strong vortex system feeding the hot, oxidizer-rich fuel toward the wall at the ±10–15 deg position is visible when examining the vorticity field in the chamber. Specifically, the vorticity component along the axial direction $\Omega_x = (\partial u_z/\partial y) - (\partial u_y/\partial z)$ is shown at selected planes in Fig. 26. Starting close to the face plate (at $x = 20$ mm), two locations with strong vorticity

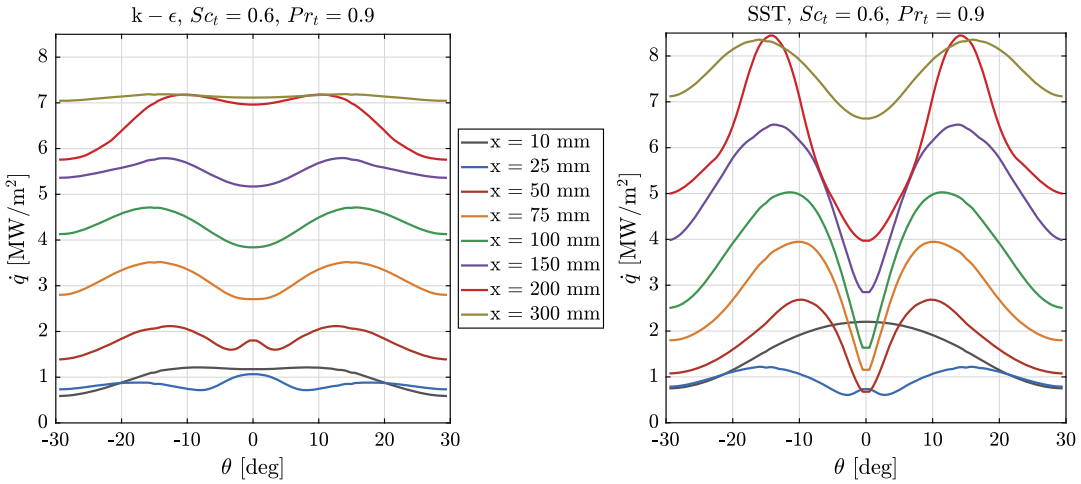

Fig. 20 Heat flux variation along the chamber angle for different axial positions.

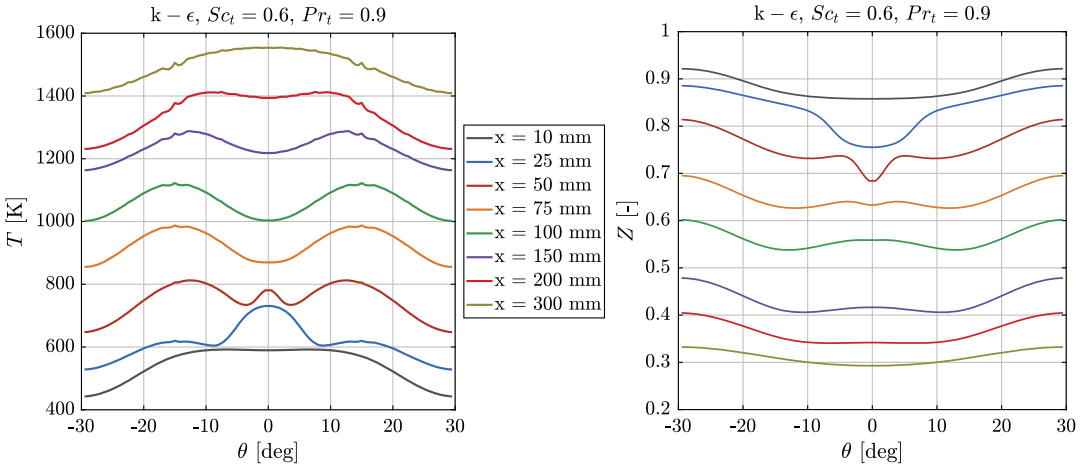

Fig. 21 Azimuthal variation of temperature and mixture fraction at the wall for the $k-\epsilon$ model.

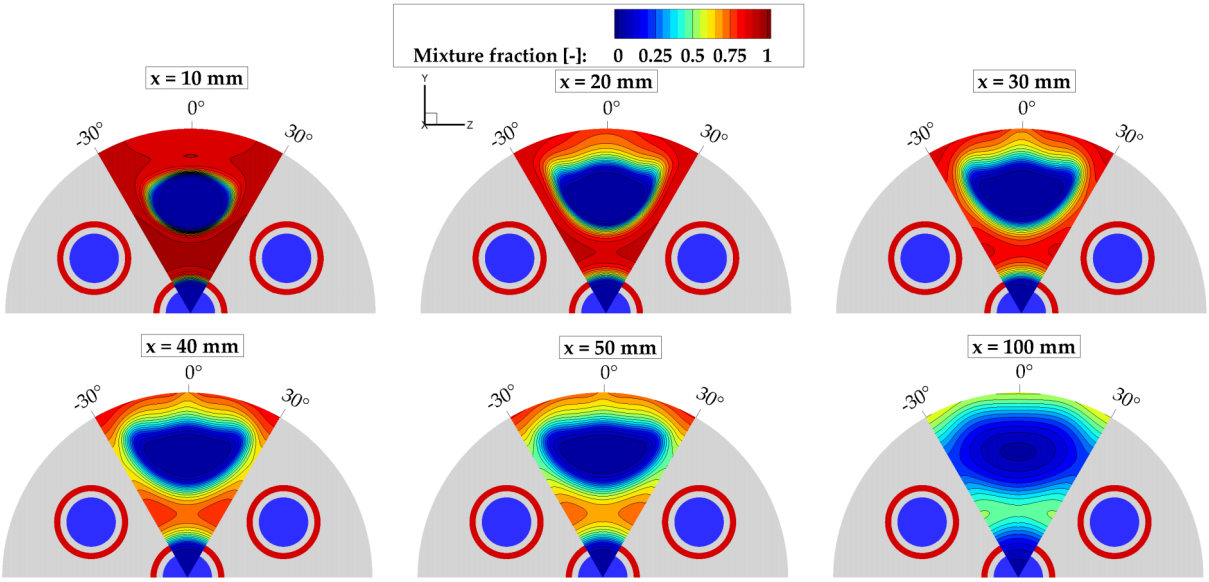

Fig. 22 Contour plot of mixture fraction at different planes in the thrust chamber.

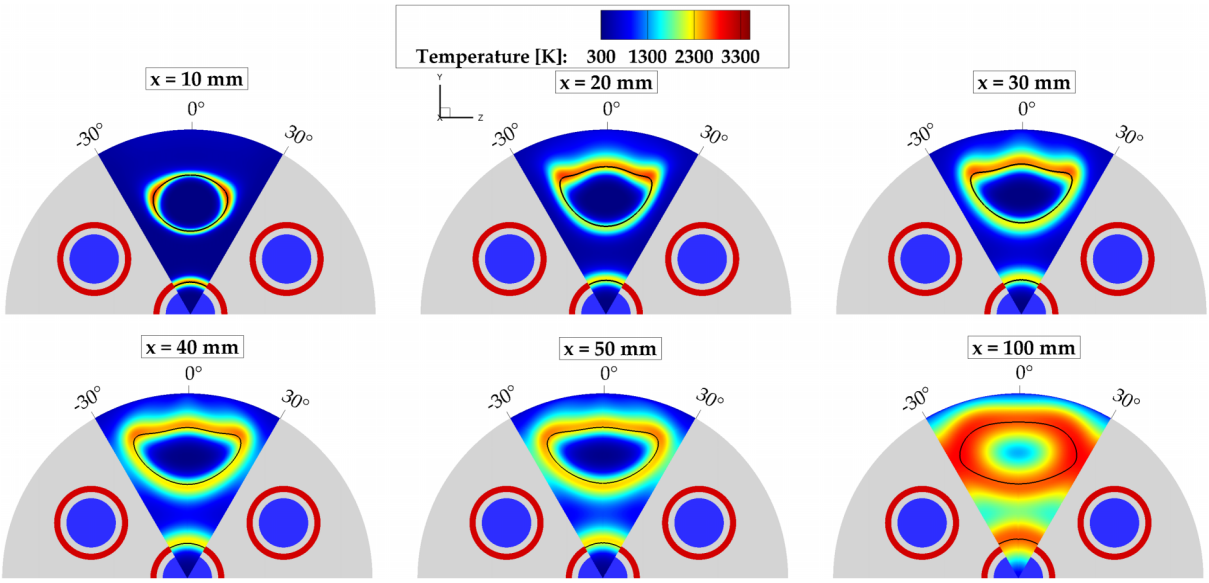

Fig. 23 Contour plot of temperature at different planes in the thrust chamber.

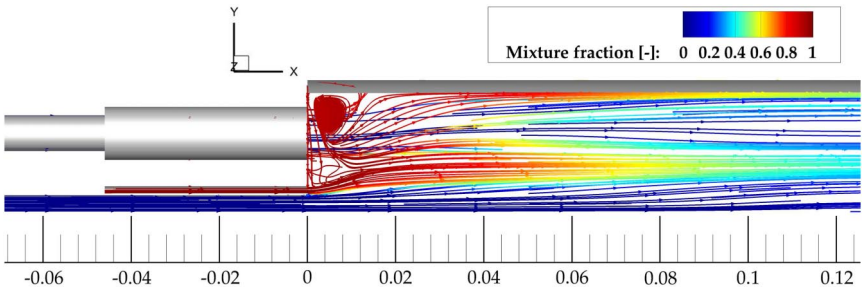

Fig. 24 Streamlines coloured by mixture fraction, showing the recirculation zone.

components appear at ±10–15 deg. This system of vortices appears to circulate hot gas from the shear layer of the coaxial injector directly onto the wall and serves as the main driving force for the increased heat transfer coefficient at this angular position. Moreover, this explains the shape of the temperature field in Fig. 23. In the first 10 mm from the face plate, the interaction between the individual flames is weak, and the expansion of the flame occurs nearly cylindrical, homogeneously in all radial directions. As soon as the jet/jet interaction is strengthened, the temperature field becomes distorted, and the expansion occurs preferably upward toward the wall. The vortex system, which is responsible for this distortion, is a consequence of the radial expansion of the individual jets and enhances the local heat loads between the injectors.

At positions farther downstream, the presence of the vortex system is still visible, but it appears to weaken after approximately 100 mm. At those positions, the individual jets are no longer dominant, and a

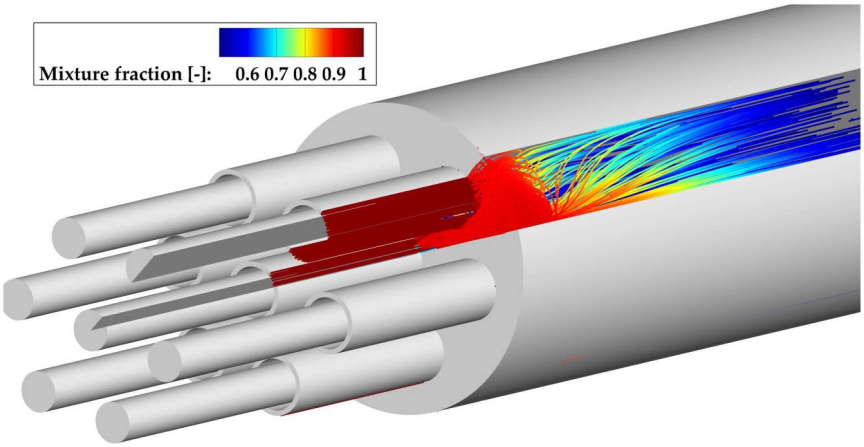

Fig. 25 Streamlines coming from the fuel inlet colored by the mixture fraction.

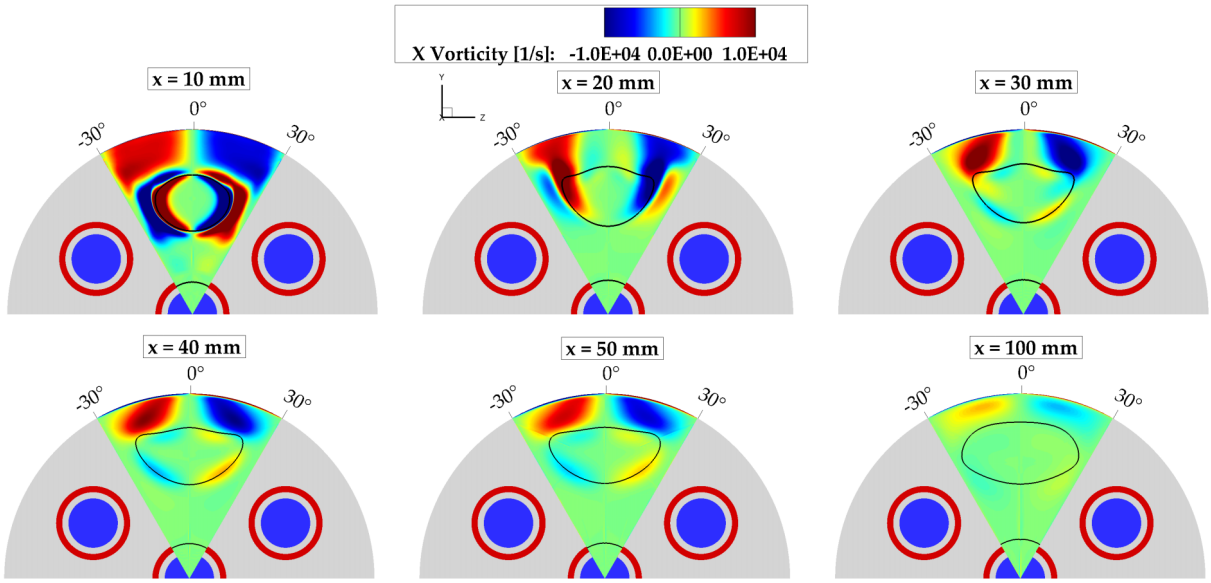

Fig. 26 Contour plot of vorticity at different planes in the thrust chamber.

homogeneous flow is achieved, which explains the absence of a strong recirculation zone. Because of the lack of a driving force for a circulation of hot gas toward the wall, at positions downstream of 100 mm, the temperature and heat flux distribution appears to smoothen, leading to a flatter profile.

To make sure that the effect is not caused by the symmetry boundary condition applied between the injectors, it was decided to extend the computational domain to include 120 deg of the rocket combustor. This has the effect of modeling two full injectors at the outer row (instead of half) as well as one direct interaction between the injectors and one through the symmetry boundary condition. To keep the computational mesh intact, the original mesh was simply reflected onto the symmetry plane to maintain the same resolution.

The results demonstrated an identical heat flux profile as the 30 deg calculation, indicating that the symmetry boundary condition is not the source of the local minimum. This is shown in Fig. 27, in which the azimuthal heat flux distribution for five different axial positions is illustrated. The 0 and 60 deg positions correspond to the two injector elements, whereas the −30, 30, and 90 deg positions correspond to the planes between injectors. The solid lines in Fig. 27 represent the solution using the 120 deg domain, whereas the symbols represent the 30 deg solution. By examining the plots, it is evident that the 30 deg symmetry is capable of resolving the azimuthal profiles with deviations smaller than 1% from the 120 deg one.

This effect is therefore a result of the turbulence model, the chemistry model, and the flow interaction between the injectors.

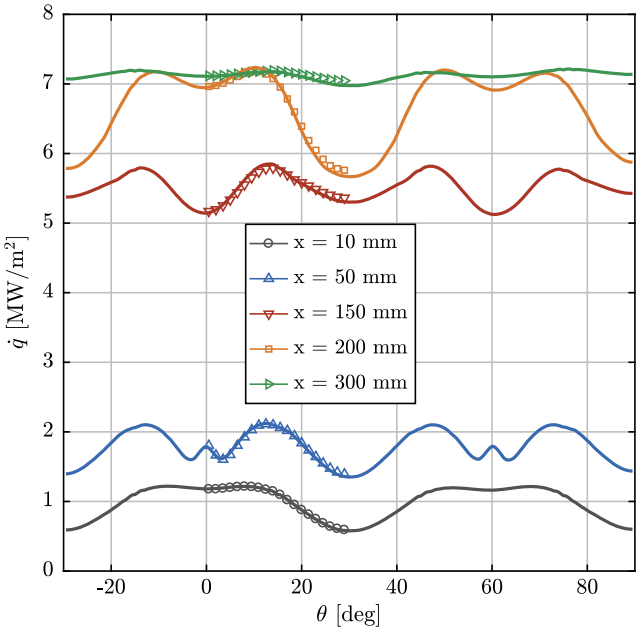

Fig. 27 Azimuthal heat flux profiles for 120 deg and 30 deg domains.

Further studies with other combustion models should be carried out to examine if this is only produced due to the use of the flamelet approach. Further measurement data such as an azimuthal heat flux profile would also be beneficial in order to allow a comparison with the CFD.

VII. Conclusions

A 3D Reynolds-averaged Navier–Stokes simulation of a seven-element rocket thrust chamber operated with GOX/GCH_4 was carried out. For the simulation, an adiabatic flamelet approach was implemented using a skeletal chemical mechanism. To allow for a comparison with experimental calorimetric heat fluxes, one-way and two-way couplings with the simulation of the structure and cooling channels were carried out.

Two different turbulence models were compared to each other, and specifically the $k-\epsilon$ with a two-layer model was compared to the $k-\omega$ shear-stress transport (SST). It was found that the $k-\epsilon$ produced more physical results in the combustion chamber, since it facilitated mixing, whereas the SST produced a very large temperature stratification, which propagated farther downstream until the nozzle. This was attributed to a much lower turbulent viscosity in the main flow. However, even the $k-\epsilon$ was found to have inefficient mixing and a lower heat release than theoretically expected. This was evident due to a high unmixedness at the exit, a high mass fraction of unburnt oxygen, and a chamber pressure lower than the experimental one by 2.5%. A further reason for the low pressure is that the adiabatic model fails to capture recombination reactions occurring at lower enthalpy levels. The heat release of those exothermic reactions that is not present in the frozen flamelet chemistry could be the culprit for the lower pressure, and nonadiabatic extensions of the model are needed to capture the effect.

Apart from the pressure, comparison with the experimental heat flux took place. The computational fluid dynamics (CFD) simulation was able to reproduce the heat flux values in the first three segments of the combustion chamber but produced a high discrepancy in the last segment and in the nozzle. To understand the nature of this deviation, a one-way coupling with the simulation of the thrust chamber structure and coolant flow was carried out using the wall heat flux from CFD as a boundary condition. This analysis showed a significant deviation between the calorimetrically measured heat flux from the one applied directly onto the hot gas wall. The source of this disagreement was found to be due to the experimental setup. An overestimated coolant mass flow rate in the nozzle produced very large thermal gradients in the structure, resulting in an unrealistically high measured heat flux in the nozzle. After taking into account this effect, very good agreement between simulation and experiment was found.

To evaluate the validity of the one-way coupling, a two-way coupling was also carried out by periodically exchanging the boundary conditions of the hot gas simulation and the cooling channel simulation until convergence. It was found that no significant change compared to the one-way coupling was present. This is attributed to the low sensitivity of the hot gas heat flux on the wall temperature boundary condition. Differences of up to 100 K in the wall temperature resulted in changes of approximately 4% in the heat flux. Therefore, carrying out simulations with approximate temperature profiles for the temperature (since wall temperature is rarely known a priori) is considered to be justified.

Finally, it was observed that the heat flux coming from the CFD had a local minimum directly above the injector position (0 deg) as opposed to a maximum. This was attributed to the interaction between the individual jets leading to low-temperature gas staying trapped directly above the injector position. A further simulation with a 120 deg domain confirmed that this effect was not a product of the symmetry boundary conditions.

Further examination of this test case is planned for the future. For an improved modeling of the heat transfer with the wall, a nonadiabatic flamelet model will be applied, which will include heat loss effects in the concentration of the species via recombination. Further evaluation of the test results is also scheduled; by developing an inverse heat transfer method, the azimuthal distribution of the heat flux could be reconstructed based on the temperature measurements at the wall. This would allow for a verification or disproving of the heat flux profile along the chamber perimeter. Simulations with large-eddy simulation will also be carried out to see if the behavior of the jet interaction remains.

Acknowledgments

Financial support has been provided by the German Research Foundation in the framework of the Sonderforschungsbereich Transregio 40: "Technological Foundation for the Thermally and Mechanically High Loaded Components of Future Space Transportation System". The authors gratefully acknowledge the Gauss Centre for Supercomputing e.V. (www.gauss-centre.eu) for funding this project by providing computing time on the Gauss Center for Supercomputing supercomputer SuperMUC at Leibniz Supercomputing Centre (www.lrz.de). The additional work on the coolant flow simulations at ArianeGroup has been supported by the Bayerische Forschungsstiftung within the project "Umweltfreundliche Treibstoffkombination LOX/Methan" and by the national technology program TARES 2020 sponsored by the DLR, German Aerospace Center, Bonn, Germany, under contract number 50RL1710.

References

[1] Frey, M., Aichner, T., Görgen, J., Ivancic, B., Kniesner, B., and Knab, O., "Modeling of Rocket Combustion Devices," *10th AIAA/ASME Joint Thermophysics and Heat Transfer Conference*, AIAA Paper 2009-5477, 2010.
doi:10.2514/6.2009-5477

[2] Urbano, A., Selle, L., Staffelbach, G., Cuenot, B., Schmitt, T., Ducruix, S., and Candel, S., "Exploration of Combustion Instability Triggering Using Large Eddy Simulation of a Multiple Injector Liquid Rocket Engine," *Combustion and Flame*, Vol. 169, July 2016, pp. 129–140.
doi:10.1016/j.combustflame.2016.03.020

[3] Oefelein, J. C., and Yang, V., "Modeling High-Pressure Mixing and Combustion Processes in Liquid Rocket Engines," *Journal of Propulsion and Power*, Vol. 14, No. 5, 1998, pp. 843–857.
doi:10.2514/2.5349

[4] Zhukov, V. P., "Computational Fluid Dynamics Simulations of a GO2/GH2 Single Element Combustor," *Journal of Propulsion and Power*, Vol. 31, No. 6, 2015, pp. 1707–1714.
doi:10.2514/1.B35654

[5] Cutrone, L., De Palma, P., Pascazio, G., and Napolitano, M., "A RANS Flamelet-Progress-Variable Method for Computing Reacting Flows of Real-Gas Mixtures," *Computers & Fluids*, Vol. 39, No. 3, 2010, pp. 485–498.
doi:10.1016/j.compfluid.2009.10.001

[6] Zips, J., Müller, H., and Pfitzner, M., "Efficient Thermo-Chemistry Tabulation for Non-Premixed Combustion at High-Pressure Conditions," *Flow, Turbulence and Combustion*, Vol. 101, No. 3, 2018, pp. 821–850.
doi:10.1007/s10494-018-9932-4

[7] Negishi, H., Daimon, Y., and Kawashima, H., "Flowfield and Heat Transfer Characteristics in the LE-X Expander Bleed Cycle Combustion Chamber," *50th AIAA/ASME/SAE/ASEE Joint Propulsion Conference*, AIAA Paper 2014-4010, 2014.
doi:10.2514/6.2014-4010

[8] Negishi, H., Kumakawa, A., Yamanishi, N., and Kurosu, A., "Heat Transfer Simulations in Liquid Rocket Engine Subscale Thrust Chambers," *44th AIAA/ASME/SAE/ASEE Joint Propulsion Conference & Exhibit*, AIAA Paper 2008-5241, 2008.
doi:10.2514/6.2008-5241

[9] Betti, B., Martelli, E., and Nasuti, F., "Heat Flux Evaluation in Oxygen/Methane Thrust Chambers by RANS Approach," *46th AIAA/ASME/SAE/ASEE Joint Propulsion Conference & Exhibit*, AIAA Paper 2010-6721, 2010.
doi:10.2514/6.2010-6721

[10] Kim, S.-K., Joh, M., Choi, H. S., and Park, T. S., "Multidisciplinary Simulation of a Regeneratively Cooled Thrust Chamber of Liquid Rocket Engine: Turbulent Combustion and Nozzle Flow," *International Journal of Heat and Mass Transfer*, Vol. 70, March 2014, pp. 1066–1077.
doi:10.1016/j.ijheatmasstransfer.2013.10.046

[11] Song, J., and Sun, B., "Coupled Numerical Simulation of Combustion and Regenerative Cooling in LOX/Methane Rocket Engines," *Applied Thermal Engineering*, Vol. 106, Aug. 2016, pp. 762–773.
doi:10.1016/j.applthermaleng.2016.05.130

[12] Silvestri, S., Celano, M. P., Schlieben, G., and Haidn, O. J., "Characterization of a Multi-Injector GOX-GCH4 Combustion Chamber," *52nd AIAA/SAE/ASEE Joint Propulsion Conference*, AIAA Paper 2016-4992, 2016.
doi:10.2514/6.2016-4992

[13] Chemnitz, A., Sattelmayer, T., Roth, C., Haidn, O., Daimon, Y., Keller, R., Gerlinger, P., Zips, J., and Pfitzner, M., "Numerical Investigation of Reacting Flow in a Methane Rocket Combustor: Turbulence Modeling," *Journal of Propulsion and Power*, Vol. 34, No. 4, 2018, pp. 864–877.
doi:10.2514/1.B36565

[14] Silvestri, S., Kirchberger, C., Schlieben, G., Celano, M. P., and Haidn, O., "Experimental and Numerical Investigation of a Multi-Injector GOX-GCH4 Combustion Chamber," *Transactions of the Japan Society for Aeronautical and Space Sciences, Aerospace Technology Japan*, Vol. 16, No. 5, 2018, pp. 374–381.
doi:10.2322/tastj.16.374

[15] Richardson, L. F., "The Approximate Arithmetical Solution by Finite Differences of Physical Problems Involving Differential Equations, with an Application to the Stresses in a Masonry Dam," *Philosophical Transactions of the Royal Society London, Series A: Mathematical and Physical Sciences*, Vol. 210, Nos. 459–470, 1911, pp. 307–357.
doi:10.1098/rsta.1911.0009

[16] Kays, W. M., "Turbulent Prandtl Number-Where Are We?" *Journal of Heat Transfer*, Vol. 116, No. 2, 1994, pp. 284–295.
doi:10.1115/1.2911398

[17] Riedmann, H., Kniesner, B., Frey, M., and Munz, C.-D., "Modeling of Combustion and Flow in a Single Element GH2/GO2 Combustor," *Council of European Aerospace Societies Space Journal*, Vol. 6, No. 1, 2014, pp. 47–59.
doi:10.1007/s12567-013-0056-3

[18] Launder, B. E., and Spalding, D. B., *Mathematical Models of Turbulence*, Academic Press, London, 1972, pp. 137–152.

[19] Wolfshtein, M., "The Velocity and Temperature Distribution in One-Dimensional Flow with Turbulence Augmentation and Pressure Gradient," *International Journal of Heat and Mass Transfer*, Vol. 12, No. 3, 1969, pp. 301–318.
doi:10.1016/0017-9310(69)90012-X

[20] Menter, F. R., "Two-Equation Eddy-Viscosity Turbulence Models for Engineering Applications," *AIAA Journal*, Vol. 32, No. 8, 1994, pp. 1598–1605.
doi:10.2514/3.12149

[21] Wilcox, D. C., *Turbulence Modeling for CFD*, Vol. 2, DCW Industries, La Canada, CA, 1998, pp. 124–128.

[22] Jones, W., and Whitelaw, J., "Calculation Methods for Reacting Turbulent Flows: A Review," *Combustion and Flame*, Vol. 48, 1982, pp. 1–26.
doi:10.1016/0010-2180(82)90112-2

[23] Peters, N., "Laminar Diffusion Flamelet Models in Non-Premixed Turbulent Combustion," *Progress in Energy and Combustion science*, Vol. 10, No. 3, 1984, pp. 319–339.
doi:10.1016/0360-1285(84)90114-X

[24] Pitsch, H., Barths, H., and Peters, N., "Three-Dimensional Modeling of NOx and Soot Formation in DI-Diesel Engines Using Detailed Chemistry Based on the Interactive Flamelet Approach," Soc. of Automotive Engineers International Paper 962057, Warrendale, PA, 1996.
doi:10.4271/962057

[25] Lee, D., Thakur, S., Wright, J., Ihme, M., and Shyy, W., "Characterization of Flow Field Structure and Species Composition in a Shear Coaxial Rocket GH2/GO2 Injector: Modeling of Wall Heat Losses," *47th AIAA/ASME/SAE/ASEE Joint Propulsion Conference & Exhibit*, AIAA Paper 2011-6125, 2011.
doi:10.2514/6.2011-6125

[26] Rahn, D., Riedmann, H., Behr, R., and Haidn, O. J., "Non–Adiabatic Flamelet Modeling for the Numerical Simulation of Methane Combustion in Rocket Thrust Chambers," *54th AIAA/SAE/ASEE Joint Propulsion Conference*, AIAA Paper 2018-4869, 2018.
doi:10.2514/6.2018-4869

[27] Perakis, N., Roth, C., and Haidn, O. J., "Development of a Non-Adiabatic Flamelet Model for Reacting Flows with Heat Loss," *Space Propulsion Conference*, Association Aéronautique et Astronautique de France Paper 171, 2018.

[28] Fiorina, B., Baron, R., Gicquel, O., Thevenin, D., Carpentier, S., and Darabiha, N., "Modelling Non-Adiabatic Partially Premixed Flames Using Flame-Prolongation of ILDM," *Combustion Theory and Modelling*, Vol. 7, No. 3, 2003, pp. 449–470.
doi:10.1088/1364-7830/7/3/301

[29] Cecere, D., Giacomazzi, E., Picchia, F. R., Arcidiacono, N., Donato, F., and Verzicco, R., "A Non-Adiabatic Flamelet Progress–Variable Approach for LES of Turbulent Premixed Flames," *Flow, Turbulence and Combustion*, Vol. 86, No. 3, 2011, pp. 667–688.
doi:10.1007/s10494-010-9319-7

[30] Marracino, B., and Lentini, D., "Radiation Modelling in Non-Luminous Nonpremixed Turbulent Flames," *Combustion Science and Technology*, Vol. 128, Nos. 1–6, 1997, pp. 23–48.
doi:10.1080/00102209708935703

[31] Chan, S., Pan, X., and Abou-Ellail, M., "Flamelet Structure of Radiating CH4-Air Flames," *Combustion and Flame*, Vol. 102, No. 4, 1995, pp. 438–446.
doi:10.1016/0010-2180(95)00037-7

[32] Proch, F., and Kempf, A., "Modeling Heat Loss Effects in the Large Eddy Simulation of a Model Gas Turbine Combustor with Premixed Flamelet Generated Manifolds," *Proceedings of the Combustion Institute*, Vol. 35, No. 3, 2015, pp. 3337–3345.
doi:10.1016/j.proci.2014.07.036

[33] Kishimoto, A., Moriai, H., Takenaka, K., Nishiie, T., Adachi, M., Ogawara, A., and Kurose, R., "Application of a Nonadiabatic Flamelet/Progress-Variable Approach to Large-Eddy Simulation of H2/O2 Combustion Under a Pressurized Condition," *Journal of Heat Transfer*, Vol. 139, No. 12, 2017.
doi:10.1115/1.4037099

[34] Ma, P. C., Wu, H., Ihme, M., and Hickey, J.-P., "Nonadiabatic Flamelet Formulation for Predicting Wall Heat Transfer in Rocket Engines," *AIAA Journal*, Vol. 56, No. 6, 2018, pp. 2336–2349.
doi:10.2514/1.J056539

[35] Slavinskaya, N., Abbasi, M., Starcke, J.-H., Mirzayeva, A., and Haidn, O. J., "Skeletal Mechanism of the Methane Oxidation for Space Propulsion Applications," *52nd AIAA/SAE/ASEE Joint Propulsion Conference*, AIAA Paper 2016-4781, 2016.
doi:10.2514/6.2016-4781

[36] Hirschfelder, J. O., Curtiss, C. F., Bird, R. B., and Mayer, M. G., *Molecular Theory of Gases and Liquids*, Wiley, New York, 1954, pp. 1167–1173.

[37] Bird, R. B., Stewart, W. E., and Lightfoot, E. N., *Transport Phenomena*, Wiley, New York, 1960, pp. 274–278.

[38] Wilke, C., "A Viscosity Equation for Gas Mixtures," *Journal of Chemical Physics*, Vol. 18, No. 4, 1950, pp. 517–519.
doi:10.1063/1.1747673

[39] Perakis, N., Roth, C., and Haidn, O., "Simulation of a Single-Element Rocket Combustor Using a Non-Adiabatic Flamelet Model," *Space Propulsion Conference 2018*, Association Aéronautique et Astronautique de France Paper 174, 2018.

[40] Kirchberger, C., Wagner, R., Kau, H.-P., Soller, S., Martin, P., Bouchez, M., and Bonzom, C., "Prediction and Analysis of Heat Transfer in Small Rocket Chambers," *46th AIAA Aerospace Sciences meeting and Exhibit*, AIAA Paper 2008-1260, 2008, pp. 7–11.
doi:10.2514/6.2008-1260

[41] Rahn, D., Eiringhaus, D., Riedmann, H., Behr, R., and Haidn, O. J., "Characterization of an Adiabatic Flamelet Combustion Model for Gaseous CH4/O2 Combustion in Rocket Thrust Chambers," *Space Propulsion Conference*, Association Aéronautique et Astronautique de France Paper 152, 2018.

[42] Daimon, Y., Negishi, H., Silvestri, S., and Haidn, O. J., "Conjugated Combustion and Heat Transfer Simulation for a 7 Element GOX/GCH4 Rocket Combustor," *2018 Joint Propulsion Conference*, AIAA Paper 2018-4553, 2018.
doi:10.2514/6.2018-4553

V. Raman
Associate Editor

6.2 NON-ADIABATIC STEADY FLAMELET

A non-adiabatic flamelet model based on an enthalpy prescription method is developed in this section. To account for the freezing of the chemical reactions, a chemical time-scale based extension of the flamelet tables is employed, delivering satisfactory results both for methane and hydrogen applications:

Wall Heat Transfer Prediction in CH_4/O_2 and H_2/O_2 Rocket Thrust Chambers Using a Non-Adiabatic Flamelet Model
Nikolaos Perakis, Oskar J. Haidn
Acta Atsronautica, Vol. (2020)
doi: https://doi.org/10.1016/j.actaastro.2020.05.008

The effect of the recombination reactions on the wall heat flux was investigated in Chapter 5, while the application of frozen models, which neglect the effect of the aforementioned reactions was explored in Section 6.1. Although frozen models were found to predict the wall heat flux with accepted accuracy within the uncertainty bounds of the experimental data, the combustion efficiency was found to be *under-predicted*.

This effect motivated the development of a non-adiabatic extension to the steady flamelet model. The method presented in this section is based on the *enthalpy prescription* that was introduced in Section 4.6.2. Laminar flamelet calculations are carried out at pre-defined enthalpy profiles corresponding to heat loss (and heat gain) profiles, thereby introducing an *additional dimension* to the flamelet tables. Investigation of the tables confirms that the recombination of CO to CO_2 is captured for decreased enthalpy levels.

However, an issue with this approach is that the only variable that describes the deviation from the chemical equilibrium conditions is the scalar dissipation. As the value of this variable *diminishes in the vicinity of the wall, the non-adiabatic model defaults to the equilibrium chemistry model*. Based on the results reported in Section 5.4, the composition within the boundary layer is significantly deviant from the equilibrium predictions and hence the flamelet model leads to an *overestimation of the degree of recombination* and the experienced wall heat flux.

The problem is solved by introducing a further dimension to the table, which accounts for the *freezing of the chemical reactions* when the temperature reaches small values close to the wall. This is carried out with the concept of the "freezing" enthalpy, i.e. the local value after which the gas composition remains constant. The estimation of this value is performed by a comparison of the dominant time-scales. The *Damköhler number* is computed based on the chemical time-scale and the flow time-scale in each cell. The minimum value of the turbulent $\tau = k/\varepsilon$ and diffusive $\tau = \frac{\rho c_p}{\lambda}\sqrt{\frac{\mu^3}{\epsilon\rho^3}} = \tau_K\sqrt{Pr}$ time-scales (with τ_k being the Kolmogorov value) is used for this purpose.

In order to validate the model, a *canonical test case* of an isothermal flat plate similar to the one simulated in Section 5.4 is deployed. Since a wide range of O/F, inlet Mach number and pressure values is examined, the cost of DNS and LES would be prohibitive, and therefore RANS is chosen, with a laminar Finite-Rate Chemistry (FRC) model for the baseline simulations. Both hydrogen/oxygen and methane/oxygen are examined as propellant combinations.

After the validation, the simulation of a single-element rocket combustor operated with GCH_4/GO_2 is performed. The frozen model, the non-adiabatic model and the time-scale extended (hybrid) model are compared and their ability to reproduce the experimental wall heat flux results reported in Section 3.1 is assessed. As expected, the non-adiabatic model without the time-scale correction over-predicts the recombination reactions and the heat flux values. On the other hand, *the hybrid and frozen models are within* 10% *of the experimental results*. The major difference between the two is the improved capability of the hybrid model to also correctly predict the combustion efficiency and absolute pressure level. As the energy release from the recombination reactions has a non-negligible contribution to the pressure increase, modeling the effect delivers a big improvement compared to the frozen model.

The model is also applied for the simulation of a hydrogen/oxygen case, where a satisfying agreement between the hybrid model results and the experimental data is observed. In this case, the time-scale extended model degenerates to a chemical equilibrium model automatically, because the chemical time-scales of hydrogen combustion are significantly faster, as Section 5.3 demonstrated.

The hybrid model is a promising extension of the steady flamelet model, allowing for a good agreement with experimental heat transfer and pressure profiles. This comes however at *the cost of an additional equation* being solved for the freezing enthalpy and a need for pre-tabulation (or in-situ calculation) of the chemical time-scales. As the additional equation is solved on an embedded mesh for each wall cell, the code implementation requires special attention.

Acta Astronautica 174 (2020) 254–269

Contents lists available at ScienceDirect

Acta Astronautica

journal homepage: www.elsevier.com/locate/actaastro

Wall heat transfer prediction in CH_4/O_2 and H_2/O_2 rocket thrust chambers using a non-adiabatic flamelet model

Nikolaos Perakis*, Oskar J. Haidn

Chair of Space Propulsion, Technical University of Munich, Boltzmannstr. 15, 85748, Garching, DE, Germany

ARTICLE INFO

Keywords:
Rocket engines
Methane combustion
Wall heat transfer
Recombination reactions
Flamelet modelling

ABSTRACT

The current work presents the extension of the flamelet model for turbulent combustion calculations to account for deviations from adiabatic conditions. The aforementioned extension is expected to significantly improve the prediction of the chemical processes occurring in the vicinity of cooled walls in rocket engine applications. A lower enthalpy level leads to an increase of the recombination reactions, which is of particular interest in the case of methane/oxygen combustion. In the present approach, the flamelet equations are solved in mixture fraction space and the energy equation is replaced by a prescription of the enthalpy profile in order to include non-adiabatic effects. To avoid the over-prediction of the recombination reactions, a local "freezing" of the chemical reactions is introduced based on the Damkoehler number close to the cold wall boundary. A pre-tabulation of the chemical time-scales in the flamelet tables enables a fast calculation of the Damkoehler number. The model is verified both for CH_4/O_2 and H_2/O_2 using the simulation of a cooled reacting boundary layer. The extended hybrid model is employed for the simulation of a single-element rocket thrust chamber using CH_2/O_2 and H_2/O_2 and is compared to the non-adiabatic and frozen flamelet models. A more accurate wall heat transfer and pressure level prediction is achieved with the hybrid model for both propellant combinations leading to great agreement with the available experimental measurements.

1. Introduction

Turbulent combustion processes are present in a large number of engineering problems. Of particular interest are the applications, which include flame-wall interaction and convective heat losses. Wall-confined reacting flows subject to heat losses to the wall are always found in gas turbine combustion chambers and rocket engine thrust chambers. In both cases, the interaction of the hot gas and the wall leads to heat loads that must be taken into account in the design process of the engine.

The proper design of the cooling system is especially crucial in the case of rocket engines. The high velocity flows with adiabatic temperature exceeding 3500 K within the thrust chamber can lead to extreme heat flux values of up to 150 MW/m_2 in the nozzle due to the steep temperature gradients [1]. Moreover, the tendency in liquid rocket engines is to use high operating pressures in order to achieve higher specific impulse, compactness of the chamber and a higher nozzle expansion ratio for a given exhaust diameter [2]. Increasing the chamber pressure however, has a direct impact on the wall heat loads, since the heat transfer coefficient is approximately linearly proportional to the chamber pressure: $\dot{q} \sim p^{0.8}$ [3]. An insufficient cooling of the structure would rapidly lead to a mechanical damage of the flight hardware and a mission failure. Therefore, the design of thrust chambers has to meet many conflicting requirements simultaneously such as high performance, reliable cooling, low weight, structural safety and costs.

Measurements of the wall heat loads with experimental methods in the design process of a rocket engine can be done with high-cost firing tests. In order to reduce the development costs of new rocket engines, expensive trial-and-error has to be kept at a minimum. For that reason, numerical methods for the accurate description of the combustion and heat transfer processes are necessary. At the same time however, the computational cost of these methods should not be too high, in order to allow for fast estimations of the performance and the heat loads in the early design process of the components and systems. The simulation of turbulent combustion within rocket engines usually needs the incorporation of detailed chemistry. In engineering applications using RANS, the Finite Rate Model and the Eddy Dissipation Concept are often utilized to account for the chemical reactions between the species. These detailed models however require the solution of $N_{sp} - 1$ additional equations for the N_{sp} species being modeled. Moreover, accounting for the Turbulence Chemistry Interaction (TCI) in those

* Corresponding author.
E-mail addresses: nikolaos.perakis@tum.de (N. Perakis).

https://doi.org/10.1016/j.actaastro.2020.05.008
Received 26 April 2020; Received in revised form 30 April 2020; Accepted 5 May 2020
Available online 12 May 2020

N. Perakis and O.J. Haidn Acta Astronautica 174 (2020) 254–269

Nomenclature

c_p	specific heat capacity [J/(kg·K)]
Da	Damkoehler number [−]
h	specific enthalpy [J/kg]
J	Jacobi matrix [1/s]
k	turbulence kinetic energy [m²/s²]
M	molecular weight [kg/mol]
$\dot{m}$	mass production rate [kg/(m³·s)]
N	upper limit index [−]
P	Probability Density Function PDF [−]
p	pressure [bar]
Pr	Prandtl number [−]
$\dot{Q}$	heat rate [W]
$\dot{q}$	heat flux [W/m²]
R	universal gas constant [J/(kg·K)]
r	grid refinement ratio [−]
Sc	Schmidt number [−]
T	temperature [K]
t	time [s]
u	velocity [m/s]
x, y	spatial coordinates [m]
Y	species mass fractions [−]
Z	mixture fraction [−]
Z''^2	mixture fraction variance [−]
ε	turbulence dissipation rate [m²/s³]
ε	numerical error [−]
ζ	normalized enthalpy [−]
λ	thermal conductivity [W/(m·K)]
μ	viscosity [Pa·s]
ρ	density [kg/m³]
τ	time-scale [s]
φ	generic variable [−]
χ	scalar dissipation rate [−]
ψ	apparent numerical order [−]
$\dot{\omega}$	reaction rate [1/s]

Subscripts

ad	adiabatic
chem	chemical
ex	extinction
ext	exact
flow	flow
fu	fuel
k	species index
min/max	minimum/maximum
n	normalized
ox	oxidizer
sp	species
st	stoichiometric value
tar	target value
t	turbulent value
wall	quantity at the wall

Abbreviations

FRC	Finite Rate Chemistry
FRF	Frozen Flamelet
HYF	Hybrid Flamelet
GCI	Grid Convergence Index
NAF	Non-adiabatic Flamelet
PDF	Probability Density Function
RANS	Reynolds Averaged Navier Stokes
TCI	Turbulence-Chemistry Interaction

models requires a closure using probability density functions (PDFs), which is complex due to the large number of transported variables requiring either multi-dimensional assumed PDFs [4] or very expensive transported PDF methods [5].

For that reason, efforts have been made in order to reduce the complexity of the turbulent combustion simulations by introducing simplified models with a smaller number of equations, which directly accelerates the computation. A common method used for the simulation of H_2/O_2 rocket engines is the assumption of chemical equilibrium and is justified by the high pressure and high temperature combustion environment as well as by the fast time-scales of the hydrogen combustion.

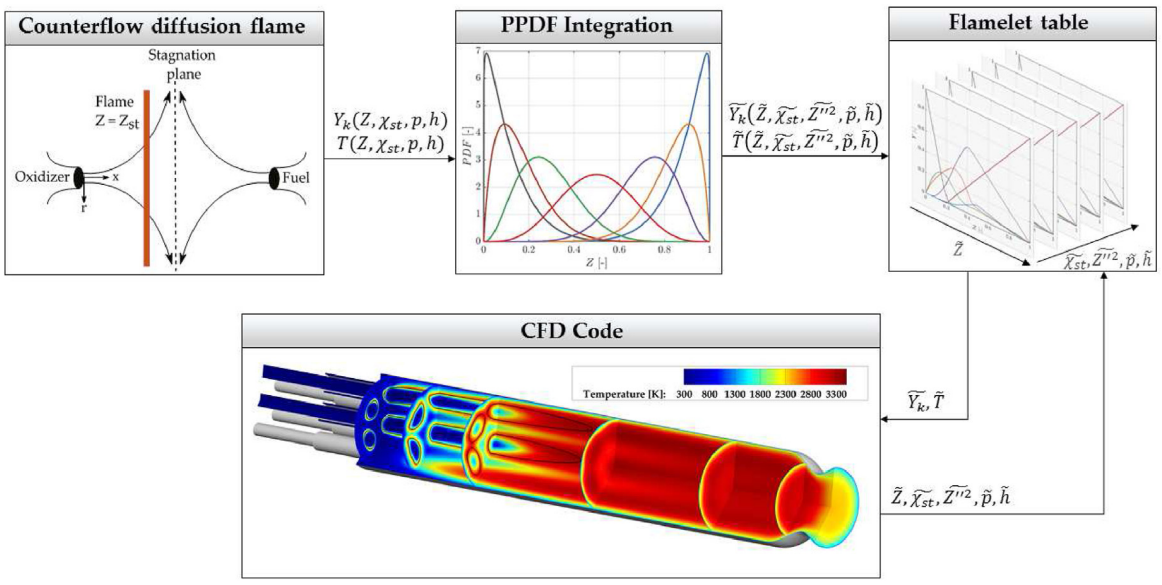

Fig. 1. Schematic illustration of the flamelet table generation and coupling with the computational fluid dynamics (CFD) solver.

In the case of hydrocarbon combustion such as CH_4/O_2 however, the assumption of chemical equilibrium is no longer valid. The increased complexity of the chemical mechanism, combined with the slow time-scales of chemical kinetics give rise to non-equilibrium effects. In order to overcome this insufficiency of the equilibrium model, the flamelet model has been widely used in many rocket engine simulations using CH_4/O_2 as propellants. The classical steady flamelet model [6], is able to capture the departure from the chemical equilibrium, but needs to be extended in order to account for changes in the gas composition in the presence of low-enthalpy regimes, as is the case in cooled rocket engine walls. In the present study, an extension of the flamelet model is undertaken, in order to capture non-adiabatic effects in the presence of wall heat losses.

2. Flamelet combustion model

In many practical engineering applications, including rocket thrust chambers, the equilibrium model has been applied in order to describe the occurring chemical processes. For the description of propellants with complex chemistry and large time-scales however, the flamelet model has been widely implemented, since it is able to capture non-equilibrium effects.

According to the flamelet turbulent combustion model, the turbulent flames are viewed as an ensemble of local flame structures with laminar nature (laminar flamelets), which are affected by the turbulent flow by being stretched and wrinkled. This assumption is valid when the relevant chemical scale is short compared to the convection and diffusion time scales, since under those conditions combustion takes place within the asymptotically thin flamelets, embedded in the turbulent flow [7].

This enables the decoupling of the chemical and turbulent processes and hence a significant reduction in computational time, while still allowing for the use of a detailed chemical reaction mechanism. The calculation of the laminar flamelets is carried out in a pre-processing step, while the presence of turbulent fluctuations is accounted for by a Presumed Probability Density Function (PPDF) [8]. The thermo-chemical data of the turbulent flamelet solutions can then be tabulated as a function of a reduced set of scalars, which results in significant speed-up of the simulation. This concludes the pre-processing step as illustrated in Fig. 1.

2.1. Laminar flamelets

The calculation of the one-dimensional local laminar flame structures (i.e. laminar flamelets) takes place by solving multiple instances of the counterflow diffusion flame problem. The solution of the 1D problem can be done either in the physical or in the mixture-fraction space. In mixture fraction space, the simplified set of the flamelet equations consists of the governing equations for the chemical species and the temperature (or enthalpy) of the one-dimensional flame structure. In this coordinate frame, only the gradients perpendicular to the iso-surface of the mixture fraction are dominant and all gradients on the iso-surface can be neglected [8]. The resulting equations are given as follows under the assumption of unity Lewis number for all chemical species [7].

$$\frac{\partial Y_k}{\partial t} = \frac{1}{2}\chi\frac{\partial^2 Y_k}{\partial Z^2} + \frac{\dot{m}_k}{\rho} \tag{1}$$

$$\frac{\partial T}{\partial t} = \frac{1}{2}\chi\frac{\partial^2 T}{\partial Z^2} - \frac{1}{\rho c_p}\sum_{k=1}^{N_{sp}} h_k\dot{m}_k + \frac{1}{2c_p}\chi\left[\frac{\partial c_p}{\partial Z} + \sum_{k=1}^{N_{sp}} c_{p,k}\frac{\partial Y_k}{\partial Z}\right]\frac{\partial T}{\partial Z} \tag{2}$$

where Y_k, $\dot{m}_k$ and h_k denote the mass fraction, mass production rate and specific enthalpy of species k respectively, while Z, T, ρ, c_p stand for the mixture fraction, temperature, density and constant-pressure specific heat capacity. Several formulations for the temperature equation exist ([7–11]), however the formula from Peters [7] is shown in the present work (Eq. (2)). The scalar dissipation rate χ represents the diffusion time scale and is a measure for the departure of the local flame structure from chemical equilibrium. Values of the scalar dissipation close to $\chi = 0$ 1/s are equivalent to the equilibrium solution, whereas higher values for χ induce a larger departure from equilibrium. This characteristic quantity in the description of non-premixed turbulent combustion is also able to describe the extinction limit of the flame. When it reaches the critical value χ_{ex}, the non-equilibrium effects are so dominant that quenching of the flame occurs. A typical profile for the scalar dissipation rate is given by the parametric distribution in Eq. (3) [8].

$$\chi(Z) = \chi_{st}\exp 2\,[erfc^{-1}(2Z_{st})]^2 - 2\,[erfc^{-1}(2Z)]^2 \tag{3}$$

χ_{st} and Z_{st} represent the scalar dissipation and mixture fraction at stoichiometry and $e\,rfc^{-1}$ the inverse of the complementary error function. The boundary value problem defined by Eqs. (1) and (2) can be solved in steady state conditions ($\partial Y_k/\partial t = \partial T/\partial t = 0$)for different values of χ_{st}, resulting in a tabulation of the resulting temperature and species mass fractions for the laminar flamelets: T, $Y_k = f(Z, \chi_{st})$. The assumption of steady-state involved in the steady flamelet model and the use of the stable burning branch does not allow for extinction and re-ignition of the flame, however this does not pose any restrictions for the test cases presented in the present work.

2.2. PDF integration

After the solution of the counterflow diffusion flame using the flamelet equations, a laminar table of the form T, $Y_k = f(Z, \chi_{st})$is obtained, while further quantities such as density, transport properties etc. can be also tabulated since they are simply a function of the gas composition Y_k and the thermodynamic state (h, p).

In order to include the effect of the Turbulence Chemistry Interaction (TCI) on the flamelets, a PPDF integration takes place using the joint PDF $P(Z, \chi_{st})$. In the present study the Favre averaged values for temperature, species mass fractions and heat capacity are calculated according to Eq. (4).

$$\tilde{\varphi} = \int_0^\infty \int_0^1 \varphi(Z, \chi_{st})\cdot P(Z, \chi_{st})\cdot dZd\chi_{st} \tag{4}$$

whereas for the transport properties (viscosity and thermal conductivity) a Reynolds averaging is used as described in Kim et al. [12].

$$\bar{\varphi} = \bar{\rho}\int_0^\infty \int_0^1 \frac{\varphi(Z, \chi_{st})}{\rho(Z, \chi_{st})}\cdot P(Z, \chi_{st})\cdot dZd\chi_{st} \tag{5}$$

$$\bar{\rho} = \frac{1}{\int_0^\infty \int_0^1 \frac{1}{\rho(Z,\chi_{st})}\cdot P(Z, \chi_{st})\cdot dZd\chi_{st}} \tag{6}$$

The assumption of statistical independence can be used to decouple the multidimensional PPDF yielding $P(Z, \chi_{st}) = P(Z)\cdot P(\chi_{st})$. For $P(Z)$, a β-PDF is usually used, the shape of which is determined by the values of $\tilde{Z}$ and its variance $\tilde{Z}''^2$. For $P(\chi_{st})$, a Dirac delta function or a log-normal distribution are implemented [8]. The flamelet calculations (laminar flamelet generation and PDF integration) are usually carried out for several values of pressure, leading to a tabulation of the gas properties as in Eq. (7).

$$\tilde{\varphi} = f(\tilde{Z}, \widetilde{Z''^2}, \tilde{\chi}_{st}, \tilde{p}) \tag{7}$$

2.3. Frozen flamelet

The flamelet equations as well as the governing equations of the counterflow diffusion flame are adiabatic. This means that the resulting profiles for species mass fractions and temperature correspond to a specific adiabatic enthalpy profile. Under the assumption of unity Lewis number this enthalpy profile is described as

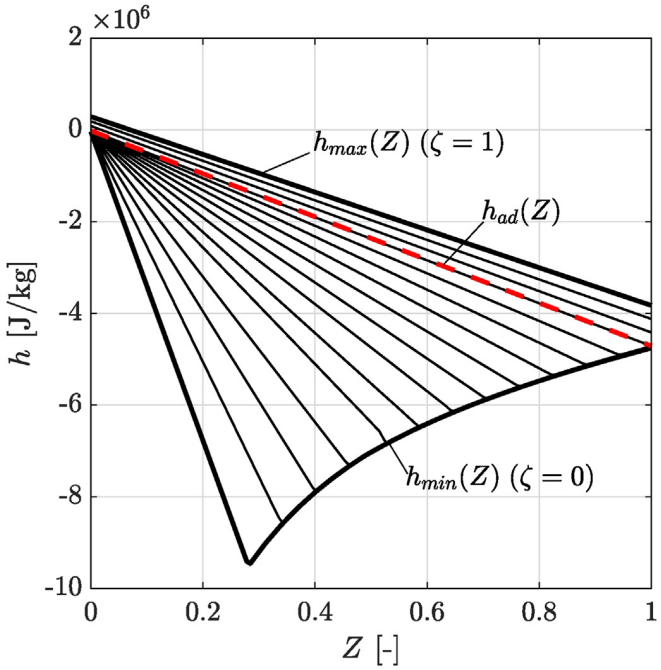

Fig. 2. Enthalpy profiles in mixture fraction space.

$$h_{ad}(Z) = h_{ox} + Z(h_{fu} - h_{ox}) \tag{8}$$

and therefore corresponds to a linear function between the boundary values of fuel and oxidizer. In most engineering applications the flow exchanges heat with its surrounding, and hence not all points of the flow are in adiabatic conditions.

In order to account for the different enthalpy, the usual extension of the adiabatic flamelet model is the concept of frozen flamelet. According to this concept, the species concentrations are assumed to be constant for all enthalpy levels and equal to the concentration at adiabatic conditions. This assumes that the change in enthalpy does not affect the reaction paths in the chemical mechanism and does not change the composition of the gas. The only effect of the non-adiabatic enthalpy level is to change the temperature, the transport and thermodynamic properties of the gas, to render the calculation thermodynamically consistent. Physically it can be interpreted as a cooling down of burned products while ignoring any recombination effects that may take place.

In the presence of cooled walls, which is the case in most rocket engine thrust chamber simulations, this method fails to predict the increase in recombination reactions which occur due to the lower enthalpy environment. The accurate description of the heat flux in the wall requires taking this effect into account and therefore an extension of the flamelet model to non-adiabatic calculations was developed.

3. Non-adiabatic extension of the flamelet model

Several approaches for the extension of the flamelet model to account for non-adiabatic effects have been proposed in the past. Libby et al. [13] used the method of activation energy asymptotics to describe the behavior and characteristics of non-adiabatic flamelets involving counterflowing reactants and products. Lee et al. [14] modeled the wall heat losses by including a source term in the unsteady flamelet equations, thereby introducing a convective heat loss process by means of a Nusselt-number correlation, whereas Fiorina et al. [15] and Cecere et al. [16] used a conductive heat loss approach in burner-stabilized flames. Marracino et al. [17] focused on the effect of radiative losses on the flamelet profiles by adjusting the boundaries of oxidizer and fuel, whereas Orich et al. [18] and Kishimoto et al. [19] reduced the chemical heat source term in the energy equation of the counterflow diffusion flame by a constant factor. Chan et al. [20] employed a radiative source in the flamelet energy equation, while Ma et al. [21] on the other hand applied a modified thermal boundary condition to the counterflow flame in the composition space in the form of a permeable wall. Rahn et al. [22] and Perakis et al. [23] introduced a source term in the energy equation of the counterflow diffusion flame and an iterative approach to obtain the wanted enthalpy levels.

3.1. Enthalpy profiles

To include the effects of sensible enthalpy decrease due to cooled walls and due to expansion in the nozzle, the enthalpy values should be first defined, for which the flamelet table is introduced. For this reason the normalized enthalpy variable ζ can be defined as in the work of Bilger [24]:

$$\zeta = \frac{h - h_{min}(Z)}{h_{max}(z) - h_{min}(Z)} \tag{9}$$

The $h_{max}$and h_{min} profiles ought to be chosen in order to contain all the energy loss or gain within the domain of interest. In the frame of this work, the enthalpy profiles coming from a 1D counterflow diffusion flame with a permeable wall (similar to the work of Ma et al. [21]) are used for the enthalpy deficit levels. The sensitivity of the chosen enthalpy profiles has been examined in the work of Breda et al. [25]. To ensure that all the points in the domain are within the limits of the tabulated enthalpy [22], enthalpy levels above the adiabatic profiles are also included. An example for CH_4/O_2 enthalpy profiles between the h_{max} ($\zeta = 1$) and h_{min} ($\zeta = 0$) lines as well as an adiabatic profile corresponding to $T_{fu} = 270$K and $T_{ox} = 275$ K are shown in Fig. 2.

The non-adiabatic extension of the flamelet model aims at obtaining profiles for mass fractions, temperature and the resulting thermochemical properties of the gas corresponding to enthalpy profiles with heat loss (and heat gain) like the ones in Fig. 2. The tabulation is then a function of the enthalpy as shown in Eq. (10).

$$\tilde{\varphi} = f(\tilde{Z}, \widetilde{Z''^2}, \tilde{\chi}_{st}, \tilde{p}, \tilde{h}) \tag{10}$$

The tabulation as a function of the pressure is justified when the length scale of pressure variations in the combustor is much larger than the flamelet length scale, an assumption which holds when for rocket engines operating in steady state in the absence of combustion instabilities [26].

3.2. Flamelet generation using enthalpy constraint

In the present work, the non-adiabatic extension of the flamelet model is implemented using the prescription of an enthalpy profile as algebraic constraint [12,23]. The idea is based on replacing the energy flamelet equation (Eq. (2)) by imposing an enthalpy profile as an equality constraint in the mixture space frame. By omitting the energy equation, the flamelet calculation is reduced to a boundary value problem consisting of the mass fraction equation (1) and an optimality constraint:

$$h(Z) = h_{tar}(Z) \tag{11}$$

Defining the linear profile of Eq. (8) as the desired enthalpy profile, the set of Eqs. (1) and (11) becomes equivalent to the system of Eqs. (1) and (2). Applying any other profile below (or above) the adiabatic enthalpy, corresponds to a heat loss (or gain) and the equations can be solved without loss of generality.

For the solution of the resulting boundary value problem, a new methodology was implemented based on an operator splitting technique by Strang [27] and Yanenko [28]. The boundary value problem in Eq. (1) consists of a transport term (diffusion term with diffusion constant $\chi/2$) and a non-linear kinetics term. By employing the

operator splitting, the non-linear algebraic equations resulting from the discretization of Eq. (1) are broken into two smaller systems:

- A kinetics equation at each cell in the Z-space, decoupled from other cells (initial value problem)
- A diffusion equation for each chemical species, decoupled from the mass fractions of the other species (parabolic problem)

The solution of the two problems is alternated repeatedly making it possible to match the accuracy of the fully coupled problem. The open-source toolbox Cantera [29] was employed for the chemical calculations and a detailed view of the algorithm is given in Ref. [23].

3.3. Comparison of frozen and non-adiabatic tables

Including non-adiabatic effects in the flamelet table generation enables capturing the effect of reactions occurring at low enthalpy levels. Such reactions are taking place along the cooled walls of rocket combustion chambers and tend to increase the observed heat flux. Specifically, the reduced enthalpy environment suppresses dissociation processes since not enough energy is present to break the chemical bonds. This translates to an increase of recombination processes and a consequent increase in the energy release. This energy release is a result of the lower building enthalpy of the stable products of the recombination reactions. A dominant reaction in the case of hydrocarbon combustion and specifically CH_4/O_2 engines is the recombination of CO to CO_2.

In order to understand the effect of the non-adiabatic flamelet formulation, the results of a frozen chemistry table are compared to the ones from the solution of the enthalpy-dependent flamelets. The load point chosen corresponds to 20 bar CH_4/O_2 combustion and a scalar dissipation rate of 1 s_{-1}. The sub-adiabatic enthalpy levels from Fig. 2 were chosen and for both cases, the chemical mechanism by Slavinskaya et al. [30] was employed.

The temperature results shown in Fig. 3 illustrate the main differences between the two approaches. In the frozen case, an enthalpy reduction has a higher temperature decrement as a consequence. This occurs due to the lower specific heat capacity of the radicals compared to the stable molecules such as CO_2 as well as their enthalpy of formation. In the case of the non-adiabatic model however the heat released from the recombination reactions leads to a smaller temperature decrease in the lower enthalpy levels.

When frozen chemistry is assumed, the lowest enthalpy levels can lead to unphysical temperatures even below 0 K. This is due to the absence of recombination heat release. The species present in the frozen composition cannot exist in such a low enthalpy environment and to avoid that, a temperature cutoff at 100 K was set in the calculation. This explains the flat line at the lowest energy level in the frozen case.

The differences between the two approaches are mainly present close to stoichiometry, whereas for fuel-richer regions the discrepancies are reduced. Since in most practical CH_4/O_2 rocket engine applications the mixture is fuel rich and since in typical co-axial injector configurations the fuel is injected on an outer annulus, the gas composition at the wall is dominantly fuel-rich. The small differences in this region explain why the conventional frozen flamelet model is able to predict reasonable values for the wall heat fluxes when applied in CFD [31].

The results of the species concentrations for different enthalpy levels are shown in Fig. 4. As expected the effect of a lower energy environment is to decrease the composition of CO and increase the CO_2 concentration. The energy release taking place in the recombination is responsible for the temperature difference in Fig. 3.

3.4. Time-scale extension

With the use of the non-adiabatic extension, the prediction of recombination reactions in low-enthalpy environments is possible. In the steady flamelet model however, the deviation from chemical equilibrium is described by the scalar dissipation rate, which is defined as $\chi = 2{\cdot}D(\nabla Z)^2$ in the CFD calculations, with D being the diffusivity. In the vicinity of the walls, as the gradient of the mixture fraction goes towards zero, the scalar dissipation becomes negligible and therefore the mixture will approach the chemical equilibrium solution. This effect leads to a considerable increase in the wall heat loads, as the state of the gas is not necessarily in chemical equilibrium at the wall, especially for low temperatures and slow chemical time-scales. The consequence is that the steady non-adiabatic flamelet model leads to an overprediction of the degree of the recombination in the boundary layer and hence an overestimation of the wall heat loads [22,32].

In order to incorporate the effect of the local chemical time-scale onto the calculation of the mixture composition, a model extension is proposed, which relies on the local Damkoehler number Da defined as the ratio of the flow time-scale τ_f and the chemical time-scale τ_c.

$$Da = \frac{\tau_f}{\tau_c} \tag{12}$$

As the characteristic flow-time scale relevant for the freezing of the

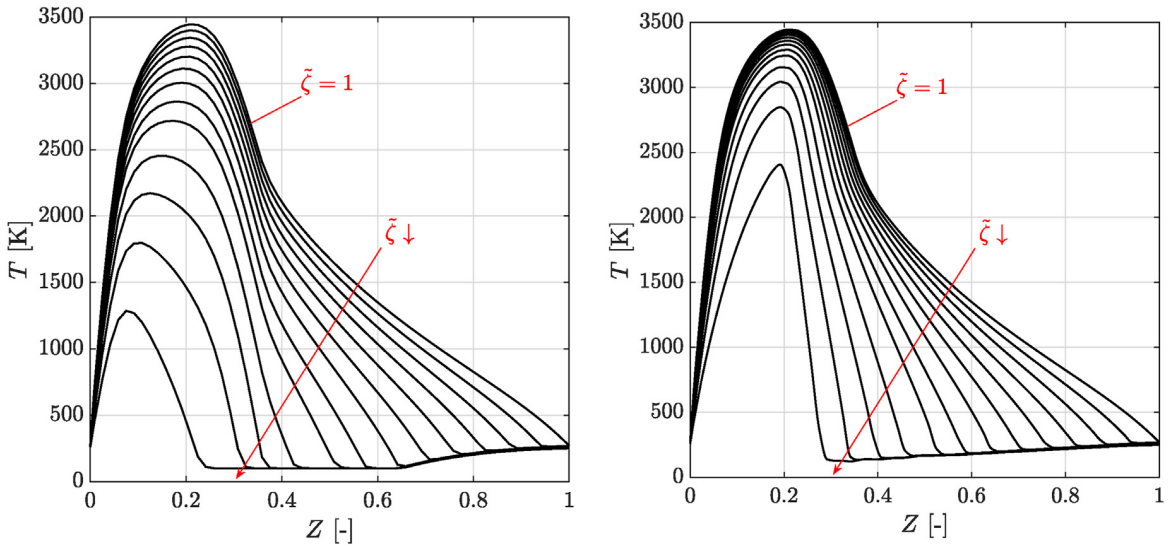

Fig. 3. Temperature profiles for different enthalpy levels in the case of the frozen (left) and non-adiabatic (right) flamelet models.

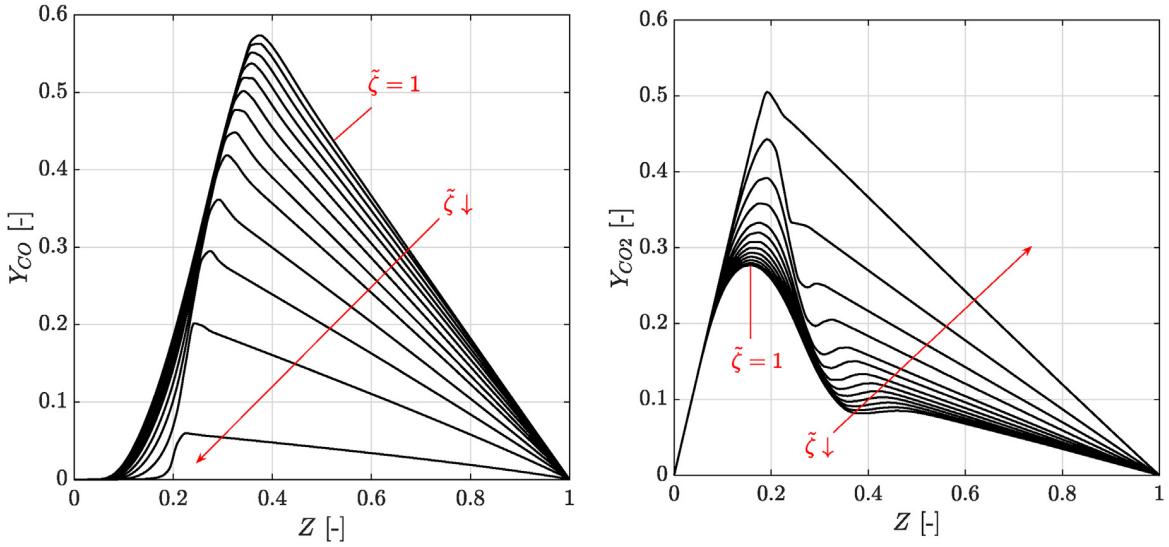

Fig. 4. CO (left) and CO_2 profiles for different enthalpy levels in the non-adiabatic flamelet table.

reactions is the heat transfer through the wall, the definition of τ_f is based on a heat diffusion time-scale equal to $\tau_K \sqrt{Pr}$. In this context $Pr$is the local Prandtl number and $\tau_K$the Kolmogorov scale, as described in Batchelor et al. [33]. For fast chemical time-scales, i.e. large Da, the flow adapts fast to external disturbances and is close to chemical equilibrium conditions [34]. Slower time-scales give rise to low Da and can lead to a frozen chemical composition, where no additional reactions take place. It is expected that for CH_4/O_2 reacting flows close to cooled walls, a freezing of the reactions could occur at the wall. This implies that within the boundary layer the composition will be changing as the distance from the wall decreases, i.e. as the enthalpy is decreasing. When the enthalpy reaches a point where no additional recombinations can occur due to the low temperature, the gas composition remains nearly constant up until the wall. The enthalpy corresponding to the freezing of the reactions is named h_f in the present work.

In the proposed model, the local composition of the gas is frozen when it reaches the freezing enthalpy $h_f$and is simply cooled down to the real enthalpy level h. This means that the species mass fractions Y_i are obtained as a function of the frozen enthalpy

$$\widetilde{Y_i} = f(\tilde{Z}, \widetilde{Z''^2}, \tilde{\chi}_{st}, \tilde{p}, \tilde{h}_f) \tag{13}$$

and the remaining thermochemical quantities (temperature, density, transport properties, heat capacity) are obtained by cooling this composition down to the local enthalpy level

$$\tilde{\varphi} = f(\widetilde{Y_i}, \tilde{p}, \tilde{h}) \tag{14}$$

In order to calculate the freezing enthalpy value as a function of the local enthalpy and the Damkoehler number, following differential equation is solved in an embedded grid along the normal to the wall $\vec{n}$:

$$\frac{\partial h_f}{\partial \vec{n}} = f \cdot \frac{\partial h}{\partial \vec{n}} \tag{15}$$

with the function f describing the effect of the local chemical and flow time-scales on the freezing enthalpy level

$$f = \frac{1 + tanh(\log_{10}(Da))}{2} \tag{16}$$

The equation is solved in the embedded grid with the boundary condition $h = h_f$ at the boundary located away from the wall. For very fast chemical time-scales we obtain $Da >> 1$, leading to $f = 1$. In that case, the frozen enthalpy and the real enthalpy coincide, meaning that no freezing of the reactions occurs. For small values $Da \ll 1$however, the discrepancy between h_f and h increases and the model converges to the frozen flamelet solution.

Several methods for the estimation of the chemical time-scale of a reacting system have been proposed and a useful summary can be found in Prüfert et al. [34] and Fox et al. [35]. In the present study the calculation of the "System Progress Timescale" is undertaken as proposed by Caudal et al. [36] and Prüfert et al. [34]. This is derived from the temporal evolution of the gas composition and temperature in a reacting chemical system, which is given by the ordinary differential equation

$$\frac{\mathrm{d}}{\mathrm{d}t}\begin{bmatrix} Y \\ T \end{bmatrix}(t) = \dot{\omega}(Y, T) = \dot{\omega}\left(Y_1, ..., Y_{N_{sp}}, T\right) \tag{17}$$

with the derivative $\dot{\omega}$ representing the reaction rate. Using a Taylor expansion around the values Y^0, T^0, the temporal evolution of the species reads

$$\frac{\mathrm{d}}{\mathrm{d}t}(Y - Y^0)(t) = J \cdot (Y - Y^0) + \mathcal{O}((Y - Y^0)^2) \tag{18}$$

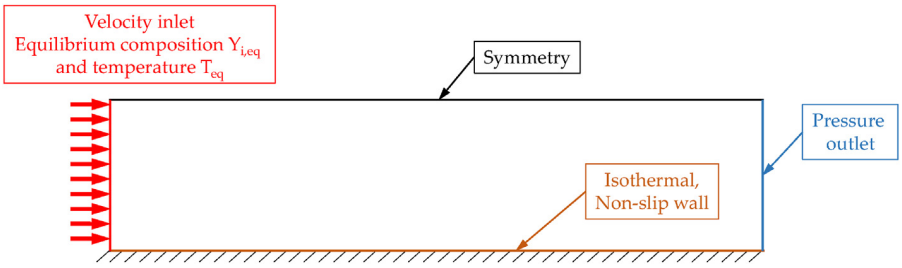

Fig. 5. Schematic illustration of the computational domain for the flat plate simulation.

The Jacobian matrix J is defined with $J := (J_{ik})_{i,k=1,\dots,N_{sp}} = \frac{\partial \dot{\omega}_i}{\partial Y_k}(Y^0)$ and the chemical time-scale τ_c can then be calculated as in Ref. [34] according to Eq. (19).

$$\tau_c = \frac{\|\dot{\omega}\|}{\|J \cdot \dot{\omega}\|} \tag{19}$$

The calculation of the chemical time-scale can be performed in situ during the CFD calculation or even tabulated along with the other thermochemical variables of the flamelet model during the pre-processing step.

4. Model Verification

In order to examine the ability of the proposed model to capture recombination effects, a simplified 2D test case of a flat plate is defined. The operating conditions defined for the plate simulation are chosen so as to resemble the flow within rocket combustion chambers. A schematic of the computational domain is shown in Fig. 5. Hot products at adiabatic equilibrium conditions are injected uniformly at the inlet. The temperature of the isothermal plate wall is prescribed at 500 K, while the exit plane is defined as a pressure outlet. The dimensions are chosen with sufficient length to allow for the development of the thermal and species boundary layer. A length of 300 mm and height of 20 mm were used. The flat plate targets the investigation of thermal boundary layer characteristics under rocket thrust chamber operating conditions. As the mixture is injected in pre-burnt conditions, it is possible to isolate the effect of reactions in the vicinity of the wall from other phenomena taking place in the chamber such as mixing and combustion.

For the verification of the model, simulations for several operating points were carried out, for different propellant combinations, mixture ratios, pressure levels and inlet Mach numbers. The variations in those conditions targeted at covering a wide range of possible operating regimes typically found in sub-scale and full-scale rocket thrust chambers. Both CH_4/O_2 and H_2/O_2 mixtures have been examined, with mixture ratios varying from 2.2 to 4.0 for methane and from 4.4 to 8.0 for hydrogen. The pressure range examined was 10–50 bar and Mach numbers between 0.1 and 0.5 were investigated, corresponding to typical contraction ratios found in flight hardware [1].

4.1. Computational setup

A mesh consisting of $50{\cdot}10^3$ finite volumes is used for the simulations, refined in the wall normal direction to ensure that the condition $y^+ < 1$ is satisfied at the wall.

The flowfield in the domain is described by the conservation equations for mass, momentum and energy:

$$\frac{\partial \bar{\rho}}{\partial t} + \frac{\partial (\bar{\rho}\tilde{u}_i)}{\partial x_i} = 0, \tag{20a}$$

$$\frac{\partial (\bar{\rho}\tilde{u}_i)}{\partial t} + \frac{\partial (\bar{\rho}\tilde{u}_i\tilde{u}_j)}{\partial x_j} = -\frac{\partial \bar{p}}{\partial x_i} + \frac{\partial}{\partial x_i}\left(\bar{\tau}_{ij} - \bar{\rho}\widetilde{u_i'' u_j''}\right), \tag{20b}$$

$$\frac{\partial (\bar{\rho}\tilde{h})}{\partial t} + \frac{\partial (\bar{\rho}\tilde{h}\tilde{u}_i)}{\partial x_i} = \frac{\partial}{\partial x_i}\left(\frac{\bar{\lambda}}{\bar{c}_p}\frac{\partial \tilde{h}}{\partial x_i} - \bar{\rho}\widetilde{u_i'' h''}\right), \tag{20c}$$

where $\bar{\rho}$ and $\bar{p}$ are the Reynolds-averaged density and pressure respectively and $\tilde{u}_i$ are the Favre-averaged velocity components in the spatial directions x_i. The viscous stress tensor is $\bar{\tau}$. The specific enthalpy is $\tilde{h}$, $\bar{c}_p$ and $\bar{\lambda}$ are the specific heat and the thermal conductivity of the fluid. NASA polynomials are implemented for the enthalpy and heat capacity of the individual species and a mass-weighting averaging is employed for the mixture values.

A pressure based scheme is used for the solution of the discretized equations with the SIMPLE scheme. Density and pressure are coupled through the ideal gas equation of state:

$$\bar{\rho} = \frac{\bar{p} M}{R\tilde{T}}, \tag{21}$$

where R is the universal gas constant, and $\tilde{T}$ and M are the fluid mixture temperature and molecular weight respectively.

The turbulent momentum flux is modeled employing the Boussinesq hypothesis, relating the Reynolds stresses to the mean velocity gradients:

$$\bar{\rho}\widetilde{u_i'' u_j''} = -\mu_t\left(\frac{\partial \tilde{u}_i}{\partial x_j} + \frac{\partial \tilde{u}_j}{\partial x_i} - \frac{2}{3}\delta_{ij}\frac{\partial \tilde{u}_k}{\partial x_k}\right) + \frac{2}{3}\bar{\rho}\tilde{k}, \tag{22}$$

where μ_t is the turbulent viscosity and k the turbulent kinetic energy. δ_{ij} is the Kronecker delta.

Turbulent closure is achieved by employing the standard k-ε model proposed by Launder and Spalding [37] and using a two-layer approach [38] for the wall. The model allows for the determination of the turbulent length and time scales by solving two additional transport equations for turbulent kinetic energy $\tilde{k}$ and its dissipation $\tilde{\varepsilon}$:

$$\frac{\partial (\bar{\rho}\tilde{k})}{\partial t} + \frac{\partial (\bar{\rho}\tilde{k}\tilde{u}_i)}{\partial x_i} = \frac{\partial}{\partial x_i}\left[\left(\mu + \frac{\mu_t}{\sigma_k}\right)\frac{\partial \tilde{k}}{\partial x_i}\right] + P_k - \bar{\rho}\tilde{\varepsilon} \tag{23}$$

$$\frac{\partial (\bar{\rho}\tilde{\varepsilon})}{\partial t} + \frac{\partial (\bar{\rho}\tilde{u}_i\tilde{\varepsilon})}{\partial x_i} = \frac{\partial}{\partial x_i}\left[\left(\mu + \frac{\mu_t}{\sigma_\varepsilon}\right)\frac{\partial \tilde{\varepsilon}}{\partial x_i}\right] + C_{\varepsilon 1}\frac{\tilde{\varepsilon}}{\tilde{k}}P_k - C_{\varepsilon 1}\bar{\rho}\frac{\tilde{\varepsilon}^2}{\tilde{k}} \tag{24}$$

The turbulent viscosity is then found by the relation $\mu_t = \bar{\rho} C_\mu \frac{\tilde{k}^2}{\tilde{\varepsilon}}$ and all modeling constants are set to the proposed standard values.

The closure of the turbulent heat flux in Eq. (20c) is achieved using the turbulent Prandtl number:

$$\bar{\rho}\widetilde{u_i'' h''} = -\frac{\lambda_t}{\bar{c}_p}\frac{\partial \tilde{h}}{\partial x_i} = -\frac{\mu_t}{Pr_t}\frac{\partial \tilde{h}}{\partial x_i} \tag{25}$$

A constant turbulent Prandtl number equal to 0.9 is chosen throughout the domain. For the molecular transport (viscosity and thermal conductivity) the Chapman-Enskog kinetic theory [39] is utilized for the individual species, combined with the Wilke mixture rule [40], leading to species- and temperature-dependent properties.

For the finite rate calculations, a transport equation for each species mass fraction Y_k is solved, according to:

$$\frac{\partial (\bar{\rho}\tilde{Y}_k)}{\partial t} + \frac{\partial (\bar{\rho}\tilde{u}_i\tilde{Y}_k)}{\partial x_i} = \frac{\partial}{\partial x_i}\left(\left(\rho D_{k,m} + \frac{\mu_t}{Sc_t}\right)\frac{\partial \tilde{Y}_k}{\partial x_i}\right) + M_k\dot{\omega}_k \tag{26}$$

For the calculation of the reaction rates $\dot{\omega}_k$, the chemical mechanism by Slavinskaya et al. [30] is employed in all methane simulations and the chemical mechanism by Ó Conaire et al. [41] for all hydrogen simulations, whereas the diffusivity of each species $D_{k,m}$is calculated according to the kinetic theory [39].

When utilizing the flamelet model, instead of solving $N_{sp} - 1$ transport equations for the N_{sp} chemical species, only one equation for the mixture fraction has to be solved:

$$\frac{\partial (\bar{\rho}\tilde{Z})}{\partial t} + \frac{\partial (\bar{\rho}\tilde{u}_i\tilde{Z})}{\partial x_i} = \frac{\partial}{\partial x_i}\left(\frac{\mu + \mu_t}{Sc_t}\frac{\partial \tilde{Z}}{\partial x_i}\right) \tag{27}$$

where Sc_t is the turbulent Schmidt number which is set to a constant value of $Sc_t = 0.6$ throughout the domain.

Non-equilibrium effects in the flamelet model are included through tabulation dependent on the scalar dissipation:

$$\tilde{\chi} = \frac{C_\chi \tilde{\varepsilon}\widetilde{Z''^2}}{\tilde{k}} \tag{28}$$

where C_χ is a constant with value of 2.0. An additional transport equation is solved for the evaluation of the mixture fraction variance field:

$$\frac{\partial(\bar{\rho}\widetilde{Z''^2})}{\partial t} + \frac{\partial(\bar{\rho}\tilde{u}_i\widetilde{Z''^2})}{\partial x_i} = \frac{\partial}{\partial x_i}\left(\frac{\mu+\mu_t}{Sc_t}\frac{\partial\widetilde{Z''^2}}{\partial x_i}\right) + C_g\mu_t\frac{\partial\tilde{Z}}{\partial x_i}\frac{\partial\tilde{Z}}{\partial x_i} - C_d\bar{\rho}\frac{\tilde{\varepsilon}}{\tilde{k}}\widetilde{Z''^2} \quad (29)$$

where C_g and C_d are constants with values of 2.86 and 2.0 respectively.

For all simulations the commercial code ANSYS Fluent (Version 18.0) was utilized, where the non-adiabatic and the extended non-adiabatic flamelet model were implemented by means of user defined functions.

4.2. Verification results

The results for two representative operating points are shown in the present section. Those correspond to a pressure level of 20 bar and inlet Mach number of 0.2. The mixture fraction for the methane case is chosen at 2.6 and for the hydrogen case at 5.5. For each case, the results form the finite rate simulation (FRC), the frozen flamelet (FRF), the non-adiabatic flamelet model (NAF) and the time-scale extended hybrid model (HYF) are presented. As the FRF model does not account for changes in species composition and since the injection at the inlet occurs at pre-mixed and pre-burnt conditions, the mass fractions remain constant along the wall normal.

Given the absence of exact solutions for the reacting boundary layer over a cooled wall with complex hydrocarbon chemistry the performance of the three flamelet models is assessed based on their ability to reproduce the finite rate results. Since in the finite rate case, the reaction time-scales are resolved and the model has been successfully applied in the past for heat flux estimations in cooled H_2/O_2 and CH_4/O_2 engines [42,43] it is considered to be the baseline reference.

Fig. 6 shows the species and temperature profiles for the flat plate simulations. For the H_2/O_2 simulation, the mass fractions of the major products responsible for the heat release in the boundary layer are plotted, namely H_2O and OH. The temperature profile from the finite rate results is also shown for reference. As the temperature decreases, the OH radical starts recombining forming additional H_2O. The available OH is consumed fast and its mass fraction drops to zero at $y^+ \approx 20$. For positions closer to the wall, both the H_2O and OH concentrations remain constant indicating the ceasing of recombination reactions.

It can be observed that both the non-adiabatic flamelet and the hybrid flamelet model appear to match the finite rate profiles with great accuracy. This is expected as the fast hydrogen chemistry leads to the flow being in chemical equilibrium even at the low temperatures found in the cooled boundary layer. This is confirmed by the Damkoehler number profile shown in the left sub-figure of Fig. 7. As expected, the Damkoehler number qualitatively follows the temperature distribution, having large values further away from the wall, indicating fast reaction rates. As the gas is approaching the wall, the Damkoehler number is reduced but still remains larger than 1 for most of the radial positions. Therefore it is also expected that the deviation between the enthalpy h and the frozen enthalpy h_f is negligible as demonstrated in the same figure.

The corresponding CH_4/O_2 results on the other hand are showing a larger discrepancy between the sub-models. The CO/CO_2 equilibrium is defining the bulk energy release within the reacting boundary layer [23] and therefore the mass fractions of those two species are plotted along the wall normal. As the temperature is reduced closer to the wall, CO is converted into CO_2, which is predicted by all three models (FRC, NAF, HYF). For radial positions larger than $y^+ \approx 40$ the three models seem to produce identical results. The non-adiabatic model however appears to over-predict the degree of conversion of CO compared to the finite rate model closer to the wall. Whereas FRC predicts that a ceasing of reactions takes place at T≈1500 K ($y^+ \approx 30$), the concentration of CO_2 keeps increasing for the NAF, even at temperatures below 800 K. This is largely attributed to the fact that for pre-burnt configurations the scalar dissipation rate is 0, meaning that the non-adiabatic flamelet degenerates to the equilibrium model. Slow processes like the conversion of CO to CO_2 are hence over-predicted.

The HYF model on the other hand closely follows the FRC and also predicts a steep reduction of the recombination reactions for $y^+ < 30$. This is explained by the Damkoehler number profile shown in Fig. 7. Similar to the H_2/O_2 case, the Damkoehler number reduces with increasing proximity to the wall, but the absolute level is lower reflecting the slower chemical time-scales [44]. The fact that the Damkoehler number reaches values as low as 10^{-3} implies that there is a large deviation between the enthalpy and the frozen enthalpy. This growing difference becomes significant for positions with $y^+ < 30$, coinciding with the freezing of the reactions in Fig. 6.

It is hence evident that the proposed extension for the non-adiabatic flamelet model is able to capture both the initiation of the recombination reactions within the thermal boundary layer as well as the ceasing of the aforementioned reactions in areas with very low enthalpy. Considering the verification of the model based on the presented flat plate simulation, a more complex rocket combustor test-case with available experimental data is chosen to evaluate the performance of the proposed model.

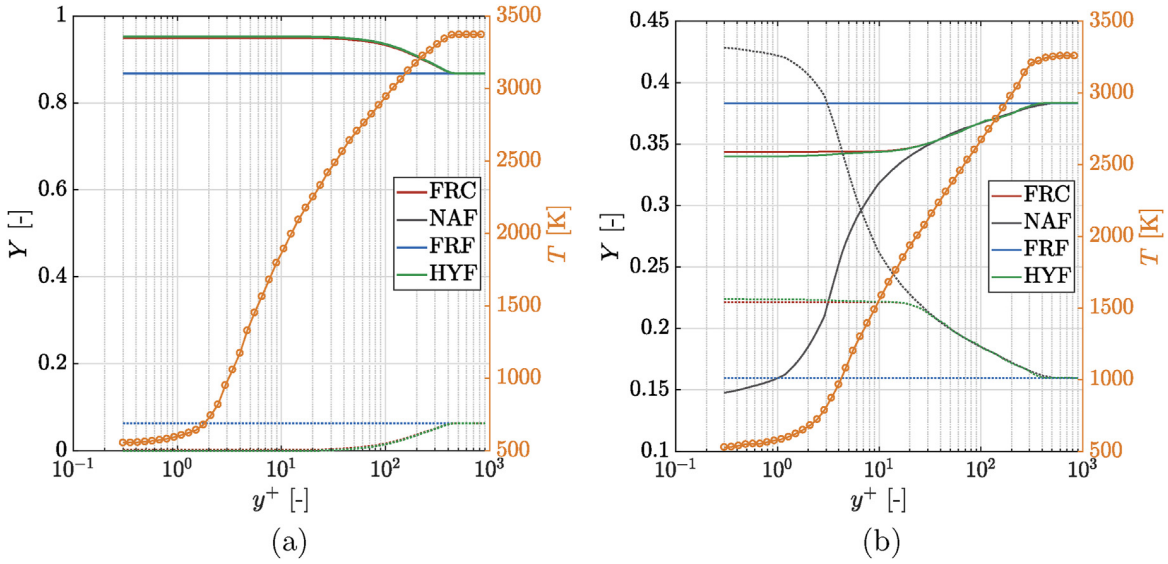

Fig. 6. Species profiles along wall normal at $Re_x = 75{\cdot}10^5$ for the H_2/O_2 (a) and the CH_4/O_2 (b) flat plate simulation.

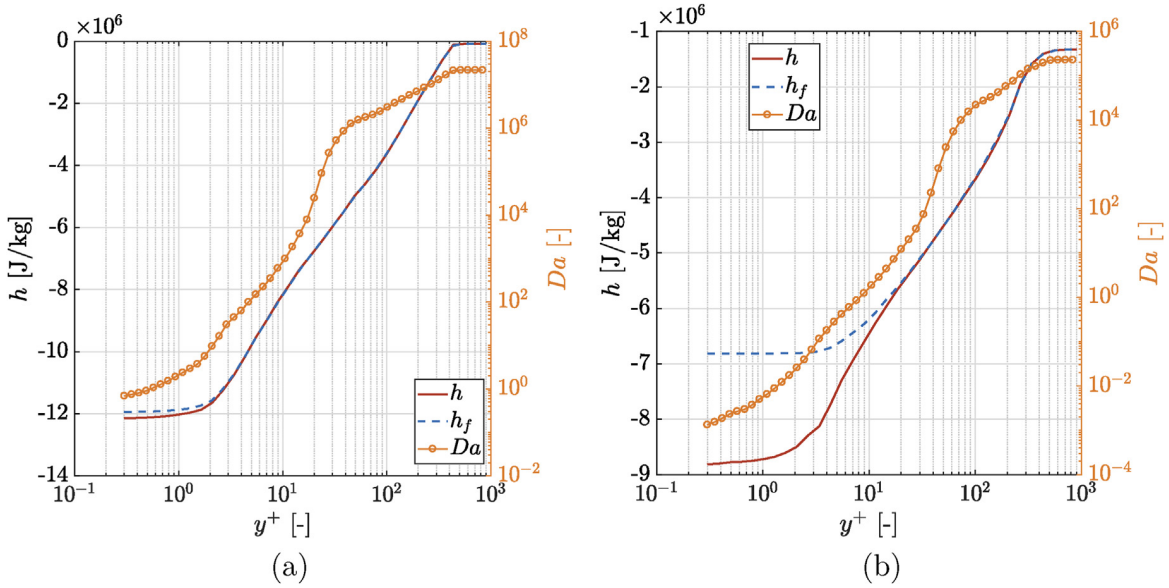

Fig. 7. Enthalpy and Damkoehler number profiles along wall normal at $Re_x = 75{\cdot}10^5$ for the H_2/O_2 (a) and the CH_4/O_2 (b) flat plate simulation.

5. Simulation of a single element rocket combustor

To assess the effects of the wall heat transfer on the flow-field structure and the performance of the extended non-adiabatic flamelet combustion model, RANS calculations of a single-element rocket combustor are carried out.

5.1. Experimental configuration

The single-element rocket combustor experimentally investigated by Silvestri et al. [45] is used for this analysis. The experimental configuration is illustrated in Fig. 8 and consists of the main rocket chamber having a diameter of 12 mm and the convergent-divergent nozzle with an contraction ratio of 2.5. Two propellant feed lines supply gaseous fuel and oxidizer to the coaxial injector. The facility has the capability of operating with both methane and hydrogen as fuel at ambient temperature. The central injector nozzle has a diameter of 4 mm whereas the fuel is supplied by an annulus surrounding the inner oxidizer stream, with inner and outer diameters of 5 and 6 mm respectively. The post separating the fuel and oxidizer stream is not recessed with respect to the injector face-plate. An operating point corresponding to a nominal chamber pressure of 20 bar has been chosen with an oxidizer to fuel ratio equal to 2.22 for the methane case. In order to demonstrate the capabilities of the non-adiabatic model to properly capture the combustion dynamics of not only $CH2/O_2$ but also H_2/O_2, the results for a load point at 20 bar with O/F = 5.85 using hydrogen as fuel is also shown. The inlet conditions for both operating points are given in Table 1.

5.2. Computational setup

The equations used for the simulation of the flowfield in the combustion chamber are already described in Section 4.1. In order to take advantage of the symmetry in the RANS simulation, a 2D axisymmetric domain is chosen consisting of the coaxial injector, combustion chamber and nozzle. The mesh consists of 75000 cells and part of it is shown in Fig. 9. At all walls, the $y^+ < 1$ condition holds.

The mass flow and temperature is defined at the inlet boundaries for oxygen and methane, whereas a pressure outlet is applied at the exit plane. The experimental temperatures obtained with an inverse method [46] are applied at the walls along with a no-slip condition.

The mesh was chosen after an extensive grid convergence study. As characteristic quantities, the maximal wall pressure p_{max} and maximal heat flux at the combustion chamber wall $\dot{q}_{max}$ (excluding the nozzle), as well as the integrated wall heat loss $\dot{Q}$, are considered for a simulation using the frozen flamelet model. To assess the convergence of the solution, the theory of the Richardson extrapolation [47] as well as the CGI approach advocated by Roache [48] were employed. The CH_4/O_2 frozen flamelet simulation was used for this analysis.

The numerical error is calculated by comparing the solutions on each grid to a value gained from Richardson extrapolation according to

$$\varphi_{ext} = \varphi_1 + \frac{\varphi_1 - \varphi_2}{r^{\psi} - 1} \tag{30}$$

where the lower indices represent the finer mesh solutions and r is the grid refinement ratio.

The results are summarized in Table 2, whereas Fig. 9 shows the numerical error as a function of the grid points. All simulations were carried out with a second order upwind scheme for all transport equations. The achieved order ψ of convergence was also estimated for each of the three variables, using the method shown in Eq. (31).

$$\psi = \frac{\log \frac{\varphi_3 - \varphi_2}{\varphi_2 - \varphi_1}}{\log r} \tag{31}$$

For the integrated heat loss, maximal pressure and maximal heat flux, apparent orders of 2.40, 2.48 and 3.28 were obtained. The relative numerical errors for the middle grid remain underneath 1.5% whereas the GCI is below 10% using the conservative formulation by Roache

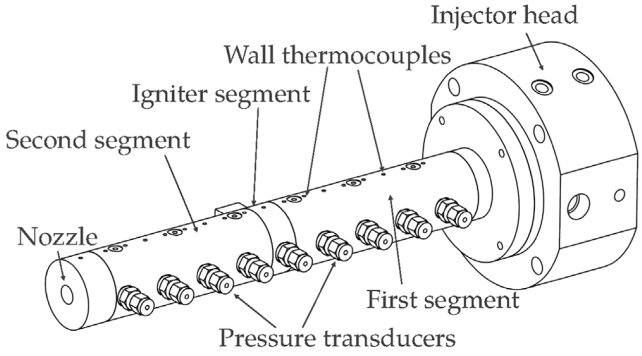

Fig. 8. Sketch of the single-element combustor.

Table 1
Summary of the experimental load points.

Case	H_2/O_2	CH_4/O_2
Nominal pressure [bar]	20	20
Mixture ratio O/F [−]	5.85	2.22
Mass flow rate fuel [g/s]	5.65	15.30
Mass flow rate oxidizer [g/s]	32.99	33.97
Fuel inlet temperature T_{fu} [K]	282	276
Oxidizer inlet temperature T_{ox} [K]	279	278
Velocity ratio u_{fu}/u_{ox} [−]	4.22	1.29

Table 2
Results of the grid convergence study.

	Coarse		Middle		Fine
Cells [−]	58000		75000		97500
r [−]		1.3		1.3	
$\dot{Q}$ [kW]	45.22		45.82		46.14
$\varepsilon_{\dot{Q}}$ [%]	2.77		1.47		0.79
p_{max} [bar]	19.12		19.35		19.47
$\varepsilon_{p_{max}}$ [%]	2.45		1.28		0.67
$\dot{q}_{max}$ [MW/m^2]	6.78		6.91		6.96
$\varepsilon_{\dot{q}_{max}}$ [%]	3.21		1.36		0.58
GCI$\dot{Q}$ [%]		8.42		1.87	
GCIp_{max} [%]		7.46		1.62	
GCI$\dot{q}_{max}$ [%]		9.78		1.72	

[48]. For that reason, the middle mesh was chosen for all simulations presented in this work.

It is important to note that in the case of simulations of reacting flows, apart from the sufficiently fine mesh, the effect of accumulated error due to numerical integration of the chemical source term, also has to be quantified, similar to the work by Smirnov et al. [49,50]. However, since the RANS equations are solved in the present work, where no explicit dynamic integration takes place, the issue of error accumulation is not relevant in this case.

5.3. Results

5.3.1. H_2/O_2 test case

Based on the results of the verification test case and the finding that NAF and HYF produce almost identical results, only the results of the hybrid model are discussed here (see Fig. 12).

Fig. 10 shows the temperature field within the chamber. A thin reaction zone appears in the shear layer of the co-axial injector which expands radially with increasing axial position. At approximately $x = 120$mm the flame reaches the wall and after this point the thermal boundary layer starts growing, indicated by a thin low-temperature zone in the vicinity of the wall. The stoichiometric line, which can be used to infer the flame length of the injector, appears to extend until $x = 140$mm. After this axial position, the temperature field is mainly homogeneous meaning that the bulk energy release due to combustion is completed. This is confirmed by the heat flux profiles in Fig. 13 which will be discussed later. The short length of the flame (compared to the total combustor length) can be explained by the large velocity ratio and the fast chemical time-scales of the H_2/O_2 combustion. A velocity ratio of 4.22 (Table 1) is responsible for a strong shear interaction close to the injector and an efficient turbulent mixing. The energy release is also taking place fast due to the small chemical scales represented by the Damkoehler values in Fig. 10. The Damkoehler number is larger than 10_6 for the majority of the flow indicating chemical equilibrium conditions. The greyed areas correspond to regions with more than 90% fuel or oxidizer, where the definition of the chemical time-scale becomes ill-posed.

The corresponding mass fractions fields for the species H_2O and OH can be found in Fig. 11. Since H_2O is the major product of H_2/O_2 combustion it reaches concentrations of up to 90% in the chamber and is mainly produced in areas with high temperature, where the main heat release takes place. Also it appears to build up close to the wall where the recombination reactions are induced due to the low enthalpy. The recombination reactions are clearly seen in the OH field as well, the concentration of which is clearly reducing in the thermal boundary layer.

A closer inspection is given in Fig. 11, where the species mass fraction and the temperature are plotted along the wall normal. For the $x = 100$mm axial position the combustion is not completed and hence low product concentrations occur close to the chamber axis ($y^+ > 10^3$). Moving closer to the wall, both the H_2O and OH mass fractions increase within the reacting shear layer. Finally for positions within the boundary layer ($y^+ < 10^2$) the OH concentration is reduced to zero, as it completely recombines to form water molecules. The profiles for $x = 200$mm are qualitatively very similar since a full recombination of OH to H_2O occurs within the thermal boundary layer. The only difference is that the flow mainly consists of pre-burnt products even close to the chamber axis and hence resembles the flat-plate results from Section 4.

The comparison of the simulation results with the available experimental pressure and heat flux data is carried out in Fig. 13. The absolute pressure level seems to be accurately captured by the HYF model, meaning that it is able to correctly predict the combustion efficiency. The pressure drop profile in the chamber is also an indicator

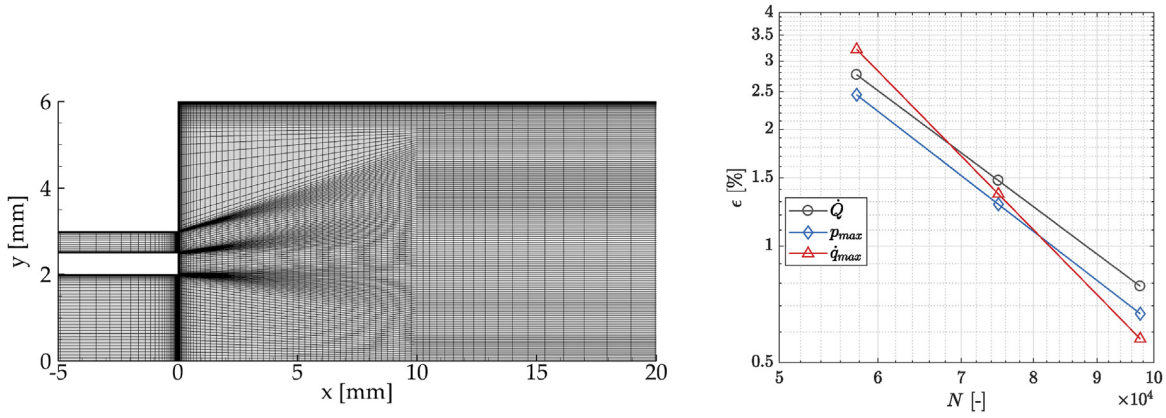

(a) Mesh in the vicinity of the injector. (b) Mesh convergence study.

Fig. 9. Mesh and numerical error as a function of the grid point number.

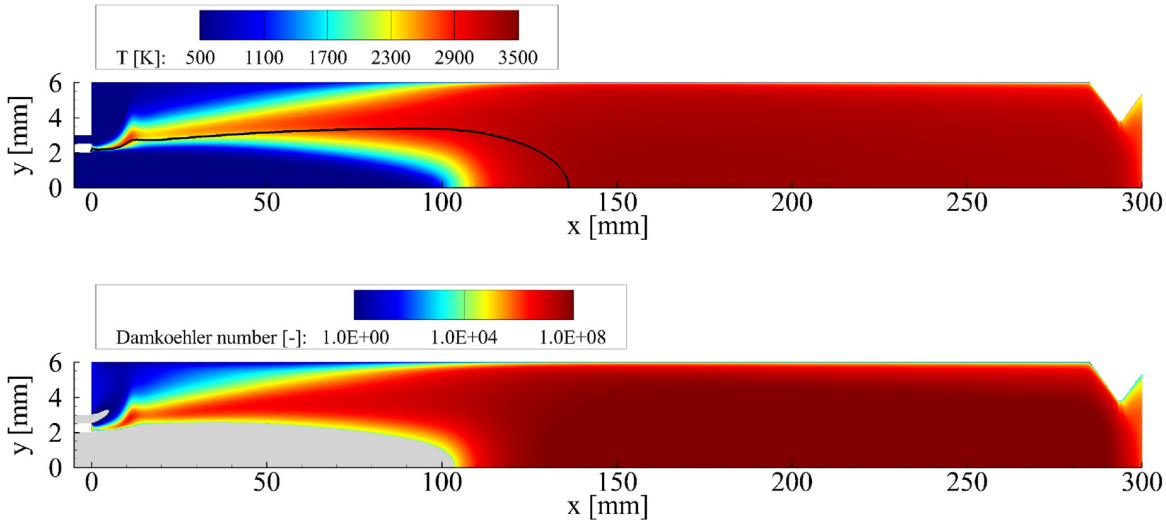

Fig. 10. Temperature (top) and Damkoehler number (bottom) fields for the H_2/O_2 simulation. The black line corresponds to the stoichiometric composition $Z_{st} = 0.111$.

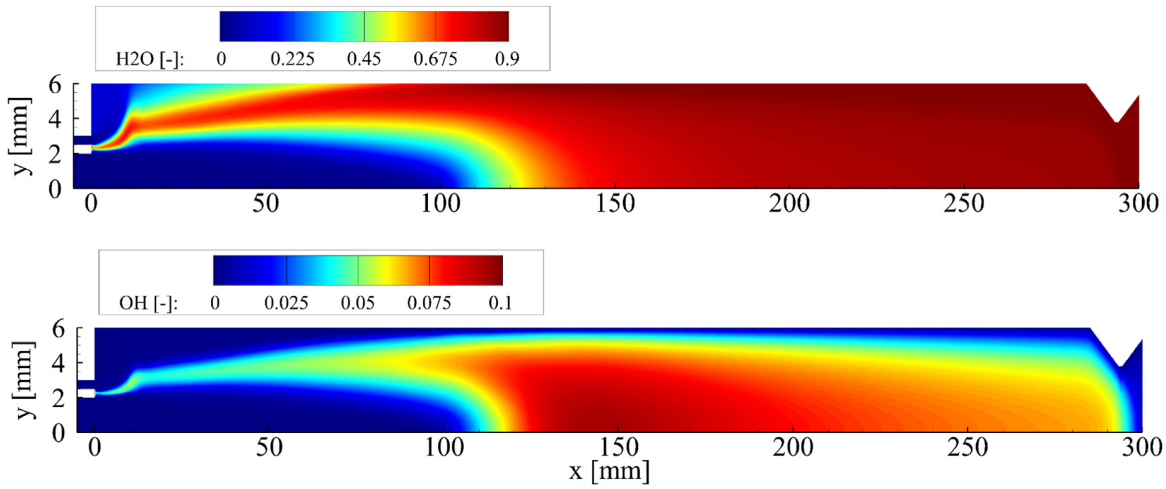

Fig. 11. H_2O (top) and OH (bottom) mass fraction fields for the H_2/O_2 simulation.

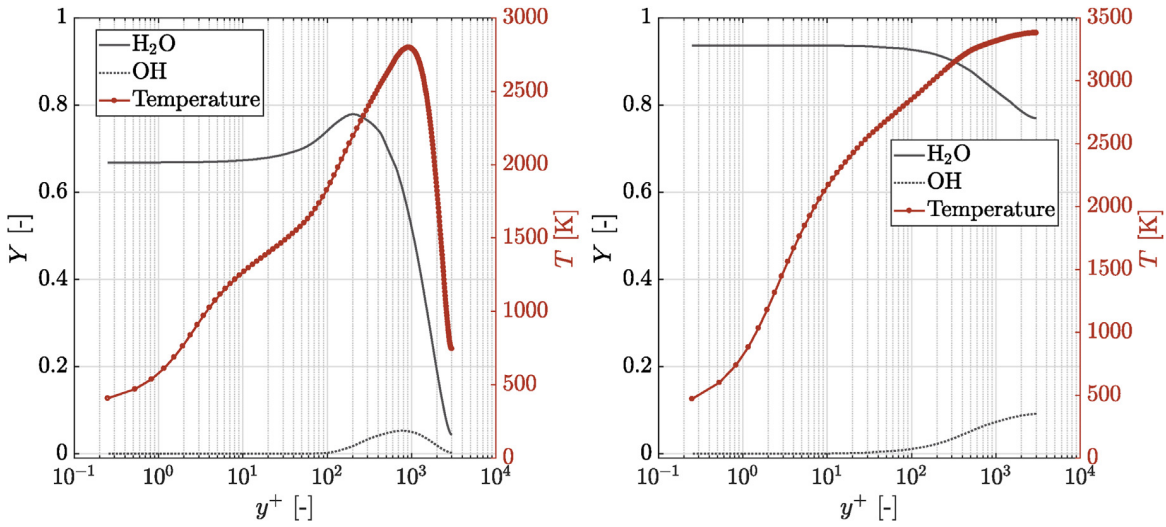

Fig. 12. Species profiles along the wall normal at x = 100 mm (left) and x = 200 mm (right) for the H_2/O_2 simulation.

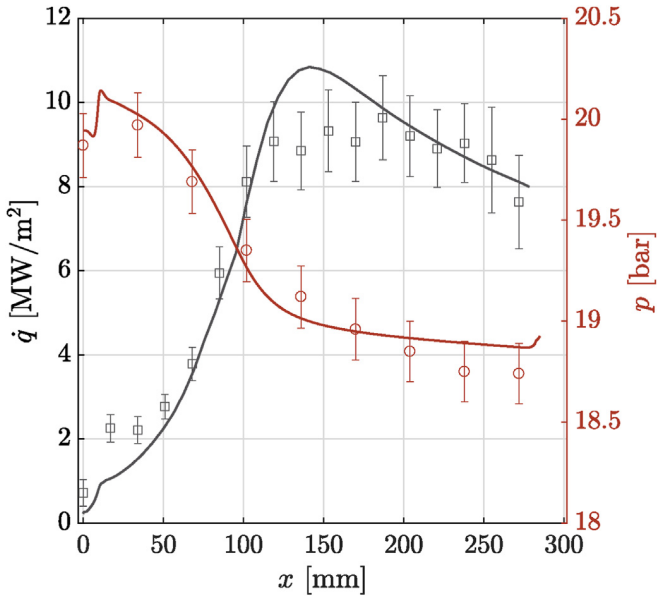

Fig. 13. Heat flux as well as pressure profiles for the H_2/O_2 simulation.

for the energy release in the chamber as it reflects the acceleration of the flow. The HYF model seems to also match the experimental pressure drop quite well. For the first 100 mm the discrepancies between simulation and experiment are minimal. Shortly before the end of the chamber, the numerical results show a flatter profile than the measured values but still within the experimental uncertainty.

A similar situation is found for when examining the wall heat flux data. The absolute heat flux level is captured with good accuracy and the profile follows the experimental measurements with small deviations. Within the recirculation zone close to the face-plate (x<50 mm), the heat flux shows a local maximum due to the stagnation flow of the reacting shear layer onto the wall. Although the simulation also displays a rise in heat flux, this is under-predicted compared to the experimental values. This difference can be attributed to the choice of the turbulence model. Since the impinging flow in the stagnation point is not isotropic, the choice of the $k-\varepsilon$ model is not ideal for capturing it. More complex RANS turbulence closure models or scale-resolving simulations would be required for this region. However, after the short recirculation zone, a steep increase in the heat flux takes place, corresponding to the position where the flame comes in contact with the wall. This is precisely re-produced in the numerical results. After the end of the bulk heat release (at $x \approx 140$mm) the heat flux reaches a plateau in the experiments and seems to drop in the simulation. The agreement of the profiles in the second half of the combustor is still satisfactory with deviations smaller than 1 MW/m^2 occurring throughout the length of the engine.

5.3.2. CH_4/O_2 test case

The results for the methane test case are presented in this section. The temperature distribution in the thrust chamber with the stoichiometric line is given in Fig. 14. Similar to the H_2/O_2 case, the temperature is high within the shear layer between the two propellants and becomes more uniform with increasing distance from the injector. A longer flame is observed compared to the hydrogen case, with the stoichiometric line extending up until $x \approx 200$mm. After this location the flow is homogeneous and no significant heat release is taking place, meaning that the flow is cooled down due to heat losses via the wall.

Lower values for the Damkoehler number are also observed throughout the thrust chamber. This is attributed both to the lower combustion temperature of the methane operating point and the slower chemical processes taking place in hydrocarbon combustion.

Only the HYF temperature results are shown in Fig. 14 since the temperature differences between the individual combustion models outside of the near-wall region are difficult to distinguish. The differences in the composition of the major species however for the three flamelet models are more obvious and are illustrated in Fig. 15. It is important to note that all three models show almost identical results in the regions with adiabatic conditions (i.e. in the main core of the flow) and only deviate in the low-enthalpy environments: the thermal boundary layer and the nozzle.

In the FRF results, CO dominates the region closer to the wall, whereas CO_2 is mainly concentrated in the energy release zone close to the chamber axis. This can be explained by the configuration of the injector, which has the fuel flowing through an outer annulus leading to fuel-rich conditions directly at the wall. For large radial positions therefore, in the absence of enough oxygen, CO_2 cannot be formed and hence CO is the final product. This segregation of the regions where CO or CO_2 are dominant is common in all three models.

The major difference is the heat loss-induced recombination directly at the wall for the NAF and HYF models, where the formation of a thin species boundary layer is evident. CO is oxidated to form CO_2 directly at the wall, a phenomenon which is expected based on previous studies regarding methane engines [44]. Although the NAF and HYF fields appear to be almost identical, large differences occur within the boundary layer.

Fig. 16 elaborates on those discrepancies by showing the species

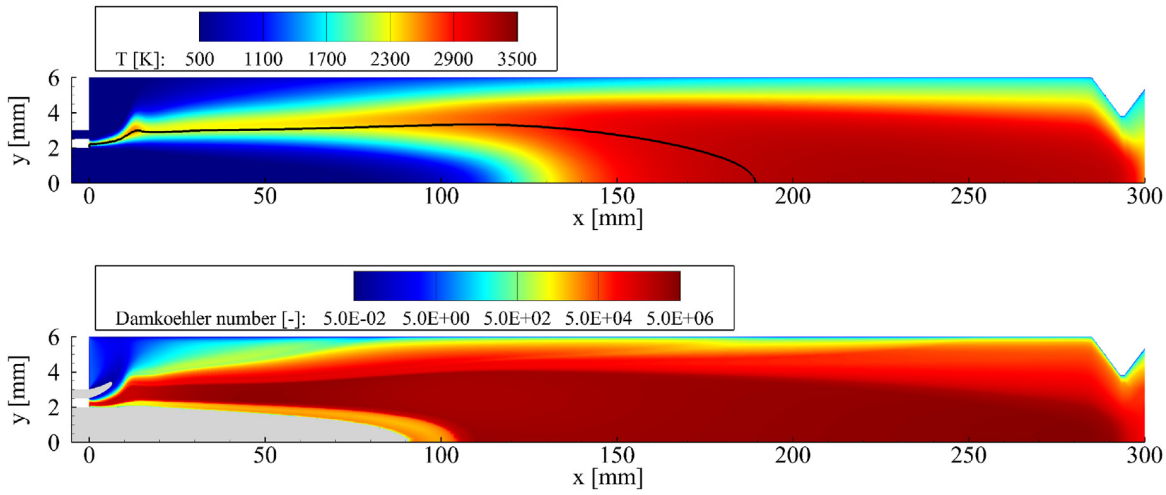

Fig. 14. Temperature (top) and Damkoehler number (bottom) fields for the CH_4/O_2 simulation. The black line represents the stoichiometric composition $Z_{st} = 0.2$.

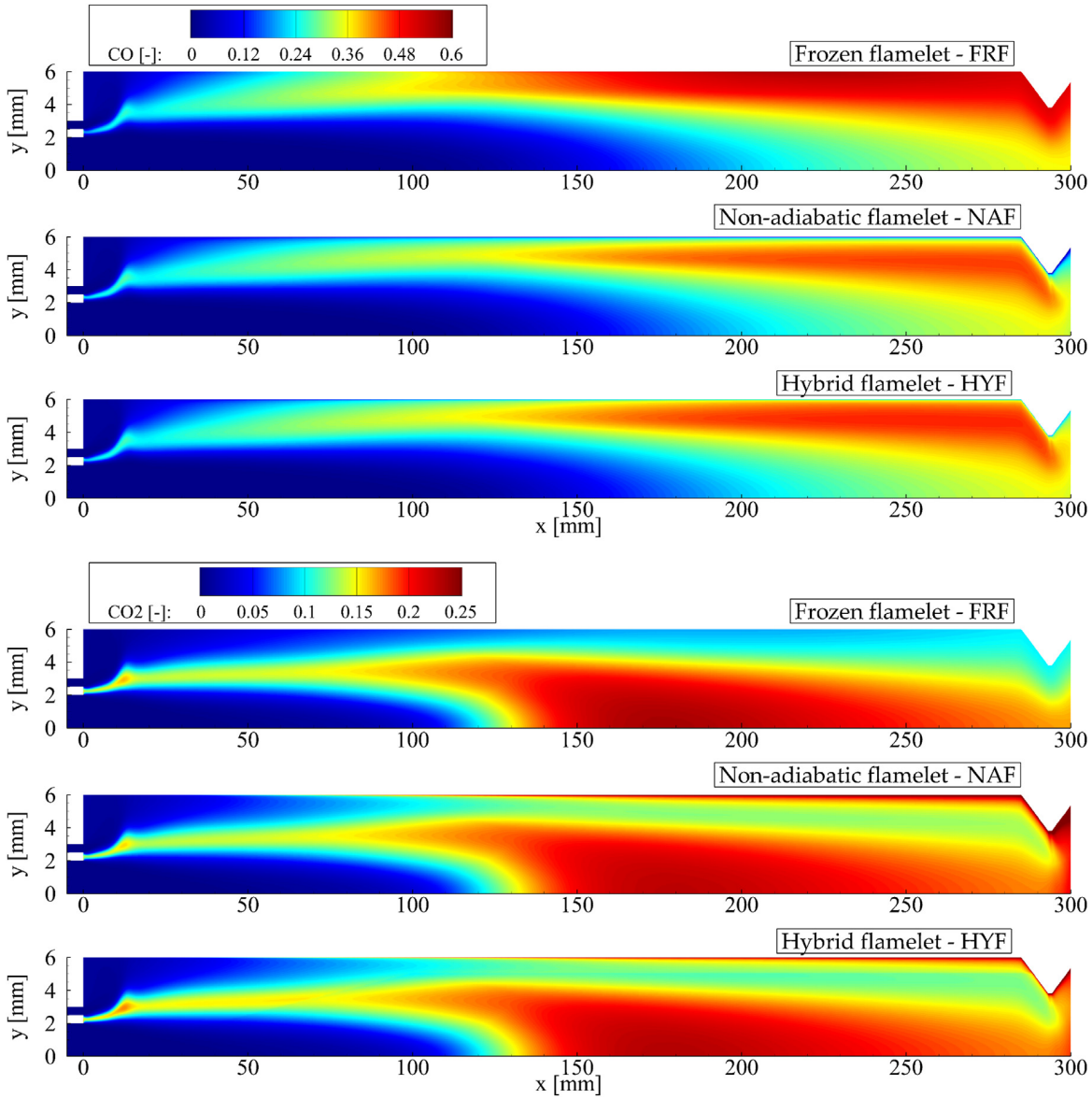

Fig. 15. CO (top) and CO_2 (bottom) species mass fraction fields for the three flamelet models.

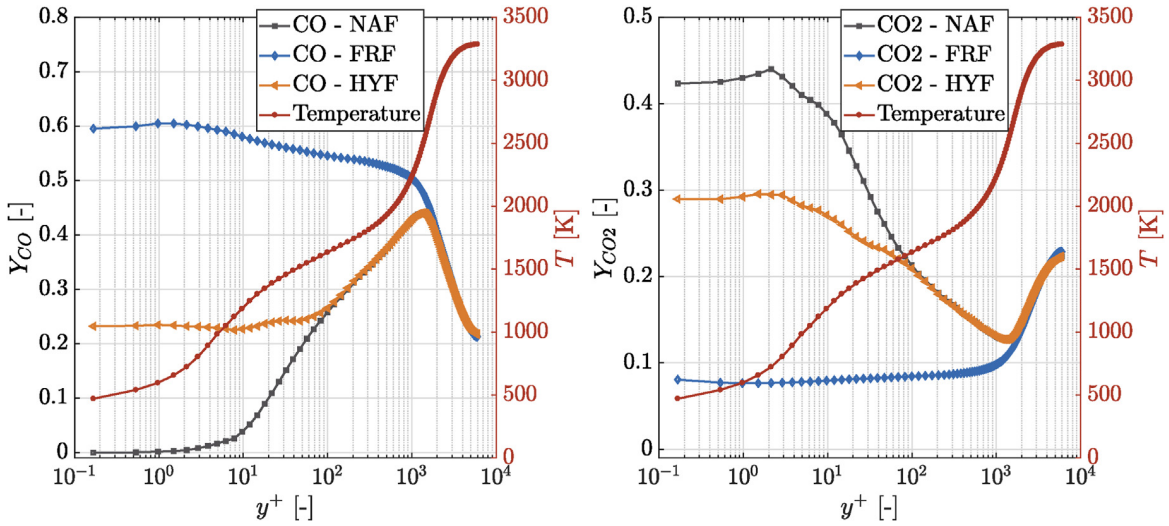

Fig. 16. CO (left) and CO_2 (right) species mass fractions along the wall normal at x = 200 mm for the CH_4/O_2 simulation.

profiles along the wall normal for $x = 200$mm. The temperature profile is also plotted as a reference. Close to the chamber axis ($y^+ > 10^3$) all three models predict nearly identical species distributions, whereas in the presence of the lower temperature environment the NAF and HYF predict the start of recombination reactions. Although the presence of those recombinations which is physically intuitive is present for both models, the degree of recombination shows some significant differences. Specifically, the conversion of CO to CO_2 in the NAF model continues even when the temperature drops below 1000 K within the viscous sub-layer. The reactions cease only when the CO is depleted and reaches a concentration of 0. The HYF model on the other hand restricts the progress rate of the CO to CO_2 conversion at $y^+ \approx 110$.

This can be attributed to the profile of the Damkoehler number shown in Fig. 17. As the chemical time-scales become larger the frozen enthalpy starts deviating from the look-up enthalpy of the flamelet tables and leads to am effective ceasing of additional reactions.

The large effect that the species concentration has on the experimentally measured values (pressure and wall heat flux) can be deduced by looking at Fig. 18. Starting with the wall heat flux in the right subfigure, the results show an expected trend: the frozen model exhibits the lowest absolute heat flux value as it does not predict any additional exothermic reactions induced by the low-enthalpy environment. The non-adiabatic model includes the aforementioned reactions but seems to excessively over-predict them, thereby leading to very large heat flux values. The results of the hybrid model on the other hand display an increased heat flux level compared to the frozen model but still in good agreement with the experimental results. Both the frozen and the hybrid model match the experimental data within 10% which is smaller than the measurement uncertainty. This means that the performance of the frozen model for the prediction of the heat flux is comparable to the hybrid one although it has an unphysical species distribution close to the wall. This explains why the frozen model has been used with success in predicting the wall heat transfer of hydrocarbon engine in the past [31].

A large difference however is evident in the pressure profile (left sub-figure) which proves the superiority of the hybrid model. Both the frozen model and the non-adiabatic model under-predict the pressure level in the combustion chamber, whereas the agreement of the hybrid model with the experimental data is very good.

To understand the reason that the NAF and FRF fail to accurately predict this performance parameter, one has to examine the total energy flow within a typical rocket engine. The energy which is released due to the reactions increases the gas temperature and can be used for either increasing the performance (higher pressure level) or can escape through the chamber walls. In the absence of sufficient heat release, the combustion pressure does not increase up to the expected level. At the same time, an excessive heat release directly at the wall increases the heat loss, thereby removing energy from the core and effectively dropping the pressure again. A predictive numerical tool hence can only be successful when it can get this energy balance correct.

It is obvious that the recombination reactions lead to a non-negligible energy release, which in turn increases the performance (pressure) of the engine. The failure of the frozen flamelet to capture those reactions explains the poor pressure prediction. The non-adiabatic model over-predicts those reactions and leads to excessive heat loss through the walls and a subsequent decrease in performance.

6. Conclusions

The current work introduces a method for extending the classic flamelet model in order to account for non-adiabatic effects. With this extension, species compositions, wall heat transfer and chamber pressure predictions can be carried out without the need for computationally expensive models based on finite rate.

For the generation of the non-adiabatic tables, an enthalpy-prescription method has been proposed. The species equations for a laminar counterflow diffusion flame are solved for different pressure, scalar dissipation and enthalpy profiles. The analysis of the flamelet tables shows that the most significant effect of the lower-enthalpy environment is that it increases the conversion of CO to CO_2.

In order to avoid an excessive predictions of the recombination reactions at the wall, the local chemical time-scale has been introduced. By pre-tabulating the chemical time-scale within the look-up table, the local Damkoehler number of the flow is obtained. Based on the value of the Damkoehler number, the reactions are defined as frozen or continue to evolve.

To verify the results of the new model, the simulation of a reacting flow over a cooled flat plate has been carried out and compared to finite rate results. Both for H_2/O_2 and CH_4/O_2 mixtures the new hybrid model exhibited great agreement with the finite rate results.

The hybrid model has been applied to the simulation of a single-element rocket combustor in realistic operating conditions. For both the H_2/O_2 and CH_4/O_2 cases, a great agreement for the wall heat flux values and pressure level is found. Without the Damkoehler number extension, the non-adiabatic flamelet model leads to an over-prediction of the heat losses through the wall and a subsequent under-prediction of the pressure level, whereas the frozen model shows a sufficiently accurate heat flux prediction but an under-estimation of the pressure level due to the absence of the exothermic recombination reactions. It is hence concluded that the correct prediction of the recombination reactions at the wall is important for the calculation of the performance and wall loads in rocket engines and that the higher fidelity hybrid model is able to capture them with minimal computational cost.

Declaration of competing interest

The authors declare that they have no known competing financial interests or personal relationships that could have appeared to influence the work reported in this paper.

Acknowledgments

Financial support has been provided by the German Research Foundation (Deutsche Forschungsgemeinschaft - DFG) in the framework of the Sonderforschungsbereich Transregio 40: "Technological Foundation for the design of thermally and mechanically high loaded

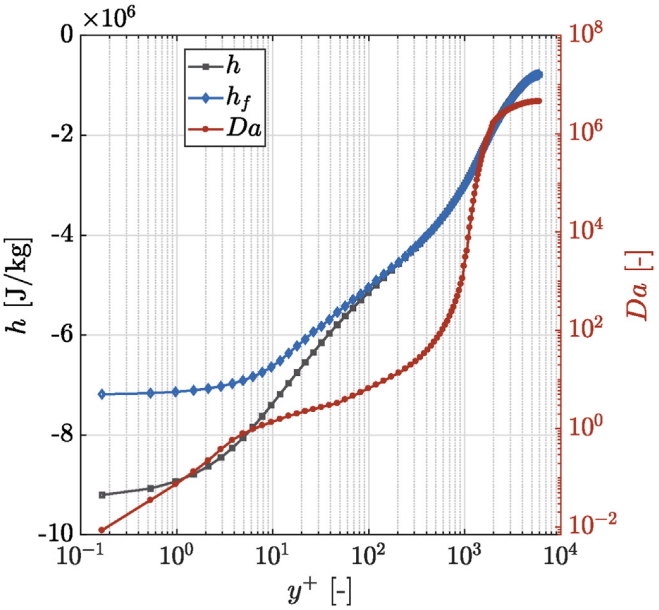

Fig. 17. Enthalpy and Damkoehler number profiles along wall normal at x = 200 mm for the CH_4/O_2 rocket combustor.

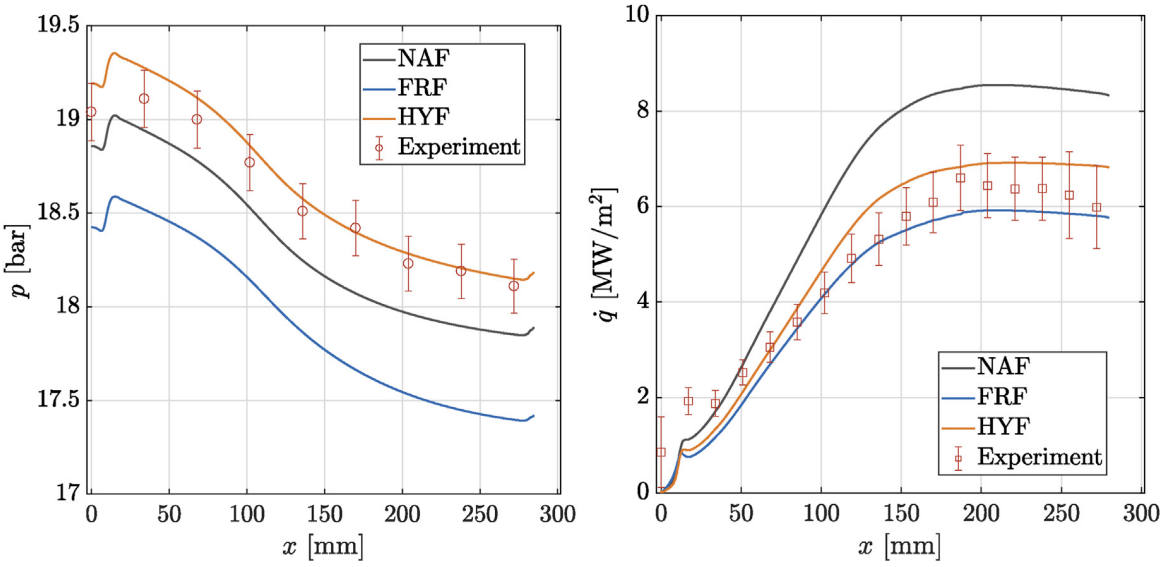

Fig. 18. Pressure (left) and wall heat flux (right) profiles along the axial direction for the CH_4/O_2 rocket combustor.

components of Future Space Transportation System". The authors gratefully acknowledge the Gauss Centre for Supercomputing e.V. (www.gauss-centre.eu) for funding this project by providing computing time on the GCS Supercomputer SuperMUC at Leibniz Supercomputing Centre (www.lrz.de).

References

[1] G.P. Sutton, O. Biblarz, Rocket Propulsion Elements, John Wiley & Sons, New York, 2016.
[2] G.P. Sutton, History of Liquid Propellant Rocket Engines, AIAA, 2006.
[3] D.R. Bartz, A simple equation for rapid estimation of rocket nozzle convective heat transfer coefficients, J. Jet Propuls. 27 (1957) 49–51, https://doi.org/10.2514/8.12572.
[4] P. Gerlinger, Investigation of an assumed pdf approach for finite-rate chemistry, Combust. Sci. Technol. 175 (5) (2003) 841–872, https://doi.org/10.1080/00102200302410.
[5] S.B. Pope, Pdf methods for turbulent reactive flows, Prog. Energy Combust. Sci. 11 (2) (1985) 119–192.
[6] N. Peters, Laminar diffusion flamelet models in non-premixed turbulent combustion, Prog. Energy Combust. Sci. 10 (3) (1984) 319–339, https://doi.org/10.1016/0360-1285(84)9011-X.
[7] N. Peters, Laminar flamelet concepts in turbulent combustion, Symposium (International) on Combustion, vol. 21, Elsevier, 1988, pp. 1231–1250, , https://doi.org/10.1016/S0082-0784(88)80355-2.
[8] N. Peters, Turbulent Combustion, Cambridge University Press, Cambridge, 2000.
[9] H. Pitsch, N. Peters, A consistent flamelet formulation for non-premixed combustion considering differential diffusion effects, Combust. Flame 114 (1–2) (1998) 26–40, https://doi.org/10.1016/S0010-2180(97)00278-2.
[10] S.-K. Kim, S.-M. Kang, Y.-M. Kim, Flamelet modeling for combustion processes and NOx formation in the turbulent nonpremixed CO/H2/N2 jet flames, Combust. Sci. Technol. 168 (1) (2001) 47–83, https://doi.org/10.1080/00102200108907831.
[11] H. Pitsch, H. Barths, N. Peters, Three-dimensional modeling of NOx and soot formation in DI-diesel engines using detailed chemistry based on the interactive flamelet approach, SAE Technical Paper, Society of Automotive Engineers International, 1996, , https://doi.org/10.4271/962057.
[12] S.-K. Kim, M. Joh, H.S. Choi, T.S. Park, Multidisciplinary simulation of a regeneratively cooled thrust chamber of liquid rocket engine: turbulent combustion and nozzle flow, Int. J. Heat Mass Tran. 70 (2014) 1066–1077, https://doi.org/10.1016/j.ijheatmasstransfer.2013.10.046.
[13] P.A. Libby, F.A. Williams, Strained premixed laminar flames under nonadiabatic conditions, Combust. Sci. Technol. 31 (1–2) (1983) 1–42, https://doi.org/10.1080/00102208308923629.
[14] D. Lee, S. Thakur, J. Wright, M. Ihme, W. Shyy, Characterization of flow field structure and species composition in a shear coaxial rocket GH2/GO2 injector: modeling of wall heat losses, 47th AIAA/ASME/SAE/ASEE Joint Propulsion Conference & Exhibit, AIAA Paper 2011-6125, 2011, p. 6125, , https://doi.org/10.2514/6.2011-6125.
[15] B. Fiorina, R. Baron, O. Gicquel, D. Thevenin, S. Carpentier, N. Darabiha, et al., Modelling non-adiabatic partially premixed flames using flame-prolongation of ILDM, Combust. Theor. Model. 7 (3) (2003) 449–470, https://doi.org/10.1088/1364-7830/7/3/301.
[16] D. Cecere, E. Giacomazzi, F.R. Picchia, N. Arcidiacono, F. Donato, R. Verzicco, A non-adiabatic flamelet progress–variable approach for LES of turbulent premixed flames, Flow, Turbul. Combust. 86 (3) (2011) 667–688, https://doi.org/10.1007/s10494-010-9319-7.
[17] B. Marracino, D. Lentini, Radiation modelling in non-luminous nonpremixed turbulent flames, Combust. Sci. Technol. 128 (1–6) (1997) 23–48, https://doi.org/10.1080/00102209708935703.
[18] F. Proch, A. Kempf, Modeling heat loss effects in the large Eddy simulation of a model gas turbine combustor with premixed flamelet generated manifolds, Proc. Combust. Inst. 35 (3) (2015) 3337–3345, https://doi.org/10.1016/j.proci.2014.07.036.
[19] A. Kishimoto, H. Moriai, K. Takenaka, T. Nishiie, M. Adachi, A. Ogawara, R. Kurose, Application of a nonadiabatic flamelet/progress-variable approach to large-eddy simulation of H2/O2 combustion under a pressurized condition, J. Heat Tran. 139 (12) (2017) 124501, https://doi.org/10.1115/1.4037099.
[20] S. Chan, X. Pan, M. Abou-Ellail, Flamelet structure of radiating ch4-air flames, Combust. Flame 102 (4) (1995) 438–446, https://doi.org/10.1016/0010-2180(95)00037-7.
[21] P.C. Ma, H. Wu, M. Ihme, J.-P. Hickey, Nonadiabatic flamelet formulation for predicting wall heat transfer in rocket engines, AIAA J. 56 (6) (2018) 2336–2349, https://doi.org/10.2514/1.J056539.
[22] D. Rahn, H. Riedmann, R. Behr, O.J. Haidn, Non-adiabatic flamelet modeling for the numerical simulation of methane combustion in rocket thrust chambers, 2018 Joint Propulsion Conference, 2018, p. 4869.
[23] N. Perakis, C. Roth, O.J. Haidn, Development of a non-adiabatic flamelet model for reacting flows with heat loss, Space Propulsion Conference, 2018.
[24] R. Bilger, Turbulent flows with nonpremixed reactants, in: P.A. Libby, F.A. Williams (Eds.), Turbulent Reacting Flows, Springer, Berlin, Heidelberg, 1980, pp. 65–113, , https://doi.org/10.1007/35401019269.
[25] P. Breda, M. Pfitzner, N. Perakis, O. Haidn, Generation of non-adiabatic flamelet manifolds: comparison of two approaches applied on a single-element GCH4/GO2 combustion chamber, 8th European Conference for Aeronautics and Space Sciences, EUCASS), 2019.
[26] T. Pant, C. Han, H. Wang, Computational investigations of the coupling between transient flame dynamics and thermo-acoustic instability in a self-excited resonance combustor, Combust. Theor. Model. (2019) 1–31.
[27] G. Strang, On the construction and comparison of difference schemes, SIAM J. Numer. Anal. 5 (3) (1968) 506–517, https://doi.org/10.1137/0705041.
[28] N.N. Janenko, The Method of Fractional Steps, Springer, Berlin, Heidelberg, 1971.
[29] D.G. Goodwin, H.K. Moffat, R.L. Speth, Cantera: an object-oriented software toolkit for chemical kinetics, thermodynamics, and transport processes, version 2.3.0 http://www.cantera.org retrieved 18 August 2018 (2017).
[30] N. Slavinskaya, M. Abbasi, J.-H. Starcke, A. Mirzayeva, O.J. Haidn, Skeletal mechanism of the methane oxidation for space propulsion applications, 52nd AIAA/SAE/ASEE Joint Propulsion Conference, AIAA Paper 2016-4781, 2016, p. 4781, , https://doi.org/10.2514/6.2016-4781.
[31] N. Perakis, D. Rahn, O.J. Haidn, D. Eiringhaus, Heat transfer and combustion simulation of seven-element O2/CH4 rocket combustor, J. Propul. Power 35 (6) (2019) 1080–1097.
[32] N. Perakis, C. Roth, O. Haidn, Simulation of a single-element rocket combustor using a non-adiabatic flamelet model, Space Propulsion Conference, 2018.
[33] G.K. Batchelor, Small-scale variation of convected quantities like temperature in turbulent fluid part 1. general discussion and the case of small conductivity, J. Fluid Mech. 5 (1) (1959) 113–133, https://doi.org/10.1017/S002211205900009X.
[34] U. Prüfert, F. Hunger, C. Hasse, The analysis of chemical time scales in a partial oxidation flame, Combust. Flame 161 (2) (2014) 416–426, https://doi.org/10.1016/j.combustflame.2013.09.001.

[35] R. Fox, Computational methods for turbulent reacting flows in the chemical process industry, Rev. Inst. Fr. Petrol 51 (2) (1996) 215–243.
[36] J. Caudal, B. Fiorina, M. Massot, B. Labégorre, N. Darabiha, O. Gicquel, Characteristic chemical time scales identification in reactive flows, Proc. Combust. Inst. 34 (1) (2013) 1357–1364, https://doi.org/10.1016/j.proci.2012.06.178.
[37] B.E. Launder, D.B. Spalding, Mathematical Models of Turbulence, Academic press, London-New York, 1972.
[38] M. Wolfshtein, The velocity and temperature distribution in one-dimensional flow with turbulence augmentation and pressure gradient, Int. J. Heat Mass Tran. 12 (3) (1969) 301–318, https://doi.org/10.1016/0017-9310(69)90012-X.
[39] R.B. Bird, W.E. Stewart, E.N. Lightfoot, Transport Phenomena, John Wiley & Sons, New York, 1960.
[40] C. Wilke, A viscosity equation for gas mixtures, J. Chem. Phys. 18 (4) (1950) 517–519, https://doi.org/10.1063/1.1747673.
[41] M. Ó Conaire, H.J. Curran, J.M. Simmie, W.J. Pitz, C.K. Westbrook, A comprehensive modeling study of hydrogen oxidation, Int. J. Chem. Kinet. 36 (11) (2004) 603–622.
[42] H. Negishi, Y. Daimon, H. Kawashima, N. Yamanishi, Conjugated combustion and heat transfer modeling for full-scale regeneratively cooled thrust chambers, 49th AIAA/ASME/SAE/ASEE Joint PropulsionConference, AIAA Paper 2013-3997, 2013, https://doi.org/10.2514/6.2013-3997.
[43] Y. Daimon, H. Negishi, S. Silvestri, O.J. Haidn, Conjugated combustion and heat transfer simulation for a 7 element gox/gch4 rocket combustor, 2018 Joint Propulsion Conference, AIAA Paper 2018-4553, 2018, https://doi.org/10.2514/6.2018-4553.
[44] B. Betti, D. Bianchi, F. Nasuti, E. Martelli, Chemical reaction effects on heat loads of CH4/O2 and H2/O2 rockets, AIAA J. 54 (1) (2016) 1693–1703, https://doi.org/10.2514/1.J054606.
[45] S. Silvestri, M.P. Celano, C. Kirchberger, G. Schlieben, O. Haidn, O. Knab, Investigation on recess variation of a shear coax injector for a single element GOX-GCH4 combustion chamber, transcations of the Japan society for aeronautical and space sciences, Aerospace Technology Japan 14 (ists30) (2016) 13–20, https://doi.org/10.2322/tastj.14.Pa13.
[46] N. Perakis, O.J. Haidn, Inverse heat transfer method applied to capacitively cooled rocket thrust chambers, Int. J. Heat Mass Tran. 131 (2019) 150–166, https://doi.org/10.1016/j.ijheatmasstransfer.2018.11.048.
[47] L.F. Richardson, The approximate arithmetical solution by finite differences of physical problems involving differential equations, with an application to the stresses in a masonry dam, Phil. Trans. Roy. Soc. Lond. 210 (459–470) (1911) 307–357, https://doi.org/10.1098/rsta.1911.0009.
[48] P.J. Roache, Perspective: a method for uniform reporting of grid refinement studies, J. Fluid Eng. 116 (3) (1994) 405–413, https://doi.org/10.1115/1.2910291.
[49] N. Smirnov, V. Betelin, V. Nikitin, L. Stamov, D. Altoukhov, Accumulation of errors in numerical simulations of chemically reacting gas dynamics, Acta Astronaut. 117 (2015) 338–355, https://doi.org/10.1016/j.actaastro.2015.08.013.
[50] N. Smirnov, V. Betelin, R. Shagaliev, V. Nikitin, I. Belyakov, Y.N. Deryuguin, S. Aksenov, D. Korchazhkin, Hydrogen fuel rocket engines simulation using logos code, Int. J. Hydrogen Energy 39 (20) (2014) 10748–10756, https://doi.org/10.1016/j.ijhydene.2014.04.150.

6.3 NON-ADIABATIC FLAMELET PROGESS VARIABLE

In this paper, a non-adiabatic FPV model is used for the simulation of a GOX/GCH4 single-element rocket combustor using LES. Comparisons with a frozen FPV model demonstrate the improved performance of the non-adiabatic model concerning the prediction of wall heat flux and pressure profiles. The recombination of CO with OH to form CO_2 is found to be the dominant heat releasing reaction in the boundary layer.

Investigation of CO recombination in the boundary layer of CH_4/O_2 rocket engines
Nikolaos Perakis, Oskar J. Haidn, Matthias Ihme
Proceedings of the Combustion Institute (2020)
doi: https://doi.org/10.1016/j.proci.2020.07.080

The application of the non-adiabatic approach in the steady flamelet model in Section 6.2 showed that a time-scale based freezing of the reactions is necessary to capture the recombination processes in the boundary layer. This was mainly needed because the scalar dissipation rate goes to zero close to the wall, thereby driving the concentration to its chemical equilibrium. In the FPV model however, this time-scale based correction is not included as the scalar dissipation rate is not one of the look-up variables.

The inclusion of the non-adiabatic effects is carried out using *the permeable wall model* by Ma et al. [305]. By examining the results obtained with this non-adiabatic model compared to a frozen approach, the areas of influence of the recombination reactions are identified. Specifically, a clear correlation between the enthalpy deficit and the CO/CO_2 mass fractions is found both in physical and mixture fraction space. With increasing distance from the injection plane, the enthalpy losses and hence the degree of recombination seem to increase. In the frozen case however, there is no correlation between enthalpy and species mass fractions. For positions outside the boundary layer both models provide very similar solutions.

By examining the reaction path diagrams at different radial distances from the wall, the progression of the chemical reactions is better understood. The hydrogen chemistry is dominant further away from the wall, with the *recombination of OH and H_2 to H_2O* having the larger contribution. This reaction remains significant for positions closer to the wall, where the *recombination of CO* following the pathway $OH + CO \longrightarrow CO_2 + H$ is also prevailing.

Macroscopically, the non-adiabatic model predicts a larger heat release and hence an amplified heat loss via the wall. The increased heat release gives rise to a *higher pressure* in the domain, which shows a better agreement with the experimental values compared to the frozen model. At the same time, the non-adiabatic model is able to closely reproduce the wall heat flux measurements as well, proving that the inclusion of non-adiabatic effects is needed for the correct estimation of heat loads and hence lifetime predictions.

Available online at www.sciencedirect.com

ScienceDirect

Proceedings of the Combustion Institute 38 (2021) 6403–6411

Proceedings of the Combustion Institute

www.elsevier.com/locate/proci

Investigation of CO recombination in the boundary layer of CH_4/O_2 rocket engines

Nikolaos Perakis [a,b,*], Oskar J. Haidn [b], Matthias Ihme [a]

[a] Department of Mechanical Engineering, Stanford University, Stanford, CA 94305, USA
[b] Chair of Space Propulsion, Technical University of Munich, Garching 85748, Germany

Received 7 November 2019; accepted 19 July 2020
Available online 2 October 2020

Abstract

In this work, the combustion and thermal recombination in the boundary layer of a single-element methane/oxygen rocket combustor is investigated using large-eddy simulations. The experimental configuration consists of a coaxial injector and an operating point with a nominal pressure of 20 bar and gaseous injection of both propellants are considered. A non-adiabatic flamelet model is utilized with the purpose of examining its capability to predict the wall heat transfer. Good agreement of the simulation results with measurements of heat flux and pressure profiles is obtained using the non-adiabatic model. By comparing results with a frozen flamelet model, the importance of the recombination reactions in the cold boundary layer is investigated. The species profiles of CO and CO_2 are examined and the reaction pathways leading to the recombination reactions at the wall were analyzed. Results from this analysis show that the reaction of OH with CO forming CO_2 is the main contributor to the additional heat release in the boundary layer.

Keywords: Reacting boundary layer; Recombination reactions; Methane combustion; Heat transfer; Rocket engines

1. Introduction

In an effort to decrease launch costs and to design reliable and efficient propulsion systems for space applications, significant research efforts have been dedicated towards advancing the maturity level of the propellant combination methane/oxygen [1–3]. This interest in methane/oxygen is attributed to the fact that it offers improved performance with reusability, sustainability and a potential cost reduction compared to conventional propellants such as H_2 and RP-1 [4,5].

Over recent years, efforts have been dedicated towards developing improved modeling techniques for a reliable prediction of combustion performance in rocket motors. However, these investigations have mainly focused on the H_2/O_2 propellant combination [6,7], while investigations of methane remain limited.

Apart from typical performance metrics such as specific impulse, thrust and characteristic velocity, combustion models have to accurately predict the

* Corresponding author at: Department of Mechanical Engineering, Stanford University, Stanford, CA 94305, USA.
E-mail address: nikolaos.perakis@tum.de (N. Perakis).

https://doi.org/10.1016/j.proci.2020.07.080
1540-7489

wall heat loads, which is of major interest in the design of rocket engines. Given the extreme heat flux values occurring at the walls of rocket thrust chambers, reaching up to 150 MW/m^2 [8], understanding the flame-wall interaction is crucial. To avoid mechanical failure of the chamber and to reduce uncertainties of the operational lifetime of the engine, a precise knowledge of the spatial distribution of the thermal load is necessary [9,10].

Compared to hydrogen, the combustion of methane evolves on slower chemical time scales, resulting in the formation of a non-equilibrium chemical state in the boundary layer at the cooled chamber wall, which requires additional modeling. Due to the wall heat loss, the hot combustion products inside the thrust chamber are abruptly cooled within the thermal boundary layer. This enthalpy reduction induces chemical reactions that enhance the wall heat flux and therefore influence the design of the cooling system and the overall cycle performance [11]. Several studies were conducted to examine the aforementioned reactions and to extend existing combustion models. Cabrit et al. [12] performed direct numerical simulations and wall-resolved large-eddy simulation (LES) of a turbulent reacting channel flow, but the operating point was not directly relevant for rocket conditions. More recently, Betti et al. [13] investigated effects of recombination reactions on the wall heat loads of methane/oxygen engines with relevance to rocket combustion. Efforts to incorporate effects of wall heat transfer in flamelet-models have been conducted. These developments include work by Ma et al. [14] in which heat loss is modeled via a permeable wall in the counterflow diffusion problem and applying the model to predict the heat loads of an H_2/O_2 rocket engine. Breda et al. [15] applied the same model in simulations of a sub-scale CH_4/O_2 rocket engine, whereas Perakis et al. [16] developed an enthalpy-constrained extension of the flamelet model to account for the recombination reactions. Furthermore, Zips et al. [17] and Maestro et al. [18] predicted the wall heat flux distribution in subscale methane/oxygen rocket engines using LES.

Previous studies have identified the recombination of CO and CO_2 as a main mechanism leading to an increase in the wall heat flux of hydrocarbon engines [13,16]. However their is a lack of fundamental understanding and predictive modeling of this effect.

The objective of the present investigation is to evaluate the ability of a non-adiabatic flamelet model to capture the recombination reactions at the wall and to predict the wall-heat transfer. By addressing this need, a validation of the model is carried out and the LES results are examined to assess the recombination kinetics and boundary layer dynamics. Despite the limitations of the model, the results give insights into the physics of recombination reactions and motivate further studies using finite-rate chemistry models. The experimental and numerical setup of the gas/gas single element rocket combustor operating with methane/oxygen is described in Section 2. Simulation results are examined in Section 3 and reaction pathways responsible for the recombination are identified. Comparisons with a frozen-chemistry flamelet model are performed to quantify the significance of recombinations on wall heat transfer augmentation.

2. Setup

2.1. Experimental configuration

The experimental configuration considered in this study corresponds to a single-element rocket combustor, operating with gaseous oxygen and gaseous methane. The experimental configuration, which is described in detail in Silvestri et al. [19,20] consists of a co-axial injector element where the oxidizer is supplied through a central jet with diameter $d_{ox} = 4$ mm, and the fuel is injected through an annulus with inner and outer diameters $d_{fu,i} = 5$ mm and $d_{fu,o} = 6$ mm respectively. The thrust chamber consists of a cylindrical combustion chamber with 12 mm diameter and a length of 285 mm as well as a nozzle with contraction ratio $\epsilon_c = 2.5$, which ensures that the Mach number in the combustion chamber is similar to typical flight configurations. The operational point chosen for the present analysis has a global oxidizer-to-fuel ratio of 2.6, a nominal operating pressure of 20 bar and the oxidizer stream is not recessed with respect to the face-plate. Thermocouples and pressure tansducers are installed along the chamber wall thereby delivering quantitative data for wall heat flux and static wall pressure.

The experimentally measured mass flow rates for the oxidizer and fuel ($\dot{m}_{O_2} = 34.82$ g/s, $\dot{m}_{CH_4} = 13.39$ g/s) as well as the corresponding inlet temperature ($T_{O_2} = 275$ K, $T_{CH_4} = 269$ K) are prescribed at the inlets and a pressure outlet is imposed at the exhaust plane. All other boundaries are defined as no-slip walls. For the thermal boundary condition at the chamber wall, the wall temperature values obtained by the inverse method of Perakis et al. [21] are applied, whereas the face-plate and injector tip are adiabatic. For the wall boundary conditions, a wall function has been used. An overview of the computational setup is given in Fig. 1. The mesh consisting of 17 million cells with 25 points across the injector lip was used for the simulation and is shown in Fig. 2. The minimum wall spacing along the chamber wall is 30 μm and a wall model was used for the viscous sublayer [22].

2.2. Governing equations

For the 3D simulations presented in the following sections, the Favre-averaged governing equations for continuity, momentum and energy are

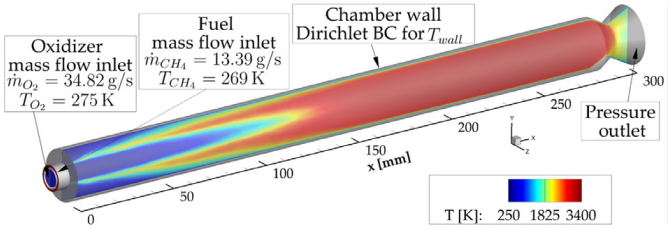

Fig. 1. Overview of the computational domain and boundary conditions.

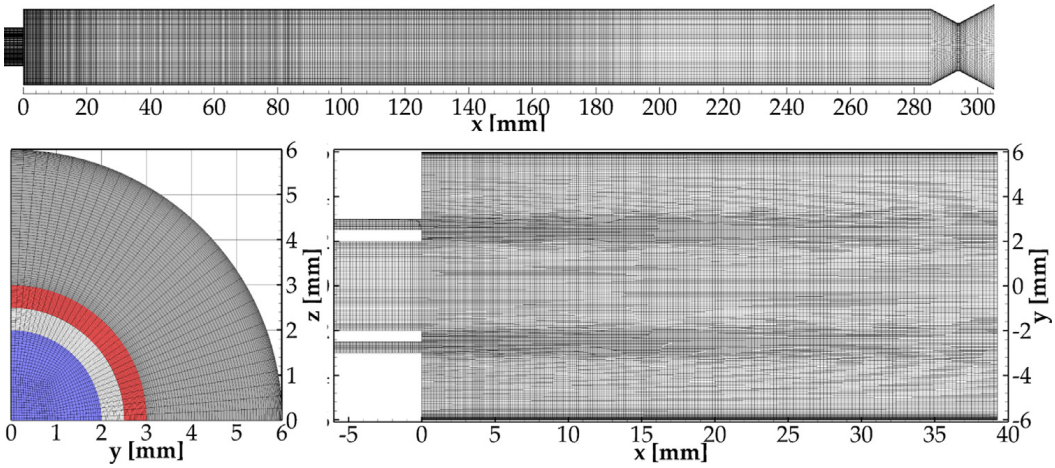

Fig. 2. Computational mesh used in the LES: side view (top), face-plate and $z = 0$ cut-plane (bottom).

solved:

$$\partial_t \bar{\rho} + \nabla \cdot (\bar{\rho}\widetilde{\boldsymbol{u}}) = 0 \tag{1}$$

$$\partial_t (\bar{\rho}\widetilde{\boldsymbol{u}}) + \nabla \cdot (\bar{\rho}\widetilde{\boldsymbol{u}}\widetilde{\boldsymbol{u}}) = -\nabla \cdot (\bar{p}\boldsymbol{I}) + \nabla \cdot (\bar{\boldsymbol{\tau}}_v + \bar{\boldsymbol{\tau}}_{SGS}) \tag{2}$$

$$\partial_t (\bar{\rho}\widetilde{E}) + \nabla \cdot [\widetilde{\boldsymbol{u}}(\bar{\rho}\widetilde{E} + \bar{p})] = \nabla \cdot [(\bar{\boldsymbol{\tau}}_v + \bar{\boldsymbol{\tau}}_{SGS}) \cdot \widetilde{\boldsymbol{u}}] - \nabla \cdot (\bar{\boldsymbol{q}}_v + \bar{\boldsymbol{q}}_{SGS}) \tag{3}$$

where ρ is the density, $\boldsymbol{u}$ is the velocity vector, p is the pressure, $\boldsymbol{\tau}$ is the viscous tensor, $\dot{\boldsymbol{q}}$ is the heat flux and E is the specific total energy combining the specific internal energy and the kinetic energy $\widetilde{E} = e + \frac{1}{2}|\widetilde{\boldsymbol{u}}|^2$ as defined in Williams [23]. Because of the low chamber pressure in the chamber which does not exceed 20bar, effects of intermolecular forces and volume correction are neglected in the definition of the energy and the ideal gas equation of state is used as closure for the system of equations.

The equations are discretized based on a finite-volume formulation and a fourth-order non-dissipative scheme is used for the convective flux discretization with a strong stability-preserving third-order Runge–Kutta scheme for time advancement [24].

2.3. Combustion modeling

To perform the LES calculation of this configuration, the Favre-filtered compressible Navier–Stokes equations are solved. A non-adiabatic flamelet progress variable (FPV) model is employed to obtain the thermo-chemical state. This model requires the solution of the filtered conservation equations for the mixture fraction, progress variable and mixture fraction variance:

$$\partial_t (\bar{\rho}\widetilde{Z}) + \nabla \cdot (\bar{\rho}\widetilde{\boldsymbol{u}}\widetilde{Z}) = \nabla \cdot \left[\left(\bar{\rho}\widetilde{D} + \frac{\mu_t}{Sc_t}\right)\nabla\widetilde{Z}\right] \tag{4}$$

$$\partial_t (\bar{\rho}\widetilde{C}) + \nabla \cdot (\bar{\rho}\widetilde{\boldsymbol{u}}\widetilde{C}) = \nabla \cdot \left[\left(\bar{\rho}\widetilde{D} + \frac{\mu_t}{Sc_t}\right)\nabla\widetilde{C}\right] + \bar{\dot{\omega}}_C \tag{5}$$

$$\partial_t (\bar{\rho}\widetilde{Z''^2}) + \nabla \cdot (\bar{\rho}\widetilde{\boldsymbol{u}}\widetilde{Z''^2}) = \nabla \cdot \left[\left(\bar{\rho}\widetilde{D} + \frac{\mu_t}{Sc_t}\right)\nabla\widetilde{Z''^2}\right] + 2\frac{\mu_t}{Sc_t}|\nabla\widetilde{Z}|^2 - \bar{\rho}\tilde{\chi} \tag{6}$$

In this non-adiabatic FPV model, an additional parameter, Z_{wall} is introduced to provide a parametrization of the flamelet solution with respect to wall distance. With this, the thermochemical state-space, consisting of chemical source term, heat release, thermo-viscous transport properties

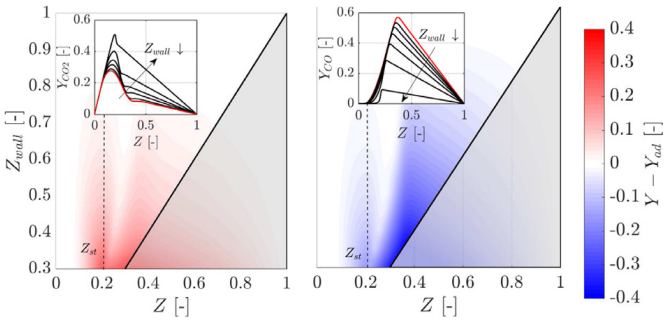

Fig. 3. CO_2 and CO mass fraction in counterflow diffusion flame calculations with the non-adiabatic wall model. Z_{wall} denotes the location of the permeable wall in mixture fraction space.

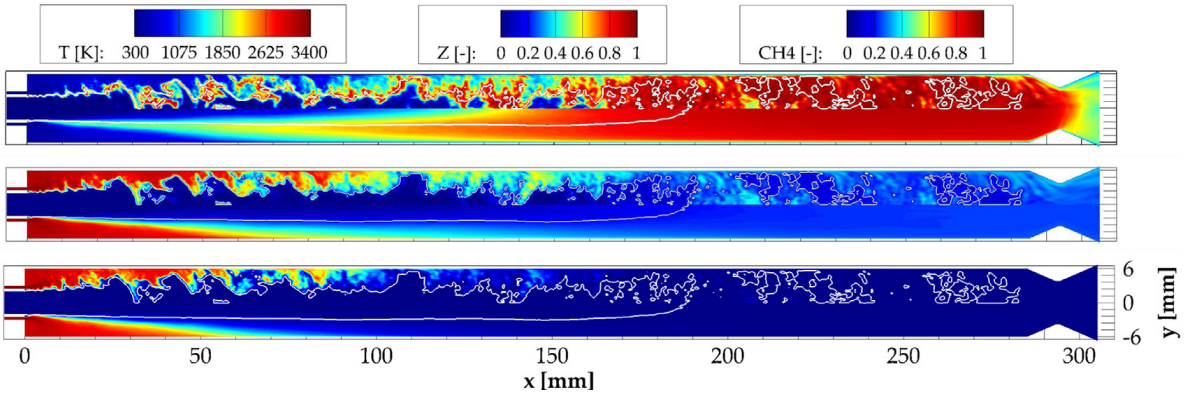

Fig. 4. Temperature, mixture fraction and methane mass fraction fields (from top to bottom) for the non-adiabatic FPV model. Upper half: instantaneous fields, bottom half: time-averaged solution. Z_{st} shown by white line.

and species mass fractions is parametrized in terms of $\widetilde{Z}$, $\widetilde{C}$, $\widetilde{Z''^2}$ and Z_{wall}, in which Z_{wall} represents the local mixture fraction at the wall. In this model, the turbulence-chemistry interaction is modeled using a presumed β-PDF and further details can be found in the work of Ma et al. [14]. The detailed GRI 3.0 mechanism is used, consisting of 35 species and 192 reactions [25]. For the closure of the turbulent viscosity μ_t the Vreman subgrid-scale model [26] is applied and a constant turbulent Schmidt number equal to 0.7 is used.

Moving the permeable wall from the fuel stream towards the flame increases the heat loss, meaning that lower values of Z_{wall} correlate to a larger enthalpy deficit and a lower temperature. At the same time, the CO mass fraction is also reduced with increasing heat loss compared to the adiabatic profile, which corresponds to the solution for $Z_{wall} = 1$.

The effect of the increased heat loss on the species mass fraction is depicted in Fig. 3, where the differences in CO and CO_2 mass fractions with respect to the adiabatic flamelet solution are plotted in mixture fraction space for different values of Z_{wall}. The line plots (shown as inlay) illustrate the evolution of the species mass fractions with varying Z_{wall}, with the red line corresponding to the adiabatic solution. The contour plots in the same figure show the deviation from the adiabatic profile ($Z_{wall} = 1$). The results correspond to a scalar dissipation rate of $\chi = 1\text{s}^{-1}$.

The black line in Fig. 3 represents the location of the permeable non-adiabatic wall. As expected, the lower enthalpy environment facilitates a significant reduction in CO mass fraction with a corresponding increase in CO_2. In the region close to stoichiometry ($Z_{st} = 0.2$) as well as the fuel-rich region an appreciable degree of CO recombination can be observed. This is explained by the larger concentration of carbon-containing species compared to the oxidizer-rich side [16]. In the following we will examine the impact of CO recombination on wall heat transfer and combustion in rocket engines.

3. LES results

Instantaneous and time-averaged flow-field results for temperature, mixture fraction and methane mass fraction are shown in Fig. 4. The injection without recess and the velocity ratio of the propellants ($u_{CH_4}/u_{O_2} \approx 0.92$) suppresses the mixing. The shear layer downstream of the injector

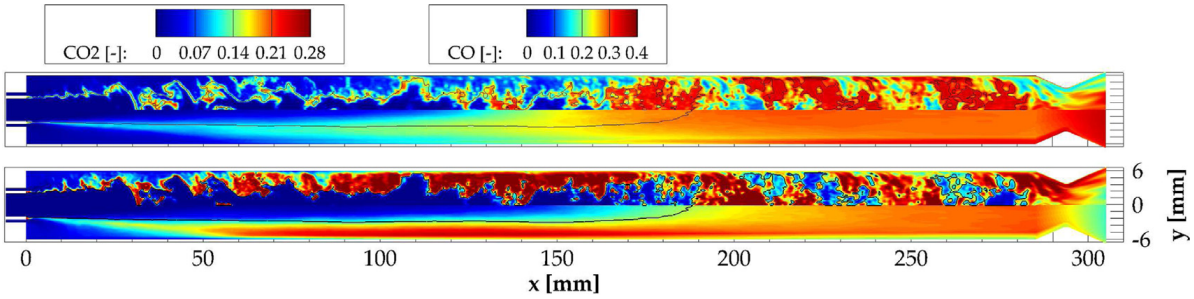

Fig. 5. CO_2 and CO mass fractions fields for the non-adiabatic FPV model. Upper half: instantaneous fields, bottom half: time-averaged solution. Z_{st} shown by black line.

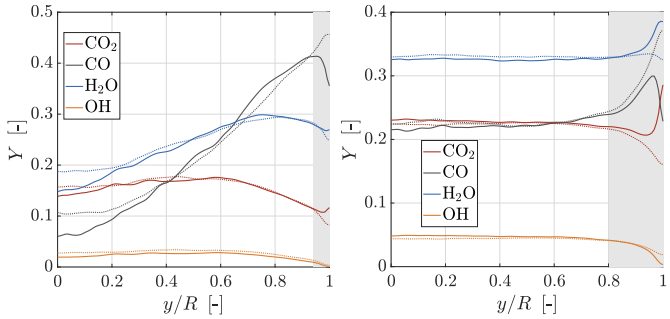

Fig. 6. Species profiles along the wall normal direction at $x = 150$ mm (left) and $x = 250$ mm (right). Dotted lines correspond to the frozen FPV model and solid lines to the non-adiabatic FPV. The gray area represents the thermal boundary layer.

exhibits small-scale Kelvin–Helmholtz instabilities, which grow with increasing axial distance. This leads to a significant radial expansion of the flame close to $x = 50$ mm and an increase in the turbulence level downstream. The stoichiometric composition ($Z_{st} = 0.2$) represented by a white line extends up to $x \approx 200$ mm, indicating a sufficient degree of mixing in the chamber. Moreover, the formation of thermal boundary layer is visible, which is a result of the enthalpy loss to the wall.

The methane, which is supplied by the outer annulus of the co-axial injector is dominant in the near-injector recirculation region but rapidly mixes and is consumed within the first half of the domain. This is also shown by the mixture fraction, with fuel-rich mixture dominating the near-wall region and oxygen-rich mixture being accumulated close to the central axis. As the mixing is enhanced however, the composition of the gas exiting the domain approaches the global mixture fraction value of 0.278. Using the definition of Danckwerts [27], an unmixedness value equal 0.021 is found at the exit plane.

The species fields of CO and CO_2 are shown in Fig. 5. It can be seen that close to the injection plane, CO and CO_2 are being formed in the reacting shear layer. As the flame expands, the CO mass fraction increases toward the radial direction closer to the wall. This is explained by the absence of oxygen near the wall to produce CO_2. With enhanced mixing, however, the CO and CO_2 exit the combustor in a more homogeneous way. Apart from the effects that the injector design and the energy release have on the CO and CO_2 mass fractions, the effect that the heat loss promotes recombination reactions can be seen near the wall throughout the domain. Specifically, a thin boundary layer is formed, where CO is converted to CO_2. The locations where recombination takes place coincide with the regions with enthalpy defect, which is defined as the difference between the local enthalpy and the adiabatic mixing enthalpy.

To elucidate the effect that the heat loss has on the species profiles, plots of the major species as a function of the wall normal direction are shown in Fig. 6. Two representative locations at $x = 150$ mm and $x = 250$ mm were chosen. The first axial position is located within the main reaction zone, while the second position is in the post-reaction zone where combustion is completed and hence the heat loss effects can be isolated. In order to quantify the effect of the recombination reactions, a simulation using the adiabatic FPV model was also carried out. For this simulation the value of Z_{wall} was set to 1. This is labeled as "frozen" model as the gas composition is unaffected by the enthalpy loss.

For both axial locations, the results obtained by the two models are in good agreement away from the wall, with small discrepancies appearing close to the chamber axis. These discrepancies occur due

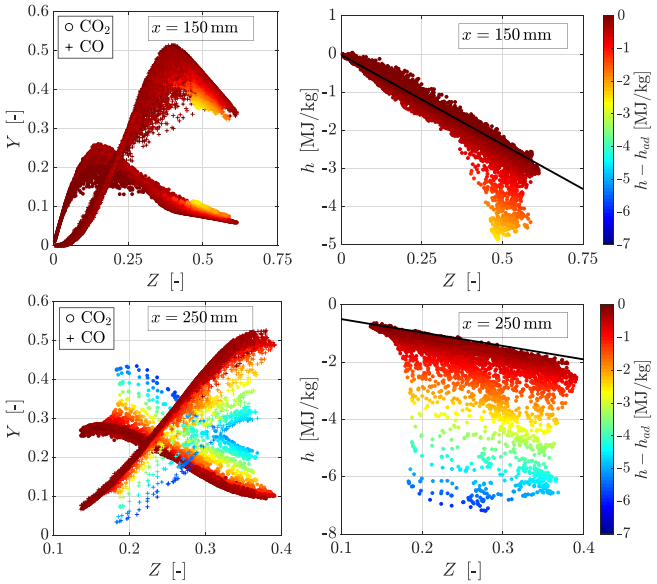

Fig. 7. Scatter plot for CO_2, CO mass fractions and enthalpy defect at $x = 150$ mm (top) and $x = 250$ mm (bottom) for the non-adiabatic FPV model. The black solid line represents the adiabatic enthalpy.

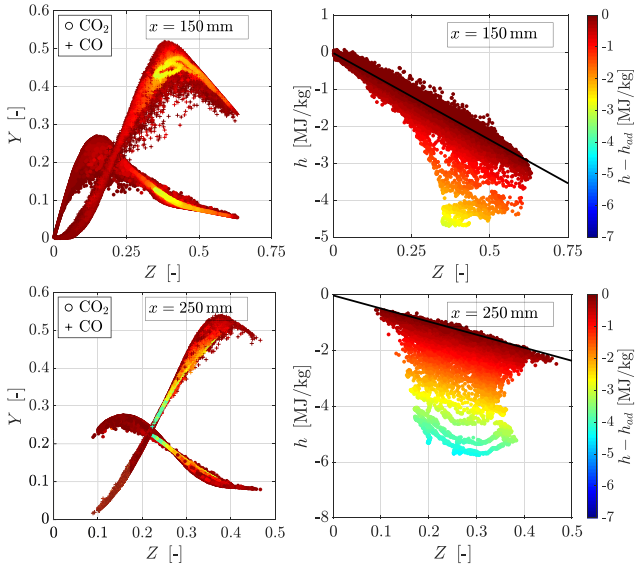

Fig. 8. Scatter plot for CO_2, CO mass fractions and enthalpy defect at $x = 150$ mm (top) and $x = 250$ mm (bottom) for the frozen FPV model. The black solid line represents the adiabatic enthalpy.

to higher heat flux obtained with the non-adiabatic FPV-solution which results in an increase in the flame length and hence a change in the gas composition along the center-line. For the first axial location, the CO mass fraction increases with decreasing distance from the wall, with a corresponding decrease in CO_2 mass fraction. This is explained by the design of the injector as shown in Fig. 5. Close to the wall, however, for $y/R > 0.9$, a species boundary layer forms, with a clear recombination of CO to CO_2 and an increase in H_2O mass fraction. For the second axial position, a homogeneous profile is observed for $y/R < 0.6$ indicating equilibrated composition. Already at $y/R = 0.8$, large deviations between the two models occur. As the thickness of the thermal boundary layer increases, the region affected by the enthalpy-defect-induced recombination broadens.

The effect of the enthalpy defect on the species composition is also illustrated in Figs. 7 and 8, where a scatter plot of the species and enthalpy defect are shown in mixture fraction space for the non-adiabatic and frozen FPV models respectively. As already established in Fig. 6, the heat loss and

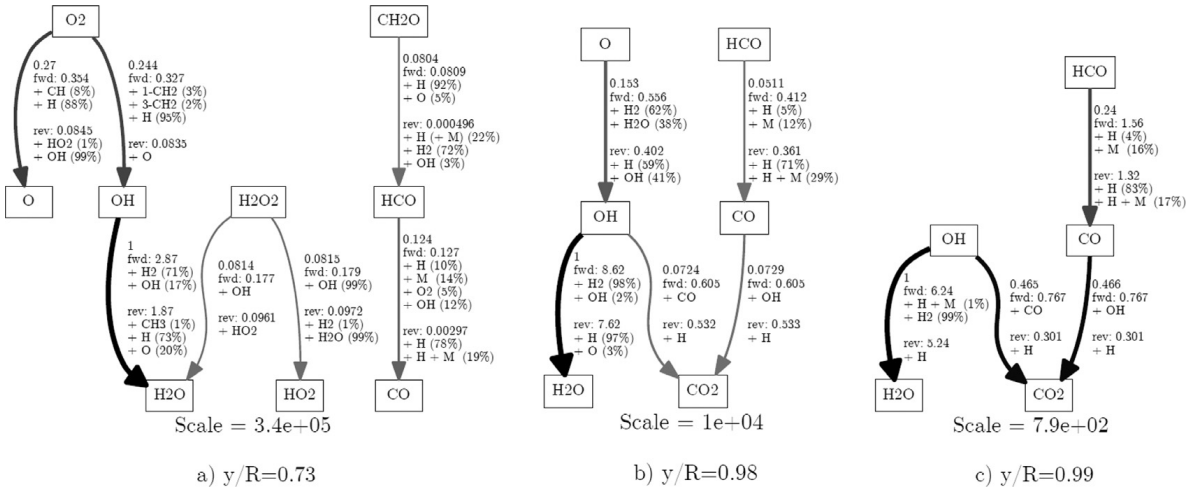

Fig. 9. Reaction path diagram at different radial locations at $x = 250$ mm. The normalized net, forward and backward atomic flux rates for the oxygen atom are included along the connecting arrows.

the recombination reactions are becoming more pronounced with increasing axial distance. This is confirmed by the large enthalpy defect at $x = 250$ mm compared to $x = 150$ mm and a resulting large degree of scattering for the CO_2 and CO mass fraction in Fig. 7. On the contrary, in the frozen model, the species mass fractions are unaffected by the low-enthalpy environment, as the scatter plot in Fig. 8 indicates.

To understand the reactions leading to the CO recombination a reaction path diagram for the oxygen atom in the non-adiabatic FPV model is performed. Results for this analysis are illustrated in Fig. 9 at three different distances from the wall for $x = 250$ mm. Before the onset of the species boundary layer ($y/R = 0.73$), the mixture is still reacting, mainly forming H_2O and CO as well as some radicals due to the high temperature combustion environment. In contrast at $y/R = 0.98$ and $y/R = 0.99$, the conversion of the previously formed CO to CO_2 and the recombination of OH to H_2O become dominant. Based on the normalized reaction rates shown in the flux diagram of Fig. 9, the reactions mainly responsible for the recombination reactions are $OH + CO \rightleftharpoons CO_2 + H$ and $H_2 + OH \rightleftharpoons H + H_2O$. As both of these reactions are exothermic, this results in a net energy release in the boundary layer, which increases the wall heat loads.

The net effect of these exothermic reactions is quantified in Fig. 11 showing a comparison of pressure and heat flux profiles from the two models along with experimental measurements [20,21]. Results from the non-adiabatic FPVA model are in good agreement with measurements. The absolute pressure level is correctly predicted with a value of approximately 18.75 bar close to the face-plate and 18 bar at the end of the combustion chamber. Apart from the absolute level, the pressure drop, which is an indicator of the acceleration and hence energy release in the combustion zone, demonstrates a satisfactory agreement with the measurements.

Within the first 30 mm from the face-plate, simulations and experiment show an increase in pressure. This is a result of the recirculation zone formed in the vicinity of the injector, feeding fuel-rich mixture directly towards the liner. After the location of peak pressure, the reduction in pressure is associated with an acceleration of the flow due to the exothermic combustion reactions. The slope of this pressure drop appears to flatten at $x \approx 200$ mm. This flattening of the pressure profile indicates a slower acceleration, and therefore a reduced heat release that characterizes the end of combustion. The location at which the change in slope occurs is in agreement with the experimentally obtained results.

The location where the chemical conversion is completed can also be inferred from the heat flux profile. Specifically, at $x = 200$ mm the maximum heat flux is observed. Subsequently for positions further downstream, the hot combustion products are cooled and the thermal boundary layer broadens, leading to a reduction in the wall heat transfer rate. Both the location and the value of the maximum heat flux (~ 7 MW/m^2) are within the experimental uncertainties.

The recirculation zone also impacts the wall heat flux values and is characterized by an increase in the local heat transfer rate at the stagnation point. After that, the heat load increases steadily before reaching the aforementioned maximum at the end of the combustion zone. Although the frozen results demonstrate a similar axial evolution of the heat flux, the absolute level is underestimated by 15%. This can be interpreted as a direct effect of the heat release resulting from the recombination reactions at the wall.

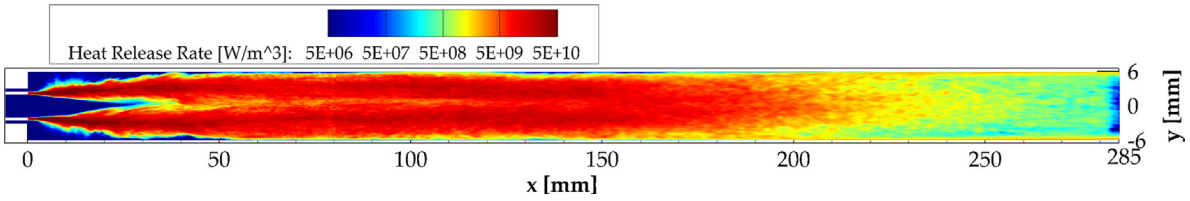

Fig. 10. Heat release rate in the combustion chamber.

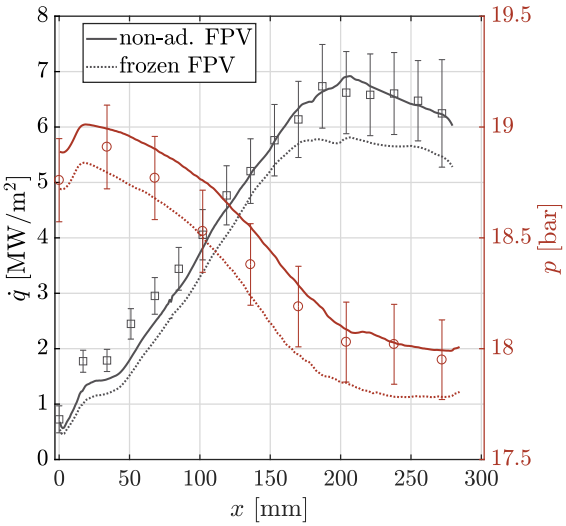

Fig. 11. Comparison of simulation results with measurements for azimuthally averaged wall heat transfer and pressure profiles.

A direct confirmation of the fact that the end of combustion occurs at approximately $x = 200$ mm is provided by the heat release rate in Fig. 10. Specifically, the bulk of the heat release appears to be taking place within the shear layer downstream of the coaxial injector. At locations further downstream, where the mixing and the combustion is completed, a gradual reduction in the heat release is observed. This decrease in the heat release is most prominent for axial locations larger than 200 mm and coincides with the experimental heat flux and pressure measurements. It is important to note that in regions where the gas is homogeneously mixed and the bulk energy release is completed, the recombination reaction in the boundary layer zone remain appreciable. In fact due to the continuing exothermic recombination reactions close to the wall, additional heat is released, thereby directly affecting the wall heat load.

4. Conclusions

A non-adiabatic flamelet model is utilized for the simulation of a methane/oxygen sub-scale rocket combustor. Comparisons with experimental results show a good agreement for both the heat flux and the pressure profiles. Simulation results are analyzed to examine the impact of CO recombination on heat flux and combustion performance.

In the low-enthalpy environment of the boundary layer the hot products recombine to form CO_2 and H_2O. These recombination reactions are exothermic and can noticeably increase the wall heat loads. By comparing the results with simulations employing frozen chemistry, it is shown that the overall contribution of the recombination to the total heat release amounts to approximately 15%. The critical reaction pathways are identified, showing that OH + CO $\rightleftharpoons$ CO_2 + H and H2 + OH $\rightleftharpoons$ H + H_2O are the main pathways.

These results illustrate the relevance of considering finite-rate chemistry and recombination reactions for the prediction of CH_4/O_2 rocket combustion. The insights given by the non-adiabatic model motivate more detailed investigations of the chemical pathways and time-scales of the reacting boundary layer in sub-scale hydrocarbon engines using DNS and finite-rate chemistry. Moreover, further analysis of the turbulent boundary-layer structure and vortex-dynamics is needed as it pertains to modeling needs for WMLES.

Declaration of Competing Interest

The authors declare that they have no known competing financial interests or personal relationships that could have appeared to influence the work reported in this paper.

Acknowledgements

The authors gratefully acknowledge the Gauss Centre for Supercomputing e.V. for providing computing time on the supercomputer SuperMUC at Leibniz Supercomputing Centre. Financial support has been provided by the Bavaria California Technology Center and the German Research Foundation (DFG) in the framework of the SFB TRR40. MI acknowledges support through AFOSR (Award No. FA9300-19P-1502) and NASA (Award No. NNX17CS15P).

References

[1] J.C. Melcher, R.L. Morehead, *AIAA Paper* (2014), doi:10.2514/6.2014-3681.
[2] A. Iannetti, N. Girard, N. Ravier, E. Edeline, D. Tchou-Kien, *AIAA Paper* (2017), doi:10.2514/6.2017-4750.
[3] M. Rudnykh, S. Carapellese, D. Liuzzi, et al., *Acta Astronaut.* 126 (2016) 364–374.
[4] O.J. Haidn, Advances on Propulsion Technology for High-Speed Aircraft, vol. 1, Research and Technology Organisation - North Atlantic Treaty Organisation, 2008, pp. 1–6.
[5] D. Preclik, G. Hagemann, O. Knab, L. Brummer, C. Mading, D. Wiedmann, P. Vuillermoz, 2005.
[6] J.C. Oefelein, V. Yang, *J. Propul. Power* 14 (5) (1998) 843–857, doi:10.2514/2.5349.
[7] V.P. Zhukov, *J. Propul. Power* 31 (6) (2015) 1707–1714, doi:10.2514/1.B35654.
[8] G.P. Sutton, O. Biblarz, *Rocket Propulsion Elements*, John Wiley & Sons, 2016.
[9] J. Riccius, O. Haidn, E. Zametaev, *AIAA Paper* (2004), doi:10.2514/6.2004-3670.
[10] F. Hötte, T. Fiedler, M.C. Haupt, P. Lungu, C.V. Sethe, O.J. Haidn, *J. Propul. Power* 35 (5) (2019) 1–11, doi:10.2514/1.B37439.
[11] R. Schuff, M. Maier, O. Sindiy, Ulrich C., Fugger S., *AIAA Paper* (2006), doi:10.2514/6.2006-4534.
[12] O. Cabrit, F. Nicoud, *Phys. Fluids* 21 (5) (2009) 055108.
[13] B. Betti, D. Bianchi, F. Nasuti, E. Martelli, *AIAA J.* 54 (1) (2016) 1693–1703, doi:10.2514/1.J054606.
[14] P.C. Ma, H. Wu, M. Ihme, J.-P. Hickey, *AIAA J.* 56 (6) (2018) 2336–2349, doi:10.2514/1.J056539.
[15] P. Breda, M. Pfitzner, N. Perakis, O. Haidn, in: Proceedings of the EUCASS, 2019.
[16] N. Perakis, C. Roth, O.J. Haidn, in: Proceedings of the Space Propulsion Conference, 2018.
[17] J. Zips, C. Traxinger, M. Pfitzner, *Int. J. Heat Mass Transf.* 143 (2019) 118474.
[18] D. Maestro, B. Cuenot, L. Selle, *Flow Turbul. Combust.* 103 (2019) 1–32.
[19] S. Silvestri, M. Celano, O. Haidn, O. Knab, in: Proceedings of the EUCASS, 2015.
[20] S. Silvestri, M.P. Celano, C. Kirchberger, G. Schlieben, O. Haidn, O. Knab, *Trans. JPN Soc. Aeron. Space Sci.* 14 (30) (2016) 13–20.
[21] N. Perakis, O.J. Haidn, *Int. J. Heat Mass Transf.* 131 (2019) 150–166, doi:10.1016/j.ijheatmasstransfer.2018.11.048.
[22] S. Kawai, J. Larsson, *Phys. Fluids* 25 (1) (2013) 015105.
[23] F.A. Williams, *Combustion Theory*, CRC Press, 2018.
[24] P.C. Ma, Y. Lv, M. Ihme, *J. Comput. Phys.* 340 (2017) 330–357, doi:10.1016/j.jcp.2017.03.022.
[25] G.P. Smith, D.M. Golden, M. Frenklach, *GRI-Mech 3.0,* (2000). http://combustion.berkeley.edu/gri-mech/
[26] A. Vreman, *Phys. Fluids* 16 (10) (2004) 3670–3681, doi:10.1063/1.1785131.
[27] P. Danckwerts, *App. Sc. Res. Sec. A* 3 (4) (1952) 279–296, doi:10.1007/BF03184936.

Part IV

CONCLUSIONS

"Begin at the beginning," the King said very gravely,
"and go on till you come to the end: then stop."

— Lewis Carroll, Alice in Wonderland

7 CONCLUSIONS

Life is the art of drawing sufficient conclusions
from insufficient premises.

— Samuel Butler

In the present work, experimental and numerical methods for the evaluation and prediction of heat transfer and combustion processes in methane/oxygen rocket engines have been presented. The simultaneous advancement of more elaborate measurement techniques and improvement of numerical combustion models is necessary for an efficient engine design process. For that reason, the studies presented here are focused on sub-scale single-element and multi-element chambers that serve as validation benchmarks for full-scale configurations.

A key driver in the development of experimental methods for the evaluation of heat flux data in this thesis was the necessity for high computational efficiency and quantified measurement uncertainty. An inverse heat transfer method was introduced for that reason with the aim to be applied on various chamber configurations.

Specifically, an inversing algorithm based on an iterative least squares minimization was used. For an effective application, the inverse method requires thermocouple measurements at distinct locations within the chamber material. Methods providing heat flux values from wall temperature data have been successfully used in the past in rocket engine applications. The benefit of the current method is its computational speed even for three-dimensional heat flux profiles. The high-computational efficiency of the method was achieved by utilizing an iterative optimization with a pre-calculated sensitivity matrix. This Jacobian matrix describes the change in temperature that a wall heat flux deviation would produce at each measurement location. Given a robust sensitivity matrix and a heat flux update method such a conjugate gradient or Newton-Raphson method, a small number of iterations was required for convergence. Convergence was defined as the reduction of the difference between calculated and measured temperature values below a pre-defined threshold.

The method was applied for investigations of four sub-scale and one full-scale thrust chambers. Both capacitively and regeneratively cooled engines were analyzed. The main differences between the two configurations entail the fact that calculations of capacitive hardware involve transient heat transfer, whereas the actively cooled hardware requires additional modeling for the the heat transfer coefficient between coolant and wall. By opting for a Nusselt number correlation for the description of the cooling channels, satisfying accuracy was combined with low computational evaluation times. In a second step, the heat transfer coefficient in the cooling channels was introduced as a second unknown, which eased the need for modeling but required the use of a larger number of thermocouples.

It was found that the inverse method was able to capture effects related to the flow and energy release within the chamber that helped quantify the performance of the injection system. First, the effect of the fuel choice, pressure level and injection parameters like velocity and momentum flux ratio on the observed heat loads was established. Moreover, the interaction between neighboring flames for the multi-element configurations was

qualitatively inferred based on the obtained wall footprints. Finally, transient heat release and heat transfer effects related to the operation of the ignition system were measured. Precise knowledge of the high heat loads obtained during transient start-up of the engines as well as local heat flux variations in azimuthal variation due to the flame/flame interaction are vital for the accurate design of rocket engines and both those effects were properly captured by the inverse method.

As far as the reliability of the measurements is concerned, the systematic errors resulting from the inverse method were extensively quantified. The first type of error defined in the study, involved the intrinsic capability of the method to predict the correct wall heat flux and coolant heat transfer coefficients in the absence of other systematic hardware-related errors. It was found that the placement of the thermocouples closer to the wall significantly reduced the measurement bias, while at the same time a larger number of sensors favored the measurement, especially when a simultaneous optimization of $\dot{q}$ and h_{cc} was carried out. It was established that the bias introduced from the choice of the Nusselt number correlation also contributes largely to the uncertainty, when an insufficient number of sensors is installed. In the second type of error, effects related to the experimental setup where considered, such as uncertainties in the position and thermal contact of the thermocouples, material property uncertainties, sensor response time etc. The main contribution to the measurement uncertainty stems from the very large temperature gradients in the vicinity of the hot-gas wall that lead to a very high sensitivity. By adding all those effects, the total uncertainty of the measurement was estimated close to 9-12%.

Using measured data for the heat flux from different experimental chambers and operating points, a database has been built up that serves as a benchmark for validation of numerical models. The focus was then placed on the development of numerical models able to accurately describe the combustion and heat transfer phenomena within the combustion chamber. Special efforts were placed in trying to derive and apply models that are able to capture the effects of chemical recombinations in the boundary layer and which directly contribute to the enhancement of the wall heat transfer coefficient.

In the first step, the properties of the recombination reactions were investigated from a physical perspective. Canonical systems with increasing degree of complexity were employed ranging from 0D chemical equilibrium calculations to 3D DNS of reacting boundary layers. The key finding of this study was that the long time-scales of chemistry within the boundary layer lead to deviations from the chemical equilibrium composition in the CH_4/O_2 case in contrast to equivalent H_2/O_2 mixtures. It was found that the main reaction paths responsible for the heat release are the recombination of H_2 and OH to H and H_2O as well as the recombination of CO and OH to produce CO_2 and H_2O. The bulk of the energy is released at distances between $y^+ \approx 10$ and $y^+ \approx 100$ from the hot gas wall. For low wall temperatures (typical in regeneratively cooled walls) a second recombination mode was established. This included mainly the recombination of the HCO radical, and was prominent in the vicinity of the wall due to the absence of an activation energy. Despite the exothermic nature of those reactions, due to the small volume where they are activated, their net heat release only accounted for approximately 5% of the total.

Using the information obtained from the fundamental investigations, two proposed extensions of non-adiabatic flamelet models were evaluated in simulations of sub-scale rocket engines. In the first one, the steady flamelet model was extended by one additional dimension (enthalpy) in order to account for the presence of recombinations in low

temperature environments. Using the scalar dissipation as a measure of the deviation from chemical equilibrium was found to be unsuitable, as the scalar dissipation drops to zero close to the wall and hence forces the composition to its equilibrium value, overestimating the heat release and heat load. As an additional parameter that accounts for the deviation from the chemical equilibrium, the local Damköhler number was utilized. In regions where an enthalpy deficit is present but the chemical time-scales are slower than the diffusion and integral scales, a freezing of the reactions occurs, establishing a more realistic composition for the near-wall gas. Including the freezing of the reactions led to a very good prediction of the wall heat flux and pressure for a single-element chamber operating with methane. The model was found suitable for the simulation of hydrogen/oxygen engines as well, as it can cover a large range in chemical time-scales.

In the second model, a Flamelet Progress Variable approach was undertaken. Due to the fact that the FPV models solves an equation for the progress variable instead of using the algebraically computed scalar dissipation rate, it does not default to chemical equilibrium close to the wall. Hence, no extension including the effect of the Damköhler number is required. Instead, the use of a reduced enthalpy dimension in the flamelet manifolds was applied. The reduced enthalpy was parametrized with the help of the "wall mixture fraction", a variable indicating the location of a permeable isothermal wall in mixture fraction space. Using the model in LES led to a good agreement with the experimental data both for heat flux and pressure, demonstrating the superiority of this model compared to a frozen flamelet approach.

The flamelet approaches tested in this thesis are manifold-based models and exploit the topological structure of the flame. The flame structure is represented in terms of reaction-transport or mixing manifolds, which are obtained from the solution of representative flame configurations, namely laminar counterflow diffusion flames. The basic motivation behind the extensions presented in this work comes from the reduced dimensionality of flamelet models, which limits them in describing certain combustion processes. To accommodate additional phenomena, the reaction-transport manifolds were extended to consider effects of wall-heat losses. The benefit compared to topology-free combustion models (such as finite-rate models) is the computational speed-up which is proportional to the number of species considered. Despite the good agreement with macroscopic data that has been presented, the model extensions substantially increase the complexity, and deteriorate the accuracy in capturing the combustion behavior for which the original model was intended. In specific regions within domain of the task at hand, physical processes may occur which extend beyond the assumptions for which the models were formulated. As an outlook for this work, the use of frameworks for the dynamic utilization of different manifold representations to describe chemically reacting flows is put forward. Efforts like the Pareto-efficient combustion model that combine different manifold representations, could enable the general adaptation of combustion sub-models to the underlying flow-field representation within the thrust chamber and lead to an accurate description of the physical complexity. Those types of frameworks could be extended to incorporate flame-wall interaction but also other phenomena such as auto-ignition, real-gas effects and soot formation, while still having a lower computational requirement than brute-force approaches.

Part V

APPENDIX

A

CHEMICAL REACTION MECHANISM VALIDATION

In the zero- and one-dimensional test cases presented in Chapter 5, the GRI-3.0 reaction mechanism [322] was used. This chemical mechanism was not initially developed for large pressures and fuel-rich mixtures and therefore validating its predictions using a more detailed mechanism as reference is important.

Previous works in literature have evaluated the prediction agreement of GRI-3.0 compared to experimental data and more detailed mechanisms [328]. Those works have also dealt with high-pressure and fuel-rich conditions similar to the ones that are relevant for rocket propulsion applications. However, the studies have been typically limited to laminar flame speed calculations and ignition delay time estimations.

In order to extend this analysis to the applications shown in Chapter 5, an abruptly cooled, ideal isothermal reactor and a stagnation flow are re-calculated with a more detailed chemical mechanism which serves as the baseline data. Chemical equilibrium calculations are not shown, as both mechanisms deliver identical results. This is due to the inclusion of all major combustion products in both of the mechanisms.

For this comparison, the detailed mechanism by Zhukov et al. [329] is chosen. This consists of 207 species and 2329 reactions and includes hydrocarbon chemistry ranging from C1 to C7, while it has been validated for a large pressure regime.

A.1 ISOTHERMAL REACTOR

The performance of the GRI-3.0 was tested for different operating points, but in this section the 20 bar isothermal, isobaric ideal reactor with $T_w = 1000\,\mathrm{K}$ is presented. This corresponds to the results shown in Figure 5.6.

A satisfying agreement is found between the two mechanisms. The operating point with the largest discrepancy is the low-O/F case ($OF = 1.5$). In fact however, it is the Zhukov mechanism that does not reach the equilibrium solution with the same accuracy as the GRI-3.0 does (5% deviation in the final CO composition). This is attributed to a poor convergence in Cantera due to the size of the mechanism.

A.2 STAGNATION FLOW

A similarly satisfying agreement is found when comparing the species profiles in the axisymmetric stagnation flow simulation for both chemical mechanisms. The results for major and minor species are shown in Figure A.2 and Figure A.3 ($O/F = 3.0$) as well as Figure A.4 and Figure A.5 ($O/F = 1.5$).

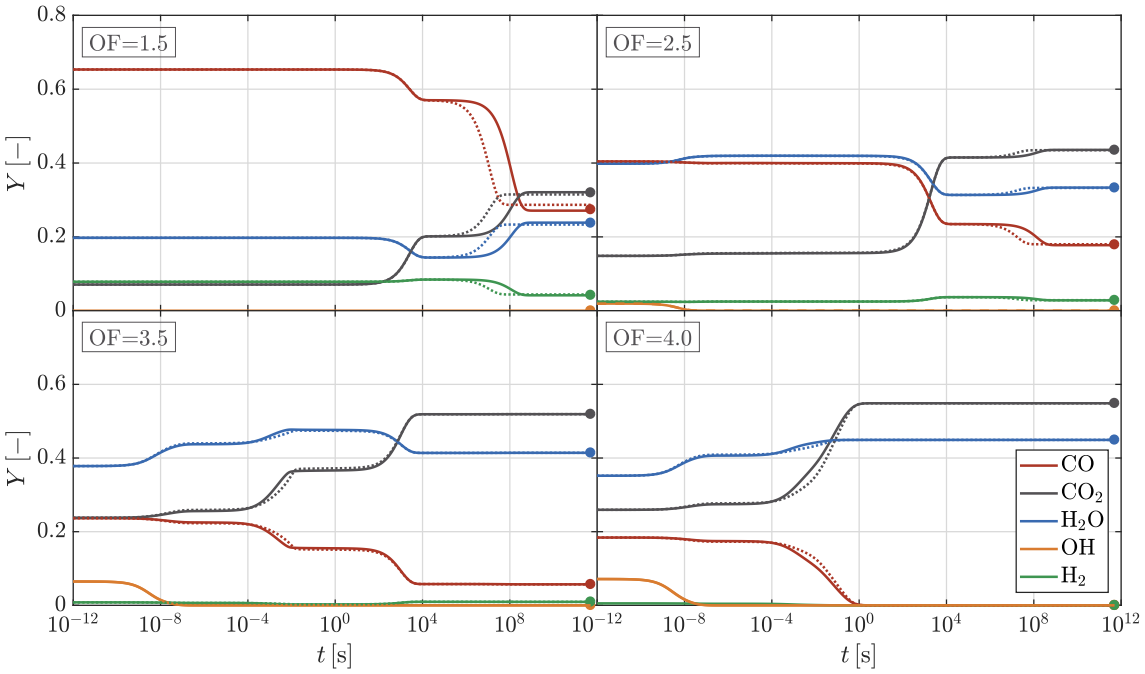

Figure A.1: Species mass fraction in the ideal isothermal reactor simulation using the Zhukov et al. mechanism [329] with the dotted line (·····) and the GRI-3.0 mechanism [322] with the solid line (——). The chosen operating point corresponds to a CH_4/O_2 mixture, $T_w = 1000\,\mathrm{K}$ and 20 bar pressure.

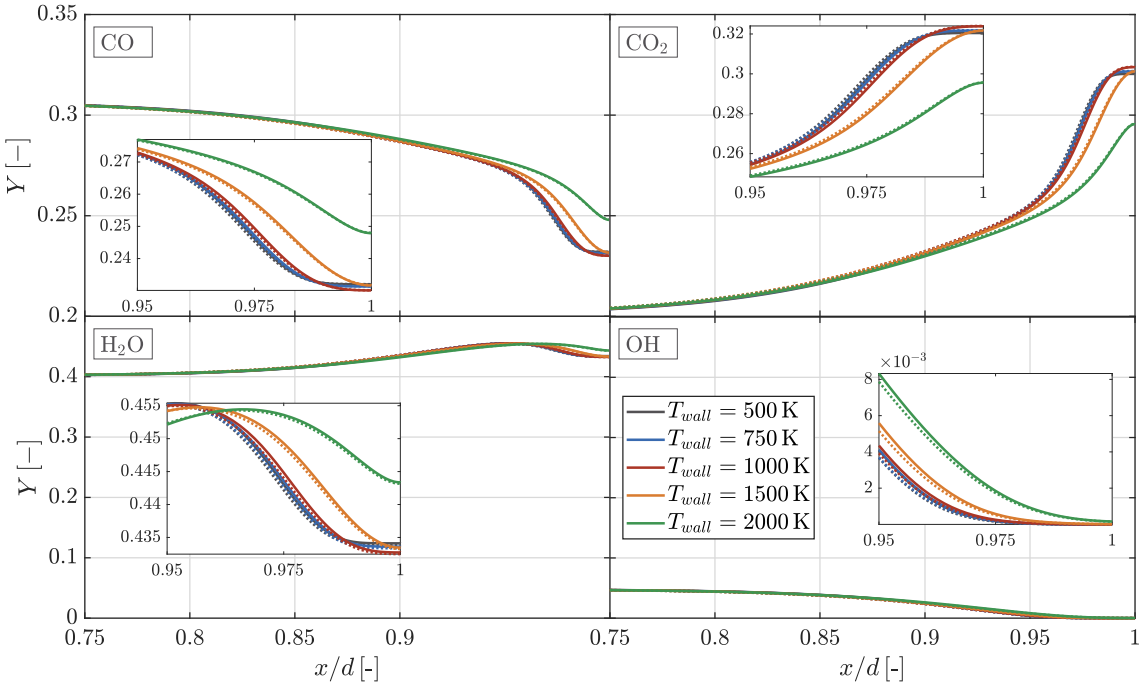

Figure A.2: Major species mass fraction in the stagnation flow simulation using the Zhukov et al. mechanism [329] with the dotted line (·····) and the GRI-3.0 mechanism [322] with the solid line (——). The chosen operating point corresponds to a CH_4/O_2 mixture, $O/F = 3.0$ and 20 bar pressure.

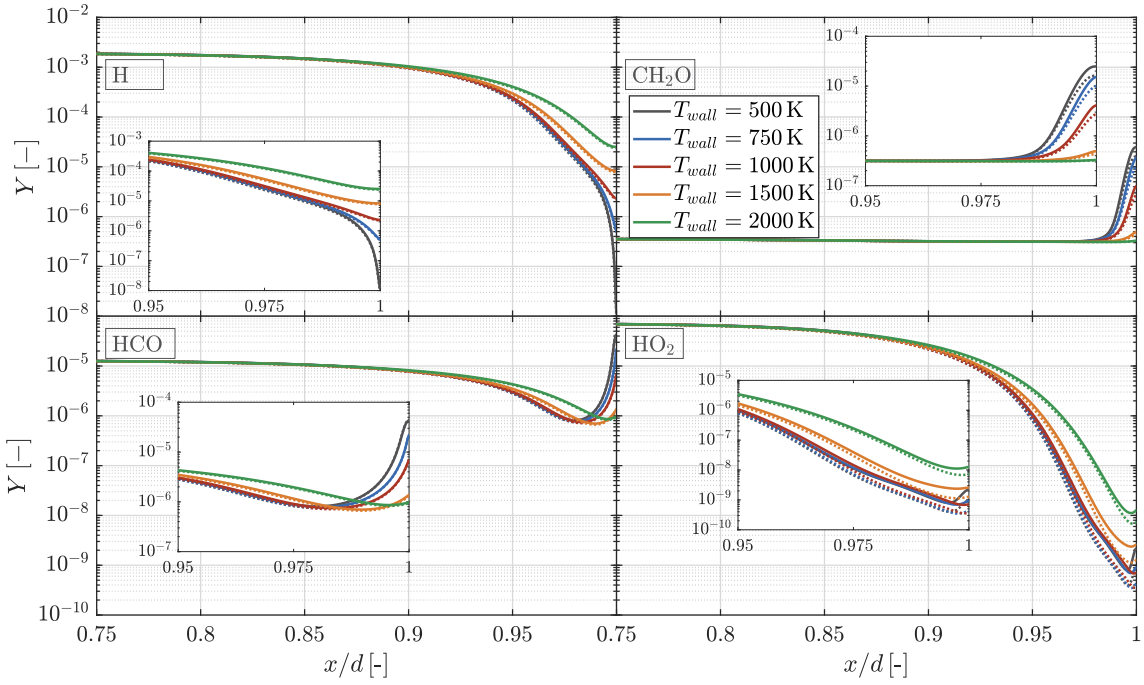

Figure A.3: Minor species mass fraction in the stagnation flow simulation using the Zhukov et al. mechanism [329] with the dotted line (·····) and the GRI-3.0 mechanism [322] with the solid line (——). The chosen operating point corresponds to a CH_4/O_2 mixture, $O/F = 3.0$ and 20 bar pressure.

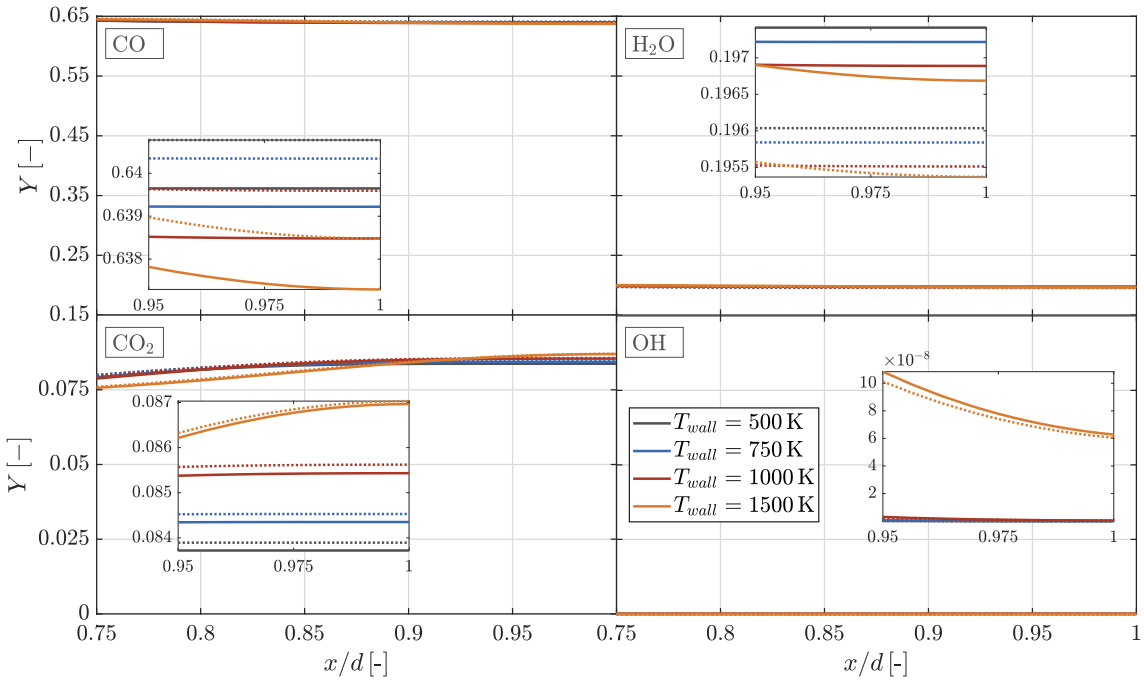

Figure A.4: Major species mass fraction in the stagnation flow simulation using the Zhukov et al. mechanism [329] with the dotted line (·····) and the GRI-3.0 mechanism [322] with the solid line (——). The chosen operating point corresponds to a CH_4/O_2 mixture, $O/F = 1.5$ and 20 bar pressure.

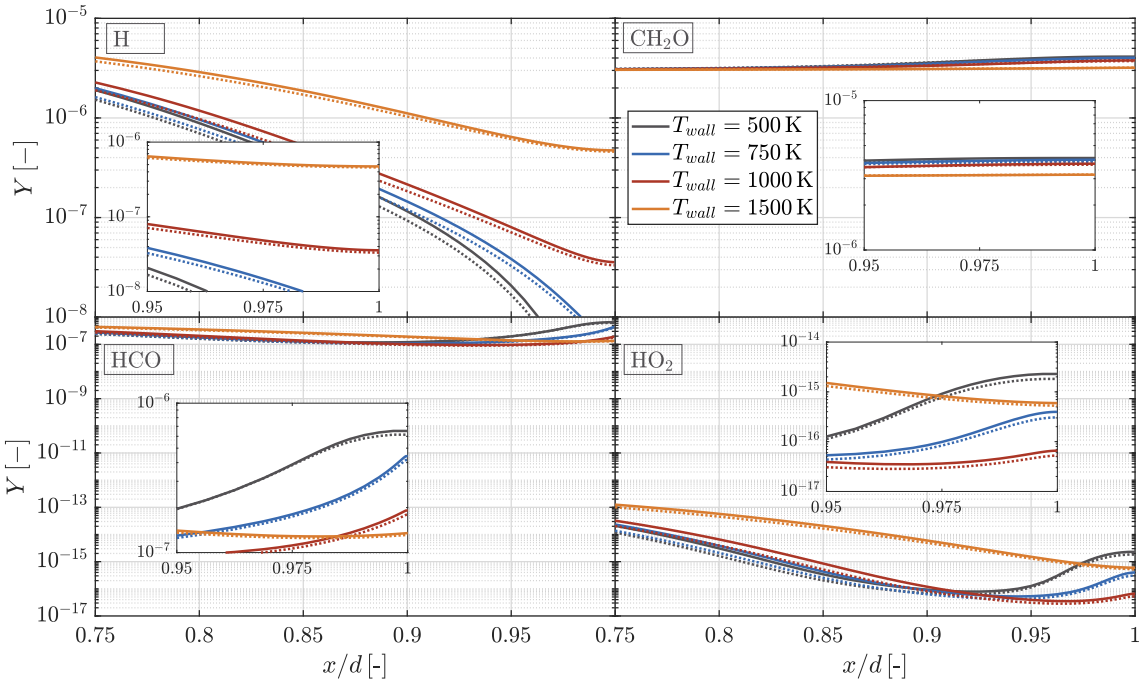

Figure A.5: Minor species mass fraction in the stagnation flow simulation using the Zhukov et al. mechanism [329] with the dotted line (·····) and the GRI-3.0 mechanism [322] with the solid line (——). The chosen operating point corresponds to a CH_4/O_2 mixture, $O/F = 1.5$ and 20 bar pressure.

B

CONTENT REUSE LICENSES

B.1 ELSEVIER

According to the Elsevier copyright agreement, "authors can use their articles, in full or in part, for a wide range of scholarly, non-commercial purposes". Amongst the listed of acceptable purposes, Elsevier's agreement states that the "inclusion in a thesis or dissertation (provided that this is not to be published commercially)" does not violate the agreement.

A detailed description of the conditions can be found in the following link:
https://www.elsevier.com/about/policies/copyright#personaluse

B.2 AMERICAN INSTITUTE OF AERONAUTICS AND ASTRONAUTICS

Copyright Clearance Center Marketplace™

American Inst of Aeronautics & Astronautics (AIAA) - License Terms and Conditions

This is a License Agreement between Nikolaos Perakis ("You") and American Inst of Aeronautics & Astronautics (AIAA) ("Publisher") provided by Copyright Clearance Center ("CCC"). The license consists of your order details, the terms and conditions provided by American Inst of Aeronautics & Astronautics (AIAA), and the CCC terms and conditions.

All payments must be made in full to CCC.

Order Date	26-May-2020	**Type of Use**	Republish in a thesis/dissertation
Order license ID	1037345-1		
ISSN	1533-3876	**Publisher**	AMERICAN INSTITUTE OF AERONAUTICS AND ASTRONAUTICS, INC.
		Portion	Chapter/article

LICENSED CONTENT

Publication Title	Journal of propulsion and power	**Country**	United States of America
Author/Editor	American Institute of Aeronautics and Astronautics.	**Rightsholder**	American Inst of Aeronautics & Astronautics (AIAA)
		Publication Type	e-Journal
Date	01/01/1985	**URL**	http://www.catchword.com/rpsv/catchword/aiaa/07484658/contp1-1.htm
Language	English		

REQUEST DETAILS

Portion Type	Chapter/article	**Rights Requested**	Main product
Page range(s)	1-18	**Distribution**	Worldwide
Total number of pages	18	**Translation**	Original language of publication
Format (select all that apply)	Print, Electronic	**Copies for the disabled?**	No
Who will republish the content?	Academic institution	**Minor editing privileges?**	No
		Incidental promotional use?	No
Duration of Use	Life of current and all future editions	**Currency**	EUR
Lifetime Unit Quantity	Up to 999		

NEW WORK DETAILS

Title	Wall Heat Transfer Measurement and Prediction in Methane/Oxygen Rocket Engines	**Institution name**	Technical University of Munich
		Expected presentation date	2020-12-01
Instructor name	Prof. Dr.-Ing. Oskar Haidn		

ADDITIONAL DETAILS

Order reference number	N/A

The requesting person / organization to appear on the license	Nikolaos Perakis

REUSE CONTENT DETAILS

Title, description or numeric reference of the portion(s)	Heat Transfer and Combustion Simulation of Seven-Element O2/CH4 Rocket Combustor	**Title of the article/chapter the portion is from**	Heat Transfer and Combustion Simulation of Seven-Element O2/CH4 Rocket Combustor
Editor of portion(s)	Venkat Raman	**Author of portion(s)**	American Institute of Aeronautics and Astronautics.
Volume of serial or monograph	35		
Page or page range of portion	1080-1097	**Issue, if republishing an article from a serial**	N/A
		Publication date of portion	2019-08-22

PUBLISHER TERMS AND CONDITIONS

Verification of copyright ownership is your responsibility. You should only submit requests for materials that are owned by AIAA. Please review the copyright statement for the source material before submitting a reprint permission request, to ensure that AIAA is the copyright owner: For AIAA meeting papers, journal papers, or books with independently authored chapters (e.g., many Progress Series volumes), look at the bottom of the first full-text page (not the cover page). There will be a footnote indicating who holds copyright. For other books, look at the copyright statement on the back of the title page. If the statement reads "Copyright by the American Institute of Aeronautics and Astronautics, Inc.," then AIAA is the copyright owner, and you may submit your request. If the statement reads otherwise, AIAA does not hold copyright, and cannot grant permission to reprint. You must seek permission from the copyright owner rather than AIAA. Preferred credit line for reprinted material: From [original title and authors]; reprinted by permission of the American Institute of Aeronautics and Astronautics, Inc. Note that the original source also should be cited in full in the reference list.

CCC Republication Terms and Conditions

1. Description of Service; Defined Terms. This Republication License enables the User to obtain licenses for republication of one or more copyrighted works as described in detail on the relevant Order Confirmation (the "Work(s)"). Copyright Clearance Center, Inc. ("CCC") grants licenses through the Service on behalf of the rightsholder identified on the Order Confirmation (the "Rightsholder"). "Republication", as used herein, generally means the inclusion of a Work, in whole or in part, in a new work or works, also as described on the Order Confirmation. "User", as used herein, means the person or entity making such republication.

2. The terms set forth in the relevant Order Confirmation, and any terms set by the Rightsholder with respect to a particular Work, govern the terms of use of Works in connection with the Service. By using the Service, the person transacting for a republication license on behalf of the User represents and warrants that he/she/it (a) has been duly authorized by the User to accept, and hereby does accept, all such terms and conditions on behalf of User, and (b) shall inform User of all such terms and conditions. In the event such person is a "freelancer" or other third party independent of User and CCC, such party shall be deemed jointly a "User" for purposes of these terms and conditions. In any event, User shall be deemed to have accepted and agreed to all such terms and conditions if User republishes the Work in any fashion.

3. Scope of License; Limitations and Obligations.

    3.1. All Works and all rights therein, including copyright rights, remain the sole and exclusive property of the Rightsholder. The license created by the exchange of an Order Confirmation (and/or any invoice) and payment by User of the full amount set forth on that document includes only those rights expressly set forth in the Order Confirmation and in these terms and conditions, and conveys no other rights in the Work(s) to User. All rights not expressly granted are hereby reserved.

    3.2. General Payment Terms: You may pay by credit card or through an account with us payable at the end of the month. If you and we agree that you may establish a standing account with CCC, then the following terms apply: Remit Payment to: Copyright Clearance Center, 29118 Network Place, Chicago, IL 60673-1291. Payments Due: Invoices are payable upon their delivery to you (or upon our notice to you that they are available to you for downloading). After 30 days, outstanding amounts will be subject to a service charge

of 1-1/2% per month or, if less, the maximum rate allowed by applicable law. Unless otherwise specifically set forth in the Order Confirmation or in a separate written agreement signed by CCC, invoices are due and payable on "net 30" terms. While User may exercise the rights licensed immediately upon issuance of the Order Confirmation, the license is automatically revoked and is null and void, as if it had never been issued, if complete payment for the license is not received on a timely basis either from User directly or through a payment agent, such as a credit card company.

3.3. Unless otherwise provided in the Order Confirmation, any grant of rights to User (i) is "one-time" (including the editions and product family specified in the license), (ii) is non-exclusive and non-transferable and (iii) is subject to any and all limitations and restrictions (such as, but not limited to, limitations on duration of use or circulation) included in the Order Confirmation or invoice and/or in these terms and conditions. Upon completion of the licensed use, User shall either secure a new permission for further use of the Work(s) or immediately cease any new use of the Work(s) and shall render inaccessible (such as by deleting or by removing or severing links or other locators) any further copies of the Work (except for copies printed on paper in accordance with this license and still in User's stock at the end of such period).

3.4. In the event that the material for which a republication license is sought includes third party materials (such as photographs, illustrations, graphs, inserts and similar materials) which are identified in such material as having been used by permission, User is responsible for identifying, and seeking separate licenses (under this Service or otherwise) for, any of such third party materials; without a separate license, such third party materials may not be used.

3.5. Use of proper copyright notice for a Work is required as a condition of any license granted under the Service. Unless otherwise provided in the Order Confirmation, a proper copyright notice will read substantially as follows: "Republished with permission of [Rightsholder's name], from [Work's title, author, volume, edition number and year of copyright]; permission conveyed through Copyright Clearance Center, Inc. " Such notice must be provided in a reasonably legible font size and must be placed either immediately adjacent to the Work as used (for example, as part of a by-line or footnote but not as a separate electronic link) or in the place where substantially all other credits or notices for the new work containing the republished Work are located. Failure to include the required notice results in loss to the Rightsholder and CCC, and the User shall be liable to pay liquidated damages for each such failure equal to twice the use fee specified in the Order Confirmation, in addition to the use fee itself and any other fees and charges specified.

3.6. User may only make alterations to the Work if and as expressly set forth in the Order Confirmation. No Work may be used in any way that is defamatory, violates the rights of third parties (including such third parties' rights of copyright, privacy, publicity, or other tangible or intangible property), or is otherwise illegal, sexually explicit or obscene. In addition, User may not conjoin a Work with any other material that may result in damage to the reputation of the Rightsholder. User agrees to inform CCC if it becomes aware of any infringement of any rights in a Work and to cooperate with any reasonable request of CCC or the Rightsholder in connection therewith.

4. Indemnity. User hereby indemnifies and agrees to defend the Rightsholder and CCC, and their respective employees and directors, against all claims, liability, damages, costs and expenses, including legal fees and expenses, arising out of any use of a Work beyond the scope of the rights granted herein, or any use of a Work which has been altered in any unauthorized way by User, including claims of defamation or infringement of rights of copyright, publicity, privacy or other tangible or intangible property.

5. Limitation of Liability. UNDER NO CIRCUMSTANCES WILL CCC OR THE RIGHTSHOLDER BE LIABLE FOR ANY DIRECT, INDIRECT, CONSEQUENTIAL OR INCIDENTAL DAMAGES (INCLUDING WITHOUT LIMITATION DAMAGES FOR LOSS OF BUSINESS PROFITS OR INFORMATION, OR FOR BUSINESS INTERRUPTION) ARISING OUT OF THE USE OR INABILITY TO USE A WORK, EVEN IF ONE OF THEM HAS BEEN ADVISED OF THE POSSIBILITY OF SUCH DAMAGES. In any event, the total liability of the Rightsholder and CCC (including their respective employees and directors) shall not exceed the total amount actually paid by User for this license. User assumes full liability for the actions and omissions of its principals, employees, agents, affiliates, successors and assigns.

6. Limited Warranties. THE WORK(S) AND RIGHT(S) ARE PROVIDED "AS IS". CCC HAS THE RIGHT TO GRANT TO USER THE RIGHTS GRANTED IN THE ORDER CONFIRMATION DOCUMENT. CCC AND THE RIGHTSHOLDER DISCLAIM ALL OTHER WARRANTIES RELATING TO THE WORK(S) AND RIGHT(S), EITHER EXPRESS OR IMPLIED, INCLUDING WITHOUT LIMITATION IMPLIED WARRANTIES OF MERCHANTABILITY OR FITNESS FOR A PARTICULAR PURPOSE. ADDITIONAL RIGHTS MAY BE REQUIRED TO USE ILLUSTRATIONS, GRAPHS, PHOTOGRAPHS, ABSTRACTS, INSERTS

OR OTHER PORTIONS OF THE WORK (AS OPPOSED TO THE ENTIRE WORK) IN A MANNER CONTEMPLATED BY USER; USER UNDERSTANDS AND AGREES THAT NEITHER CCC NOR THE RIGHTSHOLDER MAY HAVE SUCH ADDITIONAL RIGHTS TO GRANT.

7. Effect of Breach. Any failure by User to pay any amount when due, or any use by User of a Work beyond the scope of the license set forth in the Order Confirmation and/or these terms and conditions, shall be a material breach of the license created by the Order Confirmation and these terms and conditions. Any breach not cured within 30 days of written notice thereof shall result in immediate termination of such license without further notice. Any unauthorized (but licensable) use of a Work that is terminated immediately upon notice thereof may be liquidated by payment of the Rightsholder's ordinary license price therefor; any unauthorized (and unlicensable) use that is not terminated immediately for any reason (including, for example, because materials containing the Work cannot reasonably be recalled) will be subject to all remedies available at law or in equity, but in no event to a payment of less than three times the Rightsholder's ordinary license price for the most closely analogous licensable use plus Rightsholder's and/or CCC's costs and expenses incurred in collecting such payment.

8. Miscellaneous.

    8.1. User acknowledges that CCC may, from time to time, make changes or additions to the Service or to these terms and conditions, and CCC reserves the right to send notice to the User by electronic mail or otherwise for the purposes of notifying User of such changes or additions; provided that any such changes or additions shall not apply to permissions already secured and paid for.

    8.2. Use of User-related information collected through the Service is governed by CCC's privacy policy, available online here:https://marketplace.copyright.com/rs-ui-web/mp/privacy-policy

    8.3. The licensing transaction described in the Order Confirmation is personal to User. Therefore, User may not assign or transfer to any other person (whether a natural person or an organization of any kind) the license created by the Order Confirmation and these terms and conditions or any rights granted hereunder; provided, however, that User may assign such license in its entirety on written notice to CCC in the event of a transfer of all or substantially all of User's rights in the new material which includes the Work(s) licensed under this Service.

    8.4. No amendment or waiver of any terms is binding unless set forth in writing and signed by the parties. The Rightsholder and CCC hereby object to any terms contained in any writing prepared by the User or its principals, employees, agents or affiliates and purporting to govern or otherwise relate to the licensing transaction described in the Order Confirmation, which terms are in any way inconsistent with any terms set forth in the Order Confirmation and/or in these terms and conditions or CCC's standard operating procedures, whether such writing is prepared prior to, simultaneously with or subsequent to the Order Confirmation, and whether such writing appears on a copy of the Order Confirmation or in a separate instrument.

    8.5. The licensing transaction described in the Order Confirmation document shall be governed by and construed under the law of the State of New York, USA, without regard to the principles thereof of conflicts of law. Any case, controversy, suit, action, or proceeding arising out of, in connection with, or related to such licensing transaction shall be brought, at CCC's sole discretion, in any federal or state court located in the County of New York, State of New York, USA, or in any federal or state court whose geographical jurisdiction covers the location of the Rightsholder set forth in the Order Confirmation. The parties expressly submit to the personal jurisdiction and venue of each such federal or state court.If you have any comments or questions about the Service or Copyright Clearance Center, please contact us at 978-750-8400 or send an e-mail to support@copyright.com.

v 1.1

Copyright Clearance Center Marketplace™

American Inst of Aeronautics & Astronautics (AIAA) - License Terms and Conditions

This is a License Agreement between Nikolaos Perakis ("You") and American Inst of Aeronautics & Astronautics (AIAA) ("Publisher") provided by Copyright Clearance Center ("CCC"). The license consists of your order details, the terms and conditions provided by American Inst of Aeronautics & Astronautics (AIAA), and the CCC terms and conditions.

All payments must be made in full to CCC.

Order Date	01-Oct-2020	**Type of Use**	Republish in a thesis/dissertation
Order license ID	1067220-1		
ISSN	0887-8722	**Publisher**	AMERICAN INSTITUTE OF AERONAUTICS AND ASTRONAUTICS
		Portion	Chapter/article

LICENSED CONTENT

Publication Title	Journal of thermophysics and heat transfer	**Country**	United States of America
		Rightsholder	American Inst of Aeronautics & Astronautics (AIAA)
Author/Editor	AMERICAN INSTITUTE OF AERONAUTICS AND ASTRONAUTICS		
		Publication Type	Journal
Date	01/01/1987		
Language	English		

REQUEST DETAILS

Portion Type	Chapter/article	**Rights Requested**	Main product
Page range(s)	1-17	**Distribution**	Worldwide
Total number of pages	17	**Translation**	Original language of publication
Format (select all that apply)	Print, Electronic	**Copies for the disabled?**	No
Who will republish the content?	Academic institution	**Minor editing privileges?**	No
		Incidental promotional use?	No
Duration of Use	Life of current and all future editions	**Currency**	EUR
Lifetime Unit Quantity	Up to 999		

NEW WORK DETAILS

Title	Wall Heat Transfer Measurement and Prediction in Methane/Oxygen Rocket Engines	**Institution name**	Technical University of Munich
		Expected presentation date	2020-12-01
Instructor name	Prof. Dr.-Ing. Oskar Haidn		

ADDITIONAL DETAILS

Order reference number	N/A	**The requesting person / organization to appear on the license**	Nikolaos Perakis

REUSE CONTENT DETAILS

Title, description or numeric reference of the portion(s)	Wall Heat Flux Evaluation in Regeneratively Cooled Rocket Thrust Chambers	**Title of the article/chapter the portion is from**	Wall Heat Flux Evaluation in Regeneratively Cooled Rocket Thrust Chambers
Editor of portion(s)	N/A	**Author of portion(s)**	AMERICAN INSTITUTE OF AERONAUTICS AND ASTRONAUTICS
Volume of serial or monograph	N/A		
Page or page range of portion	1-17	**Issue, if republishing an article from a serial**	N/A
		Publication date of portion	2020-10-01

PUBLISHER TERMS AND CONDITIONS

Verification of copyright ownership is your responsibility. You should only submit requests for materials that are owned by AIAA. Please review the copyright statement for the source material before submitting a reprint permission request, to ensure that AIAA is the copyright owner: For AIAA meeting papers, journal papers, or books with independently authored chapters (e.g., many Progress Series volumes), look at the bottom of the first full-text page (not the cover page). There will be a footnote indicating who holds copyright. For other books, look at the copyright statement on the back of the title page. If the statement reads "Copyright by the American Institute of Aeronautics and Astronautics, Inc.," then AIAA is the copyright owner, and you may submit your request. If the statement reads otherwise, AIAA does not hold copyright, and cannot grant permission to reprint. You must seek permission from the copyright owner rather than AIAA. Preferred credit line for reprinted material: From [original title and authors]; reprinted by permission of the American Institute of Aeronautics and Astronautics, Inc. Note that the original source also should be cited in full in the reference list.

CCC Republication Terms and Conditions

1. Description of Service; Defined Terms. This Republication License enables the User to obtain licenses for republication of one or more copyrighted works as described in detail on the relevant Order Confirmation (the "Work(s)"). Copyright Clearance Center, Inc. ("CCC") grants licenses through the Service on behalf of the rightsholder identified on the Order Confirmation (the "Rightsholder"). "Republication", as used herein, generally means the inclusion of a Work, in whole or in part, in a new work or works, also as described on the Order Confirmation. "User", as used herein, means the person or entity making such republication.

2. The terms set forth in the relevant Order Confirmation, and any terms set by the Rightsholder with respect to a particular Work, govern the terms of use of Works in connection with the Service. By using the Service, the person transacting for a republication license on behalf of the User represents and warrants that he/she/it (a) has been duly authorized by the User to accept, and hereby does accept, all such terms and conditions on behalf of User, and (b) shall inform User of all such terms and conditions. In the event such person is a "freelancer" or other third party independent of User and CCC, such party shall be deemed jointly a "User" for purposes of these terms and conditions. In any event, User shall be deemed to have accepted and agreed to all such terms and conditions if User republishes the Work in any fashion.

3. Scope of License; Limitations and Obligations.

    3.1. All Works and all rights therein, including copyright rights, remain the sole and exclusive property of the Rightsholder. The license created by the exchange of an Order Confirmation (and/or any invoice) and payment by User of the full amount set forth on that document includes only those rights expressly set forth in the Order Confirmation and in these terms and conditions, and conveys no other rights in the Work(s) to User. All rights not expressly granted are hereby reserved.

    3.2. General Payment Terms: You may pay by credit card or through an account with us payable at the end of the month. If you and we agree that you may establish a standing account with CCC, then the following terms apply: Remit Payment to: Copyright Clearance Center, 29118 Network Place, Chicago, IL 60673-1291. Payments Due: Invoices are payable upon their delivery to you (or upon our notice to you that they are available to you for downloading). After 30 days, outstanding amounts will be subject to a service charge of 1-1/2% per month or, if less, the maximum rate allowed by applicable law. Unless otherwise specifically set forth in the Order Confirmation or in a separate written agreement signed by CCC, invoices are due and payable on "net 30" terms. While User may exercise the rights licensed immediately upon issuance of the Order Confirmation, the license is automatically revoked and is null and void, as if it had never been

issued, if complete payment for the license is not received on a timely basis either from User directly or through a payment agent, such as a credit card company.

3.3. Unless otherwise provided in the Order Confirmation, any grant of rights to User (i) is "one-time" (including the editions and product family specified in the license), (ii) is non-exclusive and non-transferable and (iii) is subject to any and all limitations and restrictions (such as, but not limited to, limitations on duration of use or circulation) included in the Order Confirmation or invoice and/or in these terms and conditions. Upon completion of the licensed use, User shall either secure a new permission for further use of the Work(s) or immediately cease any new use of the Work(s) and shall render inaccessible (such as by deleting or by removing or severing links or other locators) any further copies of the Work (except for copies printed on paper in accordance with this license and still in User's stock at the end of such period).

3.4. In the event that the material for which a republication license is sought includes third party materials (such as photographs, illustrations, graphs, inserts and similar materials) which are identified in such material as having been used by permission, User is responsible for identifying, and seeking separate licenses (under this Service or otherwise) for, any of such third party materials; without a separate license, such third party materials may not be used.

3.5. Use of proper copyright notice for a Work is required as a condition of any license granted under the Service. Unless otherwise provided in the Order Confirmation, a proper copyright notice will read substantially as follows: "Republished with permission of [Rightsholder's name], from [Work's title, author, volume, edition number and year of copyright]; permission conveyed through Copyright Clearance Center, Inc. " Such notice must be provided in a reasonably legible font size and must be placed either immediately adjacent to the Work as used (for example, as part of a by-line or footnote but not as a separate electronic link) or in the place where substantially all other credits or notices for the new work containing the republished Work are located. Failure to include the required notice results in loss to the Rightsholder and CCC, and the User shall be liable to pay liquidated damages for each such failure equal to twice the use fee specified in the Order Confirmation, in addition to the use fee itself and any other fees and charges specified.

3.6. User may only make alterations to the Work if and as expressly set forth in the Order Confirmation. No Work may be used in any way that is defamatory, violates the rights of third parties (including such third parties' rights of copyright, privacy, publicity, or other tangible or intangible property), or is otherwise illegal, sexually explicit or obscene. In addition, User may not conjoin a Work with any other material that may result in damage to the reputation of the Rightsholder. User agrees to inform CCC if it becomes aware of any infringement of any rights in a Work and to cooperate with any reasonable request of CCC or the Rightsholder in connection therewith.

4. Indemnity. User hereby indemnifies and agrees to defend the Rightsholder and CCC, and their respective employees and directors, against all claims, liability, damages, costs and expenses, including legal fees and expenses, arising out of any use of a Work beyond the scope of the rights granted herein, or any use of a Work which has been altered in any unauthorized way by User, including claims of defamation or infringement of rights of copyright, publicity, privacy or other tangible or intangible property.

5. Limitation of Liability. UNDER NO CIRCUMSTANCES WILL CCC OR THE RIGHTSHOLDER BE LIABLE FOR ANY DIRECT, INDIRECT, CONSEQUENTIAL OR INCIDENTAL DAMAGES (INCLUDING WITHOUT LIMITATION DAMAGES FOR LOSS OF BUSINESS PROFITS OR INFORMATION, OR FOR BUSINESS INTERRUPTION) ARISING OUT OF THE USE OR INABILITY TO USE A WORK, EVEN IF ONE OF THEM HAS BEEN ADVISED OF THE POSSIBILITY OF SUCH DAMAGES. In any event, the total liability of the Rightsholder and CCC (including their respective employees and directors) shall not exceed the total amount actually paid by User for this license. User assumes full liability for the actions and omissions of its principals, employees, agents, affiliates, successors and assigns.

6. Limited Warranties. THE WORK(S) AND RIGHT(S) ARE PROVIDED "AS IS". CCC HAS THE RIGHT TO GRANT TO USER THE RIGHTS GRANTED IN THE ORDER CONFIRMATION DOCUMENT. CCC AND THE RIGHTSHOLDER DISCLAIM ALL OTHER WARRANTIES RELATING TO THE WORK(S) AND RIGHT(S), EITHER EXPRESS OR IMPLIED, INCLUDING WITHOUT LIMITATION IMPLIED WARRANTIES OF MERCHANTABILITY OR FITNESS FOR A PARTICULAR PURPOSE. ADDITIONAL RIGHTS MAY BE REQUIRED TO USE ILLUSTRATIONS, GRAPHS, PHOTOGRAPHS, ABSTRACTS, INSERTS OR OTHER PORTIONS OF THE WORK (AS OPPOSED TO THE ENTIRE WORK) IN A MANNER CONTEMPLATED BY USER; USER UNDERSTANDS AND AGREES THAT NEITHER CCC NOR THE RIGHTSHOLDER MAY HAVE SUCH ADDITIONAL RIGHTS TO GRANT.

7. Effect of Breach. Any failure by User to pay any amount when due, or any use by User of a Work beyond the scope of the license set forth in the Order Confirmation and/or these terms and conditions, shall be a material breach of the license created by the Order Confirmation and these terms and conditions. Any breach not cured within 30 days of written notice thereof shall result in immediate termination of such license without further notice. Any unauthorized (but licensable) use of a Work that is terminated immediately upon notice thereof may be liquidated by payment of the Rightsholder's ordinary license price therefor; any unauthorized (and unlicensable) use that is not terminated immediately for any reason (including, for example, because materials containing the Work cannot reasonably be recalled) will be subject to all remedies available at law or in equity, but in no event to a payment of less than three times the Rightsholder's ordinary license price for the most closely analogous licensable use plus Rightsholder's and/or CCC's costs and expenses incurred in collecting such payment.

8. Miscellaneous.

    8.1. User acknowledges that CCC may, from time to time, make changes or additions to the Service or to these terms and conditions, and CCC reserves the right to send notice to the User by electronic mail or otherwise for the purposes of notifying User of such changes or additions; provided that any such changes or additions shall not apply to permissions already secured and paid for.

    8.2. Use of User-related information collected through the Service is governed by CCC's privacy policy, available online here:https://marketplace.copyright.com/rs-ui-web/mp/privacy-policy

    8.3. The licensing transaction described in the Order Confirmation is personal to User. Therefore, User may not assign or transfer to any other person (whether a natural person or an organization of any kind) the license created by the Order Confirmation and these terms and conditions or any rights granted hereunder; provided, however, that User may assign such license in its entirety on written notice to CCC in the event of a transfer of all or substantially all of User's rights in the new material which includes the Work(s) licensed under this Service.

    8.4. No amendment or waiver of any terms is binding unless set forth in writing and signed by the parties. The Rightsholder and CCC hereby object to any terms contained in any writing prepared by the User or its principals, employees, agents or affiliates and purporting to govern or otherwise relate to the licensing transaction described in the Order Confirmation, which terms are in any way inconsistent with any terms set forth in the Order Confirmation and/or in these terms and conditions or CCC's standard operating procedures, whether such writing is prepared prior to, simultaneously with or subsequent to the Order Confirmation, and whether such writing appears on a copy of the Order Confirmation or in a separate instrument.

    8.5. The licensing transaction described in the Order Confirmation document shall be governed by and construed under the law of the State of New York, USA, without regard to the principles thereof of conflicts of law. Any case, controversy, suit, action, or proceeding arising out of, in connection with, or related to such licensing transaction shall be brought, at CCC's sole discretion, in any federal or state court located in the County of New York, State of New York, USA, or in any federal or state court whose geographical jurisdiction covers the location of the Rightsholder set forth in the Order Confirmation. The parties expressly submit to the personal jurisdiction and venue of each such federal or state court.If you have any comments or questions about the Service or Copyright Clearance Center, please contact us at 978-750-8400 or send an e-mail to support@copyright.com.

v 1.1

BIBLIOGRAPHY

[1] I. del Portillo, B. G. Cameron, and E. F. Crawley. "A Technical Comparison of Three Low Earth Orbit Satellite Constellation Systems to Provide Global Broadband." In: *Acta Astronautica* 159 (2019), pp. 123–135. DOI: 10.1016/j.actaastro.2019.03.040.

[2] J. Yang, P. Gong, R. Fu, M. Zhang, J. Chen, S. Liang, B. Xu, J. Shi, and R. Dickinson. "The Role of Satellite Remote Sensing in Climate Change Studies." In: *Nature Climate Change* 3.10 (2013), pp. 875–883. DOI: 10.1038/nclimate1908.

[3] A. Tassa. "The Socio-Economic Value of Satellite Earth Observations: Huge, Yet to be Measured." In: *Journal of Economic Policy Reform* 23.1 (2020), pp. 34–48. DOI: 10.1080/17487870.2019.1601565.

[4] A. M. Hein, R. Matheson, and D. Fries. "A Techno-Economic Analysis of Asteroid Mining." In: *Acta Astronautica* 168 (2020), pp. 104–115. DOI: 10.1016/j.actaastro.2019.05.009.

[5] J. Griffin. "Background and Programmatic Approach for the Development of Orbital Fluid Resupply Tankers." In: *22nd Joint Propulsion Conference*. AIAA Paper 1986-1601, 1986. DOI: 10.2514/6.1986-1601.

[6] R. N. Eberhardt and W. Bailey. *Orbital Fluid Servicing and Resupply Operations*. Tech. rep. NASA-CR-180238, 1987.

[7] M. Tugnoli, M. Sarret, and M. Aliberti. "Business Perspectives for Micro Launchers." In: *European Access to Space: Business and Policy Perspectives on Micro Launchers*. Springer, 2019, pp. 29–66. DOI: 10.1007/978-3-319-78960-6_3.

[8] J. Wu and A. Giménez. "On the Maximization of the Science Output of Space Missions." In: *Space Science Reviews* 216.1 (2020), pp. 1–13. DOI: 10.1007/s11214-019-0628-4.

[9] V. S. Reddy. "The SpaceX Effect." In: *New Space* 6.2 (2018), pp. 125–134. DOI: 10.1089/space.2017.0032.

[10] D. M. Bushnell and R. W. Moses. *Commercial Space In The Age Of "New Space", Reusable Rockets and The Ongoing Tech Revolutions*. Tech. rep. NASA TM–2018-220118, 2018.

[11] M. Yoshida, T. Kimura, T. Hashimoto, S. Moriya, and S. Takada. "Overview of Research and Development Status of Reusable Rocket Engine." In: *Chemical Rocket Propulsion*. Springer, 2017, pp. 905–931. DOI: 10.1007/978-3-319-27748-6_38.

[12] C. Bonnal and M Caporicci. "Future Reusable Launch Vehicles in Europe: the FLTP (Future Launchers Technologies Programme)." In: *Acta Astronautica* 47.2 (2000), pp. 113–118. DOI: 10.1016/S0094-5765(00)00050-3.

[13] E. Musk. "Making Humans a Multi-Planetary Species." In: *New Space* 5.2 (2017), pp. 46–61. DOI: 10.1089/space.2017.29009.emu.

[14] O. J. Haidn. "Advanced Rocket Engines." In: *Advances on Propulsion Technology for High-Speed Aircraft* 1 (2008).

[15] K. Sakaki, H. Kakudo, S. Nakaya, M. Tsue, K. Suzuki, R. Kanai, T. Inagawa, and T. Hiraiwa. "Combustion Characteristics of Ethanol/Liquid-Oxygen Rocket-Engine Combustor with Planar Pintle Injector." In: *Journal of Propulsion and Power* 33.2 (2017), pp. 514–521. DOI: 10.2514/1.B36144.

[16] F. A. d. S. Mota, J. N. Hinckel, E. M. Rocco, and H. Schlingloff. "Modeling and Analysis of a LOX/Ethanol Liquid Rocket Engine." In: *Journal of Aerospace Technology and Management* 10 (2018). DOI: 10.5028/jatm.v10.914.

[17] E. W. Lemmon, I. H. Bell, M. L. Huber, and M. O. McLinden. *NIST Standard Reference Database 23: Reference Fluid Thermodynamic and Transport Properties-REFPROP, Version 10.0, National Institute of Standards and Technology*. 2018. DOI: 10.18434/T4JS3C. URL: https://www.nist.gov/srd/refprop.

[18] A. Urbano and F. Nasuti. "Parametric Analysis of Cooling Properties of Candidate Expander-Cycle Fuels." In: *Journal of Propulsion and Power* 30.1 (2014), pp. 153–163. DOI: 10.2514/1.B34852.

[19] K. Liang, B. Yang, and Z. Zhang. "Investigation of Heat Transfer and Coking Characteristics of Hydrocarbon Fuels." In: *Journal of Propulsion and Power* 14.5 (1998), pp. 789–796. DOI: 10.2514/2.5342.

[20] B. Younglove and J. F. Ely. "Thermophysical Properties of Fluids. II. Methane, Ethane, Propane, Isobutane, and Normal Butane." In: *Journal of Physical and Chemical Reference Data* 16.4 (1987), pp. 577–798. DOI: 10.1063/1.555785.

[21] R. Gross. *Combustion Performance and Heat Transfer Characterization of LOX/Hydrocarbon Type Propellants*. Tech. rep. NASA, 1980.

[22] R. Driscoll, T. Moore, B. B. Brady, S. Frolik, and J. H. Morehart. "Carbon Deposit Formation in Supercritical Methane-based, Hydrocarbon Fuels Using a Cooling Channel Surrogate." In: *AIAA Propulsion and Energy 2019 Forum*. AIAA Paper 2019-3939, 2019. DOI: 10.2514/6.2019-3939.

[23] R. C. Parsley and B. Zhang. "Thermodynamic Power Cycles for Pump-Fed Liquid Rocket Engines." In: *Liquid Rocket Thrust Chambers: Aspects of Modeling, Analysis, and Design*. Ed. by V Yang, M Habiballah, M Popp, and J Hulka. Reston, VA: AIAA, 2004. Chap. 18, pp. 621–648. DOI: 10.2514/4.866760.

[24] A. Urbano and F. Nasuti. "Onset of Heat Transfer Deterioration in Supercritical Methane Flow Channels." In: *Journal of Thermophysics and Heat Transfer* 27.2 (2013), pp. 298–308. DOI: 10.2514/1.T4001.

[25] D. Banuti. "Crossing the Widom-line–Supercritical pseudo-boiling." In: *The Journal of Supercritical Fluids* 98 (2015), pp. 12–16. DOI: 10.1016/j.supflu.2014.12.019.

[26] M. Pizzarelli, F. Nasuti, M. Onofri, P. Roncioni, R. Votta, and F. Battista. "Heat Transfer Modeling for Supercritical Methane Flowing in Rocket Engine Cooling Channels." In: *Applied Thermal Engineering* 75 (2015), pp. 600–607. DOI: 10.1016/j.applthermaleng.2014.10.008.

[27] J. Y. Yoo. "The Turbulent Flows of Supercritical Fluids with Heat Transfer." In: *Annual Review of Fluid Mechanics* 45 (2013), pp. 495–525. DOI: 10.1146/annurev-fluid-120710-101234.

[28] J. Jackson. "Fluid Flow and Convective Heat Transfer to Fluids at Supercritical Pressure." In: *Nuclear Engineering and Design* 264 (2013), pp. 24–40. DOI: 10.1016/j.nucengdes.2012.09.040.

[29] M. Pizzarelli. "The Status of the Research on the Heat Transfer Deterioration in Supercritical Fluids: A Review." In: *International Communications in Heat and Mass Transfer* 95 (2018), pp. 132–138. DOI: 10.1016/j.icheatmasstransfer.2018.04.006.

[30] J. Jackson, M. Cotton, and B. Axcell. "Studies of Mixed Convection in Vertical Tubes." In: *International Journal of Heat and Fluid Flow* 10.1 (1989), pp. 2–15. DOI: 10.1016/0142-727X(89)90049-0.

[31] J. Jackson, J. JD, and H. WB. "Influences of Buoyancy on Heat Transfer to Fluids Flowing in Vertical Tubes Under Turbulent Conditions." In: *Turbulent Forced Convection in Channels and Bundles* 2 (1979), pp. 613–640.

[32] I. L. Pioro and R. B. Duffey. "Experimental Heat Transfer in Supercritical Water Flowing Inside Channels (Survey)." In: *Nuclear Engineering and Design* 235.22 (2005), pp. 2407–2430. DOI: 10.1016/j.nucengdes.2005.05.034.

[33] R. B. Duffey and I. L. Pioro. "Experimental Heat Transfer of Supercritical Carbon Dioxide Flowing Inside Channels (Survey)." In: *Nuclear Engineering and Design* 235.8 (2005), pp. 913–924. DOI: 10.1016/j.nucengdes.2004.11.011.

[34] X. Cheng and X. Liu. "Research Status and Prospect of Supercritical Water-Cooled Reactor." In: *Atomic Energy Science and Technology* 42.2 (2008), pp. 167–172.

[35] Y. Ahn, S. J. Bae, M. Kim, S. K. Cho, S. Baik, J. I. Lee, and J. E. Cha. "Review of Supercritical CO2 Power Cycle Technology and Current Status of Research and Development." In: *Nuclear Engineering and Technology* 47.6 (2015), pp. 647–661. DOI: 10.1016/j.net.2015.06.009.

[36] J. Haemisch, D. Suslov, and M. Oschwald. "Experimental Study of Methane Heat Transfer Deterioration in a Subscale Combustion Chamber." In: *Journal of Propulsion and Power* 35.4 (2019), pp. 819–826. DOI: 10.2514/1.B37394.

[37] M. Pizzarelli, A. Urbano, and F. Nasuti. "Numerical Analysis of Deterioration in Heat Transfer to Near-Critical Rocket Propellants." In: *Numerical Heat Transfer, Part A: Applications* 57.5 (2010), pp. 297–314. DOI: 10.1080/10407780903583016.

[38] A. Urbano and F. Nasuti. "Parametric Analysis of Heat transfer to Supercritical-Pressure Methane." In: *Journal of Thermophysics and Heat Transfer* 26.3 (2012), pp. 450–463. DOI: 10.2514/1.T3840.

[39] D Haeseler, A Götz, and A Fröhlich. "Non-toxic Propellants for Future Advanced Launcher Propulsion Systems." In: *36th AIAA/ASME/SAE/ASEE Joint Propulsion Conference and Exhibit*. AIAA Paper 2000-3687, 2000. DOI: 10.2514/6.2000-3687.

[40] O. Haidn and M Habiballah. "Research on High Pressure Cryogenic Combustion." In: *Aerospace Science and Technology* 7.6 (2003), pp. 473–491. DOI: 10.1016/S1270-9638(03)00052-X.

[41] H. Vernin and P. Pempie. "LOx/CH4 and LOx/LH2 Heavy Launch Vehicle Comparison." In: *45th AIAA/ASME/SAE/ASEE Joint Propulsion Conference & Exhibit*. AIAA Paper-5133, 2009. DOI: 10.2514/6.2009-5133.

[42] T. Tsukano, N. Nagao, H. Tomaru, and T. Kuga. "Component Tests of a LOX/Methane Full-Expander Cycle Rocket Engine: Single-Shaft LOX/Methane Turbopump." In: *8TH European Conference for Aeronautics and Space Sciences (EUCASS)*. 2019. DOI: 10.13009/EUCASS2019-301.

[43] I. Klepikov, B. Katorgin, and V. Chvanov. "The New Generation of Rocket Engines, Operating by Ecologically Safe Propellant - Liquid Oxygen and Liquefied Natural Gas (Methane)." In: *Acta Astronautica* 41.4-10 (1997), pp. 209–217. DOI: 10.1016/S0094-5765(98)00076-9.

[44] P. Pempie, T. Froehlich, and H. Vernin. "LOx/Methane and LOx/Kerosene High Thrust Engine Trade-Off." In: *37th Joint Propulsion Conference and Exhibit*. AIAA Paper 2001-3542, 2001. DOI: 10.2514/6.2001-3542.

[45] H. Burkhardt, M. Sippel, A. Herbertz, and J. Klevanski. "Comparative Study of Kerosene and Methane Propellant Engines for Reusable Liquid Booster Stages." In: *4th International Conference on Launcher Technology - Space Launcher Liquid Propulsion*. 2002, pp. 3–6.

[46] H. Burkhardt, M. Sippel, A. Herbertz, and J. Klevanski. "Kerosene vs. Methane: a Propellant Tradeoff for Reusable Liquid Booster Stages." In: *Journal of Spacecraft and Rockets* 41.5 (2004), pp. 762–769. DOI: 10.2514/1.2672.

[47] G. Waxenegger, J. Riccius, E. Zametaev, J. Deeken, and J. Sand. "Implications of Cycle variants, Propellant Combinations and Operating Regimes on Fatigue Life Expectancies of Liquid Rocket Engines." In: *7th European Conference for Aeronautics and Space Sciences (EUCASS)*. 2017, pp. 3–6. DOI: 10.13009/EUCASS2017-609.

[48] W. Bouajila, J. Riccius, M. Bruchhausen, and B. Fischer. "A Prediction of Methodology for the High Cycle Fatigue Life of Hydrogen-Loaded Structures." In: *5th European Conference for Aeronautics and Space Sciences (EUCASS)*. 2013.

[49] R. E. Robinson and W. K. Meerbott. *Production of Kerosene Jet Fuels*. 1971.

[50] R. G. Miller and S. R. Sorrell. "The Future of Oil Supply." In: *Philosophical Transactions of the Royal Society A: Mathematical, Physical and Engineering Sciences* (2014). DOI: 10.1098/rsta.2013.0179.

[51] J. Benes, M. Chauvet, O. Kamenik, M. Kumhof, D. Laxton, S. Mursula, and J. Selody. "The Future of Oil: Geology Versus Technology." In: *International Journal of Forecasting* 31.1 (2015), pp. 207–221. DOI: 10.1016/j.ijforecast.2014.03.012.

[52] D. Marxer, P. Furler, J. Scheffe, H. Geerlings, C. Falter, V. Batteiger, A. Sizmann, and A. Steinfeld. "Demonstration of the Entire Production Chain to Renewable Kerosene via Solar Thermochemical Splitting of H2O and CO2." In: *Energy & Fuels* 29.5 (2015), pp. 3241–3250. DOI: 10.1021/acs.energyfuels.5b00351.

[53] M. Anand, S. A. Farooqui, R. Kumar, R. Joshi, R. Kumar, M. G. Sibi, H. Singh, and A. K. Sinha. "Optimizing Renewable Oil Hydrocracking Conditions for Aviation Bio-Kerosene Production." In: *Fuel Processing Technology* 151 (2016), pp. 50–58. DOI: 10.1016/j.fuproc.2016.05.028.

[54] A. Llamas, M.-J. García-Martínez, A.-M. Al-Lal, L. Canoira, and M. Lapuerta. "Biokerosene from Coconut and Palm Kernel Oils: Production and Properties of their Blends with Fossil Kerosene." In: *Fuel* 102 (2012), pp. 483–490. DOI: 10.1016/j.fuel.2012.06.108.

[55] N. Muradov and T. Veziroğlu. "From Hydrocarbon to Hydrogen–Carbon to Hydrogen Economy." In: *International Journal of Hydrogen Energy* 30.3 (2005), pp. 225–237. DOI: 10.1016/j.ijhydene.2004.03.033.

[56] J. Mason and K. Zweibel. "Centralized Production of Hydrogen using a Coupled Water Electrolyzer-Solar Photovoltaic System." In: *Solar Hydrogen Generation*. Springer, 2008, pp. 273–313. DOI: 10.1007\%2F978-0-387-72810-0_9.

[57] I. Dincer. "Green Methods for Hydrogen Production." In: *International Journal of Hydrogen Energy* 37.2 (2012), pp. 1954–1971. DOI: 10.1016/j.ijhydene.2011.03.173.

[58] J. A. Turner. "Sustainable Hydrogen Production." In: *Science* 305.5686 (2004), pp. 972–974. DOI: 10.1126/science.1103197.

[59] A. Züttel, A. Remhof, A. Borgschulte, and O. Friedrichs. "Hydrogen: The Future Energy Carrier." In: *Philosophical Transactions of the Royal Society A: Mathematical, Physical and Engineering Sciences* 368.1923 (2010), pp. 3329–3342. DOI: 10.1098/rsta.2010.0113.

[60] K. Taya, Y. Ishikawa, K Kimoto, and S Ishizaki. "Development and Test of the LOx/LNG Regenerative Cooled Rocket Engine (2nd report)." In: *29th International Symposium on Space Technology and Science*. 2013, pp. 2–9.

[61] J. Kopyscinski, T. J. Schildhauer, and S. M. Biollaz. "Production of Synthetic Natural Gas (SNG) from Coal and Dry Biomass–A Technology Review from 1950 to 2009." In: *Fuel* 89.8 (2010), pp. 1763–1783. DOI: 10.1016/j.fuel.2010.01.027.

[62] J. Gao, Y. Wang, Y. Ping, D. Hu, G. Xu, F. Gu, and F. Su. "A Thermodynamic Analysis of Methanation Reactions of Carbon Oxides for the Production of Synthetic Natural Gas." In: *RSC Advances* 2.6 (2012), pp. 2358–2368. DOI: 10.1039/C2RA00632D.

[63] M. Gassner and F. Maréchal. "Thermo-Economic Process Model for Thermochemical Production of Synthetic Natural Gas (SNG) from Lignocellulosic Biomass." In: *Biomass and Bioenergy* 33.11 (2009), pp. 1587–1604. DOI: 10.1016/j.biombioe.2009.08.004.

[64] W. Davis and M. Martín. "Optimal Year-Round Operation for Methane Production from CO2 and Water Using Wind Energy." In: *Energy* 69 (2014), pp. 497–505. DOI: 10.1016/j.energy.2014.03.043.

[65] A. Molino, F. Nanna, Y. Ding, B. Bikson, and G. Braccio. "Biomethane Production by Anaerobic Digestion of Organic Waste." In: *Fuel* 103 (2013), pp. 1003–1009. DOI: 10.1016/j.fuel.2012.07.070.

[66] U. USA Department of Defense. *MIL-PRF-32207: Performance Specification - Propellant, Methane*. 2006.

[67] P.-G. Han, S.-W. Lee, K.-H. Kim, and Y. Yoon. "Performance Analysis of the Thrust Chamber in Liquid Rocket Engine Using Liquefied Natural Gas as a Fuel." In: *40th AIAA/ASME/SAE/ASEE Joint Propulsion Conference and Exhibit*. AIAA Paper 2004-3860, 2004. DOI: 10.2514/6.2004-3860.

[68] A. Domashenko, A. Dovbish, R. Darbinyan, A. Lyapin, and V. Peredel'skii. "Analysis of Liquefied Methane Production Technology Depending on Methane Purity and Production Volume." In: *Chemical and Petroleum Engineering* 40.3-4 (2004), pp. 145–148. DOI: 10.1023/B:CAPE.0000033665.68451.1c.

[69] B. J. McBride, M. A. Reno, and S. Gordon. *CET93 and CETPC: An Interim Updated Version of the NASA Lewis Computer program for Calculating Complex Chemical Equilibria with Applications*. Tech. rep. NASA, 1994.

[70] K. Higashino, M. Sugioka, T. Kobayashi, R. Minato, Y. Sasayama, M. Otsuka, Y. Maru, T. Makino, and H. Sakaguchi. "Fundamental Study on Coking Characteristics of LNG Rocket Engines." In: *44th AIAA/ASME/SAE/ASEE Joint Propulsion Conference & Exhibit*. AIAA Paper 2008-4753, 2008. DOI: 10.2514/6.2008-4753.

[71] A. P. Showman. "A Whiff of Methane." In: *Nature* 452.7185 (2008), pp. 296–297. DOI: 10.1038/452296a.

[72] S. K. Atreya, E. Y. Adams, H. B. Niemann, J. E. Demick-Montelara, T. C. Owen, M. Fulchignoni, F. Ferri, and E. H. Wilson. "Titan's Methane Cycle." In: *Planetary and Space Science* 54.12 (2006), pp. 1177–1187. DOI: 10.1016/j.pss.2006.05.028.

[73] R. Ash, W. Dowler, and G Varsi. "Feasibility of Rocket Propellant Production on Mars." In: *Acta Astronautica* 5.9 (1978), pp. 705–724. DOI: 10.1016/0094-5765(78)90049-8.

[74] W. Li, H. Wang, Y. Shi, and N. Cai. "Performance and Methane Production Characteristics of H2O–CO2 Co-Electrolysis in Solid Oxide Electrolysis Cells." In: *International Journal of Hydrogen Energy* 38.25 (2013), pp. 11104–11109. DOI: 10.1016/j.ijhydene.2013.01.008.

[75] K. Sridhar, C. S. Iacomini, and J. E. Finn. "Combined H2O/CO2 Solid Oxide Electrolysis for Mars In Situ Resource Utilization." In: *Journal of Propulsion and Power* 20.5 (2004), pp. 892–901. DOI: 10.2514/1.3480.

[76] A. Muscatello and E. Santiago-Maldonado. "Mars In Situ Resource Utilization Technology Evaluation." In: *50th AIAA Aerospace Sciences Meeting Including the New Horizons Forum and Aerospace Exposition*. AIAA Paper 2012-360, 2012. DOI: 10.2514/6.2012-360.

[77] R. Zubrin, S. Price, L. Mason, and L. Clark. "An End-to-End Demonstration of a Full Scale Mars Sample Return In-Situ Propellant Production Unit." In: *31st Joint Propulsion Conference and Exhibit*. AIAA Paper 1995-2798, 1995. DOI: 10.2514/6.1995-2798.

[78] E. A. Hurlbert, H. Ueno, L. Alexander, M. D. Klem, E. Daversa, J.-M. Rualt, C. Manfletti, J.-N. Caruana, H. Asakawa, and R. J. Whitley. "International Space Exploration Coordination Group Assessment of Technology Gaps for LOX/Methane Propulsion Systems For the Global Exploration Roadmap." In: *AIAA SPACE 2016*. AIAA Paper 2016-5280, 2016. DOI: 10.2514/6.2016-5280.

[79] C. Bonhomme, M. Theron, E. Louaas, A. Beaurain, and E. Seleznev. "French–Russian Activities in the LOX/LCH4 Area." In: *57th IAF Congress, Valencia*. 2006.

[80] D. Preclik, G Hagemann, O Knab, L Brummer, C Mading, D Wiedmann, and P Vuillermoz. "LOX/Hydrocarbon Propellant Trade Considerations for Future Reusable Liquid Booster Engines." In: *41st AIAA/ASME/SAE/ASEE Joint Propulsion Conference & Exhibit*. AIAA Paper 2005-3567, 2005. DOI: 10.2514/6.2005-3567.

[81] R. Strunz, G. Hagemann, F. Grauer, L. Brummer, D. Preclik, E. Biojoux, X. Viot, G. Dantu, U. Staffilano, F. Cuoco, et al. "Main Stage Liquid Propulsion Acitivities within Europe's Future Launcher Preparatory Programme FLPP." In: *42nd AIAA/ASME/SAE/ASEE Joint Propulsion Conference & Exhibit*. AIAA Paper 2006-4698, 2006. DOI: 10.2514/6.2006-4698.

[82] A. Iannetti, N. Girard, N. Ravier, E. Edeline, and D. Tchou-Kien. "PROMETHEUS, a Low Cost LOX/CH4 Engine Prototype." In: *53rd AIAA/SAE/ASEE Joint Propulsion Conference*. AIAA Paper 2017-4750, 2017. DOI: 10.2514/6.2017-4750.

[83] P. Simontacchi, R. Blasi, E. Edeline, S. Sagnier, N. Ravier, A. Espinosa-Ramos, J. Breteau, and P. Altenhoefer. "Prometheus: Precursor of New Low-Cost Rocket Engine Family." In: *Proceedings of 8th European conference for Aeronautics and Space Sciences, EUCASS*. 2019. DOI: 10.13009/EUCASS2019-743.

[84] C. Génin and B. Vieille. "CNES/DLR Cooperation for the Preparation of Future Reusable Launcher Cryogenic Engines." In: *Proceedings of the 8th European Conference for Aeronautics and Space Sciences, EUCASS*. 2019. DOI: 10.13009/EUCASS2019-825.

[85] J. C. Deeken, M. Oschwald, and S. Schlechtriem. "LUMEN Demonstrator Project Overview." In: *32nd International Symposium on Space Technology and Science*. 2019.

[86] R. Hahn, G Waxenegger, J Deeken, M Oschwald, and S Schlechtriem. "Utilization of LOx/LCH4 for Expander-Bleed Cycle at Upper Stage Engine Application." In: *Proceedings of the 7th European Conference for Aeronautics and Space Sciences, EUCASS*. 2017. DOI: 10.13009/EUCASS2017-370.

[87] T. Traudta, R. dos Santos Hahna, H. Negishib, F. Lindemanna, S. Woidicha, B. Wagnera, D. Maiera, C. Madera, G. Waxenegger-Wilfinga, J. Deekena, et al. "Status of the Turbopump Development in the LUMEN Project." In: *69th International Astronautical Congress*. 2018, pp. 01–05.

[88] T. Traudt, R. H. Dos Santos Hahn, T. Mason, C. Mader, J. C. Deeken, M. Oschwald, and S Schlechtriem. "LUMEN Turbopump-Design and Manufacturing of the LUMEN LOX and LNG Turbopump Components." In: *32nd International Symposium on Space Technology and Science*. 2019.

[89] J. Hardi, J. C. Deeken, W. Armbruster, Y. Miene, J. Haemisch, J. Martin, D. Suslov, and M. Oschwald. "LUMEN Thrust Chamber-Injector Design and Stability Analysis." In: *32nd International Symposium on Space Technology and Science*. 2019.

[90] M. Börner, J. Hardi, D. Suslov, J. C. Deeken, and M. Oschwald. "LUMEN Thrust Chamber–Ignition Characteristics and Thrust Chamber Transients." In: *32nd International Symposium on Space Technology and Science*. 2019.

[91] G. Ordonneau, L. Vingert, N. Slavinskaya, J. Sender, D. Suslov, S. Soller, M Onofri, C Bruno, F Lentini, and M Valorani. "Oxygen/Methane Combustion Studies in In Space Propulsion Programme." In: *Proceedings of 4th European conference for Aeronautics and Space Sciences, EUCASS*. 2011.

[92] Y. Boué, P. Vinet, S. Magniant, T. Motomura, R. Blasi, and J.-P. Dutheil. "LOX/Methane Reusable Rocket Propulsion at Reach with Large Scale Demonstrators Tested." In: *Acta Astronautica* 152 (2018), pp. 542–556. DOI: 10.1016/j.actaastro.2018.06.018.

[93] S. Soller, C. Maeding, B. Kniesner, A. Preuss, N. Rackemann, and R. Blasi. "Characterisation of a LOX-LCH4 Gas Generator." In: *4th Space Propulsion Conference*. 2014.

[94] S. Soller, B. Kniesner, C. Maeding, R. Kaess, R. Behr, A. Dahlaus, and R Blasi. "Astrium's LOX/LCH4 Gas Generator Development Programme." In: *Proceedings of 5th European conference for Aeronautics and Space Sciences, EUCASS*. 2013.

[95] S Magniant, P Vinet, R Blasi, J.-P. Dutheil, and T. Motomura. "Airbus Defence and Space LOX/Methane Propulsion Demonstrator." In: *65th International Astronautical Congress*. 2014.

[96] R. Blasi and J Häberle. "LOX/Methane Thrust Chamber Demonstrator Testing." In: *5th Space Propulsion Conference*. 2016.

[97] M. Rudnykh, S. Carapellese, D. Liuzzi, L. Arione, G. Caggiano, P. Bellomi, E. D'Aversa, R. Pellegrini, S. Lobov, A. Gurtovoy, et al. "Development of LM10-MIRA LOX/LNG Expander Cycle Demonstrator Engine." In: *Acta Astronautica* 126 (2016), pp. 364–374. DOI: 10.1016/j.actaastro.2016.04.018.

[98] P Bellomi, M Rudnykh, S Carapellese, D Liuzzi, G Caggiano, L Arione, A. Gurtovoy, S. Lobov, V. Rachuk, E D'Aversa, et al. "Development of LM10-MIRA Liquid Oxygen–Liquid Natural Gas Expander Cycle Demonstrator Engine." In: *Progress in Propulsion Physics* 11 (2019), pp. 447–466. DOI: 10.1051/eucass/201911447.

[99] L Arione, N Ierardo, M Rudnykh, G Caggiano, S Lobov, A Shostak, A De Lillis, and E D'Aversa. "Development Status of the LM10-MIRA LOX-LNG Expander Cycle Engine for the LYRA Launch Vehicle." In: *2nd Space Propulsion Conference* (2010).

[100] V. Gorokhov, V. Rachuk, L. Grigorenko, and S. Kunavin. "CADB's Development of the LRE Operating with Liquefied Natural Gas and Liquid Oxygen." In: *Proceedings of the International Conference on Green Propellants for Space Propulsion*. 2001.

[101] A. Gurovoi, V. Kosmacheva, V. Rachuk, D. Scarpino, S. Carapellese, M. Biagioni, A. De Lillis, and E. D'Aversa. "Development of Thrust Chamber Assembly for LOX-LNG Expander Cycle Liquid-Propellant Rocket Engine." In: *Proceedings of the 5th European Conference for Aeronautics and Space Sciences, EUCASS*. 2013.

[102] H. Asakawa, H. Nanri, K. Aoki, I. Kubota, H. Mori, Y. Ishikawa, K. Kimoto, S. Ishihara, and S. Ishizaki. "The Status of the Research and Development of LNG Rocket Engines in Japan." In: *Chemical Rocket Propulsion*. Springer, 2017. Chap. 19, pp. 463–487. DOI: 10.1007/978-3-319-27748-6_19.

[103] I. Masuda. "JAXA's Current Activities for the Research of a LOX/LCH4 (LNG) Engine." In: *5th Space Propulsion Conference*. 2016.

[104] K. Taya, Y. Ishikawa, K. Kimoto, and S. Ishizaki. "Development Status of LOX/LCH4 Rocket Engine." In: *50th AIAA/ASME/SAE/ASEE Joint Propulsion Conference*. AIAA Paper 2014-3480, 2014. DOI: 10.2514/6.2014-3480.

[105] T. Kato, D. Terakado, H. Nanri, T. Morito, I. Masuda, H. Asakawa, H. Sakaguchi, Y. Ishikawa, T. Inoue, S. Ishihara, et al. "Subscale Firing Test for Regenerative Cooling LOX/Methane Rocket Engine." In: *Proceedings of 7th European conference for aeronatuics and space sciences, EUCASS*. 2017. DOI: 10.13009/EUCASS2017-381.

[106] S. Ukai, K. Sakaki, Y. Ishikawa, H. Sakaguchi, and S. Ishihara. "Development and Test of the LOx/LNG Regenerative Cooled Rocket Engine." In: *Proceedings of 8th European conference for aeronatuics and space sciences, EUCASS*. 2019. DOI: 10.13009/EUCASS2019-223.

[107] S. Hongming. "Review of Liquid Oxygen/Methane Rocket Engine." In: *Journal of Rocket Propulsion* 2 (2006).

[108] Z. Xiaoping, L. Chunhong, and M. Dongying. "Study on the LOX/Methane Rocket Engine Power Cycles." In: *Journal of Rocket Propulsion* 4 (2009).

[109] N. Zhang, W.-B. Wang, and J.-G. Sun. "Demonstration of a 600kN Class LOX/Methane Rocket Engine." In: *International Astronautical Congress*. 2012.

[110] J. Sun, Y Tian, L Danlin, and H. Liu. "An Experimental Study of LOX/Methane Subscale Injector." In: *International Astronautical Congress*. 2014.

[111] C.-H. Li, X.-P. Zhang, D.-Y. Ma, and H.-h. XU. "Ignition Scheme of LOX/Methane Gas Generator." In: *Journal of Rocket Propulsion* 5 (2010).

[112] D.-Y. Ma, G. Lu, X.-P. Zhang, and C.-H. Li. "Research on Hot Tests of LOX/Methane Gas Generator." In: *Journal of Rocket Propulsion* 39.3 (2013), pp. 21–26.

[113] H. Valler. *Design, Fabrication and Delivery of a High Pressure LOX-Methane Injector*. Tech. rep. NASA, 1979.

[114] A. Crocker and S. Peery. "System Sensitivity Studies of a LOX/Methane Expander Cycle Rocket Engine." In: *34th AIAA/ASME/SAE/ASEE Joint Propulsion Conference and Exhibit*. AIAA Paper 1998-3674, 1998. DOI: 10.2514/6.1998-3674.

[115] C. Brown. "Conceptual Investigations for a Methane-Fueled Expander Rocket Engine." In: *40th AIAA/ASME/SAE/ASEE Joint Propulsion Conference and Exhibit*. AIAA Paper 2004-4210, 2004. DOI: 10.2514/6.2004-4210.

[116] T. Neill, D. Judd, E. Veith, and D. Rousar. "Practical Uses of Liquid Methane in Rocket Engine Applications." In: *Acta Astronautica* 65.5-6 (2009), pp. 696–705. DOI: 10.1016/j.actaastro.2009.01.052.

[117] J. J. Hart and J. D. Mitchell. "Morpheus Lander Testing Campaign." In: *2012 IEEE Aerospace Conference*. IEEE. 2012, pp. 1–12. DOI: 10.1109/AERO.2012.6187304.

[118] J. B. Olansen. "Project Morpheus: Lander Technology Development." In: *AIAA SPACE 2014 Conference and Exposition*. AIAA Paper 2014-4314, 2014. DOI: 10.2514/6.2014-4314.

[119] R. Morehead. "Project Morpheus Main Engine Development and Preliminary Flight Testing." In: *47th AIAA/ASME/SAE/ASEE Joint Propulsion Conference & Exhibit*. AIAA Paper 2011-5927, 2011. DOI: 10.2514/6.2011-5927.

[120] J. C. Melcher and R. L. Morehead. "Combustion Stability Characteristics of the Project Morpheus Liquid Oxygen/Liquid Methane Main Engine." In: *50th AIAA/ASME/SAE/ASEE Joint Propulsion Conference*. AIAA Paper 2014-3681, 2014. DOI: 10.2514/6.2014-3681.

[121] M. Harris. "The Heavy Lift: Blue Origin's Next Rocket Engine Could Power Our Return to the Moon." In: *IEEE Spectrum* 56.7 (2019), pp. 26–30. DOI: 10.1109/MSPEC.2019.8747308.

[122] O Knab, H Riedmann, B Ivancic, C Höglauer, M Frey, and T Aichner. "Consequences of Modeling Demands on Numerical Rocket Thrust Chamber Flow Simulation Tools." In: *Progress in Propulsion Physics* 11 (2019), pp. 317–346. DOI: 10.1051/eucass/201911317.

[123] F. F. Winter, N. Perakis, and O. J. Haidn. "Emission Imaging and CFD Simulation of a Coaxial Single-Element GOX/GCH4 Rocket Combustor." In: *2018 Joint Propulsion Conference*. AIAA Paper 2018-4764, 2018. DOI: 10.2514/6.2018-4764.

[124] N. Perakis, D. Rahn, O. J. Haidn, and D. Eiringhaus. "Heat Transfer and Combustion Simulation of Seven-Element O2/CH4 Rocket Combustor." In: *Journal of Propulsion and Power* 35.6 (2019), pp. 1080–1097. DOI: 10.2514/1.B37402.

[125] S. Silvestri. "Investigation on Heat Transfer and Injector Design Criteria for Methane / Oxygen Rocket Combustion Chambers." PhD thesis. Technische Universität München, 2019.

[126] N. Perakis, L. Preis, and O. J. Haidn. "Wall Heat Flux Evaluation in Regeneratively Cooled Rocket Thrust Chambers." In: *Journal of Thermophysics and Heat Transfer* (2020), pp. 1–15. DOI: 10.2514/1.T6056.

[127] N. Adams, W. Schröder, R. Radespiel, O. Haidn, T. Sattelmayer, C. Stemmer, and B. Weigand. *Future Space-Transport-System Components under High Thermal and Mechanical Loads*. 1st ed. Vol. 1. 156. Basel: Springer International Publishing, 2021. ISBN: 978-3-030-53847-7. DOI: 10.1007/978-3-030-53847-7.

[128] O. J. Haidn, N. Adams, R. Radespiel, W. Schröder, C. Stemmer, T. Sattelmayer, and B. Weigand. "Fundamental Technologies for the Development of Future Space Transportsystem Components under high Thermal and Mechanical Loads." In: *2018 Joint Propulsion Conference*. AIAA Paper 2018-4466, 2018. DOI: 10.2514/6.2018-4466.

[129] S. Penner. "On the Development of Rational Scaling Procedures for Liquid-Fuel Rocket Engines." In: *Journal of Jet Propulsion* 27.2 (1957), pp. 156–161. DOI: 10.2514/8.12611.

[130] G. Nickerson et al. *JANNAF Rocket Engine Performance Prediction and Evaluation Manual*. Tech. rep. CPIA Publication, 1975.

[131] T. Fiala and T. Sattelmayer. "On the Use of OH* Radiation as a Marker for the Heat Release Rate in High-Pressure Hydrogen Liquid Rocket Combustion." In: *49th AIAA/ASME/SAE/ASEE Joint PropulsionConference*. AIAA Paper 2013-3780, 2013. DOI: 10.2514/6.2013-3780.

[132] J. J. Smith, G. Schneider, D. Suslov, M. Oschwald, and O. Haidn. "Steady-State High Pressure LOx/H2 Rocket Engine Combustion." In: *Aerospace Science and Technology* 11.1 (2007), pp. 39–47. DOI: 10.1016/j.ast.2006.08.007.

[133] N. Fdida, L. Vingert, Y. Mauriot, L.-H. Dorey, and M. Théron. "Comparison of LOX/Methane and LOX/Hydrogen Cryogenic Spray Combustion with Simultaneous Optical Diagnostics." In: *Proceedings of 8th European conference for Aeronautics and Space Sciences, EUCASS*. 2019. DOI: 10.13009/EUCASS2019-862.

[134] F. Winter, S. Silvestri, M. P. Celano, G. Schlieben, and O Haidn. "High-Speed and Emission Imaging of a Coaxial Single Element GOX/GCH4 Rocket Combustion Chamber." In: *Proceedings of 7th European conference for Aeronautics and Space Sciences, EUCASS*. 2017. DOI: 10.13009/EUCASS2017-340.

[135] J. Lux and O. Haidn. "Flame Stabilization in High-Pressure Liquid Oxygen/Methane Rocket Engine Combustion." In: *Journal of Propulsion and Power* 25.1 (2009), pp. 15–23. DOI: 10.2514/1.36852.

[136] J. Hardi, M. Oschwald, and B. Dally. "Flame Response to Acoustic Excitation in a Rectangular Rocket Combustor with LOx/H2 Propellants." In: *CEAS Space Journal* 2.1-4 (2011), pp. 41–49. DOI: 10.1007/s12567-011-0020-z.

[137] W. Armbruster, J. S. Hardi, D. Suslov, and M. Oschwald. "Injector-Driven Flame Dynamics in a High-Pressure Multi-Element Oxygen–Hydrogen Rocket Thrust Chamber." In: *Journal of Propulsion and Power* 35.3 (2019), pp. 632–644. DOI: 10.2514/1.B37406.

[138] G. E. Choi, Y. J. Moon, and C. Lee. "Combustion Dynamics in Postchamber of Hybrid Rocket Using CH* Radical Chemiluminescence Images." In: *Journal of Propulsion and Power* (2017), pp. 176–186. DOI: 10.2514/1.B35999.

[139] M. J. Bedard, T. L. Fuller, S. Sardeshmukh, and W. E. Anderson. "Chemiluminescence as a Diagnostic in Studying Combustion Instability in a Practical Combustor." In: *Combustion and Flame* 213 (2020), pp. 211–225. DOI: 10.1016/j.combustflame.2019.11.039.

[140] T. Fiala, T. Sattelmayer, S. Gröning, J. Hardi, R. Stützer, S. Webster, and M. Oschwald. "Comparison Between Excited Hydroxyl Radical and Blue Radiation from Hydrogen Rocket Combustion." In: *Journal of Propulsion and Power* 33.2 (2017), pp. 490–500. DOI: 10.2514/1.B36280.

[141] R. Snyder, G. Herding, J. C. Rolon, and S. Candel. "Analysis of Flame Patterns in Cryogenic Propellant Combustion." In: *Combustion Science and Technology* 124.1-6 (1997), pp. 331–370. DOI: 10.1080/00102209708935651.

[142] D. Salgues, A.-G. Mouis, S.-Y. Lee, D. Kalitan, S. Pal, and R. Santoro. "Shear and Swirl Coaxial Injector Studies of LOX/GCH4 Rocket Combustion Using Non-Intrusive Laser Diagnostics." In: *44th AIAA Aerospace Sciences Meeting and Exhibit*. AIAA Paper 2006-757, 2006. DOI: 10.2514/6.2006-757.

[143] U. Brummund, A. Cessou, and A. Vogel. "PLIF Imaging Measurements of a Co-Axial Rocket Injector Spray at Elevated Pressure." In: *Symposium (International) on Combustion*. Vol. 26. 1. Elsevier. 1996, pp. 1687–1695. DOI: 10.1016/S0082-0784(96)80393-6.

[144] R. Woodward, K. Miller, V. Bazarov, G. Guerin, S. Pal, and R. Santoro. "Injector Research for Shuttle OMS Upgrade Using LOX/Ethanol Propellants." In: *34th AIAA/ASME/SAE/ASEE Joint Propulsion Conference and Exhibit*. AIAA Paper 1998-3816, 1998. DOI: 10.2514/6.1998-3816.

[145] R. Woodward, S. Pal, S. Farhangi, G. Jensen, and R. Santoro. "LOX/GH2 Shear Coaxial Injector Atomization Studies: Effect of Recess and Non-Concentricity." In: *45th AIAA Aerospace Sciences Meeting and Exhibit*. AIAA Paper 2007-571, 2007. DOI: 10.2514/6.2007-571.

[146] C. Manfletti. "Laser Ignition of an Experimental Cryogenic Reaction and Control Thruster: Ignition Energies." In: *Journal of Propulsion and Power* 30.4 (2014), pp. 952–961. DOI: 10.2514/1.B35115.

[147] F. Ommi, K Nekofar, and E Movahednejad. "Designing and Experimental Investigation of Characteristics of a Double-Base Swirl Injector in a Liquid Rocket Propellant Engine." In: *Journal Applied Sciences Research* 5.8 (2009), pp. 955–968.

[148] M. Luo, Y. Wu, and O. J. Haidn. "Temperature and Size Measurements of Cryogenic Spray Droplets with Global Rainbow Refractometry." In: *Journal of Propulsion and Power* 35.2 (2019), pp. 359–368. DOI: 10.2514/1.B36750.

[149] F. Grisch, P. Bouchardy, and W. Clauss. "CARS Thermometry in High Pressure Rocket Combustors." In: *Aerospace Science and Technology* 7.4 (2003), pp. 317–330. DOI: 10.1016/S1270-9638(03)00017-8.

[150] F. Grisch, E. Bertseva, M. Habiballah, E. Jourdanneau, F. Chaussard, R. Saint-Loup, T. Gabard, and H. Berger. "CARS Spectroscopy of CH4 for Implication of Temperature Measurements in Supercritical LOX/CH4 Combustion." In: *Aerospace Science and Technology* 11.1 (2007), pp. 48–54. DOI: 10.1016/j.ast.2006.07.005.

[151] F. A. Bendana, D. D. Lee, S. A. Schumaker, S. A. Danczyk, and R. M. Spearrin. "Cross-Band Infrared Laser Absorption of Carbon Monoxide for Thermometry and Species Sensing in High-Pressure Rocket Flows." In: *Applied Physics B* 125.11 (2019), p. 204. DOI: 10.1007/s00340-019-7320-y.

[152] J.-M. Hartmann, H. Tran, R. Armante, C. Boulet, A. Campargue, F. Forget, L. Gianfrani, I. Gordon, S. Guerlet, M. Gustafsson, et al. "Recent Advances in Collisional Effects on Spectra of Molecular Gases and their Practical Consequences." In: *Journal of Quantitative Spectroscopy and Radiative Transfer* 213 (2018), pp. 178–227. DOI: 10.1016/j.jqsrt.2018.03.016.

[153] C. U. Kirchberger. "Investigation on Heat Transfer in Small Hydrocarbon Rocket Combustion Chambers." PhD thesis. Technische Universität München, 2014.

[154] D. R. Bartz. "A Simple Equation for Rapid Estimation of Rocket Nozzle Convective Heat Transfer Coefficients." In: *Jet Propulsion* 27.1 (1957), pp. 49–51. DOI: 10.2514/8.12572.

[155] D. Bartz. *Survey of the Relationship Between Theory and Experiment for Convective Heat Transfer from Rocket Combustion Gases*. Tech. rep. NASA, 1968.

[156] R. Schacht and R. Quentmeyer. *Axial and Circumferential Variations of Hot-Gas-Side Heat-Transfer Rates in a Hydrogen-Oxygen Rocket*. Tech. rep. NASA, 1971.

[157] G. Sinyarev and M. Dobrovolsky. *Liquid Rocket Engines-Theory and Design*. Moscow, USSR, 1955.

[158] P. Pempie. *Moteur Fusées à Ergols Liquides*. Tech. rep. CNES/DLA/AET/A 331/00, 2000.

[159] G. Schmidt. *Technik der Flüssigkeits-Raketentriebwerke*. Munich, Germany: Daimler Chrysler, 1999.

[160] M. H. Ostrander. "Emissivity Calculations for Carbon Monoxide." PhD thesis. California Institute of Technology, 1951.

[161] F. Goebel, B. Kniesner, M. Frey, O. Knab, and C. Mundt. "Radiative Heat Transfer Analysis in Modern Rocket Combustion Chambers." In: *CEAS Space Journal* 6.2 (2014), pp. 79–98. DOI: 10.1007/s12567-014-0060-2.

[162] M. Barrére, A. Jaumotte, B. F. De Veubeke, and J. Vandenkerchkhove. *Raketenantriebe*. Elsevier Publishing Company, 1961.

[163] A. Schack. *Der industrielle Wärmeübergang*. Verlag Stahleisen, 1969.

[164] D. Marty. *Conception des véhicules spatiaux*. Masson, 1986.

[165] T.-S. Wang. "Multidimensional Unstructured-Grid Liquid Rocket-Engine Nozzle Performance and Heat Transfer Analysis." In: *Journal of Propulsion and Power* 22.1 (2006), pp. 78–84. DOI: 10.2514/1.14699.

[166] T Badinand and T. H. Fransson. "Radiative Heat Transfer in Film-Cooled Liquid Rocket Engine Nozzles." In: *Journal of Thermophysics and Heat Transfer* 17.1 (2003), pp. 29–34. DOI: 10.2514/2.6748.

[167] W. Dalzell and A. Sarofim. "Optical Constants of Soot and their Application to Heat-Flux Calculations." In: *Journal of Heat Transfer* (1969). DOI: 10.1115/1.3580063.

[168] D. Byun and S. W. Baek. "Numerical Investigation of Combustion with Non-Gray Thermal Radiation and Soot Formation Effect in a Liquid Rocket Engine." In: *International Journal of Heat and Mass Transfer* 50.3-4 (2007), pp. 412–422. DOI: 10.1016/j.ijheatmasstransfer.2006.09.020.

[169] C. Dexter, M. Fisher, J. Hulka, K. Denisov, A. Shibanov, and A. Agarkov. "Scaling Techniques for Design, Development, and Test." In: *Liquid Rocket Thrust Chambers: Aspects of Modeling, Analysis, and Design*. Ed. by V Yang, M Habiballah, M Popp, and J Hulka. Reston, VA: AIAA, 2004. Chap. 16, pp. 553–600. DOI: 10.2514/4.866760.

[170] H Kraussold. "Die Wärmeübertragung an Flüssigkeiten in Rohren bei turbulenter Strömung." In: *Forschung auf dem Gebiet des Ingenieurwesens A* 4.1 (1933), pp. 39–44.

[171] W. H. Mcadams. *Heat Transmission: 3rd Ed*. McGraw-Hill, 1954.

[172] V. Gnielinski. "New Equations for Heat and Mass Transfer in Turbulent Pipe and Channel Flow." In: *International Chemical Engineering* 16.2 (1976), pp. 359–368.

[173] R. Roback, E. Szetela, and L. J. Spadaccini. *Deposit Formation in Hydrocarbon Rocket Fuels*. Tech. rep. NASA-TM-82911, 1981.

[174] R. W. Michel. *Combustion Performance and Heat Transfer Characterization of LOX/Hydrocarbon Type Propellants*. Tech. rep. NASA-CR-171712, 1983.

[175] F. Kirby. *Methane Heat Transfer Investigation*. Tech. rep. NASA-CR-171199, 1984.

[176] M. Pizzarelli, F. Nasuti, and M. Onofri. "Analysis of Curved-Cooling-Channel Flow and Heat Transfer in Rocket Engines." In: *Journal of Propulsion and Power* 27.5 (2011), pp. 1045–1053. DOI: 10.2514/1.B34163.

[177] M. Pizzarelli, F. Nasuti, R. Paciorri, and M. Onofri. "Numerical Analysis of Three-Dimensional Flow of Supercritical Fluid in Cooling Channels." In: *AIAA Journal* 47.11 (2009), pp. 2534–2543. DOI: 10.2514/1.38542.

[178] M. Pizzarelli, F. Nasuti, and M. Onofri. "Effect of Cooling Channel Aspect Ratio on Rocket Thermal behavior." In: *Journal of Thermophysics and Heat Transfer* 28.3 (2014), pp. 410–416. DOI: 10.2514/1.T4299.

[179] G. Dang, F. Zhong, Y. Zhang, and X. Zhang. "Numerical Study of Heat Transfer Deterioration of Turbulent Supercritical Kerosene Flow in Heated Circular Tube." In: *International Journal of Heat and Mass Transfer* 85 (2015), pp. 1003–1011. DOI: 10.1016/j.ijheatmasstransfer.2015.02.052.

[180] J. B. Calvo and K. Hannemann. "Analysis of the Heat Transfer in Liquid Rocket Engine Cooling Channels." In: *New Results in Numerical and Experimental Fluid Mechanics VII*. Springer, 2010, pp. 441–448. DOI: 10.1007/978-3-642-14243-7_54.

[181] L. Hernandez, R. Palacios, D. Ortega, J. Adams, L. I. Bugarin, M. M. Rahman, and A. R. Choudhuri. "The Effect of Surface Roughness on LCH4 Boiling Heat Transfer Performance of Conventionally and Additively Manufactured Rocket Engine Regenerative Cooling Channels." In: *AIAA Propulsion and Energy 2019 Forum*. AIAA Paper 2019-4363, 2019. DOI: 10.2514/6.2019-4363.

[182] G. Waxenegger-Wilfing, K. Dresia, J. C. Deeken, and M. Oschwald. "Heat Transfer Prediction for Methane in Regenerative Cooling Channels with Neural Networks." In: *Journal of Thermophysics and Heat Transfer* 34.2 (2020), pp. 347–357. DOI: 10.2514/1.T5865.

[183] A Fröhlich, M Popp, G Schmidt, and D Thelemann. "Heat Transfer Characteristics of H2/O2-Combustion Chambers." In: *29th Joint Propulsion Conference and Exhibit*. AIAA Paper 1993-1826, 1993. DOI: 10.2514/6.1993-1826.

[184] W. E. Welsh Jr and A. B. Witte. "A Comparison of Analytical and Experimental Local Heat Fluxes in Liquid-Propellant Rocket Thrust Chambers." In: *Journal of Heat Transfer* (1962). DOI: 10.1115/1.3684282.

[185] C. Kirchberger, G. Schlieben, and O. J. Haidn. "Investigation on Film Cooling in a GOX/Kerosene Rocket Combustion Chamber." In: *29th International Symposium on Space Technology and Science*. 2013.

[186] G. Schlieben, C. U. Kirchberger, O. J. Haidn, C. Höglauer, B. Kniesner, and O. Knab. "Experimental and Numerical Film Cooling Investigations in a GOX/Kerosene Rocket Combustion Chamber." In: *50th AIAA/ASME/SAE/ASEE Joint Propulsion Conference*. AIAA Paper 2014-4008, 2014. DOI: 10.2514/6.2014-4008.

[187] C. Höglauer, B. Kniesner, O. Knab, C. Kirchberger, G. Schlieben, and H.-P. Kau. "Simulation of a GOX–Kerosene Subscale Rocket Combustion Chamber." In: *CEAS Space Journal* 2.1-4 (2011), pp. 31–40. DOI: 10.1007/s12567-011-0017-7.

[188] P. A. Masters, E. S. Armstrong, and H. G. Price. *High-Pressure Calorimeter Chamber Tests for Liquid Oxygen/Kerosene (LOX/RP-1) Rocket Combustion*. Tech. rep. NASA, 1988.

[189] K. Ahn, J.-G. Kim, and H.-S. Choi. "Effects of Injector Recess on Heat Flux in a Combustion Chamber with Cooling Channels." In: *Aerospace Science and Technology* 37 (2014), pp. 110–116. DOI: 10.1016/j.ast.2014.05.012.

[190] D. Suslov, B Betti, T Aichner, S Soller, F Nasuti, and O Haidn. "Experimental Investigation and CFD-Simulation of the Film Cooling in an O2/CH4 Subscale Combustion Chamber." In: *3rd Space Propulsion Conference*. 2012.

[191] S. Silvestri, M. P. Celano, G. Schlieben, and O. J. Haidn. "Characterization of a Multi-Injector GOX/CH4 Combustion Chamber." In: *52nd AIAA/SAE/ASEE Joint Propulsion Conference*. AIAA Paper 2016-4992, 2016. DOI: 10.2514/6.2016-4992.

[192] S. Silvestri, C. Kirchberger, G. Schieben, M. P. Celano, and O. Haidn. "Experimental and Numerical Investigation of a Multi-Injector GOX-GCH4 Combustion Chamber." In: *Transactions of the Japan Society for Aeronautical and Space Sciences, Aerospace Technology Japan* 16.5 (2018), pp. 374–381. DOI: 10.2322/tastj.16.374.

[193] N. Perakis, O. J. Haidn, D. Eiringhaus, D. Rahn, S. Zhang, Y. Daimon, S. Karl, and T. Horchler. "Qualitative and Quantitative Comparison of RANS Simulation Results for a 7-Element GOX/GCH4 Rocket Combustor." In: *2018 Joint Propulsion Conference*. AIAA Paper 2018-4556, 2018. DOI: 10.2514/6.2018-4556.

[194] Y. Daimon, H. Negishi, S. Silvestri, and O. J. Haidn. "Conjugated Combustion and Heat Transfer Simulation for a 7 Element GOx/GCH4 Rocket Combustor." In: *2018 Joint Propulsion Conference*. AIAA Paper 2018-4553, 2018. DOI: 10.2514/6.2018-4553.

[195] J. Wei, M. Ye, S. Zhang, J. Qin, and O. J. Haidn. "Modeling of a 7-Elements GOX/GCH4 Combustion Chamber using RANS with Eddy-Dissipation Concept Model." In: *Aerospace Science and Technology* 99 (2020). DOI: 10.1016/j.ast.2020.105762.

[196] D. Preclik, D. Wiedmann, W. Oechslein, and J. Kretschmer. "Cryogenic Rocket Calorimeter Chamber Experiments and Heat Transfer Simulations." In: *34th AIAA/ASME/SAE/ASEE Joint Propulsion Conference and Exhibit*. AIAA 1998-3440, 1998. DOI: 10.2514/6.1998-3440.

[197] M. Masquelet, S. Menon, Y. Jin, and R. Friedrich. "Simulation of Unsteady Combustion in a LOX-GH2 Fueled Rocket Engine." In: *Aerospace Science and Technology* 13.8 (2009), pp. 466–474. DOI: 10.1016/j.ast.2009.07.005.

[198] D. Suslov, A. Woschnak, J. Sender, M. Oschwald, and O. Haidn. "Test Specimen Design and Measurement Technique for Investigation of Heat Transfer Processes in Cooling Channels of Rocket Engines under Real Thermal Conditions." In: *39th AIAA/ASME/SAE/ASEE Joint Propulsion Conference and Exhibit*. AIAA Paper 2003-4613, 2003. DOI: 10.2514/6.2003-4613.

[199] D. Suslov, A. Woschnak, D. Greuel, and M. Oschwald. "Measurement Techniques for Investigation of Heat Transfer Processes at European Research and Technology Test Facility P8." In: *Proceedings of 1st European conference for Aeronautics and Space Sciences, EUCASS*. 2005.

[200] R. Arnold, D. I. Suslov, and O. Haidn. "Film Cooling in a High-Pressure Subscale Combustion Chamber." In: *Journal of Propulsion and Power* 26.3 (2010), pp. 428–438. DOI: 10.2514/1.47148.

[201] R. Arnold, D. Suslov, and O. Haidn. "Circumferential Film Cooling Effectiveness in a LOX/H2 Subscale Combustion Chamber." In: *Journal of Propulsion and Power* 25.3 (2009), pp. 760–770. DOI: 10.2514/1.40305.

[202] J. Locke, S. Pal, and R. Woodward. "Chamber Wall Heat Flux Measurements for a LOx/CH4 Propellant Uni-element Rocket." In: *43rd AIAA/ASME/SAE/ASEE Joint Propulsion Conference & Exhibit*. AIAA Paper 2007-5547, 2007. DOI: 10.2514/6.2007-5547.

[203] L. Droppers, R. Schuff, and W. Anderson. "Study of Heat Transfer in a Gaseous Hydrogen Liquid Oxygen Multi-Element Combustor." In: *43rd AIAA/ASME/SAE/ASEE Joint Propulsion Conference & Exhibit*. AIAA Paper 2007-5550, 2007. DOI: 10.2514/6.2007-5550.

[204] J. T. Nakos. *Description of Heat Flux Measurement Methods used in Hydrocarbon and Propellant Fuel Fires at Sandia*. Tech. rep. Sandia National Laboratories Albuquerque, New Mexico, USA, 2010.

[205] M. Celano, S. Silvestri, J. Pauw, N. Perakis, F. Schily, D. Suslov, and O. J. Haidn. "Heat Flux Evaluation Methods for a Single Element Heat-Sink Chamber." In: *Proceedings of 6th European conference for Aeronautics and Space Sciences, EUCASS*. 2015.

[206] M. N. Ozisik. *Inverse Heat Transfer: Fundamentals and Applications*. Boca Raton, FL: CRC Press/Taylor & Francis, 2000.

[207] M Fernández-Torrijos, C Sobrino, J. Almendros-Ibáñez, C Marugán-Cruz, and D Santana. "Inverse Heat Problem of Determining Unknown Surface Heat Flux in a Molten Salt Loop." In: *International Journal of Heat and Mass Transfer* 139 (2019), pp. 503–516. DOI: 10.1016/j.ijheatmasstransfer.2019.05.002.

[208] L. Zhang, L. Li, H. Ju, and B. Zhu. "Inverse Identification of Interfacial Heat Transfer Coefficient between the Casting and Metal Mold Using Neural Network." In: *Energy Conversion and Management* 51.10 (2010), pp. 1898–1904. DOI: 10.1016/j.enconman.2010.02.020.

[209] C.-H. Huang and C.-T. Lee. "An Inverse Problem to Estimate Simultaneously Six Internal Heat Fluxes for a Square Combustion Chamber." In: *International Journal of Thermal Sciences* 88 (2015), pp. 59–76. DOI: 10.1016/j.ijthermalsci.2014.08.021.

[210] A. Dąbrowski and L. Dąbrowski. "Inverse Heat Transfer Problem Solution of Sounding Rocket Using Moving Window Optimization." In: *PloS one* 14.6 (2019). DOI: 10.1371/journal.pone.0218600.

[211] J. Luo and A. J. Shih. "Inverse Heat Transfer Solution of the Heat Flux Due to Induction Heating." In: *Journal of Manufacturing Science and Engineering* 127.3 (July 2004), pp. 555–563. ISSN: 1087-1357. DOI: 10.1115/1.1949617. eprint: https://asmedigitalcollection.asme.org/manufacturingscience/article-pdf/127/3/555/5608880/555_1.pdf.

[212] C.-H. Huang and Y.-L. Tsai. "A Transient 3-D Inverse Problem in Imaging the Time-Dependent Local Heat Transfer Coefficients for Plate Fin." In: *Applied Thermal Engineering* 25.14-15 (2005), pp. 2478–2495. DOI: 10.1016/j.applthermaleng.2004.12.003.

[213] N. Perakis, J. Strauß, and O. J. Haidn. "Heat Flux Evaluation in a Multi-Element CH4/O2 Rocket Combustor Using an Inverse Heat Transfer Method." In: *International Journal of Heat and Mass Transfer* 142 (2019), pp. 1–16. DOI: 10.1016/j.ijheatmasstransfer.2019.07.075.

[214] T. Wang, B. Sun, J. Xiang, and D. Liu. "Wall Heat Flux Measurements in a GO2/GH2 Heat-Sink Combustion Chamber." In: *Journal of Thermal Science and Technology* 13.1 (2018), pp. 1–17. DOI: 10.1299/jtst.2018jtst0016.

[215] S. K. Singh, M. K. Yadav, R. Sonawane, S. Khandekar, and K Muralidhar. "Estimation of Time-Dependent Wall Heat Flux from Single Thermocouple Data." In: *International Journal of Thermal Sciences* 115 (2017), pp. 1–15. DOI: 10.1016/j.ijthermalsci.2017.01.010.

[216] M. Raudenskỳ, K. A. Woodbury, J Kral, and T. Brezina. "Genetic Algorithm in Solution of Inverse Heat Conduction Problems." In: *Numerical Heat Transfer, Part B Fundamentals* 28.3 (1995), pp. 293–306. DOI: 10.1080/10407799508928835.

[217] S. Szénási and I. Felde. "Configuring Genetic Algorithm to Solve the Inverse Heat Conduction Problem." In: *2017 IEEE 15th International Symposium on Applied Machine Intelligence and Informatics (SAMI)*. IEEE. 2017, pp. 387–392. DOI: 10.1109/SAMI.2017.7880340.

[218] B. Yu, W. Yao, Q. Gao, H. Zhou, and C. Xu. "A Novel Non-Iterative Inverse Method for Estimating Boundary Condition of the Furnace Inner Wall." In: *International Communications in Heat and Mass Transfer* 87 (2017), pp. 91–97. DOI: 10.1016/j.icheatmasstransfer.2017.06.0170.

[219] B. Yu, C. Xu, W. Yao, and Z. Meng. "Estimation of Boundary Condition on the Furnace Inner Wall Based on Precise Integration BEM Without Iteration." In: *International Journal of Heat and Mass Transfer* 122 (2018), pp. 823–845. DOI: 10.1016/j.ijheatmasstransfer.2018.02.039.

[220] C. Nie and B. Yu. "Inversing Heat Flux Boundary Conditions Based on Precise Integration FEM Without Iteration and Estimation of Thermal Stress in FGMs." In: *International Journal of Thermal Sciences* 140 (2019), pp. 201–224. DOI: 10.1016/j.ijthermalsci.2019.03.003.

[221] D. Kuhl, O. Haidn, and A. Holzer. "Computational Solution of the Inverse Heat Conduction Problem of Rocket Combustion Chambers." In: *35th Joint Propulsion Conference and Exhibit*. AIAA Paper 1999-2913, 1999. DOI: 10.2514/6.1999-2913.

[222] D. Suslov, R Arnold, and O Haidn. "Investigation of Film Cooling Efficiency in a High Pressure Subscale LOX/H2 Combustion Chamber." In: *47th AIAA/ASME/SAE/ASEE Joint Propulsion Conference & Exhibit*. AIAA Paper 2011-5778, 2011. DOI: 10.2514/6.2011-5778.

[223] J Haemisch, D Suslov, and M Oschwald. "Experimental Analysis of Heat Transfer Processes in Cooling Channels of a Subscale Combustion Chamber at Real Thermal Conditions for Cryogenic Hydrogen and Methane." In: *6th Space Propulsion Conference*. 2018.

[224] M. P. Celano, S. Silvestri, C. Bauer, N. Perakis, G. Schlieben, and O. J. Haidn. "Comparison of Single and Multi-Injector GOX/CH4 Combustion Chambers." In: *52nd AIAA/SAE/ASEE Joint Propulsion Conference*. AIAA Paper 2016-4990, 2016. DOI: 10.2514/6.2016-4990.

[225] Y. Hong, Z. Liu, S. Silvestri, M. P. Celano, O. J. Haidn, and Z. Yu. "An Experimental and Modelling Study of Heat Loads on a Subscale Methane Rocket Motor." In: *Acta Astronautica* 164 (2019), pp. 112–120. DOI: 10.1016/j.actaastro.2019.07.011.

[226] C. Roth, O. J. Haidn, A. Chemnitz, T. Sattelmayer, Y. Daimon, G. Frank, M. Pfitzner, R. Keller, P. Gerlinger, H. Riedmann, et al. "Numerical Investigation of Flow and Combustion in a Single-Element GCH4/GOX Rocket Combustor: Chemistry Modeling and Turbulence-Combustion Interaction." In: AIAA Paper 2016-4995, 2016. DOI: 10.2514/6.2016-4995.

[227] D. Maestro, B. Cuenot, A. Chemnitz, T. Sattelmayer, C. Roth, O. J. Haidn, Y. Daimon, R. Keller, P. M. Gerlinger, G. Frank, et al. "Numerical Investigation of Flow and Combustion in a Single-Element GCH4/GOX Rocket Combustor: Chemistry Modeling and Turbulence-Combustion Interaction." In: *52nd AIAA/SAE/ASEE Joint Propulsion Conference*. AIAA Paper 2016-4996, 2016.

[228] D Maestro, B Cuenot, and L Selle. "Large Eddy Simulation of Combustion and Heat Transfer in a Single Element GCH4/GOx Rocket Combustor." In: *Flow, Turbulence and Combustion* 103.3 (2019), pp. 699–730. DOI: 10.1007/s10494-019-00036-w.

[229] J. Zips, C. Traxinger, and M. Pfitzner. "Time-Resolved Flow Field and Thermal Loads in a Single-Element GOx/GCH4 Rocket Combustor." In: *International Journal of Heat and Mass Transfer* 143 (2019). DOI: 10.1016/j.ijheatmasstransfer.2019.118474.

[230] M. Oschwald, D. Suslov, J. Haemisch, O. Haidn, M. P. Celano, C. Kirchberger, N. Rackemann, A. Preuss, and D. Wiedmann. "Measurement of Heat Transfer in Liquid Rocket Combustors." In: *High Pressure Flows for Propulsion Applications*. Ed. by J. Bellan. Reston, VA: AIAA, 2020. Chap. 7, pp. 281–332. DOI: 10.2514/4.105814.

[231] A. Woschnak, D. Suslov, and M. Oschwald. "Experimental and Numerical Investigation of Thermal Stratification Effects." In: *39th AIAA/ASME/SAE/ASEE Joint Propulsion Conference and Exhibit*. AIAA Paper 2003-4615, 2003. DOI: 10.2514/6.2003-4615.

[232] R. C. Hendricks, R. Friedman, and R. Graham. *Experimental Heat-Transfer Results for Cryogenic Hydrogen Flowing in Tubes at Subcritical and Supercritical Pressures to 800 Pounds per Square Inch Absolute*. Tech. rep. NASA, 1966.

[233] N. Perakis and O. J. Haidn. "Inverse Heat Transfer Method Applied to Capacitively Cooled Rocket Thrust Chambers." In: *International Journal of Heat and Mass Transfer* 131 (2019), pp. 150–166. DOI: 10.1016/j.ijheatmasstransfer.2018.11.048.

[234] K. Funazaki. "Studies on Wake-Affected Heat Transfer Around the Circular Leading Edge of Blunt Body." In: *Journal of Turbomachinery* 118.3 (1996), pp. 452–460. DOI: 10.1115/1.2836688.

[235] M. G. Dunn, H. L. Martin, and M. J. Stanek. "Heat-Flux and Pressure Measurements and Comparison With Prediction for a Low-Aspect-Ratio Turbine Stage." In: *Journal of Turbomachinery* 108.1 (1986), pp. 108–115. DOI: 10.1115/1.3262008.

[236] D. Holmberg and T. Diller. "High-Frequency Heat Flux Sensor Calibration and Modeling." In: *Journal of Fluid Engineering* 117 (1995). DOI: 10.1115/1.2817319.

[237] M. F. Taylor. *Correlation of Local Heat-Transfer Coefficients for Single-Phase Turbulent Flow of Hydrogen in Tubes with Temperature Ratios to 23*. National Aeronautics and Space Administration, 1968.

[238] M. Meyer. "Electrically Heated Tube Investigation of Cooling Channel Geometry Effects." In: *31st Joint Propulsion Conference and Exhibit*. AIAA Paper 1995-2500, 1995. DOI: 10.2514/6.1995-2500.

[239] D. Suslov. *Zum Einfluss periodisch instationärer Nachlaufströmungen auf das aerothermische Verhalten konvektiv gekühlter Gasturbinenschaufeln*. Logos-Verlag, 2002.

[240] D. Eiringhaus, H. Riedmann, O. Knab, and O. J. Haidn. "Full-Scale Virtual Thrust Chamber Demonstrators as Numerical Testbeds within SFB-TRR 40." In: *Joint Propulsion Conference*. AIAA Paper 2018-4469, 2018. DOI: 10.2514/6.2018-4469.

[241] T. Wang, B. Sun, D. Liu, and J. Xiang. "Experimental Investigation of Two-Dimensional Wall Thermal Loads in the Near-Injector Region of a Film-Cooled Combustion Chamber." In: *Applied Thermal Engineering* 138 (2018), pp. 913–923. DOI: 10.1016/j.applthermaleng.2018.03.108.

[242] L. Di, S. Bing, W. Taiping, S. Jiawen, and J. Zhang. "Thermo-Structural Analysis of Regenerative Cooling Thrust Chamber Cylinder Segment Based on Experimental Data." In: *Chinese Journal of Aeronautics* 33.1 (2020), pp. 102–115. DOI: 10.1016/j.cja.2019.09.023.

[243] D. Suslov, R. Arnold, and O. Haidn. "Investigation of Two Dimensional Thermal Loads in the Region near the Injector Head of a High Pressure Subscale Combustion Chamber." In: *47th AIAA Aerospace Sciences Meeting including The New Horizons Forum and Aerospace Exposition*. AIAA Paper 2009-450, 2009. DOI: 10.2514/6.2009-450.

[244] J. O. Hirschfelder, C. F. Curtiss, R. B. Bird, and M. G. Mayer. *Molecular Theory of Gases and Liquids*. Vol. 2. New York, NY: Wiley, 1964.

[245] J. Zips, H. Müller, and M. Pfitzner. "Efficient Thermo-Chemistry Tabulation for Non-Premixed Combustion at High-Pressure Conditions." In: *Flow, Turbulence and Combustion* 101.3 (2018), pp. 821–850. DOI: 10.1007/s10494-018-9932-4.

[246] J.-P. Hickey and M. Ihme. "Large Eddy Simulation of Supercritical Mixing and Combustion for Rocket Applications." In: *52nd Aerospace Sciences Meeting*. AIAA Paper 2014-0138, 2014. DOI: 10.2514/6.2014-0138.

[247] S. Fechter, T. Horchler, S. Karl, K. Hannemann, D. Suslov, J. Hardi, and M. Oschwald. "Efficient Handling of Cryogenic Equation of State for the Simulation of Rocket Combustion Chambers." In: *International Seminar on Non-Ideal Compressible-Fluid Dynamics for Propulsion & Power*. Springer. 2018, pp. 19–30. DOI: 10.1007/978-3-030-49626-5_2.

[248] B. E. Poling, J. M. Prausnitz, J. P. O'connell, et al. *The Properties of Gases and Liquids*. Vol. 5. New York: McGraw-Hill, 2001.

[249] J. Warnatz and N. Peters. *Numerical Methods in Flame Propagation*. Wiesbaden: Vieweg and Sohn, 1982.

[250] C. Wilke. "A Viscosity Equation for Gas Mixtures." In: *The Journal of Chemical Physics* 18.4 (1950), pp. 517–519. DOI: 10.1063/1.1747673.

[251] S. Mathur, P. Tondon, and S. Saxena. "Thermal Conductivity of Binary, Ternary and Quaternary Mixtures of Rare Gases." In: *Molecular Physics* 12.6 (1967), pp. 569–579. DOI: 10.1080/00268976700100731.

[252] A. N. Kolmogorov. "The Local Structure of Turbulence in Incompressible Viscous Fluid for Very Large Reynolds Numbers." In: *The Proceedings of the USSR Academy of Sciences* 30 (1941), pp. 301–305.

[253] F. G. Schmitt. "About Boussinesq's Turbulent Viscosity Hypothesis: Historical Remarks and a Direct Evaluation of its Validity." In: *Comptes Rendus Mécanique* 335.9-10 (2007), pp. 617–627. DOI: 10.1016/j.crme.2007.08.004.

[254] D. Leslie and G. Quarini. "The Application of Turbulence Theory to the Formulation of Subgrid Modelling Procedures." In: *Journal of Fluid Mechanics* 91.1 (1979), pp. 65–91. DOI: 10.1017/S0022112079000045.

[255] J. Ferziger. "Large Eddy Simulation: An Introduction and Perspective." In: *New Tools in Turbulence Modelling*. Springer, 1997, pp. 29–47.

[256] M Lesieur. "Recent Approaches in Large-Eddy Simulations of Turbulence." In: *New Tools in Turbulence Modelling*. Springer, 1997, pp. 1–28.

[257] U. Piomelli. "Large-Eddy Simulation: Achievements and Challenges." In: *Progress in Aerospace Sciences* 35.4 (1999), pp. 335–362. DOI: 10.1016/S0376-0421(98)00014-1.

[258] J. Smagorinsky. "General Circulation Experiments with the Primitive Equations: I. The Basic Experiment." In: *Monthly Weather Review* 91.3 (1963), pp. 99–164. DOI: 10.1175/1520-0493(1963)091<0099:GCEWTP>2.3.CO;2.

[259] K. Lilly. "The Representation of Small-Scale Turbulence in Numerical Simulation Experiments." In: *In Proceedings of the IBM Scientific Computing Symposium on Environmental Sciences* (1966).

[260] M. Germano, U. Piomelli, P. Moin, and W. H. Cabot. "A Dynamic Subgrid-Scale Eddy Viscosity Model." In: *Physics of Fluids A: Fluid Dynamics* 3.7 (1991), pp. 1760–1765. DOI: 10.1063/1.857955.

[261] T. Poinsot and D. Veynante. *Theoretical and Numerical Combustion*. RT Edwards, Inc., 2005.

[262] F. Ducros, F. Nicoud, and T. Poinsot. "Wall-Adapting Local Eddy-Viscosity Models for Simulations in Complex Geometries." In: *Numerical Methods for Fluid Dynamics VI* (1998), pp. 293–299.

[263] F. Nicoud, H. B. Toda, O. Cabrit, S. Bose, and J. Lee. "Using Singular Values to Build a Subgrid-Scale Model for Large Eddy Simulations." In: *Physics of fluids* 23.8 (2011). DOI: 10.1063/1.3623274.

[264] A. Vreman. "An Eddy-Viscosity Subgrid-Scale Model for Turbulent Shear Flow: Algebraic Theory and Applications." In: *Physics of Fluids* 16.10 (2004), pp. 3670–3681. DOI: 10.1063/1.1785131.

[265] A. Favre. "Statistical Equations of Turbulent Gases." In: *Problems of Hydrodynamics and Continuum Mechanics* (1969), pp. 231–266.

[266] L. Prandtl. "Investigations on Turbulent Flow." In: *Zeitschrift fur angewandte Mathematik und Mechanik* 5 (1925), p. 136.

[267] P. Spalart and S. Allmaras. "A One-Equation Turbulence Model for Aerodynamic Flows." In: *30th Aerospace Sciences Meeting and Exhibit*. AIAA Paper 1992-439, 1992. DOI: 10.2514/6.1992-439.

[268] B. E. Launder and D. B. Spalding. *Mathematical Models of Turbulence*. Academic press, London-New York, 1972.

[269] V. Yakhot and S. A. Orszag. "Renormalization Group Analysis of Turbulence. I. Basic heory." In: *Journal of Scientific Computing* 1.1 (1986), pp. 3–51. DOI: 10.1007\%252FBF01061452.

[270] W. Liou, A Shabbir, Z. Yang, and J Zhu. "A New Eddy Viscosity Model for High Reynolds Number Turbulent Flows." In: *Computers and Fluids* 24.3 (1995), pp. 227–238.

[271] D. C. Wilcox et al. *Turbulence Modeling for CFD*. Vol. 2. La Canada, CA: DCW Industries, 1998.

[272] F. R. Menter. "Two-Equation Eddy-Viscosity Turbulence Models for Engineering Applications." In: *AIAA Journal* 32.8 (1994), pp. 1598–1605. DOI: 10.2514/3.12149.

[273] M. Hallbäck, A. V. Johansson, and A. D. Burden. "The Basics of Turbulence Modelling." In: *Turbulence and Transition Modelling*. Springer, 1996, pp. 81–154.

[274] D. Veynante and L. Vervisch. "Turbulent Combustion Modeling." In: *Progress in Energy and Combustion Science* 28.3 (2002), pp. 193–266. DOI: 10.1016/S0360-1285(01)00017-X.

[275] M. Germano, A. Maffio, S. Sello, and G. Mariotti. "On the Extension of the Dynamic Modelling Procedure to Turbulent Reacting Flows." In: *Direct and Large-Eddy Simulation II*. Springer, 1997, pp. 291–300. DOI: 10.1007/978-94-011-5624-0.

[276] P. E. DesJardin and S. H. Frankel. "Large Eddy Simulation of a Nonpremixed Reacting Jet: Application and Assessment of Subgrid-Scale Combustion Models." In: *Physics of Fluids* 10.9 (1998), pp. 2298–2314. DOI: 10.1063/1.869749.

[277] B. F. Magnussen. "The Eddy Dissipation Concept: A Bridge Between Science and Technology." In: *ECCOMAS Thematic Conference on Computational Combustion*. Vol. 21. 2005, p. 24.

[278] L. Vervisch and D. Veynante. "Interlinks Between Approaches for Modeling Turbulent Flames." In: *Proceedings of the Combustion Institute* 28.1 (2000), pp. 175–183. DOI: 10.1016/S0082-0784(00)80209-X.

[279] S. B. Pope. "PDF Methods for Turbulent Reactive Flows." In: *Progress in Energy and Combustion Science* 11.2 (1985), pp. 119–192. DOI: 10.1016/0360-1285(85)90002-4.

[280] A. Y. Klimenko and R. W. Bilger. "Conditional Moment Closure for Turbulent Combustion." In: *Progress in Energy and Combustion Science* 25.6 (1999), pp. 595–687. DOI: 10.1016/S0360-1285(99)00006-4.

[281] R. Borghi. "On the Structure and Morphology of Turbulent Premixed Flames." In: *Recent Advances in the Aerospace Sciences*. Springer, 1985, pp. 117–138.

[282] B. Cuenot and T. Poinsot. "Effects of Curvature and Unsteadiness in Diffusion Flames. Implications for Turbulent Diffusion Combustion." In: *Symposium (International) on Combustion*. Vol. 25. 1. Elsevier. 1994, pp. 1383–1390. DOI: 10.1016/s0082-0784(06)80781-2.

[283] N. Peters. *Turbulent combustion*. 2001.

[284] H. Pitsch and N. Peters. "A Consistent Flamelet Formulation for Non-Premixed Combustion Considering Differential Diffusion Effects." In: *Combustion and Flame* 114.1-2 (1998), pp. 26–40. DOI: 10.1016/S0010-2180(97)00278-2.

[285] S.-K. Kim, S.-M. Kang, and Y.-M. Kim. "Flamelet Modeling for Combustion Processes and NOx Formation in the Turbulent Nonpremixed CO/H2/N2 Jet Flames." In: *Combustion Science and Technology* 168.1 (2001), pp. 47–83. DOI: 10.1080/00102200108907831.

[286] N. Peters. "Laminar Flamelet Concepts in Turbulent Combustion." In: *Symposium (International) on Combustion*. Vol. 21. 1. Elsevier. 1988, pp. 1231–1250. DOI: 10.1016/S0082-0784(88)80355-2.

[287] H. Pitsch, M Chen, and N. Peters. "Unsteady Flamelet Modeling of Turbulent Hydrogen-Air Diffusion Flames." In: *Symposium (International) on combustion*. Vol. 27. 1. Elsevier. 1998, pp. 1057–1064. DOI: 10.1016/S0082-0784(98)80506-7.

[288] E Effelsberg and N Peters. "Scalar Dissipation Rates in Turbulent Jets and Jet Diffusion Flames." In: *Symposium (International) on Combustion*. Vol. 22. 1. Elsevier. 1989, pp. 693–700. DOI: 10.1016/S0082-0784(89)80077-3.

[289] C. D Pierce and P. Moin. "Progress-Variable Approach for Large-Eddy Simulation of Non-Premixed Turbulent Combustion." In: *Journal of Fluid Mechanics* 504 (2004), p. 73. DOI: 10.1017/S0022112004008213.

[290] M. Ihme, L. Shunn, and J. Zhang. "Regularization of Reaction Progress Variable for Application to Flamelet-Based Combustion Models." In: *Journal of Computational Physics* 231.23 (2012), pp. 7715–7721. DOI: 10.1016/j.jcp.2012.06.029.

[291] B. Fiorina, R. Baron, O. Gicquel, D Thevenin, S. Carpentier, N. Darabiha, et al. "Modelling Non-adiabatic Partially Premixed Flames Using Flame-Prolongation of ILDM." In: *Combustion Theory and Modelling* 7.3 (2003), pp. 449–470. DOI: 10.1088/1364-7830/7/3/301.

[292] M. Ihme and H. Pitsch. "Prediction of Extinction and Reignition in Nonpremixed Turbulent Flames using a Flamelet/Progress Variable Model: 2. Application in LES of Sandia flames D and E." In: *Combustion and Flame* 155.1-2 (2008), pp. 90–107. DOI: 10.1016/j.combustflame.2008.04.015.

[293] B. Marracino and D. Lentini. "Radiation Modelling in Non-Luminous Nonpremixed Turbulent Flames." In: *Combustion Science and Technology* 128.1-6 (1997), pp. 23–48. DOI: 10.1080/00102209708935703.

[294] S. Chan, X. Pan, and M. Abou-Ellail. "Flamelet Structure of Radiating CH4-Air Flames." In: *Combustion and Flame* 102.4 (1995), pp. 438–446. DOI: 10.1016/0010-2180(95)00037-7.

[295] F. Proch and A. M. Kempf. "Modeling Heat Loss Effects in the Large Eddy Simulation of a Model Gas Turbine Combustor with Premixed Flamelet Generated Manifolds." In: *Proceedings of the Combustion Institute* 35.3 (2015), pp. 3337–3345. DOI: 10.1016/j.proci.2014.07.036.

[296] A. Kishimoto, H. Moriai, K. Takenaka, T. Nishiie, M. Adachi, A. Ogawara, and R. Kurose. "Application of a Nonadiabatic Flamelet/Progress-Variable Approach to Large-Eddy Simulation of H2/O2 Combustion Under a Pressurized Condition." In: *Journal of Heat Transfer* 139.12 (2017), p. 124501. DOI: 10.1115/1.4037099.

[297] D. Cecere, E. Giacomazzi, F. R. Picchia, N. Arcidiacono, F. Donato, and R. Verzicco. "A Non-Adiabatic Flamelet Progress–Variable Approach for LES of Turbulent Premixed Flames." In: *Flow, Turbulence and Combustion* 86.3 (2011), pp. 667–688. DOI: 10.1007/s10494-010-9319-7.

[298] N. Perakis, C. Roth, and O. J. Haidn. "Development of a Non-Adiabatic Flamelet Model for Reacting Flows with Heat Loss." In: *Space Propulsion Conference* (2018).

[299] D. Rahn, H. Riedmann, R. Behr, and O. J. Haidn. "Non-Adiabatic Flamelet Modeling for the Numerical Simulation of Methane Combustion in Rocket Thrust Chambers." In: *2018 Joint Propulsion Conference*. AIAA Paper 2018-4869, 2018. DOI: 10.2514/6.2018-4869.

[300] S.-K. Kim, M. Joh, H. S. Choi, and T. S. Park. "Multidisciplinary Simulation of a Regeneratively Cooled Thrust Chamber of Liquid Rocket Engine: Turbulent Combustion and Nozzle Flow." In: *International Journal of Heat and Mass Transfer* 70 (2014), pp. 1066–1077. DOI: 10.1016/j.ijheatmasstransfer.2013.10.046.

[301] G. Strang. "On the Construction and Comparison of Difference Schemes." In: *SIAM Journal on Numerical Analysis* 5.3 (1968), pp. 506–517. DOI: 10.1137/0705041.

[302] N. N. Yanenko. *The Method of Fractional Steps*. Springer, Berlin, Heidelberg, 1971.

[303] P. Breda, M. Pfitzner, N. Perakis, and O. Haidn. "Generation of Non-Adiabatic Flamelet Manifolds: Comparison of Two Approaches Applied on a Single-Element GCH4/GO2 Combustion Chamber." In: *8th European Conference for Aeronautics and Space Sciences (EUCASS)*. 2019. DOI: 10.13009/EUCASS2019-121.

[304] H. Wu and M. Ihme. "Modeling of Wall Heat Transfer and Flame/Wall Interaction a Flamelet Model With Heat-Loss Effects." In: *9th US National Combustion Meeting*. Central States Section of the Combustion Institute. 2015, pp. 17–20.

[305] P. C. Ma, H. Wu, M. Ihme, and J.-P. Hickey. "Nonadiabatic Flamelet Formulation for Predicting Wall Heat Transfer in Rocket Engines." In: *AIAA Journal* 56.6 (2018), pp. 2336–2349. DOI: 10.2514/1.J056539.

[306] J. Zips, C. Traxinger, P. Breda, and M. Pfitzner. "Assessment of Presumed/Transported Probability Density Function Methods for Rocket Combustion Simulations." In: *Journal of Propulsion and Power* 35.4 (2019), pp. 747–764. DOI: 10.2514/1.B37331.

[307] D. R. Chapman. "Computational Aerodynamics Development and Outlook." In: *AIAA Journal* 17.12 (1979), pp. 1293–1313. DOI: 10.2514/3.61311.

[308] U. Piomelli. "Wall-Layer Models for Large-Eddy Simulations." In: *Progress in Aerospace Sciences* 44.6 (2008), pp. 437–446. DOI: 10.1016/j.paerosci.2008.06.001.

[309] L. Potier. "Large Eddy Simulation of the combustion and heat transfer in sub-critical rocket engines." PhD thesis. 2018.

[310] U. Piomelli and E. Balaras. "Wall-Layer Models for Large-Eddy Simulations." In: *Annual Review of Fluid Mechanics* 34.1 (2002), pp. 349–374. DOI: 10.1146/annurev.fluid.34.082901.144919.

[311] P. R. Spalart. "Detached-Eddy Simulation." In: *Annual Review of Fluid Mechanics* 41 (2009), pp. 181–202. DOI: 10.1146/annurev.fluid.010908.165130.

[312] W. M. Kays, M. E. Crawford, and B. Weigand. *Convective Heat and Mass Transfer*. Tata McGraw-Hill Education, 2012.

[313] O. Cabrit. "Modélisation des flux pariétaux sur les tuyères des moteurs à propergol solide." PhD thesis. Montpellier 2, 2009.

[314] Z. Chen, A. Devesa, S. Hickel, C. Stemmer, and N. A. Adams. "A Wall Model Based on Simplified Thin Boundary Layer Equations for Implicit Large Eddy Simulation of Turbulent Channel Flow." In: *New Results in Numerical and Experimental Fluid Mechanics VII*. Springer, 2010, pp. 59–66. DOI: 10.1007/978-3-642-14243-7_8.

[315] W. Cabot and P. Moin. "Approximate Wall Boundary Conditions in the Large-Eddy Simulation of High Reynolds Number Flow." In: *Flow, Turbulence and Combustion* 63.1-4 (2000), pp. 269–291. DOI: 10.1023/A:1009958917113.

[316] S. Kawai and J. Larsson. "Dynamic Non-Equilibrium Wall-Modeling for Large Eddy Simulation at High Reynolds Numbers." In: *Physics of Fluids* 25.1 (2013), p. 015105. DOI: 10.1063/1.4775363.

[317] A. Devesa. "Modélisation de paroi pour la simulation d'écoulements instationnaires non-isothermes." PhD thesis. Montpellier 2, 2006.

[318] D. Muto, Y. Daimon, T. Shimizu, and H. Negishi. "An Equilibrium Wall Model for Reacting Turbulent Flows with Heat Transfer." In: *International Journal of Heat and Mass Transfer* 141 (2019), pp. 1187–1195. DOI: 10.1016/j.ijheatmasstransfer.2019.05.101.

[319] D. G. Goodwin, H. K. Moffat, and R. L. Speth. *Cantera: An Object-Oriented Software Toolkit for Chemical Kinetics, Thermodynamics, and Transport Processes, Version 2.2.1*. 2016. URL: http://www.cantera.org.

[320] P. Atkins, J. d. Paula, and J. Keeler. *Physical Chemistry*. New York, NY: WH Freeman and Company, 2014.

[321] B. Betti, D. Bianchi, F. Nasuti, and E. Martelli. "Chemical Reaction Effects on Heat Loads of CH4/O2 and H2/O2 Rockets." In: *AIAA Journal* 54.5 (2016), pp. 1693–1703. DOI: 10.2514/1.J054606.

[322] G. P. Smith, D. M. Golden, M. Frenklach, N. W. Moriarty, B. Eiteneer, M. Goldenberg, C. T. Bowman, R. K. Hanson, S. Song, W. C. Gardiner Jr, et al. *GRI 3.0 Mechanism*. 1999. URL: http://www.me.berkeley.edu/gri_mech.

[323] R. J. Kee, M. E. Coltrin, and P. Glarborg. *Chemically Reacting flow: Theory and Practice*. Hoboken, NJ: John Wiley & Sons, 2005.

[324] P. Popp and M. Baum. "Analysis of Wall Heat Fluxes, Reaction Mechanisms, and Unburnt Hydrocarbons During the Head-on Quenching of a Laminar Methane Flame." In: *Combustion and Flame* 108.3 (1997), pp. 327–348. DOI: 10.1016/S0010-2180(96)00144-7.

[325] J. Song and B. Sun. "Coupled Numerical Simulation of Combustion and Regenerative Cooling in LOX/Methane Rocket Engines." In: *Applied Thermal Engineering* 106 (2016), pp. 762–773. DOI: 10.1016/j.actaastro.2016.12.026.

[326] H. Negishi, A. Kumakawa, N. Yamanishi, and A. Kurosu. "Heat Transfer Simulations in Liquid Rocket Engine Subscale Thrust Chambers." In: *44th AIAA/ASME/SAE/ASEE Joint Propulsion Conference & Exhibit*. AIAA Paper 2008-5241, 2008. DOI: 10.2514/6.2008-5241.

[327] N. Perakis. "Flamelet Modeling and Simulation of CH4/O2 Rocket Thrust Chambers." MA thesis. Garching, Germany: Technical University of Munich, 2016.

[328] U. Rana. "Validation of Kinetic Model of Methane Oxidation at High Pressures." MA thesis. Garching, Germany: Technical University of Munich, 2017.

[329] V. Zhukov, V. Sechenov, and A. Y. Starikovskii. "Autoignition of a Lean Propane-Air Mixture at High Pressures." In: *Kinetics and Catalysis* 46.3 (2005), pp. 319–327. DOI: 10.1007/s10975-005-0079-7.